Fabrication of Graphene-based Electrodes for Electrochemical Energy Storage Devices

by

Gillian Hawes

A thesis

presented to the University of Waterloo

in fulfillment of the

thesis requirement for the degree of

Doctor of Philosophy

in

Chemical Engineering (Nanotechnology)

Waterloo, Ontario, Canada, 2023

Examining Committee Membership

The following served on the Examining Committee for this thesis. The decision of the Examining Committee is by majority vote.

External Examiner:	Prof. Dominik Barz Associate Professor Department of Chemical Engineering, Queen's University
Supervisor:	Prof. Michael Pope Associate Professor Department of Chemical Engineering, University of Waterloo
Internal Member:	Prof. Milad Kamkar Assistant Professor Department of Chemical Engineering, University of Waterloo
Internal Member:	Prof. Mark Pritzker Adjunct Professor Emeritus Department of Chemical Engineering, University of Waterloo
Internal-External Member:	Prof. Rodney Smith Associate Professor Department of Chemistry, University of Waterloo

Author's Declaration

This thesis consists of material all of which I authored or co-authored: see Statement of Contributions included in the thesis. This is a true copy of the thesis, including any required final revisions, as accepted by my examiners.

I understand that my thesis may be made electronically available to the public.

Statement of Contributions

The body of this thesis is based upon a combination of published and unpublished works.

Parts of **Chapter 2** are adapted with permission from: **Hawes, G. F.**; Rehman, S.; Rangom, Y.; Pope, M.A. Advanced Manufacturing Approaches for Electrochemical Energy Storage Devices. *International Materials Reviews.* **2022**, *68* (3), 323–364. DOI: 10.1080/09506608.2022.2086388. Copyright 2022 Taylor & Francis.

I am the first author of this review paper, and was responsible for the literature review, analysis, and writing of all drafts. Dr. Sarish Rehman assisted in the literature review for the 3D printing section and Dr. Yverick Rangom assisted in the literature review and writing for the traditional manufacturing approach section. Dr. Michael Pope reviewed and edited the manuscript.

Chapter 3 is adapted with permission from: **Hawes, G. F.**; Yilman, D.; Noremberg, B. S.; Pope, M. A. Supercapacitors Fabricated via Laser-Induced Carbonization of Biomass-Derived Poly(furfuryl alcohol)/Graphene Oxide Composites. *ACS Applied Nano Materials.* **2019**, *2* (10), 6312–6324. DOI: 10.1021/acsanm.9b01284. Copyright 2019 American Chemical Society.

I am the first author of this paper, and was responsible for all experiment planning, methodology, data collection and analysis, and draft writing and editing. Dilara Yilman and Dr. Bruno Noremberg assisted in performing initial experiments. Dr. Michael Pope assisted in supervision, experiment planning, and reviewing and editing the manuscript.

Chapter 4 is adapted with permission from: **Hawes, G. F.**; Verma, P.; Uceda, M.; Karimi, G.; Noremberg, B. S.; Pope, M. A. Salt-Induced Doping and Templating of Laser-Induced Graphene Supercapacitors. *ACS Appl. Mater. Interfaces.* **2023**, *15* (8) 10570–10584. DOI: 10.1021/acsami.2c17476. Copyright 2023 American Chemical Society.

I am the first author of this paper, and was responsible for all experiment planning, methodology, data collection and analysis, and draft writing and editing. Priyanka Verma assisted in carrying out experiments under my direction. Dr. Marianna Uceda assisted with XRD analysis, and assisted in experiment planning and reviewing and editing the manuscript. Dr. Gholamreza Karimi assisted with the computational modelling. Dr. Bruno Noremberg assisted in carrying out initial experiments. Dr. Michael Pope assisted in supervision, experiment planning, and reviewing and editing the manuscript. A patent for this work has also been filed.

Chapter 5 is adapted from: **Hawes, G. F.**; Alidina, A.; Pope, M. A. Investigation of Lithium Nucleation on Laser-Induced Graphene as Lithium Metal Anode Host. Manuscript in preparation.

I am the first author of this work, and was responsible for all experiment planning, methodology, data collection and analysis, and draft writing and editing. Alina Alidina assisted in carrying out experiments under my direction. Dr. Michael Pope assisted in supervision, experiment planning, and reviewing and editing the manuscript.

Chapter 6 is adapted with permission from: **Hawes, G.F.**; Punckt, C.; Pope, M. A. Probing Sulfur Deposition onto Carbon Nanomaterials from Aqueous, Elemental Sulfur Sols for Lithium-Sulfur Batteries. *ACS Appl. Mater. Interfaces.* **2021**, *13* (27) 31569–31582. DOI: 10.1021/acsami.1c04484. Copyright 2021 American Chemical Society.

I am the first author of this paper, and was responsible for all experiment planning, methodology, data collection and analysis, and draft writing and editing. Dr. Christian Punckt and Dr. Michael Pope assisted in supervision, experiment planning, and reviewing and editing the manuscript.

Other published works beyond the scope of this thesis:

Hawes, G. F.; Rehman, S.; Pope, M. A. Rapid prototyping of electrochemical energy storage devices based on two dimensional materials. *Current Opinion in Electrochemistry.* **2020**, *20* 36–45. DOI: 10.1016/j.coelec.2020.02.006

Abstract

Amid a global climate crisis, the urgent transition to net zero carbon emissions necessitates the development of improved electrochemical energy storage (EES) devices, such as batteries and supercapacitors. One of the most promising next-generation battery chemistries is lithium-sulfur, which possesses a theoretical energy density an order of magnitude higher than today's widely used lithium-ion batteries. However, the effectively infinite volume change and unstable solid electrolyte interphase of the lithium anode along with the insulating nature of the sulfur cathode material remain critical challenges that limit the cycle life and energy density of current cells. Simultaneously, applications in regenerative braking, grid stabilization, and consumer electronics require devices with higher power densities and longer cycle life, which could be addressed via the use of supercapacitors, but the energy density of these devices requires improvement.

Graphene-based materials possess high specific surface areas and conductivities, as well as tunable morphologies, pore structures, and surface chemistries, making them particularly suited for EES electrode applications. However, processing of graphene-based electrodes introduces many challenges, including aggregation of graphene in the solid state, which limits the accessible surface area, and the frequent use of toxic solvents in solution-based processing. As such, this thesis focuses on the development of graphene-based electrodes for both supercapacitors and next-generation batteries via novel processing methods with the potential for improving sustainability.

In the first part of this thesis, we explore the fabrication of graphene-based electrodes via the laser-induced graphenization of polymer precursors, known as laser-induced graphene (LIG). This process enables the rapid production of porous, defective graphene active material as well as the patterning of advanced architectures. While LIG formation has previously been demonstrated on a range of materials, the areal capacitance of most devices has been limited, with high-performing devices nearly exclusively prepared from costly, petroleum-derived polyimide (PI, Kapton^{TM}, ~4-9 mF/cm^2). As such, we first study and introduce a new, easily processable, biomass-derived LIG precursor, poly(furfuryl alcohol) (PFA). We further study the implementation of additives into the PFA precursor to improve its surface area and capacitance. We demonstrate that supercapacitors prepared from composites of PFA microspheres and graphene oxide exhibit areal capacitances as high as 16.0 mF/cm^2 at 0.05 mA/cm^2, outperforming both GO and PI-based LIG supercapacitors reported to date. Following this work, we demonstrate that salt microparticle additives act as a template during LIG formation, resulting in BET

surface areas that are an order of magnitude higher than LIG from pristine PFA, while simultaneously doping the LIG with different heteroatoms depending on the salt. As such, the multifunctional nature of these salts results in capacitances up to ~25 mF/cm^2 at 0.05 mA/cm^2, 2-4 orders of magnitude above that of LIG from pristine PFA, and among the highest capacitances reported for LIG to date.

Following the optimization of the LIG material, we study its implementation as a porous, 3D host for lithium metal anodes. While host structures are a common strategy to address the lithium volume change, little fundamental study has been reported to date on their rational design, with one of the guiding principles in literature thus far being that heteroatom doping of carbon hosts can improve lithium nucleation. As such, we study the nucleation of lithium metal on different LIG materials for the first time. We demonstrate that doping of the LIG with lithiophilic functional groups enables lower overpotentials for lithium nucleation, but also that doped samples exhibit shorter cycle life, indicating that careful optimization of the degree of doping is critical for lithium host design.

Finally, we develop a novel processing strategy to utilize graphene as a conductive scaffold for sulfur cathodes. Most fabrication methods for carbon/sulfur composites employ dry carbon powders, and are impractical for materials such as graphene, which are highly aggregated in solid powder form. Moreover, solution-based approaches typically use toxic organic solvents or costly electrochemically-inactive sulfur precursors. We demonstrate that high performance sulfur cathodes can be prepared via the nucleation and growth of sulfur on graphene from thus far relatively unexplored hydrophobic sulfur sols. Cathodes exhibit capacities as high as 1300 mAh/g_{sulfur} (~4.8 mAh/cm^2) and energy densities as high as 468 Wh/kg at 0.1C, demonstrating that this method can serve as a simple, scalable, aqueous-based route for the fabrication of high energy density cathodes.

Acknowledgements

First and foremost, I want to thank my supervisor, Dr. Michael Pope. Your guidance, support, enthusiasm for research, unfailing optimism, and belief in me have been invaluable for the last six years, and I am tremendously grateful that I had this opportunity to learn from you. I have grown so much as a researcher and person from your mentorship, and I will take what I have learned here with me wherever I go.

I want to thank all of my committee members – Dr. Mark Pritzker, Dr. Milad Kamkar, Dr. Rodney Smith, and Dr. Dominik Barz – for taking the time to read my thesis and provide their valuable feedback. I want to particularly thank Dr. Pritzker for serving on my committee and attending my defence even after his retirement. I also want to specifically thank Dr. Kamkar for stepping in as a replacement committee member on short notice when my previous committee member was unavailable.

I also want to thank Dr. Juewen Liu, Dr. Eric Prouzet, and Dr. Neil McManus for the use of their lab facilities. Thank you to Judy Caron and Chris Kleven for their help on many occasions throughout my PhD.

The work presented in this thesis would not be possible without the many wonderful collaborators I have had the privilege of working with in the last several years. Thank you to Dr. Christian Punckt for his insight and thoughtful discussions on the sulfur cathode work. Thank you to my co-op students Priyanka Verma and Alina Alidina for their experimental LIG work – it was a joy to mentor you both. Thank you to Dr. Marianna Uceda, Dilara Yilman Lenos, and Dr. Bruno Noremberg for their contributions to the LIG work as well. I would also like to thank Dr. Reza Karimi for his help with the thermal modeling and Dr. Yverick Rangom and Dr. Sarish Rehman for their assistance with drafting of the review paper which is partially implemented in the literature review of this thesis.

One of the highlights of my PhD has been the opportunity to work with so many talented, hardworking, and wonderful people. I want to thank the entire Pope group, past and present, for being so welcoming, kind, and supportive, and for making the lab such a fun place to be that we all hung out in QNC even when the lab work was done. Thank you especially to Mariam, Tahani, Sima, Manila, Irene, Mursal, and Azam for your friendship and moral support. I want to particularly thank Amanda, for your fierce dedication to making the lab the best it can be and for being at my side from the first to last day of this degree, through every up and down. I also want to specifically thank Marianna for

spending days on the floor fixing the laser with me, providing constant support, and cheering me on through every challenge. I want to thank the WatECS team, past and present, for their passion for electrochemistry and for giving me the opportunity to connect with so many excellent scientists and engineers.

I would not have made it through this degree or the last several years without the encouragement of my friends and family. I want to thank my friends, particularly Hayley and Kristen, for their endless patience, support, and belief in me over the last several years. Finally, I want to thank my family – my brother Andrew, and my parents Kathryn and Robert. Your love and support are the foundation that enables me to pursue my dreams and believe that I am capable of anything. I would not be where I am today without your sacrifices, support, and faith in me. I also want to thank Lily for brightening every day of this experience. Last but certainly not least, I want to thank my partner, Nick. Thank you for being my anchor, confidant, sounding board, support system, and best friend through this entire journey, and for making me laugh every single day for the last nine years. I love you.

Dedication

Dedicated to my family –

to my parents and to Nick, for their patience, support, and unconditional love.

Table of Contents

List of Figures

List of Tables

List of Abbreviations

AFM	Atomic force microscopy
ATR-FTIR	Attenuated total reflectance Fourier-transform infrared spectroscopy
BET	Brunauer-Emmett-Teller surface area analysis
CV	Cyclic voltammetry
DLS	Dynamic light scattering
EDS	Energy-dispersive x-ray spectroscopy
FA	Furfuryl alcohol
FTIR	Fourier-transform infrared spectroscopy
GCD	Galvanostatic charge and discharge
GO	Graphene oxide
HAADF	High-angle annular dark-field
HOPG	Highly oriented pyrolytic graphite
HR-TEM	High-resolution transmission electron microscopy
KB	Ketjen black
LIG	Laser-induced graphene
OM	Optical microscopy
PEI	Polyethylenimine
PFA	Poly(furfuryl alcohol)
PI	Polyimide
rGO	Reduced graphene oxide
SAED	Selected area electron diffraction
SEM	Scanning electron microscopy
TEM	Transmission electron microscopy
TGA	Thermogravimetric analysis
XPS	X-ray photoelectron spectroscopy
XRD	X-ray diffraction

Chapter 1:
Introduction

The sixth assessment report from the Intergovernmental Panel on Climate Change states that greenhouse gas emissions from human activity, primarily the burning of fossil fuels, have led to an increase in global temperature of 1.1 °C above pre-industrial levels.[1] Further warming beyond 1.5 °C above pre-industrial levels will strongly impact food and water availability and biodiversity, and lead to increased flooding, wildfires, community displacement and infrastructure damage.[1]

Along with many other countries around the world, the government of Canada has pledged to reach net zero carbon emissions by 2050.[2] The transportation sector accounts for 25% of Canada's greenhouse gas emissions.[2] As of 2020, automakers had announced investments of $300 billion globally into vehicle electrification, and the Canadian government has set a sales target for zero-emission vehicles of 30% by 2030 and 100% by 2040.[2] Further national commitments include electrifying public transit, increasing renewable power generation via wind and solar, and establishing electric grid storage of these inherently intermittent renewable energy sources.[2] Electrification of diesel-powered equipment and vehicles in the industrial sector is also essential to reach net zero, as this sector contributes 37% of Canada's greenhouse gas emissions.[2]

As such, electrochemical energy storage devices have become critical in the fight against climate change. Lithium-ion batteries are the most widely used electrochemical energy storage device and have become ubiquitous in day-to-day life, used in all portable electronics and electric vehicles. While decades of engineering of lithium-ion batteries have enabled significant advancements in electrification, they are approaching their fundamental energy density limits and so a critical need to develop and transition towards next-generation energy storage technologies exists.

The development of next-generation battery chemistries is therefore critical to enable the global transition to net zero, by enabling higher energy densities and greater access to and implementation of energy storage technologies via the use of electrodes prepared from inexpensive and abundant materials. One promising next-generation battery chemistry is the lithium-sulfur battery. Lithium-sulfur batteries replace the graphite anode and lithium transition metal oxide cathode of lithium-ion batteries with a lithium metal anode and sulfur cathode. This chemistry possesses a theoretical energy density an order of magnitude higher than lithium-ion batteries (2500 Wh/kg vs. 390 Wh/kg),[3–6] and the abundant nature of sulfur makes it significantly cheaper. However, a number of challenges have

hindered the widespread implementation of lithium-sulfur batteries. The lithium metal anode possesses a limited cycle life, due to the formation of an unstable solid electrolyte interphase and an effectively infinite volume change during cycling.[5,7] Furthermore, the insulating nature of elemental sulfur requires the fabrication of composites of sulfur and a conductive additive, typically carbon, to enable electron transport.[3,4,8] The fabrication of these composites is energy intensive or requires the use of toxic organic solvents, and the addition of the inactive carbon material limits the achievable energy density of the cell.[9] These issues, among others, such as the dissolution of intermediate polysulfide species into the electrolyte,[3,10] have limited both the energy density and cycle life of lithium-sulfur batteries.

Simultaneously, other electrochemical energy storage devices can assist in addressing some of the limitations of rechargeable batteries. Supercapacitors, which employ physical rather than chemical charge storage, possess lower energy densities than batteries, but much higher power densities and significantly longer cycle life, making them desirable for applications in which large bursts of power need to be captured or provided.[11–13] This high power density makes them useful in combination with batteries in electric vehicles for short term acceleration or regenerative braking, extending the lifetime of the battery by limiting the rapid charging and discharging steps.[11–13] They have also been employed in a range of other applications, including consumer electronics, memory back-up systems and power buffers for the grid.[11–13] The electrodes of most supercapacitors are prepared from high surface area, lightweight, conductive carbon materials, such as activated carbons.[11–13] The relative simplicity of the supercapacitor architecture also makes it an excellent model system to investigate wearable and flexible energy storage devices, as well as novel and advanced manufacturing approaches. However, the low capacitance and energy density remain major limiting factors for many energy storage applications.

While the charge storage mechanism is different for batteries and supercapacitors, both electrochemical energy storage devices consist of two electrodes submerged in an electrolyte, and the electrode material and design are critical to the achievable energy density, power density, and cycle life. Electrodes must be electrically conductive, lightweight, and contain as few inactive additives as possible, while possessing controlled morphologies and porosity. The design of high-performance electrodes is critical, and the development and inclusion of novel materials such as nanomaterials can enable these performance improvements.

In 2004 Geim and Novoselov demonstrated that a single 2D atomic layer of carbon, referred to as graphene, could be isolated from a graphite crystal by repeatedly cleaving layers with Scotch tape,

leading them to receive the 2010 Nobel prize in Physics.[14,15] Graphene possesses exceptional material properties, including high electrical conductivity, mechanical strength, and high specific surface area.[16,17] Following its discovery, the subsequent two decades of research have enabled a host of methods to synthesize graphene at scale, tune its specific surface area, and introduce various defects, dopants and functional groups onto the surface.[17–19] As such, graphene is a promising electrode material for electrochemical energy storage devices such as supercapacitors and next-generation battery chemistries.

While much research in electrochemical engineering has focused on the development of novel electrode materials, an area which has received less attention is device fabrication. Electrodes are conventionally prepared via the slurry casting of electrode materials onto conductive foils.[20] This process typically employs large quantities of organic solvent, and often leads to cracking or distortion of electrodes beyond a certain thickness, making higher electrode loadings – which is essential for increased energy density – challenging to produce.[20] Moreover, it limits device architectures to a conventional sandwich configuration, while next generation architectures such as interdigitated designs may lead to improved performance.[21,22] As such, next-generation approaches are needed for electrode and device fabrication. This may include processing of electrodes with aqueous, non-organic solvents, or the avoidance of solvent entirely through dry-pressing of electrodes. More notably, advanced manufacturing methods such as laser-based processing may enable the patterning of unique electrode architectures and enable active material synthesis and electrode fabrication in a single step.[23] Particularly, the laser-induced graphenization of polymer precursors has emerged as a promising, inexpensive approach to prepare porous, defective graphene foam known as laser-induced graphene (LIG).[24] The porous, high surface area, and highly conductive graphene is uniquely suited for supercapacitor or battery electrodes, while laser processing enables the formation of novel electrode architectures. Nonetheless, nearly all LIG prepared to date has been produced from petroleum-based precursors, and the areal capacitance remains limited.[23]

The conductive, high surface area, porous and tunable nature of graphene-based electrodes make them uniquely suited to address many of the challenges of next-generation EES devices, such as lithium-sulfur batteries. However, several major challenges in processing graphene-based electrodes must be overcome. While graphene could be an ideal conductive scaffold for sulfur cathodes, few processing methods exist to effectively couple elemental sulfur and graphene into conductive, high sulfur-loading composites. Most fabrication strategies involve processing carbon scaffolds in a dry

powder form, which leads to aggregation of the graphene sheets and reduces their surface area, limiting cathode performance compared to other carbon additives.[9] Solution-based strategies either employ toxic organic solvents or costly electrochemically-inactive sulfur precursors.[9] Conversely, porous, defective LIG could be uniquely suited to act as a host for the lithium metal anode, providing a lithiophilic surface for lithium nucleation, void space to accommodate the lithium volume change, and the opportunity to pattern advanced 3D architectures. However, nearly all high-performance LIG prepared to date is from costly, petroleum-derived, commercial polyimide (PI, Kapton^{TM}).[23] Thus, a need exists for both more sustainable and easily processable polymer precursors, which could be easily modified via various additives, as well as better control over the surface area, carbon yield, and surface chemistry of the resulting LIG.

The overall objective of this research project is to develop novel and sustainable fabrication strategies to employ graphene as an electrode material in EES devices. This work will both advance fundamental scientific knowledge pertaining to processing of graphene-based electrodes and improve the performance of the resulting devices. This will be accomplished by first developing an easily processable, biomass-derived LIG precursor system, and optimizing the LIG material properties by implementing different additives and studying its performance first as a supercapacitor. Following this, we will investigate the optimized LIG as a host for the lithium metal anode. Finally, we will develop an aqueous, solution-based strategy to fabricate graphene-sulfur composites for sulfur cathodes. Before outlining the specific objectives of this thesis, a comprehensive background and literature review on supercapacitors, batteries, electrode fabrication and graphene-based electrodes will be provided in the next chapter.

Chapter 2:
Literature Review

2.1 Operating Principles of Electrochemical Energy Storage (EES) Devices

As shown schematically in **Figure 2.1**, conventional EES devices are composed of two electrically conductive electrodes which typically contain the active electrode material bound together as a film with a polymer binder. These are laminated onto current collectors such as Al or Cu foil which better distribute the electronic charge to the less conductive electrode material which is limited in thickness to 10-100 μm to minimize ohmic losses. The electrodes are electronically isolated from each other, typically by using a porous polymeric separator. Ionic conduction between the two electrodes is facilitated by a liquid, solid, or gel electrolyte which fills the pore space within the separator and electrode materials.

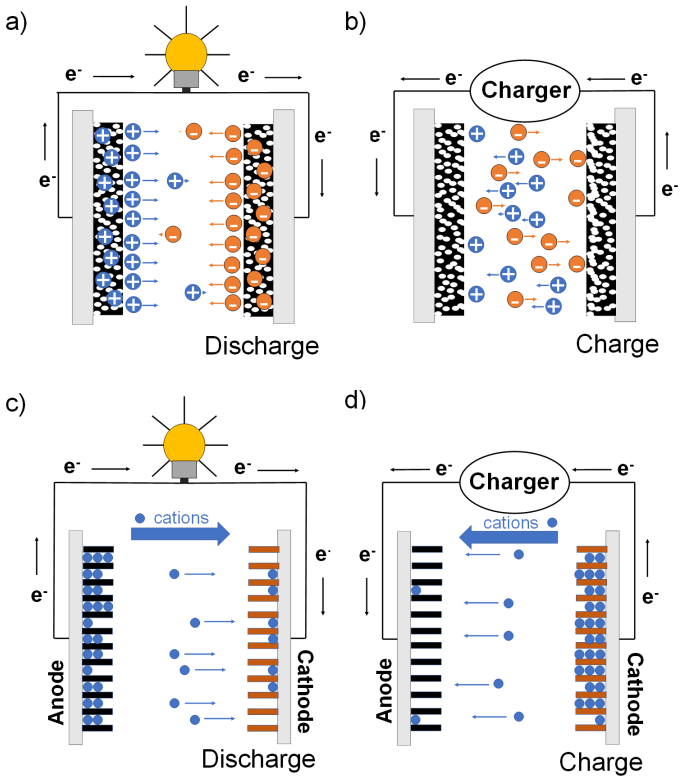

Figure 2.1: Schematic of an EDLC supercapacitor: a) discharging from a mostly charged state, b) charging from a mostly discharged state, and of an alkali-ion, intercalation-type battery: c) discharging from a mostly charged state, d) charging from a mostly discharged state. Figure and caption adapted from our review paper, [23], with permission from Taylor & Francis.

2.1.1 Supercapacitors

Electrochemical capacitors or supercapacitors are EES devices in which charge is stored either through purely physical electric double-layer formation (known as electrochemical double layer capacitors or EDLCs) or via rapid surface redox reactions (pseudocapacitors).

In EDLCs, applying a negative potential to the negative electrode causes the accumulation of positive charge adjacent the electrode/electrolyte interface, otherwise known as the formation of the electrical double layer. The electrical double layer was first introduced by Helmholtz in 1879, who postulated that a compact layer of ions forms on the surface of an electrically conductive electrode in solution, known as the Helmholtz layer.[11] A subsequent model by Gouy and Chapman included thermal effects, and suggested the formation of a diffuse layer of ions instead, following the Poisson-Boltzmann equation.[11] A final model, the Stern model, combined the work of Helmholtz and Gouy and Chapman, to suggest that both a compact, rigid layer of ions closest to the electrode surface (known as the Stern or Helmholtz layer), followed by a diffuse layer of ions, exist as seen in **Figure 2.2**.[11] However, due to the high ionic strength of most commonly employed electrolytes in EDLCs, the diffuse layer is suppressed and the Helmholtz model is most relevant for this system.

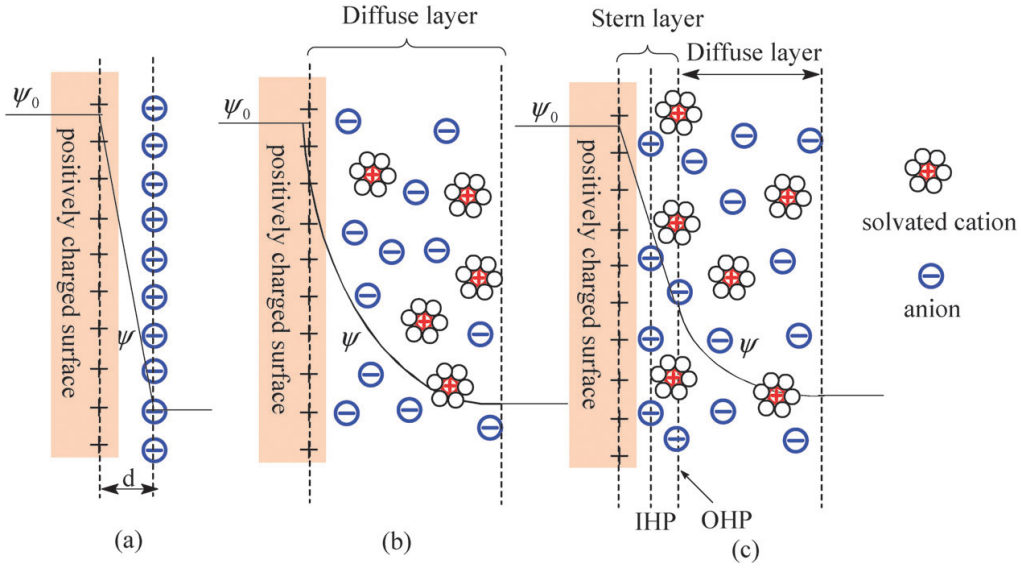

Figure 2.2: Model of the electrical double layer at a positively charged surface. a) Helmholtz model. *d* is the thickness of the double layer in this model. b) Gouy-Chapman Model. c) Stern Model. IHP denotes the inner Helmholtz plane, which is the distance of closest approach of specifically adsorbed ions, and OHP denotes the outer Helmholtz plane, which is the distance of closest approach of non-specifically adsorbed ions, and also where the diffuse layer begins. Ψ_0 is the potential at the electrode surface and Ψ is the potential at the electrode/electrolyte interface with distance. Figure and caption adapted from [11] with permission from Royal Society of Chemistry.

EDLCs store charge based on this electrical double layer formation. The capacitance (C) is the amount of charge (q) stored in the electrical double layer per unit volt applied (V):

$$C = \frac{q}{V} \tag{2.1}$$

Experimentally, either the differential capacitance (C_{diff}) or integral capacitance (C_{int}) is measured, where:

$$C_{diff} = \frac{dq}{dV} \tag{2.2}$$

and:

$$C_{int} = \frac{q}{V} \tag{2.3}$$

The capacitance of a conventional parallel plate capacitor is:

$$C = \frac{\varepsilon A}{\delta} \tag{2.4}$$

where ε is the permittivity of the dielectric, A is the area of the plates, and δ is the thickness of the dielectric. In an EDLC, a capacitor akin to a parallel plate capacitor is formed at the double layer between the closely spaced electronic and ionic charge separated by a dielectric with a thickness of less than a few solvent-layers (δ< 1 nm). When a material with high mass specific surface area (A_{m}) is used, such as an activated carbon which can have A_{m} ~1000 m^2/g, the mass-specific capacitance (C'_{m}) is many orders of magnitude higher than conventional dielectric or electrolytic capacitors. Using some order of magnitude estimates for typical parameters:

$$C'_{\mathrm{m}} = \frac{\varepsilon}{\delta} A_{\mathrm{m}} \sim \frac{10 \cdot 8.85 \times 10^{-12}\,\mathrm{F/m}}{1 \times 10^{-9}\,\mathrm{m}} \times 1000\ \mathrm{m^2/g} = \sim 100\ \mathrm{F/g} \tag{2.5}$$

where ε is the effective permittivity of the solvent or ligand between the electronic and ionic charge which is typically reduced from bulk values due to the high electric field within this layer.[25,26]

Moving beyond the charge that can be stored in the double-layer alone, pseudocapacitors employ rapid and highly reversible surface or near-surface Faradaic charge transfer reactions which possess theoretical capacitances that are an order of magnitude higher than EDLCs.[27] Materials which exhibit pseudocapacitance (in parallel with double layer capacitance) include conducting polymers or metal oxides, which store charge by either highly reversible protonation/deprotonation reactions, electrochemical intercalation or adsorption processes.[27] Each of these mechanisms results in a change

in the oxidation state of the pseudocapacitive material, which unlike in a battery, is distributed over a wide voltage, as opposed to a single redox potential. For example, metal oxide pseudocapacitive materials possess high theoretical capacitances of > 1000 F/g, but values of ≤ 400 F/g are typically achieved. While promising, some combination of limited voltage window or low stability reduce their energy density or applicability as a supercapacitor and few examples have yet to be commercialized.[28]

2.1.2 Batteries

In a battery, the negative electrode (the anode during discharge) contains an active electrode material or redox electrolyte which supports a half-cell reaction with a more negative redox potential ($E_{\text{rev, a}}$). The positive electrode (the cathode during discharge) supports another electrochemical reaction with a more positive redox potential ($E_{\text{rev, c}}$). The difference between the redox potentials ($E_{\text{cell}} = E_{\text{rev, c}} - E_{\text{rev, a}}$) sets up the driving force for a spontaneous galvanic process that converts chemical energy into electrical energy as electrons flow through the external circuit (as opposed to short-circuiting if the two electrodes were in physical contact as is the case with corrosion – another spontaneous galvanic process). The amount of charge that can flow through this external circuit is dictated by the capacity of the active material and is often normalized by the mass or volume of each active material. In SI units, the specific capacity is reported in C/g but more commonly mAh/g is used where 1 mAh = 3.6 C. This is known as the mass specific capacity (C_{m}) of the active material and the theoretical maximum for a given half-cell reaction ($C_{\text{m,theor}}$) can be determined by Faraday's law based on the number of electrons transferred (n) per formula unit in the half-cell reaction, Faraday's constant (F) and the molar mass (M) of the active material:

$$C_{m,theor} = \frac{nF}{M} \tag{2.6}$$

2.2 Performance Metrics of EES Devices

2.2.1 Supercapacitors

As defined in Equation 2.5, the gravimetric capacitance is a critical parameter for EDLC supercapacitors, and is directly related to the mass specific surface area of the electrode material and the distance of closest approach of ions. The capacitance can also be normalized volumetrically:

$$C'_{\text{V}} = C'_m \rho \tag{2.7}$$

where ρ is the electrode density, or even areally:

$$C_A' = C_m' t_m \tag{2.8}$$

where t_m is the areal mass loading of the electrode material, usually reported in mg/cm^2. Areal capacitances are of particular interest as these are the most commonly reported benchmarks for advanced manufacturing approaches, such as laser-induced graphene-based devices, both due to the fact that the electrode area is explicitly controlled in these methods, while the volume and mass may be unknown, and because many of these devices may have applications in microelectronics that are already lightweight.

The maximum voltage (V_{max}) achieved by a supercapacitor depends on the electrochemical stability window of the electrodes and electrolyte used. For aqueous electrolytes, the thermodynamic stability window is 1.23 V but this can be extended to nearly 2 V when using materials with high overpotentials for oxygen and hydrogen evolution reactions. Most commercial supercapacitors operate above 2.7 V by using organic electrolytes while ionic liquid electrolytes can achieve 3.5-4 V. Since the charge stored by a capacitor depends on the voltage, it is challenging to talk about supercapacitors in terms of capacity as the charge must be integrated over the voltage range which continuously falls upon discharge.

In a symmetric design, where both positive and negative electrodes are the same mass (m) and exhibit the same capacitance ($C'_+ = C'_- = C'$), the reciprocal of the total absolute capacitance is equal to the sum of each electrode's reciprocal capacitance as each electrode acts in series:

$$\frac{1}{C'_{\text{total}}} = \frac{1}{C'_+} + \frac{1}{C'_-} = \frac{2}{C'} \text{ and thus, } C'_{\text{total}} = C'/2 \tag{2.9}$$

When considering the areal capacitance for full symmetric devices, for all works in this thesis, the areal capacitance is normalized by the full two electrode area (i.e., ¼ of the single electrode capacitance). While supercapacitors are conventionally prepared in sandwich configurations, which would often be normalized by the single electrode or device area, interdigitated and other complex geometries are more frequently employed by advanced manufacturing approaches, and in these methods the full two electrode area is more commonly used for normalization. As such, we will use this normalization for device capacitance throughout this thesis.

From Equation 2.9, the total, theoretical cell-level Gibbs free energy stored in such a symmetric supercapacitor is given by:

$$\Delta G'_{cell,m,theor} = \frac{\int_0^{Vmax} (C'/2)\mathrm{V}d\mathrm{V}}{2m} = \frac{1}{8}\frac{C'}{m} V_{max}^2 = \frac{1}{8} C_m' V_{max}^2 \tag{2.10}$$

where, the $2m$ accounts for the mass of two identical electrodes of mass m in the symmetric cell with C'_m being the single electrode capacitance which is what would be measured in a 3-electrode cell. However, this equation merely predicts the theoretical energy density. This value cannot be achieved in practice, as cells consist of many essential components beyond the active material. Practical energy densities can be calculated by introducing a correction factor, F_m:

$$\Delta G'_{cell,m} = \frac{F_m}{8} C'_m V^2_{max} \tag{2.11}$$

F_m is the mass fraction active material (in wt%) corresponding to both electrode active materials. It accounts for the, usually dominant, mass of all other cell components which do not contribute to the capacitance such as the current collectors and separator. F_m is largely controlled by the areal mass loading of the electrode material (t_m), making this one of the most important parameters for assessing the practical energy density of a design and thus its commercial promise. F_m is related to t_m by the following relationship:

$$F_m = \frac{t_m}{f_\infty t_m + f_0} \tag{2.12}$$

where f_∞ is the total mass of other materials that scale in direct proportion to the active material. For example, the amount of binder used and the amount of electrolyte used to fill a given electrode porosity would scale with the loading. If the electrode were made infinitely thick, these masses would still need to be accounted for while the total mass of fixed components such as the current collectors, membrane separator and electrolyte within the membrane separator, represented by f_0, would become a smaller and smaller proportion of the device mass. **Table 2.1** illustrates typical masses of cell components in supercapacitors that contribute to f_∞ and f_0.

As illustrated in Equation 2.11, the square dependence of the maximum voltage makes it preferable to work with materials and electrolytes with high electrochemical stability windows. In a well-designed supercapacitor, with high loading, dense electrodes, F_m would approach 30 wt.% and capacitances achievable in commercialized activated carbon electrodes (~150 F/g) in an organic electrolyte (V_{max} ~ 3 V) leads to $\Delta G'_{cell,m} = \frac{0.3}{8} \cdot 150 \cdot 3^2 = 50.6 \frac{J}{g} or\ 14\ \mathrm{Wh/kg}$. Some optimized designs can reportedly achieve 20-30 Wh/kg which is not too far off from the aforementioned estimate. It is important to note that while we have used $\Delta G'_{cell,m}$ here to represent the theoretical maximum energy stored in a supercapacitor, practical cell energy densities are lower due to inefficiencies and losses.

Table 2.1: Mass of cell components that scale with active material loading (f_∞) and that do not scale with active material loading (f_0) for typical supercapacitors. Table adapted from our review paper, [23], with permission from Taylor & Francis.

Cell Component	f_∞ **(mg/mg)**[i]
Electrolyte	0.62 (Aqueous), 0.49 (Organic), 0.95 (IL)
Binder	0.22
Electrode 1	1.00
Electrode 2	1.00
Total f_∞	*2.84 (Aqueous), 2.71 (Organic), 3.17 (IL)*
Cell Component	f_0 **(mg/cm^2)**[ii]
Al current collector for electrode 1	4.32
Al current collector for electrode 2	4.32
Membrane separator	1.03
Electrolyte in membrane	1.38 (Aqueous), 1.08, (Organic), 2.10 (IL)
Total f_0	*11.05 (Aqueous), 10.75 (Organic), 11.77 (IL)*

i) Assumptions: No additional conductive material, symmetric supercapacitor with two electrodes of identical loading, single electrode capacitance (C'_m of 100 F/g); Electrode porosity of (ε) = 0.35 used to calculate electrolyte mass; Electrolyte density = 0.997 g/cm^3 for aqueous electrolyte, Electrolyte density = 0.783 g/cm^3 for organic electrolyte (acetonitrile), Electrolyte density = 1.52 g/cm^3 for ionic liquid electrolyte (1-ethyl-3-methylimidazolium bis(trifluoromethylsulfonyl)imide, (EMIM-TFSI)), Carbon active material density = 2.2 g/cm^3; Binder density (PVDF) = 1.78 g/cm^3, and 10 wt.% binder assumed. ii) Assumptions: 25 µm polypropylene (density = 0.91g/cm^3) membrane with a porosity of 55% was assumed to calculate mass of electrolyte in separator; 16 µm thick Al foil current collectors.

The mass-specific power density in W/kg is directly related to the energy density:

$$P'_{cell,m} = \Delta G'_{cell,m}/t \tag{2.13}$$

where t is the discharge time. Finally, another critical assessment of performance is the cycle life of the full supercapacitor device, which is typically reported as the percentage of capacitance retention after a specific number of charging and discharging cycles (for example, 10,000) at a specific current density.

2.2.2 Batteries

Similar performance metrics are used for batteries, with some key differences. The theoretical gravimetric capacity of an electrode material, as introduced in Equation 2.6, is a critical parameter. As discussed with supercapacitors, the capacity can also be normalized volumetrically or areally, in a similar manner as Equations 2.7 and 2.8. For batteries, the areal capacity of both the individual electrodes and the full cell are normalized to the single electrode area, which typically corresponds to the geometric device area, as most batteries are prepared in a sandwich or stacked configuration, even via advanced manufacturing approaches. Also similarly to supercapacitors, the theoretical capacity of the full cell can be determined from the individual theoretical capacities of the anode and cathode, by considering them as two capacitors in series, with the absolute capacity of each electrode being equivalent:[29]

$$C_{total} = \frac{1}{\frac{1}{C_{anode}} + \frac{1}{C_{cathode}}} \tag{2.14}$$

However, in practice, the capacity of a full cell is typically limited by the electrode with lower capacity.

Unlike EDLC supercapacitors, in which the cell voltage is purely dependent on the stable voltage window of the electrolyte, the battery cell voltage is dictated by the reduction potentials of the cathode and anode. The cell reaction emf, E_{cell}, is:[29,30]

$$E_{cell} = E_{cathode} - E_{anode} \tag{2.15}$$

where E_{cathode} and E_{anode} are the electrode potentials of the cathodic and anodic reactions, respectively. These reduction potentials are related to both the standard reduction potential of the electrode, as well as the activities of the oxidized and reduced species through the Nernst equation:[29,30]

$$E = E^0 + \frac{RT}{zF} ln\left(\frac{a_O^{\nu_O}}{a_R^{\nu_R}}\right) \tag{2.16}$$

where E^0 is the standard reduction potential of the electrode, R is the gas constant, T is the temperature, z is the stoichiometric number of electrons transferred in the half-reaction, F is Faraday's constant, a_0 and a_{R} are the activities of the oxidized and reduced species, and ν_{O} and ν_{R} are their respective stoichiometric coefficients. It should be noted that both Equations 2.15 and 2.16 assume that no current is flowing. When current is flowing, overpotentials at the two electrodes and ohmic resistance must also be included when determining the cell potentials. Equation 2.16 can be further simplified by using the formal potential, $E^{0'}$, which is the measured potential of the half-cell when the oxidized and reduced species are present in concentrations such that $\frac{C_O^{\nu_O}}{C_R^{\nu_R}} = 1$ and any other conditions such as pH or ionic strength are specified. For example, for the case where the stoichiometric coefficients ν_{O} and ν_{R} are both unity, the formal potential incorporates the standard reduction potential of the electrode and the activity coefficients γ_{O} and γ_{R} as follows:

$$E^{0\prime} = E^0 + \frac{RT}{zF} ln\left(\frac{\gamma_O}{\gamma_R}\right) \tag{2.17}$$

which enables the Nernst equation to be more conveniently written as a function of the formal potential and the concentrations of the oxidized and reduced species, C_{O} and C_{R}:

$$E = E^{0\prime} + \frac{RT}{zF} ln\left(\frac{C_O}{C_R}\right) \quad (2.18)$$

However, it should be noted that one of the downsides of this formulation is that the formal potential depends on concentration, as the activity coefficients may depend on concentration as well.

Assuming that E_{cell} does not change as a function of the extent of charge or discharge, the mass-specific Gibbs free energy (constant temperature and pressure) stored in a battery is given by:

$$\Delta G_{cell,m} = F_m C_m E_{cell} \quad (2.19)$$

where in this case, F_{m} is the mass fraction active material (in wt%) corresponding to the electrode material used for C_{m}. F_{m} has the same form for the supercapacitor as in the battery, but in this case, since the anode and cathode are not prepared from identical materials, the other electrode whose capacity must at least match that of the first, also must be considered. **Table 2.2** shows typical cell components that contribute to f_∞ and f_0 for lithium-ion batteries. It is worth noting that practically, E_{cell} does vary depending on the state of charge, and thus, the energy density calculated in Equation 2.19 is an estimate.

Table 2.2: Mass of cell components that scale with active material loading (f_∞) and that do not scale with active material loading (f_0) for typical lithium-ion batteries. Table adapted from our review paper, [23], with permission from Taylor & Francis.

Cell Component	$\boldsymbol{f_\infty}$ **(mg/mg)**[i]
Electrolyte in Cathode	0.28
Electrolyte in Anode	0.25
Binder in Cathode	0.11
Binder in Anode	0.08
Conductive Additive in Cathode	0.03
Conductive Additive in Anode	0.02
Cathode Material	1.00
Anode Material	0.74
Total f_∞	*2.52*
Cell Component	$\boldsymbol{f_0}$ **(mg/cm²)**[ii]
Al current collector	4.3
Membrane separator	1.0
Electrolyte in membrane	1.7
Cu current collector	9.9
Total f_0	*16.9*

i) Assumptions: Ratio of active material to conductive additive assumed to be 30; A stoichiometric amount of graphite anode was assumed and a cathode theoretical capacity of 160 mAh/g; Cathode and anode porosity (ε) = 0.35 used to calculate electrolyte mass; Electrolyte density = 1.195 g/cm^3, which is an average of pure EC and DMC; Cathode active material density = 2.8 g/cm^3 based on LCO, Carbon conductive additive and graphite material density = 2.2 g/cm^3 ; Binder density (PVDF) = 1.78 g/cm^3, and 10 wt.% binder assumed. ii) Assumptions: 25 µm polypropylene (density = 0.91g/cm^3) membrane with a porosity of 55% was assumed to calculate mass of electrolyte in separator; 16 µm thick Al foil current collector; 11 µm thick Cu foil current collector.

For parameters typical of commercial lithium-ion batteries (**Table 2.2**), the high loadings used (15-20 mg cathode/cm^2) and compactness of the electrodes (reduced porosity for electrolyte deadweight) enable devices to be roughly 30 wt.% active material, while ~40 wt.% could be achieved at infinite active material loading. This results in current, commercial Li-ion full-cells which are capable of reaching energy densities exceeding 250 Wh/kg. EDLC-type supercapacitors offer only one tenth of this energy density, being more similar to lead-acid batteries but with significantly improved power density, cycle life, reliability and safety. The power density of batteries is calculated in the same manner as for supercapacitors, using Equation 2.13.

Assessments of battery capacity and energy density are essential battery metrics, but equally important are metrics quantifying the cycle life. This is typically quantified through the coulombic efficiency of the cell which can be calculated as:[31]

$$CE = \frac{Discharge\ Capacity}{Charge\ Capacity} \times 100\% \tag{2.20}$$

For an ideal theoretical cell, the discharge capacity would perfectly equal the charge capacity, and the coulombic efficiency would equal 100%. For any real cell, this value is less than 100% due to various side reactions and consumption of active material. The coulombic efficiency of the cell after a certain number of cycles can demonstrate the stability and cycle life of a cell.

Finally, it is important to assess the rate of charge and discharge of the cell. For batteries, this is typically expressed as a "C rate". A C rate of 1C means that a constant current is applied such that the battery should be fully charged or discharged in 1 hour.[29] Higher C rates refer to higher currents used; thus at 2C a cell would take 30 minutes to discharge, while at 0.1C it would require 10 hours to discharge.[29] The cycle life and capacity of cells are strongly influenced by the rate of charge and discharge.

2.2.3 Comparison of Supercapacitor and Battery Performance:

For all EES devices, a tradeoff exists between energy density and power density,[27,32] and different EES devices fall into different ranges between the two, as seen in the Ragone plot in **Figure 2.3.** Batteries exhibit the highest energy densities, but limited power density, while parallel plate capacitors such as dielectric and electrolytic capacitors used in electronic circuits can achieve the highest power densities, but very limited energy densities. Supercapacitors exist over a range of power and energy

densities and bridge the gap between capacitors and batteries, with improved power density over batteries, but lower energy densities.

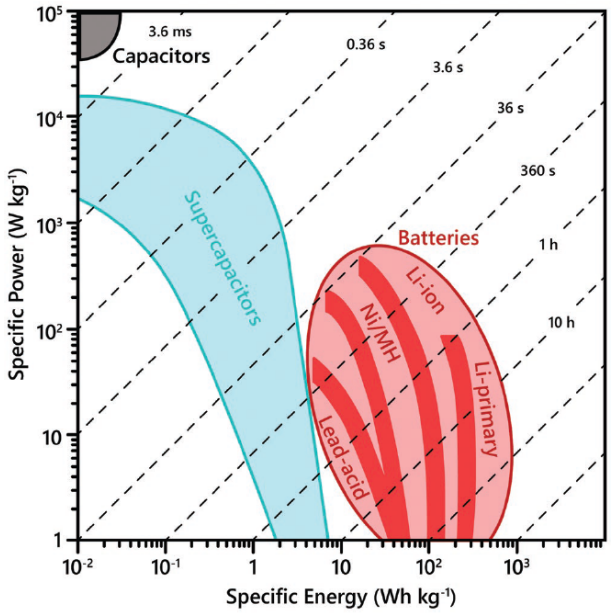

Figure 2.3: Ragone plot showing the energy and power relationships of current electrochemical energy storage technologies with their associated time constant regimes. Figure and caption adapted from [33] with permission from John Wiley and Sons.

While we have mainly discussed energy density thus far, the requirements for maximum energy density typically oppose those for high power density.[32] Higher power density requires design criteria which lower the equivalent series resistance in EES devices. Some considerations are summarized in **Table 2.3** which affect various ohmic and mass transport resistances in an EES device. Depending on the system, kinetic overpotentials can also play a role. Different manufacturers use different approaches to optimize their cells for high energy density or high power density.

Table 2.3: Design parameters used to optimize LIBs in terms of energy density and power density. Table adapted from our review paper, [23], with permission from Taylor & Francis.

Component	Energy Density	Power Density
Electrode	High loading t_m (mg/cm^2) Low electrode porosity ε (%) Larger primary particle size Low conductive additive content Minimum possible binder content	Lower electrode loading Higher electrode porosity Smaller particle size High conductive carbon content Minimum possible binder content
Current collector	Thinner Coated to improve adhesion	Thicker Coated to reduce resistance
Seperator	Thin	Thin
Electrolyte	High conductivity	High conductivity

2.3 Current Electrode Materials

2.3.1 Supercapacitors

EDLC-type supercapacitors typically employ carbonaceous materials as electrode materials, due to their high electrical conductivity, chemical stability, corrosion-resistance, and specific surface area. Moreover, porous carbon materials can be prepared from a variety of methods and with a variety of surface areas and pore structures, enabling tuning of key electrode properties. Smaller pore sizes generally result in higher specific surface areas, boosting capacitance, but also limit electrolyte access, lowering power density. As such, the porous carbon structure needs to be carefully optimized to enable the desired device performance.

The first and still most commonly used carbon-based electrode material is activated carbon.[11,13] Activated carbon is prepared via either physical or chemical activation of precursors such as waste, coal, nutshells, and wood.[11,13] Physical activation involves the use of high-temperature (700 – 1200 °C) thermal treatments of precursors with oxidizing or reducing agents, such as air, CO_2, and steam, while chemical activation employs lower temperatures (400 – 700 °C) along with chemicals such as oxyacids, hydroxides, and metal chlorides.[12] These activation processes enable the formation of carbon materials with conductivities ranging from 1250 – 2500 S/m and extremely high BET surface areas of up to 2500-3000 m^2/g.[13,34] The pore structure of activated carbons consist of macropores, mesopores, and micropores. Depending on the quantity of micropores, the BET surface area may be much higher than the electrolyte-accessible surface area, otherwise known as the electrochemical surface area (ECSA), which is what determines the achievable double-layer capacitance. Nonetheless, the high specific surface area and ability to prepare activated carbons via inexpensive and widely used industrial processes have made them the most widely employed electrode material for commercial supercapacitors to date, typically achieving electrode specific capacitances of up to ~300 F/g and ~150-180 F/g in aqueous and organic electrolytes respectively.[12] Higher capacitances are achieved with aqueous electrolytes than organic since the organic electrolyte ions are typically larger, and thus a larger quantity of the activated carbon pores remain inaccessible and do not contribute to charge storage.[12]

2.3.2 Batteries

The first officially reported battery, called the voltaic pile, was developed by Alessandro Volta in 1800 and consisted of stacks of alternating copper and zinc plates, separated by cloths soaked in brine.[35] In

the subsequent centuries, a range of different active materials have been utilized to form batteries, including lead-acid batteries, which have been used in nearly all internal combustion engine vehicles to power starter motors, and nickel metal hydride batteries, widely used in consumer electronics and first-generation electric vehicles. In 1991, Sony released the first lithium-ion battery.[36] The cell utilized graphite as the anode material. The relatively reversible intercalation and deintercalation of lithium ions between the graphite sheets enables the anode to have a theoretical capacity of 372 mAh/g:[36]

$$Li^+ + C_6 + e^- \rightleftharpoons LiC_6 \tag{2.21}$$

This knowledge was combined with work from the Goodenough group, which found that lithium ions can also reversibly intercalate into and deintercalate from a lithium transition metal oxide compound such as lithium cobalt oxide ($LiCoO_2$), enabling its use as a cathode material:[37]

$$LiCoO_2 \rightleftharpoons xLi^+ + xe^- + Li_{1-x}CoO_2 \tag{2.22}$$

The cells utilized a microporous polyethylene separator to prevent contact between the anode and cathode, and an ethylene carbonate-based electrolyte.[36] During battery charge, lithium ions are transported from the lithium transition metal oxide cathode towards the graphite anode, where they are intercalated within the graphite sheets, while during discharge, the opposite occurs, giving a cell voltage of 3.3 – 4.2 V. Since 1991, various other lithium-ion cathode materials have been developed, including lithium iron phosphate ($LiFePO_4$), lithium manganese oxide ($LiMnO_2$), and lithium nickel manganese cobalt oxide (LiNMC, $Li(Ni_{1/3}Mn_{1/3}Co_{1/3})O_2$), among others, which enable cathode theoretical capacities of 140 – 200 mAh/g, and thus full cell theoretical capacities of 100 – 130 mAh/g.[3,5] Decades of engineering have enabled improvements in cathode capacity and voltage, while increasing the correction factor F_m by reducing electrolyte volume, separator thickness, and the mass and volume of current collectors and packaging. However, these engineering improvements are reaching fundamental limits, as certain volumes of electrolyte and separator thicknesses are necessary for safe and reasonable cell operation. As such, next-generation battery chemistries and active materials beyond lithium-ion are needed to achieve substantial increases in energy density.

2.4 Next-Generation Electrode Materials: Graphene

Graphene is a carbon nanomaterial consisting of a single layer of carbon atoms in a hexagonal lattice. As mentioned in the introduction, it was first isolated by Geim and Novoselov in 2004 via micromechanical cleavage from a graphite crystal using adhesive tape, otherwise known as the Scotch

tape method.[14,15] Geim and Novoselov were awarded the Nobel Prize in Physics in 2010 for their discovery. Graphene has found applications in nearly all fields of science and technology, including electronics, drug delivery, composites and coatings, membranes, and sensors. Pristine graphene has exceptional material properties, including a specific surface area of 2630 m^2/g, high Young's modulus (1 TPa) and intrinsic strength of ~130 Gpa, high thermal conductivity (5000 W/mK), strong chemical resistance, high optical transmittance (97.7%), and high electron mobility (2.5 x 10^5 cm^2/Vs).[16,17] While the Scotch tape method demonstrated the possibility of isolating single graphene sheets, the limited scalability of the approach led to the development of many other synthesis approaches to prepare graphene-based materials.

2.4.1 Current Synthesis Methods

All graphene synthesis methods can be characterized as either bottom-up or top-down approaches. Bottom-up approaches include chemical synthesis, SiC epitaxial growth, or, most commonly, chemical vapor deposition (CVD). In the CVD approach, graphene is grown on a metallic catalyst such as nickel or copper via the high temperature decomposition of H_2/CH_4 gas, followed by the dissolution of carbon atoms into the metal catalyst to form a solid solution.[18] Cooling then occurs, allowing carbon atoms to diffuse out of the solid solution and grow graphene on the catalyst surface.[18] This process has been useful for preparing single layers of highly conductive crystalline graphene, but is costly and has limited scalability for bulk synthesis.

One category of top-down methods expands on the micromechanical cleavage initially utilized by Geim and Novoselov, by directly exfoliating graphite into graphene via methods such as ball-milling or liquid-phase exfoliation methods such as sonication and high shear mixing.[17] While this can produce graphene materials with a low ratio of defects, yields are relatively low and significant lateral size and sheet number variations are common.[16]

One of the most commonly employed top-down methods to prepare scalable amounts of graphene is the reduction of graphene oxide (GO). GO can be prepared via the oxidation of graphite to form graphite oxide, followed by subsequent exfoliation to form GO. GO synthesis was first demonstrated by Brodie in 1859, by oxidizing graphite with potassium chlorate in fuming nitric acid.[19,38] This was improved upon by Staudenmaier in 1898, via adding the chlorate in multiple aliquots, and employing a mixture of concentrated sulfuric and fuming nitric acid.[19,39] This was further optimized in 1958 by Hummers, who used a mixture of potassium permanganate and sodium nitrate in concentrated sulfuric acid.[19,40]

The most commonly employed method today is Tour's method, developed in 2010.[19] In this method, potassium permanganate is used as an oxidizer, in a 9:1 mixture of oxidizing acids sulfuric and phosphoric acid. This approach avoids the formation of toxic nitrogen dioxide and dinitrogen tetroxide gases, and the toxic and explosive gas chlorine dioxide, which were formed in previous approaches.[19] As such, this method is both the most scalable and safest, and also produces the most oxidized GO, with the least hydrophobic unreacted material left over.[19]

The conversion of graphite into GO occurs through a three-step process.[41] The first step is the intercalation of the sulfuric acid into the graphite sheets to form a stage 1, or fully intercalated, graphite compound.[41] In the second step, this graphite intercalation compound is converted into graphite oxide, via the diffusion of the oxidizing agent into the graphite galleries.[41] This is the rate-determining step of the reaction.[41] The third and final step occurs when the graphite oxide is exposed to water, which hydrolyzes covalent sulfate bonds and exfoliates the graphite oxide into GO.[41]

Despite over a century of synthesis, the exact chemical structure of GO is not fully known. A common model for GO is the Lerf-Klinowski model, as shown in **Figure 2.4**, which consists of a graphene sheet with oxidized domains, possessing oxygen-containing functional groups such as hydroxyl, epoxy, and ketone groups on the graphene plane, along with carboxylic acid groups at the sheet edge.[42] NMR studies have also shown that ester groups are present on the surface, and 6- and 5-membered lactol rings are present at the edges,[42] and residual sulfate groups are also known to be present.[41] These oxygen-containing functional groups disrupt the otherwise flat and pristine sp^2 graphene lattice, introducing some sp^3 carbon atoms, which are distorted to above or below the graphene plane.[42] Nonetheless, this model and all models to date are non-stoichiometric in nature, and variation in the quantity of the different oxygen-containing functional groups is common among different reports. GO can be considered a 2D material with a random distribution of oxidized regions, possessing oxygen-containing functional groups, and regions with preserved sp^2 graphene structure.

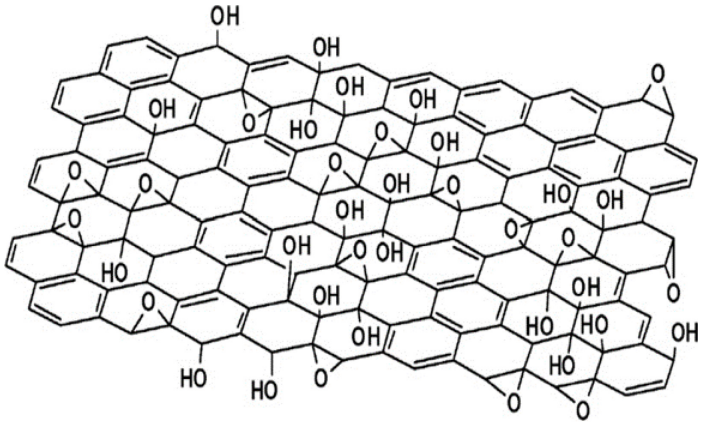

Figure 2.4: Lerf-Klinowski model of GO. Some minor groups at the plane edge have been omitted (carbonyl, carboxyl, ester, etc.). Figure and caption reproduced from [42–44] with permission from Elsevier and the American Chemical Society.

This structure has made GO an interesting material for many applications. While it is still a 2D material with a high specific surface area, it is unlike graphene as it is electrically insulating and highly hydrophilic in nature, enabling its easy dispersion in aqueous systems. This has motivated its use in a variety of fields, including membranes, sensors, and biomedical applications.[45,46] Moreover, it can be reduced via a range of methods to produce reduced graphene oxide (rGO). The two most common methods to reduce GO are chemical and thermal reduction methods.

Chemical reduction of GO utilizes chemical reducing agents, such as hydrazine, sodium borohydride, ascorbic acid, or hydroiodic acid. This process can typically be done in an aqueous dispersion at relatively low temperatures, which also prevents the possible aggregation and re-stacking of the GO or rGO during drying steps. However, chemically reduced GO is typically only partially reduced. A common metric to assess the degree of reduction is the C/O ratio, which is typically 8 – 12 via chemical reduction, though some methods have reported C/O ratios up to 15.[42,47,48]

Thermal reduction involves heating GO at high temperature, and is typically performed on dried GO powders or films. The drying process introduces challenges, as the sheets may restack or aggregate, and methods such as spray-drying or freeze-drying are often used to attempt to preserve the high surface area of the material. However, rapid thermal reduction can be used to simultaneously reduce and exfoliate graphite oxide, or restacked GO.[42,49] Rapid heating (>2000 °C) causes the oxygen-containing functional groups on the GO surface to rapidly decompose into CO and CO_2 gases and the pressure of this rapid gas evolution can exfoliate the rGO during a simultaneous reduction.[42,49] As such, this is a

scalable method to produce large quantities of rGO. Moreover, the high temperatures used typically result in a more highly reduced rGO than chemical reduction methods, with C/O ratios of ~15 typically achieved, though this is dependent on the reduction temperature used.[42] However, it should be noted that thermal reduction also leads to some structure deformation of the rGO – the sheets are typically wrinkled in nature and possess lattice defects, as some of the carbon of the GO is lost during the rapid gas formation.[42,49] Moreover, thermal reduction is energy intensive and requires extremely high temperatures (>1000 °C) for highly reduced, high surface area rGO to be produced.[42]

While chemical and thermal reduction of GO are the most widely used reduction methods, a number of other methods have been proposed, including electrochemical reduction,[50] solvothermal reduction,[51] photocatalyst reduction,[52] microwave reduction,[53] and photothermal methods.[54] Microwave and photothermal methods employ a similar mechanism as thermal annealing reduction methods, but utilize microwaves or photo energy, for example from a xenon lamp, as the thermal energy source for reduction. These methods may enable rapid and localized GO reduction, without the need for energy intensive high-temperature furnaces. This approach has been expanded via the use of lasers to photothermally reduce GO, which can enable rapid, inexpensive patterning of rGO electrodes.[55–57] We will discuss this method in further detail later in this chapter.

2.4.2 Graphene in Supercapacitors

The high specific surface area and conductivity of graphene has made it extremely attractive as a supercapacitor electrode material. The intrinsic double layer capacitance of graphene has been measured to be 21 μF/cm^2 (without considering quantum capacitance limitations, to be discussed below).[58] With a theoretical specific surface area of 2630 m^2/g, this enables an extremely high theoretical capacitance of 550 F/g.[59] Moreover, depending on the electrode fabrication method, graphene electrodes could possess significantly less microporosity than activated carbon, making more of this high BET surface area electrochemically accessible. In fact, the structure of graphene sheets has been proposed to improve ionic conductivity and electrolyte penetration into supercapacitor electrodes by allowing channels for ionic transport. In 2010, Miller et al. demonstrated that supercapacitors prepared from vertically oriented graphene grown directly on a metal current collector could be charged and discharged in under a millisecond – a similar time scale to dielectric and electrolytic capacitors, but with ten times the volumetric capacitance.[60] As such, significant research has focused on developing graphene-based electrodes.

However, several issues have limited the performance of graphene electrodes thus far. One of the major challenges is the re-stacking of graphene sheets in solid, powder form. While graphene and rGO can be dispersed and stabilized in dispersion with specific solvents or surfactants, strong π-π interactions between graphene sheets lead to restacking and aggregation during any drying process. This restacking limits the actual accessible surface area of graphene electrodes. Consequently, significant research effort has focused on methods to limit restacking. One avenue is to employ physical spacers between the graphene sheets, such as other carbon nanomaterials[61,62] or some form of electrolyte, such as a microemulsion[63] or surfactant complex,[64] while other strategies focus on altering the graphene morphology via the use of curved or crumpled graphene structures to attempt to limit restacking.[65,66] Notably, laser-induced graphene synthesis, which will be introduced fully in section 2.8, enables simultaneous graphene synthesis and electrode fabrication from a precursor substrate without drying of a graphene dispersion, thereby avoiding the restacking issue entirely.

Another key consideration in employing graphene-based materials is their inherent semimetallic nature. For supercapacitors prepared from materials with a low density of states such as graphene,[58] the total capacitance (C_T) is dependent on both the double layer capacitance (C_{DL}) and the quantum capacitance (C_Q):

$$\frac{1}{C_T} = \frac{1}{C_Q} + \frac{1}{C_{DL}} \tag{2.23}$$

The quantum capacitance is intrinsic to the electrode material, and depends upon its electronic properties:

$$C_Q(V) = \frac{1}{SV}\int_0^V eD(\varepsilon_F - eV')dV' \tag{2.24}$$

where S is the surface area, V is the applied voltage, D is the density of states, ε_F is the Fermi level, and e is the electron charge.[24] As the quantum capacitance is often less than the double layer capacitance, it is typically a limiting value for graphene-based supercapacitors. However, several studies have demonstrated that doping of the graphene with different heteroatoms can increase the density of states near the Fermi level and thereby increase the quantum capacitance.[67–69]

2.4.3 Graphene in Batteries

Graphene has also found a wide range of applications in batteries. Most notably, it has been used as an anode material in lithium-ion batteries, to replace graphite. The theoretical capacity of conventional

graphite anodes is limited to 372 mAh/g, which corresponds to the formation of LiC_6, a stage I intercalation compound. However, higher capacity carbon materials have been demonstrated via other mechanisms, including the adsorption of lithium onto carbon sheets and the binding of lithium on hydrogen-terminated graphene edges.[70,71] Since graphene-based materials can facilitate lithium adsorption onto both sides of each sheet, this could lead to an effective doubling in capacity compared to graphite, forming Li_2C_6, and resulting in a theoretical capacity of 744 mAh/g.[70] However, it has also been proposed that lithium can be stored in microcavities in carbon materials, which can enable a further increase in capacity.[70] In one of the first reports of graphene-based lithium-ion anodes, Wang et al. demonstrated a reversible capacity of 650 mAh/g at 1C.[70]

While graphene has been investigated as a potential lithium-ion anode material, its most widely explored applications have been in next-generation battery chemistries, such as lithium-sulfur batteries (to be discussed more thoroughly in subsequent sections). While it is not used as the main active material in these next-generation batteries, its conductivity, high specific surface area, and tunable morphology and surface chemistry have made it a widely employed additive for both lithium metal anodes and sulfur cathodes.

2.5 Cell Manufacturing

2.5.1 Manufacturing Process

The cell assembly of both batteries and supercapacitors follows a similar process. The current production of lithium-ion batteries (LIBs) follows a fairly well-known sequence of manufacturing steps as presented in **Figure 2.5**.

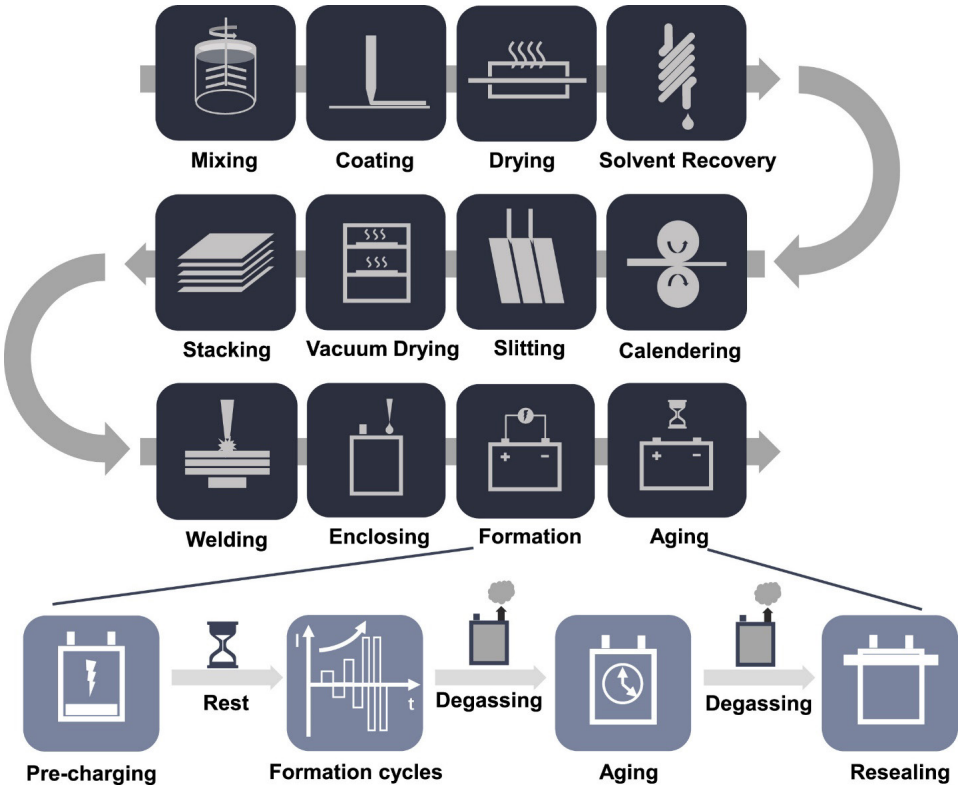

Figure 2.5: Schematic of current Li-ion battery manufacturing process. Figure and caption adapted from [20] with permission from Elsevier under a Creative Commons Attribution-Non-Commercial-No Derivatives License.

2.5.2 Electrode Preparation

Electrode preparation includes the mixing, coating, drying and solvent recovery steps. This is an important part of the fabrication of a battery as its performance depends significantly on the morphology of the electrode at the micron length scale. In particular, the proper dispersion and homogenization of electrode particles is critical, as the electronic pathways generated by the carbon additive and the ionic pathways in-between these particles are key to battery performance.[72] The mixing phase can be done with high-shear mixing equipment, ball milling or via ultrasonication.[73] The coating phase traditionally involves the application of a "wet" slurry onto a metal sheet current collector (copper for anode and aluminum for cathode) through a slot die on a roll-to-roll system.[20] Subsequent drying is conducted in ovens, under conditions that depend on the solvent used. Typically, anode slurries are water-based with a mixture of sodium carboxymethylcellulose and styrene-butadiene as binders. On the cathode side, slurries typically use N-methyl-2-pyrrolidone, an organic solvent that has a higher boiling point than water (~200 °C). Organic solvents not only require higher temperatures to evaporate, but their toxicity also mandates using a solvent recovery process.[74] Organic solvents are often necessary

because most lithium-ion cathode materials are water-sensitive.[75] To reduce energy consumption and drying time, the industry is moving toward thicker slurries with a lower amount of solvent. Finally, the calendaring of electrodes is achieved by pressing them in between rollers that are adjusted to achieve a certain thickness and compression of the coating in order to enhance adhesion with the current collector and control porosity.[76]

2.5.3 Electrode Conditioning

Electrode conditioning is comprised of slitting and vacuum drying. Slitting refers to the cutting of the electrodes to a prescribed width. This operation increasingly makes use of laser cutting rather than mechanical cutting.[77] Laser cutting improves edge quality that helps prevent potential short-circuiting when the battery is assembled. The vacuum drying step removes traces of water in the anode. Drying is one of the most energy intensive steps as shown in **Table 2.4**.[78] This step consists of placing the electrode in a low pressure environment at temperatures up to 150 °C for several hours. However, it has been demonstrated that using argon purges at lower temperatures prevents PVDF and CMC binders from being degraded and produces higher performing electrodes.[79]

Table 2.4: Manufacturing and energy cost of the various steps of production of Li-ion batteries. Table adapted from [20] with permission from Elsevier under a Creative Commons Attribution-Non-Commercial-No Derivatives License.

Manufacturing process	**Cost per year [$]***	**Percentage [%]**	**Throughput**	**Manufacturing processes**	**Energy consumption per cell [kWh]**	**Percentage [%]**
Slurry mixing	7,396,000	7.91	30 min – 5 h	**Slurry mixing**	0.11	0.83
Coating/drying	13,984,000	14.96	35-80 m/min	**Coating**	0.18	1.36
Solvent recovery	4,296,000	4.60	NA	**Drying/solvent recovery**	6.22	46.84
Calendering	4,849,000	5.19	60-100 m/min	**Calendering**	0.38	2.86
Slitting	2,891,000	3.09	80-150 m/min	**Sitting**	0.71	5.35
Vacuum drying	2,990,000	3.20	12-30 h	**Stacking**	0.77	5.80
Stacking	8,086,000	8.65	NA	**Welding**	0.25	1.88
Welding	6,864,000	7.34	NA	**Enclosing**	0.69	5.20
Enclosing	11,636,000	12.45	Depend on the cell design	**Formation/aging**	0.07	0.53
Formation/aging	30,482,750	32.61	Up to 1.5-3 weeks	**Dry room**	3.9	29.37

*The manufacturing cost includes equipment depreciation, labor cost, and plant floor space cost.

2.5.4 Battery Assembly

In the final stages of cell assembly, anodes and cathodes are stacked and welded. External containers are assembled with the introduction of electrolyte and the formation and aging steps are conducted. Welding is done using ultrasonic and spot-welding techniques for pouch cells and cylindrical or prismatic cells respectively. This step also involves the welding of a tab at the end of each electrode rolls of the battery, which is used as electrical connection to the battery terminals.[80] After introduction of the electrolyte, the formation and aging steps consist of cycling the battery at a very slow rate to form a robust solid electrolyte interphase (SEI) layer and promote wetting of the active material. During these steps, the battery is also degassed to increase operational safety. These steps take weeks and can account for more than 30% of the total cost of production.[20]

2.5.5 Limitations

While conventional manufacturing approaches have enabled large-scale production of both supercapacitors and batteries with a variety of active materials and a number of cell geometries (coin, cylindrical, pouch, etc.), they face various limitations which slow innovative design changes and restrict design possibilities. For example, the high capital costs associated with the various required manufacturing equipment prohibit any major change to the manufacturing process such as form factor. Thus, it is currently infeasible to build a battery that fits a specific design whereas, these days, the design is normally built around a battery with set form factor. Furthermore, the relatively thick sandwich-type design of laminated batteries make them relatively inflexible which precludes their use in wearable and flexible electronics. Most microbatteries or microsupercapacitors employed in miniaturized electronics are fabricated using costly cleanroom processes such as chemical vapor deposition and thermal evaporation for thin-film designs, and photolithography and plasma etching for interdigitated architectures, which also suffer from a slow design loop.[81,82] On the other hand, thicker/higher active material loadings are required to increase F_m to improve device energy density. With this in mind, even improvements to energy density in the sandwich configuration by slurry casting is limited in terms of achievable active material loadings/thicknesses due to high stresses that develop during the drying process which are exacerbated with increased thickness and fast drying times.[83] Furthermore, thicker active material films have lower ionic and electronic conductivity which could severely limit power density and charge/discharge rates.

2.6 Advanced Manufacturing Approaches

While significant research attention has focused on the development of new and advanced materials for EES systems, less attention has been paid to advancing electrode and device manufacturing. Advanced manufacturing techniques such as additive manufacturing and laser-based methods can potentially overcome many of the limitations of conventional slurry casting processes and possess other unique advantages. Firstly, these methods can enable the fabrication of electrodes and devices with unique form factors beyond conventional planar sandwich structures, including interdigitated and lattice structures, and even coaxial, parallel and twisted fiber designs. These novel structures possess unique advantages in terms of electrochemical performance. The most commonly employed advanced architecture is a planar, interdigitated design, which enables increased electrode-electrolyte contact area, and also simplifies device manufacturing by entirely eliminating the need for a polymeric separator between the anode and cathode.[21,22] The design prevents short circuiting via control of the distance between the interdigitated fingers and can enable very short ion transport distances and improved device power density by shortening the distance between each finger. These advantages are particularly critical for thick and high-loading electrodes that would otherwise limit power density in a standard sandwich configuration. For thick electrodes, interdigitated designs may also enable increased electrolyte penetration into the electrode and thus higher electrochemical utilization of active material.[22] Moreover, via the careful preparation of precursor substrates, a number of high loading electrodes with novel architectures have been fabricated without the need for additives or polymer binders as well as free-standing electrodes which do not require current collectors, all of which typically lower the overall device energy density.

In addition to their potential electrochemical performance enhancements, unique cell form factors can imbue devices with added functionality, such as flexibility, stretchability, and wearability.[84–86] Moreover, while traditional cells are too bulky for implementation into microelectronics, advanced manufacturing methods are uniquely suited to prepare microsupercapacitors and microbatteries, as they enable the patterning of individual traces ranging from 100 nm to hundreds of microns. Compared to traditional manufacturing techniques, these advanced manufacturing methods are also considered low-cost rapid prototyping methods that enable quick and easy design changes via computer control without re-tooling an entire manufacturing line. Some advanced manufacturing methods, such as laser-based methods, also enable simultaneous active material synthesis and electrode fabrication in a single step, simplifying the overall device manufacturing process. Furthermore, using specific precursor materials,

not only conductive but electrically insulating structures can also be prepared, enabling printing and patterning of all components of an EES device in one step.

2.7 Direct Laser Writing

While the rapid and room-temperature nature of laser-based synthesis methods, including laser-based carbonization, has been widely employed for bulk synthesis of electrochemical active materials, laser-based patterning approaches, often referred to as direct laser writing, can enable the simultaneous synthesis of active materials from a suitable precursor and the rapid patterning of electrodes. These processes utilize a 2D computer model to raster a pattern on a substrate using a laser. The high energy of the laser beam can cause photothermal or photochemical reactions to occur, and can convert many insulating materials into carbonaceous, conductive traces. In 2010, the laser reduction of graphene oxide (GO) to conductive reduced graphene oxide (rGO), termed laser reduced graphene (LRG) was first demonstrated.[55–57] A range of different lasers were used for this purpose, ranging in wavelength from 355 nm to 663 nm. Sokolov et. al observed the formation of CO and CO_2, and the release of H_2O during laser irradiation.[56] With a 663 nm laser, under an air environment, Zhou et al. observed oxidative burning or ablation of the GO, but under inert environments they observed the reduction of the GO.[55] They measured the local temperature of irradiated GO to be >500°C, suggesting a photothermal reduction mechanism.[55] Others with shorter wavelength lasers and different laser powers observed reduction under ambient conditions, indicating that careful control of the laser energy is needed to facilitate reduction of the GO without ablation. El-Kady et al. expanded upon this work in 2012 by using a Lightscribe optical DVD laser (788 nm, 5 mW) to reduce GO and prepare LRG supercapacitors, as seen in **Figure 2.6**.[87] The LRG from this work was highly conductive (1738 S/m), possessed extremely high specific surface areas of 1520 m^2/g, and was very mechanically robust and flexible, with only ~1% change in the resistance after 1000 bending cycles.[87] The rapid nature of the photothermal laser reduction causes simultaneous reduction of the GO and exfoliation, as the rapidly escaping gases push apart the LRG sheets.[87] It was used directly as an electrode for supercapacitors, without the need for binder, additional conductive additives, or current collectors, and resulted in capacitances of 5.02 mF/cm^2 (276 $F/g_{LRG/electrode}$) at 1 $A/g_{LRG/electrode}$.[87] Following these seminal works, the use of laser-processing to fabricate graphene-based devices has rapidly expanded.[88–91]

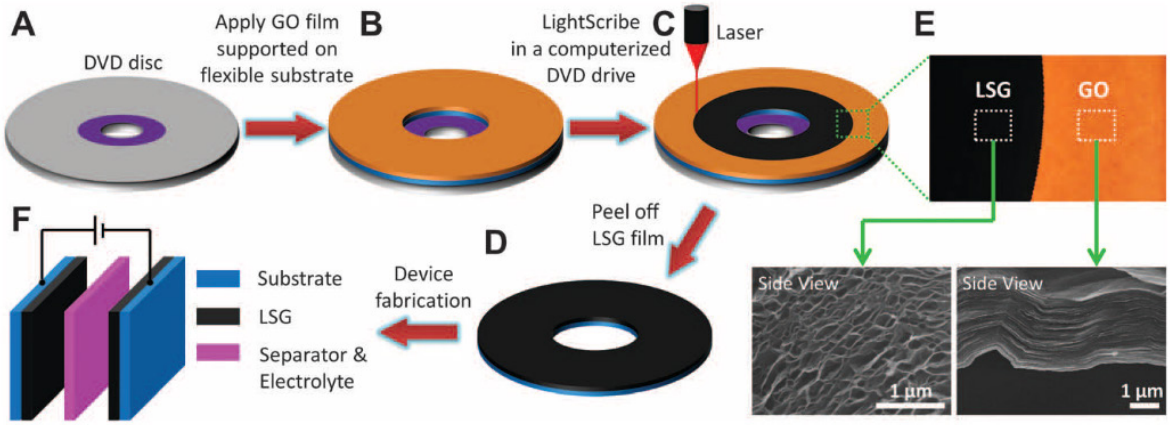

Figure 2.6: Schematic of the fabrication of LRG supercapacitors (referred to in this figure as "laser-scribed graphene, LSG"). a-d) A GO film on a flexible substrate is placed on a Lightscribe-enabled DVD disc. A computer image is then irradiated onto the GO in a Lightscribe DVD drive. e) As shown in the photo, the golden brown GO is converted into black LRG. The low power IR laser changes the stacked GO sheets immediately into exfoliated, few-layered LRG, as seen in the SEM images. f) A symmetric supercapacitor is prepared from two identical LRG electrodes, a separator, and electrolyte. Figure and caption adapted from [87] with permission from AAAS.

2.8 Laser-Induced Graphene

Direct laser writing of graphene was further advanced in 2014, when the Tour group demonstrated that an IR laser could be used to convert commercial polymers such as polyimide (PI, Kapton™) to laser induced graphene (LIG) (**Figure 2.7**).[24] The LIG process is appealing as it is rapid – the large thermal cross-section of traces (~100 µm) allows large areas to be converted in one pass converting ~cm^2 areas in seconds and enabling the possibility of medium-throughput manufacturing. While a range of different laser wavelengths and powers have been employed, most of the field has focused on the use of widely available and inexpensive CO_2 IR lasers that are commonly used in industry and by hobbyists for laser cutting and engraving. Furthermore, LIG formed from PI possesses highly desirable properties for the fabrication of electrodes for electrochemical energy storage, including a high conductivity of ~25 S/cm, and a unique three-dimensional porous structure, due to the rapid escape of gases during the carbonization, which results in a high specific surface area.[24] Furthermore, the LIG material is highly defective, with a number of five- and seven-membered ring defects that can contribute to capacitive energy storage by increasing the density of electronic states in the carbon near the Fermi level.[92] While LIG is not a metal, this increased density of states makes it more "metallic" than pristine graphene, which is a semimetal.[24] Moreover, laser irradiation combines both graphene production and device fabrication and patterning into one rapid step. Since its discovery, this method has been used

extensively for the production of flexible and miniaturizable devices for a wide array of different applications, including energy storage devices such as supercapacitors,[24,93–97] batteries,[98–106] water splitting electrodes,[107] sensors,[108–110] microfluidics[111] and superhydrophobic membranes for water purification.[112,113] In particular, this technology has enabled the miniaturization of supercapacitors, facilitating their integration into microcomputers, lab-on-a-chip, and wearable devices.[109,114,115]

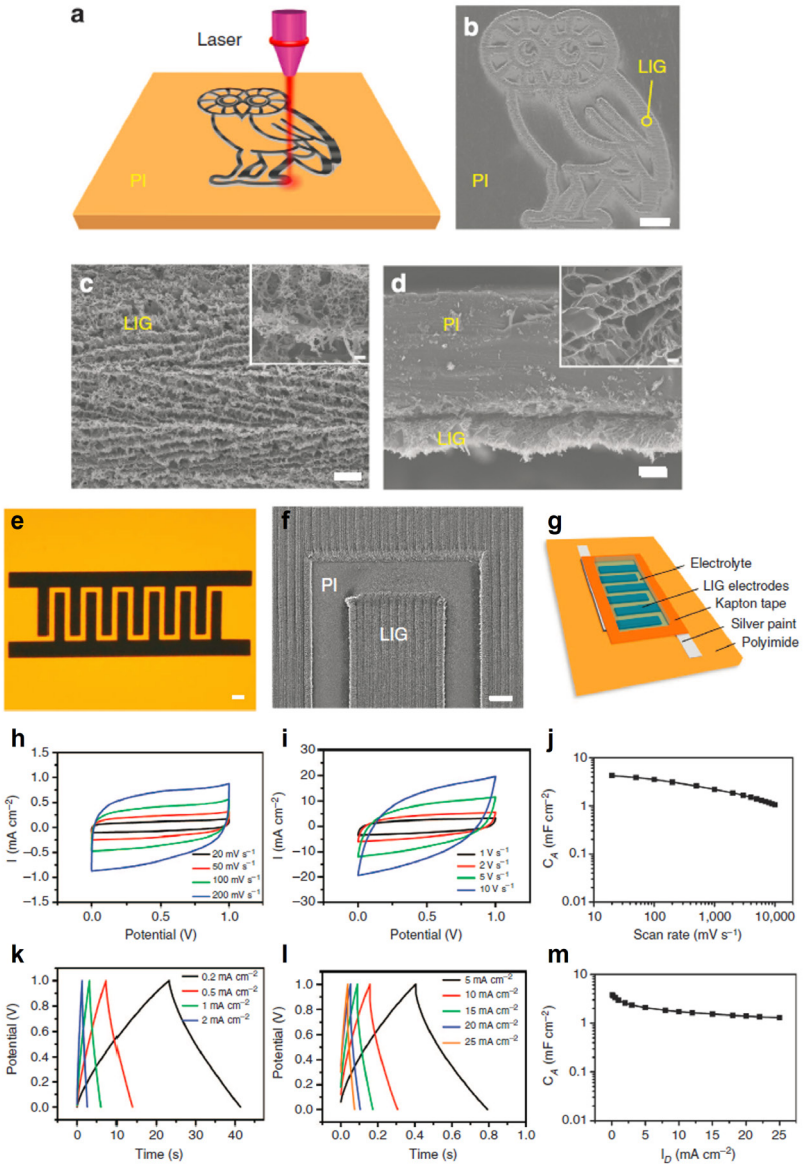

Figure 2.7: Demonstration of LIG process and material. a) Schematic of the synthesis process of LIG from PI. b) SEM image of LIG patterned into an owl shape; scale bar, 1 mm. The bright contrast corresponds to LIG surrounded by the darker-colored insulating PI substrates. c) SEM image of the LIG film circled in b); scale bar, 10 µm. Inset is the corresponding higher magnification SEM image; scale bar, 1 µm. d) Cross-sectional SEM image of the LIG film on the PI substrate; scale bar, 20 µm. Inset is the SEM image showing the porous morphology of LIG; scale bar, 1 µm. Electrochemical performances of LIG-microsupercapacitor (MSC) devices in 1M H_2SO_4. e) A digital photograph of LIG-MSCs with 12 interdigital electrodes; scale bar, 1 mm. f) SEM image of LIG electrodes; scale bar, 200 µm. g) Schematic diagram of LIG-MSCs device architecture. h),i) CV curves of LIG-MSCs at scan rates from 20 to 10,000 mV/s. j) Specific areal capacitance (C_A) calculated from CV curves as a function of scan rates. k),l) CC curves of LIG-MSCs at discharge current densities (I_D) varied from 0.2 to 25 mA/cm^2. m) C_A calculated from CC curves versus I_D. Figure and caption adapted from [24] with permission from Springer Nature.

2.8.1 Laser-Induced Graphene Supercapacitors

In their seminal paper on the LIG process, Lin et al. demonstrated that LIG-based supercapacitors could be prepared from PI in an interdigitated architecture, with the insulating PI between each finger acting as a separator, preventing short circuiting.[24] These initial LIG supercapacitors resulted in areal capacitances of 4 mF/cm^2,[24] which was rapidly increased in their following report to 9 mF/cm^2 when using a stacked architecture and a polyvinyl alcohol (PVA)/sulfuric acid (H_2SO_4) polymer gel electrolyte.[93] Since this report, PVA/H_2SO_4 and PVA/H_3PO_4 gel electrolytes have been widely used with LIG-based supercapacitors, reducing the need for leakproof packaging for liquid electrolytes.[23] Following these initial studies, significant research attention has focused on improving the areal capacitance of LIG prepared from PI, as seen in **Figure 2.8**. One strategy involved doping the PI, by incorporating boric acid during PI synthesis, resulting in B-doped LIG with an areal capacitances of 16.5 mF/cm^2 at 0.05 mA/cm^2,[94] and use of a fluorinated PI substrate which improved performance to 27.5 mF/cm^2.[116] Further strategies to boost areal capacitance have focused on modification of the LIG material to introduce further defects and improve wetting of the electrolyte. Application of an oxygen plasma treatment after laser scribing with a blue laser boosted performance to 31.9 mF/cm^2.[97] Lasing in an O_2 environment enabled capacitances as high as 37 mF/cm^2 – although the addition of sealed gas chambers may limit both the substrate size and the ease and accessibility of the method.[113]

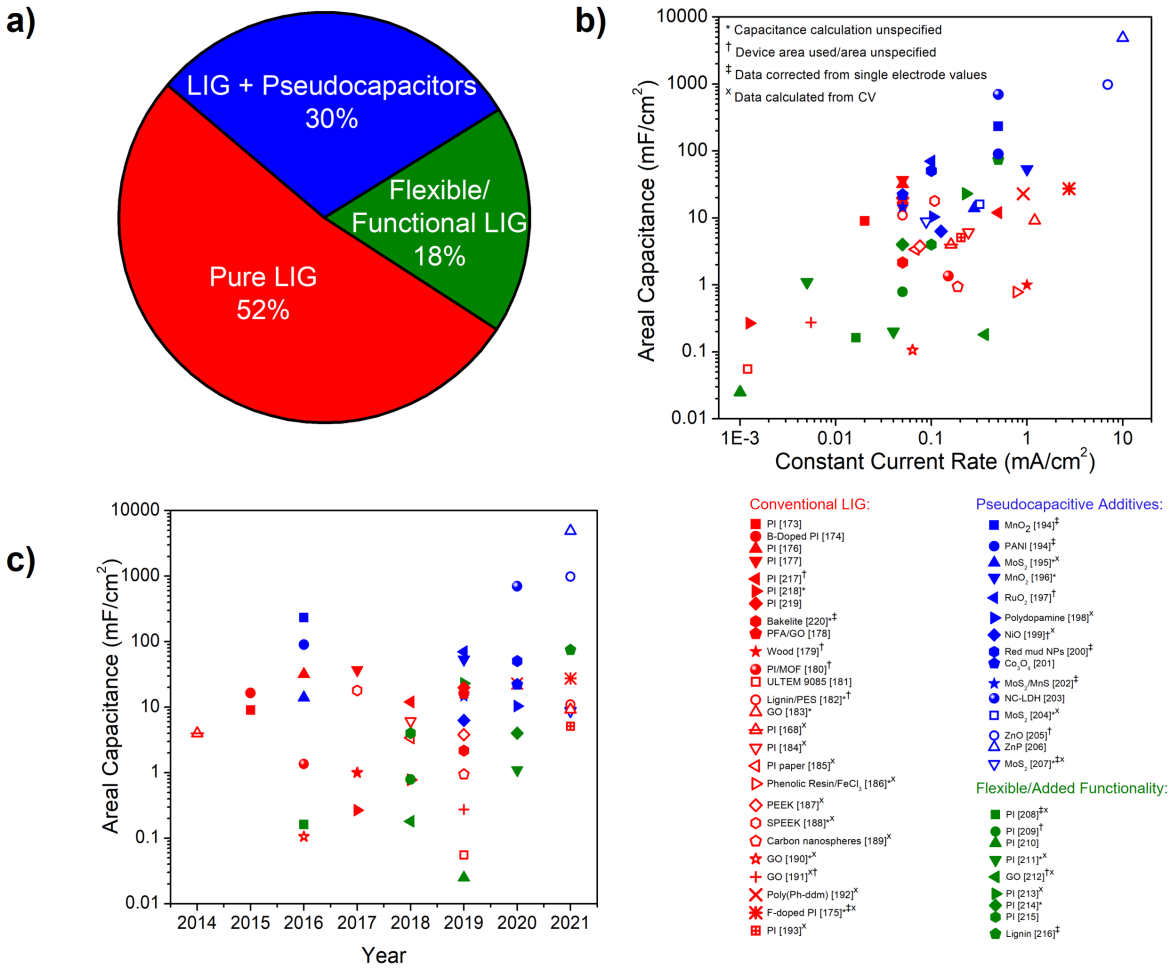

Figure 2.8: Summary of LIG-based supercapacitors prepared from various materials. a) Pie chart of LIG-based supercapacitors. b) Areal capacitance with constant current rate. c) Maximum reported areal capacitance with publication year. Red – Conventional LIG, blue – LIG and pseudocapacitive additives, green – LIG devices with added functionality (i.e. flexibility, etc.). Figure and caption reproduced from our review paper, [23], with permission from Taylor & Francis.

LIG preparation is currently limited to a select set of materials – typically PI, made from precursors, 4,4'-oxydianiline and pyromellitic dianhydride, that are costly, toxic, and derived from petroleum or coal. Thus, great interest has been shown in preparing LIG from inexpensive and green precursors. Methods to expand the range of LIG-precursors, such as through pre-treatment of substrates with fire retardants,[117] the use of lasers of different wavelengths,[95,96] and fabrication in inert environments[117,118] have achieved some success but all of these approaches pose significant challenges that hinder the widespread implementation of LIG devices. Furthermore, the electrochemical performance of current LIG-based electrode materials requires further improvement. LIG-based supercapacitors achieve

relatively low capacitance per area compared to conventional supercapacitors, with higher performance essentially limited to PI-based LIG. Though LIG formation has been expanded to other polymers and resins such as Bakelite,[95] phenolic resin,[96] PEEK,[119] PEI,[24,120] and poly(Ph-ddm),[121,122] all of these materials are also prepared from petroleum-based precursors, and either result in lower capacitances than PI or require complex, multi-step syntheses. Consequently, the need exists for novel LIG precursors that are inexpensive, abundant, easily processable, and based on green or sustainable precursors. While LIG has also been prepared from wood and other biomaterial precursors,[117,118,123–125] most reported capacitances from these bulk materials are around ~1 mF/cm^2. Thus the preparation of high performance devices from sustainable and easily processable materials remains challenging, explaining why PI still remains the most widely used LIG precursor to date.[23]

2.8.2 Laser-Induced Graphene Batteries

While the LIG method has been widely used to prepare supercapacitors, its application for the fabrication of battery electrodes or current collectors is less widely reported and still a developing field.[126] Since the mass loading of LIG formed cannot easily be measured or controlled, it is not typically used as an active material directly, but rather as a porous, conductive scaffold to which active materials can be added. In most examples, LIG has been used in metal-air batteries, as a three-dimensional, carbonaceous framework that can potentially act as a catalyst support, or a catalyst itself for the OER/ORR reaction at the air cathode.[98–101]

While air cathodes have dominated the LIG battery literature, a few studies have recently been reported of the method's extension into other battery chemistries. LIG and LIG-based composites have been recently used as anode materials for lithium-ion batteries,[102–104] but their areal capacities remain far below the 4 mAh/cm^2 typically achieved via slurry casting (typically <1 mAh/cm^2) due to the low loadings of active material (1-3 mg/cm^2), which are far below those used in slurry casting. Recent work has moved instead towards the preparation of LIG/sulfur cathodes, which achieve higher gravimetric capacities (~950-1300 mAh/g),[105,106] with the LIG acting as a conductive framework to imbibe insulating sulfur. However, sulfur loadings reported to date remain low. Only one report achieves an areal capacity above 4 mAh/cm^2 (6.4 mAh/cm^2 at 6.7 mg$_{sulfur}$/cm^2).[106] Thus, LIG-based batteries remain an exciting if relatively unexplored field, particularly for applications as a conductive, porous scaffold for active material deposition in next-generation battery chemistries.

2.9 Lithium-Sulfur Batteries

One of the most promising battery chemistries to replace lithium-ion is the lithium-sulfur battery, which consists of a sulfur cathode and lithium metal anode, as seen in **Figure 2.9**. During discharge at the cathode, elemental sulfur in the form S_8 is reduced to form Li_2S:[3,5]

$$S_8 + 16Li^+ + 16e^- \rightleftharpoons 8Li_2S \tag{2.25}$$

This reaction provides a theoretical capacity of 1672 mAh/g sulfur, an order of magnitude greater than lithium-ion battery transition metal oxide cathode materials.[3,5] During discharge at the anode side, the oxidation of lithium metal to lithium ions occurs:[7]

$$Li_{(s)} \rightleftharpoons Li^+ + e^- \tag{2.26}$$

During charge, Li_2S is converted back into elemental sulfur at the cathode and lithium ions are reduced to plate lithium metal at the anode. The utilization of a lithium metal anode instead of an intercalation compound such as graphite provides a theoretical capacity of 3860 mAh/g, the highest capacity of any anode material, as well as the lowest electrochemical reduction potential, at -3.04 V vs SHE.[7] Cells utilize a microporous polyethylene or polypropylene separator which prevents short circuiting and enables electrolyte transport. The electrolyte typically consists of ether-based solvents, as polysulfide species generated during cycling react irreversibly with the carbonate solvents optimized for the lithium-ion system.[127] A 1:1 mixture of 1,3-dioxolane (DOL) and 1,2-dimethoxyethane (DME) is the most common solvent mixture utilized, with the current optimized salt being 1 M lithium bis(trifluoromethanesulfonyl)imide (LiTFSI). 0.1 to 0.2 M lithium nitrate ($LiNO_3$) is also commonly added to improve cycling by forming a more stable SEI on lithium metal, and preventing the irreversible decomposition of polysulfides.[128] Overall, the full lithium-sulfur cell possesses a voltage of approximately 2.2 V, which is less than that of lithium-ion cells, but due to the high capacity of the active materials, the full cell can provide a theoretical energy density of 2567 Wh/kg,[3] as seen in **Table 2.5**.

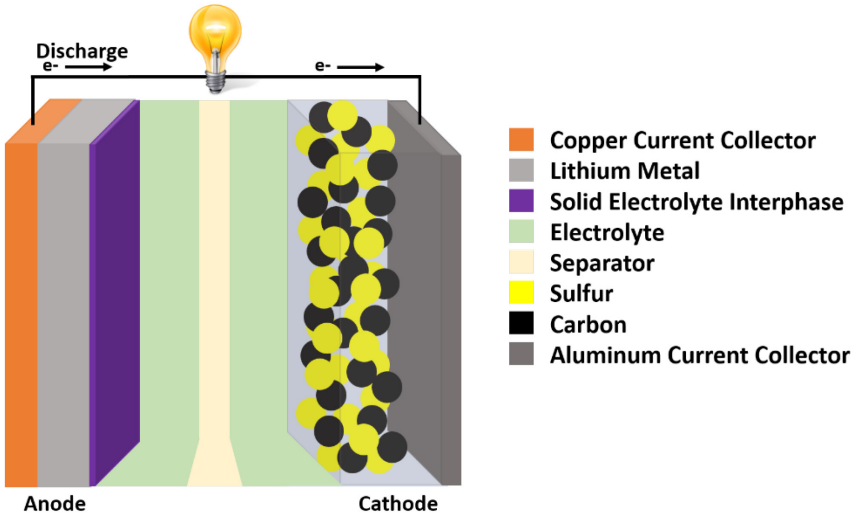

Figure 2.9: Schematic of lithium-sulfur battery.

Table 2.5: Comparison of lithium-ion and lithium-sulfur batteries.

	Lithium-Ion	Lithium-Sulfur
Anode	Graphite	Lithium metal
Cathode	Lithium transition metal oxide	Sulfur
Electrolyte	Carbonate-based	Ether-based
Separator	Polyethylene/Polypropylene	Polyethylene/Polypropylene
Anode Theoretical Capacity (mAh/g)	372 [5]	3860 [3]
Cathode Theoretical Capacity (mAh/g)	140-200 [3,5]	1672 [3]
Full Cell Theoretical Capacity (mAh/g)	100-130 [3,5]	1167 [3]
Voltage (V)	3.3-4.2 [5]	2.2 [3]
Theoretical Gravimetric Energy Density (Wh/kg)	390 [5]	2500 [3,4,6]
Current Achievable Gravimetric Energy Density (Wh/kg)	250 [7]	400 [6]
Theoretical Volumetric Energy Density (Wh/L)	1015 [5]	2200 [5]
Current Achievable Volumetric Energy Density (Wh/L)	700 [7]	700 [129]
Cost ($/kWh)	~150 [130]	~100 (projected) [131]

2.10 Lithium Anode

While much progress has been made in the past sixty years on the sulfur cathode, one of the most formidable challenges of the lithium-sulfur battery remains the lithium anode. Lithium metal is the ultimate anode material, possessing the highest theoretical capacity of any anode at 3860 mAh/g as well as the most negative electrochemical reduction potential of -3.04 V vs the standard hydrogen electrode.[5,7] Furthermore, high capacity, next-generation chemistries such as lithium-sulfur possess non-lithiated cathodes and thereby require lithium anodes to function.

Despite their exceptional theoretical capacities and energy densities, lithium anodes face a host of challenges limiting the safety and cycle life of full cells, as seen in **Figure 2.10**. Firstly, unlike intercalation compounds, lithium metal anodes are "hostless" and undergo an effectively infinite volume change during cycling.[7] This leads to breakage of the solid electrolyte interphase (SEI) layer that initially passivates the lithium metal in the electrolyte.[7] Breakage of this layer leads to exposure of fresh lithium metal to the electrolyte, allowing for further parasitic reactions, consuming both lithium and electrolyte, and forming a thick, resistive SEI layer.[7] These breaks in the SEI layer also contribute to one of lithium metal's greatest challenges – its tendency to electrodeposit as dendritic or mossy morphologies. The needle-like dendrites formed during the charging process can pierce through the battery separator, leading to short circuiting and cell failure.[7] Furthermore, the long, fragile dendrites can break from the anode surface, leading to the accumulation of "dead lithium", which is no longer electrically contacted.[7] This results in loss of active material, and the formation of a thick, resistive dead lithium layer, preventing transport within the cell and leading to steady capacity decay over time.[7] Much research in the last three decades has focused on understanding the mechanisms of dendrite formation during lithium electrodeposition, as well as the structure, composition, and properties of the SEI layer on lithium anodes, in order to control the morphology and efficiency of lithium plating.

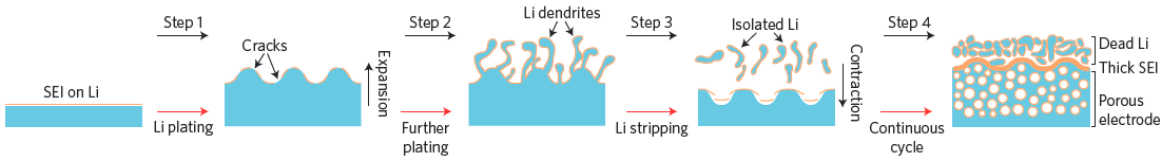

Figure 2.10: Summary of challenges facing lithium anodes. Step 1: Li plating causes volume expansion, which cracks the SEI film. Step 2: further plating causes Li dendrites to shoot out through the cracks. Step 3: Li stripping produces isolated Li which becomes part of the "dead" Li, while volume contraction results in further SEI fracture. Step 4: Continuous cycling causes steps 1–3 to occur repeatedly, and this finally results in accumulated dead Li, thick SEI and porous Li electrode. Figure and caption adapted from [7] with permission from Springer Nature.

2.10.1 Dendritic Lithium Deposition

Dendritic electrodeposition has been observed for several metals at high current densities, including copper and zinc[132] and can be explained by the classical Chazalviel model.[133] At current densities greater than a mass transfer-limited current, the cations in the solution can only supply the applied current for a time referred to as Sand's time before they are depleted, destroying the electroneutrality in solution at the electrode surface.[133] Because of this, a localized space charge develops, which leads

to the formation of dendrite structures.[133] While this theory can explain the formation of dendrites at high current densities, lithium metal forms dendritic morphologies at current densities far below a mass transfer limited current, requiring further understanding of the process of lithium plating at the electrode surface.[132]

Unlike the metals mentioned above, the high reactivity of lithium metal leads to the spontaneous formation of an SEI layer when submerged in electrolyte. Various models are proposed for the SEI layer, but all suggest that the layer is an inhomogeneous mixture of different lithium compounds and salts, with varying lithium ion conductivity.[134] This causes inhomogeneities in ion transport at the electrode surface leading to inhomogeneous nucleation and growth of lithium metal.[134] Additionally, the breakage of this layer due to the severe volume changes of the lithium anode during cycling exposes areas of fresh lithium metal.[7] Lithium plating on this fresh exposed lithium metal requires a much lower overpotential, as it avoids the more resistive path of lithium ion conduction through the SEI layer.[7] Thus, dendrites can more easily form at these cracks.

Another important consideration is that dendrite growth is self-propagating, with lithium deposition occurring more rapidly at dendrite tips than at their sides or at the bulk lithium surface.[7] Some theories suggest that this is due to an increased electrical field surrounding dendrite tips due to their curved structure, while others suggest that three-dimensional diffusion can occur around the tips, while only one-dimensional diffusion can occur at the planar electrode surface.[7] Due to this self-propagating phenomenon, it is essential to minimize the initial heterogeneous lithium ion transport and nucleation that leads to the formation of dendrites.

2.10.2 Solid Electrolyte Interphase

Due to its extremely negative electrochemical reduction potential, when submerged in any electrolyte, lithium will immediately react with the electrolyte components to form a solid electrolyte interphase (SEI).[134] This SEI is formed from the deposition of various solid decomposition products on the anode surface. Typically, this layer is approximately 20 nm thick, ionically conductive and electrically insulating, and passivates the lithium metal surface, preventing further reaction between the lithium metal and the electrolyte.[134] Thus, while the formation of this layer consumes active material and electrolyte, it also plays a key role in enabling proper cell function. While many electrodes, including graphite-based lithium-ion anodes, form an SEI during initial galvanostatic cell cycling, lithium metal

is unique in that it is one of the few electrode materials that spontaneously form an SEI upon submersion in the electrolyte, due to its exceptionally negative standard reduction potential.[134]

The various decomposition products that make up the SEI layer on lithium are dictated by the electrolyte used in the cell. Ether-based solvents such as 1,3-dioxolane and dimethyl ether containing lithium salts such as lithium bis(trifluoromethanesulfonyl)imide (LiTFSI) and lithium nitrate are typically utilized in lithium-sulfur battery research. Decomposition products are a mixture of inorganic and organic lithium salts, including $ROCO_2Li$, ROLi, Li_2CO_3, LiOH, Li_2O, LiF, Li_3N, and oligomers of polydioxolane.[134] X-ray photoelectron spectroscopy (XPS) studies have shown that the decomposition products in an inner, compact layer closest to the anode surface consist mainly of inorganic lithium salts with low oxidation states, such as Li_2O, Li_3N, LiF and lithiated carbon species.[134] The outer side of the SEI layer is porous and consists mainly of organic lithium salts, such as $ROCO_2Li$, ROLi, LiOH, $RCOO_2Li$, and polydioxolane oligomers.[134] These oligomers are formed from the decomposition of 1,3-dioxolane with lithium metal, and are elastomeric in nature, enabling reduced breakage of the flexible SEI layer during cycling in comparison to other electrolytes.[134]

2.10.3 Electrolyte Modifications

One major research direction in overcoming the challenges of lithium anodes is the use of a solid-state electrolyte (SSE). Various types of SSEs have been investigated, including ceramics, such as oxide and sulfide-based lithium compounds, as well as solid and gel polymer-based systems.[135] These systems are attractive as they eliminate many of the hazards of organic electrolytes, such as flammability and low flash point, and eradicate polysulfide shuttling.[135] Solid state electrolytes are especially appealing for lithium metal batteries. In 2005, Monroe and Newman predicted that a solid electrolyte with a shear modulus approximately twice that of lithium metal could suppress dendrite formation.[136] However, despite these advantages, solid state electrolytes remain far from full cell implementation, as most suffer from low room-temperature lithium ion conductivities and exhibit poor interfacial contact and stability.[135]

Another strategy in implementing lithium metal anodes involves tailoring the electrolyte composition through various additives to form a more chemically stable, ionically conductive, mechanically robust, and homogenous solid electrolyte interphase. This includes the use of different lithium salts as the main ion source in the electrolyte, including $LiAsF_6$, $LiPF_6$, and LiTFSI, as well as different electrolyte additives, including lithium nitrate,[128] polyphosphoric acid,[137] Li_2S_6 and P_2S_5 mixtures,[138] indium halide

salts[139] or $In(TFSI)_3$,[140] and cesium or rubidium ions,[141] among others. "Solvent in salt" systems using extremely high lithium salt concentrations have also been explored[142] but remain impractical as the large quantities of the lithium salts utilized are typically prohibitively expensive. While the use of electrolyte additives is a scalable and simple approach to improve the structure and stability of the SEI layer, the additives are typically expensive or not commercially available, and results in full cells – particularly lithium-sulfur cells – are limited. In addition, due to their limited concentration, additives are typically fully consumed during cell cycling, minimizing the overall efficacy of this strategy.

2.10.4 Protective Films

As tailoring of the SEI layer with electrolyte additives has yet to address many of the fundamental challenges facing lithium anodes, much research attention has focused on ex situ methods to implement artificial SEI layers. These layers, like an ideal SEI, should be mechanically robust, chemically stable against lithium metal, and possess high lithium-ion conductivity.

Ex situ approaches can enable uniform coatings of a single, homogeneous lithium salt. One method to prepare these coatings is a vapour phase deposition method, which can enable conformal and pinhole-free coatings. This method has been used to prepare coatings of Li_3N by exposing fresh lithium metal to a nitrogen atmosphere,[143] as well as lithium fluoride coatings using freon gas as the fluoride source.[144] Both coatings improved cycle life of symmetric cells, but the coulombic efficiency of Li_3N-coated lithium cells remained low, at 92%.[143] For LiF-coated cells, fluorine-containing additives further improved cycling performance, indicating that the LiF layer still forms cracks and pinholes during long-term cycling.[144]

One of the benefits of ex-situ coatings is that a wide variety of different materials can be used to prepare protective layers, rather than purely lithium salts. Other inorganic materials, such as Al_2O_3, have been utilized through a direct spin-coating approach on lithium foil.[145] Additionally, a variety of polymer layers have been utilized, including polydimethylsiloxane[146] and copolymers of PEDOT-co-PEO.[147] Much attention has also focused on utilizing atomic layer deposition (ALD), molecular layer deposition (MLD) and vapor phase methods to develop hybrid organic-inorganic coatings, such as alucone layers,[148] composite lithium silicate and mercaptopropyl group coatings,[149] and bilayers of ceramic lithium-ion conductor lithium phosphorus oxy-nitride (LIPON) and an elastomer developed from cycling the lithium anode in a dioxolane electrolyte.[150] While these methods show improvement in cycling stability, increases in cell resistance are still observed during cycling even though fairly low

current densities and charging rates are utilized for testing. Additionally, costly, low-throughput methods such as ALD and MLD are impractical for widespread battery fabrication. Other hybrid methods involve mixing organic and inorganic species together and coating using a traditional method. Various mixtures such as TiO_2 in Nafion have proven successful,[151] but the lithium transport through these films is limited by the degree of mixing. If an inhomogeneous mixing of the inorganic filler is obtained, lithium transport through the film will also be inhomogeneous, resulting in higher localized current densities.

Another direction of ex-situ film research focuses on carbonaceous coatings. Carbon materials are lightweight, easily prepared from a variety of precursors, and their ability to easily intercalate lithium ions at a variety of rates is the backbone of the success of lithium-ion cells. One of the seminal papers in this area came from Yi Cui's group, who utilized a hollow carbon nanosphere film prepared from the flash evaporation of carbon fibers onto self-assembled polystyrene nanoparticles.[152] This film could be utilized directly on copper substrates or the film could be etched from the copper surface and transferred onto lithium metal.[152] Another study from the same group utilized 2D materials such as graphene prepared via chemical vapor deposition onto copper substrates as a protective coating.[153] Still other approaches have utilized films prepared from carbon-coated electrospun polymer fibers[154] and carbon paper interlayers[155] as protective layers. A final novel approach utilized a graphite-lithium metal hybrid anode, which enabled lithium ions to intercalate into the graphite layer before reaching the lithium surface, creating a stable SEI on the graphite surface rather than the lithium.[156] A lithium-sulfur cell prepared from this design maintained a capacity above 800 mAh/g after 400 cycles at 1C, sustaining a coulombic efficiency of over 99%.[156] While these approaches are promising, all of these carbon layers are porous in nature, and cannot fully block the electrolyte from reaching the lithium surface, and therefore an unstable, heterogeneous, and fragile SEI layer will still form and be broken during cycling. Thus, the benefits of these layers lie mainly in mechanically suppressing dendrites rather than being impermeable, electrolyte-blocking and protective. Furthermore, the fabrication of thin, robust, ex-situ carbon films is challenging. Most critically, controlling the location of lithium plating with a carbon coating remains an unsolved issue. For a carbon coating to be effective, lithium ions must move through it and undergo deposition by nucleation and growth beneath it, rather than on the electronically conductive carbon surface. This is challenging since solid-state diffusion through the carbon film can be rate-limiting and promote nucleation on the carbon surface. While innovative approaches have been taken to deal with this, such as using evaporated carbon with a relatively electrically insulating

surface[152] and by connecting a graphite electrode in parallel with the lithium anode,[156] this remains a fundamental challenge with all carbon-based artificial SEI layers.

2.10.5 3D Current Collectors and Host Structures

Both in situ and ex situ films can provide significant advances in suppressing dendrite growth, nucleating and growing smooth morphologies of lithium metal, controlling lithium-ion diffusion, and forming stable, mechanically robust interfaces. However, despite these advances, the exceptionally large volume change of the lithium metal anode during cycling remains a critical issue and leads to some breakage of even the most robust films. Consequently, a great deal of research has focused on designing three-dimensional porous structures that can adequately host lithium metal, as this is the only strategy that can mitigate the overall volume change of the electrode and prevent breakage of the SEI layer.

This can either be done by using a 3D current collector or a host structure. Both consist of porous, conductive scaffolds for lithium metal deposition. However, 3D current collectors are unsealed – the deposited lithium metal is still exposed to electrolyte, and SEI will still form, though the mitigation of the lithium volume change may prevent breakage of the SEI layer. An ideal host structure would possess void space for lithium to deposit, but would be sealed from the electrolyte, preventing the formation of the SEI layer on lithium metal directly. While some hollow structures have been developed, in practice, fully sealing the host structure from a liquid electrolyte is exceedingly challenging, and most host structures to date involve some exposure of the lithium metal to the electrolyte. As such, we will refer to all of these porous scaffolds as lithium metal hosts.

A variety of materials can be utilized as a 3D current collector or host for lithium metal. One of the simplest approaches to introduce 3D void space is the use of a porous copper mesh as a current collector, rather than the conventional copper foil.[157] Lithium-silicon host composites have also been designed by reacting SiO with an overstoichiometric amount of lithium, resulting in a $Li_xSi–Li_2O$ host.[158] However, carbonaceous materials make up the largest body of lithium host research. Carbon-based hosts are extremely promising due to their high electrical conductivity and lightweight nature, as well as their ability to transport lithium ions in the solid state. A variety of carbonaceous lithium hosts have been explored. Lin et al. utilized a spark reaction between graphene oxide and molten lithium to form a layered reduced graphene oxide/lithium anode that maintains 3390 mAh/g capacity and retains approximately 1.16 and 14 times greater capacity than lithium foil in a $Li/LiCoO_2$ cell at 4C and 10C

respectively.[159] Graphene foams have also been utilized as three-dimensional scaffolds for lithium metal, due to their large surface area and flexibility.[160] Symmetric cells prepared from these host structures exhibit stable cycling for over 2000 cycles at 10 mA/cm^2, but only for low amounts of lithium plated, at 0.5 mAh/cm^2.[160] Xie. et al. utilized hollow carbon nanospheres as a lithium host, with an ALD-deposited alumina layer to both fill small pores in the carbon nanospheres, and mechanically induce lithium plating within the nanospheres, and not on their surfaces.[161] Symmetric cells maintained an average 99% coulombic efficiency at 0.5 mA/cm^2 for over 500 cycles.[161] Still other carbon materials including mesoporous carbon,[162] hard carbon,[163] MOF-derived porous carbon,[164] carbon fibers,[165,166] and carbon nanotube/carbon fiber composites[167] have also been explored as host materials.

While these carbon hosts have been promising, many require complex fabrication steps, such as utilizing molten lithium,[159] hydrofluoric acid etching,[161] or costly, low throughput ALD methods.[161] Additionally, few report results in full cells (without significantly excess lithium and electrolyte), and especially in lithium-sulfur cells, indicating that a dire need exists for further research in this field.

Yi et al. addressed some of these challenges in the only study to date to investigate the use of LIG as a lithium metal host.[168] By selectively lasing copper foil covered with PI tape, they fabricated 3D PI pillars, coated with LIG, as seen in **Figure 2.11**.[168] This unique architecture exhibited a higher cycle life than both conventional LIG films and copper at a range of current densities.[168] Moreover, it demonstrated less than 10% capacity loss after 250 cycles at 1C when assembled in a full cell, with a high loading (15 mg/cm^2) lithium iron phosphate cathode.[168] While this study illustrates the potential of LIG as a host material, it is only the first to date, and thus further study into optimizing the properties of the LIG as a lithium nucleation substrate and porous host is needed.

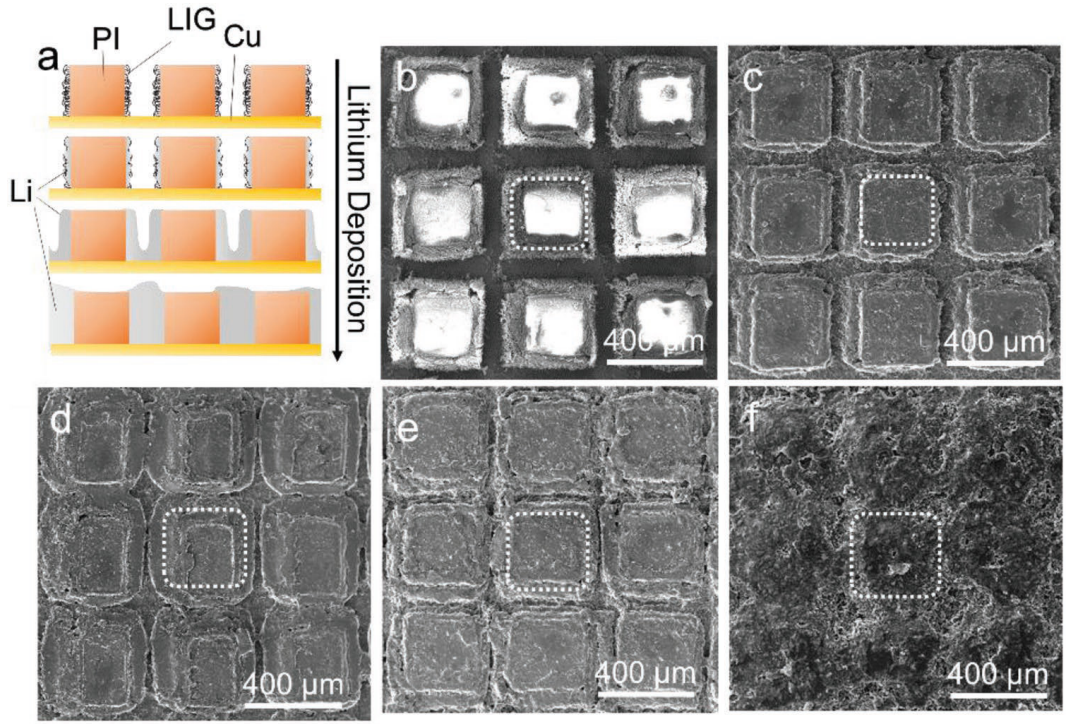

Figure 2.11: Lithium deposition characteristics in LIG host. a) Illustration of the mode of lithium nucleation and growth in LIG host. SEM of Li deposited in LIG host with a specific capacity of b) 0, c) 0.5, d) 2, e) 5, and f) 10 mAh/cm^2 at the current density of 1 mA/cm^2. The white box indicates the position of the PI pillar. Figure and caption adapted from [168] with permission from John Wiley and Sons.

2.10.6 Lithium Host Design

Critically, while many promising host structures have been demonstrated, little fundamental work has been done on host structure and material design. Host materials should be electronically conductive, lightweight so as to introduce as little electrochemically inactive mass as possible, possess void space for lithium deposition, and be lithiophilic. The lithiophilicity of a material is a measure of how well lithium metal deposits on or wets a material. This is a term frequently used in lithium metal anode research, but is challenging to quantitatively measure. The lithiophilicity of a material can be visualized by examining the contact angle of molten lithium on a substrate, as seen in **Figure 2.12**. Due to the challenges associated with performing this measurement in a glovebox above the melting point of lithium metal (~180 °C), this is typically done qualitatively (i.e. by assessing if the contact angle is low or high, without numerical measurement), where low contact angles of lithium indicate a lithiophilic material, while high contact angles indicate a lithiophobic material.

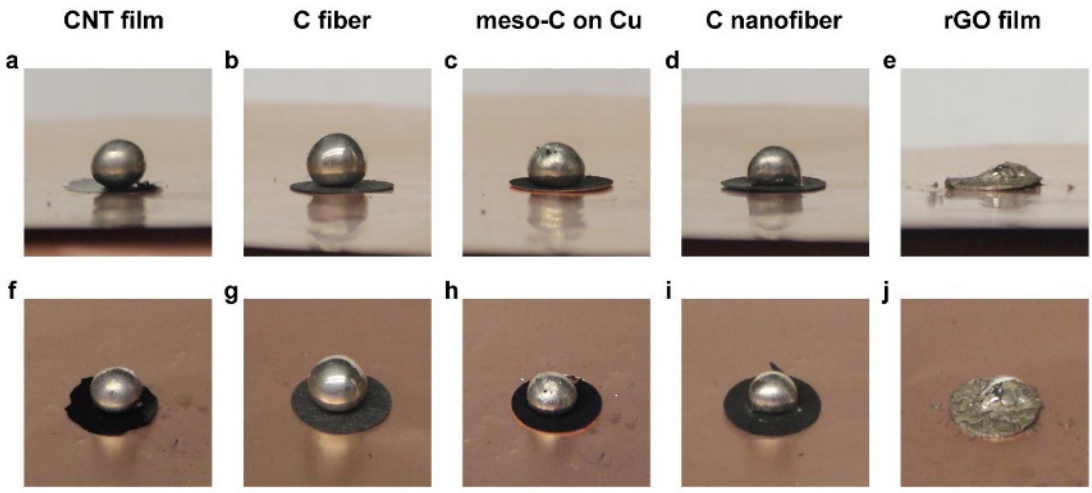

Figure 2.12: Lithiophilicity of various carbon materials, as indicated by molten lithium wetting on a,f) CNT film, b,g) carbon fiber, c,h) mesoporous carbon, d,i) carbon nanofiber, and e,j) rGO film. The rGO film is lithiophilic while the other carbon materials are lithiophobic. Figure and caption adapted from [159] with permission from Springer Nature.

The importance of the lithiophilicity of the lithium host can be further elucidated by considering the electrochemical nucleation of lithium on a surface via classical nucleation theory. Classically, nucleation is controlled by the decrease in free energy associated with forming a new phase, which is the driving force of the nucleation process, and the increase in surface energy from the formation of a new interface, which controls the thermodynamic nucleation barrier.[169]

For homogeneous nucleation of a spherical nucleus, the Gibbs free energy change as a function of the nucleus radius, r, is:[170]

$$\Delta G_{hom} = -\frac{4}{3}\pi r^3 \Delta G_v + 4\pi r^2 \gamma_{LE} \tag{2.27}$$

where γ_{LE} is the surface energy of, in this case, the lithium-electrolyte interface and ΔG_v is the free energy change per volume, which for electrodeposition is related to the magnitude of the deposition overpotential, η,:[170]

$$\Delta G_v = \frac{F|\eta|}{V_m} \tag{2.28}$$

where F is Faraday's constant and V_m is the molar volume of lithium. An overpotential (η) is the potential difference between the non-equilibrium and equilibrium potential for a redox event:

$$\eta = E_{non-equilibrium} - E_{equilibrium} \tag{2.29}$$

Increasing the magnitude of the overpotential effectively lowers the nucleation energy barrier, by changing the electrochemical supersaturation at the working electrode.[170] For heterogeneous nucleation, the nucleation barrier is lowered compared to homogeneous nucleation, via the multiplication of a factor related to the contact angle, θ:[171]

$$\Delta G_{het} = f(\theta)\Delta G_{hom} \tag{2.30}$$

where

$$f(\theta) = \frac{2-3\cos\theta+\cos^3\theta}{4} \tag{2.31}$$

and where the contact angle, θ, is defined as:[171]

$$\cos\theta = \frac{\gamma_{SE}-\gamma_{SL}}{\gamma_{LE}} \tag{2.32}$$

where γ_{SE} and γ_{SL} are the surface and interfacial energies of the substrate-electrolyte and substrate-lithium interfaces respectively. Changes in the lithium nucleation substrate will affect both γ_{SE} and γ_{SL}. Choosing an effectively lithiophilic material will lower the substrate-lithium interfacial energy, lowering the contact angle and thus the nucleation barrier. While lithium electrodeposition is much more complex in practice, and deviates from classical nucleation behaviour in many ways, including the presence of the SEI layer and the formation of deposits of varying morphologies,[172] these general principles still guide lithium host design.

As measuring the molten lithium contact angle is experimentally challenging, Yan et al. demonstrated that a more quantitative and direct measure of lithiophilicity is the overpotential for lithium nucleation on a material.[173] When lithium is galvanostatically plated on a substrate, the voltage profile follows a shape similar to that seen in **Figure 2.13a)**, where below 0 V vs. Li/Li^+, there is an initial dip in the voltage profile, associated with lithium nucleation, before it plateaus at a voltage slightly below zero as the lithium nuclei steadily grow in size. The voltage difference between the bottom of this initial dip and the voltage plateau is thus the lithium nucleation overpotential, η_{nuc}, while the voltage difference between the voltage plateau and 0 V is the lithium deposition overpotential, η_{dep}. Thus, measurement of the magnitude of the lithium nucleation overpotential provides direct insight into the magnitude of the lithium nucleation barrier on different materials.

Yan et al. electrochemically plated lithium metal on a range of different metallic substrates and observed dramatically different overpotentials for lithium nucleation, depending on the material, as

seen in **Figure 2.13**.[173] For example, a significant overpotential for lithium nucleation is observed on copper substrates (~40 mV at 10 μA/cm^2), the commonly employed lithium anode current collector.[173] However, nearly zero overpotential is observed on gold.[173] The overpotential for this heterogenous nucleation of lithium onto another solid surface is dependent on the interfacial energy between lithium metal and the substrate, which in turn is increased by a mismatch of the crystal structures of lithium and the solid substrate.[173] In the cases of both copper and gold however, a crystal structure mismatch occurs with lithium metal (both are FCC crystals, while lithium is BCC).[173] However, the phase diagrams of lithium/copper and lithium/gold reveal that while no stable alloys or mixed phases of lithium and copper form, several alloys of lithium and gold exist.[173] Notably, at an atomic ratio of lithium of nearly 100%, gold exhibits some limited solubility in lithium.[173] This solid solution enables the deposition of lithium metal on gold with effectively zero overpotential. Similarly, a range of different overpotential behaviour is observed on other conductive substrates, including Pt, Al, Mg, Zn, Ag, Si, Sn, Ni and C.[173] This lithiophilic behaviour of gold is exploited to prepared hollow carbon shells that contain gold nanoparticles as a lithium host, and lithium is found to preferentially deposit on the gold within the shells, rather than on the surface.[173] This demonstrates that the development of a lithiophilic host material with a low lithium nucleation overpotential is critical to control lithium deposition. Indeed, since this seminal work, the addition of lithiophilic materials such as gold, silver, and zinc oxide into host materials in order to control lithium nucleation and growth has been widely employed in the field.[174–177]

It is worth noting at this point that the lithium nucleation process is very complicated and influenced by both kinetics and thermodynamics. Lithium ions are driven to the electrode surface via an electric field, concentration gradient, and electrostatic interactions with electronegative sites on the electrode.[169] They bind to electronegative sites on the electrode surface, and following adsorption, are reduced to form lithium metal via electron transfer.[169] Consequently, the experimentally measured lithium nucleation overpotential has contributions from many processes: charge transfer, mass transport, chemical reaction, and crystallization.[170,178] While Yan et al. utilize low plating current densities and thus assume that the overpotentials they measure are purely controlled by the thermodynamic differences in the nucleation process on different substrates, in practice, kinetics and mass transport may also contribute.

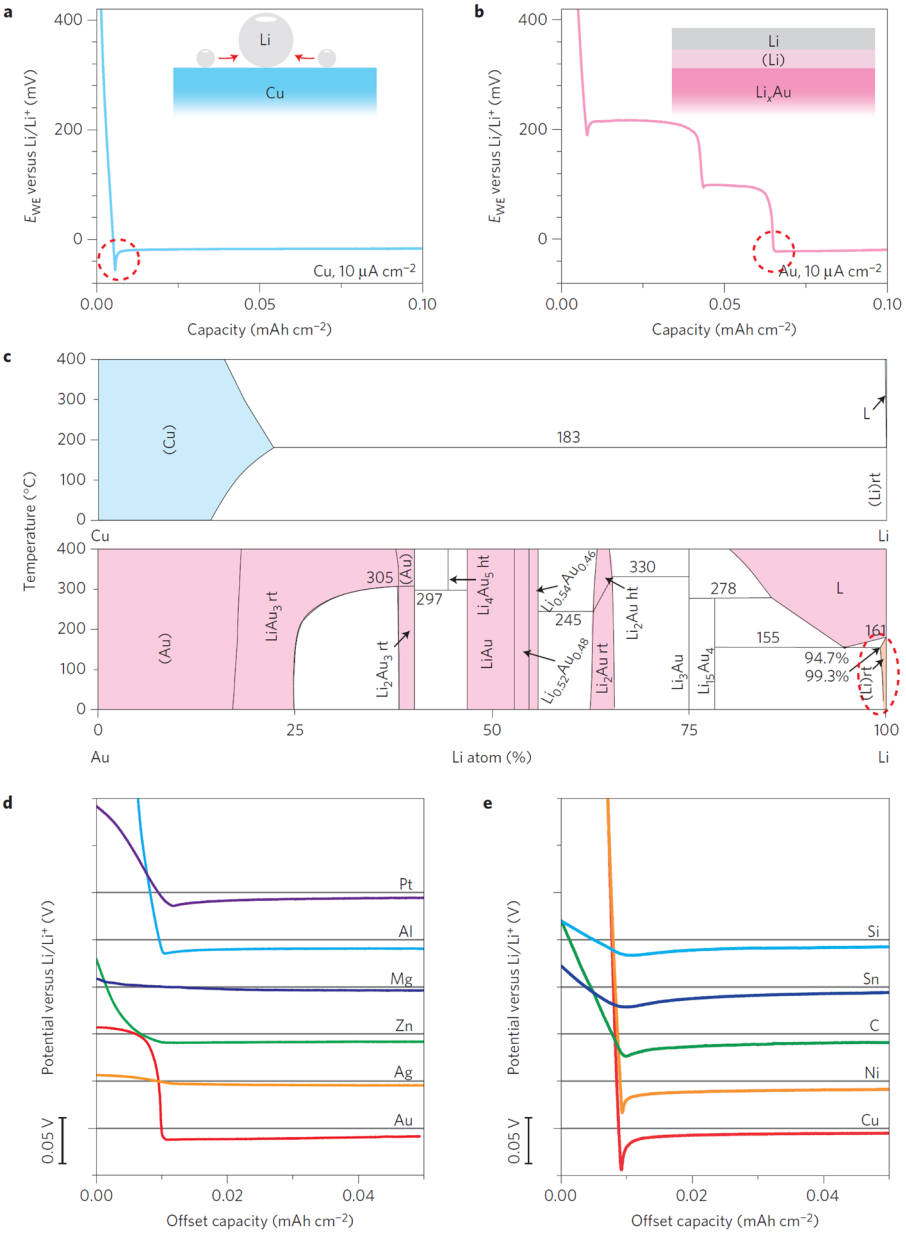

Figure 2.13: Overpotential for lithium deposition on different substrates. a) Voltage profile of galvanostatic Li deposition on a copper substrate at 10 μA/cm^2. E_{WE} refers to the potential of the working electrode. A clear overpotential was observed, as circled by the dashed line. The inset shows a schematic mechanism of Li nucleation, which explains the extra energy involved. b) Voltage profile of galvanostatic Li deposition on a gold substrate at 10 μA/cm^2. As indicated by the dashed circle, no overpotential was observed at the onset of Li metal plating. The inset shows a schematic of how the solid solution buffer layer of Au dissolved in Li reduces the nucleation energy. c) Phase diagrams of lithium with copper (top) and gold (bottom). The region where Au dissolved in Li is circled by the dashed line. L refers to liquid, whereas (Li)rt means lithium metal phase at room temperature. d,e) Voltage profiles of various materials during lithium deposition. Figure and caption adapted from [173] with permission from Springer Nature.

Nonetheless, the use of costly gold or silver nanoparticles is not practical for large-scale battery fabrication. Moreover, as previously discussed, nearly all host materials used for lithium metal to date are carbon-based due to their inexpensive, lightweight, and conductive nature. Thus, controlling the lithiophilicity of carbonaceous hosts directly is key to designing lithium host materials. This could potentially be done via doping of the carbon with different functional groups and heteroatoms that could significantly alter the surface chemistry of the material. A key parameter that defines the lithiophilicity of a surface is the strength of the electrostatic interaction between a lithium ion and an electronegative group on the material surface. Chen et al. computationally investigated the lithiophilicity of heteroatom doped-graphene by calculating the binding energy of lithium to various functional groups on the graphene surface.[169] As seen in **Figure 2.14**, many of these groups possess more negative binding energies with lithium than pristine graphene (G), indicating that heteroatom doping is one strategy to create a lithiophilic host material.[169] Notably, the dopants that result in the strongest binding energies include B, P, N, S, and O, though for N, S, and O, this is dependent on the specific functional group formed.[169] However, this is one of the only studies to date on the effect of doping on a carbon material's lithiophilicity, and it is mainly computational in nature, with only one experimental proof-of-concept included. More fundamental studies on the overpotential of lithium nucleation on different carbon materials would be invaluable in designing improved lithium metal hosts.

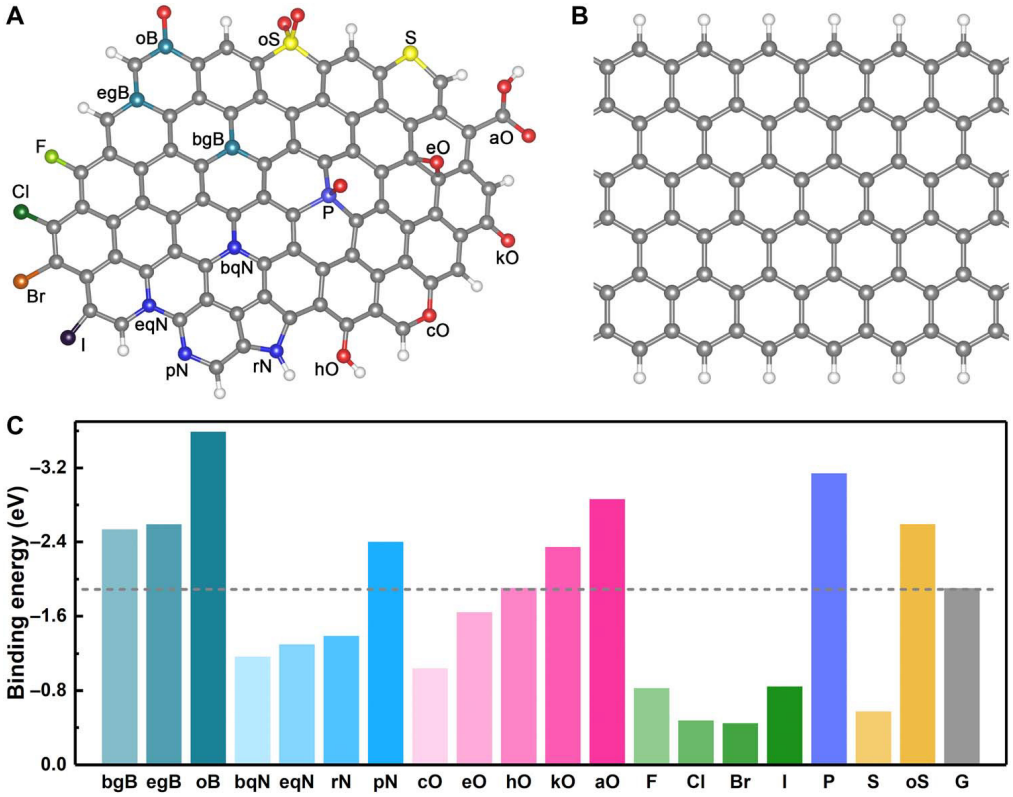

Figure 2.14: Summary of computationally calculated binding energies for different heteratom-containing functional groups on graphene. a) Heteroatom-doped graphene model. b) Pristine graphene model. c) Summary of binding energies for different functional groups. G denotes pristine graphene. Adapted from [169] with permission from AAAS under a Creative Commons Attribution-Non-Commercial license.

2.11 Sulfur Cathode

Sulfur possesses the highest theoretical capacity for any solid cathode material.[8,179] This stems from the combination of both its relatively low molecular weight, and the fact that each sulfur atom can react with two lithium ions.[3] Beyond its high capacity, sulfur is the tenth most abundant element in the universe[8] and is also a common byproduct of the fossil fuel industry, making it extremely cheap.[8] Additionally, its non-toxicity and low melting point can be an added benefit in manufacturing cathodes in simple, green, and energy-efficient methods.[3] These combined factors make sulfur a compelling replacement for current lithium-ion battery cathodes, which contain toxic, expensive, and rare transition metals.

However, since initial work on sulfur cathodes in the 1960s, many challenges have limited their widespread implementation. The first critical issue is that sulfur and its final discharge product, Li_2S, are electrically insulating, with a room temperature conductivity of 5×10^{-30} S/cm.[180] This necessitates

the addition of high surface area conductive material into the cathode in order for charge transfer processes to occur, adding inactive mass and limiting the fraction of active material in the cathode.[3,4,8] A second key issue is the formation of soluble polysulfide species during the charging and discharging processes, which results in "the shuttle effect", in which these species migrate out of the cathode and can react with the lithium anode to form insoluble Li_2S at the anode surface.[10]

Another challenge of the sulfur cathode is its effective volume change during cycling. As sulfur cathodes take in two lithium ions per sulfur atom, they undergo an approximately 180% volume change,[8] which is enormous compared to typical lithium ion cathodes, which undergo a nearly 0% volume change.[181] This volume change can lead to mechanical failure of the cathode if it is unable to accommodate it. Finally, sulfur cathodes cannot be employed with the carbonate-based electrolytes typically used for lithium-ion batteries, as soluble polysulfides react immediately and irreversibly with these solvents.[127] This necessitates the use of ether-based electrolytes, which possess high vapor pressures, posing challenges for vacuum-based processing and flammability concerns.[3]

2.11.1 Conductive Additives for Sulfur Cathodes

Due to the intrinsically low conductivity of sulfur and Li_2S, various conductive additives have been explored to facilitate charge transport within sulfur cathodes. These additives should possess a high electrical conductivity, high specific surface area, and be lightweight, so as to limit the mass of inactive additives within the cathode. While many different types of additives have been explored, including conductive polymers,[182] metal foams,[183] and metal organic frameworks,[184] most cathode designs utilize carbon-based materials, due to their high specific surface areas, low density, high conductivity, and low cost, enabling good rate performance with low carbon loadings.[8,9] Furthermore, a wide array of high surface area carbon materials can be synthesized, with tunable surface chemistry and porosity, including mesoporous carbon materials,[185] carbon nanotubes,[186] activated carbons,[187] carbon fibers,[188] carbon blacks,[180] and graphene-based materials.

Among these carbon materials, great attention has been placed on the use of graphene as a conductive scaffold, as it possesses extremely high electrical conductivity and exceptional specific surface area (theoretical SSA of 2630 m^2/g).[8] Furthermore, due to its monolayer structure, graphene sheets possess superior mechanical properties and flexibility, which are important to accommodate volume changes during cycling,[8] making graphene an ideal candidate material to provide a lightweight conductive scaffold for sulfur cathodes.

The solubility of intermediate polysulfides in the Li-S electrolyte leads to redistribution of sulfur during cycling[189–191] which is why understanding and optimizing processes to achieve highly intimate mixing of sulfur and carbon filler have not garnered much attention in the research community. However, the development of strategies to uniformly coat carbon materials with sulfur remains critical, as large insulating sulfur particles are not fully electrochemically converted during cycling, leading to low sulfur utilization and poor capacity.[192] Similarly, one key failure mode of sulfur cathodes is their mechanical degradation due to the large volume change of the cathode during charge and discharge (80%), which leads to pulverization and loss of electrical contact.[193–195] The uniform distribution of sulfur in the cathode is critical to ensure that the mechanical stress caused by the volume change during cycling is well-distributed about the cathode. This is critical for maintaining mechanical integrity of the cathode, particularly for increased sulfur loadings, which are essential to achieve high energy densities. Furthermore, as the field moves toward the use of solid state electrolytes, in which polysulfides remain insoluble,[135,193,196–198] the redistribution of sulfur cannot be relied upon for high performance, necessitating the development of simple, cost-effective and scalable approaches for the fabrication of well-distributed sulfur/carbon composites.

Several methods have been established to mix insulating sulfur intimately with conductive additives, as seen in **Figure 2.15**.[9] The simplest and most common approach is melt imbibition, in which sulfur is melted at ~160 °C and subsequently coats the solid carbonaceous material while in the liquid state.[185,199–201] Though effective, melt imbibition is time-consuming, hard to control, energy intensive, and often requires post-treatments to improve sulfur distribution and remove large insulating aggregates.[9] Furthermore, the melt imbibition approach is only suitable for carbonaceous materials which possess a well-defined internal porosity, such as mesoporous carbon.[9] Various other methods can be utilized, including mechanical mixing of carbon and sulfur, as well as vapor phase infiltration of gaseous sulfur into the pores of the carbonaceous material.[9] However, all of these traditional forms of sulfur-carbon composite formation involve mixing sulfur with a solid carbon phase, which is challenging when utilizing nanomaterials such as graphene, as the strong $\pi - \pi$ interactions between the graphene sheets will cause re-stacking and aggregation, limiting the exposed surface area during the sulfur coating. Thus, to fully enable the use of these materials, the development of feasible solution-based processing routes where the carbonaceous nanomaterial is coated while in a de-aggregated and dispersed state is essential.

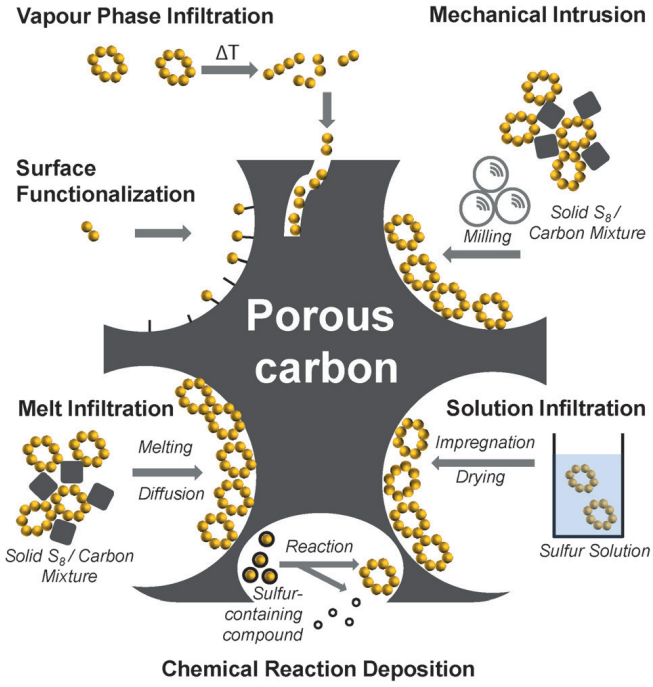

Figure 2.15: Different methods for preparing carbon/sulfur composites. Figure and caption adapted from [9] with permission from John Wiley and Sons.

Several solution-based methods have been investigated for the purpose of coating graphene and other carbonaceous nanomaterials with sulfur, but all are fraught with limitations. Sulfur is insoluble in water and most organic solvents, and thus, many solution-based approaches involve dissolving sulfur in CS_2,[202,203] which is highly toxic and impractical for large-scale synthesis.[9] Other approaches look at forming sulfur in situ from hydrophilic sulfur sols. These strategies utilize a sulfur precursor, which undergoes a chemical reaction in dispersion with the carbonaceous material to produce sulfur microparticles known as sols. Evers et al. demonstrated the use of this approach by mixing sodium polysulfides (Na_2S_x) with a dispersion of graphene oxide (GO) and 5% HCl, where the polysulfides were oxidized in situ to produce sulfur particles wrapped with slightly reduced graphene oxide.[204] While composites with sulfur content as high as 87% were prepared with this one-pot approach, the particles were micron-sized, leading to limited capacity. Zu et al. utilized a similar approach to prepare sulfur particles from sodium thiosulfate ($Na_2S_2O_3$) precursors in dispersion with hydroxylated graphene nanosheets, achieving high initial capacities of 1277 mAh/g at C/2, although the specific areal sulfur loading was not reported.[205] Other studies have employed similar strategies, using precursors such as Li_2S_8[206] and other polysulfides,[207] as well as sulfur-amine chemistry, in which sulfur nanoparticles can

be formed from the decomposition of complexes of sulfur and amines such as ethylenediamine (EDA).[193,208,209]

While these approaches have enabled solution-based processing of graphene/sulfur nanocomposites, they all utilize hydrophilic sulfur sols, in which the sulfur particles are prepared in situ from chemical precursors, which are typically much more costly than inexpensive elemental sulfur. Furthermore, hydrophilic sols possess unreacted sulfur precursor and electrochemically inactive groups at the surface of the sulfur particles,[210,211] which remain present in the final active material and may result in side reactions resulting in limited faradaic efficiency and capacity loss. Despite the large amount of research on this topic, a need remains for simple, green and cost-effective methods to effectively and directly coat carbonaceous materials with elemental sulfur in uniform, thin, and conformal coatings.

Conversely, hydrophobic sulfur sols, also known as Weimarn sols,[212,213] remain largely unexplored for applications in sulfur cathode preparation. Weimarn sols are prepared via the dissolution of sulfur in a suitable water-miscible organic solvent, followed by the rapid addition of this solution into a large volume of water.[210] The extremely low solubility of sulfur in water (5×10^{-6} g/L at 25°C) produces submicron sulfur particles, which have been shown to consist of liquid or amorphous sulfur.[210] This approach is simpler, scalable and utilizes elemental sulfur and aqueous processing, making it an attractive alternative to hydrophilic sol-based processing methods for the fabrication of high performance sulfur cathodes. Recent work from our group demonstrated the use of these hydrophobic sulfur sols to prepare sulfur cathodes by trapping of sol particles within a network of GO and polyethyleneimine (PEI), followed by a hydrothermal step to both reduce the GO and melt the sulfur particles for improved distribution, as seen in **Figure 2.16**, resulting in practical energy densities of >400 Wh/kg.[214] While demonstrating the simplicity and promise of hydrophobic sulfur sols, this approach merely trapped the sols in solution, and relied on a secondary heat treatment to enable better coating of the carbon materials with sulfur. Furthermore, the reduced graphene oxide (rGO) used in this method is prepared via a low temperature heat treatment, resulting in a carbon material with many remaining oxygen-containing functional groups and poor conductivity. Further fundamental studies on the interaction of these unexplored hydrophobic sulfur sols with carbon and graphene-based materials are critical to develop aqueous processes in which carbon nanomaterials can be coated with sulfur in dispersion.

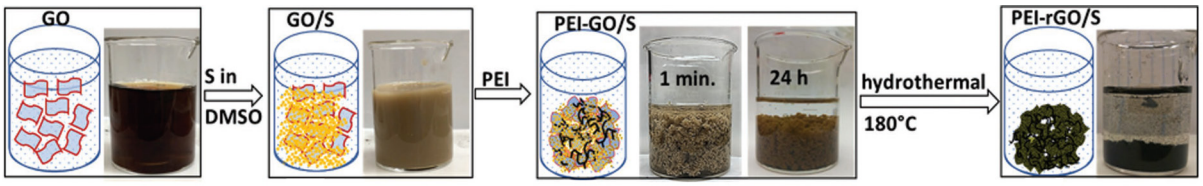

Figure 2.16: Schematic of the synthesis of PEI–rGO/S composite starting from the GO suspension followed by the addition of dissolved sulfur in DMSO to form a hydrophobic sulfur sol, followed by modification with PEI and its hydrothermal treatment along with the digital images of these steps of the synthesis. Figure and caption adapted from [214] with permission from John Wiley and Sons.

2.11.2 Polysulfide Scavengers and Blocking Agents

Beyond the insulating nature of sulfur and Li_2S, the other significant challenge impeding sulfur cathodes is the dissolution of intermediate polysulfide species during charge and discharge. During the discharge process of a lithium-sulfur cell, elemental sulfur in the form of S_8 is first converted to long-chain polysulfides such as Li_2S_8 and Li_2S_6, which are then converted into shorter polysulfides such as Li_2S_4 and Li_2S_2, and finally to Li_2S, as seen in **Figure 2.17**.[3] These polysulfide species are soluble in the ether-based electrolytes utilized in lithium-sulfur cells, and thus redistribution of the sulfur species occurs within the cathode during cycling.[3] Because sulfur itself is not ionically conductive, it is critical that the sulfur species in the cathode are accessible to the electrolyte of the cell for the electrochemical reactions to proceed; however, this enables migration of the soluble polysulfides out of the cathode.[3] These species can then diffuse towards the lithium anode, at which they irreversibly reduce to form Li_2S, resulting in permanent capacity fade.[10]

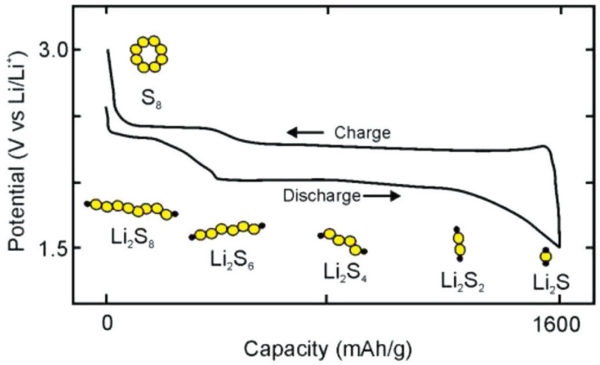

Figure 2.17: Charging and discharging voltage profile for a lithium-sulfur cell, illustrating the formation of intermediate polysulfides. Figure and caption adapted from [3] with permission from John Wiley and Sons.

Two overall approaches are typically utilized in order to prevent polysulfide migration. The first involves modifying the battery separator with species that can either interact strongly with and trap polysulfide species, or with coatings that limit the diffusion of the polysulfide species through the

separator.[215] While this approach has demonstrated improvements in cycle life, it does not solve the fundamental issue of the migration of polysulfides out of the heart of the cathode, and instead merely traps them at the cathode surface. The second strategy involves modifying the cathode itself with additives that interact with polysulfide species, preventing their migration out of the cathode. A variety of additives can be used for this purpose, but polymers are commonly employed, as they can also act as an adhesive and flexible binder for the electrode, which can be critical to enable its large volume change. A wide variety of polymers containing polar heteroatoms such as oxygen and nitrogen have been employed to interact with and trap polysulfides through either hydrogen bonding or polar-polar interactions, including polypyrrole,[216] polyethyleneimine (PEI),[214] polydopamine,[217] polyvinylpyrrolidone,[218] and poly(ethylene oxide) (PEO),[185] among others. As discussed earlier, previous work from our group demonstrated that cathodes prepared from sulfur composites with rGO and PEI could be prepared with high energy densities. Importantly, the inclusion of PEI also limited polysulfide shuttling, and enabled excellent cycle life, with 0.028% capacity loss per cycle over 810 cycles at 0.75C, indicating that this is a promising strategy to overcome the polysulfide shuttling challenge.[214]

2.12 Research Objectives

The overarching objective of this thesis is to develop graphene-based electrodes for supercapacitors and next-generation batteries via advanced and sustainable fabrication methods. This work has value for both fundamental science and device engineering, as it will explore fundamental mechanistic studies, including the formation of LIG from different precursors and the nucleation of active materials such as lithium and sulfur onto graphene, as well as focusing on fabricating devices with improved capacitance, capacity, and energy density.

The specific objectives are as follows:

1. Develop a new, biomass-derived carbon precursor for the fabrication of LIG-based electrodes.

2. Improve the surface area and areal capacitance of LIG traces via the implementation of precursor additives.

3. Develop strategies to introduce heteroatom dopants into LIG in order to improve lithiophilicity for controlled lithium plating for lithium metal anodes.

4. Develop a method to better couple elemental sulfur with graphene through aqueous solution processing.

2.13 Thesis Outline

This thesis is organized into seven chapters. The previous chapter, Chapter 1, provides an introduction to the thesis and motivation for the work. The present chapter, Chapter 2, provides a comprehensive literature review of batteries, supercapacitors, performance metrics, and graphene electrodes. Chapter 3 focuses on the formation of LIG from PFA, a biomass-derived sustainable resin which has never previously been studied as an LIG precursor, as well as the use of GO as a carbonization aid, and the development of PFA/GO-derived LIG supercapacitors. Chapter 4 focuses on the development of LIG supercapacitors from composites of PFA and inexpensive, abundant sodium salt microparticles which can simultaneously boost the LIG surface area via a templating effect and dope the LIG formed with different heteroatoms depending on the salt employed. Following the optimization of the surface area and surface chemistry of the LIG via studying its performance as a supercapacitor, Chapter 5 focuses on the investigation of different LIG materials from Chapter 3 and Chapter 4 as potential lithium metal anode hosts, by studying the nucleation of lithium metal on the LIG surface. Chapter 6 focuses on the aqueous solution-based, room-temperature fabrication of graphene/sulfur composites for high energy density sulfur cathodes. Finally, the conclusions of this thesis and recommendations for future work are presented in Chapter 7. A schematic outline of the four main projects discussed in Chapters 3, 4, 5, and 6 can be seen in **Figure 2.18**.

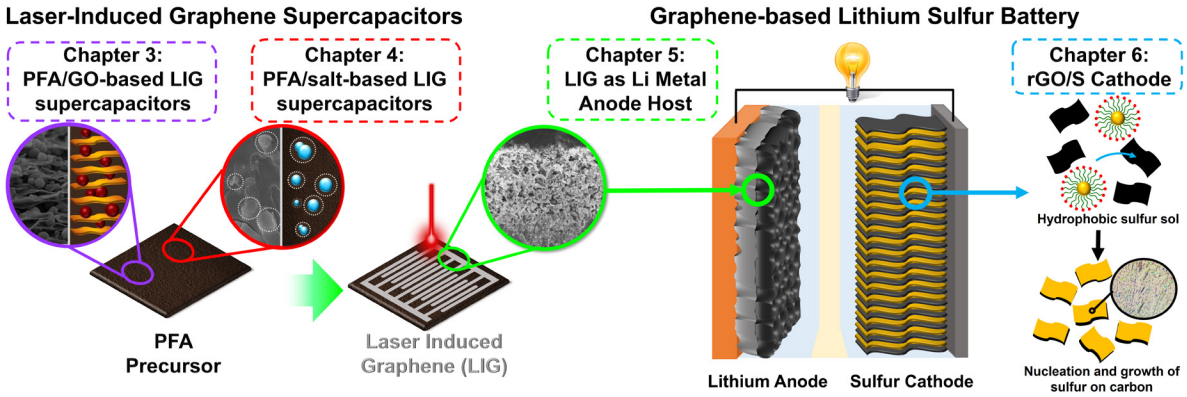

Figure 2.18: Overall thesis outline schematic.

Chapter 3:
Supercapacitors Fabricated via Laser-Induced Carbonization of Biomass-Derived Poly(furfuryl alcohol)/Graphene Oxide Composites

3.1 Introduction

As discussed in Chapter 2, the LIG method is promising for the simultaneous synthesis and fabrication of graphene-based electrodes with high conductivity, surface area, and porosity. However, thus far, high performance LIG formation has been effectively limited to PI-based LIG, which is prepared from petroleum and coal-based precursors. Moreover, the areal capacitance remains limited. Consequently, a need exists for the fabrication of high-performance LIG from inexpensive, easily processable, and sustainable precursors.

Poly(furfuryl alcohol) (PFA) is a thermosetting polymer resin and a common carbon precursor. Its pyrolysis product has been utilized to prepare carbon materials for a wide array of applications, including the first lithium-ion battery anode by Sony in 1990,[36,219] as well as glassy carbon MEMs,[220] electrodes,[221] and sensors,[222] and carbonaceous membranes for water desalination[223] and gas separation.[224] While it self-polymerizes via a simple acid catalyzed polycondensation reaction, various branching reactions lead to a highly crosslinked structure with aromatic rings, which is a common feature of nearly all LIG precursors. Its chemical structure is similar to phenol-formaldehyde resins, which have been previously utilized to form LIG-based supercapacitors, albeit with much lower specific capacitances than PI.[95,96] However, unlike petroleum-based PF resin, PFA is also a sustainable and green polymer. Its monomer, furfuryl alcohol (FA), is prepared from the hydrogenation of furfural, which is easily prepared in large quantities from a variety of biomass waste derivatives, such as corn cobs, rice hulls, bagasse, and wood.[225,226] As such, it is a compelling choice as a precursor for the formation of LIG.

Notably, PFA has been widely used as a precursor to glassy carbon, rather than graphene. However, for high performance LIG-based supercapacitors, it is not critical that the carbonaceous electrodes are graphene-based. In fact, pristine graphene is a poor candidate as a supercapacitor material, as it is limited by its low quantum capacitance.[58] It has been shown by us[92] and others[227,228] that defects and functional groups similar to those on glassy carbon are beneficial for enhancing the area-specific

capacitance. Glassy carbon is thought to be a more "metallic" form of carbon, as it has a higher density of states near the Fermi level, and is not limited by these effects.[92]

The first paper on LIG from Lin et al. noted that the high capacitance of LIG prepared from PI was aided by the polycrystalline nature of the LIG, which consists of grain boundaries made up of defects such as five and seven-membered rings that enhance the "metallic" nature and charge storage performance of the material.[24] In fact, the best electrochemical performance reported for LIG devices to date was for PI-based devices that were plasma-treated to introduce further oxygen-containing groups and defects to increase the hydrophilicity and wettability of the electrodes, further indicating the benefits of defects on device performance.[97]

Furthermore, the unique properties of glassy carbon, including high inertness and corrosion resistance, excellent electrical conductivity, exceptional mechanical properties, and tunable surface chemistry make it a superior material for a host of applications. It has been widely employed as a chemically inert electrode for analytical electrochemistry, and its surface has been functionalized with a variety of small molecules for use in sensors and biosensors. Its high conductivity and mechanical properties have propelled its widespread use in MEMS devices,[220] and, unlike graphite or graphene, it is able to intercalate sodium ions, making it the most promising candidate for sodium-ion batteries to date.[229]

However, glassy carbon is commonly prepared from high temperature pyrolysis of crosslinked polymers, which is a slow and energy-intensive process. Preparation of glassy carbon through direct laser writing is a rapid and simple synthesis approach, and further enables patterning of complex architectures, which has previously only been achieved through expensive and complex multi-step lithography methods.[220] The ease and speed of this approach would expand the application space of glassy carbon, further motivating the investigation of laser-induced carbonization of PFA.

In this work, we investigate for the first time the laser-induced carbonization of PFA according to the approach described in **Figure 3.1**. Surprisingly, while PFA typically exhibits a high carbon yield under normal thermal processing in a furnace, under all laser conditions tried (varying powers, defocusing, multiple lasing) no significant laser-induced carbonization could be achieved with our IR laser. In an attempt to bypass this challenge, we explore the use of graphene oxide (GO) as an aid for successful carbonization and LIG-formation. We demonstrate that the addition of loadings as low as 1 wt. % of GO to PFA enables its carbonization via an IR laser under ambient conditions to a porous,

conductive material with properties similar to glassy carbon. As this material is prepared via the LIG method, we will also refer to this material as LIG throughout, although its structure and properties are more similar to a glassy carbon than graphene. Furthermore, we develop a novel strategy to utilize PFA microspheres (μPFA), prepared from an emulsion polymerization approach, in order to increase the surface area and porosity of the PFA/GO composite films, resulting in LIG microsupercapacitors (MSCs) with high specific areal capacitances of 11.7 mF/cm^2 at 5 mV/s. This specific capacitance increases to 14.5 mF/cm^2 after 11 days due to increased electrolyte wetting, outperforming current PI and GO-based LIG MSCs prepared by similar methods. The devices reach a maximum capacitance of 16.0 mF/cm^2 at 0.05 mA/cm^2, which is among the highest capacitances reported for LIG-based devices, and also cycle stably for over 10,000 cycles with over 97% capacitance retention.

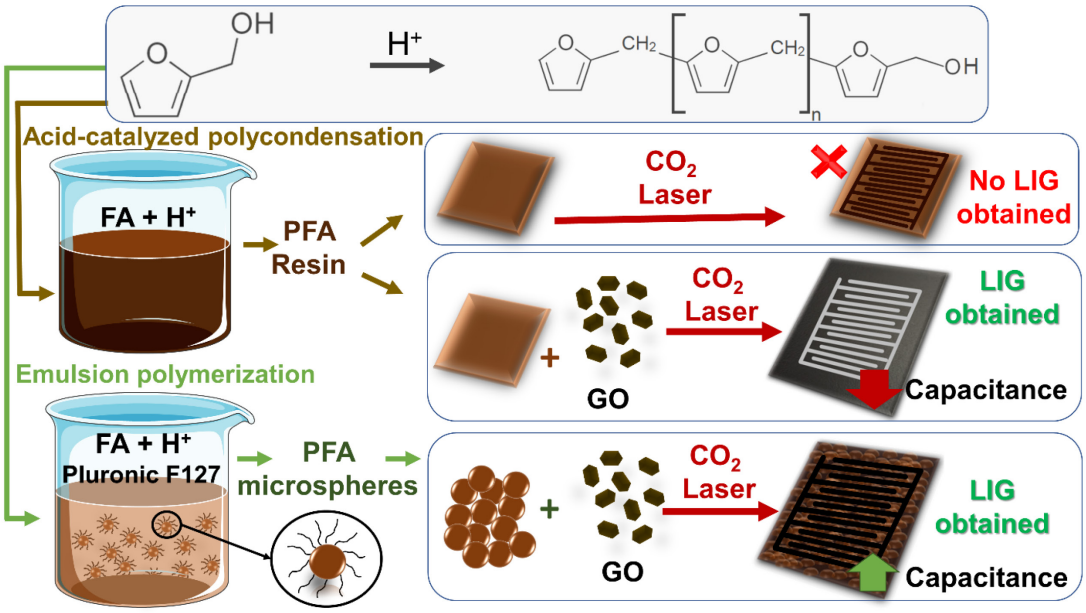

Figure 3.1: Scheme of strategies to induce carbonization of PFA and to introduce further porosity through the use of composites of PFA microspheres and GO. The interconnected and highly crosslinked nature of the PFA chemical structure is not shown.

3.2 Experimental Methods

3.2.1 GO Synthesis and Characterization

Graphene oxide synthesis was conducted according to Marcano et al.'s improved Hummer's method,[19] where 1 g of graphite flakes (Natural, 99.9%, -10 mesh, metal basis, Alfa-Aesar) and 6 g of potassium permanganate (EMD Millipore), were stirred in a 9:1 mixture of sulfuric (98%, Sigma-Aldrich) and phosphoric acid (85 wt.% in H_2O, 97%, Sigma-Aldrich) for 16 h at 45 °C. After the oxidation process the mixture was cooled and then slowly transferred to a beaker with 130 mL of deionized water placed in an ice bath. Then approximately 5 mL of H_2O_2 (30 wt.% in H_2O, Sigma-Aldrich) was added until the mixture changed color from purple to golden yellow. The final mixture was then washed two times with 10% hydrochloric acid solution (ACS Reagent 37 wt.% in H_2O, Sigma-Aldrich) followed by four washes with ethanol, with each washing step followed by centrifugation (Thermo-IEC Centra-CL2) conducted at 3500 rpm for 30 min. The final precipitate was dispersed in ethanol, resulting in a dispersion of ~20-40 mg/mL. The elemental composition of the graphene oxide material was determined by spray drying an aqueous dispersion (Buchi Mini Spray Dryer B-290), pressing the material into a pellet, and using energy dispersive x-ray spectroscopy (EDS) on a Zeiss Leo 1530 scanning electron microscope operating with a 20 kV acceleration voltage. The graphene oxide possessed an average C/O ratio of 2.06, with the elemental atomic composition of carbon: 66.5% ± 0.8%, oxygen: 32% ± 1%, sulfur: 0.9% ± 0.2%, chlorine: 0.13% ± 0.02%, potassium: 0.09% ± 0.03%, sodium: 0.04% ± 0.06%, phosphorus: 0.02% ± 0.02%, and silicon: 0.02% ± 0.03%.

Atomic force microscopy (AFM) of the graphene oxide sheets was conducted by spin-coating a dispersion of 0.01 wt.% graphene oxide in ethanol on atomically flat muscovite mica substrates. AFM images were obtained with a NP-STT10 tip (Bruker) and a Nanoscope MultiMode AFM (Veeco).

3.2.2 Preparation of PFA Resin Films With and Without GO

PFA resin was prepared via the acid-catalyzed polycondensation of furfuryl alcohol (FA). For samples without GO, 25 mg of oxalic acid (99.5%, EMD) was dissolved in 5 mL of FA (98%, Sigma Aldrich), and the mixture was polymerized at 70 °C for 21 hours, to form a viscous black liquid. Initial samples of PFA resins with varying contents of GO, ranging from 0.1 wt.% to 1 wt.%, were prepared via the mixing and ultrasonic dispersion of the corresponding amount of GO (from a ~20-40 mg/mL dispersion of GO in ethanol) in FA with no oxalic acid. The samples were sonicated with an ultrasonic probe at

60% power (BioLogics, Inc., Model 150 V/T Ultrasonic Homogenizer, 150 W) for 15 minutes in an ice bath, and then allowed to react for 24 hours at room temperature. In order to shorten the reaction time and improve the throughput of the process, samples were also prepared by mixing 1 wt.% GO with FA and 0.75 wt.% oxalic acid, sonicating with an ultrasonic probe for 15 minutes at 60% power in an ice bath, and polymerizing at 75 °C for 3 hours to form a viscous black liquid. Films were then either drop-cast or spin-coated onto PET or glass substrates and allowed to solidify on a 75 °C hotplate overnight.

3.2.3 Preparation of PFA Microspheres

The emulsion polymerization procedure was adapted from Yao et al.[230] 3 g of Pluronic F127 (Sigma-Aldrich) was dissolved in 20 mL of a 7:3 ratio (v/v) ethanol to water mixture. To this solution, 1.4 g of 37% HCl was dissolved as a catalyst for the polycondensation reaction. This solution was stirred for 5 min before adding 3 g of FA dropwise. The polymerization was carried out for 24 hours at room temperature and pressure. Following this, approximately 11.9 mL of 9 M H_2SO_4 were added into the polymer mixture in order to induce further crosslinking within each microsphere and prevent particle aggregation. The mixture was then allowed to evaporate at 90 °C for one hour, resulting in a dark brown, viscous dispersion. This was diluted with water and vacuum-filtered and the filter cake rinsed with 100 mL DI water four times to remove any unreacted monomer, surfactant and acid. The filter cake was left to dry under vacuum overnight.

3.2.4 Preparation of μPFA/GO Films

Dispersions of 12 mg/mL PFA microspheres and graphene oxide in ethanol were prepared, by sonicating each for 15 minutes at 60% power in an ice bath. Then, the two dispersions were mixed in the desired mass ratio (i.e. 2:3 PFA:GO) and sonicated for an additional 5 min. Approximately 1.2 mL of the final dispersion was drop-cast onto 2.5 x 2.5 cm PET substrates, resulting in loadings of approximately 2.2-2.3 mg/cm^2.

3.2.5 Laser-Induced Carbonization and Electrode Assembly

To fabricate the microsupercapacitors, a CO_2 infrared laser machine (BossLaser 1416L - 50W) was used to carbonize a selected area of the film. The pattern used (interdigitated finger) was designed in RDWorks, v.8.0 (**Fig. A1**). The full device was composed of 28 fingers, 14 on each electrode, with each finger being 1.5 cm in length and 350 μm in width, with 450 μm of space between each other.

Images of a scribed device design can be seen in **Figure 3.2**. The active area of both electrodes for this design is ~0.98 cm^2. The power and speed settings utilized in scribing the devices were determined by which conditions resulted in the lowest sheet resistance, with the effect of the laser power on sheet resistance discussed in section 3.3. Sheet resistances were determined by laser scribing a rectangle of 6.07 mm x 2.70 mm and measuring the resistance with a two-probe measurement using a multimeter. While this two-point measurement is not as accurate as a four-point probe measurement due to contact resistances, it can still provide a comparative estimate between different materials. This characterization was conducted every time that a device was prepared, as slight variations in the laser power are common over time. The sheet resistance was calculated with the following formula:

$$R_S = \frac{RW}{L} \tag{3.1}$$

In this equation R is the measured resistance, W is the width of the scribed rectangle, and L is the length of the scribed rectangle.

To assemble the MSC, the electrode area was coated with 230 mg of the electrolyte, which was prepared by dissolving 1 g of polyvinyl alcohol (165 kDa molecular weight, hydrolyzed, 98%, Fisher Scientific) in 5.2 mL concentrated phosphoric acid (85 wt.% in H_2O, 97%, Sigma-Aldrich) and 10 mL DI water at 85°C for 2 h, after which a gel was formed. The MSC was then assembled utilizing titanium foil current collectors (Alfa Aesar, 0.5 mm thick, annealed, 99% metals basis) and a custom laser-cut PMMA cell. Devices were tested 24 hours after electrolyte application to enable the gel-based electrolyte to penetrate into the pores of the laser-scribed material. A representative illustration of the steps is shown in **Fig. A2**.

3.2.6 Materials Characterization

Optical microscope images of the laser-scribed PFA films were obtained with a Leica DM2700M microscope at 10× or 20× magnification, as indicated. ATR-FTIR spectroscopy of the PFA resin films was conducted with a Bruker Tensor 27 Fourier-Transform Infrared Spectrometer with Pike attenuated total reflectance (ATR) attachment possessing a ZnSe crystal. Thermogravimetric analysis (TGA) was carried out utilizing a TA Instruments Q500 at a 20 °C/min ramp rate from 30 °C to 800 °C, under nitrogen atmosphere, to best approximate the rapid heating of laser irradiation. To assess the differences in the thermal diffusivity of the samples, TGA was also done at ramp rates of 5 °C/min and 10 °C/min. The LIG material was examined using Raman spectroscopy using a Horiba Jobin-Yvon HR800 Raman

system equipped with an Olympus BX 41 microscope with a 50 mW, 532 nm laser operating at 25% laser power. Raman spectroscopy was carried out directly on a laser-scribed substrate for µPFA/GO samples, but was done on LIG powder scraped off of the substrate for PFA/1% GO samples, in order to eliminate any fluorescent background from remaining PFA beneath the carbonized trace. Raman spectra of pyrolyzed PFA were obtained from either solidified PFA resin ground into a powder or µPFA powder, by heating in a Carbolite Gero tube furnace under an argon environment at a ramp rate of 5 °C/min to a temperature of 700 °C, followed by heating at 700 °C for 2 hours. A minimum of 3 Raman scans were performed on different areas of each sample in order to obtain a representative measurement. The D and G peaks were fit with a Lorentzian and Breit-Wigner-Fano (BWF) fit,[231] and the 2D peak was fit with a Lorentzian fit. The I_D/I_G and I_G/I_{2D} ratios were calculated from the fitted peak heights or intensities. Flammability testing was done on solid, free-standing pieces of PFA with 0% and 1% GO prepared via polymerization within a PDMS mold, with dimensions 4 cm x 2.5 cm x 0.1 cm. Each sample was ignited for 3 seconds with a butane torch possessing a flame height of 2 cm, positioned 1 cm away from the sample. Burn tests were carried out inside an acrylic box within a fumehood, to limit the influence of air flow on the burning process. Scanning electron microscopy (SEM) to assess the material morphology was done on cryogenically fractured cross-sections of both the polymer/GO films and the LIG material, with a Zeiss Leo 1530 with energy dispersive X-ray spectroscopy (EDS) operating at an acceleration voltage of 10 kV. X-ray photoelectron spectroscopy (Thermal Scientific KAlpha XPS spectrometer, 150 eV) was carried out on LIG powders scraped off of films of polyimide and µPFA/GO 2:3 composite. The spectra were fitted using CasaXPS software.

3.2.7 Electrochemical Characterization

The MSCs were tested at ambient conditions using a Biologic SP-300 potentiostat. Cyclic voltammetry (CV) was conducted at 5, 10, 50, 100, 250 and 500 mV/s, with a voltage window of 0 – 1 V. The specific areal capacitance based on CV measurement was calculated according to Eq. (3.2), where I_{avg} is the average current at the center of the voltage window of CV (i.e. at 0.5 V), v is the scan rate, and A is the active area of both electrodes (~0.98 cm²). This calculation method was utilized in order to avoid any contribution to the capacitance from the faradaic signal at the edges of the voltage window.

$$C_{\mathrm{CV}} = \frac{I_{\mathrm{avg}}}{v \cdot A} \tag{3.2}$$

Galvanostatic charge and discharge (GCD) curves were obtained at varying current densities, ranging from 0.05 mA/cm^2 to 0.3 mA/cm^2. Specific areal capacitances were calculated from the discharge curves in GCD according to Eq. (3.3), where I_{appl} is the applied current and dV/dt is the slope of the discharge curve.

$$C_{\mathrm{GCD}} = \frac{I_{\mathrm{appl}}}{dV/dt \cdot A} \tag{3.3}$$

Electrochemical impedance spectroscopy (EIS) was carried out between 1 MHz to 1 Hz using a sinusoidal perturbation of amplitude 10 mV at a constant 0 V DC. Long term cycling of the devices was done at a single electrode current density of 0.3 mA/cm².

3.3 Results and Discussion

3.3.1 Laser-Induced Carbonization of PFA Resin

As shown in **Figure 3.2a)**, when a film of neat PFA resin was irradiated with an IR laser under ambient conditions, only a brown, insulating decomposition product could be formed. A variety of different laser conditions were examined, including varying the power from 4 W to 5 W (**Fig. A3**). At powers below 4 W, no change in the material was observed, while the brown insulating product was formed in power ranges of 4 W to 4.65 W. At higher powers than this, the PFA film appears fully ablated, indicating that the PFA resin does not carbonize within this range of laser parameters, but rather directly forms gaseous decomposition products. We also examined the strategy of multiple lasings[117] to enable carbonization and did form a black product after 10 scans at 4.5 W power and 1 mm/s scan speed (**Fig. A4**), but only thin, disconnected lines of the black material were formed, and nearly all of the initial polymer film appears ablated, resulting in an insulating film. We further explored using a defocusing approach, as introduced by Chyan et al.,[117] to enable the carbonization of PFA. While a defocusing of 1.7 mm and a power of 4.65 W did result in the formation of a black material rather than the insulating brown film (**Fig. A5**), nearly all of the initial polymer material again appears ablated. Supercapacitors assembled from this material exhibit extremely noisy CV curves, with average currents in the nA range at 500 mV/s (**Fig. A6**), indicating that the poor conductivity and significant ablation of material under these conditions make this approach unfeasible for the fabrication of microsupercapacitors or other devices from PFA. Thus, under no laser conditions were we able to obtain LIG or conductive, carbonaceous material from pure PFA resin that was viable as an electrode material.

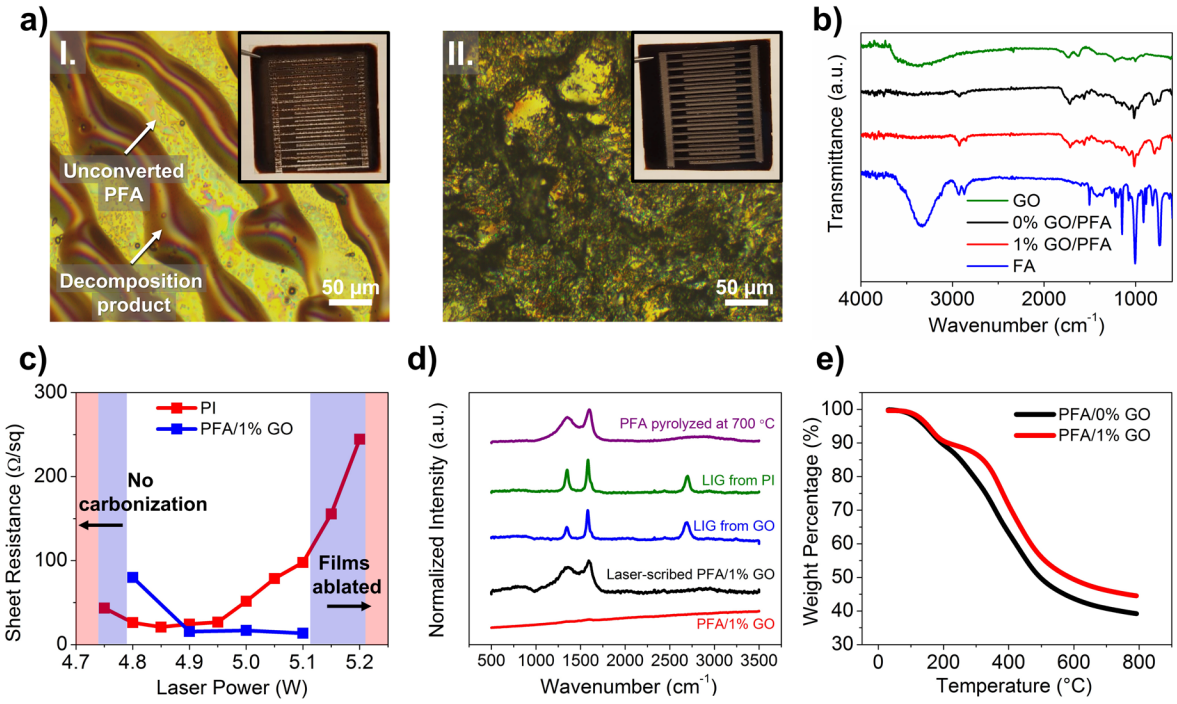

Figure 3.2: Characterization of the effect of 1% GO on carbonization of PFA. a) I. PFA/0% GO thin film laser-scribed at 4.5 W, 1 mm/s. Brown areas correspond to solid decomposition product, while yellow areas correspond to unconverted PFA. Inset: Interdigitated electrode laser-scribed onto PFA/0% GO film on PET substrate at 4.5 W and 10 mm/s, and 1.7 mm defocus. II. PFA/1% GO thin film laser-scribed at 4.5 W, 1 mm/s. Black, conductive material is formed over the entire film area. Inset: Interdigitated electrode laser-scribed onto PFA/1% GO film on PET substrate at 4.9 W and 10 mm/s. b) FTIR spectra of GO, PFA/0% GO, PFA/1% GO, and furfuryl alcohol monomer. c) Sheet resistances of laser-scribed PFA/1% GO and PI films, where PFA/1% GO films were laser scribed at 10 mm/s and PI films were laser scribed at 30 mm/s. d) Raman spectra of PFA/1% GO prior to laser-scribing (red), laser-scribed PFA/1% GO (black), LIG from GO (blue), LIG from PI (green), and PFA pyrolyzed at 700 °C (violet). e) TGA curves of PFA/0% GO and PFA/1% GO, performed at a ramp rate of 20 °C/min in nitrogen.

Following this, small percentages of a GO dispersion in ethanol were added to the resin during the polymerization to serve as an aid for carbonization and the formation of LIG. Atomic force microscopy (AFM) analysis of spin-coated GO from this dispersion demonstrates that the sheets have an average thickness of 1.1 nm ± 0.3 nm, indicating that they have been exfoliated into monolayers, and possess lateral flake sizes ranging from sub-100 nm to 1.4 micron (**Fig. A7**). The FTIR spectra of GO, FA monomer and PFA with 0% GO and 1% GO are presented in **Figure 3.2b)**. The FTIR spectrum of GO corresponds well with results from Marcano et al.'s improved synthesis of graphene oxide.[19] The major peaks consist of a broad OH stretching peak at ~3300 cm^{-1}, C=O stretching peak at 1728 cm^{-1}, C=C

stretching peak at 1622 cm^{-1}, and C-O stretching peak at 1226 cm^{-1} and 1001 cm^{-1}.[19] From FTIR analysis, no significant difference appears in the structure of PFA formed when percentages up to 1 wt.% of GO were present during the polymerization. The FTIR spectra confirm that both resins with and without GO are fully polymerized. This is most apparent due to the disappearance of the OH stretching peak present in the FA monomer at ~3330 cm^{-1} and further confirmed by the appearance of a peak at ~1715 cm^{-1}, which can be attributed to the stretching of the carbonyl (C=O) groups of di-ketones which are formed from the furan rings during the crosslinking of the resin.[232] The intensity of the 1005 cm^{-1} and 1150 cm^{-1} peaks associated with C-O stretches in the FA monomer decreases significantly.[232–234] Other weak peaks are present in the polymer samples, including peaks at 2920 cm^{-1} and 2852 cm^{-1} arising from aliphatic -C-H stretches, 1660-1670 cm^{-1} associated with ring stretching of 2,3-bisubstituted furan rings, ~1562 cm^{-1} arising from the stretching mode of conjugated C=C bonds or ring vibrations, 1350 cm^{-1} from C-H ring deformation, 1215-1180 cm^{-1} and ~1015 cm^{-1} arising from =C-O-C asymmetric and symmetric stretching, 793 cm^{-1} from 2,5-disubstituted furan rings, and 735 cm^{-1} from monosubstituted furan heterocycles.[232–235]

When amounts of GO ranging from 0.1 wt.% to 0.5 wt.% were added to the PFA resin, the material behaved similarly to pure PFA resin, with the formation of a brown, insulating film at low laser powers, and complete ablation at higher powers (**Fig. A8, A9**). However, when 1 wt.% of GO was added into the PFA resin, a black, conductive material was formed upon laser irradiation under ambient conditions (**Fig. 3.2a)**). Loadings above 1 wt. % were not investigated due to the challenge of dispersing higher loadings without increasing the composite viscosity beyond film processing limits. We tested a range of different laser powers and found that the black, conductive material was formed in a laser power range of 4.4 W to 4.65 W at a scanning speed of 1 mm/s and a range of 4.8 to 5.1 W at a scanning speed of 10 mm/s (**Fig. A10**). Above these powers, the film appears cut or ablated. At powers slightly below this range, (i.e., 4 W to 4.4 W at 1 mm/s), black circles of presumably carbonized material are present in optical microscope images of the films, but are disconnected and do not result in a conductive network. At even lower powers, no change is observed in the morphology or colour of the films, indicating that the laser power is too low to induce any carbonization or degradation of the PFA/GO composite.

The sheet resistance of the laser-scribed films was also measured and compared to LIG prepared from PI at various laser powers. It should be noted that the range of laser powers that enable carbonization of the PFA was narrower than PI (4.8 W to 5.1 W, compared to 4.75 W to 5.2 W). The

conductivity of the laser scribed films was quite high, with sheet resistances ranging from 13-80 Ω/sq over the range of powers that induce carbonization (**Fig. 3.2c)**). These values were higher than those of LIG films prepared from PI, which possessed sheet resistances ranging from 21 – 245 Ω/sq. Taking into account the thickness of the LIG layer formed in each case, which was 84 μm ± 7 μm for LIG from PI and 81 μm ± 6 μm for LIG from PFA/1% GO (as estimated from cross-sectional SEM), this results in conductivities of 6 S/cm ± 0.5 S/cm and 9 S/cm ± 0.7 S/cm respectively. These values are lower than the conductivity of LIG from PI reported by Lin et al. (25 S/cm),[24] which may stem from contact resistances, due to our measurement being a two-point probe measurement, while theirs was a four-point probe measurement. Differences in the conductivity of the LIG material prepared from PFA and PI may stem from different morphologies and porosities of these materials (to be discussed below).

Raman spectroscopy of the laser-scribed PFA/1% GO material further confirms the conversion of the polymer into carbon (**Fig. 3.2d)**). Three major peaks are typically observable in the Raman spectrum of graphitic carbon: the D peak at ~1350 cm^{-1}, the G peak at ~1580 cm^{-1}, and the 2D peak at ~2700 cm^{-1}. The D peak is typically absent for pristine graphene and is associated with defects and disorder in the graphene material.[236] The G peak is indicative of a graphitic sp^2 carbon structure, while the 2D peak arises from second order zone boundary phonons and can be utilized to assess the number of layers of graphene.[236] Two major peaks are visible in the Raman spectrum of laser-scribed PFA/1% GO: the D peak at ~1350 cm^{-1}, and the G peak at ~1580 cm^{-1}. A faint 2D peak at ~2700 cm^{-1} can also be observed. Prior to laser-scribing, the PFA/1% GO composite possesses no significant peaks, with a sloping background due to the fluorescence of the PFA under the 532 nm laser. The formation of the D and G peaks confirm the conversion of the polymer into a carbonaceous material under laser irradiation; however, the broadness of the peaks and lack of a sharp and strong 2D peak indicate that the material is more similar to glassy carbon than graphene. The ratio of the D peak intensity (I_D) to the G peak intensity (I_G) or I_D/I_G ratio of the laser-scribed PFA/1% GO material is 0.79 ± 0.03. While some variation in the I_D/I_G ratio of the LIG prepared from GO and PI films is observed, all spectra display sharp peaks and a strong 2D peak, making the laser-scribed PFA/1% GO spectrum significantly different than both. The laser-scribed PFA/1% GO material most closely resembles that of a glassy carbon prepared from pyrolysis of PFA at high temperature (700 °C).

Further investigation on the effect of GO on the thermal degradation of PFA was performed through thermogravimetric analysis (TGA) (**Fig. 3.2e)**). PFA/0% GO and PFA/1% GO were heated at high ramp rates of 20 °C/min under nitrogen to a maximum temperature of 800 °C to best approximate the

rapid, high-temperature laser-scribing process. The laser heating is much faster (>1000 °C/s),[237] and thus TGA can only provide some indirect insight into the decomposition process with and without GO. The TGA profiles of the two materials are similar, with a slow and steady mass loss as the polymer carbonizes, up until approximately 500 °C, where the curves plateau. However, the TGA curve for PFA/1% GO possesses a distinct plateau from approximately 200 °C to 300 °C and possesses a carbon yield of 44.7% at 800 °C, while the PFA/0% GO material has a carbon yield of 39.3%. This yield difference of 5.4% cannot be explained by the mass difference of the 1 wt.% GO added into the PFA/1% GO material alone, suggesting that the GO plays a role in acting as a carbon-forming aid in the PFA system.

The morphology and microstructure of the laser-scribed PFA/1% GO was further investigated via SEM imaging. The SEM images of a freeze-fractured cross-section of the film indicate that a fibrous, porous structure is formed upon laser irradiation (**Fig. 3.3a),c)**). EDS mapping indicates that this film consists of 96.8 at.% carbon and 3.2 at.% oxygen (**Fig. A11**), further confirming the conversion of the polymer into a highly carbonized structure. This material possesses a distinctly different morphology and pore structure than LIG formed from PI (**Fig. 3.3b),d)**). The thickness of the carbonized film on PFA/1% GO is approximately 80 μm, and appears cut into the PFA resin, exhibiting a different structure than LIG from PI, which appears to both cut into the PI film by ~25-45 μm and expand significantly (~45-70 μm) above the polymer surface. The difference in the morphology and expansion of the carbonized material between PFA and PI is suspected to arise from the different chemical structures of the polymer precursors, which dictate the quantity and identity of the gaseous products formed, the kinetics of the gas evolution and carbon formation reactions, and the carbon yield of the rapid laser-induced carbonization process.

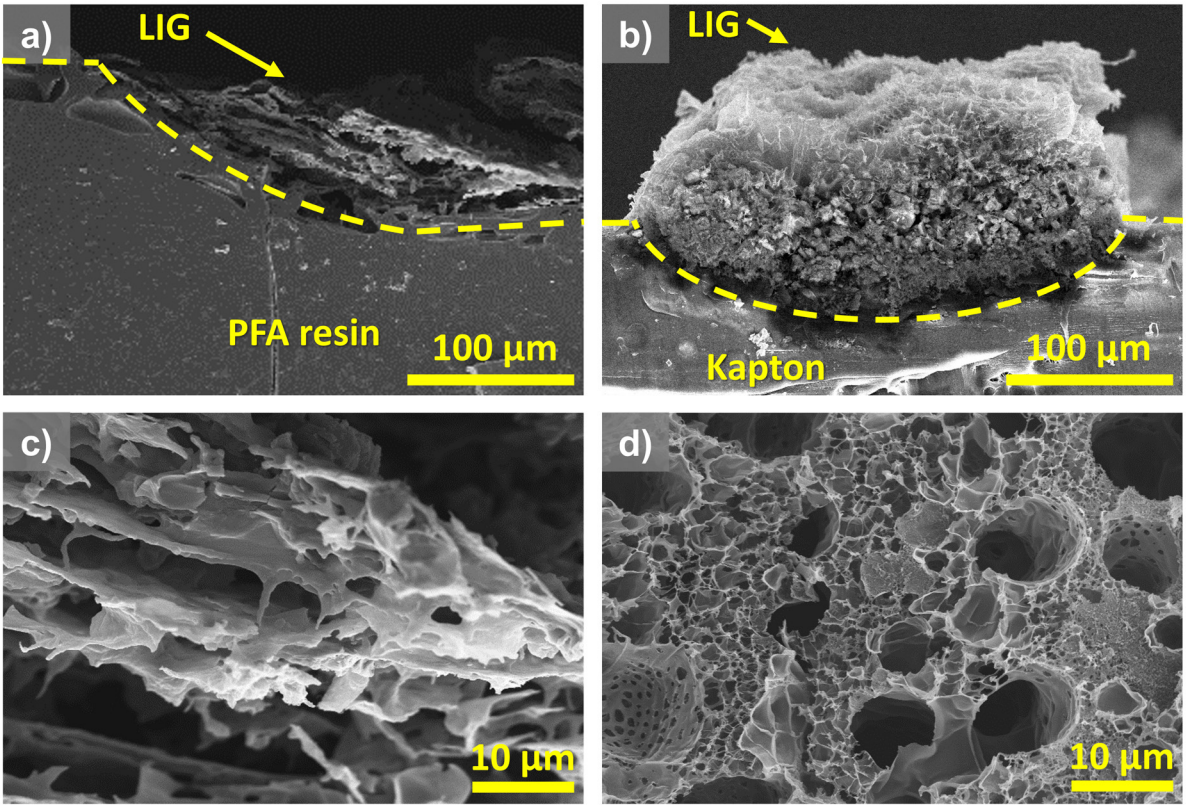

Figure 3.3: SEM images of laser-scribed PFA/1% GO and PI. Freeze-fractured cross-sectional SEM images of a) laser-scribed PFA/1% GO and b) LIG from PI. c) Higher magnification image of laser-scribed PFA/1% GO. d) Higher magnification image of LIG from PI. Dashed yellow lines indicate where the substrate or polymer film ends and where the LIG material begins. LIG from PFA/1% GO appears cut into the PFA resin, while LIG from PI appears to both cut into the polymer and expand above its surface.

These results indicate that the addition of even 1 wt.% of GO can enable the carbonization of PFA through laser irradiation. Several possible explanations can be given for this effect. Firstly, it is possible that the carbonized material formed is purely from the carbonization of the 1 wt.% GO, while all PFA material is ablated during the process. This is unlikely, as the morphology of the carbonized material via SEM imaging is fibrous in nature and does not resemble LIG produced from pure GO films, which typically display clearly visible stacked reduced graphene oxide (rGO) sheets.[87] In addition, the amorphous nature of the carbon material formed, as revealed by the Raman spectrum, indicates that the material cannot be purely rGO. The more likely explanation is that GO is able to facilitate or aid in the carbonization of the PFA material. Graphene oxide has been previously shown to catalyze the hydrothermal carbonization of glucose, both significantly altering the carbonized product morphology and resulting in higher carbon yields in shorter reaction times.[50] GO can play a few possible roles in

facilitating the carbonization of PFA. Firstly, Chyan et al. found that green materials such as wood, paper, cardboard, and cotton fabric could be converted to LIG, but needed to be pre-treated with a phosphoric acid or phosphate-based fire retardant prior to lasing to dehydrate the materials and increase the char yield.[117,238] Notably, graphene oxide and graphite oxides have been widely utilized as fire retardants in a variety of polymeric nanocomposites.[239–242] GO can act as a flame retardant via two different mechanisms. As a 2D nanomaterial, GO can act as a physical barrier in the composite to prevent the diffusion of heat, gases, and thermal degradation products.[239–242] Furthermore, GO can also act as an intumescent flame retardant. When heated, gases such as CO_2 and H_2O are evolved from the GO, and a charred foam is then formed, which then can block transport of heat and combustible gases to the remaining polymer or substrate.[239–242] In this manner, the GO may act as a flame retardant and char-forming agent for PFA during laser irradiation.

To investigate the role of GO as a flame retardant in this system, solid pieces of PFA resin with 0% and 1% GO were burned with a butane torch in order to assess their flammability and self-extinguish time. As a crosslinked, thermosetting resin, PFA is not highly flammable, and will self-extinguish rather than melt or drip after ignition. No significant differences in the self-extinguish time of samples with and without GO was measured, but differences in the burning process were observed, such as breakage of the samples without GO and the formation of a liquid residue, neither of which occurred for samples with GO. The chars formed during the flammability testing were imaged via SEM (**Fig. A12**), and dramatic differences in morphology are observed. For samples without GO, large cracks or pores are formed on the surface, exposing a porous sample interior. These cracks are 100 – 200 μm wide, and span ~0.5 – 2 mm long. However, chars from samples with GO do not display any of these large cracks, instead possessing small, crescent-shaped pores or divots on the surface, that do not expose a porous interior. These pores range from 50 – 200 μm in size. The dramatic difference in char morphology indicates that the 2D sheet structure of GO may limit the release of gases during burning of the sample, preventing the formation of large cracks in the sample surface. Thus, while it appears that GO does not significantly change the flammability of the PFA, it is expected that the effect of GO on the gas transport during burning would be analogous to its effect on gas transport during laser irradiation of the samples, which may be a key part of the laser-induced carbonization mechanism.

GO may play further roles in the carbonization of PFA. For example, GO is known to absorb IR radiation very strongly,[243,244] and thus it is expected that the GO is fully reduced to form rGO during laser irradiation – an exothermic reaction[245,246] that may distribute heat throughout the PFA resin. Both

GO and rGO have been hypothesized to interact strongly with π-conjugated systems, templating and controlling their assembly, and potentially acting as seeds or nucleation sites for the formation of graphene sheets.[247] Furthermore, it has been well-documented that the addition of small amounts of graphene or rGO into polymer nanocomposites increases the thermal conductivity of the composites.[248,249] Thus the rGO formed in situ may distribute the laser photothermal energy throughout the thermally insulating PFA.

To investigate the effect of GO on the thermal conductivity and thermal stability of PFA, TGA was carried out at varying heating rates ranging from 5 °C/min to 20 °C/min (**Fig. A13**). Shifts in the profile of the TGA curve are expected at different heating rates, with curves shifting to higher temperatures at higher heating rates.[250,251] This effect results partly from the kinetics of the decomposition, and partly from thermal lag, which is attributed to heat transfer limitations.[250,251] The magnitude of thermal lag has been related to the thermal diffusivity of the measured material, which is, in turn, directly related to the thermal conductivity of the material.[252,253] Thus, it is expected that smaller shifts in the TGA curves should be observed for materials with higher thermal diffusivity, and larger changes should be observed for materials with lower thermal diffusivity. Analysis of the derivative TGA curves demonstrate two major weight loss regions, with maxima in the ranges of 130 – 170 °C and 350 – 420 °C. Due to the irregular shape of the weight loss peak in the 350 – 420 °C range, changes in the T_{max} value for the 130 – 170 °C range were investigated. The percent change in the T_{max} value with varying heating rate for samples with and without GO are similar, indicating that there is not a significant difference in the thermal diffusivity. Assuming a similar heat capacity and density of the two materials, there is no significant difference in the thermal conductivity of the two samples in this temperature range (**Table A1**). However, all samples with GO exhibit a stable plateau observed in the 200 – 300 °C region, which is absent in samples without GO. This plateau, which may result from the ability of GO to block the release of gases during carbonization, indicates the increased thermal stability of all samples with GO, resulting in repeatable higher overall carbon yields. While the TGA results do not indicate significant differences in the thermal conductivity, the higher thermal stability of the samples with GO should limit ablation of material at higher laser powers. Experimentally, we observe this in our optical microscopy analysis, which indicates that PFA/0% GO is fully ablated at 4.75 W (**Fig. A3**), while PFA/1% GO still retains some carbon material at this power (**Fig. A10**).

It is challenging to isolate a single mechanism to explain the effect of GO on the carbonization of PFA, and it is likely that many of these mechanisms may play a role simultaneously. The SEM images

of the chars of burned PFA and the TGA studies suggest that GO affects both the thermal stability of the PFA and gas transport during laser irradiation. These effects, paired with further possible templating effects of GO, enable the carbonization of the PFA/1% GO composite at laser powers that only degrade the pure PFA resin into a brown insulating product. Zhang et. al found that the formation of LIG from phenol-formaldehyde resins with an IR laser was very challenging due to the high power density of the laser and high IR absorptivity of the material, resulting in the laser either having no effect or fully ablating or burning the polymer.[96] We observe a similar phenomenon with the PFA resin, where the carbonization process is highly sensitive to the laser power, and the power control of the laser is too coarse to result in carbonization of the resin alone. However, the addition of 1% of GO enables the carbonization within a reasonable and controllable range of laser powers.

3.3.2 Electrochemical Performance of PFA/GO-based Resins

Following the successful carbonization of the PFA/1% GO composite, electrodes were scribed in an interdigitated pattern and a microsupercapacitor was assembled with a PVA/H_3PO_4 electrolyte for electrochemical characterization. The PFA/1%GO supercapacitor exhibits the expected rectangular shape by cyclic voltammetry (CV), with the absence of faradaic peaks (**Fig. A14**). While the addition of 1 wt. % of GO enables the laser-induced carbonization of PFA and produced a higher electrical conductivity than LIG from PI, the electrochemical performance of supercapacitors prepared from the material is poor compared to reports of LIG-based supercapacitors in literature, with a specific areal capacitance of only 34 μF/cm² at 5 mV/s (**Fig. A14**). It is expected that this low capacitance is a result of the fibrous morphology, resulting in a dense material with low surface area and limited porosity.

3.3.3 Laser-Induced Carbonization of PFA Microsphere System

To achieve more competitive specific capacitances, we investigated a strategy to increase the surface area and porosity of the PFA-based LIG through the use of PFA microspheres (μPFA). As the monolithic PFA resin previously utilized is highly dense and nonporous, its conversion into a highly porous, high surface area LIG material is challenging. Thus, by directly using films consisting of microspheres of the PFA material prepared from a simple emulsion polymerization approach as the LIG precursor, a significant increase in porosity in the initial polymer film can be achieved. SEM images of the μPFA prepared via this approach display the spherical nature of the particles, which range in size from approximately 280 nm to 1.5 μm and possess an average diameter of 670 nm (**Fig. A15**). TGA analysis of the μPFA indicates that it possesses a nearly identical carbon yield as PFA resin, at

39.2% (**Fig. A16**). Again, it was found that the μPFA material would not carbonize under laser irradiation alone, and thus GO was added to the material in order to facilitate the carbonization. However, unlike the PFA resin, uniform and crack-free film formation at both very low and very high GO content was extremely challenging by solution casting. Four ratios of μPFA/GO were investigated: 1:4, 2:3, 1:1, and 3:2. All ratios, when laser-scribed, resulted in the formation of conductive, carbonaceous material, and supercapacitors were prepared from each ratio. The performance of these supercapacitors was again assessed via cyclic voltammetry at a variety of scan rates (**Fig. A17**). It was found that at all scan rates tested, the μPFA/GO 2:3 ratio performed the best, and as such, this optimal ratio was selected for further investigation and characterization.

Cross-sectional SEM images of the μPFA/GO composite display the microspheres of PFA wrapped among the GO sheets (**Fig. 3.4a)**). These images indicate that a highly porous composite of PFA and GO is formed during the film preparation process, with the microspheres and GO sheets well distributed amongst each other. Following laser irradiation and carbonization, this highly porous structure remains mostly intact (**Fig. 3.4b)**), with both the carbonized spheres and rGO sheets remaining visible, although the number of spheres appears slightly decreased, indicating that some of the PFA material may be ablated during this process. Larger voids are evident in the structure between 1-2 μm thick domains of μPFA/GO after carbonization, likely due to the rapid gas evolution during photothermal heating. Furthermore, lower magnification images (**Fig. A18**), indicate that the LIG composite exists in larger flakes, with some of the sheets and layers peeling apart from each other due to the rapid gas evolution during the laser irradiation process. Notably, some of the carbonized PFA spheres appear broken and opened (**Fig. A18**), which may also occur due to gas escaping during the carbonization process. EDS mapping (**Fig. A19, A20**) of the μPFA/GO composite before carbonization indicates that the composite consists of 18.7 at.% oxygen and 81.3 at.% carbon, which is reduced to 0.9 at.% oxygen and 99.1 at.% carbon following laser irradiation. Furthermore, both before and after carbonization, the oxygen content is randomly distributed across both the spheres and sheets of the composite, indicating that both the GO and PFA are carbonized in the laser irradiation process.

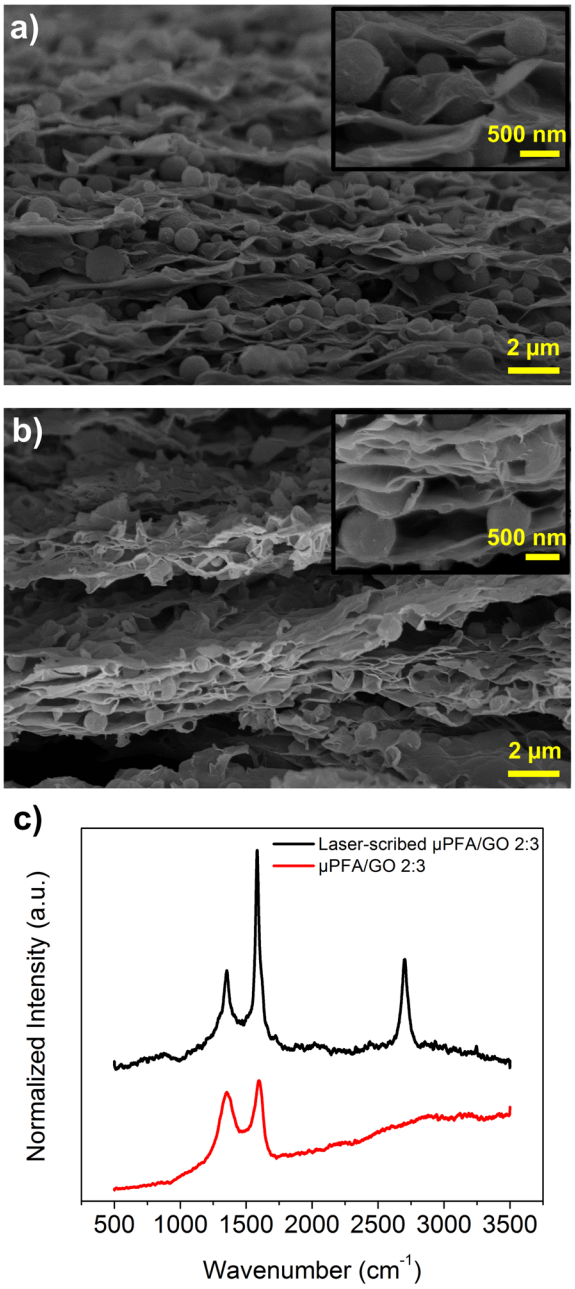

Figure 3.4: Materials characterization of µPFA/GO and LIG from µPFA/GO. a) Cross-sectional SEM image of µPFA/GO composite. b) Cross-sectional SEM image of LIG from µPFA/GO composite. c) Raman spectrum of LIG from µPFA/GO 2:3. Scale bars in lower magnification SEM images are 2 µm, and scale bars in higher magnification inset are 500 nm.

X-ray photoelectron spectroscopy (XPS) analysis of the laser-scribed µPFA/GO 2:3 composite reveals a C/O ratio of 11.2, compared to 16 for LIG from PI (**Fig. A21**). The C1s peak consists of a

dominant C-C peak, with weak C=O and C-O peaks. The C1s and O1s peaks of laser-scribed μPFA/GO 2:3 and LIG from PI are very similar, with the only significant difference being a more dominant C-O peak than C=O peak in the μPFA/GO 2:3 O1s peak. This corresponds well with the chemical structures of the polymer precursors, as PFA possesses more C-O bonds and fewer C=O bonds than PI. The sheet resistance of carbonized material from the μPFA/GO composite was also measured and compared to that of carbonized PFA/1% GO and LIG from PI (**Fig. A22**) and possesses a similar range to both (25 – 440 Ω/sq). However, the thinner LIG layer formed from this material (20 μm ± 10 μm), results in a higher conductivity of 20 S/cm ± 15 S/cm, although this value is also affected by contact resistances during measurement and the porous nature of the LIG formed. Notably, PFA/1% GO carbonizes at higher laser powers (4.8 to 5.1 W) compared to the μPFA/GO composite (4.65 to 4.85 W). The lower laser power required to carbonize PFA/GO composites with increased GO content further reinforces that GO acts to assist carbonization in both PFA/GO composites.

The Raman spectrum of the μPFA/GO composite displays a structure similar to LIG or rGO rather than an amorphous carbon material (**Fig. 3.4c)**). Although multiple spectra were obtained over different areas of the composite, in no case does the spectrum resemble the glassy or amorphous carbon signature of the laser-scribed PFA/1% GO, indicating that either the rGO signal dominates the spectrum, or the PFA is converted into a more graphene-like structure in this composite. The spectra of the laser-scribed μPFA/GO composites possess an average I_D/I_G ratio of 0.37 ± 0.05. The relatively high D peak can result from a variety of factors including the bending of the graphene sheets in the porous graphene structure, residual oxygen functional groups, and other defects in the graphene such as the formation of pentagon and heptagon ring structures, which have been previously suggested to form in PI-based LIG.[24] The μPFA/GO-based LIG possesses an average I_G/I_{2D} ratio of 2.1 ± 0.2. The 2D peak can be fit with a single Lorentzian curve centered at ~2700 cm^{-1}, with a FWHM of ~54 cm^{-1}, which is similar to the Raman spectrum of LIG prepared from PI, and indicates that a few-layer graphene structure is formed.[24] While the Raman spectrum of the μPFA/GO composite prior to laser-scribing also possesses D and G peaks, these stem from the GO in the composite. No 2D peak is evident, indicating the transformation of the composite into LIG following laser irradiation.

It is challenging to experimentally assess the structure of the carbonized PFA within the composite, as it is not easily isolated from the surrounding rGO. In order to better elucidate the nature of the carbonized μPFA in the LIG, Raman analysis was carried out for LIG prepared from various ratios of μPFA/GO (3:2, 1:1, 2:3), as well as LIG prepared from pure GO films, and thermally pyrolyzed μPFA

(**Fig. A23**). Various parameters were assessed, including the I_D/I_G ratio, I_G/I_{2D} ratio, and the FWHM of the D, G, and 2D peaks. In order to assess if the LIG consists purely of a physical mixture of glassy carbon and rGO, these parameters were compared to theoretical values calculated from fitting of linear combinations of spectra of LIG from GO and of thermally carbonized μPFA (**Fig. A24**). The values were further compared to weighted averages of each individual parameter from LIG from GO and thermally carbonized μPFA. For all parameters investigated, and most notably for the I_D/I_G ratios and I_G/I_{2D} ratios, significant differences are observed for experimental LIG prepared from ratios of μPFA/GO compared to a theoretical physical mixture of glassy carbon and rGO. This leads us to conclude that in the μPFA/GO composite, μPFA is converted into a more graphene-like material, along with the GO.

It is difficult to experimentally evaluate the mechanism of this process. However, while PFA is most widely known as a precursor to glassy carbon, researchers have utilized it to prepare graphene. Beckert et al. prepared nitrogenated graphene from PFA and mixtures of urea and dicyandiamide.[254] In this approach, the PFA is pyrolyzed in the presence of these nitrogen-containing agents, to cause the in situ formation of C_3N_4 nanosheets, which act as sheet-like templates for the generation of graphene from PFA.[254] The C_3N_4 sheets are then removed through higher temperature pyrolysis.[254]

This approach demonstrates the potential of sheet-like nanomaterials to act as templates that can guide and manipulate the carbonization of PFA, altering its structure from the disordered graphitic crystallites formed to produce glassy carbon, into single or few-layer graphene sheets. This utilization of a 2D sheet-like material as a template to form graphene from a carbonizable precursor has been extended to various materials, including dopamine,[255] hydroxypropyl methylcellulose,[256] and citric acid.[257] The ability of GO, as a sheet-like nanomaterial, to template the carbonization of materials is supported by Krishnan et al., who demonstrated that GO can act as a catalyst for the hydrothermal carbonization of biomass such as glucose and cellulose, resulting in increased carbon yields and altering the morphology of the carbon product from spheres to sheets.[247] They suggest that GO can template the formation of sheet-like carbon structures during the carbonization process, potentially acting as nucleation sites for the growth of graphene sheets. [247] This process should be even more favourable for polymers such as PFA which contain aromatic ring structures that can interact strongly with graphene and graphene oxide materials through π-π stacking interactions. Thus, we expect that the graphene oxide in the PFA/GO nanocomposite acts as a template and as nucleation sites for the formation of a graphene-like material from PFA during laser irradiation.

Despite differences in the structure of the carbon material formed, the mechanisms of the laser-induced carbonization of PFA/1%GO and μPFA/GO are related to one another. While the microstructures of the two composites investigated differ, the main difference in the carbonization process is in the GO content. In the resin-based PFA/1%GO, GO-lean conditions are utilized, while in the μPFA/GO system, GO-rich conditions are employed. Our studies on the PFA/1%GO system suggest that the increased thermal stability of composites with GO, and the effect of GO on gas transport and escape both play a role in the carbonization of this material. It is also possible that GO may act as a template or as nucleation sites during the carbonization, and the combination of these effects lead to the formation of a glassy carbon material following laser irradiation. We suspect that all of these effects are also key in the carbonization of μPFA/GO, but this is more challenging to investigate due to the high GO content of the samples, which may dominate characterization methods. We hypothesize that the more graphene-like material formed from μPFA is due to the much higher GO content of these samples than the resin-based PFA/1%GO samples, enabling a higher degree of templating of PFA during carbonization and thereby changing its carbonized structure.

3.3.4 Electrochemical Performance of Laser-Scribed μPFA/GO System

Microsupercapacitors prepared from laser-scribed μPFA/GO composites display the expected pseudo-rectangular shape in CV at varying scan rates (**Fig. 3.5a)**), indicating a lack of any faradaic peaks or pseudocapacitance. From the CV curves, the device exhibits specific areal capacitances as high as 11.7 mF/cm^2 at 5 mV/s. Galvanostatic charging and discharging (GCD) was also performed on the device at different current densities (**Fig. 3.5b)**). The GCD curves display the expected triangular shape, with the device displaying a specific areal capacitance of 11.3 mF/cm^2 at 0.15 mA/cm^2. The rate performance demonstrates that the device loses little capacitance with increased scan rates (**Fig. 3.5c)**), with specific areal capacitances as high as 4.70 mF/cm^2 still obtained at scan rates as high as 500 mV/s. Furthermore, the specific areal capacitance of the device increases after 11 days of aging, achieving values of 14.5 mF/cm^2 and 14.0 mF/cm^2 from CV at 5 mV/s and GCD at 0.15 mA/cm^2 respectively (**Fig. A25**). This can be attributed to the gel-based electrolyte wetting and wicking into the LIG pores over time, accessing more electrode surface area. At low current densities of 0.05 mA/cm^2, the device obtains a specific areal capacitance of 16.0 mF/cm^2 which is comparable to the 16.5 mF/cm^2 specific capacitance of boron-doped LIG devices at 0.05 mA/cm^2, which are the highest specific areal capacitances reported for LIG-based devices prepared directly from an IR laser-scribing process.[94] Additionally, the areal capacitance of the devices is currently limited by the thickness of the μPFA/GO

film, which is approximately 5-10 μm thick and fully converted into LIG during laser irradiation; thus, even higher areal capacitances could be achieved through irradiation of thicker films. The long-term cycle life of the device has also been thoroughly tested via galvanostatic cycling at a current density of 0.3 mA/cm^2. Excellent long-term cycle life is displayed (**Fig. 3.5d)**), with capacitance retention of 97.2% after 5000 cycles, and 97.4% at 10,000 cycles. Furthermore, no significant increase in cell resistance or leakage current is observed with cycling. The profile of the galvanostatic charge and discharge curve at cycles 0, 5000, and 10,000, overlap with little observable difference, indicating the long-term stability of the device.

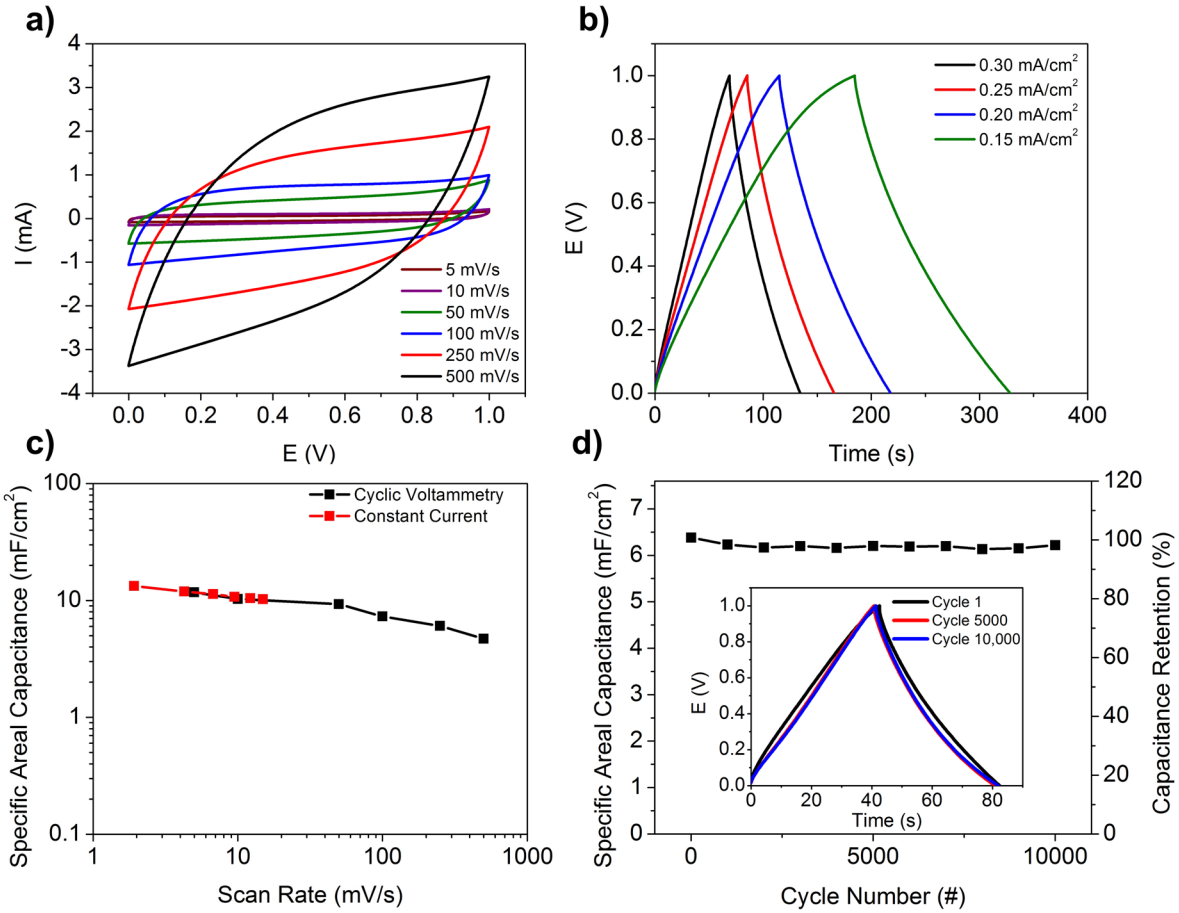

Figure 3.5: Electrochemical characterization of microsupercapacitor prepared from laser-scribed μPFA/GO. a) Cyclic voltammetry (CV) curves with varying scan rates. b) Galvanostatic charge and discharge (GCD) curves with varying current densities. c) Specific areal capacitances with varying scan rates from both CV and GCD results. d) Specific areal capacitance and capacitance retention with long-term cycling of microsupercapacitor at 0.3 mA/cm².

The electrochemical performance of the μPFA/GO supercapacitors was then compared to supercapacitors prepared from common LIG precursors in literature: PI and GO. MSCs with the same interdigitated design were scribed on commercial PI films and drop cast GO films on PET substrates, and their performance was assessed by CV and GCD testing (**Fig. A26**). Both μPFA/GO-based and PI-based LIG films dramatically outperform GO-based LIG films (**Fig. 3.6a)**), which only possess a specific areal capacitance of 0.97 mF/cm^2 at 5 mV/s. This lower capacitance may have been limited by the lower loading and thickness of the GO films (1.1-1.3 mg/cm^2), but if the capacitance is assumed to scale with loading, GO films with twice the thickness would possess similar loadings as μPFA/GO films, and still achieve capacitances less than 2 mF/cm^2. Furthermore, μPFA/GO-based films outperform literature reports of GO-based LIG supercapacitors which have reached a specific capacitance of 4-5 mF/cm^2 at current densities of 1 A/$g_{LSG/electrode}$.[87] From the structure of the laser-scribed μPFA/GO 2:3 composite in SEM analysis, as well as the strong rGO Raman signal, it could be argued that the high specific capacitance of this material arises purely from the rGO sheets, with the PFA spheres acting simply as spacers to maintain exfoliation of the sheets. However, previous literature on GO-based LIG indicates that the material is well-exfoliated, with re-agglomeration prevented by the 3D porous structure, and these materials possess significantly lower capacitance than the μPFA/GO 2:3 composite.[87] Furthermore, we have previously demonstrated that carbonized μPFA is also present following laser irradiation, leading us to hypothesize that it is the unique microstructured nature of this composite that is the origin of its high capacitance.

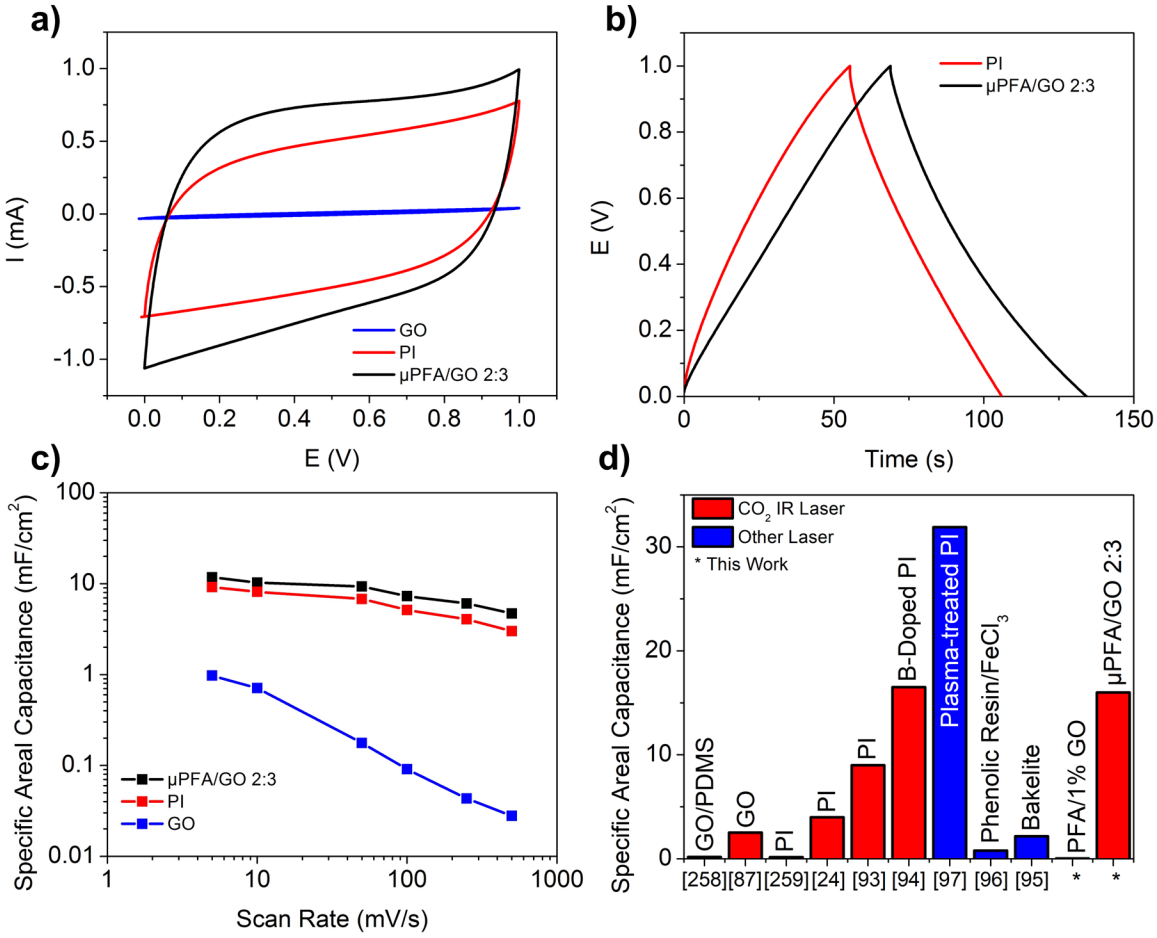

Figure 3.6: Comparison of µPFA/GO 2:3 LIG supercapacitor performance with PI and GO-based LIG. a) Comparison of CV curves for MSCs at 100 mV/s. b) Comparison of GCD curves at 0.3 mA/cm^2. c) Comparison of specific capacitance from CV at different scan rates. d) Comparison of specific areal capacitance of MSCs to literature values. All capacitances reported are device capacitances (not single electrode) and are normalized by the two-electrode area. Reference numbers for each material are listed below each bar. Bars for this work are highlighted with an asterisk.

When PFA-based LIG supercapacitors are compared to results from PI-based LIG, the µPFA/GO composite outperforms PI in both CV and GCD testing (**Fig. 3.6a),b)**), where PI achieves a specific capacitance of 9.2 mF/cm^2 at 5 mV/s. The µPFA/GO composites also possess excellent rate performance as seen in **Figure 3.6c)**, exhibiting higher specific capacitances than both GO and PI-based composites at all scan rates tested, up to a maximum of 500 mV/s. Electrochemical impedance spectroscopy (EIS) (**Fig. A27**) curves for the µPFA/GO and PI-based devices are similar; however the slope of the µPFA/GO composite in the low-frequency regime is higher than that of the PI-based device, further indicating the stronger capacitive behaviour of the µPFA/GO-based device.

Finally, the performance of the PFA-based MSCs prepared in this work has been compared to reported literature performance for various LIG-based MSCs (**Fig. 3.6d)**). In order to compare reported values fairly, the specific areal capacitance of the full MSC device was compared, where the capacitance was normalized with the two-electrode area (area of both electrodes covered by the electrolyte). If the values reported in literature were for a single-electrode capacitance, these values were divided by four in order to account for both the area of the two electrodes, as well as the two electrodes in series making up the device. The quantitative comparison of results is challenging due to the varying methods of measuring and calculating the specific capacitance, which is reported both by CV and GCD at varying scan rates and current densities, but here we compare the highest specific capacitances reported for each MSC. It can be confirmed that the µPFA/GO composite fabricated in this work outperforms current reported results for GO-based LIG,[87,258] and for PI scribed under similar laser conditions.[24,93,259] Notably, the capacitance of the µPFA/GO composite also dramatically surpasses recent reports on LIG prepared from petroleum-based Bakelite[95] and phenol-formaldehyde (PF) resins[96] which possess similar chemical structures and properties as PFA. The µPFA/GO composite achieves a maximum capacitance of 16.0 mF/cm^2 at a current density of 0.05 mA/cm^2 which is highly comparable to the 16.5 mF/cm^2 capacitance (also reported at 0.05 mA/cm^2) achieved by boron-doped PI, which is the highest specific capacitance reported for LIG prepared with a conventional IR laser.[94] While a PI-based LIG device has been prepared with a specific capacitance of 31.9 mF/cm^2 at 0.05 mA/cm^2, this approach utilized a semiconductor blue-violet laser, followed by a plasma treatment to enhance wettability.[97] Thus, the performance of the µPFA/GO-based LIG is among the highest of any LIG-based device prepared from an IR laser, without the need for semiconductor lasers, inert atmospheres, plasma surface treatments, multiple lasings, or laser defocusing. Furthermore, these excellent electrochemical results are achieved utilizing an easily synthesized, cost-effective, green polymer rather than unsustainable coal or petroleum-based polymers.

3.4 Conclusion

In summary, we have demonstrated the laser-induced carbonization of inexpensive, renewable, and easily processable poly(furfuryl alcohol) films for the first time. This process utilizes ambient conditions and the most cost-effective and commonly utilized IR laser source, with no need for inert atmosphere, multiple lasings, or substrate pre-treatment, through the addition of graphene oxide as a carbonization aid. GO content as low as 1 wt.% can enable the carbonization of PFA, which would

otherwise form an insulating brown degradation product or be fully ablated by the laser irradiation. The laser-induced glassy carbon prepared from this approach exhibits excellent conductivity, with sheet resistances as low as 13 Ω/sq, which are lower than that of LIG from PI. This method utilizes only a small fraction of the more synthetically complex and costly GO additive, making this platform cost-effective and promising for further applications outside of energy storage in a variety of electronic devices, including sensors, RFID antennas, sodium-ion batteries, MEMS, and other conductive traces. Furthermore, we have demonstrated that composites of PFA microspheres and GO sheets result in a highly porous film structure, both before and after laser exposure. Microsupercapacitors prepared from this material possess specific areal capacitances as high as 11.7 mF/cm^2 at 5 mV/s, which increases to 14.5 mF/cm^2 after 11 days due to further electrolyte penetration into the pore structure. The device achieves a maximum capacitance of 16.0 mF/cm^2 at 0.05 mA/cm^2, making it among the highest reported specific capacitances for LIG-based MSCs, and outperforming LIG prepared via the same approach from commonly utilized GO films and commercial PI. The MSCs also demonstrate impressive cycle life, with capacitance retention of 97.4% at 10,000 cycles. Furthermore, as all components of these microsupercapacitors are flexible and mechanically robust, the devices could have potential future applications in flexible and wearable electronics. The high performance, simplicity, low cost, and use of biomass-derived materials make this approach a facile, practical green alternative to conventional GO and PI-based LIG devices, demonstrating the promise of PFA/GO-based LIG for implementation into the next generation of miniaturized energy storage devices and electronics.

Chapter 4:
Salt-Induced Doping and Templating of Laser-Induced Graphene Supercapacitors

4.1 Introduction

In Chapter 3, we demonstrated the formation of LIG from composites of poly(furfuryl alcohol) (PFA) and graphene oxide (GO).[260] As discussed, PFA is an inexpensive, easily processable, sustainable material with a highly crosslinked structure similar to that of many other LIG precursors. Despite this, we previously found that neat PFA could not be carbonized successfully with a CO_2 laser, and thus we introduced GO as a carbonization aid. Composites of PFA resin and 1 wt.% GO exhibited highly conductive carbonized traces, but achieved low capacitances (34 μF/cm^2 at 5 mV/s) due to the low surface area of the fibrous carbon material formed. To circumvent this, composites of PFA microspheres and GO were prepared, which demonstrated capacitances higher than that of GO or PI-based LIG. However, unlike PFA resin, both GO and PFA microspheres are prepared through complex, lengthy syntheses using toxic chemicals and strong acids and resulted in fragile films compared to dense, polymer-based substrates such as PI, making it unfeasible to form thick or free-standing films. PFA resins have similar mechanical properties to other thermosetting resins[261] and PI (Young's modulus of 2.3 GPa and yield point of ~70 MPa),[262] with a Young's modulus of ~0.8 GPa and tensile yield strength of ~10 MPa.[263,264] Thus, formation of LIG directly from PFA resins, which are more mechanically robust and easily processable than PFA microspheres, would be desirable.

In this work, for the first time, we have investigated the use of inexpensive and abundant salts as templates and carbonization aids to increase the surface area and capacitance of PFA-based LIG. Salts have been previously used to activate carbon materials and increase their surface areas at high temperatures.[265] As the local temperatures during laser scribing can reach thousands of degrees,[237] the presence of salt in the PFA material may result in a similar effect during laser irradiation. Likewise, salt particles have been previously utilized as templating and pore-forming agents in order to increase the porosity and surface area of carbon materials.[266]

Herein, we demonstrate that the addition of micron-sized particles of sodium salts such as sodium chloride (NaCl) and sodium sulfate (Na_2SO_4) into PFA dramatically changes the resulting LIG material after laser irradiation, as seen in **Figure 4.1**. The addition of salt particles increases the BET surface

area of the LIG formed by over an order of magnitude and also results in the formation of either Cl- or S-doped LIG depending on the salt used, resulting in LIG electrodes which exhibit a ~2,500× capacitance increase compared to pristine PFA. We demonstrate that the simultaneous effect of the salt particles on the LIG surface area, chemical structure, and carbon yield enables composites of PFA/25% Na_2SO_4 to exhibit average areal capacitances of ~20 mF/cm^2 at 5 mV/s and ~25 mF/cm^2 at 0.05 mA/cm^2, with some individual PFA/20% Na_2SO_4 devices exhibiting capacitances as high as 38 mF/cm^2 at 5 mV/s and 80 mF/cm^2 at 0.05 mA/cm^2, outperforming previously reported values for GO, PI, and PFA/GO-based LIG devices, and providing a key step towards sustainable, high-performance LIG-based supercapacitors.

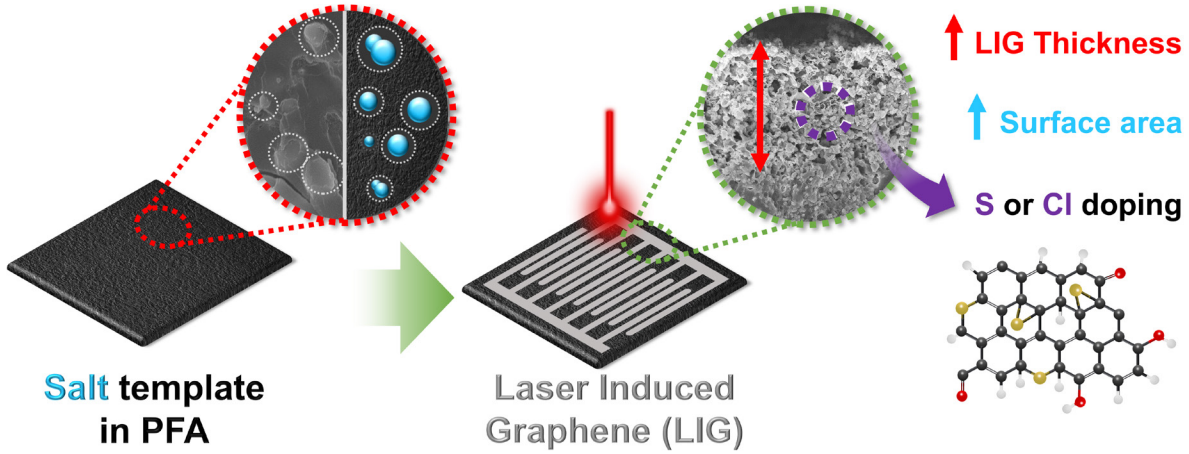

Figure 4.1: Scheme of preparation of LIG from PFA/salt composites.

4.2 Experimental Methods

4.2.1 Spray Drying of Salt Particles

The size and morphology of the salts used were modified using a spray dryer (BÜCHI Mini Spray Dryer B-290). The spray dryer conditions were optimized to yield the smallest distinct particles, while limiting fusion of the particles. The solutions were prepared by dissolving 6 g of either NaCl (EMD, ≥99.5%) or Na_2SO_4 (Sigma-Aldrich, ≥99.0%) in 100 mL of DI water. This mixture was spray-dried at an inlet temperature of 200 °C, with the aspirator set to 100%, the pump set to 30%, and the nitrogen flow set to 473 L/h.

4.2.2 Preparation of PFA Resin Films with and without Salt

PFA resin was prepared via the acid-catalyzed polycondensation of furfuryl alcohol (FA), using a procedure adapted from our previous work with PFA resin and GO.[260] PFA resin without salt was prepared by dissolving 34 mg of oxalic acid (EMD, 99.5%) into a mixture of 1.19 mL ethanol and 4 mL FA (Thermo Scientific™, Acros Organics, 98%), and then allowing the polymerization reaction to occur for 5.5 hours in a 75 °C oil bath to form a viscous black resin that could then be either drop-cast or doctor-bladed. PFA resins with varying salt loadings ranging from 1% to 30%, were prepared by adding 34 mg of oxalic acid and the corresponding amount of salt into 1.19 mL ethanol and 4 mL FA. The weight percentages used are ratios with respect to the monomer added, (i.e. m_{salt}/m_{FA}). While the final amount of salt in the PFA/salt composite is expected to be higher, due to loss of water and other byproducts during polymerization and crosslinking, we have maintained this naming convention for simplicity. Following addition of salt and oxalic acid into ethanol and FA, the samples were sonicated with an ultrasonic probe at 60% power (Sonics & Materials Inc., VCX 750, 750 W, 20 kHz) for 15 minutes in an ice bath, and then allowed to react at 75 °C until a viscous black liquid formed. For 1-15% Na_2SO_4, the reaction time was ~5.5 h, while for all NaCl samples and 20-30% Na_2SO_4 the reaction time was ~2-3 h. Films were then either drop-cast onto PET substrates (1.25" x 1.25") to prepare supercapacitors, or doctor-bladed onto aluminum foil (Fisherbrand, 18 μm thick) using a wet gap of 1000 μm for the preparation of large-scale films. Following film casting, the films were allowed to cure and solidify in an oven at 80 °C overnight.

4.2.3 Laser-Induced Carbonization and Electrode Assembly

A CO_2 IR laser (BossLaser 1416L – 50 W) was used to selectively irradiate the PFA films. Supercapacitors were prepared using an interdigitated finger architecture designed in RDWorks, v.8.0 (**Figure B1**). The full device was composed of 28 fingers, 14 on each electrode, with each finger being 1.5 cm in length and 350 μm in width, with 450 μm of space between each other. This is roughly the minimum electrode spacing that can be achieved with the laser in order to avoid short circuiting, which was occasionally observed due to some widening of the electrode fingers when scribing. The active area of both electrodes for this design is ~0.98 cm^2. Devices were prepared using a scan rate of 10 mm/s, and scribing the electrode pattern two times. A number of different laser powers were investigated, and a laser power of 11.7% (5.85 W) was selected based on the Raman analysis, and as such was used to prepare all devices.

For assembly, the electrode area was coated with 230 mg of the electrolyte, which was prepared by dissolving 1 g of polyvinyl alcohol (146-186 kDa molecular weight, 99+% hydrolyzed, Sigma-Aldrich™) in 5.2 mL concentrated phosphoric acid (85 wt.% in H_2O, 97%, Sigma-Aldrich) and 10 mL DI water at 85°C for 2 h, after which a gel was formed. The supercapacitors were then assembled with titanium foil current collectors (Alfa Aesar, 0.5 mm thick, annealed, 99% metals basis) and a custom laser-cut PMMA cell (**Figure B1**). Electrochemical testing of devices was performed 24 hours after electrolyte application to enable the gel-based electrolyte to penetrate into the pores of the LIG.

4.2.4 Materials Characterization

Attenuated total reflectance Fourier-transform infrared (ATR-FTIR) spectroscopy of the PFA films with varying salt content was conducted with a Bruker Tensor 27 Fourier-Transform Infrared Spectrometer with Pike ATR attachment possessing a ZnSe crystal.

Thermogravimetric analysis (TGA) of PFA and PFA/salt composites was carried out utilizing a TA Instruments Q500 at a 20 °C/min ramp rate from 30 °C to 750 °C, under nitrogen atmosphere, to best approximate the rapid heating of laser irradiation. As CO_2 laser irradiation can enable local heating of >1000 °C/s, the much slower heating of TGA can only act as an indirect model of the laser carbonization process, but can provide insight into the thermal degradation of PFA with and without salt. PFA samples for TGA analysis were prepared by drop-casting resins into a silicone mold instead of onto PET, and ground into a powder following overnight curing. The values reported here are the averages obtained from three samples for each salt loading. The TGA data was corrected for the initial salt content in the PFA/10% NaCl and PFA/25% Na_2SO_4 samples, such that the weight % only reflects the mass of PFA in the sample, for a clearer comparison between the samples. It should be noted that the salt content in the sample is in reference to the monomer, prior to polymerization. Since water and other small molecules are formed as byproducts of the polymerization and are expected to evaporate during polymerization, cross-linking, and curing of the resins, the actual salt content in the PFA/salt samples is expected to be higher than the initial loading in the monomer. As such, the carbon yields determined from these samples are only estimates and can only provide general insight into the thermal degradation of the PFA composites.

Sheet resistances of LIG samples were determined by laser scribing a rectangle of 6.07 mm x 2.70 mm and measuring the sheet resistance with a four-point probe measurement (Ossila). To compare the effect of different laser powers, all films were scribed at the same speed (10 mm/s) and all areas were

scribed twice to ensure complete carbonization. All sheet resistance measurements were performed directly on the PFA or PI substrates after laser scribing. However, for PFA/25% Na_2SO_4 samples, after initial sheet resistance measurements, samples were soaked in DI water overnight and then dried under vacuum overnight, and the sheet resistance was re-measured to determine if dissolving surface coatings of salt could improve sheet resistance.

X-ray diffraction (XRD) was conducted on spray-dried salt powders and LIG powders scraped off of the doctor-bladed PFA substrates. All LIG powders were prepared under the same laser conditions for effective comparison, and were irradiated at 5.85 W laser power, using a laser speed of 10 mm/s, with each area scribed twice. XRD was performed with a Rigaku Miniflex II at a scan rate of 2 degrees/minute, from 2θ values of 10-100.

Raman spectroscopy was carried out on LIG directly on the substrate surface with a Horiba Jobin-Yvon HR800 Raman system equipped with an Olympus BX 41 microscope with a 50 mW, 532 nm laser operating at 25% laser power. The D, G, and 2D peaks of the Raman spectra were fit with Lorentzian peaks, as this provided the best fit. The I_{2D}/I_G ratio was calculated from the fitted peak heights or intensities.

Scanning electron microscopy (SEM) to assess the material morphology was conducted on spray-dried salt particles and on both the surface of LIG and PFA/salt films and on gold-coated cryogenically fractured cross-sections, with a Zeiss Leo 1530 with energy dispersive X-ray spectroscopy (EDS) operating at an acceleration voltage of 20 kV. Image analysis of the spray-dried salt particle size was done using ImageJ software.

Brunauer–Emmett–Teller (BET) surface area was measured for spray-dried salt powders and for LIG powders using a Micromeritics Gemini VII 2390, with nitrogen as the gaseous adsorbate. Full nitrogen adsorption and desorption isotherms were obtained using a Quantachrome Instruments Autosorb IQ. The LIG from PFA/no salt was measured directly, but LIG from PFA/10% NaCl and PFA/25% Na_2SO_4 were first stirred in DI water overnight to dissolve salt, in order to measure the surface area of only the LIG. The samples were then centrifuged at 3500 rpm, transferred into ethanol and re-centrifuged. This step was repeated once more to remove all water, to prevent any capillary forces during drying, in order to limit any drying-induced changes to the surface area. The samples were then dried under vacuum overnight before conducting the BET analysis. From the BET analysis, surface areas of 192 m^2/g and 209 m^2/g were obtained for PFA/10% NaCl and PFA/25% Na_2SO_4,

respectively. Following BET analysis, TGA was performed on the LIG powders from PFA/10% NaCl and PFA/25% Na_2SO_4 at 5 °C/min under an air environment, to burn off all LIG material, and determine how much salt remained in each composite, even after soaking in water overnight (**Figure B22**). The residual mass at 800 °C was attributed to remaining salt, which was determined to be 2.96% in the case of PFA/10% NaCl and 12.32% in the case of PFA/25% Na_2SO_4. BET surface area was also measured for the salt microparticles directly, which possess extremely low BET surface areas (<5 m^2/g). By assuming that the salts contribute effectively nothing to the BET surface area, we can correct the BET surface areas of the LIG alone (without remaining salt) from PFA/10% NaCl and PFA/25% Na_2SO_4 to be 198 m^2/g and 239 m^2/g respectively. The BET surface area of LIG from PFA/no salt and PFA/10% NaCl was determined from the typical BET pressure range, 0.05-0.3 $p/p°$, but as LIG from PFA/25% Na_2SO_4 exhibited significant microporous behaviour, the BET surface area of this sample was determined from a lower pressure range of 0.005-0.05 $p/p°$.

TEM analysis was conducted on LIG powders directly scraped off of the PFA substrate and on powders where salt was dissolved out, following the procedure for BET. The samples were prepared by mixing the powder in 6 mL of high purity ethanol, sonicating for 5 minutes, drop-casting on a carbon supported TEM grid and air drying. Samples without salt were imaged with a Thermo Fisher Scientific Spectra Ultra operated at 300 kV, while samples containing salt were imaged with a Thermo Fisher Scientific Talos 200X operated at 200 kV. HAADF was performed with a spot size less than 1 nm. EDS maps were acquired using Velox from Thermo Fisher Scientific.

X-ray photoelectron spectroscopy (XPS) was carried out on LIG powders scraped off of the PFA substrate with a Thermal Scientific KAlpha XPS spectrometer, 150 eV, and spectra were fitted using CasaXPS software.

4.2.5 Electrochemical Characterization

The electrochemical performance of the supercapacitors was evaluated using a Biologic SP-300 or VSP potentiostat. Cyclic voltammetry (CV) was carried out at 5, 10, 50, 100, 250 and 500 mV/s, with a voltage window of 0 – 1 V. The specific areal capacitance based on CV measurement was calculated according to Eq. (4.1), where I_{avg} is the average current at the center of the voltage window of CV (i.e. at 0.5 V), v is the scan rate, and A is the active area of both electrodes (~0.98 cm^2). This calculation method was utilized in order to avoid any contribution to the capacitance from faradaic signal at the edges of the voltage window.

$$C_{\mathrm{CV}} = \frac{I_{\mathrm{avg}}}{v \cdot A} \tag{4.1}$$

Galvanostatic charge and discharge (GCD) curves were obtained at varying current densities (normalized by a single electrode area), ranging from 0.05 mA/cm^2 to 4 mA/cm^2. Specific areal capacitances were calculated from the discharge curves in GCD according to Eq. (4.2), where I_{appl} is the applied current and dV/dt is the slope of the discharge curve.

$$C_{\mathrm{GCD}} = \frac{I_{\mathrm{appl}}}{dV/dt \cdot A} \tag{4.2}$$

Long term cycling of the devices was performed at a single electrode current density of 0.5 mA/cm².

In nearly all previous LIG studies, capacitance has been typically reported areally, as the patterned area is controlled during fabrication. It is challenging to report the capacitance of LIG-based devices gravimetrically as the LIG material is synthesized during electrode patterning, and the mass of LIG formed is unknown. However, we attempted to estimate the gravimetric capacitance of our material by scraping the LIG off of the PFA surface and weighing it. A large degree of error is associated with this measurement, and thus this is only a rough estimate of the gravimetric capacitance. For PFA with no salt, the LIG loading is ~0.7 ± 0.3 mg/cm^2, which results in a very low gravimetric capacitance of 0.012 F/g_{LIG} at 5 mV/s. For PFA/25% Na_2SO_4, the loading of LIG and salt is ~6.1 ± 0.6 mg/cm^2. Following dissolution of the salt, using the same procedure used for BET and TEM analyses, 20.1% of the LIG/salt composite is retained as LIG, leading to an LIG loading of 1.2 mg/cm^2. This gives a full device gravimetric capacitance of 16.0 F/g_{LIG} at 5 mV/s and 20.0 F/g_{LIG} at 0.05 mA/cm^2. We note that from our TGA analysis of soaked LIG powders, some residual salt is likely still present (12%), and as such the actual gravimetric capacitance may be slightly higher.

4.2.6 Thermal Modeling

All assumptions for the physical constants used in the thermal modeling are available in **Table B3**, and full details of the thermal modeling equations can be found in Appendix B.

4.3 Results and Discussion

4.3.1 Characterization of Spray-Dried Salts and PFA/Salt Composites

In Chapter 3, PFA films polymerized using 5 mg/mL of oxalic acid, a typical recipe found in the literature, were found to not carbonize under any focused laser conditions. Following this work, we found that PFA carbonization could be facilitated using either laser defocus, shown by Chyan *et al*. to be successful in forming LIG from materials that would not otherwise carbonize effectively under the laser,[117] or by using higher concentrations of oxalic acid. However, the capacitance of the LIG formed from pristine PFA under these conditions is extremely low, ~8 μF/cm^2 on average at 5 mV/s (**Figure B2**), making this material unsuitable for the fabrication of high-performance supercapacitors. The limited electrochemical performance was similar to PFA resin filled with 1 wt% GO, as shown in Chapter 3. Since GO can also act as an acid catalyst for the polycondensation of furfuryl alcohol into PFA, the ability to carbonize this system and the one with the higher oxalic acid loading may point towards carbonization being facilitated by a change in the crosslinked structure (e.g., higher crosslink density) which one might expect to occur with an increase in the acid catalyst. In any case, the capacitance is far too low for any practical electrochemical device and significant improvements must be made if this material system is to be used for anything but a conductive trace.

To introduce salts into the PFA resin, we altered the size distribution of commercially available NaCl and Na_2SO_4 by dissolving them in water and spray drying the resulting solutions to obtain micron-sized particles, as seen in **Figure 4.2a)** and **4.2b)**. Spray-dried NaCl particles appear cubic in shape, with an average size of 6.2 ± 2.5 μm (**Figure 4.2c)**). Na_2SO_4 particles instead appear mainly spherical in shape, but apparent holes and pores indicate that they may consist of smaller particles fused together. SEM images indicate that a significant variety in the Na_2SO_4 particle shape exists (**Figure B3**), with the appearance of some needle-like structures and non-uniform globules. As such, the Na_2SO_4 particle size was measured from the spherical particles, and is smaller than NaCl particles, with an average size of 2.4 ± 1.3 μm. These results appear consistent with the known crystallization behavior of these salts – NaCl is known to form only the anhydrous halite salt via evaporation above 0°C, while the crystallization behavior of Na_2SO_4 is fairly complex, and can result in the formation of hydrates such as mirabilite ($Na_2SO_4 \cdot 10H_2O$) and the heptahydrate ($Na_2SO_4 \cdot 7H_2O$), as well as a number of different anhydrous phases, including thenardite (Na_2SO_4 phase V), which is the stable anhydrous phase at room temperature, and the metastable phase III.[267]

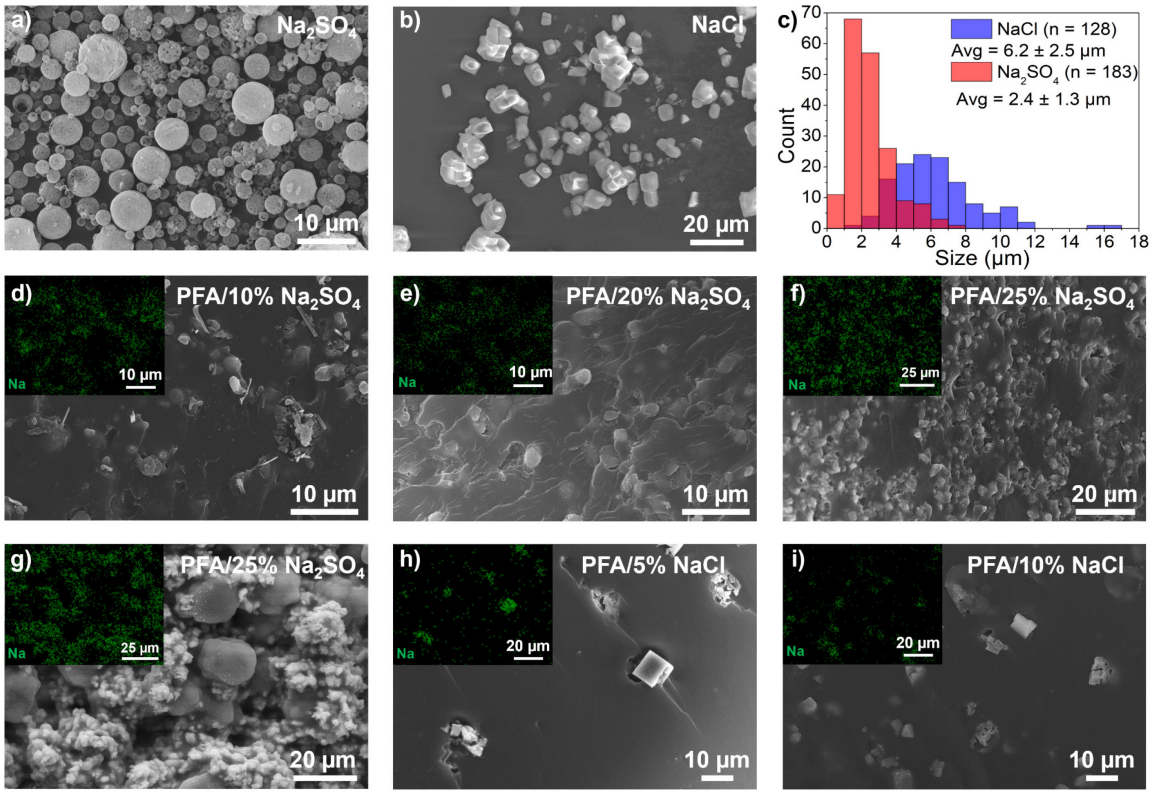

Figure 4.2: SEM and EDS analysis of spray-dried salts and PFA/salt composites. SEM images of a) spray dried Na_2SO_4 particles and b) spray dried NaCl particles. c) Histogram of spray-dried Na_2SO_4 and NaCl particle size. SEM images of a freeze-fractured cross-section of d) PFA/10% Na_2SO_4, e) PFA/20% Na_2SO_4, and f) PFA25% Na_2SO_4. g) Top-down image of PFA/25% Na_2SO_4 surface. SEM images of a freeze-fractured cross-section of h) PFA/5% NaCl, and i) PFA/10% NaCl. Insets in d)-i) show EDS maps for Na Kα, demonstrating the distribution of the salts in the final composites.

Thin films of the resin cast with and without salt were mechanically robust and flexible after sufficient curing (**Figure B4** and discussion in Appendix B). Freeze-fractured cross-sections of PFA resin prepared with 10%-25% Na_2SO_4 can be seen in **Figure 4.2d)-f)**, showing that PFA forms a uniform and non-porous resin, and that salt particles remain as discrete, micron-sized particles, uniformly dispersed throughout the PFA matrix at all salt loadings. Lower magnification SEM images at high salt loadings of 25% Na_2SO_4 indicate that salt particles remain dispersed across the entire PFA film thickness (**Figure B5**). For the most part, the salt particles appear to retain their shape. The Na Kα EDS maps can be seen in the insets of **Figure 4.2d)-f)**, along with complete EDS mapping in **Figure B5** and **B6**, which confirm that the particles are Na_2SO_4 and that some salt is found around these particles potentially arising from dissolution in the PFA matrix. For high salt loadings of 25% Na_2SO_4,

top-down SEM images and EDS mapping of the surface of this composite (**Figure 4.2g)**) demonstrate that, unlike the smooth PFA resin observable in the cross-sectional images, the surface of these films is highly porous, with channels of Na_2SO_4 surrounding separate PFA structures that appear akin to PFA microspheres. Composites prepared with spray-dried NaCl display similar results to Na_2SO_4 (**Figure 4.2h)**,**i)** and **Figure B7**). NaCl particles remain as discrete, micron-sized cubic particles dispersed throughout the PFA matrix, with some Na Kα and Cl Kα signal seen throughout the PFA.

As seen in **Figure 4.3a)**, FTIR spectra of the PFA/salt composites confirm the complete polymerization of the PFA resin, via the disappearance of the OH stretching peak present in the FA monomer at ~3300 cm^{-1}, and the formation of carbonyl (C=O) stretching peaks at ~1715 cm^{-1}, which can be attributed to the formation of diketones via the breaking of the furan rings during PFA crosslinking.[232] The spectra of the PFA resins without salt and with 10% NaCl or Na_2SO_4 all appear identical to one another, indicating that the presence of spray-dried salt particles during the polymerization does not alter the final PFA chemical structure. An expanded view of the fingerprint region, with labels, can be seen in **Figure B8**. However, at high loadings of salt, such as PFA/25% Na_2SO_4, the FTIR spectrum becomes noisier, and the dominant peak present is at ~1100 cm^{-1}, which is attributed to the asymmetric stretching of the SO_4^{2-} ion in Na_2SO_4.[268] As such, it is challenging to determine whether the presence of large quantities of salt affect the polymerization process and final PFA structure, as the salt dominates the FTIR spectrum. We do not observe an SO_4^{2-} ion peak in the PFA/10% Na_2SO_4 spectra, which may be due to some settling of the salt particles during polymerization and curing at low salt loadings (**Figure B9**). As the salt particles are coated in the PFA and present at higher concentrations deeper into the sample, the limited penetration depth (~0.5 – 2 μm) of the ATR-FTIR measurement may not detect any SO_4^{2-} signal. At high salt loadings, the system behaves more as a polymer-in-salt system than a salt-in-polymer system, and the jamming of the salt particles prevents any settling.

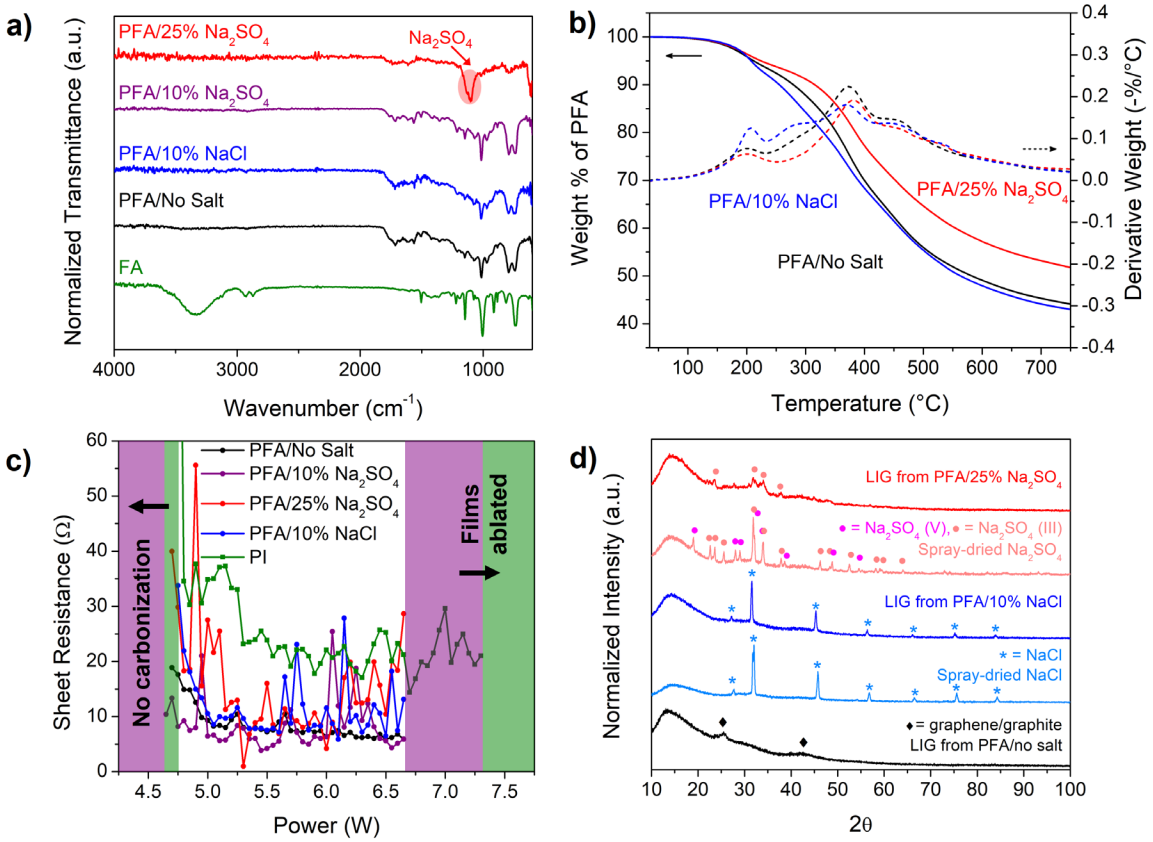

Figure 4.3: Materials characterization of PFA/salt composites and resulting LIG. a) FTIR spectra of FA monomer and PFA films with varying salt content, including PFA/no salt, PFA/10% NaCl, PFA/10% Na_2SO_4, and PFA/25% Na_2SO_4. b) TGA of PFA/no salt, PFA/10% NaCl and PFA/25% Na_2SO_4, along with the derivative TGA curves on the second axis. TGA curves were corrected for the initial salt content in the sample as discussed in the Experimental Methods section. c) Sheet resistance of LIG from PFA/no salt, PFA/10% NaCl, PFA/10% Na_2SO_4, PFA/25% Na_2SO_4, and PI. d) XRD of spray-dried NaCl and Na_2SO_4, as well as LIG from PFA/no salt, PFA/10% NaCl and PFA/25% Na_2SO_4.

TGA data for PFA/no salt, PFA/10% NaCl and PFA/25% Na_2SO_4 can be seen in **Figure 4.3b)**. The TGA curves for PFA/no salt and PFA/10% NaCl are similar, with carbon yields of 44.1 ± 2.5% and 43.0 ± 1.4%, respectively. However, the PFA/25% Na_2SO_4 sample possesses an increased carbon yield of 51.8 ± 2.0%, 7.7% higher than PFA/no salt, indicating that a high loading of Na_2SO_4 in the PFA composite may improve carbon yield to a small but significant extent. Moreover, derivative TGA curves show a peak at ~200 °C for samples with and without salt, which we attribute to the loss of volatile and low molecular weight species in the resin. This peak is strongest in the PFA/10% NaCl sample, indicating more volatile species may be present in this composite. At higher temperatures, two peaks appear for PFA/no salt, at ~370 °C and ~450 °C, which are very similar for PFA/10% NaCl, at

~370 °C and ~440 °C. However, for PFA/25% Na_2SO_4, the two main derivative peaks are shifted slightly to higher temperatures of ~380 °C and ~460 °C. The shifts in the derivative peaks indicate that this sample possesses improved thermal stability, and that under laser irradiation, this may enable the formation of a larger quantity of carbon and result in less material ablation.

4.3.2 Characterization of LIG formed from PFA/Salt Composites

Samples were irradiated with a range of different laser powers, and the sheet resistance of the samples was measured with a four-point probe, as seen in **Figure 4.3c)**. The carbonization power range is similar for PFA-based samples and PI, although PFA is ablated at lower laser powers of 6.7 W, while PI still carbonizes up to 7.3 W. Notably, the sheet resistance of LIG prepared from PFA/no salt is quite reproducible, with an average of 8.6 ± 3.1 Ω/square across all carbonizing laser powers. This sheet resistance is also very low and is consistently lower than LIG from PI (26.2 ± 16.3 Ω/square). The sheet resistances of LIG from salt-containing samples exhibit a larger variation with laser power. The average sheet resistances increase only slightly with the percentage of salt added, but remain lower than that of PI. Moreover, the sheet resistance of all samples remains relatively constant across the entire carbonization range. To determine whether variations in electrical resistance stem from remaining salt in the LIG, we dissolved away the salt, and re-measured the sheet resistance (**Figure B10**). While variation still exists, some of the very high sheet resistance values are significantly lowered. Even with this surface-coating salt present, LIG from PFA and PFA/salt composites exhibits sheet resistances similar to or lower than those reported in literature for LIG from PI (15 – 35 Ω/square),[24] phenolic resin (44 Ω/square),[96] and wood (10 Ω/square).[118]

XRD was conducted on the spray-dried NaCl and Na_2SO_4 salt particles, and also on LIG powder scraped off of the PFA/salt substrates as shown in **Figure 4.3d)**. The diffractogram for LIG from PFA/no salt possesses peaks at 2θ values of 25.4° and 42.0°, corresponding to the (002) and (100) peaks of graphitic domains, similar to XRD diffractograms of LIG from PI.[24] The diffractogram of NaCl possesses clear peaks for cubic NaCl, and the same peaks are apparent in the LIG powder from PFA/10% NaCl, indicating that the NaCl structure is preserved and still present in the LIG after laser irradiation. Full peak assignments are available in **Tables B1** and **B2**. The diffractogram of spray-dried Na_2SO_4 is more complex, as Na_2SO_4 undergoes different polymorphic transitions with temperature, and five different Na_2SO_4 polymorphs have been identified in the literature.[269] Two different polymorphs of anhydrous Na_2SO_4 are observable via XRD in the spray-dried Na_2SO_4. One set of peaks corresponds

to orthorhombic phase V Na_2SO_4, also known as thenardite, which is the stable Na_2SO_4 phase at room temperature. The remaining peaks correspond to anhydrous phase III Na_2SO_4, which is a metastable phase of Na_2SO_4 at room temperature, but has been observed to form as precipitates from solution at room temperature,[269] and when Na_2SO_4 is heated to high temperatures.[270] The diffractogram of LIG from PFA/25% Na_2SO_4 possesses some peaks that correspond to Na_2SO_4, mostly corresponding to phase III, but the peaks are very broad and weak, indicating that the photothermal energy from laser irradiation may induce some reaction or degradation of the Na_2SO_4, with only some phase III Na_2SO_4 remaining afterwards.

To further investigate the LIG material formed, and the effect of different salt loadings and laser powers, Raman spectroscopy was conducted. As seen for PFA/no salt in **Figure 4.4a)**, variations in the laser power result in changes in the Raman spectra, and thereby in the carbon material formed. In all spectra, the G and D peak are visible, at ~1580 cm^{-1} and ~1350 cm^{-1}, respectively. The G peak corresponds to an sp^2 hybridized, graphitic carbon structure, while the D peak corresponds to aromatic domains but is enhanced with defects and disorder in the material. However, only at 5.6 – 5.9 W is a 2D peak clearly visible, at ~2700 cm^{-1}. The 2D peak arises from second order zone boundary phonons, and can be used to assess the number of single graphene layers in the material.[236,271] Similarly to LIG from PI, the I_D/I_G ratio of LIG from PFA/no salt varies with laser power and an optimal laser power results in the lowest I_D/I_G ratio[24] – in our case, 5.85 W. The decrease in I_D/I_G ratio with laser power is related to the formation of larger graphitic crystalline domains along the a axis, while the subsequent increase after an optimal laser power may be due to partial oxidation of the LIG in air.[24] However, further investigation of the PFA/no salt LIG at 5.85 W indicates significant variation in the Raman spectra obtained on different areas of the sample, including in the I_D/I_G ratio (**Figure B11**). This is an expected phenomenon with LIG, and has been observed in LIG from PI as well, as the rastering laser beam induces non-uniform temperatures across each individual laser trace, resulting in differences in the carbon material formed at the center and edge of each laser trace.[272]

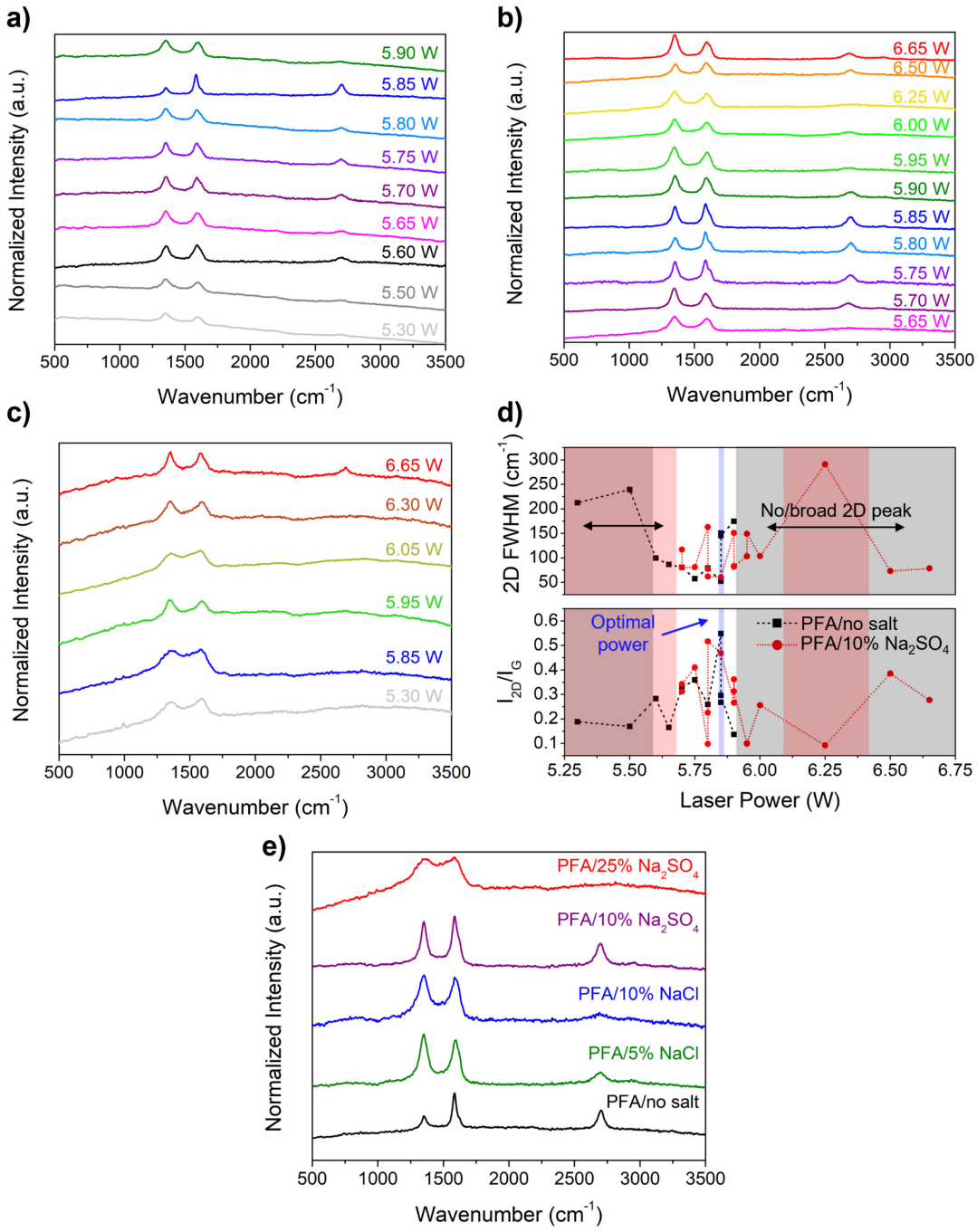

Figure 4.4: Raman spectroscopy analysis of LIG from PFA and PFA/salt composites. Raman spectra of LIG prepared at varying laser powers from a) PFA/no salt, b) PFA/10% Na_2SO_4, and c) PFA/25% Na_2SO_4. d) FWHM of 2D peak and I_{2D}/I_G ratio with laser power for PFA/no salt and PFA/10% Na_2SO_4. Black and red shaded areas indicate power ranges that result in either no 2D peak or a very broad and weak 2D peak. The blue shaded area indicates the optimal power of 5.85 W for the formation of a 2D peak with a minimum FWHM and maximum I_{2D}/I_G ratio. e) Raman spectra at 5.85 W for LIG from PFA/no salt, PFA/5% NaCl, PFA/10% NaCl, PFA/10% Na_2SO_4, and PFA/25% Na_2SO_4.

Similar behavior is observed for LIG formed from PFA/10% Na_2SO_4 (**Figure 4.4b)**), where clear G and D peaks are observed, but a 2D peak is only present in certain power rangers of 5.7 – 5.9 W and 6.5 – 6.65 W. Raman spectra of LIG formed from PFA/25% Na_2SO_4 exhibit significant differences compared to PFA without salt or with lower salt loadings (**Figure 4.4c)**). At most laser powers, the D and G peak do not appear as distinctive peaks, but instead are broad and slightly overlapped, strongly resembling an amorphous or glassy carbon signal, and is similar both to PFA prepared via high temperature furnace carbonization, and the signal obtained in previous work from PFA/1% GO.[260] Furthermore, the 2D peak is completely absent at most laser powers. Only at extreme laser powers of 6.65 W, just below the ablation threshold of the composite, is some separation in the G and D peaks and the appearance of a 2D peak observed, although significant variations in the spectra obtained across the sample area are again observed (**Figure B12**). The changes in the carbon structure formed at high Na_2SO_4 loadings may stem from changes in the PFA structure, or in the carbonization process. PFA/25% Na_2SO_4 resins are drop-cast after shorter polymerization times, due to the increased viscosity of the resin at high salt loadings, which could alter the PFA structure, but this is challenging to confirm with FTIR, due to the strong SO_4^{2-} signal. However, as indicated by the TGA data, the presence of the salt particles may also alter the carbonization process, resulting in a more amorphous carbon at higher salt loadings.

The evolution of the 2D peak behavior for PFA/no salt and PFA/10% Na_2SO_4 is summarized in **Figure 4.4d)**. While the behaviour of both systems varies significantly with laser power, an optimum level exists for both PFA/no salt and PFA/10% Na_2SO_4 samples, from 5.7 W – 5.9 W, that results in the formation of a 2D peak with minimal FWHM and maximum intensity. This corresponds well with results reported in the literature, such as LIG from wood,[118] Bakelite resin,[95] and poly(Ph-ddm)[122] which all exhibit a similar behavior of the I_{2D}/I_G ratio and 2D FWHM with laser power. As we observed no clear trend in sheet resistance with laser power, we selected 5.85 W to use for all further characterization and electrochemical testing, as it resulted in the lowest 2D FWHM and the highest I_{2D}/I_G ratio for PFA/no salt samples and is far enough from both the minimum and maximum carbonization power thresholds to ensure that PFA is fully converted into carbon without risk of significant ablation. In **Figure 4.4e)**, the Raman spectra of LIG prepared from various PFA/salt composites at a laser power of 5.85 W are displayed. The 2D peak is clearly visible for LIG from PFA/no salt, PFA/5% NaCl, and PFA/10% Na_2SO_4, but at higher salt loadings of PFA/10% NaCl and PFA/25% Na_2SO_4, the peak broadens or is not visible, and the highest salt loading of Na_2SO_4 is the only sample which exhibits the

broad, overlapping D and G peaks characteristic of amorphous, glassy carbon. This laser power was then used to prepare all remaining samples, to enable comparisons between LIG prepared from different salt composites.

The LIG material formed from varying PFA/salt composites was then imaged via SEM, both from a top-down surface view, and via freeze-fracturing of cross-sections of the composites. As seen in **Figure 4.5a)-c)**, LIG formed from PFA/no salt is highly fibrous and stringy in nature. The LIG formed is approximately 50 µm thick and the laser appears to have cut into the PFA resin surface. Little carbon material is present, indicating that a significant amount of PFA has vaporized instead of carbonized. Moreover, in the top-down surface view in **Figure 4.5a)**, while pores are present in the LIG, the LIG surface appears mainly smooth and non-porous, with little available surface area for electrolyte to access.

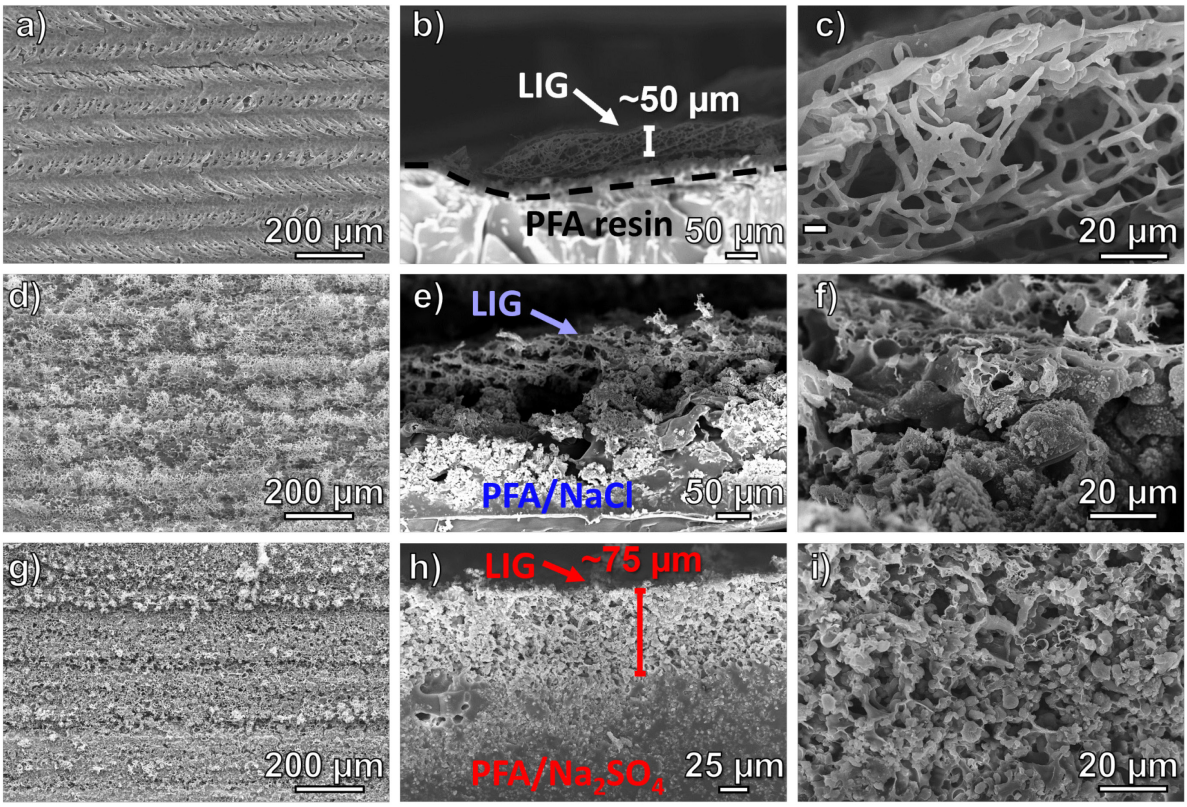

Figure 4.5: SEM images of LIG from PFA and PFA/salt composites. SEM images of LIG formed from a-c) PFA/no salt, d-f), PFA/10% NaCl, g-i) PFA/25% Na_2SO_4. a), d), and g) are top-down views of LIG, while b), e), and h) are cross-sections of the LIG formed on the PFA surface, and c), f), and i) are higher resolution cross-sections of the LIG material formed for each composite.

As seen in **Figure 4.5d)-f)**, LIG formed from PFA/10% NaCl has a much different morphology than the LIG from PFA/no salt. The top surface exhibits a spiky, almost branch-like morphology, while the cross-sections indicate that a less fibrous carbon structure is formed, with what appears to be more carbon material formed, and smaller pores. EDS mapping of the top surface (**Figure B13**) and cross-section (**Figure B14**) indicate that a mainly carbon-based material is formed, with some oxygen still present, and NaCl still distributed throughout and on top of the carbon material.

Finally, as seen in **Figure 4.5g)-i)**, LIG prepared from PFA/25% Na_2SO_4 appears to possess a morphology unique from the previous two samples, with a less branch-like surface, but still appearing highly porous, with a high degree of electrolyte-accessible surface area. The LIG morphology is unique, with some areas appearing like hollow spheres, which may be from PFA that was wrapped around spherical Na_2SO_4 particles or may stem from structuring of the PFA itself at the film surface into a spherical morphology, as the SEM images of this composite demonstrated. EDS mapping of the top surface (**Figure B15**) and cross-section (**Figure B16**) of the LIG indicate that a large quantity of Na_2SO_4 is still present, coating the LIG material. The LIG layer formed from PFA/25% Na_2SO_4 is thicker than that from PFA/no salt, at ~75 μm thick, and notably it appears that significantly more carbon is formed than without salt, indicating that less material is fully ablated or converted into gaseous byproducts. This corresponds well with the TGA data which demonstrates that higher carbon yields are achieved upon the addition of 25% Na_2SO_4, which is not observed with 10% NaCl. Notably, Ming *et al*. found that sodium salts behaved as carbonization catalysts in the hydrothermal carbonization of glucose, with Na_2SO_4 performing the best of various sodium salts evaluated, dramatically increasing the carbon yield and changing the particle morphology.[273] We suspect that Na_2SO_4 may play a similar catalytic role in our system, promoting the conversion of PFA into carbon rather than volatile species, although further analysis of the exact catalytic mechanism is needed. Moreover, we believe that the increased LIG thickness may be because inclusion of the dispersed salt particles increases the effective thermal conductivity and diffusivity of the PFA/salt composite, such that when the IR laser irradiates the sample, the laser power is distributed further across and into the composite, enabling a greater volume to be carbonized. We modeled the effect of dispersed NaCl and Na_2SO_4 particles on the thermal properties of PFA composites (full details in Appendix B and **Table B3**), and as seen in **Figure B17**, we observed an increase in the thermal conductivity and thermal diffusivity of the composites, with a higher increase observed with NaCl than with Na_2SO_4. From this calculated thermal diffusivity, we

were able to estimate the thermal penetration depth into a PFA sample and observed an increase upon the inclusion of salt particles (**Figure B18**).

HR-TEM analysis demonstrates that LIG from PFA/no salt possesses a wrinkled, few-layer graphene structure similar to LIG from PI, and a SAED pattern indicative of a polycrystalline graphitic structure, as seen in **Figure 4.6a)-c)**. The two main rings visible correspond to interplanar distances of 2.15 Å and 1.25 Å, which can be attributed to the (100) and (110) planes of graphitic carbon. The HR-TEM images and SAED patterns for LIG from PFA/10% NaCl and PFA/25% Na_2SO_4 in **Figure 4.6d)-f)** and **Figure 4.6g)-i)** indicate that as the salt loading increases, the material becomes more amorphous and disordered, with the rings in the SAED patterns becoming more diffuse. However, even in the highly amorphous LIG from 25% Na_2SO_4, some areas remain with clear few-layer graphene structure. A lattice spacing of 3.4 Å can be measured from the rippled graphene structures in all samples, which corresponds to the (002) spacing in graphitic crystallites. The graphene sheet number range is estimated to be ~3-13 sheets, but varies significantly across each sample, making it more suitable to refer to this as a few or multi-layer graphene. HAADF images and EDS maps of LIG from 10% NaCl and PFA/25% Na_2SO_4 in **Figure 4.6j)-l)** and **Figure 4.6m)-o)** demonstrate that discrete salt particles remain in the composite, and that the LIG material wraps around these salt particles, indicating that they behave as a template for pore formation. Higher magnification EDS mapping of LIG from 10% NaCl and 25% Na_2SO_4 in **Figure B19** and **B20** shows weak Cl and S signal distributed throughout each LIG material as well.

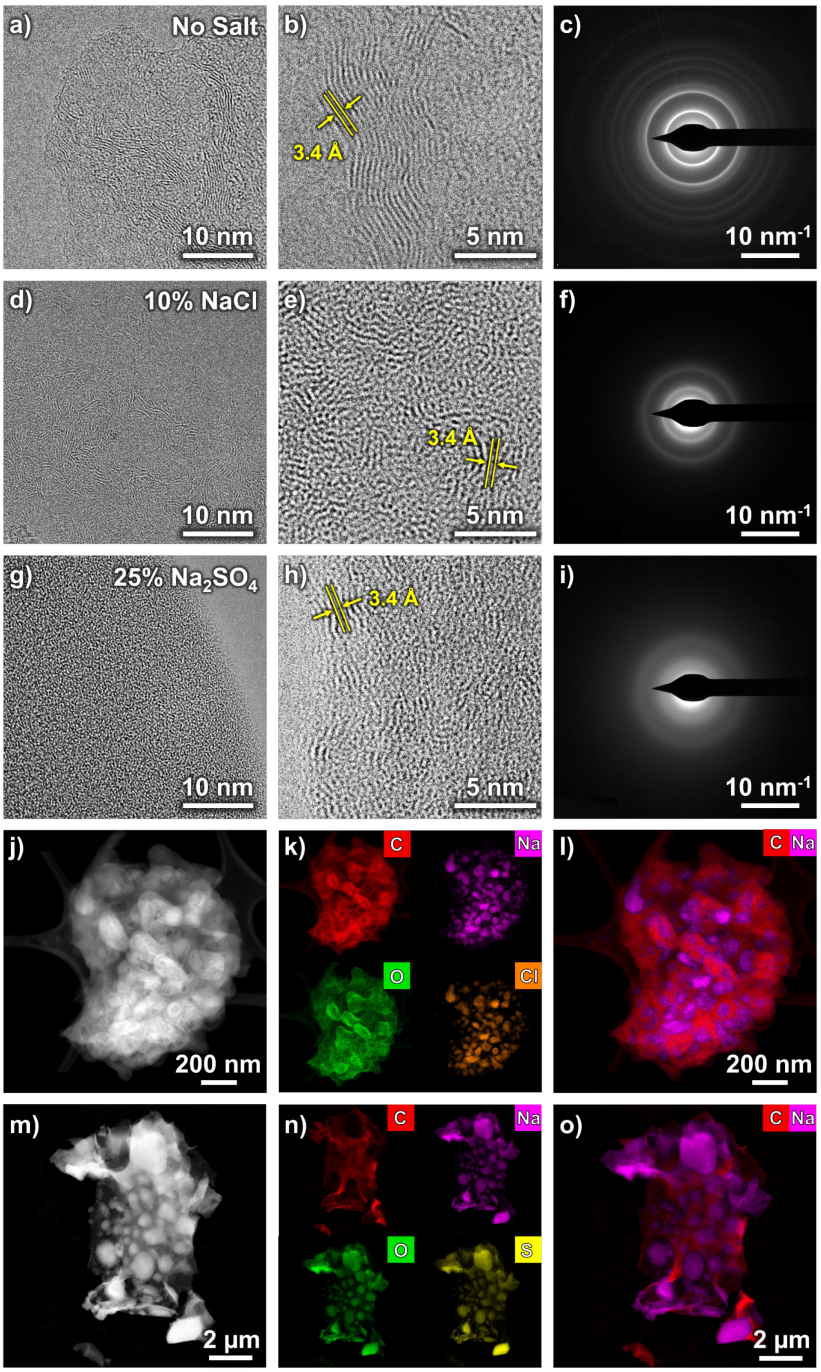

Figure 4.6: HR-TEM, EDS, and SAED analysis of LIG from PFA and PFA/salt composites. HR-TEM images and SAED patterns of LIG formed from a-c) PFA/no salt, d-f), PFA/10% NaCl, g-i) PFA/25% Na_2SO_4. For images d) and g), and all SAED patterns, salts were dissolved out of the LIG material prior to analysis, while for images e) and h), salts remain in the LIG. j-l) HAADF images and EDS mapping of LIG from PFA/10% NaCl. m-o) HAADF images and EDS mapping of LIG from PFA/25% Na_2SO_4. Figures l) and o) show overlaid C and Na maps, showing carbon wrapping around salt particles.

BET surface area analysis of LIG powders further confirms significant differences in the LIG formed from PFA with and without salt. LIG powder from PFA/no salt possesses a very low BET surface area of 22.4 m^2/g, congruent with its highly fibrous nature as seen in the SEM images. Following dissolution of residual salt, the LIG powders from PFA/salt composites both exhibited microporous behavior, which was not observed with PFA/no salt, and possessed substantially higher surface areas of 198 m^2/g and 239 m^2/g for PFA/10% NaCl and PFA/25% Na_2SO_4, respectively. The pore size distributions indicate that both samples are microporous and mesoporous in nature (**Figure B21** and **B22**). The samples possess similar cumulative pore volumes, with 10% NaCl's being slightly higher. As much of the pore volume for LIG from PFA/25% Na_2SO_4 consists of micropores, while LIG from PFA/10% NaCl possesses larger pore sizes, the ion accessible surface area of the two samples is expected to be similar. The differences in the pore sizes and structure may stem from the different initial sizes of the spray-dried salt particles. The surface area values are similar to those reported for LIG from PI (~340 m^2/g),[24] and fall within the range of surface areas reported for other LIG precursors such as Bakelite (55 m^2/g),[95] B-doped PI (191 m^2/g),[94] and poly(Ph-ddm) (883 m^2/g).[122] From this data, along with the TEM images, which demonstrate wrapping of the LIG around embedded salt particles, we believe that the salt particles act as a template or porogen in the PFA composite, enabling the formation of a higher surface area carbon material. Salt particles such as LiCl have been utilized in this manner as a hard template during the hydrothermal carbonization of lignin, to result in a higher surface area carbon material,[266] and salts such as $ZnCl_2$ and Na_2CO_3 have been employed in the chemical activation of carbons at high temperature to boost carbon surface areas.[265]

XPS analysis was then conducted on the LIG powders to further investigate their chemical structures. The high resolution C1s spectra can be seen in **Figure 4.7a)**. The LIG from PFA/no salt possesses a narrow C1s peak, made up of C-C, C-O, and C=O bonds.[24,94,260,274] The complete peak assignments and fitting parameters for all XPS spectra are listed in **Tables B4-B6**. However, the C1s peak from samples with salt is much broader overall, indicative of a higher degree of oxygen-containing functional groups. This is further confirmed by the decrease in intensity of the C-C peak. The C1s peak for PFA/10% NaCl is made up of C-C, C-O, and C=O/C-Cl bonds, as with PFA/no salt, but also possesses a small peak corresponding to carboxylic acids, -COO.[274] Notably, the peak at 286.8 eV may correspond to both C=O bonds as well as C-Cl bonds, which typically appear at 286.6 eV for chlorinated graphene.[275] The C1s spectrum for PFA/25% Na_2SO_4 is similar to PFA/10% NaCl, with C-C, C-O/C-S, and C=O peaks, as well as a much larger carboxylic acid peak, -COO. The peak at 285.5 eV may correspond to

both C-O functional groups as well as C-S bonding, which appear at approximately the same binding energy.[276] Moreover, it is clear that while both salts result in a higher degree of oxygen-containing functional groups, the quantity of specific groups formed is different depending on the specific sodium salt used. This is also clear in the high resolution O1s spectra, as seen in **Figure 4.7b)**. The O1s peak for PFA/no salt indicates a similar amount of oxygen present as both C-O and C=O bonds.[277] As the PFA/no salt C1s spectrum indicated that more carbon is present as C-O than C=O, this is an indication that more epoxide groups may be present in the LIG than alcohols. The O1s spectrum of PFA/10% NaCl possesses more C-O than C=O. PFA/25% Na_2SO_4 consists mainly of C=O bonds and very few C-O bonds, but also possesses a peak for SO_4^{2-}, from the remaining Na_2SO_4 in the system. The Cl2p peak for the LIG powder from PFA/10% NaCl is shown in **Figure 4.7c)**. A set of peaks corresponding to Cl^- from NaCl is visible. However, most chlorine is actually present as organic chlorine (i.e. covalent C-Cl bonds, 51.3%),[275] indicating that while some NaCl is retained after laser irradiation, some reacts with the PFA during laser carbonization, to produce Cl-doped LIG. The S2p peak for LIG powder from PFA/25% Na_2SO_4 can be seen in **Figure 4.7d)** and indicates that this is also the case with Na_2SO_4. While peaks are visible for SO_4^{2-},[278] peaks are also present that indicate covalent C-S bonding (20.8%).[276,279] Finally, a small peak is present that corresponds to $Na_2(SO_3)_2$,[280] indicating that, while some Na_2SO_4 remains intact following laser irradiation, some is converted into $Na_2(SO_3)_2$, and more still reacts with the PFA during the laser carbonization, to yield S-doped LIG. From the survey spectra of each powder (**Figure B23**), the C/O ratio of LIG from PFA/no salt, PFA/10% NaCl and PFA/25% Na_2SO_4 are 4.78, 2.98, and 1.59, respectively, with the PFA/25% Na_2SO_4 oxygen content estimated from the C-O and C=O peaks in the O1s spectrum, excluding the SO_4^{2-} peak. We expect that these fairly low C/O ratios correspond only to the surface composition of the LIG, not the bulk. The C/O ratios obtained from EDS of the LIG cross-sections for PFA/no salt, PFA/10% NaCl and PFA/25% Na_2SO_4 are much higher, at 27.52, 17.19, and 2.99 respectively. Notably, the EDS of the PFA/25% Na_2SO_4 cannot distinguish between the presence of oxygen in the LIG material and oxygen remaining in the form of Na_2SO_4, and as such the bulk C/O ratio for the LIG material alone is expected to be much higher.

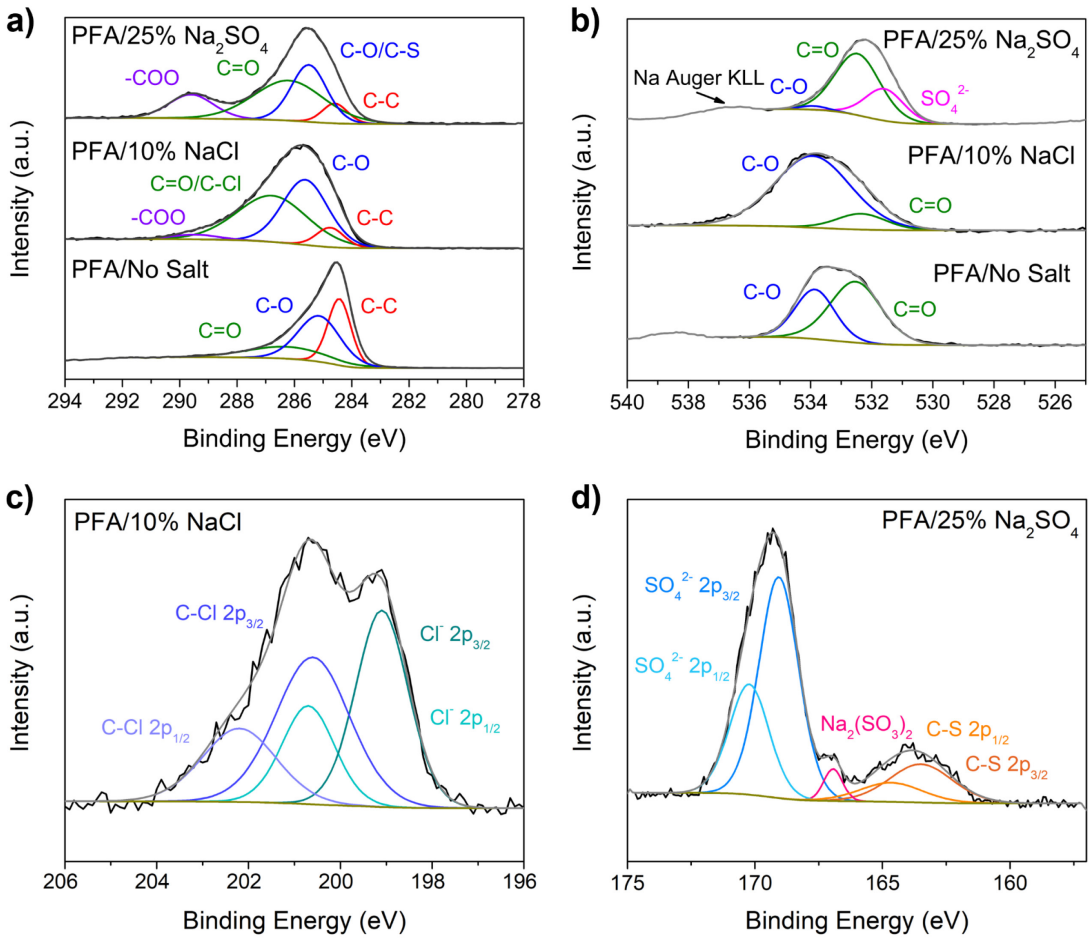

Figure 4.7: High resolution XPS spectra of LIG powders from PFA/no salt, PFA/10% NaCl, and PFA/25% Na_2SO_4. a) C1s spectra for all three samples, b) O1s spectra for all 3 samples, c) Cl2p spectrum for PFA/10% NaCl, and d) S2p spectrum for PFA/25% Na_2SO_4.

4.3.3 Electrochemical Performance of PFA/Salt-based LIG Supercapacitors

The average areal capacitances of devices prepared from various salt loadings, as determined from CV, can be seen in **Figure 4.8a)**. While devices prepared from PFA/no salt exhibit very low average areal capacitances of 8 μF/cm^2 at 5 mV/s, all devices with ≥ 5% salt achieve capacitances that are two or three orders of magnitude higher than PFA/no salt. In the case of NaCl, PFA/5% NaCl devices achieve an average capacitance of 6.5 mF/cm^2 at 5 mV/s and 0.35 mF/cm^2 at 500 mV/s, while increasing the NaCl content to 10% results in a slight decrease in capacitance at low scan rates, to 5.7 mF/cm^2, but higher performance at high scan rates, with 0.64 mF/cm^2 at 500 mV/s. As little difference was observed

between the 5% and 10% results, higher NaCl loadings were not explored. In the case of Na_2SO_4, average areal capacitance steadily increases with salt loading from 0.99 mF/cm^2 for PFA/5% Na_2SO_4, up to 25.6 mF/cm^2 at PFA/20% Na_2SO_4. At loadings above 20% Na_2SO_4, a slight decrease in average areal capacitance is observed, with capacitances of 19.7 mF/cm^2 and 15.2 mF/cm^2 at 5 mV/s achieved for PFA/25% Na_2SO_4 and PFA/30% Na_2SO_4, respectively. Complete values of the average areal capacitance with salt loading at 5 mV/s are listed in **Table B7**. Moreover, while both NaCl and Na_2SO_4 result in significant improvements in capacitance, the capacitance improvement more clearly scales with salt loading in the case of Na_2SO_4 than NaCl, which appears to result in a performance plateau. Furthermore, Na_2SO_4-based samples also exhibit better rate performance than NaCl-based samples, with PFA/Na_2SO_4 samples retaining ~22% of their 5 mV/s capacitance when tested at 500 mV/s, compared to ~8% capacitance retention for PFA/NaCl-based samples. Samples were also tested where the salt particles were removed prior to polymerization to determine the impact of any dissolved salt on the capacitive performance. For example, removing the micron-sized $NaSO_4$ particles results in very poor capacitances of 0.8 μF/cm^2 at 5 mV/s, with similar results obtained for NaCl (see **Figure B24** and associated discussion).

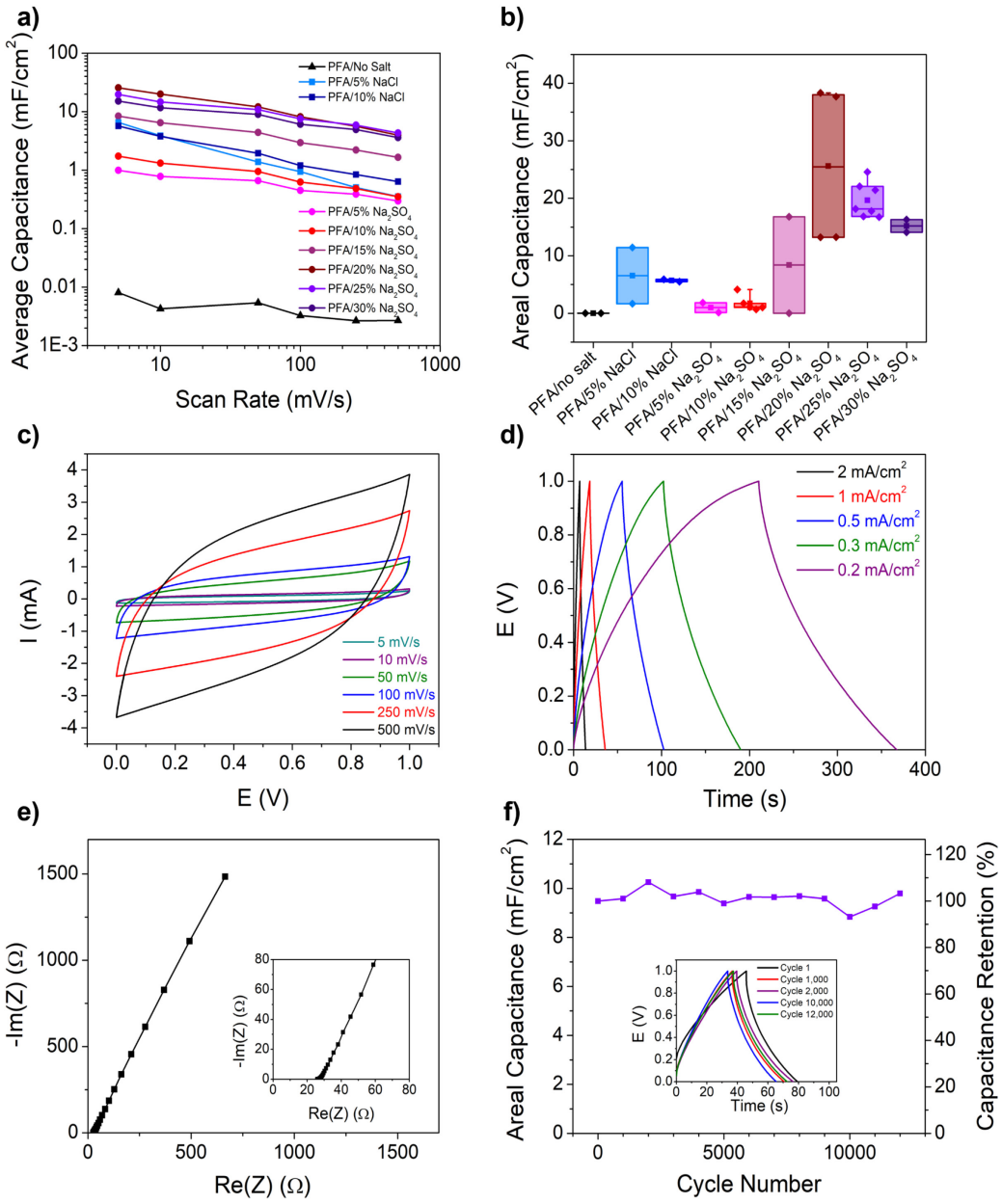

Figure 4.8: Electrochemical performance of PFA/salt-based LIG supercapacitors. a) Average areal capacitances with scan rate, as determined via CV, for PFA with no salt and with varying loadings of NaCl and Na_2SO_4. b) Box and whisker plot of areal capacitance for PFA with no salt and varying loadings of NaCl and Na_2SO_4 at 5 mV/s. Upper and lower bounds of the box represent the upper and lower quartile of the data, center line represents the median, square symbol represents the mean, and whiskers represent the minimum and maximum values. Each individual data point is represented with a diamond. c) CV curves of PFA/25% Na_2SO_4 at scan rates ranging from 5 mV/s to 500 mV/s. d) GCD curves of PFA/25% Na_2SO_4 at current densities ranging from 0.2 mA/cm^2 to 2 mA/cm^2. e) Nyquist plot of EIS data for supercapacitors prepared from LIG from PFA/25% Na_2SO_4. f) Long-term cycling of PFA/25% Na_2SO_4 at 0.5 mA/cm^2, with inset showing charging and discharging behavior at 1, 1,000, 2,000, 10,000, and 12,000 cycles.

While the average areal capacitance is a key performance metric for these supercapacitors, the repeatability of the performance is also critical. Consequently, we also examined the variation in the areal capacitance of the supercapacitors with varying salt content, from 2-7 devices prepared for each salt loading. In **Figure 4.8b)**, the areal capacitance for each salt loading at 5 mV/s is plotted as a box and whisker plot. The variability is lowest for the high salt loading samples (i.e., 10% NaCl and 25% $NaSO_4$) which we expect is due to a more homogeneous distribution of salt throughout the composite due to jamming of the particles and the resulting higher viscosity of the resin during casting. Lower loadings of 15% and 20% Na_2SO_4 may not be high enough to reach a threshold for jamming of the particles, resulting in more variability due to some settling of salt particles during curing. While individual PFA/20% Na_2SO_4 devices demonstrate the best performance among all devices at low rates, PFA/25% Na_2SO_4 devices were selected as the optimal salt loading, as they provided both high areal capacitance and excellent repeatability.

The performance of the optimized PFA/25% Na_2SO_4 devices is presented in the CV and GCD data in **Figure 4.8c)** and **Figure 4.8d)**. The CV curves are mainly rectangular in shape, and do not exhibit any faradaic or pseudocapacitive peaks, indicating the purely capacitive behavior of the PFA/25% Na_2SO_4 devices. The average areal capacitances achieved with scan rate for PFA/25% Na_2SO_4 are listed in **Table B8**. EIS data (**Figure 4.8e)**) demonstrates that the ESR for a typical device is relatively low at ~ 26 Ω, and the plot possesses a 45° slope at mid to low frequencies, characteristic of Warburg behavior and diffusion-limited processes, which is likely due to limited ionic transport through the gel electrolyte and pores of the LIG. A full discussion of the sources of cell resistance is available in Appendix B. Moreover, the GCD data demonstrates similar behavior, with fairly triangular charging and discharging profiles. Some curving of the GCD profiles is observed at low scan rates, which may be a result of some pseudocapacitive behavior resulting from unconverted PFA or dangling functional groups. As seen in **Figure B25**, the average areal capacitances calculated from CV and GCD agree with one another well, with average areal capacitances from GCD listed in **Table B9**, achieving 24.7 ± 3.8 mF/cm^2 at 0.05 mA/cm^2 and 5.5 ± 1.0 mF/cm^2 at 4 mA/cm^2. We further estimated the gravimetric capacitance of PFA/25% Na_2SO_4 devices to be 16.0 F/g_{LIG} at 5 mV/s and 20.0 F/g_{LIG} at 0.05 mA/cm^2. While more variability is observed in the PFA/20% Na_2SO_4 devices, the individual high-performing devices at this loading exhibit the highest capacitances of all devices in GCD, as seen in **Figure B26** and **Table B10**, with an average areal capacitance of 80.4 mF/cm^2 at 0.05 mA/cm^2. As discussed further

in Appendix B (**Figure B27**), removing salt before electrochemical testing resulted in only a slight improvement to electrode performance.

The long-term cycling of the PFA/25% Na_2SO_4 devices was tested via GCD at 0.5 mA/cm^2 as seen in **Figure 4.8f)**. The device initially exhibited a capacitance of 9.5 mF/cm^2 at 0.5 mA/cm^2 and displays stable cycling for 12,000 cycles. The capacitance retention varies slightly with cycling, with an increase at 2,000 cycles (10.2 mF/cm^2, 108.1% capacitance retention), and the lowest capacitance reported at 10,000 cycles (8.8 mF/cm^2, 93.2% capacitance retention). After 12,000 cycles, the device exhibits a capacitance of 9.79 mF/cm^2, with a capacitance retention of 103.3%. We expect that the variation in device capacitance over time stems from a few factors. Firstly, over time, we expect that surface-coating salt may dissolve into the gel electrolyte, which may lead to slight increases in capacitance, as we observed in **Figure B27**. Secondly, the cell architecture is not sealed, but rather open to the environment, and is therefore susceptible to changes in temperature and humidity in the lab, particularly over evenings and weekends as lab air flow may vary. Slight increases in the device capacitance with time may also occur due to further penetration of the electrolyte into the pores of the LIG. We observed a similar increase in capacitance of devices after resting without cycling (**Figure B28**), indicating that this is likely due to changes in the electrolyte rather than any degradation of the device itself. The shape of the charging and discharging voltage profile can be seen in an inset in **Figure 4.8f)**. While the first cycle appears slightly shifted from following cycles, this appears to be mainly due to a slightly increased charging capacitance in the first cycle, which may result from some initial irreversible reaction of remaining functional groups in the system. This does not appear to have an impact on the initial discharge capacitance, which then remains relatively constant for all other cycles. Moreover, the shape of the discharge curves for cycles 1,000, 2,000, 10,000, and 12,000 are nearly identical, indicating the stable cycling behavior of LIG-based supercapacitors from PFA/25% Na_2SO_4.

In **Figure 4.9**, we compare the performance of our PFA/salt-based supercapacitors to other LIG-based supercapacitors reported in the literature. We included the average areal capacitances of PFA/no salt and PFA/25% Na_2SO_4 devices, and also the average performance of the two highest performing PFA/20% Na_2SO_4 devices. It can be seen that while PFA/no salt devices exhibit areal capacitances several orders of magnitude below literature reports, PFA/Na_2SO_4 devices exhibit areal capacitances among the highest reported to date, outperforming most PI-based devices,[24,93,94] and various other LIG precursors, such as wood,[118] Bakelite,[95] and phenolic resin.[96] PFA/Na_2SO_4 devices similarly outperform μPFA/GO devices prepared in our previous work,[260] while also being more easily processable and

mechanically robust. Moreover, PFA/Na_2SO_4 devices are prepared using an inexpensive and widely available CO_2 laser under ambient conditions, while many other LIG-based devices have required the use of more costly lasers of other wavelengths[95–97] and inert gas atmospheres during lasing.[95,118] Notably, our devices exhibit similar capacitances to devices prepared through much more complex and less scalable processes, including plasma-treated PI-based LIG[97] and PI-based LIG prepared via lasing in a sealed chamber under O_2 gas,[113] as well as lignin[125] and poly(Ph-ddm)[122] devices which are prepared via use of much higher laser powers (~16-20 W).

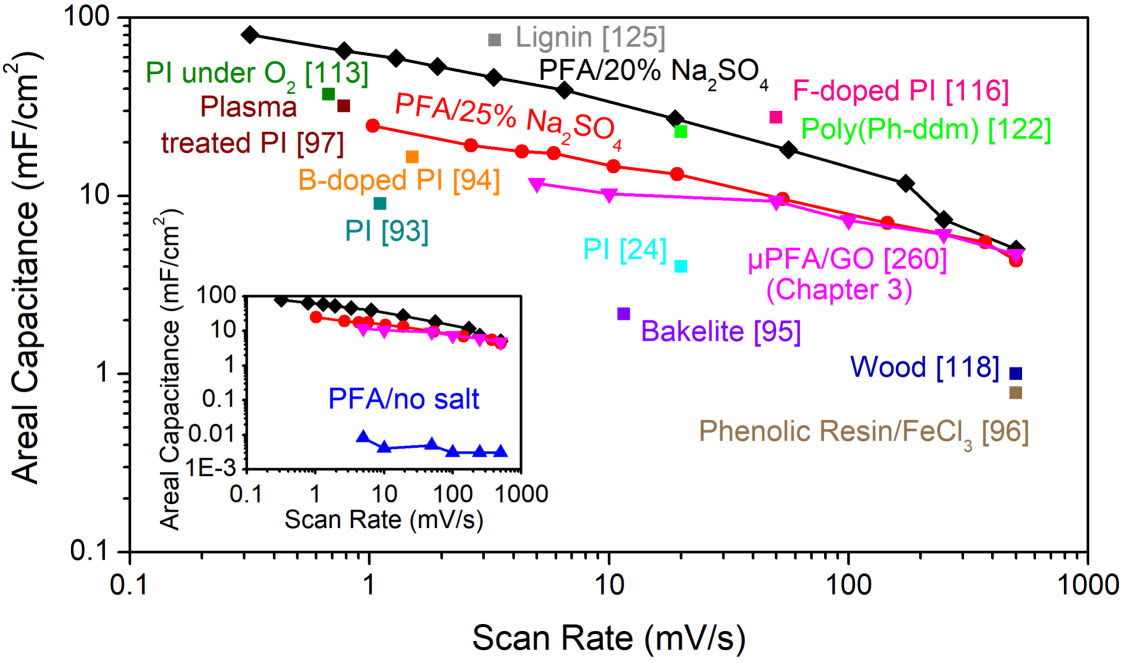

Figure 4.9: Comparison of electrochemical performance of PFA/salt-based supercapacitors with other LIG-based supercapacitors reported in literature. For all reports, the areal capacitance was normalized by the full two electrode area of the device, and any literature values that were normalized by a single electrode area or device area were corrected such that all data could be fairly compared.

As discussed above, the inclusion of micron-sized salt particles into the PFA significantly enhanced the BET surface area of the resulting LIG due to its templating effect and enhanced the thermal penetration depth, leading to increased LIG thickness and higher carbon yields. TGA analysis demonstrated that the carbon yield is higher for the Na_2SO_4 case, which could be one explanation for its increased capacitance over the NaCl-templated material despite the two electrode materials having similar mass specific surface areas measured by gas adsorption. In the Na_2SO_4 case, simply more high

surface area material was present after laser irradiation. On the other hand, via XPS we observed Cl-doping for the NaCl case and S-doping for the $NaSO_4$ case. Several studies have shown that the doping of heteroatoms such as Cl[88,281,282] and S[282,283] into graphene can improve its capacitance, which is attributed to a change in the quantum capacitance of the LIG. As discussed in section 2.4.2, for supercapacitors prepared from materials with a low density of states such as graphene,[58] the total capacitance is dependent on both the double layer capacitance and the quantum capacitance, as shown in Equations 2.23 and 2.24.

In the seminal publication on LIG, Tour's group demonstrated that defects in the LIG material, such as pentagon and heptagon pairs, can be more "metallic" in nature, effectively increasing the density of states in the material near the Fermi level, and increasing the quantum capacitance – thereby increasing the total capacitance.[24] For these reasons, amorphous or glassy carbons may be more suitable than graphene for use in supercapacitors, as their defects and functional groups have been shown to boost capacitance.[69,92,228] Likewise, other DFT studies have shown that doping of graphene with covalently-bound heteroatoms increases its quantum capacitance.[67–69] While we expect that both dopants improve the capacitance of the LIG material, it is possible that S doping may result in a more significant capacitance boost than Cl. We also observed a more amorphous structure for LIG from Na_2SO_4 via SAED, and the combination of these effects may enable the maximum capacitances to be achieved from Na_2SO_4-based samples. However, due to the multifunctional nature of the salt particles in the PFA composites, it is challenging to determine which of these effects is the most critical in boosting electrochemical performance. Overall, we expect that the salt particles act as multi-faceted additives, simultaneously improving the thermal properties of the PFA, acting as pore-forming agents and carbonization aids, and enabling heteroatom doping into the LIG structure, resulting in the remarkable capacitance increase observed in PFA/salt-based devices over PFA/no salt.

4.4 Conclusion

In summary, we have demonstrated for the first time that LIG-based supercapacitors prepared via dispersing of sodium salt microparticles throughout a carbon precursor such as PFA can result in a 2-4 order of magnitude increase in the areal capacitance. Supercapacitors prepared from PFA/25% Na_2SO_4 exhibit extremely high average areal capacitances of 19.7 ± 3.0 mF/cm^2 at 5 mV/s and 24.7 ± 3.8 mF/cm^2 at 0.05 mA/cm^2, with individual PFA/20% Na_2SO_4 devices achieving capacitances as high as 38 mF/cm^2 at 5 mV/s and 80 mF/cm^2 at 0.05 mA/cm^2, which are among the highest areal capacitances

reported for pure LIG-based supercapacitors to date. This approach employs inexpensive, abundant, and non-toxic sodium salts to enable high-performance LIG-based supercapacitors from PFA resin, an easily processable and biomass-derived polymer. Moreover, the improved capacitance is achieved without the need for inert atmospheres or surface treatments, while using an inexpensive and widely available CO_2 IR laser. In most previous studies thus far, the performance of LIG-based devices has been dictated mainly by the chemistry of the LIG precursor. Many materials carbonize successfully under laser irradiation but do not result in high surface area materials. The incorporation of multi-functional salt particles as dopant precursors, thermally conductive additives, pore-forming agents, and carbonization aids may enable a new level of control over device performance. While we have only demonstrated this concept with PFA thus far, the inert nature of the salts used and the ease and scalability of spray-drying as a manufacturing method demonstrate the widespread applicability of this approach for improving the porosity and performance of LIG from various precursors.

Chapter 5:
Evaluating Lithium Nucleation onto Laser-Induced Graphene for Lithium Metal Anodes

5.1 Introduction

Chapters 3 and 4 of this thesis have focused on the development of PFA as a novel, sustainable and easily processable precursor for the formation of LIG. Moreover, via the addition of GO and salt additives, we demonstrated the ability to optimize the surface area, carbon yield, and surface chemistry of the resulting LIG. While we have thus far focused on the optimization of these properties via the fabrication of LIG-based supercapacitors, the ultimate goal of this work was the intentional design of a porous, high surface area, heteroatom-doped LIG as a host material for lithium metal anodes.

As discussed in detail in Chapter 2, the lithium metal anode possesses the lowest standard reduction potential (-3.04 V vs. SHE) and one of the highest theoretical capacities (3860 mAh/g) of any anode material, making it an incredibly desirable anode choice.[5,7] However, its formation of an unstable SEI layer and its effectively infinite volume change during plating and stripping – thereby leading to breakage of the SEI layer, dendrite formation, and accumulation of a thick SEI layer and inactive, "dead" lithium – have limited the cycle life of all lithium metal cells. A variety of strategies have been investigated to improve its performance, including the use of electrolyte additives which can stabilize the SEI,[128,137–141] the formation of ex situ artificial SEI layers on the lithium or copper current collector surface,[143–156] and the use of porous, conductive materials to act as a host or scaffold to accommodate the lithium volume change and lower the effective current densities during plating.[158–161] While 3D current collectors and hosts for lithium are a promising route to address the challenges associated with the lithium anode, little fundamental work has been done to address how to effectively design a lithium host.

An ideal host material should be electronically conductive, lightweight, possess a high surface area to lower the effective current density, void space to accommodate lithium deposition, and be lithiophilic – meaning that lithium will plate on the material easily, with a low overpotential for lithium nucleation. Yan et al. demonstrated that different metals exhibit different overpotentials for the heterogeneous nucleation of lithium, with gold possessing an effectively zero overpotential due to the non-zero solubility of lithium in gold at high lithium content phases.[173] They demonstrated that a lithiophilic

material such as gold can be used to guide and control the deposition of lithium within a host structure.[173] However, nearly all host structures studied to date are carbonaceous. Preparation of a lithiophilic surface from purely carbon-based materials, rather than costly and heavy materials such as gold, would be desirable. Chen et al. demonstrated computationally that the inclusion of specific heteroatom dopants and functional groups on the surface of graphene materials can increase the binding energy between lithium ions and the graphene substrate, particularly functional groups containing boron and phosphorus, along with certain functional groups containing oxygen, nitrogen, and sulfur.[169] However, few experimental studies have demonstrated the impact of heteroatom doping on the nucleation of lithium on carbon host materials.

LIG is a promising material for a lithium host, as it is a conductive, high surface area material with substantial porosity to accommodate lithium plating. Due to the limited loadings achieved by laser scribing, LIG is more practical as a scaffold material in batteries, rather than a direct active material, as shown by the wide number of studies that have employed it as the porous carbon scaffold for air cathodes.[98–101] In the only study of its kind to date, Yi et al. prepared a unique LIG architecture to act as a host for lithium metal by placing PI tape on copper foil and selectively scribing it to form PI pillars coated with LIG.[168] They demonstrated that this material possesses low overpotentials for lithium nucleation even at extremely high current densities up to 10 mA/cm^2, and outperforms conventional LIG and copper.[168] The authors illustrated from further computational analysis that this is due to the formation of lithiophilic oxygen and nitrogen-containing functional groups on the LIG, although it should be noted that some inconsistencies in the lithiophilic nature of specific functional groups exist between these different computational studies.

In Chapter 4, we demonstrated the formation of high surface area LIG from PFA/salt composites, and notably, discovered that the LIG could be doped with different heteroatoms depending on the salt used. The LIG formed from these PFA/salt composites is particularly suited for the fundamental study of lithium nucleation on different doped graphene materials.

In this chapter, we first investigate if LIG can be prepared from composites of PFA and lithium salts and as a proof-of-concept measure the capacitance of the resulting LIG materials. Following material characterization, we identify four model materials for investigation as lithium hosts – LIG from PI, LIG from PFA, LIG from PFA/25% Na_2SO_4, and LIG from PFA/10% Li_2SO_4. We then conduct a lithium nucleation and plating study by evaluation of the lithium nucleation overpotential at various current

densities on the different LIG materials, as seen in **Figure 5.1**. Notably, we also study the effect of pre-lithiating the LIG materials before lithium nucleation on the resulting plating overpotentials. We attempt to identify trends in the overpotentials and charge transfer resistances and to deconvolute the various factors that can influence plating, such as the doping, surface area, and loading. We demonstrate that LIG from PFA/25% Na_2SO_4 and PFA/10% Li_2SO_4 exhibit lower overpotentials and charge transfer resistances than undoped LIG from pristine PFA. We also study the cycling performance of these cells and suggest strategies to improve performance.

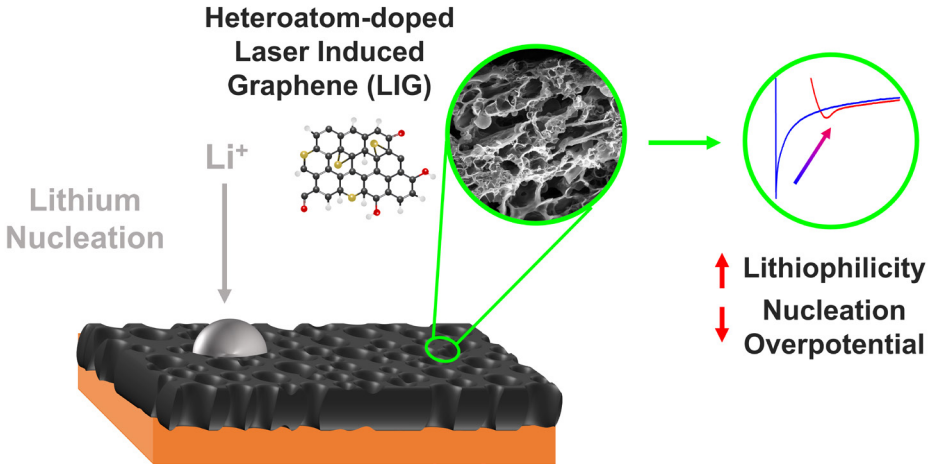

Figure 5.1: Scheme for investigation of lithium nucleation on heteroatom-doped LIG.

5.2 Experimental Methods

5.2.1 LIG Synthesis

PFA and PFA/25% Na_2SO_4 were prepared following the procedure outlined in Chapter 4. Li_2SO_4 (Sigma-Aldrich, ≥98.5%) and K_2SO_4 (Sigma-Aldrich, Reagent Plus®, ≥99.0%) were spray-dried following the protocol used for NaCl and Na_2SO_4 in Chapter 4. Li_3PO_4 (Sigma-Aldrich, 338893) and $Li_2B_4O_7$ (Sigma-Aldrich, ≥99.9%) were used directly. PFA/Li_2SO_4, PFA/K_2SO_4, and PFA/Li_3PO_4 films were prepared following the same procedure as PFA/NaCl and PFA/Na_2SO_4, but with polymerization times of 3-4 hours. All LIG was prepared using a speed of 10 mm/s and two laser passes. A range of laser powers was investigated for sheet resistance testing, but otherwise, the optimized laser power from Chapter 4, 5.85 W, was used for all other testing. LIG from PI was prepared from commercial Kapton film (McMaster-Carr, Electrical-Grade, 0.0050" thick), using 5.85 W, 10 mm/s, and a single laser pass, as a second started to cut through the film.

5.2.2 Materials Characterization

Sheet resistances of LIG samples were obtained by laser scribing a rectangle of 6.07 mm x 2.70 mm and measuring the sheet resistance with a four-point probe measurement (Ossila). All sheet resistance measurements were performed directly on the PFA or PI substrates after laser scribing.

Raman spectroscopy was conducted on LIG directly on the substrate surface with a Horiba Jobin-Yvon HR800 Raman system equipped with an Olympus BX 41 microscope with a 50 mW, 532 nm laser operating at 25% laser power.

Scanning electron microscopy (SEM) to assess the material morphology was carried out on spray-dried salt particles and on gold-coated cryogenically fractured cross-sections of the PFA/salt composites, LIG, and LIG after salt dissolution, with a Zeiss Leo 1530 with energy dispersive X-ray spectroscopy (EDS) operating at an acceleration voltage of 20 kV. Salts were dissolved by soaking the entire PFA substrate after LIG formation in DI water for 24 hours, followed by rinsing the surface with DI water and drying under vacuum for 24 hours. Image analysis of the spray-dried salt particle size was performed with ImageJ software.

X-ray photoelectron spectroscopy (XPS) was conducted with a Thermal Scientific KAlpha XPS spectrometer, 150 eV, and spectra were fitted using CasaXPS software. For LIG from PI, XPS was carried out directly on the LIG powder scraped off the PI substrate, while for LIG from PFA/Li_2SO_4 samples, the salt was dissolved out of the LIG powder first. To do this, the same protocol used to remove the salt from LIG from PFA/25% Na_2SO_4 in Chapter 4 was used – samples were stirred in 15 mL of DI water for 24 hours. They were then centrifuged at 3500 rpm, transferred into ethanol and re-centrifuged. This step was repeated once more to remove all water, to prevent any capillary forces during drying, in order to limit any drying-induced changes to the surface area. The samples were then dried under vacuum overnight. As charge compensation was used during XPS measurement, which can cause shifts in the binding energy, the XPS spectra for Li_2SO_4 samples were charge-corrected so that the C-C peak appeared at 284.4 eV.

5.2.3 Electrode Fabrication

Graphite electrodes were prepared by mixing 1.71 g of graphite (MTI Artificial Graphite Powder for Li-ion battery anode) with 3 mL of 30 mg/mL PVDF (Sigma-Aldrich, Mw ~534,000, powder) in NMP (Fisher Chemical, Laboratory grade) to prepare a slurry with 600 mg/mL loading and a ratio of 95:5

graphite:PVDF. Slurries were homogenized for 30 seconds with a CATX120 homogenizer with a T6 shaft at 33,000 rpm. Slurries were then doctor-bladed onto 10 μm thick copper foil at a wet-gap of 250 μm. LIG-based electrodes were prepared by mixing LIG (following dissolution of any salt using the procedure above), 30 mg/mL PVDF in NMP binder solution, and NMP to form a slurry with 95:5 LIG:PVDF by mass, and a loading of 400 mg/mL. Slurries were homogenized using the same procedure as graphite. Films were doctor-bladed using a wet-gap of 100 μm. All electrode films were dried overnight under vacuum at 80 °C. Electrodes were then punched to form discs (15/32" diameter) and pressed at 1 US ton for 1 minute. Copper electrodes were prepared by punching discs (15/32" diameter) from copper foil. Gold-coated copper electrodes were prepared by sputtering gold (Polaron Instruments, E5100) onto copper foil at 20 mA for 5 minutes to form a 75 nm thick layer on the copper foil.

5.2.4 Electrochemical Testing

Capacitance of LIG with varying salts and loadings was tested using a symmetric, interdigitated design, identical to that used in Chapter 4.

Electrochemical testing of graphite was conducted in a three-electrode split cell (MTI Corp., EQ-3ESTC), using 700 μL of electrolyte consisting of 1 M $LiPF_6$ in 1:1 EC:DMC (Sigma-Aldrich, battery grade). Graphite was used as the working electrode, while 9/16" diameter lithium metal (Sigma-Aldrich, 0.75 mm thick, 99.9% trace metals basis) was used as the counter electrode and a lithium metal ring (24 mm OD and 5/8" ID) was used as the reference electrode. The surface layer of the lithium was removed prior to assembly with a brush and rolling between two metal rollers to provide a clean, bare lithium surface. Whatman GF/A glass microfiber separators were used, with a 24 mm OD separator between the working electrode and reference electrode, and a 24 mm OD and 15/32" ID separator ring between the reference electrode and counter electrode. All cells were assembled in an Ar-filled glovebox, with ≤0.1 ppm water and ≤0.7 ppm oxygen. The graphite working electrode was subjected to an initial work-in cycle at 0.05C (discharging to 0.005 V and charging to 2 V) and then discharged to 5 mV at 0.1C before plating studies were carried out. Plating was carried out at current densities of 100 $\mu A/cm^2$, 50 $\mu A/cm^2$, 300 $\mu A/cm^2$, and 500 $\mu A/cm^2$, with stripping at 100 $\mu A/cm^2$ until a cut-off voltage of 35 mV was reached. Following stripping, for 300 and 500 $\mu A/cm^2$ current densities, the electrodes were first re-lithiated to 5 mV at 100 $\mu A/cm^2$, followed by plating at the higher current densities.

Electrochemical testing of copper, gold-coated copper and LIG-based electrodes was performed in CR2032 coin cells (MTI Corp.) with a polypropylene separator (MTI Corp.) and 7/16" diameter lithium metal foil anode. The lithium surface was cleaned using the same procedure as for the graphite cells. Cells were assembled with 90 µL of electrolyte, consisting of 1 M lithium bis(trifluoromethanesulfonyl)imide (LiTFSI, Aldrich Chemistry, 99.95% trace metals basis) and 0.1 M lithium nitrate ($LiNO_3$, Acros Organics, 99+%) in 1:1 v/v 1,2-dimethoxyethane (DME, Sigma-Aldrich, anhydrous, 99.5%)/1,3-dioxolane (DOL, Sigma-Aldrich, anhydrous, 99.8%). All cells were assembled in an Ar-filled glovebox, with ≤0.1 ppm water and ≤0.7 ppm oxygen. All cells were rested for 6 hours before testing. For the lithium nucleation study, LIG samples were tested via two protocols: lithiated and unlithiated. Lithiated cells were first discharged to 0.005 V and charged to 2 V at 0.1C, followed by a second discharge at 0.1C to 0.005 V. Lithium was then plated at 100 µA/cm^2 to a capacity of 1.5 mAh/cm^2. Lithium was then stripped to a cut-off voltage of 50 mV, as this was experimentally observed to be the point at which the stripping plateau began to rapidly increase in voltage, indicating that all plated lithium had been stripped away and delithiation of the LIG was occurring. Following this, lithium was plated at a range of current densities in the following random order, to avoid any additive effects on the overpotential over time: 100 µA/cm^2, 50 µA/cm^2, 300 µA/cm^2, 500 µA/cm^2, 100 µA/cm^2 repeat, 1 mA/cm^2, 2 mA/cm^2, 5 mA/cm^2, 50 µA/cm^2 repeat. Stripping for all steps was performed at 100 µA/cm^2 until the 50 mV cut-off. Unlithiated samples were tested similarly, but with no initial discharge, charge, and discharge cycle. Rather lithium was plated at 100 µA/cm^2 with no work-in cycle. Plating was performed at the same current densities, in the same order, with all stripping done at 100 µA/cm^2, but done to a cut-off voltage of 2 V, to fully delithiate the carbon. Long term cycling was conducted using a LAND CT2001A battery tester, with lithium plating at 1 mA/cm^2 and 1 mAh/cm^2, and lithium stripping at 1 mA/cm^2 with a cut-off voltage of 1 V. The electrochemically active surface area (ECSA) was determined via cyclic voltammetry on Li/LIG half-cell coin cells at 5 mV/s in the non-faradaic region between 2 and 2.5 V. It is assumed that the Li CE does not contribute to the capacitance and impacts of doping on the capacitance are ignored here – as such, this can only serve as an estimate. The double layer capacitance, C_{DL}, was determined as:

$$C_{DL} = i_{avg}/\nu \tag{5.1}$$

where i_{avg} is the average current at the midpoint (2.25 V) of the CV curves and ν is the scan rate. The ECSA was calculated as:[284–286]

$$ECSA = \frac{C_{DL}}{C_s m} \quad (5.2)$$

where m is the mass loading of the LIG and C_s is the specific capacitance for carbon, which was assumed to be 20 μF/cm^2. Values of 10 – 20 μF/cm^2 have been reported for carbon, and we used 20 μF/cm^2 to provide a lower estimate of the surface area.[58,285,286]

5.3 Results and Discussion

5.3.1 Formation of LIG from PFA/Lithium Salt Composites

In Chapter 4, we demonstrated that introducing spray-dried NaCl and Na_2SO_4 microparticles into PFA lead to doping and templating of the resulting LIG formed. While these heteroatom-doped and high surface area LIG materials could be promising lithium metal host materials, the electrodes previously prepared still contained significant quantities of residual salt after laser scribing. We previously hypothesized that this salt could dissolve in the aqueous, gel electrolyte used to prepare LIG-based supercapacitors. While residual salt could be dissolved out from the LIG in water, it would make more sense for a lithium anode application to investigate the use of lithium salts in preparing LIG, such that any remaining salt not removed via dissolution could potentially dissolve in the electrolyte or form part of the SEI, and contribute to lithium transport. As such, we first investigated expanding our previous PFA/salt composite work to use lithium-based salts to form LIG. Moreover, since lithium nucleation has been theoretically shown to be highly dependent on heteroatom-doping, we specifically targeted lithium salts that could potentially introduce heteroatom dopants that would facilitate low nucleation overpotentials, such as O, N, S, P, and B. Consequently, we first investigated the preparation of PFA/salt composites from $LiNO_3$, Li_2SO_4, Li_3PO_4, $Li_2B_4O_7$, and, for comparison to our previous work with NaCl and as a negative control, LiCl, as Cl doping is expected to make the material more lithiophobic and lead to higher lithium nucleation overpotentials.

However, processing of most PFA/lithium salt composites proved challenging. While NaCl and Na_2SO_4 were both insoluble in the FA monomer and ethanol solvent, LiCl and $LiNO_3$ were soluble. Thus, they could not remain as solid salt microparticles, which is essential for the templating of the PFA, and thus the formation of a high surface area LIG material. Moreover, their dissolution led to an extremely rapid polymerization of the PFA, likely due to the reaction of the salts with the oxalic acid catalyst, producing lithium oxalate and either nitric or hydrochloric acid, which caused the

polymerization to occur violently, within a few seconds. As a result, these salts were incompatible with the PFA synthesis process and could not be used.

Similarly, the use of $Li_2B_4O_7$ led to the formation of brittle, inhomogeneous films, likely due to some dissolution and reaction of the salt, as seen in **Figure C1**. Only two lithium salts could be used to prepare PFA/salt composites: Li_2SO_4 and Li_3PO_4. However, the inclusion of Li_3PO_4 also had an impact on the PFA polymerization. While typical PFA films were cured after drop-casting at 80 °C overnight, we observed that PFA/Li_3PO_4 films would not fully cure unless four times the oxalic acid catalyst concentration was used and extended cure times of 48 hours at 80 °C were employed, likely due to Li_3PO_4 acting as a weak base in the system.

SEM images of the different spray-dried salt particles investigated can be seen in **Figure C2** and histograms of the salt size distributions as measured from SEM can be seen in **Figure 5.2a)**. The salt size distributions for NaCl and Na_2SO_4 were previously reported in Chapter 4, but are compared here to the size of the spray-dried Li_2SO_4 particles, and for sake of completion of the sulfate salt series, K_2SO_4. Li_3PO_4 could not be spray-dried due to its limited water solubility. However, it could be purchased as a fine powder, rather than large crystals. While a quantitative size estimate was not possible due to aggregation of the particles in SEM, we estimate that it is on the same size scale as the other salts employed, even without spray-drying. Na_2SO_4 and K_2SO_4 possess the same average particle size – the smallest, at 2.4 μm ± 1.3 μm and 2.4 μm ± 0.5 μm respectively, with Li_2SO_4 possessing an average size of 4.7 ± 1.9 μm and NaCl possessing the highest, at 6.2 ± 2.5 μm. We expect that this trend in particle size is due to the different densities of the different salts employed. Na_2SO_4 and K_2SO_4 possess the same density, 2.66 g/cm^3, while the densities of Li_2SO_4 and NaCl are 2.22 and 2.16 g/cm^3 respectively. As all salts are spray-dried at the same concentration in g/L, the denser salts result in smaller particles after drying.

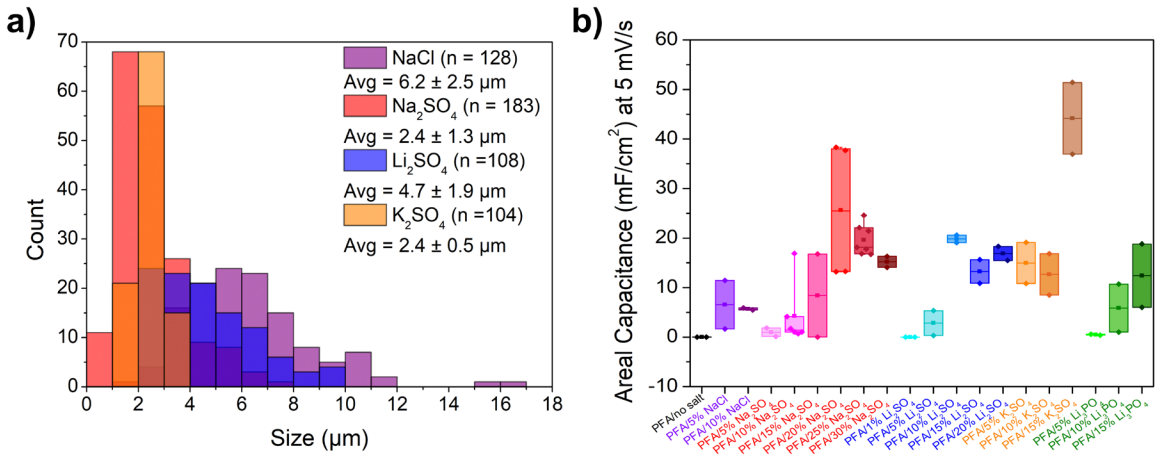

Figure 5.2: Size distribution of salt particles and areal capacitance summary for PFA/salt-based LIG. a) Size distribution of spray-dried salts, as measured from SEM. b) Summary of areal capacitance at 5 mV/s for LIG supercapacitors prepared from PFA with various salts and salt loadings.

PFA/salt composites were prepared from Li_2SO_4, K_2SO_4, and Li_3PO_4, with varying salt loadings, ranging from 1 – 20%, and were laser scribed using the same optimized parameters described in Chapter 4. While the capacitance of the LIG is not necessarily a parameter indicating a good Li host material, it is directly related to both the surface area and the doping of the carbon. Furthermore, it can be determined by a rapid test and can help to identify promising salt loadings for further investigation. Thus, the capacitance of interdigitated LIG supercapacitors prepared from different salts and loadings was measured, identically to the testing done in Chapter 4. The areal capacitance at 5 mV/s of all salts and loadings investigated can be seen in a box and whisker plot in **Figure 5.2b)**, and on a logarithmic scale in **Figure C3**. High quality LIG material can be prepared from each of these salts, expanding the list of salts beyond NaCl and Na_2SO_4, which were studied in detail in the previous chapter. As observed for the sodium salts, areal capacitances for low salt loadings are low, and increase with salt loading. The optimal salt loading for Li_2SO_4 is 10%, which results in an average areal capacitance of 19.8 ± 1.1 mF/cm^2, quite similar to that of 25% Na_2SO_4, beyond which loading the capacitance appears to decrease or plateau. LIG from PFA/15% K_2SO_4 results in the highest capacitances of all salts tested, of 44 ± 10.2 mF/cm^2, but with significant variation between samples. Higher loadings of K_2SO_4 were explored but led to either short-circuited samples due to widening of the LIG fingers or cutting through the PFA film during lasing. Though there are many complicating factors that can contribute to the capacitance, such as heteroatom doping, a relationship exists between the salt particle size and the highest achievable capacitance of LIG from each salt, indicative of the templating effect of the salt particles. K_2SO_4 and

Na_2SO_4, while possessing some variability between samples, exhibit the highest individual capacitances, and the smallest particle sizes, while Li_2SO_4, with a slightly larger particle size, yields slightly lower capacitance, and NaCl, with even larger particle size, even lower maximum capacitance. This can be seen in **Figure C4**. The highest performance for Li_3PO_4 films was observed at 15%, with an areal capacitance of 12 ± 9.0 mF/cm^2, but again with significant variation observed among samples. The areal capacitance for optimal salt loadings with scan rate can be seen in **Figure C5a)**, demonstrating that the inclusion of any salt tested boosts the capacitance of LIG by 2 – 4 orders of magnitude over LIG from pristine PFA. The performance of the optimal ratios for sulfate salts can be seen in **Figure C5b)**. This indicates no significant trend in capacitance with the variation of the cation of the sulfate salt. While K_2SO_4 results in the highest capacitance at low scan rates, it also possesses the worst rate capability, with the lowest performance at high scan rates. The performance of Li_2SO_4 and Na_2SO_4 are quite similar to one another, with slightly better rate performance observed for Na_2SO_4.

In selecting LIG materials for further investigation as a host material for a lithium anode, we eliminated LIG prepared from PFA/Li_3PO_4 and PFA/K_2SO_4 as both possessed significant variation in performance, along with the increased catalyst content and cure times for processing PFA/Li_3PO_4 and K_2SO_4 not being a lithium salt. Consequently, we chose to focus on LIG prepared from PFA/25% Na_2SO_4 and PFA/10% Li_2SO_4. As demonstrated in Chapter 4, LIG from PFA/25% Na_2SO_4 is a high surface area carbon material with O and S doping, and we expect that LIG from PFA/10% Li_2SO_4 may have similar properties. Moreover, capacitance results from both indicate highly repeatable and consistent performance.

To further investigate the LIG material prepared from PFA/Li_2SO_4 composites, cryogenically fractured cross-sections were examined using SEM and EDS, as seen in **Figure 5.3**. As seen in the cross-sections of the PFA/salt composites at 5, 10, and 15% Li_2SO_4 in **Figure 5.3a), d), and g)**, the salt particles remain as discrete particles, analogous to the Na_2SO_4 system. Similarly, as seen in **Figure 5.3b), e), and h)**, the LIG formed possesses a similar morphology and porous structure, and EDS mapping indicates that sulfur and oxygen are uniformly present across the surface, indicating the presence of residual Li_2SO_4 after laser irradiation. To determine if this surface salt could be removed, samples were then imaged after dissolving out the salt in DI water, as seen in **Figure 5.3c), f) and i)**, and the porous LIG structure is preserved after salt dissolution. Moreover, a significant difference is observed in the EDS maps, which demonstrate a strong decrease in the signal of both S and O, with the

dominant signal being C. This indicates that dissolution of the salt is possible without damaging the LIG structure, and can be done before testing the materials as a lithium host.

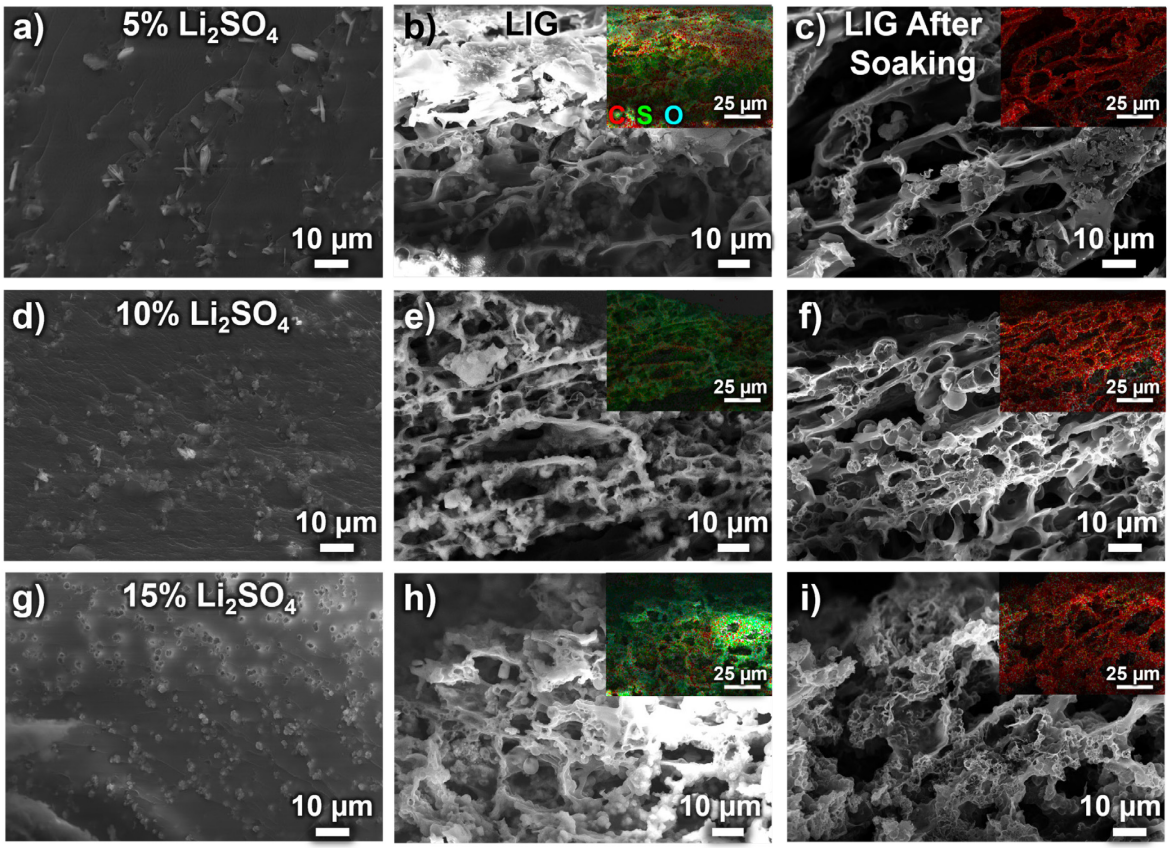

Figure 5.3: SEM and EDS analysis of LIG prepared from PFA/Li_2SO_4 composites. a-c) 5% Li_2SO_4, d-f) 10% Li_2SO_4, g-i) 15% Li_2SO_4. a), d), and g) show cross-sections of the salt particles dispersed in the PFA resin, b), e) and h) show cross-sections of the LIG formed, and c), f), and i) show cross-sections of the LIG formed after the salt has been dissolved out. The insets in b), e), h), c), f), and i) show EDS mapping, with carbon in red, sulfur in green, and oxygen in cyan.

LIG material prepared from 5, 10 and 15% Li_2SO_4 was examined by XPS after dissolution of the salt. The high resolution C1s, O1s, and S2p spectra can be seen in **Figure 5.4a), b), and c)**, with the survey spectrum in **Figure 5.4d)**. In the high resolution C1s spectrum in **Figure 5.4a)**, the typical C-C, C-O/C-S, C=O, and COO bonds previously observed for LIG from PFA/salt are present. However, significant differences are observed in these spectra compared to LIG from PFA/25% Na_2SO_4. In the Li_2SO_4 case, the C-C peak is the dominant peak, and the C=O and COO peaks are much smaller than those observed for LIG from PFA/25% Na_2SO_4. This is consistent with the overall oxygen content determined from the survey spectra, which is 37.85% for LIG from PFA/25% Na_2SO_4, but only 15.52%,

17.52%, and 20.19% for 5, 10 and 15% Li_2SO_4, respectively – which are not very different than LIG from pristine PFA (17.31%). The S2p spectra shown in **Figure 5.4c)** demonstrate that some residual sulfate is present in the system, even after salt dissolution, which was also observed in Chapter 4 for the Na_2SO_4 system, via TGA analysis. It is also possible that these sulfate groups are covalently attached to the LIG, but based on the previous TGA analysis, we have assumed that this is from residual undissolved surface salt. As in LIG from PFA/Na_2SO_4, sulfur doping (C-S) is also present in these samples. However, two previously unobserved S-containing functional groups are also formed – sulfone groups (CSO_2C, $2p_{3/2}$ of 168.0 eV) and sulfoxide groups (CSOC, $2p_{3/2}$ of ~165 eV). It is possible that some small amount of sulfone formation occurs in the case of Na_2SO_4-based LIG, and is obscured by the significant SO_4^{2-} peak. However, in the case of Li_2SO_4, significant sulfone formation is observed, with a similar sulfone and sulfide content, or even greater sulfone content than sulfides. Notably, the sulfone and SO_4^{2-} contents increase with rising Li_2SO_4 salt loading. The amount of total sulfur doping increases with salt loading and is 0.64%, 0.69%, and 0.97% for LIG from 5% Li_2SO_4, 10% Li_2SO_4, and 15% Li_2SO_4 respectively, after correcting for residual SO_4^{2-}. These values are also consistent with PFA/25% Na_2SO_4, which exhibited a sulfur doping content of 2.15%. The O1s spectra in **Figure 5.4b)** possess the same C-O and C=O peaks previously observed, but also a CSO_2C peak, which overlaps with the C=O peak. The sulfoxide O1s peak also likely overlaps here, but few examples of the O1s peak for sulfoxide groups beyond liquid and gas phase DMSO have been reported.[287] Moreover, a small sulfate peak would also be expected to overlap here (532.6 eV),[278] but the peak is likely too small to be visible. The fitting parameters used for all XPS analysis can be found in **Tables C1-C3**. Thus, while both Na_2SO_4 and Li_2SO_4 salts result in sulfur doping and similar areal capacitance, the LIG materials formed are significantly different.

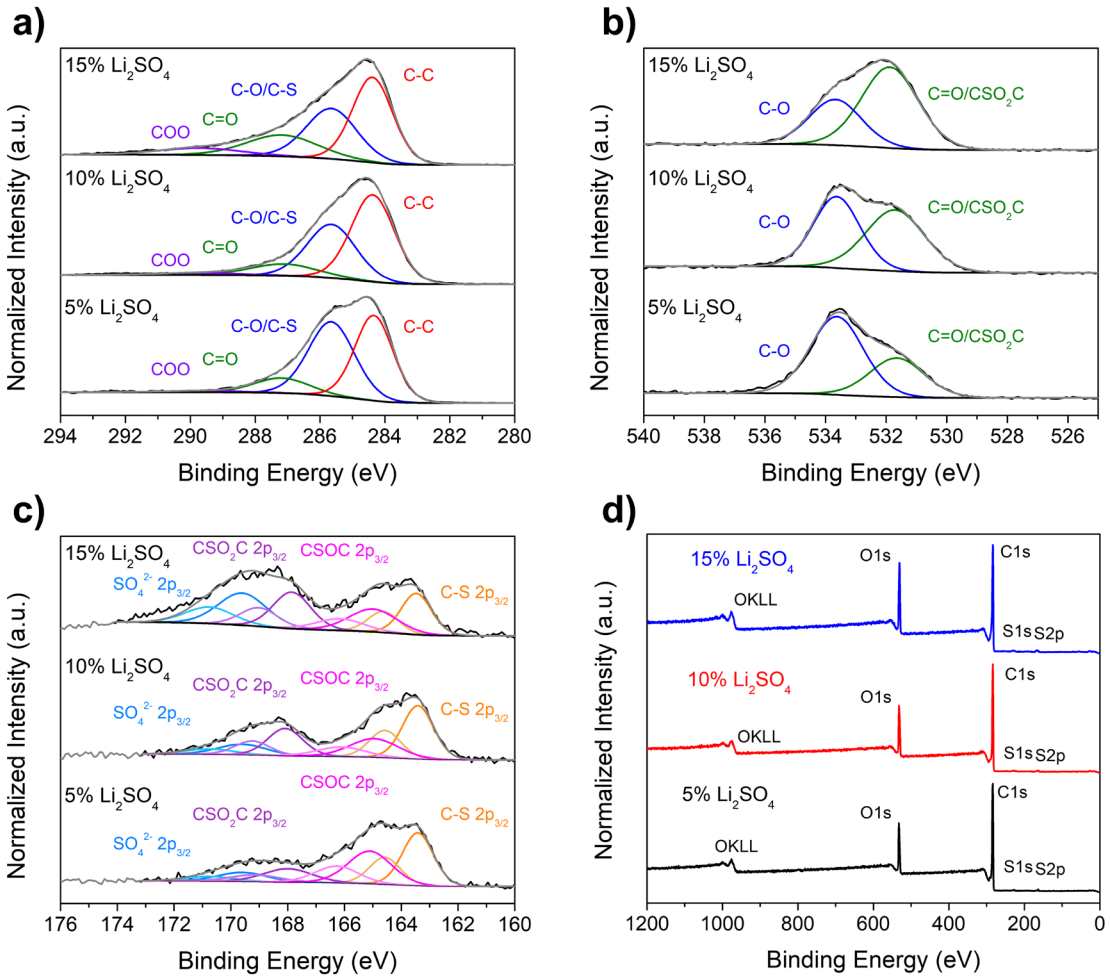

Figure 5.4: XPS analysis of LIG formed from 5, 10, and 15% Li_2SO_4. High resolution a) C1s, b) O1s, and c) S2p spectra, along with d) survey spectra. Note that only the $2p_{3/2}$ peaks are labelled in c), and not the $2p_{1/2}$ peaks, for readability.

Further sheet resistance and Raman spectroscopy analysis, seen in **Figures C6** and **C7**, indicated that little difference is apparent in the conductivity or carbon structure of the LIG material prepared from 5, 10, or 15% Li_2SO_4. While the XPS results indicate a slight increase in the sulfur content with increasing salt content, 10% Li_2SO_4 was selected as the optimal salt loading for investigation of the LIG as a lithium metal host, as it led to the highest capacitance and the least variation between samples.

5.3.2 Materials Characterization of LIG for Lithium Host

We selected four LIG materials to investigate as potential hosts for lithium: LIG from pristine PFA, LIG from PI, and due to their observed differences in XPS, both LIG from PFA/25% Na_2SO_4 and LIG

from PFA/10% Li_2SO_4. The full XPS characterization of LIG from PFA and PFA/25% Na_2SO_4 is discussed in Chapter 4, and the XPS for LIG from PI can be seen in **Figure C8**, with all peaks tabulated in **Table C4**. LIG from PI possesses less oxygen content than PFA-based samples, but possesses similar functional groups. While significant overlap of the different C-N functional groups (imine, imide, amine, amide, pyrrole and pyridine groups) occurs in the N1s spectrum, making any deconvolution challenging, nitrogen doping and C-N bonding are present. The chemical composition of the different LIG materials is summarized in **Table 5.1**.

Table 5.1: Chemical composition of different LIG materials, as determined by XPS.

Sample*	C (%)	O (%)	N (%)	S (%)	Key Functional Groups
LIG from PFA	82.69	17.31	N/A	N/A	C-O, C=O
LIG from PI	90.72	6.39	2.89	N/A	C-O, C=O, COO, CON, C-N
LIG from PFA/25% Na_2SO_4	60.00	37.85	N/A	2.15	C-O, C=O, COO, C-S
LIG from PFA/10% Li_2SO_4	81.69	17.52	N/A	0.69	C-O, C=O, COO, C-S, C-SO-C, C-SO_2-C

*For LIG from PFA/25% Na_2SO_4 and PFA/10% Li_2SO_4, chemical composition has been corrected to remove salt, such that only the composition of the LIG is reported here. The functional groups present in each sample are colour-coded based on Chen et al.'s computational study, with green indicating lithiophilic groups, red indicating lithiophobic groups, black indicating functional groups that were not considered in the study, and orange indicating groups that have similar lithiophilicity to pristine graphene or a range of different values reported, i.e. values for epoxides, alcohols, and ethers all vary among the C-O group.[169]

The sheet resistance of all LIG materials is reported in **Figure 5.5a)**, before salt dissolution for PFA/salt samples. The sheet resistances of all PFA-based LIG samples are similar and vary very little with laser power. The sheet resistance of PI-based LIG is higher than that of all PFA-based samples. As laser power has very little effect on sheet resistance, the optimized laser power settings used in Chapter 4 were used for all samples here (5.85 W). Raman spectra of the LIG materials can be seen in **Figure 5.5b)**. LIG from the pristine polymers, PFA and PI, exhibits a graphene-like spectrum, with distinct D (~1350 cm^{-1}), G (~1580 cm^{-1}), and 2D (~2700 cm^{-1}) peaks. As discussed thoroughly in Chapter 4, the spectrum of LIG from PFA/25% Na_2SO_4 is indicative of an amorphous carbon material, with broad, overlapping D and G peaks, and no 2D peak. The spectrum of LIG from 10% Li_2SO_4 is very similar to that of 25% Na_2SO_4, indicating a similarly amorphous structure. It should be noted that despite this amorphous structure, graphitic domains were still observed in LIG from 25% Na_2SO_4 in TEM, which could also be the case with the 10% Li_2SO_4 sample.

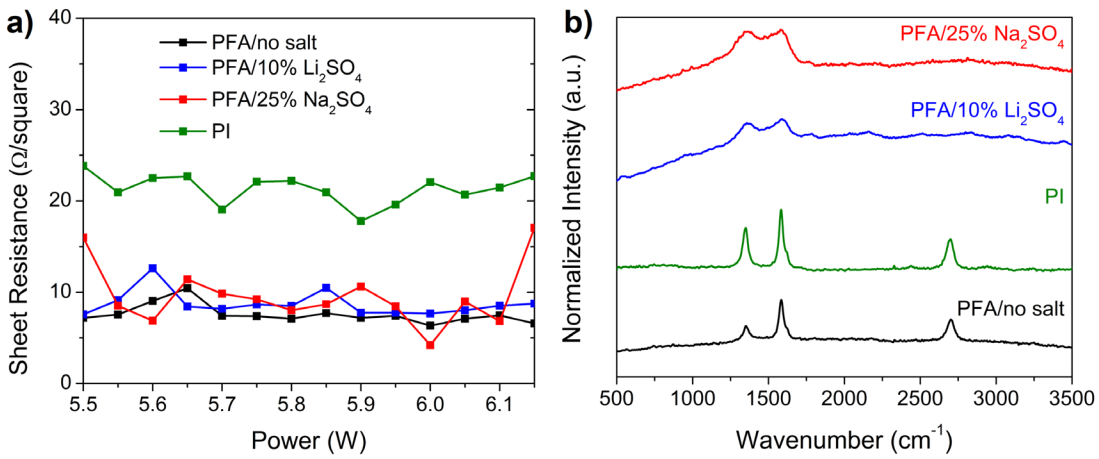

Figure 5.5: Sheet resistance and Raman spectroscopy of different LIG materials. a) Sheet resistance of LIG from PFA, PFA/10% Li_2SO_4, PFA/25% Na_2SO_4, and PI at various laser powers. b) Raman spectra of LIG from the same precursors at selected laser power of 5.85 W.

5.3.3 Lithium Nucleation on Graphite

To assess the performance of various materials as a lithium metal host, we sought to measure the overpotential for lithium nucleation at different current densities on the materials of interest. As a proof of concept, we first studied graphite electrodes, which have been used as lithium-ion anodes for decades. Initial proof-of-concept testing was performed in a three-electrode split test cell, using a lithium metal disc as the counter electrode, and lithium metal ring as the reference electrode (**Figure C9**). The graphite working electrode was subjected to an initial work-in cycle at 0.05C and then discharged to 5 mV at 0.1C before plating studies were carried out. This testing procedure and the voltage profiles for lithium plating on lithiated graphite can be seen in **Figure C10a) – c)**. The lithium plating voltage profiles follow the expected shape, with an initial dip followed by a plateau, indicative of lithium nucleation and growth. Moreover, testing of three separate cells at different current densities indicates repeatable results with little variation, and a linear relationship of the overpotential with current density (**Figure C10d)**).

While these initial results were promising, we experienced several issues associated with the use of the three-electrode test cell. Firstly, we frequently observed disconnection between the lithium ring reference electrode and the cell during assembly, leading to inaccurate or noisy voltage measurements (**Figure C10e)**). We also observed frequent short-circuiting of the reference and counter electrodes. While this is challenging to confirm via voltage alone as both the reference and counter electrodes are

lithium metal, and thus possess a nearly 0 V potential difference, this can be confirmed via the appearance of a second dip in the lithium plating voltage profiles at higher current densities (300 and 500 μA/cm^2) and capacities of lithium plated. In two-electrode symmetric Li|Li cells, this second dip stems from changes in the lithium counter electrode potential – the initial plateau during plating is due to stripping of lithium metal from dendrites formed on the counter electrode surface, and the second dip occurs after the dendrites have been consumed and once stripping begins to occur from the bulk counter electrode surface.[288,289] However, this should not occur in a three-electrode setup since the voltage measured is with respect to the Li reference electrode. Thus, the presence of this second dip is indicative of the short circuiting of the reference and counter electrodes. Moreover, the high cost of the three-electrode cell and incompatibility of the sealing o-rings with ether-based electrolytes used for LiS cells makes it unsuitable for scalable testing. We compared the voltage profiles for lithium nucleation on graphite in the three-electrode cell and two-electrode coin cells and observed very similar overpotentials at low current densities (**Figure C10f)**). At higher current densities, the coin cells actually exhibited lower overpotentials and IR drops, which could be due to electrolyte evaporation and sealing issues in the three-electrode cell (**Figure C10g)**). Consequently, although three-electrode testing would provide the most accurate overpotential measurements without the influence of the lithium counter electrode, we performed all remaining testing in a two-electrode coin cell configuration, due to its scalability, compatibility with electrolyte, and use to date in literature.[168]

5.3.4 Lithium Nucleation on LIG

Initial plating tests were first carried out on two model materials, copper, and gold-coated copper. Copper is the typical current collector employed for lithium metal anodes, and the benchmark for most lithium anode performance comparisons. As discussed above, lithium possesses an effectively zero overpotential for nucleation on gold, due to the formation of lithium-gold alloys and a solid solution of lithium in gold at high atomic ratios of lithium. As such, these two materials can act as a negative and positive control for lithium nucleation, with copper as a lithiophobic material that should exhibit high nucleation overpotentials, and gold as a lithiophilic material that should exhibit low nucleation overpotentials. All tests were carried out in a DOL/DME-based electrolyte typically used for LiS cells.

The voltage profiles for lithium nucleation and plating on copper are shown in **Figure 5.6a)**. The voltage profiles follow the expected shape for lithium nucleation and growth: an initial voltage dip, immediately followed by a plateau, with the initial dip stemming from lithium nucleation, and the

following voltage plateau corresponding to lithium plating and growth, following nucleation. The magnitude of the voltage difference between this initial dip and plateau is the overpotential, η, for lithium nucleation. With increasing current density (*j*), the overpotential increases as well. While an unchanging plateau is observed during lithium plating up to the maximum plating capacity of 1.5 mAh/cm^2 at most current densities, at some current densities, a second dip in the voltage profile is observed, which, as discussed with the graphite results, stems from the lithium metal counter electrode, and occurs from a transition from stripping from surface dendrites to stripping from the lithium bulk.

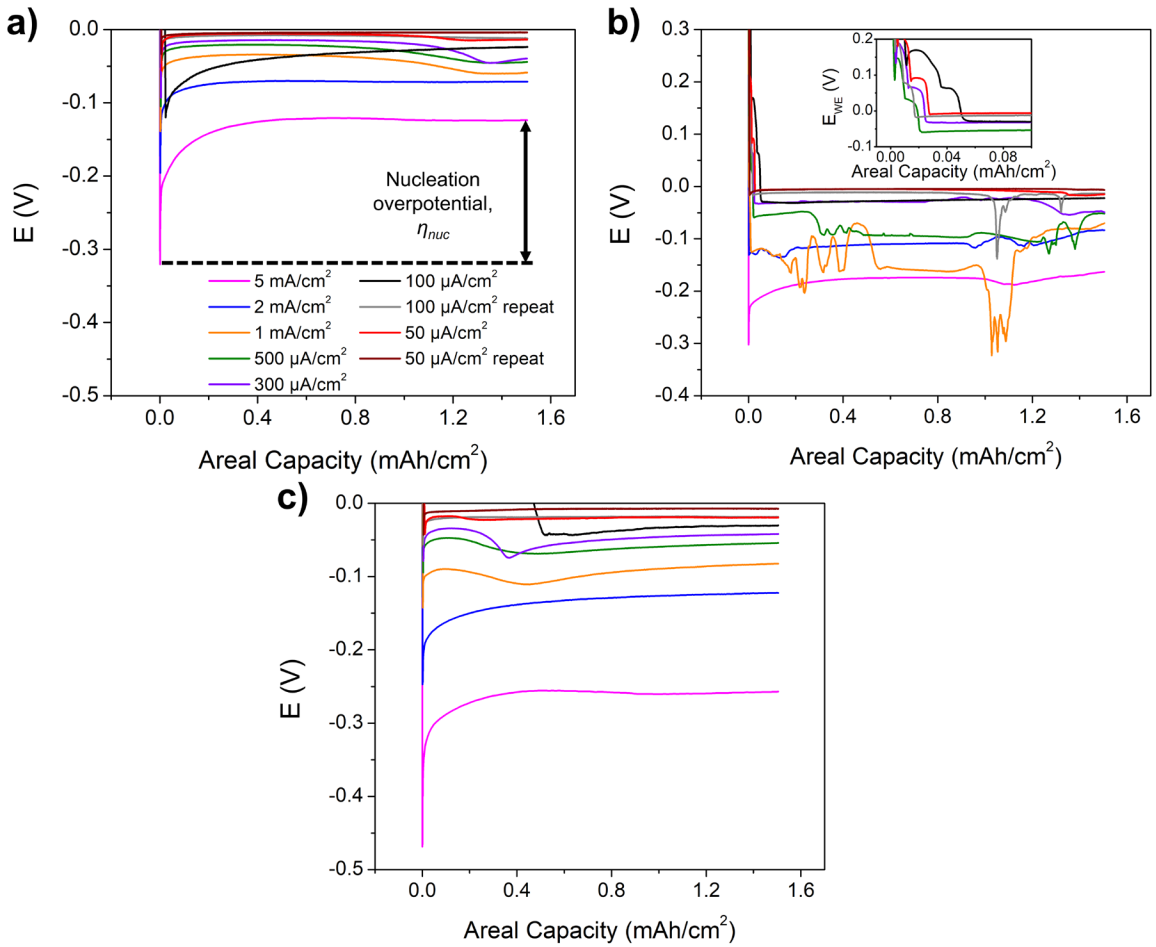

Figure 5.6: Voltage profiles for lithium nucleation and plating on different materials. Voltage profiles for plating on a) copper, b) gold-coated copper, and c) unlithiated LIG from PFA/25% Na_2SO_4.

However, the lithium plating on gold-coated copper (**Figure 5.6b)**) does not follow expected behaviour based on literature. The voltage curves for initial plating at low current densities (100 and

50 μA/cm^2) exhibit the expected behaviour – the formation of Li-Au alloys can be confirmed by the presence of multiple voltage plateaus below 0.2 V, and the subsequent nucleation overpotential for these current densities is effectively zero, with no initial dip in the voltage profile observed, but rather an immediate voltage plateau. The Li-Au alloy voltage plateaus and lack of an overpotential matches well with the studies performed by Yan et al., which were performed at very low current densities of 10 – 100 μA/cm^2.[173] However, at higher current densities, large dips and variations are present in the voltage profiles at higher lithium plating capacities, which was repeatedly observed in multiple cells. We hypothesize that these variations occur due to some delamination of the gold from the copper substrate during plating. The gold surface was prepared via sputtering of ~75 nm of gold onto copper foil, with no intermediate adhesion layer, and the large volume change of the gold during alloying could result in enough mechanical stress to cause delamination. While we investigated gold-coated copper here as a positive control of a lithiophilic surface with a low overpotential for lithium nucleation, these results suggest further challenges associated with gold, beyond its cost, and that simple gold-coating of copper current collectors is not a solution for a stable lithium metal anode.

Studying the lithium nucleation and plating on LIG is more complex, as LIG materials have been previously studied as lithium-ion anodes, and can therefore store lithium via adsorption of lithium onto each side of the graphene sheets, and via binding to the sheet edges. For any carbon anode that can be lithiated, lithiation and lithium plating are both possible processes – in fact, lithium deposition usually proceeds by adsorption as the first step. Furthermore, unlike copper and gold films, where lithium can plate on a flat, effectively 2D surface, LIG electrodes consist of a thick layer of porous electrode material, held together with binder and immersed in electrolyte. For any electrode beyond a nominal thickness, mass transport of Li^+ is a limiting factor that could impact the measured overpotential. We can confirm that mass transport in the liquid electrolyte is not a limiting condition that will impact the overpotential, as the diffusion limiting current density for DOL/DME electrolytes is 198 mA/cm^2 in a typical coin cell configuration, and the currents investigated here are two to three orders of magnitude lower.[290] However, for materials that can be lithiated, solid state transport of lithium ions in the material during lithiation can be a limiting step. To ensure that mass transport of lithium ions in the LIG does not contribute to the overpotential, we studied the nucleation of lithium on LIG electrodes that had been fully pre-lithiated. However, while these measurements can provide fundamental information on lithium plating on LIG materials, they do not represent how LIG materials would be used as a lithium metal host in practice, during which lithium would need to plate on the LIG surface with no pre-

lithiation step. Consequently, we also tested LIG materials without any pre-lithiation, referred to from hereon as unlithiated samples. Plots showing the specific charge and discharge steps for both the lithiated and unlithiated testing protocols can be seen in **Figure C11**. Few studies, if any, have been reported on the effect of pre-lithiation on lithium nucleation.

The voltage profile for lithium nucleation and plating on unlithiated LIG from PFA/25% Na_2SO_4 can be seen in **Figure 5.6c)**. The voltage profiles for plating on other LIG materials are presented in **Figure C12**. Similarly to copper, the voltage profiles possess the expected shape, with an initial dip from lithium nucleation followed by a plateau. Again, at several intermediate current densities, a second dip is observed in the plating profiles, stemming from the counter electrode. At these current densities, the overpotential was calculated at both the initial plateau and final plateau in the data, to account for any differences, as labelled in **Figure C13**. The individual calculated overpotentials for all samples are plotted in **Figure C14**, with 2 – 4 cells measured for each sample. It should be noted that for all samples, significant differences in the overpotential at 100 $\mu A/cm^2$ are observed from the first lithium plating cycle to the 5^{th}, due to the formation and stabilization of the SEI layer, as seen in **Figure C15**.

Plots of the variation of the average lithium nucleation overpotential with current density for all LIG materials can be seen in **Figure 5.7**. It should be noted that the overpotentials are all negative for the plating process, but the overpotential magnitude is plotted for simplicity. All LIG materials exhibit similar overpotentials at low current densities, but significant deviations can be observed at higher current densities. In all cases, pre-lithiated cells exhibit very repeatable results, with small error bars across different samples. However, unlithiated PFA and PI samples exhibit significant variation – particularly PFA samples, which possess extremely large error bars in overpotential at high current densities. In contrast, PFA/salt samples exhibit little variation among both lithiated and unlithiated cells. While the variation is lower for PFA/10% Li_2SO_4 cells than PFA/25% Na_2SO_4 cells, it should be noted that more PFA/25% Na_2SO_4 cells were tested, including cells prepared from separate batches of LIG material, which only exhibited very slight differences in measured overpotential. This is significant, as the LIG process is known to lead to large variations in material. As discussed in Chapter 4, significant differences have been observed in Raman spectra of LIG formed at the center and edge of each rastered trace, due to the thermal gradient formed in the material during lasing.[272] In the previous chapter, we suggested, via thermal modeling, that the inclusion of salt particles in the PFA could lead to increased thermal conductivity and diffusivity, which could also lead to a less extreme thermal gradient during

lasing, and a more uniform LIG material. This could explain the extremely repeatable results achieved from PFA/Na_2SO_4 and PFA/Li_2SO_4, despite the significant variation from pristine PFA.

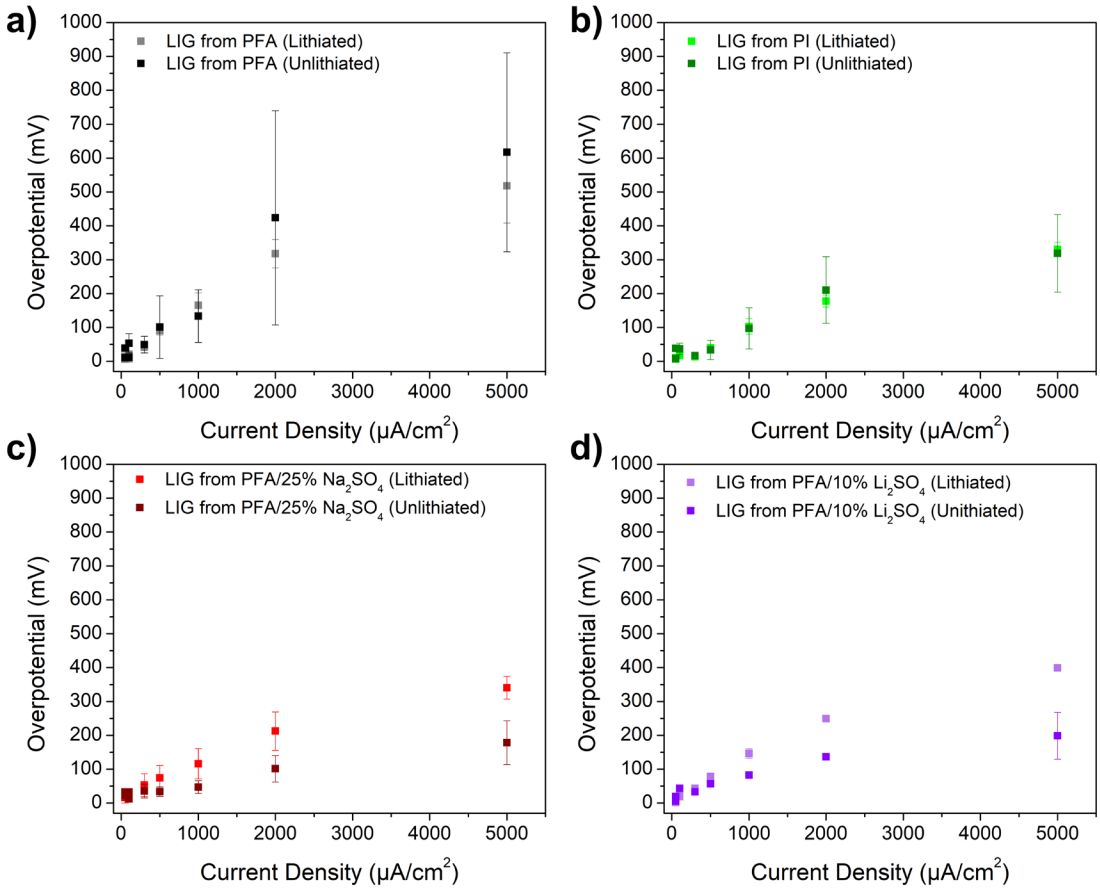

Figure 5.7: Average lithium nucleation overpotentials with current density for different LIG materials. Nucleation overpotentials for a) LIG from PFA, b) LIG from PI, c) LIG from PFA/25% Na_2SO_4, and d) LIG from PFA/10% Li_2SO_4.

LIG from PFA, both lithiated and unlithiated, exhibits the highest overpotentials of the LIG materials, with substantially higher overpotentials than LIG from PI, PFA/25% Na_2SO_4 and PFA/10% Li_2SO_4. This appears to match our initial hypothesis, that the lower surface area and lack of doping with lithiophilic functional groups leads to higher overpotentials for lithium nucleation. The performance of LIG from PI, PFA/25% Na_2SO_4 and PFA/10% Li_2SO_4 are similar to one another. Notably, for both LIG from PFA and LIG from PI, despite variation in the unlithiated cell performance, the average overpotentials for lithiated and unlithiated cells are similar to one another. However, for LIG from PFA/salt, in both cases, the overpotentials for lithiated cells are higher than that of unlithiated cells at

high current densities. This is an unexpected result. A fully lithiated carbon material is expected to provide a more lithiophilic surface for lithium nucleation. Moreover, the fully lithiated structure should eliminate any increase in the overpotential due to mass transport resistance during solid state Li^+ diffusion. One possible explanation is that the lithiated samples are less stable, and that during the plating study, the longer periods of time spent at lower voltages leads to more accumulation of SEI, resulting in increased overpotentials at higher current densities, applied in subsequent plating steps. However, this unexpected result requires further investigation.

The average overpotentials for all lithiated samples are compared with one another and the average values for copper in **Figure 5.8a)**. The overpotentials measured for copper correspond well with other literature reports in the same electrolyte.[168] At low current densities (<500 $\mu A/cm^2$), copper exhibits the highest overpotentials of all samples. However, at higher current densities, LIG samples perform more poorly than copper, with LIG from PFA exhibiting the highest overpotentials, and LIG from PI, 25% Na_2SO_4, and 10% Li_2SO_4 exhibiting similar performance. In **Figure 5.8b)**, the performance of the unlithiated LIG samples is compared. In this case, again, copper exhibits the highest overpotentials at low current densities, but at higher current densities LIG from PFA/25% Na_2SO_4 exhibits essentially equal overpotentials, with LIG from 10% Li_2SO_4 exhibiting only slightly higher overpotentials. LIG from PI and LIG from PFA each exhibit much higher overpotentials. This provides some indication that the introduction of lithiophilic functional groups in LIG from PFA/salt has lowered the lithium nucleation overpotential in comparison to LIG from pristine PFA. However, it is surprising that the high surface area LIG materials possess higher overpotentials than copper at high current densities. Mass transport effects could lead to increased overpotentials at high current densities, which could stem from the formation of different compositions of SEI on the different LIG surfaces or from increased consumption of electrolyte in the porous, high surface area LIG electrodes. However, excess electrolyte was used in all tests. Moreover, we observe relatively linear behaviour of the overpotential with current density. We do not observe the sharp increase in the overpotential we would expect if approaching the mass transfer limited current density.

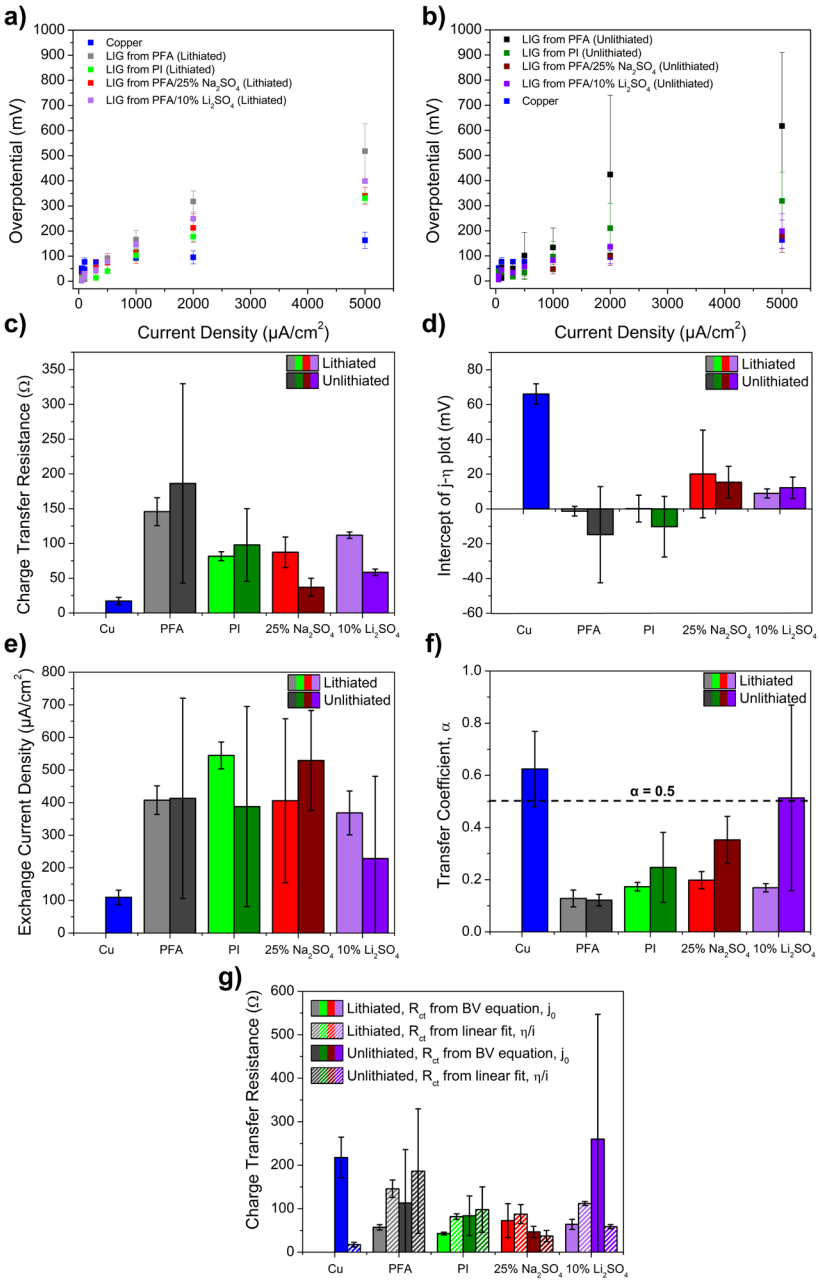

Figure 5.8: Summary of overpotentials for different materials and extracted kinetic parameters. Comparison of average overpotentials with current density for copper and a) all lithiated LIG samples and b) all unlithiated LIG samples. c) Comparison of charge transfer resistance (calculated from the slope of the current-overpotential plots) for lithium nucleation for all samples using linear fit of data. d) Comparison of the intercept of the current density-overpotential plots, for all samples, using linear fit of data. e) Comparison of exchange current density, j_0, for all samples using fit of data to full Butler-Volmer equation. f) Comparison of transfer coefficient, α, for all samples, using fit of data to full Butler-Volmer equation. g) Comparison of charge transfer resistance for all samples, as calculated from both a linear fit of the data and fitting to the full Butler-Volmer equation.

The relationship between the overpotential for an electrochemical reaction and the current is described by the current-overpotential equation in the Butler-Volmer model:

$$i = i_0 \left[\frac{C_O(0,t)}{C_O^*} e^{-\alpha f \eta} - \frac{C_R(0,t)}{C_R^*} e^{(1-\alpha) f \eta} \right] \tag{5.3}$$

where i_0 is the exchange current (j_0 is the exchange current density), α is the transfer coefficient, f is a constant ($f = F/RT$), $C_O(0,t)$ and $C_R(0,t)$ are the concentrations of the oxidized and reduced species at the electrode surface, and C_O^* and C_R^* are the bulk concentrations of the oxidized and reduced species. If we assume no mass transfer effects, the equation simplifies to:

$$i = i_0 \left[e^{-\alpha f \eta} - e^{(1-\alpha) f \eta} \right] \tag{5.4}$$

At small overpotentials, since for small x, $e^x \approx 1 + x$:

$$i = -i_0 f \eta \tag{5.5}$$

Equation 5.5 shows that a linear relationship exists between the current or current density and overpotential when the overpotential is small. This linear relationship can be related to the charge transfer resistance for the reaction:

$$-\frac{\eta}{i} = R_{CT} = \frac{RT}{F i_0} \tag{5.6}$$

This linear relationship is typically valid when the current is ≤10% of the mass transfer limiting current.[30] As discussed previously, this is certainly true for mass transfer in the liquid electrolyte and for all lithiated cells. While this is harder to prove for unlithiated cells, we do not observe behaviour indicative of approaching the mass transfer limiting current in the overpotential plots. Rather, for the most part, the overpotential-current density plots all exhibit relatively linear behaviour. The low overpotential regime of the Butler-Volmer equation is also expected to no longer be valid for overpotentials >118 mV, as this typically marks the transition to the Tafel regime.[30] However, the magnitude of the nucleation overpotentials in our system is determined by both the electron transfer kinetics, which conventionally follow Butler-Volmer theory, and the energy barrier required for nucleation to occur, which is related to the thermodynamic mismatch of lithium and the nucleation substrate, along with any other contributions from mass transfer or SEI formation. It is extremely challenging to deconvolute the contributions of these many different processes – reaction, charge transfer, diffusion, and crystallization[170] – on the total measured overpotential. However, the magnitude of the experimental overpotential is expected to be higher than that of a purely kinetically controlled

system, and as such the typical overpotential cutoffs (such as 118 mV defining the beginning of the Tafel regime) may no longer be valid. It is furthermore worth noting that, to the best of our knowledge, the lithium nucleation overpotentials on a non-lithium surface have not been fit to a kinetic model before, due to the complexity of the system. Moreover, most fitting of current-overpotential data is done via voltage sweeping, which results in a much higher number of data points. As we investigated the lithium plating galvanostatically (in order to be as close in operation to a practical lithium metal anode as possible), the number of data points is more limited, and any fit to a kinetic model can only be done roughly. Finally, we note that the form of the Butler-Volmer equation presented here is very simple, and more rigorous lithium deposition models have been proposed in the literature to date,[172,291–294] such as Monroe and Newman's 2004 study that accounted for mechanical stress between the substrate and deposit.[295] While we did not examine fitting of our data to these models, this should be explored in future work to provide further insight into the nucleation behaviour on these materials.

As such, we first linearly fit the average overpotential-current density data for all samples, using the low-overpotential Butler-Volmer approximation. For LIG-based samples, we observed the best linear fits when excluding the highest current density (5000 μA/cm^2) data point (i.e., for data from 50 to 2000 μA/cm^2). We also excluded the repeat data points at 50 and 100 μA/cm^2 for all samples, as these led to poorer fits, and are expected to vary based on SEI accumulation. However, for copper, we observed a significantly improved linear fit when including the highest current density (5000 μA/cm^2) data point (R^2 of 0.94 vs. 0.63). Optimized linear fits of all data demonstrated high R^2 values of 0.89 – 0.99 for each individual cell. The linear fits of the average overpotentials for all samples can be seen in **Figure C16**.

From the linear fits, we calculated a charge transfer resistance from the slope for all samples following Equation 5.6. A comparison of the calculated charge transfer resistances from the linear fits can be seen in **Figure 5.8c)**. It is clear that unlithiated and lithiated LIG from PFA exhibit the highest charge transfer resistance among all samples. R_{CT} for lithiated LIG from PI, LIG from PFA/25% Na_2SO_4 and LIG from PFA/10% Li_2SO_4 are all similar to one another, but R_{CT} clearly decreases for unlithiated LIG from PFA/25% Na_2SO_4 and LIG from PFA/10% Li_2SO_4. These values are very similar to that of copper. Notably, they are also only 20-35% that of the R_{CT} for LIG from PFA/no salt, indicating that the inclusion of the salt particles into the LIG has dramatically improved the kinetics of the charge transfer reaction.

According to Butler-Volmer theory, the intercept of the low overpotential/linear regime of the current density-overpotential plot should be zero. In **Figure 5.8d)** we plot the calculated intercept of the overpotential-current density plot. For many samples, particularly lithiated PFA and PI, this value is extremely close to zero (-1.3 mV and 0.2 mV respectively). Overpotentials for other LIG materials are higher, but are all lower than that of copper, which possesses an intercept of 66 mV, indicating a significant deviation from Butler-Volmer theory. However, this corresponds well with the work of Yan et al., which demonstrated that copper possesses an extremely high overpotential for lithium nucleation (~40 mV) even at extremely low current densities of 10 μA/cm^2.[173] This may be because the thermodynamic mismatch between the lithiophobic copper surface and lithium is much greater than for the lithiophilic LIG. The thermodynamic energy barrier of the nucleation process on an unfavourable substrate may manifest in non-zero intercepts of the current-overpotential plot. Thus the magnitude of the intercept could provide some insight into the lithiophilicity and substrate-lithium interfacial energy, while the charge transfer resistance provided insight regarding the kinetics of the system. The results from the linear fit suggest that the kinetics of the charge transfer reaction on copper may be faster, potentially due to a more crystalline or conductive surface, but that the lithiophilicity of the LIG materials is significantly improved compared to copper, based on the intercept data. Moreover, significant improvements in the kinetics are observed for the doped LIG samples when compared to LIG from pristine PFA.

We also fit our data to the full Butler-Volmer equation using non-linear least squares regression, assuming no mass transfer effects, as written in Equation 5.4, resulting in R^2 values ranging from 0.90 – 0.99 for each individual cell. The fits of the average current density-overpotential data can be seen in **Figure C17**. It should be noted that in order to fit the model effectively, the cathodic currents are labelled as positive following the Texas convention, the overpotentials are labelled as negative values, and the current density and overpotential axes are switched from our previous plots, to follow Butler-Volmer convention. From these fits, we are able to extract the exchange current density (j_0) and transfer coefficient (α), which can be seen in **Figures 5.8e)** and **f)**. The findings from the full Butler-Volmer fit exhibit differences from the previous linear fit. In this case, we observe higher exchange current densities for all LIG-based samples than copper, indicating improved kinetics for LIG. Moreover, significant differences are observed in the calculated transfer coefficients. Copper possesses an α value close to 0.5, which is the expected value for most electrochemical reactions, and indicates a symmetric energy barrier for reaction. However, most LIG samples possess low α values, with only the best

performing samples (unlithiated 25% Na_2SO_4 and 10% Li_2SO_4) exhibiting α values close to 0.5. This would indicate asymmetric reaction energy barriers for most LIG samples, meaning that the overpotential for lithium nucleation is much higher than the overpotential for lithium stripping. While we did not investigate the dependence of the stripping overpotential with current density, this asymmetric behaviour has been commonly observed in other systems, such as lead-acid batteries, which exhibit increased charge polarization compared to the discharge process.[296] While α values as low as 0.16 have been reported for some systems, such as the reduction of Ce^{4+} to Ce^{3+} on gold,[297] such low α values are rare (with as low as 0.12 observed here for PFA) and such significant differences between LIG and copper are surprising. It should be noted that the Butler-Volmer equation specifically applies to elementary reactions. As such, mechanisms that involve a series of elementary steps can result in observed transfer coefficients for the overall mechanism that differ from 0.5. We also note that a high standard deviation between unlithiated 10% Li_2SO_4 samples is observed. It can be seen in **Figure C14h)** that the overpotential data for the unlithiated 10% Li_2SO_4 cells is nearly identical except for deviation in the final, 5000 $\mu A/cm^2$ data point, which leads to significantly different estimates of both j_0 and α, and illustrates the dependence of this fit on the limited high current density data, and the need for more measurements at high current density to improve the fit and estimations from the full Butler-Volmer equation.

From the exchange current densities calculated from the fit to the full Butler-Volmer equation, we are able to calculate the charge transfer resistance from the second half of Equation 5.6. We compare the calculated charge transfer resistances from the two fitting methods in **Figure 5.8g)**. Good agreement is achieved between the two fitting methods for most LIG samples, particularly for LIG from PI and PFA/25% Na_2SO_4. The most significant discrepancies between the two models occur for copper and for PFA/10% Li_2SO_4, both of which possess low charge transfer resistances based on the linear fit and high charge transfer resistances from the fit to the full Butler-Volmer equation. As discussed above, the deviations in the Li_2SO_4 fit stem from differences in the final, highest current density data point, which is excluded from the linear fit. The data obtained on copper on the other hand exhibits the worst fit to both the linear and full Butler-Volmer equation, with R^2 values of 0.91 and 0.92 when averaging the results for each individual copper sample. This indicates that lithium nucleation on copper possesses the most significant deviations from Butler-Volmer kinetics and further investigation is needed.

Boyle et al. recently reported a transient voltammetry study of lithium electrodeposition with ultramicroelectrodes.[298] They observed that the $Li^+ + e^- \rightarrow Li$ reaction kinetics deviate from Butler-

Volmer kinetics at high overpotentials, and that the lithium electrodeposition more accurately follows Marcus kinetics. In Marcus theory, the potential energy surface is represented by two parabolas, which represent the solvent coordinate in the initial and final states of the reaction. This does not change the form of the current-overpotential equation in Equation 5.4, but does introduce a potential dependence to α:

$$\alpha = \frac{1}{2} + \frac{e\eta}{4\lambda} \tag{5.7}$$

where e is the elementary charge and λ is the reorganization energy, which represents the energy needed to reorganize the solvent due to the differing charge distributions in the initial and final reaction states. While Marcus and Butler-Volmer kinetics are identical at small overpotentials, the potential dependence of α in Marcus theory leads to curvature of the Tafel plot at higher overpotentials. We did not further investigate fitting our data to Marcus theory, particularly as more high current density data points are needed, but this could explain some deviations in our data from symmetric Butler-Volmer kinetics. Notably, Boyle et al. do observe symmetric kinetic behaviour, but study the kinetics of the lithium stripping after lithium nucleation on the ultramicroelectrode surface (i.e. for a symmetric Li|Li system). The kinetics are studied in the absence of a nucleation energy barrier, which exists in our system, and it remains unclear if these findings fully apply to the nucleation process on copper and LIG.

Despite some discrepancies in the extracted parameters for copper and 10% Li_2SO_4, both fit models demonstrate that PFA/25% Na_2SO_4 and PI exhibit lower charge transfer resistances than PFA, indicating that doping of the LIG facilitates improved electron transfer kinetics. Moreover, both methods indicate that lithium nucleation follows Butler-Volmer kinetics, at least at low overpotentials, but that modifications from the theory are needed to fully describe the overpotential-current density behaviour. Higher thermodynamic nucleation barriers, indicative of lithiophobic materials and high substrate-lithium interfacial energies, may manifest as deviations in the theory via either a non-zero intercept in the linear regime or an asymmetric transfer coefficient, though the asymmetry could also stem from a multi-step reaction mechanism. Improved models that can better decouple these kinetic and thermodynamic effects can lead to better understanding of the complexities of the nucleation process.

Whether kinetically or thermodynamically driven, we observe smaller nucleation overpotentials for LIG from PFA/salt and PI than from pristine PFA, particularly for unlithiated PFA/salt samples. In

order to confirm that the improved performance of the LIG from PFA/salt stems from the formation of lithiophilic functional groups, we have plotted the calculated kinetic parameters from both the linear and full Butler-Volmer fit with other varying properties of the LIG materials and electrodes. As demonstrated via BET and capacitance in Chapter 4, the inclusion of the salt particles during lasing leads to the formation of a higher surface area LIG material. However, the BET surface areas of the LIG materials are not reflective of the actual surface area that is accessible to electrolyte. Pore size analysis of LIG from PFA/25% Na_2SO_4 indicated that significant micropores were present, which would not be accessible to electrolyte, and moreover, the fabrication of LIG electrodes via slurry casting with binder and subsequent electrode pressing is expected to dramatically change the accessible surface area. Consequently, we estimated the electrode surface areas by conducting cyclic voltammetry on the electrodes in a non-faradaic region, 2.0-2.5 V, before cycling, as seen in **Figure C18**. From this, the electrochemically active surface area (ECSA) was estimated to be 5.0, 9.2, 14.8, and 23.1 m^2/g for LIG from PFA, LIG from PFA/25% Na_2SO_4, LIG from PFA/10% Li_2SO_4, and LIG from PI respectively. We note that the current densities employed in our nucleation study were normalized by the geometric electrode area, not the ECSA, and thus as the ECSA varies among the LIG samples, the effective current density also varies for the different samples, which could lead to differences in the nucleation behaviour. However, current densities are conventionally defined in this manner in lithium plating studies, and thus were similarly defined in our testing protocol. It is extremely challenging to deconvolute or control the various changing properties of the LIG, including the surface area. Moreover, despite the differences in ECSA, and thereby effective current density, we demonstrate below that the surface area is not strongly correlated with the overpotential measurements across different LIG samples.

In **Figure 5.9a)**, the charge transfer resistance calculated via a linear fit of the data is plotted along with the calculated electrode surface area, based on the ECSA and electrode loading for all LIG samples. A linear fit of all data points provides a very poor R^2 value of 0.15, which indicates that the correlation between charge transfer resistance and electrode surface area is not strong. It should be noted that within each sample type, it appears that the charge transfer resistance is inversely related to the electrode surface area (for example, for unlithiated PI, increases in surface area lower the charge transfer resistance). However, due to the limited number of data points for each sample, this is challenging to measure quantitatively. Nonetheless, we expect that an increase in surface area leads to lower charge transfer resistance, and this appears to be true within each sample type, when it is the only

changing variable. However, across the different LIG materials, this is not the case, and the highest surface area sample does not result in the lowest R_{CT}, indicating that the chemical differences between the LIG materials are more critical. Similarly, as seen in **Figure 5.9b)**, while samples were all prepared within a relatively narrow loading range, no observable trend between the electrode loading and R_{CT} (R^2 of 0.015) is apparent. Likewise, as seen in **Figure 5.9c)** and **d)**, no relationship appears to exist between the intercept of the current density-overpotential plot and the electrode surface area (R^2 of 0.0002) and loading (R^2 of 0.007). Parameters extracted from fitting the data to the full Butler-Volmer equation show similar behaviour, as seen in **Figure 5.9e)-h)**, with no clear relationship between either the exchange current density or transfer coefficient and electrode surface area (R^2 of 0.01 and 0.04) and loading (R^2 of 0.10 and 0.003).

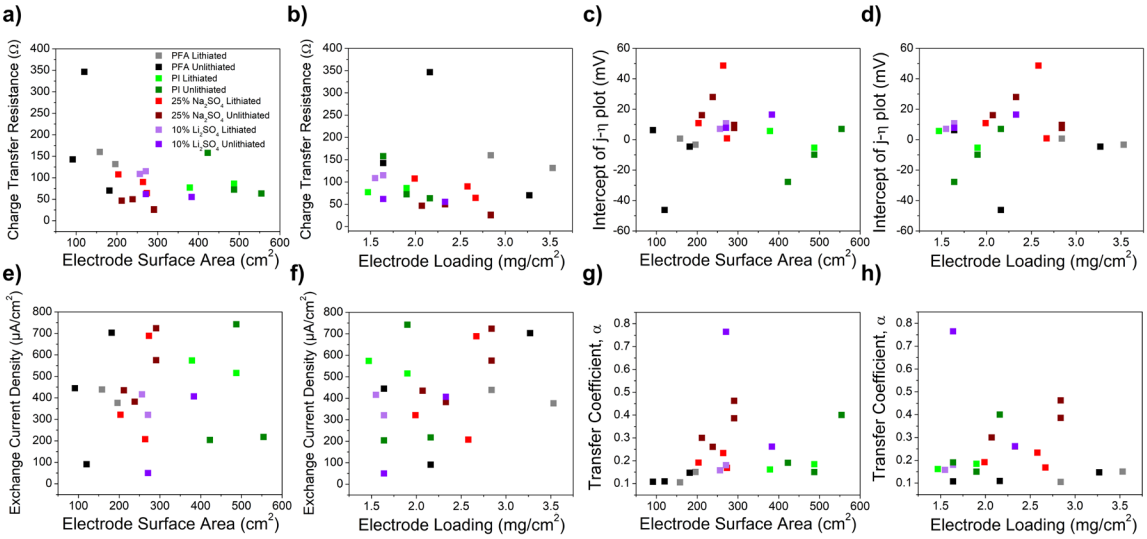

Figure 5.9: Plots of calculated kinetic parameters with electrode loading and surface area. Charge transfer resistance calculated from linear fit with a) electrode surface area and b) electrode loading and intercept of the current density-overpotential plot calculated from linear fit with c) electrode surface area and d) electrode loading for LIG samples. Exchange current density calculated from fit to full Butler-Volmer equation with e) electrode surface area and f) electrode loading and transfer coefficient with g) electrode surface area and h) electrode loading.

As no clear relationship is observed between the current-overpotential behaviour and the electrode surface areas and loadings, the most critical factor impacting this behaviour is likely the chemical composition of the different LIG materials. It is not possible to statistically prove a relationship between the LIG functional groups and overpotential behaviour, as each LIG material possesses multiple different functional groups, with varying degrees of lithiophilicity. Moreover, discrepancies exist in the computational studies published to date as to the lithiophilicity of certain functional groups. While both

Chen et al. and Yi et al. report high binding and adsorption energies for ketones and carboxylic acids,[168,169] discrepancies exist as to whether epoxide groups are lithiophilic or not, and hydroxyl and ether groups show lithiophobic behaviour. While XPS analysis can provide some insight into whether C-O or C=O groups are formed, it is challenging to assess specifically which functional groups are formed without further characterization, and their low quantity in the LIG structure can make them challenging to measure through other methods such as FTIR. Nonetheless, qualitative trends can be drawn from the LIG samples investigated. LIG from PFA only possesses oxygen doping, with C-O and C=O groups, with C=O groups being the only lithiophilic group present, making this the material containing the least lithiophilic groups. LIG from PI possesses the same groups, with the addition of lithiophilic carboxylic acid groups, and C-N doping. While discrepancies also exist in the computational studies regarding nitrogen functional groups, pyridine groups are shown to possess high binding and adsorption energies for lithium, making them lithiophilic.[168,169] While LIG from PI possesses several lithiophilic groups and 2.89% N-doping, it possesses the lowest oxygen content of any of the samples, at only 6.39%, limiting the lithiophilic impact of these groups. LIG from PFA/25% Na_2SO_4 possesses similar oxygen containing functional groups as LIG from PI – C-O, C=O, and COO groups. It also possesses sulfide bonds, which are expected to be lithiophobic in nature. However, it possesses the highest oxygen content of any sample, by far, at 37.85%, with only 2.15% of the lithiophobic sulfur doping. This indicates that the lithiophilic oxygen-containing functional groups play the most critical role here. Notably, from the O1s XPS for this material, significantly more oxygen is present in C=O bonds than C-O bonds, indicating that most oxygen is present in a lithiophilic functional group. Finally, LIG from PFA/10% Li_2SO_4 possesses C-O and C=O functional groups, with a very small quantity of COO groups. It also possesses lithiophobic sulfide groups. However, sulfone groups are also present, which are lithiophilic, along with sulfoxide groups, which have not been computationally investigated. The oxygen content for this sample is similar to that of LIG from PFA (17.52% vs. 17.31% respectively), and the only major difference between these samples is the presence of the different S-containing functional groups. While the total sulfur content is quite low (0.69%), the data from PI indicates that the presence of even a small quantity of highly lithiophilic groups can significantly change the overpotential behaviour, indicating that the presence of the sulfone – and possibly sulfoxide – groups are the most critical influence on the plating behaviour for this sample.

Lithium half-cells of the different LIG materials and copper were prepared and cycled to test their long-term cycling performance at a current density of 1 mA/cm^2 and lithium plating capacity of 1

mAh/cm^2, with a 1 V cutoff during lithium stripping. The coulombic efficiency of the cells can be seen in **Figure 5.10a)**, which demonstrates that all cells have limited cycling performance. All LIG materials possess very low initial coulombic efficiencies in the first few cycles as their higher surface area leads to more initial Li consumption during SEI formation. The LIG cells all reach a maximum coulombic efficiency around 10 cycles. Notably, despite their very different overpotential performance, LIG from PFA and LIG from PFA/10% Li_2SO_4 achieve the highest coulombic efficiencies, similar to copper, at 91 – 93%. However, all LIG samples experience a rapid decrease in coulombic efficiency beyond this point, particularly LIG from PFA/25% Na_2SO_4 and PFA/10% Li_2SO_4. While the coulombic efficiencies of LIG from PFA and PI both show a substantial drop as well, they begin to increase after ~20 cycles, surpassing copper.

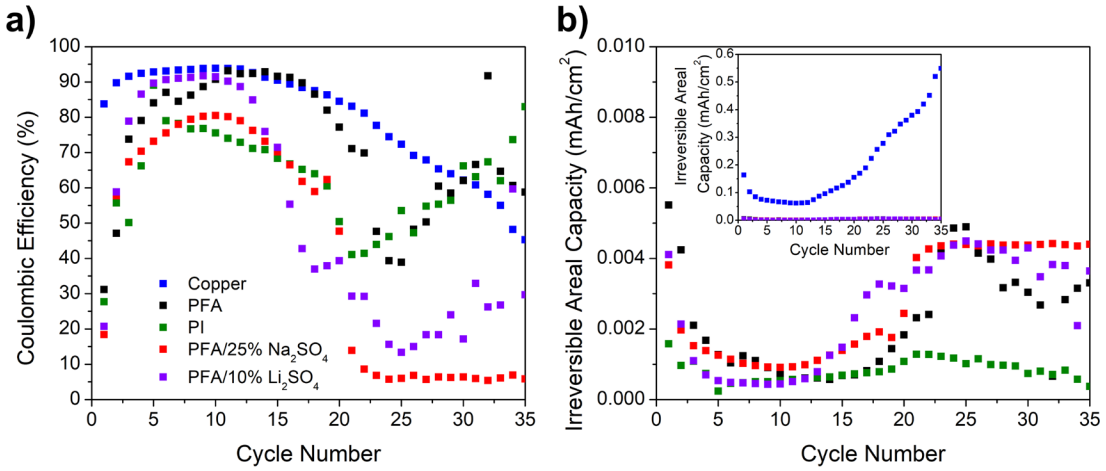

Figure 5.10: Cycling of Li half cells. a) Coulombic efficiency and b) irreversible areal capacity with cycle number. Lithium was plated at 1 mA/cm^2, 1 mAh/cm^2, and stripped to a 1 V cutoff.

The high surface area of the LIG material can both positively and negatively affect the electrode performance. While it can lead to lower effective current densities, if the SEI layer formed is not stable on this high surface area material and is still continuously breaking and reforming, the effectively much larger SEI layer on LIG will lead to substantially more irreversible capacity loss, which is the difference between the discharge and charge capacity per cycle. To normalize this behaviour, the irreversible areal capacity is plotted with cycle number in **Figure 5.10b)**. For the LIG materials, the ECSA was used to determine the effective actual area of each electrode, based on loading, while the copper surface is estimated to be relatively flat and planar, and thus the geometric electrode area was used here as an estimate. For all electrodes, some initial irreversible capacity loss is observed in the first few cycles as

the SEI layer is established, and then stable cycling is observed for ~10-15 cycles before more substantial irreversible capacity loss is observed. This occurs for all samples, copper and LIG alike, but the irreversible capacity loss per area is two orders of magnitude higher for copper, indicating a more unstable SEI layer is formed on the copper surface. The LIG structure can provide a lithiophilic surface for lithium deposition, and an open, 3D structure with void space to accommodate the significant volume change during stripping and plating and which also lowers the effective current density during lithium plating. All of this leads to a more areally stable SEI layer that experiences less strain than the SEI on copper – meaning that fewer cracks are formed and less extensive outward SEI growth occurs per area. However, the much higher total surface area of the LIG surface compared to copper means that the total sum of SEI growth – and thus irreversible capacity – is still larger on LIG than on copper. As such the practical cell performance and coulombic efficiency are not improved, and require further optimization, indicating that the surface area of the lithium host is a parameter that needs to be carefully tuned in order to optimize performance.

It is interesting to note that the worst coulombic efficiency for the LIG samples is actually observed for LIG from PFA/25% Na_2SO_4 and PFA/10% Li_2SO_4 – the two most lithiophilic samples, which exhibited the lowest overpotentials for lithium nucleation. While defects can lead to lower carrier mobility due to scattering of electrons, which can effectively increase local current densities,[168] we did not observe any substantial increase in the sheet resistance of doped samples, so this factor is not expected to play a significant role here. One possible explanation for this limited coulombic efficiency is that defects can also catalyze parasitic reactions that can lead to increased SEI formation and voltage hysteresis.[168] Another possibility is that this limited performance is related to the specific carbon structure of the different LIG materials. LIG from PFA/salt is fairly amorphous in nature, while LIG from PFA and PI exhibited more pristine graphene structures. Because the LIG materials can be lithiated, the coulombic efficiency of these cells is related not only to the stripping of the lithium metal, but also the delithiation of the LIG materials. It is known that hard or disordered carbons exhibit limited coulombic efficiencies and high irreversible capacity as lithium-ion anodes, as it is challenging to fully delithiate them.[299] We expect that this may be the source of the lower coulombic efficiency for LIG from PFA/25% Na_2SO_4 and LIG from PFA/10% Li_2SO_4 compared to other LIG samples. This is supported by evaluating the coulombic efficiency of the various plating and stripping steps in the lithium nucleation study on lithiated and unlithiated LIG. As seen in **Figure C19**, significant variation is observed in the coulombic efficiency of the PFA/25% Na_2SO_4 samples, some of which we believe is

due to batch-to-batch variation. However, the lithiated LIG from PFA/10% Li_2SO_4 samples possess higher coulombic efficiencies than their unlithiated counterparts, suggesting that the delithiation process is limiting. This is further supported by the fact that PFA/25% Na_2SO_4, which possesses the highest oxygen content and thereby the highest level of doping – and thus, the most disordered structure – also possesses the worst coulombic efficiency of all samples. This finding indicates that, as with the LIG surface area, the degree of doping is another parameter that needs to be finely tuned to optimize plating performance – too high of doping leads to the formation of a much more amorphous structure that cannot be delithiated easily, while too little leads to a lithiophobic surface. This is a critical finding, as nearly all studies to date have focused on the lithiophilicity of specific functional groups, but little emphasis has been placed on the optimal degree of doping. In fact, Yi et al. attempted to investigate this in their study of lithium plating on LIG, by varying the laser parameters to achieve different I_D/I_G ratios. However, they could not decouple other factors such as the changing LIG surface area, and found that the variation in each LIG material was too significant to draw any conclusions.[168] Our study is the first to date to demonstrate that high levels of doping, while resulting in a lithiophilic material, can limit cycling performance. Thus, lower levels of salt doping could be one strategy to prepare improved hosts – LIG from PFA/10% Na_2SO_4 exhibited a much less amorphous and more graphene-like structure via Raman spectroscopy, but would be expected to possess similar functional groups to LIG from PFA/25% Na_2SO_4, and could be a promising material for further study.

The LIG structures investigated in this chapter possess an open, 3D current collector-type lithium host architecture. As discussed above, while this structure can provide void space, lowered effective current density, and a tailored surface for lithium nucleation, this approach does not mitigate SEI formation in the way that a fully sealed host structure can. We have demonstrated in this work that dopants can be controllably introduced into the LIG structure via salt doping, and, as predicted computationally, these doped LIG materials exhibit lower overpotentials for lithium nucleation, with the LIG doping being the most critical parameter controlling the overpotential, over the electrode surface area and loading. Electrodes prepared from this LIG exhibit improved areal irreversible capacity loss than copper, but very poor overall coulombic efficiencies, indicating that further optimization of their surface areas and doping is necessary. It is worth mentioning that the only study to date that evaluated LIG as a lithium metal host used LIG formed from PI tape on copper directly, meaning that a very low LIG loading was used[168] (typically <0.5 mg/cm^2)[23], while we studied slurry-cast electrodes with much higher LIG loadings and electrode densities, which could further limit their performance.

Moreover, Yi et al. observed significant improvements in anode performance by controlled patterning of the LIG host in order to fabricate specific 3D architectures,[168] which we did not further investigate in this study. With these further modifications, LIG is still a promising material as a 3D current collector. However, even more promisingly, the lithiophilic nature of the doped LIG could be utilized in a sealed 3D lithium host, with a more lithiophobic structure surrounding it. This type of structure could prevent substantial SEI formation while leading to guided lithium plating within the host structure. The work in this chapter demonstrates that tuning of the lithiophilicity of LIG is possible with doping and that rationally-designed lithium host structures with guided lithium deposition are possible from purely carbon-based materials.

5.4 Conclusion

In conclusion, in this chapter we studied lithium nucleation and plating on different doped LIG materials for the first time. We demonstrated that doped, high surface area LIG could be prepared from composites of PFA and lithium salts, such as Li_2SO_4, for the first time, and that the chemical composition of the LIG formed varies significantly based on the salt precursor, even within the family of sulfate salts. We also showed that surface salt could be removed from the PFA structure by dissolution in water without impacting the LIG structure. We performed the first in-depth study of lithium nucleation and growth on different, doped LIG materials, accounting for the different chemical structures, functional groups, surface areas, and loadings of electrodes. We also studied the impact of pre-lithiating the LIG or not on the lithium nucleation overpotential – one of the first studies on lithiated vs. unlithiated carbon host materials to date – and demonstrated the unexpected finding that pre-lithiating LIG from PFA/salt composites leads to an increase in lithium nucleation overpotential, possibly due to the formation of more SEI. We demonstrated that LIG materials prepared from PFA/salt possess more lithiophilic functional groups, lower overpotentials for lithium nucleation, and via fitting the nucleation overpotential to kinetic models for the first time, lower charge transfer resistances than LIG from pristine PFA for most samples. While LIG materials exhibited less irreversible capacity per area than copper controls, cell coulombic efficiencies are limited and further optimization of surface area, doping degree, and SEI formation are needed for practical implementation as a lithium metal host. Nonetheless, this fundamental study provides key insight into the lithium nucleation behaviour on LIG which is essential for the future rational design of LIG host materials.

Chapter 6:
Probing Sulfur Deposition onto Carbon Nanomaterials from Aqueous, Elemental Sulfur Sols for Lithium−Sulfur Batteries

6.1 Introduction

While Chapter 5 focused on the use of LIG as a potential host material to address some of the challenges associated with the lithium metal anode, the sulfur cathode also faces several challenges preventing the commercialization of lithium-sulfur batteries. One of the most significant challenges is the poor electrical conductivity of sulfur (5×10^{-30} S/cm) and its discharge product, Li_2S, which necessitates that the active material be intimately mixed with typically inactive, electrically conductive additives for rapid electron transport.[3,8,9,300,301] Another critical challenge is the dissolution of intermediate polysulfide species into the ether-based electrolyte during cycling. These polysulfides may "shuttle" to the anode side of the cell, resulting in capacity fade over time.[3,300,301]

This chapter aims to address one of the primary challenges in preparing sulfur cathodes, which is the scalable fabrication of an architecture in which sulfur is intimately mixed with a conductive carbonaceous scaffold. As discussed in Chapter 2, most fabrication methods, including the most widely used melt imbibition approach, utilize aggregated carbon powders, limiting the accessible surface area of the material that can be coated with sulfur. Moreover, solution-based approaches investigated thus far either employ toxic solvents such as CS_2 or hydrophilic sulfur sols, which are converted into elemental sulfur in situ, but are much more costly than elemental sulfur and typically result in residual unreacted precursor that remains on the sulfur surface and may result in side reactions, leading to capacity loss. Consequently, the development of scalable, aqueous-based, solution-processing for carbon/sulfur composites is crucial.

Hydrophobic or Weimarn sols, prepared via the rapid dilution of a water-miscible, organic sulfur solution into large quantities of water, have been relatively unexplored for the preparation of sulfur cathodes. This process results in submicron particles of amorphous sulfur due to the low solubility of sulfur in water. These sols are prepared via elemental sulfur directly through simple, scalable, aqueous-based processing. Previous work from our group demonstrated that trapping hydrophobic sols in networks of GO and polyethylenimine, followed by a heat treatment to reduce the GO and improve the sulfur distribution via melting, enables the formation of rGO/S cathodes with energy densities >400

mAh/g.[214] However, this strategy only involved physically trapping sol particles, with improved sulfur distribution achieved via subsequent melting steps. Furthermore, the GO in this system was reduced at low temperatures, resulting in a low C/O ratio and low conductivity. Moreover, few fundamental studies on these hydrophobic sulfur sol systems and their interaction with carbon nanomaterials have been reported. These could provide key insights into novel carbon/sulfur composite fabrication methods.

In Chapters 3, 4, and 5, we investigated the use of LIG as an electrode material for both supercapacitor electrodes and lithium metal anodes. While LIG-based sulfur cathodes have been previously demonstrated, most employ conventional melt imbibition processing or employ extremely toxic solvents, and achieve limited loadings.[105,106] While LIG is porous and possesses high surface areas via BET measurement (Chapter 4), our studies of LIG electrodes in Chapter 5 demonstrated much lower specific surface areas following typical electrode processing steps of slurry-casting with a binder and pressing. While rGO powders prepared via thermal reduction of GO possess similar BET surface areas to LIG, they are expected to possess significantly higher surface areas once they are no longer solid aggregated powders, but dispersed in solution. Moreover, while the LIG process is ideal for patterning of novel electrode architectures, yields of bulk LIG (which must be scraped off of the precursor substrate) remain low for larger scale processing. Consequently, in this final study, thermally reduced rGO powder was used rather than the LIG investigated in previous chapters.

In this chapter, we study the interaction of hydrophobic sulfur sols with carbon nanomaterial dispersions for the first time. We demonstrate that when dispersed with carbon-based nanomaterials such as rGO, hydrophobic sulfur sols dissolve and then deposit sulfur on the carbon surface through an Ostwald ripening-like mechanism (**Figure 6.1**), providing a simple, one-step, aqueous-based strategy to directly coat carbon-based nanomaterials in a de-aggregated and dispersed state. Moreover, we demonstrate that rGO/S cathodes prepared directly from these composites exhibit capacities as high as 1300 mAh/g_{sulfur} (~4.8 mAh/cm^2) at 0.1C, outperforming melt-imbibed cells prepared from the same materials. Cells without added binder or conductive material attain energy densities as high as 468 Wh/kg at 0.1C, demonstrating the promise of this approach for the fabrication of high capacity sulfur cathodes.

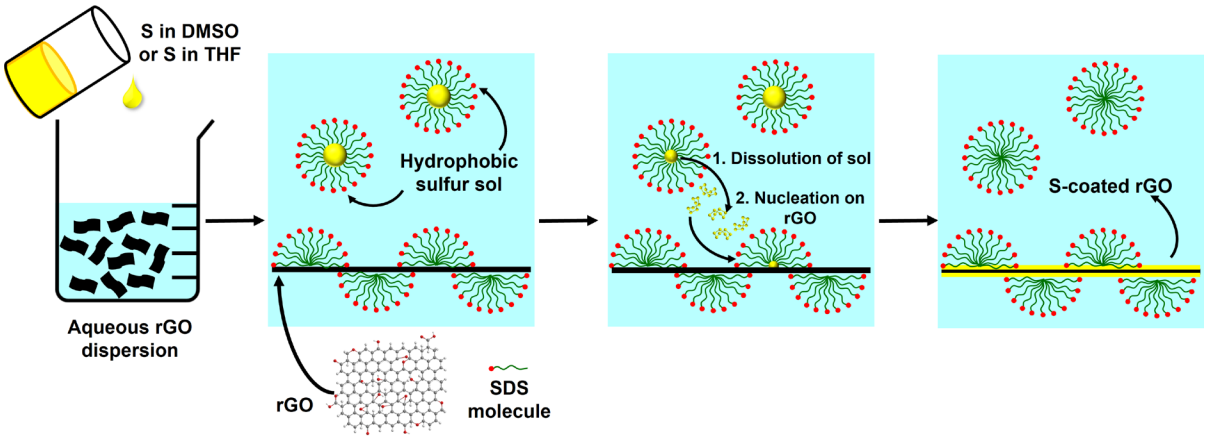

Figure 6.1: Strategy for solution processing of rGO/S composites via the deposition of sulfur from hydrophobic sulfur sols.

6.2 Experimental Methods

6.2.1 Materials Synthesis

Graphene oxide (GO) was synthesized according to Marcano et al.'s improved Hummer's method,[19] whereby 3 g of graphite flakes (Asbury) and 18 g of potassium permanganate (EMD Millipore), were stirred in 360 mL sulfuric acid (98%, Sigma-Aldrich) and 40 mL phosphoric acid (85 wt.% in H_2O, 97%, Sigma-Aldrich) for 16 h at 45 °C. Following the reaction, the mixture was cooled to room temperature and then slowly transferred to a beaker with 400 mL of ice. Then approximately 5 mL of H_2O_2 (30 wt.% in H_2O, Sigma-Aldrich) was added until the mixture changed colour from purple to golden yellow. The GO was then washed two times with 10% hydrochloric acid solution (ACS Reagent 37 wt.% in H_2O, Sigma-Aldrich) followed by four washes with ethanol, with each washing step followed by centrifugation (Thermo-IEC Centra-CL2) conducted at 3500 rpm for 30 min. The final precipitate was dispersed in water, to reach a concentration of 1.6 mg/mL. This dispersion was sonicated for 30 minutes with an ultrasonic probe (BioLogics, Inc., Model 150 V/T Ultrasonic Homogenizer, 150 W) at 70% power in an ice bath while stirring at 300 rpm. The material was then spray-dried (Buchi Mini Spray Dryer B-290), using 100% aspirator, 180 °C inlet temperature, 30% pump, and 667 L/h nitrogen flow. The material was stored under flowing nitrogen until reduction. Reduced graphene oxide (rGO) was prepared through thermal reduction and expansion. 100 mg of spray-dried GO was added to a quartz tube, closed on one side, using an aluminum foil funnel. Nitrogen was gently blown into the tube to ensure that no GO remained on the walls of the tube. The tube was evacuated, and then flushed with argon (ultra high purity, 99.999%) and evacuated 12 times, finally

holding the tube under vacuum for 5 minutes. The tube, still under vacuum, was placed in a 1100 °C tube furnace for 2 minutes, leading to a rapid thermal reduction and expansion of the GO. The tube was removed from the furnace after 2 minutes, and allowed to cool to room temperature. The tube was flushed with argon, and then connected to a custom vacuum filtration device, consisting of a plastic collection vessel with a filter, a long copper tube, and a 3D-printed end matching the diameter of the quartz tube. This rGO was used for optical microscopy and DLS measurements as it dispersed more easily due to a lower C/O ratio (~14), making it suitable for sensitive DLS analysis. However, we chose to use commercially available rGO (Global Graphene Group, Gi-PW-B050 (N002-PDR)) for the preparation of rGO/S composites for SEM analysis and electrochemical testing, both due to its higher C/O ratio (~63), and its availability in large quantities for scalable cathode processing. The graphene has carbon content of ≥95 wt.%, oxygen content of ≤2.00 wt.%, hydrogen content of ≤2.00 wt.%, nitrogen content of ≤0.50 wt.%, with a C/O ratio of ~63 and a BET surface area of 449 m^2/g. A comparison of the Raman spectra of these two materials can be seen in **Figure D1**. rGO/S composites were prepared following the same procedure as for DLS. Following 2 hours of deposition, the samples were flocculated with NaCl, vacuum filtered, and dried at 80 °C.

6.2.2 Materials Characterization

The elemental composition of the GO and rGO was assessed via SEM/EDS. Both materials were pressed into a pellet using a stainless steel die (MTI Corp.), and examined using a Zeiss Leo 1530 scanning electron microscope operating with a 20 kV acceleration voltage. The GO possessed an average C/O ratio of 1.68 ± 0.04, with an elemental atomic composition of carbon: 62.0 ± 0.5%, oxygen: 36.8% ± 0.5%, sulfur: 1.00% ± 0.09%, chlorine: 0.12% ± 0.01%, potassium: 0.12% ± 0.03%. The synthesized rGO possessed an average C/O ratio of 14.4 ±3.6, with the elemental atomic composition of carbon: 89.5± 1.8%, oxygen: 6.5% ± 1.5%, sulfur: 0.95% ± 0.04%, chlorine: 0.39% ± 0.03%, potassium: 0.43% ± 0.02%, sodium: 0.17% ± 0.03%, phosphorus: 0.09% ± 0.01%, and silicon: 2.05% ± 0.32%, and a BET surface area of 565 m^2/g. BET surface area measurements were obtained for synthesized rGO, commercial rGO and Ketjen black (KB, EC600) using a Micromeritics Gemini VII 2390, with nitrogen as the gaseous adsorbate.

Sulfur sols were prepared via dissolution of sulfur (Alfa Aesar, powder, -325 mesh, 99.5%) in either THF (Sigma-Aldrich, ≥99.0%) or DMSO (Fisher BioReagents, ≥99.7%) at a given concentration. Dissolution in THF was carried out on a hotplate at 35 °C while dissolution in DMSO was conducted

on a hotplate at 85 °C. The dissolution of sulfur occurs in approximately 15-20 minutes. For optical microscopy studies on HOPG, sulfur sols were immediately crashed (i.e. rapidly added) into either DI water or solutions of SDS (Fisher BioReagents, Micropellets) in DI water, and 40 µL was drop-cast onto an HOPG substrate and covered with a glass coverslip. Optical microscope images were obtained with a Leica DM2700M microscope with a 20× objective lens, as indicated. The bulk solutions examined by optical microscopy (OM) were prepared by crashing a hot sulfur solution (0.2 M) into a dispersion of the specific carbon nanomaterial in SDS and water (0.5 mg/mL, 1:10 ratio of solvent to 35 mM SDS/water solution, 45% carbon material to 55% sulfur), following tip sonication (BioLogics, Inc., Model 150 V/T Ultrasonic Homogenizer, 150 W) at 70% power in an ice bath. A 40 µL aliquot was taken from the bottom of the vial after each analysis time and pipetted onto a glass coverslip, covered with a second coverslip, and imaged.

DLS was conducted with a Malvern Zetasizer Nano 90 at a 90° angle, with three measurements collected for each sample at each time interval, and three separate repeats run for each sample type. rGO samples (0.5 mg/mL, 1:10 ratio of solvent to 4 mM SDS/water solution) were tip-sonicated for 20 minutes at 70% power in an ice bath, with stirring at 300 rpm before sulfur addition. rGO dispersions for "rGO Alone" and "rGO/S" samples were prepared identically – the same mass and concentration of rGO, volume of 4 mM SDS solution, sonication time, and sonication power were used – in order for an accurate comparison between samples, and so that the effect of the sonication step on rGO sheet size/morphology is identical. Sample aliquots were taken at each analysis time and diluted 100x in DI water. Solid powder composites of rGO/S, GO/S, and KB/S were prepared by crashing a hot sulfur solution (0.2 M) into a dispersion of the specific carbon nanomaterial in SDS and water (0.5 mg/mL, 1:10 ratio of solvent to 4 mM SDS/water solution, 45% carbon material to 55% sulfur), enabling sulfur deposition in the solution with stirring for 2 hours, flocculation of the material with NaCl, vacuum filtration, drying of the material at 80 °C, and finally grinding into a fine powder in a mortar and pestle. SEM imaging and EDS mapping of the rGO/S, GO/S, and KB/S composites were carried out using a FEI Quanta FEG 250 ESEM under environmental/low vacuum mode to limit sulfur sublimation. Raman spectroscopy was performed on the rGO materials, sulfur controls, and rGO/S composites with a Horiba Jobin-Yvon HR800 Raman system equipped with an Olympus BX 41 microscope with a 50 mW, 532 nm laser operating at 25% laser power. A minimum of five Raman scans were performed on different areas of each sample to obtain a representative measurement. The D and G peaks were fit with a Lorentzian and Breit−Wigner−Fano (BWF) function respectively.[92,231] The I_D/I_G ratio was calculated

from the fitted peak heights or intensities. TGA analysis was performed using a TA Instruments Q500 at a 5 °C/min ramp rate from 30 °C to 800 °C under nitrogen. TGA analysis of the rGO/S powder prepared in a ratio of 45% rGO and 55% sulfur demonstrates that the final composite consists of 55.5% sulfur, indicating that none is lost during the filtration and drying process (**Fig. D2**).

6.2.3 Electrode Fabrication

80 mg of rGO was dispersed in 160 mL of 4 mM SDS in water via tip sonication at 70% power for 1 hour in an ice bath, with stirring at 250 rpm. 97.8 mg sulfur was dissolved in 16 mL of THF or DMSO and then was crashed into the rGO dispersion to result in a 45:55 ratio of rGO/S. The mixture was stirred for 2 hours to enable sulfur deposition on rGO. Following 2 hours, for all samples without PEI, ~3 g of NaCl was added to the solution to flocculate the rGO. For samples with 5% or 10% PEI (Sigma-Aldrich, average M_w ~25,000 by LS, average M_n ~10,000 by GPC, branched), after 2 hours, the solution pH was adjusted to ~8 using 0.2 mM NaOH, and then 0.790 mL (5%) or 1.693 mL (10%) of 15 mg/mL PEI solution in water was added to flocculate the rGO, and to yield a ratio of 5% or 10% PEI in the final cathode. All samples were then vacuum filtered, rinsed three times with DI water to remove solvent and surfactant, and dried at 80 °C. Removal of the surfactant during this process was further supported via TGA analysis of the final isolated rGO/S powder in which no mass loss attributed to SDS was observed. Active material powder was then pulverized in a mortar and pestle to form a fine powder. Cathodes were then assembled by pressing the dry powder onto an aluminum foil current collector using a ½" stainless steel pressing die and a force of 25 US tons (~22,680 kg). Cells without binder or conductive additive were pressed directly. Cells with binder and conductive additive were prepared by first mixing the active material with PVDF binder (Sigma-Aldrich, Mw ~534,000) and carbon black (MTI Corp., TIMCAL Graphite and Carbon Super P® Conductive Carbon Black) in a 70:10:20 ratio in NMP (Fisher Chemical, Laboratory Grade), fully drying the powder at 80 °C, re-pulverizing the material in a mortar and pestle, and then pressing the cathodes. Cells with PEI were prepared by mixing the active material/PEI mixture with carbon black in NMP such that the final ratio was either 75:5:20 AM:PEI:CB (5% PEI) or 70:10:20 AM:PEI:CB (10% PEI) fully drying the powder at 80 °C, re-pulverizing the material in a mortar and pestle, and then pressing the cathodes. The cathodes were assembled in CR2032 coin cells (MTI Corp.) with a polypropylene separator (MTI Corp.) and lithium metal foil anode (Xiamen Tmax Battery Equipments Limited), and excess (90 μL) electrolyte, consisting of 1 M lithium bis(trifluoromethanesulfonyl)imide (LiTFSI, Aldrich Chemistry, 99.95% trace metals basis) and 0.1 M lithium nitrate ($LiNO_3$, Acros Organics, 99+%) in 1:1 v/v 1,2-

dimethoxyethane (DME, Sigma-Aldrich, anhydrous, 99.5%)/1,3-dioxolane (DOL, Sigma-Aldrich, anhydrous, 99.8%). All cells were assembled in an Ar-filled glovebox, with ≤0.1 ppm water and ≤0.7 ppm oxygen.

6.2.4 Electrochemical Characterization

Electrochemical impedance spectroscopy (EIS) was performed on the assembled coin cells at OCV 2 hours after assembly, to enable electrolyte penetration into the cathode. A Biologic SP-300 potentiostat was used to perform EIS between 200 kHz to 100 mHz using a sinusoidal perturbation of amplitude 10 mV. Coin cells were then cycled using an Arbin BT2000 battery tester (Arbin Instruments) using constant current charge-discharge testing with potential limits of 1.7 and 2.7 V vs. Li metal to avoid decomposition of the nitrate salt and oxidation of the Al current collector. Charging currents were limited to 2.25 mA (1.12 mA/cm^2) to prevent dendrite formation and failure of the lithium metal anode. A value of 55% sulfur was used to calculate C-rate current values and specific capacities for each sample.

6.3 Results and Discussion

6.3.1 Sulfur Nucleation and Growth on Model Surface

We first studied the interactions between hydrophobic sulfur sols and a model carbonaceous surface, highly oriented pyrolytic graphite (HOPG). Sols were first prepared, then drop-cast onto the surface of an HOPG substrate, and finally observed via OM, as shown schematically in **Figure 6.2a)**. **Figure 6.2b)** shows results obtained with sols prepared from sulfur dissolved in DMSO, rapidly added to deionized water. When the sulfur solution is added to water, a cloudy, opaque white sol is immediately formed. After the initiation of the experiment, the HOPG surface is visible, with various lines and defects. The sol particles are also visible as small, spherical particles that are mobile on the surface of the HOPG, and move due to Brownian motion during imaging. Initially, these are the only particles visible on the surface. Then, over time, crystals are observed to grow. After 30 minutes, sol particles are still clearly visible and mobile on the surface of the HOPG, but additional needle-like crystals have formed on the surface. Some crystals are situated at visible cracks and defects on the HOPG surface, while others appear to grow on more uniform, flat areas. After 2 hours, the initial crystals have grown in size. A quantitative plot of the growth of the lateral size of the crystals labelled “1” and “2” can be seen in **Figure D3**. Both crystals exhibit similar growth behaviour, with initial rapid growth which then

plateaus after 30 minutes. Over time, the crystal color changes as well, due to thin film interference. An example of this can be seen in **Figure D4**, demonstrating that the crystal color oscillates over time as the thickness increases. After 2 hours, sol particles are still present, but notably appear to be absent in the areas directly surrounding each crystal, as highlighted with white dashed lines.

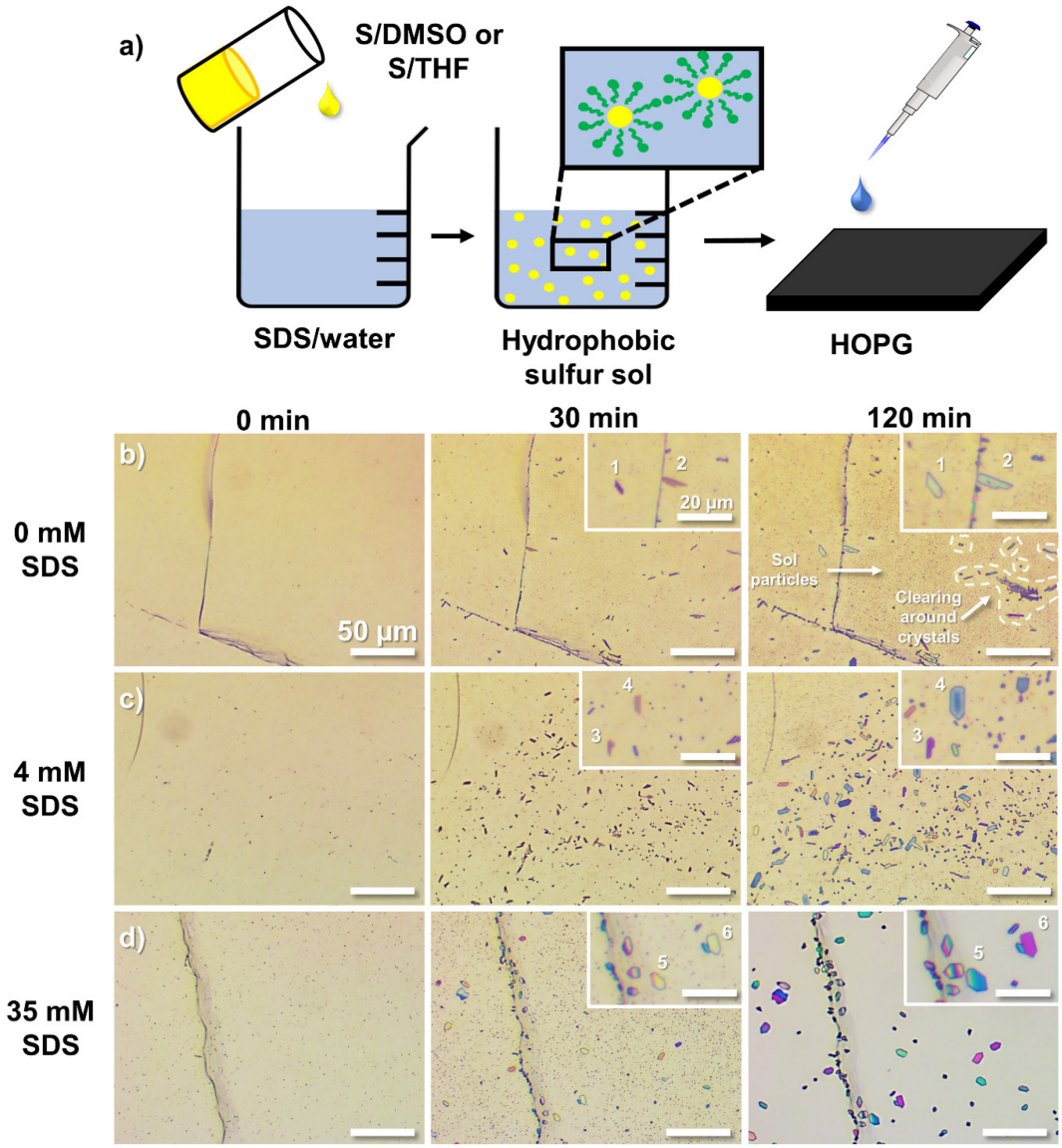

Figure 6.2: Optical microscopy study of sulfur crystal growth on HOPG from DMSO-based sols. a) Scheme of strategy to investigate sol interaction and crystal growth on HOPG substrate as model system. b-d) OM images of sulfur crystal growth on HOPG substrate using 0.2 M sulfur dissolved in DMSO, a 1:10 ratio of DMSO/water, and SDS concentrations of b) 0 mM, c) 4 mM, and d) 35 mM. Scale bars are 50 µm in low magnification images and 20 µm in high magnification insets. Crystals in insets at 30 min and 120 min are numbered for identification.

As seen in **Figure 6.2c)** and **6.2d)**, we then investigated the effect of adding a surfactant into the aqueous phase. Surfactants are often used to form stable aqueous dispersions of relatively hydrophobic carbonaceous nanomaterials. Thus, we investigated the use of SDS, as it is known to be a suitable surfactant for the dispersion of graphene. A concentration of 4 mM SDS was used as this is below the critical micelle concentration (CMC), but above the critical surface aggregation concentration.[302] The value of 35 mM is chosen to lie above the CMC of SDS in water. In both cases, crystal nucleation and growth are observed on the surface of the HOPG. In the 4 mM case, mobile sol particles are again visible initially. After 30 min, a larger number of crystals have formed on the surface compared to the case without surfactant. After 2 hours, some mobile sol remain, but a large number of crystals with varying morphology are present.

In the 35 mM SDS case, mobile sol particles are also initially visible, and remain after 30 min. However, unlike the other two cases, after 2 hours, no sol particles remain. The crystals formed in the 35 mM case all possess the same morphology, appearing flat and hexagonal, suggesting that the surfactant may adsorb to specific crystal planes and promote specific, ordered crystal growth. The lateral crystal growth behaviour for both concentrations of SDS follow a similar trend as the sample without SDS (**Fig. D3**). When hydrophobic sulfur sols were drop-cast onto glass substrates for comparison, rather than onto HOPG, no crystal formation was observed, (**Fig. D5**), suggesting that the crystal nucleation and growth occurs because of favorable interactions of the sulfur with the sp^2 carbon surface.

We hypothesize that the mechanism of nucleation and growth of the sulfur crystals on the surface of the HOPG follows a mechanism comparable to Ostwald ripening,[303] in which the sulfur sols exist as liquid or amorphous sulfur particles dispersed in the aqueous phase. Small amounts of sulfur dissolve out of the sol particles and diffuse through the aqueous phase, where they can nucleate on the surface of the hydrophobic carbon material. This is most evident when examining large crystals in all cases after 2 hours of growth. In the cases of 0 mM and 4 mM SDS, sol particles are still present, but are absent in the areas surrounding each crystal. This suggests that crystal growth does not occur via direct contact or fusion of sol particles with the crystals, but rather that sol particles slowly shrink at the expense of the growing sulfur crystals. When a surfactant such as SDS is added to the system, it is suggested that the surfactant particles coat the surface of the sol particles as in an emulsion.[210] Surfactants such as SDS are known to both stabilize hydrophobic sulfur sols and increase the solubility of sulfur in water.[210] Hydrophobic sulfur sols are known to be metastable at room temperature, and will

eventually precipitate through a homogeneous nucleation process to form crystalline sulfur. The stability of the sol is greatly improved in surfactant solutions, which delays their precipitation and crystallization by several days, as the surfactant molecules on the sol surface prevent the aggregation and fusion of the particles.[210]

We observe that higher concentrations of surfactant result in faster crystal growth and removal of sol particles, as evidenced by the complete clearing of the sol after 2 hours in 35 mM SDS, while sol particles remain when using 4 mM SDS or no surfactant. As the addition of surfactants minimizes mechanisms based on particle fusion, but leads to increased solubility of sulfur in the aqueous phase, the observation of increased crystal growth at higher SDS concentration supports our conjecture of an Ostwald ripening-like growth mechanism. We hypothesize that the mechanism of the sulfur deposition onto carbon stems from a favourable hydrophobic-hydrophobic interaction between sulfur and carbon: Fan et al. demonstrated through DFT calculations that an S_8 molecule has a stronger adsorption energy with a carbon nanotube (CNT) than with other S_8 molecules, suggesting that sp^2-hybridized carbons offer low energy sites for heterogeneous nucleation of sulfur.[304] This finding was then used to develop a strategy to recrystallize sulfur from concentrated solutions in acetone onto CNTs. This demonstration of an interaction between sulfur and carbon that results in heterogeneous nucleation on CNTs provides further supporting evidence of the heterogeneous nucleation process we observe from sulfur sols on HOPG. Furthermore, studies of the wetting behaviour of molten sulfur on a range of different carbon materials, including glassy carbon, and microcrystalline and nanocrystalline graphites, all demonstrate that sulfur wets carbon surfaces very well.[305] All samples exhibit contact angles of approximately 50°, despite the interaction between the two being determined by weak van der Waals forces, providing further support of interfacial interactions between sulfur and carbon surfaces that could result in heterogeneous nucleation of sulfur on carbon.[305]

OM studies using THF as the solvent for sulfur demonstrate similar results, as seen in **Figure 6.3**. Without surfactant, crystals of a variety of different morphologies are observed (**Fig. 6.3a)**), while the addition of surfactant (**Fig. 6.3b),c)**) mainly results in crystals with a flat morphology, although, unlike the DMSO case, not all are hexagonal in shape. Rather, many exist as large aggregates of crystals of varying morphology. Again, we observe that at higher concentrations of SDS, the growth process is faster, with larger sulfur crystals formed more rapidly, and, likewise, sol particles depleted more quickly. Interestingly, the crystal nucleation and growth appears to be faster in THF, particularly with 4 mM and 35 mM SDS. In the 35 mM case, large aggregates of crystals over 100 μm in lateral size are

visible after only 10 minutes of growth. We hypothesize that this is at least partly due to the higher room temperature solubility of sulfur in THF than DMSO. The observations are also in agreement with our suggestion that the growth process is an Ostwald ripening-like process, as it is accelerated by raising the solubility of sulfur.

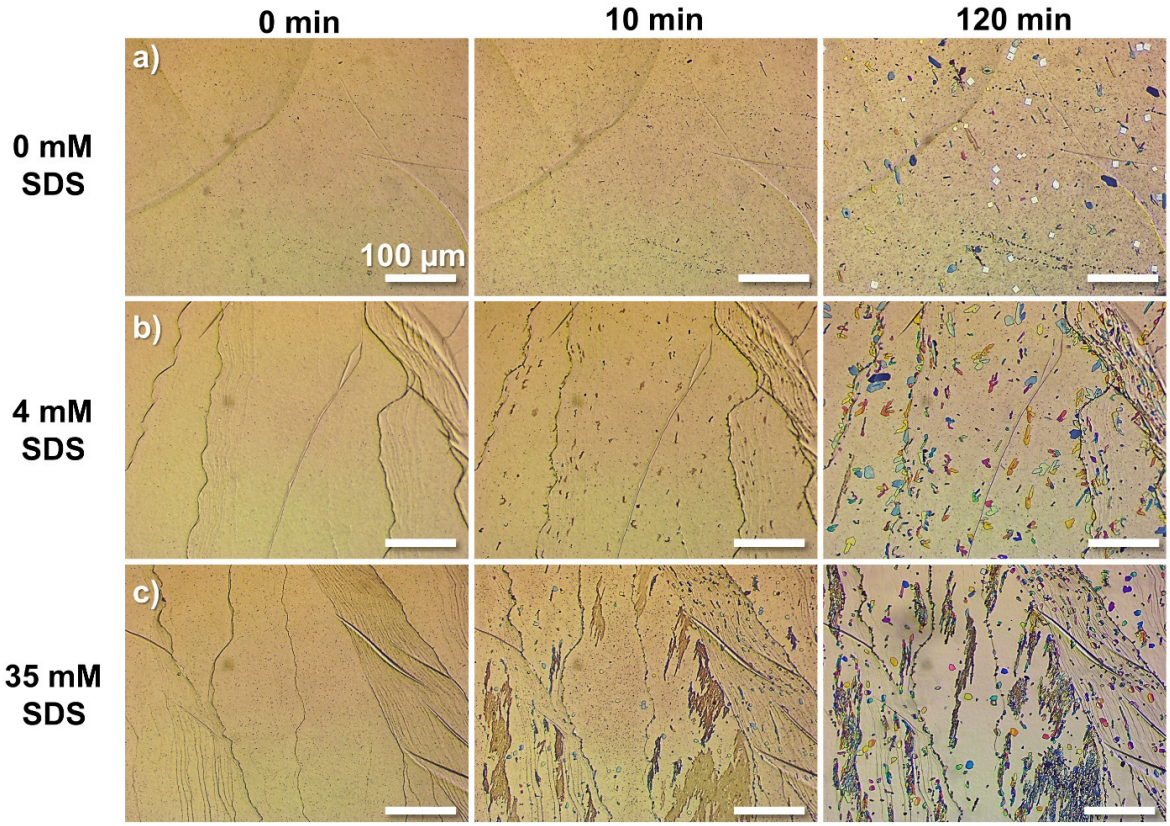

Figure 6.3: Optical microscopy study of sulfur crystal growth on HOPG from THF-based sols. OM images of sulfur crystal growth on HOPG substrate using 0.2 M sulfur dissolved in THF, a 1:10 ratio of THF/water, and SDS concentrations of a) 0 mM, b) 4 mM, and c) 35 mM. Scale bars are 100 µm.

The effect of higher sulfur concentrations, which correspond to higher sulfur/carbon ratios, was also studied. At increased concentrations of 0.37 M (11.8 mg/mL), which is the approximate saturation point for sulfur in THF, a larger number of sol particles are initially visible on the HOPG surface, for samples prepared from both DMSO (**Fig. D6**) and THF (**Fig. D7**). In the case of THF, this leads to the growth of large crystals of >100 µm length within 5 minutes, while the growth process in DMSO is much slower, resulting in much smaller crystals. The sol particles are fully depleted after 2.5 hours for THF, but sol particles are still present after 4.5 hours with DMSO. However, in both cases, the crystallization

process still occurs. Furthermore, in the DMSO case, the increased number of sol particles clearly shows the localized depletion of sol particles in areas surrounding the growing crystals. We also examined a much higher sulfur concentration of 1.25 M (40 mg/mL) in DMSO, which approaches the saturation point of sulfur in this solvent (**Fig. D8**). A very high number of sol particles are observed in this case, and after 2 hours, only a few flat crystals are observed. Instead, a third type of bipyramidal particle is observed in large numbers on the HOPG surface. After 5 hours and 15 minutes, more of the sol has cleared, and three types of particles are visible on the surface: (i) flat crystals similar to those observed previously, (ii) bipyramidal crystals that had not been previously observed, and (iii) other settled particles that appear to be aggregates of particles smaller than the resolution limit of the optical microscope.

We assume that both the bipyramidal crystals as well as the other observed particles result from homogeneous nucleation processes, which at high sulfur concentrations or sulfur/carbon ratios may become more favorable than heterogeneous nucleation on carbon. Bipyramidal sulfur crystals have been previously observed during the homogeneous nucleation of sulfur crystals from hydrophilic sulfur sols by Fu et al. in the presence of a surfactant.[306] To confirm this, sulfur sols prepared from the same high sulfur concentration (1.25 M) in DMSO were drop-cast onto glass (**Fig. D9**). After five hours, no flat crystals like those formed on HOPG are observed, but the other two particle types – bipyramidal crystals and other small settled aggregates – are visible, suggesting that these originate from homogeneous nucleation in concentrated sol dispersions.

Finally, we briefly examined the role different surfactants have on the growth process. While we first focused on the use of SDS, an anionic surfactant, due to its known qualities for dispersing graphene, we also examined the growth of sulfur on HOPG with Triton X-100, a non-ionic surfactant, and CTAB, a cationic surfactant (**Fig. D10**). In all cases, crystal growth was still observed, though the crystal morphologies differed with different surfactants, suggesting that the surfactants may bind to different crystal planes, and promote the growth of different morphologies. However, as crystal morphology is not critical for final rGO/S cathode performance (morphology will change during electrochemical cycling), the mere fact of observing crystal growth in a variety of surfactants indicates the universality of this method for coating sp^2-hybridized carbon with sulfur.

6.3.2 Sulfur Coating on rGO and Other Nanocarbons

The OM studies on HOPG demonstrated that the deposition of sulfur from hydrophobic sulfur sols onto the surface of sp^2-hybridized carbon. However, this HOPG model system represents a much higher ratio of sulfur to available surface area of carbon than is present in a sulfur cathode. Thus, we next conducted OM on dispersions of different carbon-based materials after adding sulfur sols. Specifically, we examined aliquots from dispersions of rGO, GO, and a control with no carbonaceous nanomaterial after 1, 2, and 3 days. Images of the bulk solution behaviour over time can be seen in **Fig. D11**. As seen in **Figure 6.4a)** and **d)**, after 3 days, the control sample contains sulfur crystals formed from the homogeneous nucleation of the metastable sulfur sol. The sample with GO (**Figure 6.4b)** and **e)**) contains a large number of sulfur crystals, with morphologies ranging from flat hexagonal crystals similar to those observed on HOPG to bipyramidal crystals, indicating that GO sheets may act as a site for heterogeneous nucleation, but the observed flat hexagonal crystals do not remain bound to the surface of the GO. Instead, they precipitate and collect at the bottom of the vial. In the case of rGO (**Figure 6.4c)** and **f)**), aggregates of rGO are visible, but no sediment of sulfur crystals is observed. This suggests that instead of nucleating homogeneously, the sulfur preferentially forms nuclei on the dispersed rGO and coats it rapidly. Results for THF-based sols (**Fig. D12** and **D13**) confirm the findings obtained with DMSO, with sulfur crystals observed for both control and GO samples, and no crystals observed for rGO.

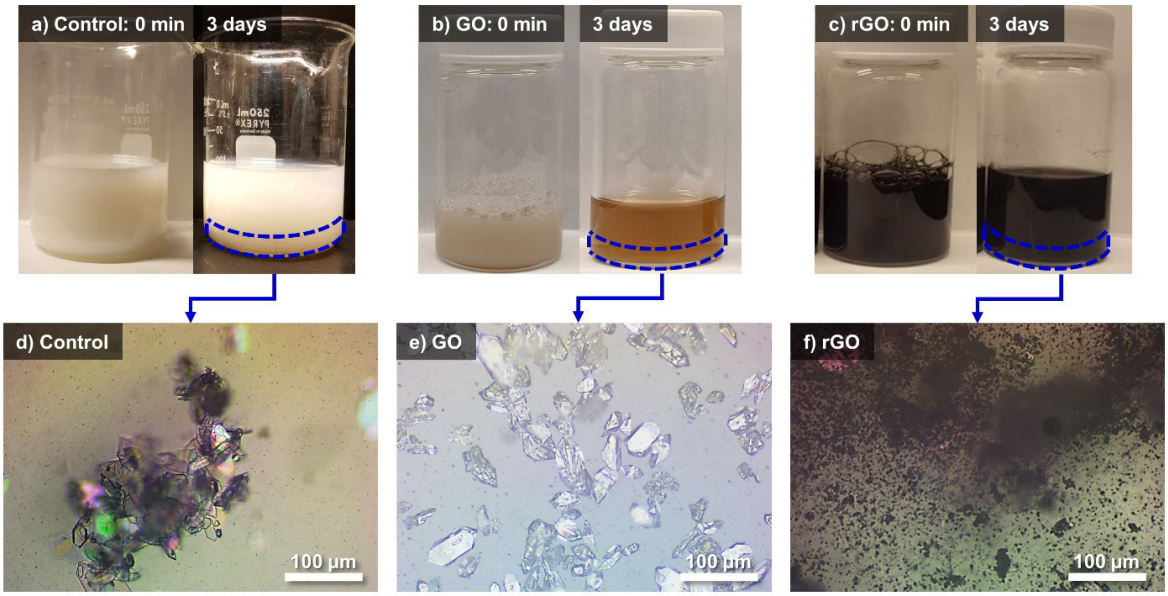

Figure 6.4: Optical microscopy of bulk carbon nanomaterial dispersions and sulfur sols over time. Images of bulk solutions immediately after and 3 days after the formation of hydrophobic sulfur sols using 35 mM SDS, 0.2 M sulfur, and a 1:10 ratio of DMSO/water for a) control sample with no carbon material, b) GO, and c) rGO. The ratio of carbon nanomaterial to sulfur was 45% to 55% to mimic a conventional sulfur cathode. OM images of settled material from bulk solutions 3 days after sol formation for d) control sample with no carbon material, e) GO, and f) rGO.

We also used dynamic light scattering (DLS) to follow changes in particle size and count rate with time, immediately after forming a sulfur sol. The derived count rate in DLS is directly related to both the number density of particles and the size of the particles, and thus can provide information on the behaviour of the sulfur sol over time. Particularly, if the particle size is constant, the count rate can be directly related to the number density of particles.[307] We first studied sulfur sols alone, without rGO. A surfactant concentration of 4 mM SDS was used for all further studies, as this provides enough surfactant to stabilize dispersions of rGO, but a low enough concentration to easily wash out and remove the SDS later on, simplifying cathode processing. As seen in **Figure 6.5a)**, sulfur sols prepared from THF and DMSO possess initial count rates of 1970 kcps ± 117 kcps and 1775 kcps ± 108 kcps which increases until 1 hour later, at which point it decreases. **Figure 6.5b)** demonstrates that THF-based sols possess an initial particle diameter of 180 nm ± 14.9 nm, which reach a size of 266 nm ± 11.5 nm after 2 hours, while DMSO-based sols possess an initial size of 164 nm ± 5.7 nm, which grows to a size of 247 ± 1.9 nm. As the sol particles continuously increase in size, the initial increase in count rate can be attributed to the particle growth, while the decrease after 1 hour can be attributed to the decreasing

number of particles as smaller particles are depleted and eventually fully dissolved in the Ostwald ripening-like growth. Particle sizes are similar to, but slightly larger than, sizes reported for hydrophobic sulfur sols prepared from methanol/water.[308]

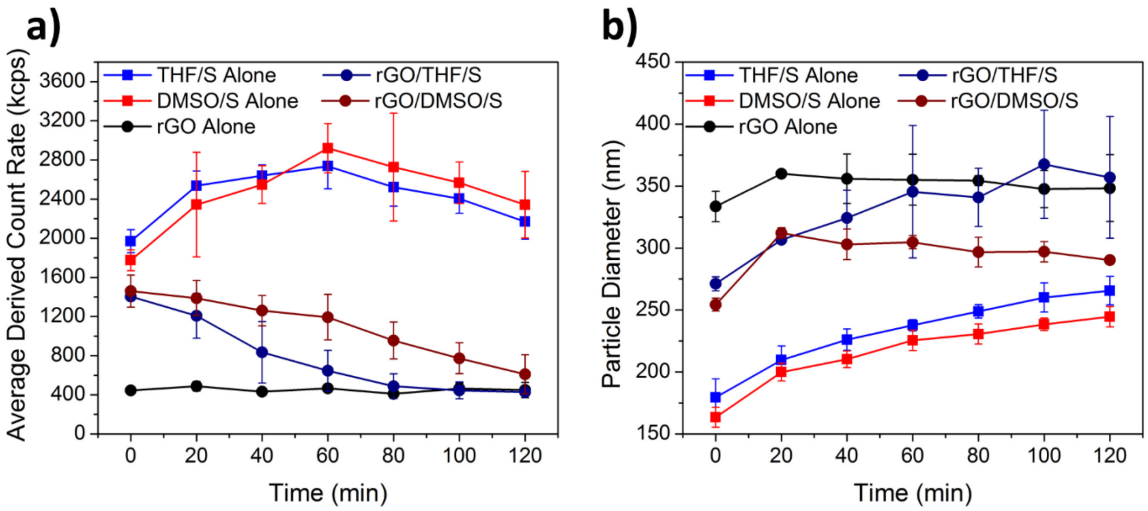

Figure 6.5: DLS analysis of carbon nanomaterial dispersions and sulfur sols over time. a) Average derived count rate data and b) average particle diameter for sulfur sols alone (THF/S/Alone, DMSO/S/Alone), rGO alone, and mixtures of rGO/sulfur sols (rGO/THF/S, rGO/DMSO/S). Error bars represent the standard deviation across three separate repeats for each sample and time.

DLS measurements of a dispersion of rGO in 4 mM SDS in water demonstrate a near-constant count rate of approximately 450 kcps over the course of two hours, and a near-constant particle size of approximately 350 nm. These results indicate that a sonicated dispersion of rGO in 4 mM SDS is stable over the course of 2 hours, with little to no aggregation. We then analyzed the behaviour of samples in which the sulfur sol was rapidly added into a dispersion of rGO in 4 mM SDS over time. For both DMSO and THF-based samples, initial count rates were very similar to that of the sulfur sols alone, at 1459 kcps ± 164 kcps and 1404 kcps ± 32 kcps, respectively. Over the course of 2 hours, both DMSO and THF-based samples exhibit decreases in their count rates, with both eventually meeting the count rate of the dispersion of rGO alone, with values of 610 kcps ± 199 kcps and 429 kcps ± 28 kcps, respectively. Notably, the THF-based samples experience this decrease in count rate much earlier in time, meeting the "rGO-alone" count rate within 80-100 minutes, while the DMSO-based samples take the full 2 hours or slightly longer. Both samples possess an initial average hydrodynamic diameter in between that of the sulfur sols and rGO sheets, with DMSO-based samples and THF-based samples possessing an initial average hydrodynamic diameter of 254 nm ± 5 nm and 271 nm ± 6 nm,

respectively. Over the course of 2 hours, the THF-based samples exhibit increases in average hydrodynamic diameter, with the final average value matching that of the rGO alone (357 nm ± 49 nm), while DMSO-based samples exhibit increases in average hydrodynamic diameter, but the final average value remains less than that of rGO alone, at 290 nm ± 3 nm. The polydispersity index (PDI) of all samples can be seen in **Figure D14**, demonstrating a similar trend as the particle size, in which the sols alone possess low PDI values of ~0.1, and the rGO alone possesses a higher PDI of ~0.45. rGO/S samples possess initial PDI values between these two, with an increase in the PDI over the course of the 2 hour experiment.

We also used DLS to examine the effect of temperature on the behaviour of the dispersions, and found that for DMSO-based sols, samples consisting of rGO/S and rGO alone at 50 °C exhibited similar behaviour (**Figure D15**). The rGO/S sample at 50 °C displayed a slightly faster drop in count rate than the room temperature sample, but within the error of each measurement. The sulfur sol alone at 50 °C had a similar initial hydrodynamic diameter of 165.8 nm ± 2.2 nm, but exhibited an increased growth rate, and after one hour, large homogeneously nucleated crystals were visible in the sample, leading to an effective count rate of ~0, and a PDI of 0.9, making the sample no longer suitable for DLS analysis. This behaviour corresponds well with that of methanol-based Weimarn sols, which demonstrated increased particle growth rates with increasing temperature, owing to increased solubility of sulfur in the aqueous phase and an Ostwald ripening growth mechanism.[308]

These results lead us to conclude that in samples with both sulfur sols and dispersed rGO sheets, the sulfur sol immediately forms upon addition of the dissolved sulfur into the aqueous surfactant solution, resulting in the high initial count rate. Over time, sulfur dissolves out of the sols, into the aqueous phase, and deposits on the surface of the rGO, depleting the sol particles. As the smaller sol particles dissolve and the sulfur coats the rGO, this leads to an increase in the average hydrodynamic diameter determined for the sol/dispersion mixture, and a decrease in the count rate (as the sol particles disappear). Furthermore, this process is faster in THF, where the solubility of sulfur is higher, resulting in complete consumption of the sol particles within 80-100 minutes. The process is slower in DMSO, and the smaller final average hydrodynamic diameter of the dispersion indicates that some small sol particles may remain after 2 hours. While it is possible that the results could also indicate the trapping of the sol particles within aggregates of the rGO, rather than deposition of the sol, the fact that the count rate of the rGO/S samples meets the rGO alone data indicates that this is unlikely. Furthermore, the formation of large aggregates would be expected to lead to increases in the count rate or decreased stability of the

rGO dispersion, which is not observed. While the initial count rates for the rGO/S samples are expected to be higher than sulfur sols alone, we expect that this discrepancy is a result of some initial deposition of sol particles onto the rGO during the approximately 30 seconds between the formation of the sol and the start of the measurement, during which the sample is diluted and added to the cuvette.

The nucleation and growth of sulfur on the rGO surface is further confirmed via SEM imaging and energy dispersive X-ray spectroscopy (EDS) mapping of rGO/S composites prepared via this approach. Powders were imaged under low vacuum conditions to mitigate any evaporation of sulfur during imaging. The sublimation of sulfur was found to be quite rapid under high vacuum conditions, as seen in **Figure D16**, where sulfur crystals with lateral sizes of a few to tens of microns were nearly completed removed after 3 minutes of imaging, preventing any analysis of the sulfur composites under conventional high vacuum SEM or TEM. As seen in high magnification images and sulfur EDS maps of rGO/S prepared from DMSO-based sols in **Figure 6.6a)-d)**, sulfur is uniformly distributed on the surface of the rGO. Versions of these images obtained with a backscattered electron detector (BSE) can be seen in **Figure D17** and further low and high magnification images of the rGO/S active material can be seen in **Figure D18**. In most of the SEM images in **Figure 6.6** and **Figures D17** and **D18**, some larger sulfur aggregates are present, indicated by both bright spots in the SEM images and S EDS maps. One of these sulfur aggregates, approximately 1.6 μm in size, is marked in **Figure 6.6a)**. These aggregates might have formed during the fusion and agglomeration of remaining sol particles during filtration and drying steps, or due to trapping and agglomeration of some sol particles in rGO aggregates. As seen in the EDS map in **Figure 6.6b)**, while the sulfur aggregate exhibits the strongest sulfur signal, the remaining rGO sheets surrounding it also contain sulfur. Furthermore, even areas of the rGO/S composite with few to no sulfur aggregates visible still exhibit a uniform sulfur signal, as seen in **Figure 6.6c)** and **d)**, indicating that, while some sulfur aggregates are present, our proposed mechanism, in which sulfur dissolves out of sol particles to uniformly coat the surface of the rGO sheets, also occurs. Moreover, while the sulfur EDS signal in areas without large sulfur aggregates is lower, this corresponds well with a thin coating of sulfur on the rGO sheets. Lower magnification images of the rGO/S composite (**Figure 6.6e)** and **f)**) illustrate similar behaviour across the composite as a whole, with some sulfur aggregates present, but also the uniform distribution of sulfur across the rGO material on a large scale. While it could be suggested that the uniform sulfur signal in EDS mapping stems from sulfur particles that are buried under rGO sheets, the penetration depth of EDS is typically only a few microns into the sample,[309] and the sulfur aggregates observed are typically a few

microns in size. With BSE imaging, the sulfur particles, which possess a higher atomic number than carbon, are highly visible, making it unlikely that any aggregates could present an EDS signal without being visible in the BSE images. Furthermore, these large particles would result in clusters of bright signal in the EDS, rather than a uniform sulfur signal. As such, the EDS mapping provides strong evidence that sulfur is present in a uniformly distributed thin coating on the rGO surface. Furthermore, consistent with our optical microscopy studies, no large crystals of sulfur are observed, suggesting that undesirable homogenous nucleation of sulfur is suppressed, and that nearly all sulfur is instead deposited on the rGO surface or present as remaining sulfur aggregates. SEM images and EDS mapping of THF-based composites demonstrates similar results (**Fig. D19**). Raman analysis of rGO/S composites do not exhibit any of the characteristic peaks found for elemental sulfur (153, 217, and 473 cm^{-1}),[310] but rather only the D and G peaks of the rGO material, indicating that the sulfur in the composite is uniformly distributed, and largely amorphous in nature (**Fig. D20**).

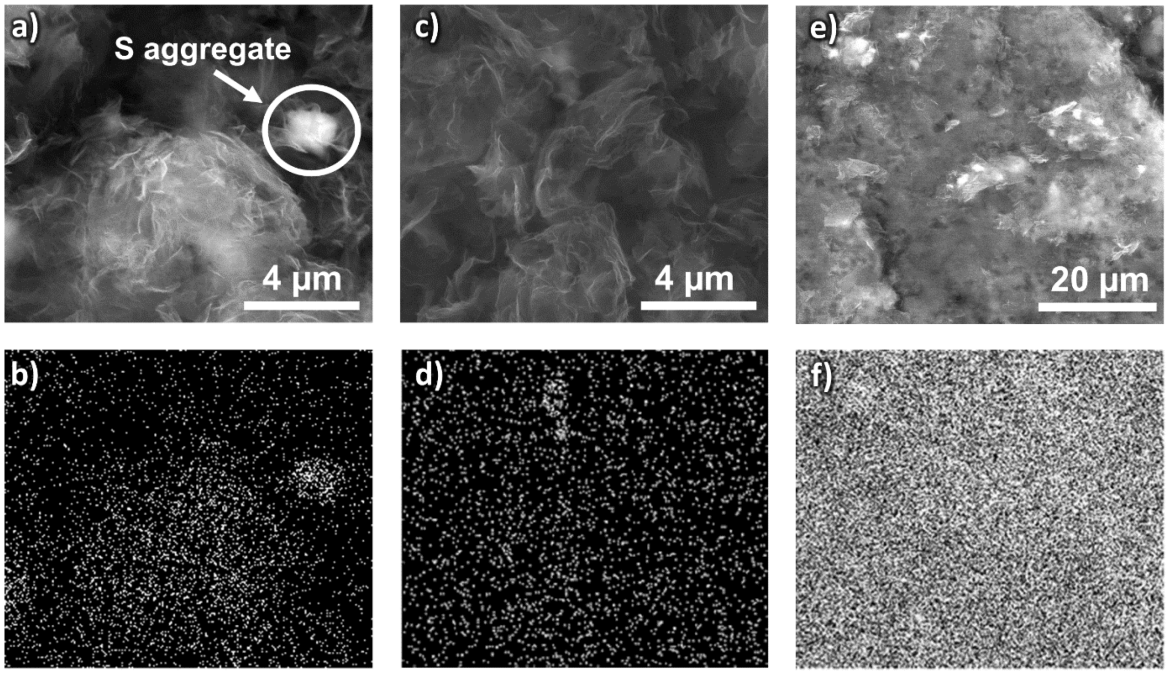

Figure 6.6: SEM and EDS analysis of rGO/S composite. a) SEM image of morphology of rGO/S composite prepared from DMSO-based sol with a sulfur aggregate and b) corresponding S EDS map. c) SEM image of rGO/S in area with no sulfur aggregates and d) corresponding S EDS map. e) Lower magnification SEM image of the rGO/S composite and f) corresponding S EDS map.

To better understand this mechanism, we prepared composites of sulfur with other carbon-based materials, Ketjen black (KB) and GO in the same way. As seen in **Figure 6.7a), b),** and **c)**, SEM images

and EDS maps of KB samples demonstrate that some areas of the carbon particles are uniformly coated with sulfur, while other areas are covered in bipyramidal sulfur crystals, which appear to be wrapped with KB particles. GO/S composites (**Figure 6.7d), e),** and **f)**) show large numbers of bipyramidal sulfur crystals, consistent with the optical microscopy studies with bulk GO solutions. As discussed earlier, we suggest that these bipyramidal crystals are formed from the homogeneous nucleation of sulfur in surfactant solutions. However, in the SEM images, it is clear that the sulfur crystals are wrapped in GO sheets, with the sheets clearly visible in the secondary electron (SE) image (**Figure 6.7e)**), and the sharp bipyramidal crystals clear in the backscattered (BSE) electron image (**Figure 6.7f)**), in which the GO sheets are less visible due to their lighter atomic mass. Further SE and BSE images demonstrating this are presented in **Figure D21**. Thus, we conclude that in the case of GO, sulfur either nucleates homogeneously in solution, or the GO sheets may act as nucleation sites, but in stark contrast to rGO, sulfur does not coat the surface of the GO sheet. This is consistent with previous work from our group that used mixtures of GO and hydrophobic sulfur sols to prepare sulfur cathodes, in which no deposition of the sulfur onto the GO was observed.[214] We hypothesize that this is because the many oxygen-containing functional groups in GO result in weaker interactions with sulfur than between carbon and sulfur, making the deposition process unfavourable. The presence of large bipyramidal crystals with KB and GO samples highlights that the mechanism for the rGO/S composite, in which no bipyramidal crystals are observed, is different, and does not merely involve wrapping of homogeneously nucleated sulfur.

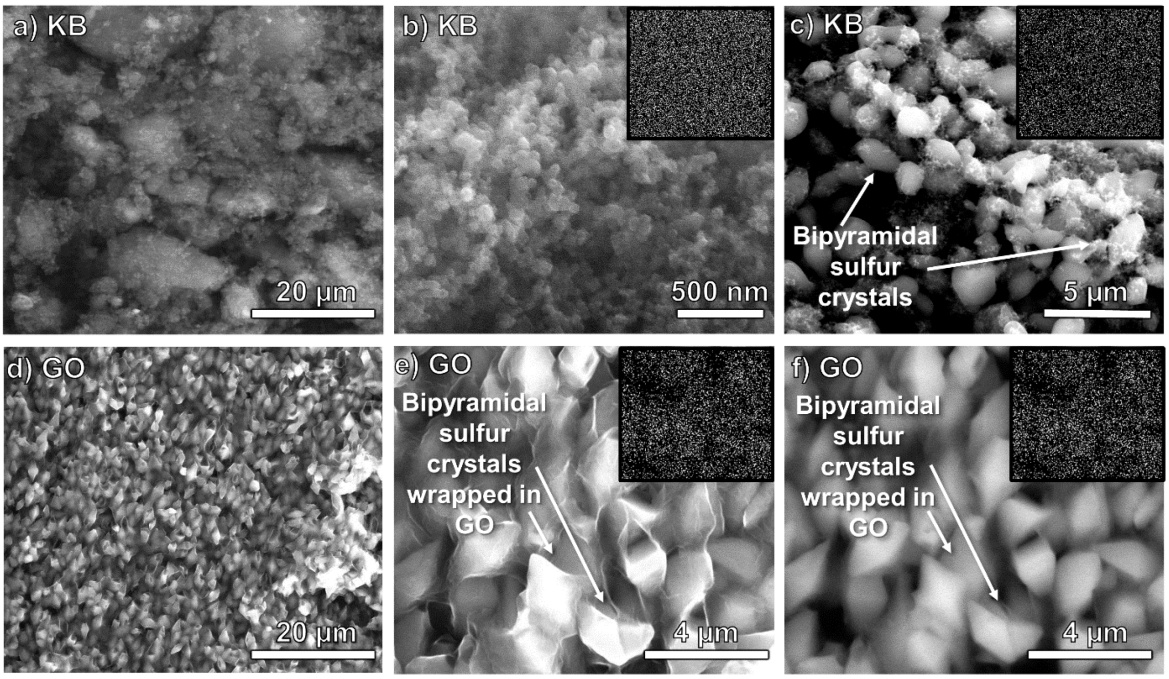

Figure 6.7: SEM and EDS analysis of KB/S and GO/S composites. SEM images of sulfur deposited on a)-c) KB and d)-f) GO. a) Low magnification SEM image of sulfur deposited on KB. b), c) Higher magnification SEM images of sulfur deposited on two different areas of KB, demonstrating both uniform coating of KB particles (b) and the formation of a large number of homogeneously nucleated bipyramidal crystals (c). d) Low magnification SEM image of sulfur deposited on GO. e), f) Higher magnification SEM images of sulfur deposited on GO using a secondary electron detector (e) and backscattered electron detector (f), demonstrating that only bipyramidal crystals are present in the sample, which are wrapped in GO sheets. Insets are EDS maps of sulfur distribution for each image, showing uniform sulfur signal across each high magnification image.

In the case of KB, sulfur does nucleate and grow, but some homogeneous nucleation occurs, unlike the situation with rGO. We suggest that this stems from differences in the structure of the two carbon materials. While KB exhibits a high nitrogen-accessible surface area via BET measurement (1379 m^2/g) vs rGO (449 m^2/g for commercial rGO or 565 m^2/g for in-house synthesized rGO), higher surface areas of up to 1850 m^2/g have been reported for rGO after deaggregation in dispersion via methylene blue adsorption.[311] Furthermore, the surface area of KB particles stems largely from internal pores that might be blocked upon initial sulfur deposition. Thus, the presence of homogeneous nucleation in KB samples may stem from differences in the accessible surface area in dispersion. Additionally, both the higher degree of sp^2-hybridized graphene-like (i.e., carbon atoms in hexagonal arrangement) surface and sheet-like morphology of rGO may play a role in promoting sulfur crystallization over the more amorphous, spherically-shaped KB. Nonetheless, while some homogeneous nucleation is observed in KB/S composites, the deposition of the sulfur onto the KB surface from the hydrophobic sulfur sol still

occurs, indicating the possible generalization of this approach to prepare carbon/sulfur composites from a variety of carbon materials, such as carbon nanotubes, nanofibers, or glassy/amorphous carbons.

6.3.3 Fabrication and Testing of Li-S Battery Cathode

Following the sulfur deposition, flocculation, filtration, and drying of the rGO/S composites, the powders were directly used to prepare cathodes for electrochemical characterization. **Figure 6.8a)** shows the voltage profiles for charge and discharge of a full cell with a rGO/S cathode. The cell achieves capacities as high as 1242 mAh/g_{sulfur} (~4.8 mAh/cm^2) for the first cycle and 1211 mAh/g_{sulfur} for the second cycle at 0.1C, 1112 mAh/g_{sulfur} at 0.2C, 1024 mAh/g_{sulfur} at 0.4C, 736 mAh/g_{sulfur} at 0.8C, 543 mAh/g_{sulfur} at 1C (6.5 mA/cm^2), and 74 mAh/g_{sulfur} at 2C. The first cycle coulombic efficiency is 93%. In **Figure 6.8b)**, the electrochemical performance was compared to a cathode prepared through a traditional melt imbibition approach (labelled rGO/S/MI), in which rGO and sulfur were mixed together, combined in an autoclave under argon, and heated to 160 °C for 12 hours. At all C rates, the discharge capacity of the rGO/DMSO/S cells is higher than the rGO/S/MI cells, particularly at higher C rates, despite the fact that the sulfur loading of the rGO/DMSO/S cell is higher than the rGO/S/MI cell, with loadings of 3.90 mg/cm^2 and 3.42 mg/cm^2 respectively. At 0.8C and 1C, the rGO/DMSO/S cell exhibits a discharge capacity of 635 mAh/g_{sulfur} and 472 mAh/g_{sulfur} higher than the rGO/S/MI cell at the same C rate.

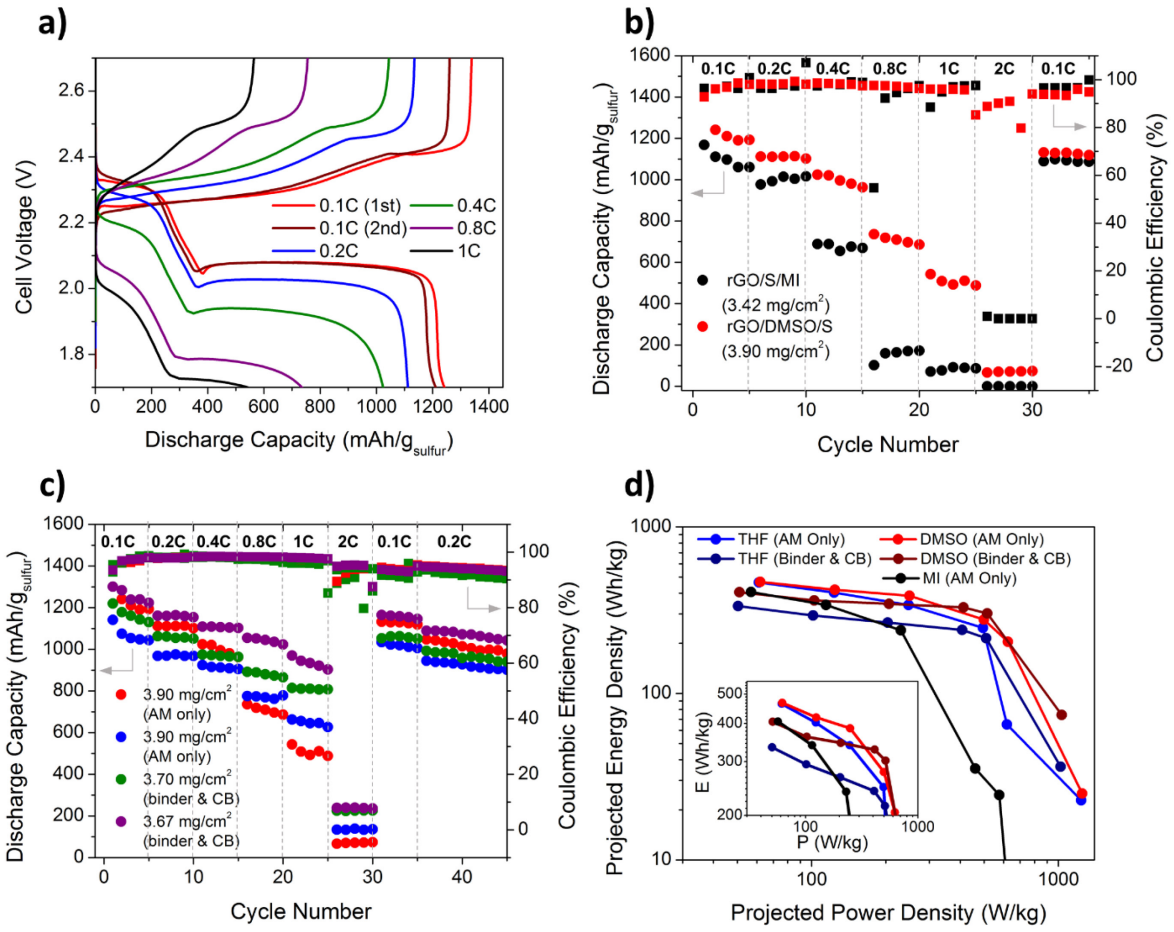

Figure 6.8: Electrochemical characterization of rGO/S cathodes. a) Charge and discharge profiles of lithium-sulfur coin cell with 45% rGO, 55% sulfur cathode with no added binder or conductive material, with a sulfur loading of 3.90 mg/cm^2 at varying C rates. b) Discharge capacity and coulombic efficiency with cycling of rGO/S/MI (sulfur loading of 3.42 mg/cm^2) and rGO/DMSO/S (sulfur loading of 3.90 mg/cm^2). c) Discharge capacity and coulombic efficiency with cycling of two different rGO/DMSO/S cells with loadings of 3.90 mg/cm^2 and two rGO/DMSO/S cells with added PVDF binder and carbon black, with loadings of 3.70 mg/cm^2 and 3.67 mg/cm^2. d) Ragone plot of projected practical energy density vs. power density for cells prepared via heterogeneous nucleation method from THF-based sols (with and without binder/carbon black) and DMSO-based sols (with and without binder/carbon black) and cells prepared via conventional melt imbibition approach.

We also investigated the addition of a binder and further conductive additive into the sulfur cathode, as is traditionally done in sulfur cathode fabrication. We prepared cells using the same rGO/DMSO/S active material, with added PVDF binder and carbon black (CB), in a 70:10:20 ratio. The performance of two of these cells, with sulfur loadings of 3.70 mg/cm^2 and 3.67 mg/cm^2 is shown in **Figure 6.8c)**, and is compared to two different rGO/DMSO/S cells with no added binder or carbon black, both with

sulfur loadings of 3.90 mg/cm^2. Cells with binder and CB possess similar or slightly higher initial capacities of 1219 mAh/g_{sulfur} to 1300 mAh/g_{sulfur} at 0.1C (~4.8 mAh/cm^2), and higher capacities of 894 mAh/g_{sulfur} to 1094 mAh/g_{sulfur} at higher rates of 1C (~6.1 mA/cm^2). These results demonstrate the promise of this approach, as well as the repeatability, with multiple cells of different sulfur loadings exhibiting high discharge capacities at a range of C rates.

rGO/THF/S cells exhibit similar initial discharge capacities at low C rates (**Fig. D22**), but lower capacities at higher discharge rates of 1C and 2C. This result may seem counterintuitive, as the nucleation and growth process in THF occurs more quickly, consuming more of the sol particles. However, the rapidity of the nucleation and growth process may lead to the formation of larger or thicker sulfur crystals, as observed via OM images, while the slower DMSO process may result in more uniform or thinner coatings. In the case of THF, the larger sulfur particles likely have a detrimental effect on Li ion and electron transport in the cathode. This is supported by EIS analysis (**Fig. D23**), in which THF-based samples exhibit increased charge transfer resistances, and significant variability among different samples.

Cells were also prepared from the KB/S (45% KB, 55% S, THF-based sol) composite material (**Fig. D24**) with no added binder or conductive additive, and exhibit initial discharge capacities of 1056 mAh/g_{sulfur} at 0.1C for a cell with a sulfur loading of 3.51 mg/cm^2, indicating the possible generalization of this strategy for the preparation of sulfur cathodes from a variety of carbon materials. However, KB/S cells prepared from this approach demonstrate lower capacities than KB/S cells prepared via melt imbibition. This is congruent with the SEM images, which indicate that, while some sulfur is nucleated and coats the KB surface, a large number of homogeneously nucleated bipyramidal sulfur crystals are also present. This suggests that the sulfur does not coat the full surface area of the KB material due to blockage of the internal pore structure, and thus this method is more suitable for materials such as rGO or CNTs, where the high specific surface area is fully accessible for sulfur deposition.

Long term cycling of rGO/DMSO/S cells with and without binder at 0.5C can be seen in **Figure D25**, along with melt-imbibed rGO/S cells for comparison. All cells demonstrate very limited cycle life, with significant capacity fading, and loss of nearly all capacity within 100 cycles. This is to be expected, since this work has focused on the scalable fabrication of rGO/S composites with nano-scaled sulfur coatings, and we did not address polysulfide shuttling leading to active material loss on the cathode side or SEI growth and degradation of lithium on the anode side. While optimization of the

long term cycle life of these cells is beyond the scope of this work, we demonstrate that the addition of a polysulfide retention agent in the cathode, polyethylenimine (PEI), leads to a dramatic improvement in capacity retention within the first 100 cycles, with cells containing 10% PEI exhibiting 82.2% capacity retention after 100 cycles. Cycle life testing was not continued beyond this point. Studies have previously shown that PEI interacts with any residual functional groups on rGO and crosslinks the sheets, while additionally interacting with polysulfides via its amine groups, limiting polysulfide diffusion out of the cathode.[214] While this is still an unoptimized system, it demonstrates that with the inclusion of polysulfide-retention additives in the cathode, this system has the potential to demonstrate both high initial capacities and good long term cycle life. It should further be noted that we did not address the challenges of the lithium anode in this system, which is also critical for long term cycle life. Several studies have demonstrated that optimization of the lithium anode, whether via SEI design,[312] use of a protective layer,[146,148] or use of a three-dimensional lithium host,[313] results in significant improvement in lithium-sulfur cycle life, making this critical for future work.

The projected practical energy density (*E*) of all cells, considering all inactive cell components, was also calculated using a correction factor approach suggested by Pope et al.[3] and detailed in Appendix D. We performed the energy density calculation under three different scenarios to demonstrate the effect of different assumptions on the calculated values – 1) assuming 5% stoichiometric excess of lithium, 2) assuming excess lithium with a commercially available foil with constant thickness of 125 μm, and 3) again assuming a 125 μm lithium foil and taking into account the use of excess electrolyte, which is necessary in practical cells both to wet all cell components and to compensate for the formation and growth of the SEI layer on the unoptimized lithium anode. Using the first calculation method, cathodes without any added binder or carbon black achieve energy densities as high as 530 – 540 Wh/kg at 0.1C (**Tables D1-D8**), representing the absolute maximum energy density achievable with these cathodes when paired with a perfect lithium anode. In the second calculation method, assuming excess lithium via a commercially available lithium metal foil,[3,129,214] a more practical estimate of the energy density is obtained (**Tables D9-D14**). Cells without binder or carbon black are capable of achieving practical energy densities as high as 468 Wh/kg at 0.1C, and 250 Wh/kg at 1C. The practical energy densities for two different rGO/DMSO/S cells prepared with PVDF binder and CB were also calculated and are tabulated in **Table D14**. These cells exhibit energy densities of as high as 405 Wh/kg at 0.1C, but slightly improved energy densities of as high as 302 Wh/kg at 1C. It should further be noted that no additives are present in these cells to address polysulfide dissolution or shuttling, and as such, some

capacity fade may occur during rate testing and cycling, meaning that higher capacities and energy densities may be possible with these additions.

Finally, in the third calculation method, we also calculated the energy density of our cells when taking into account the large excess of electrolyte used in our testing (90 μL per cell). When considering this excess electrolyte, the energy density of the full cells without binder or carbon black drops by over 50% to 217 Wh/kg at 0.1C (**Tables D15-D20**), demonstrating the detrimental effect of excess electrolyte on energy density. A summary of the energy densities calculated using all three methods is presented in **Tables D21** and **D22**. While excess electrolyte is necessary to wet all cell components, it is also critical in order to compensate for the degradation and failure of the lithium anode during cycling. While optimization of the anode was not the focus of this chapter, other studies have demonstrated that protection and stabilization of the anode enables the use of much leaner electrolyte conditions, highlighting the importance of anode optimization in future work.[314–316] These studies demonstrate that lean electrolyte conditions are possible with further anode optimization, but the use of extremely thin lithium foils remains technically challenging. Thus, for comparison of the performance of the sulfur cathodes prepared in this work, we have used energy densities calculated using the second calculation method, taking into account excess lithium but not excess electrolyte, to provide a realistic estimate of the cathode performance when paired with an optimized lithium anode.

To fully compare the electrochemical results from the different approaches, a Ragone plot was prepared using the practical energy density and power density for each synthesis method (using the second calculation method) and can be seen in **Figure 6.8d)**. The DMSO-based cells with no added binder or carbon black demonstrate the highest energy densities at all rates, but THF-based cells with no added binder or carbon black achieve similar values at low rates (0.1 and 0.2C). DMSO-based cells with binder and carbon black demonstrate slightly lower energy densities at low rates, but improved performance at high rates (1C). Notably, when comparing cells with no added binder or carbon black, both THF and DMSO-based cells prepared from the heterogeneous nucleation method outperform conventional melt-imbibed cells in terms of both energy density and power density at all rates, indicating that the heterogeneous nucleation approach enables excellent sulfur distribution in a simple, scalable, inexpensive, and room-temperature solution-based approach.

6.4 Conclusion

Via optical microscopy, SEM, and DLS studies, we have thoroughly investigated the interaction of carbonaceous materials with hydrophobic sulfur sols, which have been broadly overlooked in comparison to their hydrophilic counterparts for the fabrication of high performance sulfur cathodes. In both model studies on highly ordered pyrolytic graphite and on various dispersed carbonaceous nanomaterials, we find that hydrophobic sulfur sols form and sulfur is redistributed via an Ostwald ripening type mechanism to uniformly coat the surface of the carbon material. Our approach works with multiple surfactants, organic solvents and different carbon materials, such as rGO and KB, indicating the universality of this method for the fabrication of sulfur/carbon composites. Moreover, we use solution-based processing to enable coating of a higher accessible surface area of dispersed carbon materials when compared to their aggregated solid powders used in most other fabrication routes, all under room-temperature conditions. Solution-based processing can introduce challenges in that the solvent used in the process exists as waste following electrode fabrication, and all current approaches that use elemental sulfur rather than hydrophilic sulfur sols to prepare carbon/sulfur composites employ large volumes of toxic organic solvents. However, the solvent in this process is ~90% water, making it a greener alternative while still coating the full accessible surface area of rGO in solution. Furthermore, it can be completed in a simple 2 hour process, compared to lengthy (>12 hour) high temperature melt imbibition approaches, and uses inexpensive, widely available elemental sulfur, unlike processes based on hydrophilic sulfur sols which typically require the use of precursors. Our synthesis and processing yields cathodes with capacities as high as 1300 mAh/g_{sulfur} (~4.8 mAh/cm^2) at 0.1C and discharge capacities that are a factor of 7 times higher than melt imbibed cells at 0.8C and 1C. Furthermore, cells without any added binder or conductive material demonstrate impressive energy densities of 468 Wh/kg at 0.1C, and 250 Wh/kg at 1C, without any added polysulfide trapping agents. As such, we believe the deposition of hydrophobic sulfur sols onto carbon-based materials is a promising route for rapid, scalable processing of sulfur cathodes, providing a key step towards the commercialization of Li-S technology.

Chapter 7:
Conclusions and Future Work

7.1 Conclusion

In this thesis, four distinct projects focusing on the development and fabrication of graphene-based electrodes for electrochemical energy storage devices, including both supercapacitors and next-generation batteries, were presented. In each study, we developed devices with increased capacitance or capacity or contributed to furthering the fundamental understanding of key processes for these devices, such as lithium nucleation.

In Chapter 3, we investigated the use of PFA as a sustainable, biomass-derived resin for the formation of LIG for the first time. We demonstrated that pristine PFA could not easily be carbonized via laser irradiation, but highly conductive traces of LIG could be formed via the introduction of 1% GO as a carbonization aid. We also demonstrated the formation of composites of PFA microspheres and GO and their subsequent conversion into LIG. We showed that the PFA microspheres are converted into LIG and act as spacers between the laser-reduced graphene sheets, resulting in supercapacitors that exhibited a capacitance of 16.0 mF/cm^2 at 0.05 mA/cm^2. These devices outperform nearly all reported PI-based LIG and GO-based LRG to date, while demonstrating a stable cycle life, with 97.4% capacitance retention after 10,000 cycles.

In Chapter 4, we investigated the addition of inexpensive, abundant sodium salt microparticles, NaCl and Na_2SO_4, into PFA resin precursors, and demonstrated that LIG formed from these composites possesses BET surface areas that are an order of magnitude larger than LIG from pristine PFA, as the salt particles act as a template for pore formation. Furthermore, LIG formed from PFA/salt composites is simultaneously doped with heteroatoms from the salt of choice – forming Cl-doped LIG from NaCl and S-doped LIG from Na_2SO_4, which can contribute to increasing the quantum capacitance of the LIG. We further demonstrated via thermal modeling that the inclusion of salt particles may lead to increased laser penetration depths and thicker layers of LIG, and that salt particles may also act as carbonization aids, improving the carbon yield during lasing. After fully investigating the mechanism behind the changes in the LIG properties with the inclusion of salt, we demonstrated that the multifunctional nature of the salt additives results in capacitances that are 2-4 orders of magnitude higher than that of LIG from pristine PFA, with capacitances of ~25 mF/cm^2 at 0.05 mA/cm^2 for PFA/25% Na_2SO_4, and with

some individual PFA/20% Na_2SO_4 devices exhibiting capacitances as high as 80 mF/cm^2 at 0.05 mA/cm^2. These devices outperform nearly all LIG-based supercapacitors to date. Moreover, due to the wide array of materials that carbonize under laser irradiation but do not result in high surface area, high capacitance LIG, and the abundant and inert nature of the salts employed, this is potentially a simple, scalable approach to improve the performance of LIG from a range of materials.

In Chapter 5, we investigated the use of LIG as a porous, conductive host material for lithium metal anodes. Expanding upon the LIG material developed and characterized in Chapter 4, we demonstrated a further array of salts that can be used to prepare high capacitance LIG, including lithium salts such as Li_2SO_4, and further showed that residual salt could be removed from these electrode materials via dissolution without damaging the LIG structure. We performed a lithium nucleation study on LIG electrodes prepared from PI, PFA, PFA/25% Na_2SO_4, and PFA/10% Li_2SO_4, which each possessed different chemical structures and functional groups, and further investigated the effect of pre-lithiating each LIG structure before lithium plating or not. We related the overpotential-current density behaviour for lithium nucleation to Butler-Volmer kinetics for the first time, and were able to extract charge transfer resistances, exchange current densities, and transfer coefficients via two different fitting methods. We demonstrated that the nucleation process follows Butler-Volmer kinetics, but with high thermodynamic nucleation barriers potentially manifesting as modifications to the theory via either non-zero intercepts or asymmetric ($\alpha \neq 0.5$) behaviour. We demonstrated that unlithiated LIG from PFA/salt composites exhibited the lowest overpotentials for lithium nucleation – particularly at high current densities – and, for the most part, lower charge transfer resistances than LIG from pristine PFA. We evaluated this behaviour in comparison to other parameters such as electrode surface area and loading to confirm that the presence of lithiophilic functional groups is the most critical determining factor in the overpotential behaviour. We studied the cycling behaviour of the different LIG materials, and observed that the more lithiophilic LIG from PFA/salt composites surprisingly resulted in lower coulombic efficiencies, which we hypothesized is due to both increased parasitic reactions on the doped LIG and the more amorphous LIG structure, which is not easily delithiated, thus determining that the optimization of the degree of doping is a key, and thus far overlooked, parameter for lithium host design.

Finally, in Chapter 6, we investigated the heterogeneous nucleation of hydrophobic sulfur sols – which had been thus far widely unexplored for the fabrication of sulfur cathodes – on carbonaceous and graphene-based materials. Via detailed optical microscopy and DLS studies, we demonstrated that

hydrophobic sulfur sols prepared in an aqueous, room-temperature process, deposit on the surface of graphene-based materials in dispersion via an Ostwald ripening mechanism, coating them with a thin, uniform layer of elemental sulfur. This process does not require lengthy, high temperature melting steps or toxic solvents typically utilized to dissolve sulfur, and occurs in dispersion, enabling the full use of the graphene surface area. Moreover, this is the first study to date to employ hydrophobic, aqueous-based sulfur sols to prepare graphene/sulfur composites directly, without the need for any subsequent reduction or melting steps. Sulfur cathodes prepared from this process exhibit high capacities of 1300 mAh/g_{sulfur} (~4.8 mAh/cm^2) at 0.1C, and discharge capacities 7 times higher than melt imbibed cells at 0.8C and 1C. They also possess energy densities of 468 Wh/kg at 0.1C, and 250 Wh/kg at 1C.

The key contributions of this work are as follows:

- Demonstration of PFA as a novel, easily processable, biomass-derived LIG precursor and development of high-capacitance LIG supercapacitors from composites of PFA and GO.
- Development of high-capacitance LIG supercapacitors from PFA resin/salt composites that exhibit a capacitance 2-4 orders of magnitude that of LIG from pristine PFA, via multifunctional salt additives which simultaneously template the LIG to achieve high surface area, dope the LIG with heteroatoms, and increase the thermal diffusivity and carbon yield during lasing.
- Improved understanding of the preparation of lithiophilic lithium host materials via the study of lithium nucleation on doped LIG materials and identifying the degree of doping as a thus far unknown but critical parameter for host design.
- Increased fundamental understanding of hydrophobic sulfur sols and their subsequent nucleation on different carbon nanomaterials, and the development of a scalable, aqueous-based process to prepare high energy density graphene-based sulfur cathodes from hydrophobic sulfur sols.

7.2 Future Work

7.2.1 LIG Supercapacitors

7.2.1.1 Increasing the Energy Density of LIG Supercapacitors

Implementation of Smaller Salt Particles for Increased Capacitance

In Chapter 4, we demonstrated that the inclusion of microparticles of sodium salts in the PFA prior to lasing resulted in a templating effect, boosting the surface area and capacitance of the resulting LIG. The salt particles used were micron-sized in scale, as this is the size recoverable via spray-drying. However, we expect that using even smaller salt particles would further increase the surface area and capacitance of the resulting LIG. Sodium chloride nanoparticles have recently been synthesized using a microemulsion reaction for cancer therapeutics.[317] If scalable quantities of salt nanoparticles can be prepared in this method, this could be one strategy to further boost the capacitance, and thereby the energy density, of LIG from PFA/salt composites.

Transition to Electrolytes with Wider Voltage Window

The focus of Chapters 3 and 4 was on improving the areal capacitance of LIG-based electrodes, and as such, all testing was performed with the most commonly employed electrolyte for LIG supercapacitors – a gel-based electrolyte consisting of PVA and H_3PO_4. While this gel-based system is most practical for LIG devices as it is flexible and does not require the leakproof packaging that a liquid electrolyte would, its aqueous nature limits its potential window to ~1.2 V. While we did not directly calculate the energy density of our devices in this work, the square dependence of the energy density on voltage indicates that this limited voltage window of the electrolyte is a critical factor for improving the energy density. Thus, a focus on developing gel-based electrolyte from organic (~2.7 V) or ionic liquid-based (3.5 – 4 V) systems with increased voltage windows is critical for the future of LIG-based supercapacitors.

Densifying LIG

One of the remaining challenges limiting the energy density of LIG-based supercapacitors is the relatively low loading of LIG formed after irradiation. The loading of nearly all LIG is <1 mg/cm^2, with many reports of <0.5 mg/cm^2. These low loadings and the low density (<0.06 g/cm^3) of LIG limit both the areal and volumetric capacitances, but also F_m, and thus the achievable energy density of LIG-based

supercapacitors. Kim et al. demonstrated that one way to overcome this is by applying a second coating of LIG precursor onto the formed LIG, and laser scribing a second time, to form a densified LIG.[318] This strategy has only been demonstrated with PI, but this should be investigated with our PFA system to enable further increases in areal and volumetric capacitance and energy density.

Pseudocapacitive Materials

While the focus of this thesis was on employing LIG directly as an EDLC-type supercapacitor, further improvements to the energy density are possible by incorporating pseudocapacitive materials, such as transition metal oxides. These materials can provide higher capacitance and fill some of the void space in the LIG, leading to higher loadings and increasing energy density. While a number of different pseudocapacitive materials have been implemented into LIG,[319–321] including high loadings (10 mg/cm^2) of ZnP nanosheets, which enabled extremely high areal capacitances of 4.9 F/cm^2,[321] all work thus far used GO or PI-based LIG. The higher conductivity of PFA-based LIG, as demonstrated via our sheet resistance results, indicates that it may be a more promising scaffold for pseudocapacitive materials and enable higher power densities than PI-based LIG/pseudocapacitive composites.

7.2.1.2 Improving Flexibility

In Chapter 3, we demonstrated the formation of LIG supercapacitors from μPFA/GO composites, which possessed limited mechanical properties – only relatively thin films could be prepared without cracking and the films were fairly brittle. Transitioning to the use of PFA resin in Chapter 4 enabled the formation of thicker and more mechanically robust films. However, the addition of large quantities of salt (i.e. 25% Na_2SO_4) made the films more brittle. In order to improve the flexibility of the LIG devices, a few different strategies can be employed. Firstly, since the flexibility of PFA depends on cure time, shorter cure times could be investigated to form LIG on a more flexible PFA substrate. Moreover, the salt templating and doping approach is potentially generalizable to a range of different polymers and precursors that can be carbonized but do not result in high performance LIG. This strategy should be investigated with more elastomeric precursors, or composites of PFA with elastomeric precursors.

7.2.1.3 Combination of LIG Method with Other Advanced Manufacturing Methods

The thickness of LIG-based electrodes that can be fabricated is currently limited as the LIG thickness is ultimately controlled by the penetration depth of the laser into the substrate, which is typically 25 – 350 μm. Moreover, thicknesses beyond ~50 μm are rare, and typically limited to the formation of LIG

fibers, which exhibit much lower conductivities than typical LIG.[322] One strategy to overcome the electrode thickness limitations of the LIG method is to combine it with other advanced manufacturing techniques, such as additive manufacturing. Luong et al. demonstrated that LIG electrodes of mm – cm thickness could be prepared via laminated objected manufacturing of multiple layers of LIG, and fiber lasers could be used to selectively mill these 3D structures for further architectural control.[323] While this work is an initial proof-of-concept, and automation of this process is needed for further scalability, this is one step towards increased LIG thicknesses and complete 3D electrode design. Another strategy to implement further control over the LIG process and improve scalability is the use of multiple laser heads to pattern simultaneously – a concept that has been implemented via the use of multiple print heads in additive manufacturing.[324,325]

7.2.1.4 Increasing the Throughput of the LIG Method

While the LIG process is uniquely suited for the patterning of novel electrode architectures, the laser-based method has some key limitations. Firstly, as discussed several times throughout this thesis, the LIG material formed is non-uniform due to the thermal gradient during lasing and so the properties of the LIG formed at the center of the laser trace can be very different than those of the LIG at the edge. Secondly, since each rastered laser trace is ~100 μm thick, long processing times would be required to prepare large electrode areas using the laser speeds employed in this work (i.e. 10 mm/s). One strategy to overcome both of these issues is to modify the laser optics to produce a line beam instead,[326] which can convert larger areas of precursor at once and result in more uniform graphenization. While this approach cannot be used to pattern high-resolution structures, it may be more suitable for the scalable production of bulk LIG material.

7.2.2 Lithium-Sulfur Batteries

7.2.2.1 Improving the Cycle Life of LIG Lithium Hosts

Investigation of Intermediate Salt Loadings for Preparation of LIG Lithium Host

The nucleation study carried out in Chapter 5 demonstrated that doping of LIG with lithiophilic functional groups enables lower overpotentials and charge transfer resistances for lithium nucleation, which are critical for the design of a lithiophilic lithium host. However, it also demonstrated that high levels of doping, while increasing lithiophilicity, can also limit the coulombic efficiency and cycle life due to side reactions and the formation of more amorphous carbons that are not easily delithiated. This highlighted that a key factor governing the design of lithium host structures is the degree of doping, which has been thus far overlooked. As we investigated the highest capacitance LIG from PFA/Na_2SO_4 and PFA/Li_2SO_4, we naturally studied the most highly doped materials. However, examining the lithium nucleation on LIG from lower salt content (for example, PFA/10% Na_2SO_4), which would yield a less amorphous carbon and a lower degree of doping, is one strategy to fabricate a LIG host that is still lithiophilic but also possesses longer cycle life.

Investigation of Other LIG Doping Strategies

In our lithium nucleation study, we examined doped LIG prepared from PFA/salt composites. While these LIG materials possessed several lithiophilic functional groups, the dopants that resulted in the most lithiophilic materials in theoretical studies to date are boron and phosphorus. We found that B- and P-containing lithium salts were either incompatible with PFA processing or extended the processing and cure times significantly, and so B- and P-doped LIG could not be assessed. However, strategies have been developed to prepare B- and P-doped LIG from PI, via the incorporation of H_3BO_3 or H_3PO_4 into PI precursors, for high-performance supercapacitors.[94,327] These are promising materials for further study as lithium hosts. We performed initial experiments on the preparation of B-doped LIG from PI, but faced significant challenges with film processing and cracking, which must be overcome in order to prepare these materials for further study.

Investigation of Impact of Different LIG Architectures for Lithium Host

Our nucleation study was conducted on LIG materials that were scraped off of the substrate, slurry-cast with binder onto copper, and finally pressed to prepare electrodes with comparable loadings and surface areas, in order to deconvolute the effects of different parameters on the overpotential results. However,

Yi et al. demonstrated that the LIG architecture plays a role in the plating overpotential, as the unique design of LIG-coated PI pillars on a copper substrate exhibited lower overpotentials and significantly improved cycle life over a conventional LIG film prepared from the same materials.[168] One of the unique advantages of the LIG approach is the ability to pattern novel electrode architectures. Further investigation into the design of 3D LIG architectures for lithium deposition is necessary to optimize SEI formation and void space for lithium deposition for future LIG-based lithium anodes.

Development of Bilayer Host Architecture

Our findings in Chapter 5 demonstrated the ability to tune the lithiophilicity and thus lithium nucleation overpotential of different LIG materials via doping. However, the cycle life of the LIG materials was limited. One strategy to overcome this could be through the development of a bilayer host, with a lithiophilic layer just above the current collector and a lithiophobic layer on top. Bilayer structures such as these have been previously demonstrated and enable selective lithium deposition deeper within the host structure, preventing plating from being limited to the top surface of the porous host material.[177] This could be achieved via the same method discussed above for densifying the LIG, by preparing LIG from PFA/salt, and then casting a second layer of pure PFA and lasing this layer, to form a lithiophobic-lithiophilic bilayer structure which could enable improved performance.

Development of Sealed Host Architecture

As discussed in Chapter 5, while the LIG materials developed in this work are lithiophilic in nature and result in a more areally stable SEI layer (with less irreversible capacity per area), the open nature of the LIG structure still results in significant SEI formation and the volume change during cycling still leads to breakage of the SEI layer. One of the only possibilities to mitigate this is to develop host structures that are sealed from the electrolyte. Developing these host materials is extremely challenging – they need to be leakproof to prevent liquid electrolyte from entering them and causing SEI formation and must be electronically conductive but simultaneously must facilitate lithium nucleation within the host, not on the surface. This requires the inside of the host to be lithiophilic, while the outside should be lithiophobic and enable rapid lithium diffusion into the internal structure. Studies such as ours in Chapter 5 can assist in making progress towards this design by identifying how to design lithiophilic and lithiophobic materials for this purpose, but further studies on how to fabricate these structures and fundamental studies on lithium diffusivity through outer host materials are needed.

7.2.2.2 Improving the Capacity and Cycle Life of Graphene/Sulfur Cathodes

Investigation of Higher Sulfur Content Cathodes

In Chapter 6, we demonstrated the formation of rGO/S cathodes, with a relatively high sulfur loading of 3.9 mg/cm^2 and a ratio of 45:55 of rGO:S. While high energy densities were achieved without the addition of binder or other conductive materials (468 Wh/kg at 0.1C), we did not investigate higher ratios of sulfur to rGO, which would enable a push to higher energy densities. Furthermore, for samples with added binder and conductive additive, this lowers the sulfur content to only 38.5% of the cathode. Moreover, inclusion of any further additives to suppress polysulfide shuttling will reduce sulfur content in the cathode, thus requiring a push to even higher sulfur content. Increasing the sulfur content leads to decreased electrical conductivity and lower capacities, and requires further optimization and engineering of the rGO/S composite formation.

Investigation of the Use of Exfoliated Graphite

In our development of graphene/sulfur composites for sulfur cathodes, we employed thermally reduced rGO, which was available in large quantities and was highly reduced, with a very high C/O ratio for thermally reduced rGO of 63, a carbon content of ≥95 wt.%, oxygen content of ≤2.00 wt.%, hydrogen content of ≤2.00 wt.%, nitrogen content of ≤0.50 wt.%. Throughout our study, we observed that the nucleation of sulfur onto carbon nanomaterials from hydrophobic sulfur sols is dependent on the hydrophobic interactions between the sulfur and graphene, and that sulfur is more likely to deposit on a pure carbon surface than one with oxygen-containing functional groups. For example, it will not deposit at all on GO. While the thermally reduced rGO used in this work has a high C/O ratio, any increase in this C/O ratio could be expected to enable the deposition of sulfur from hydrophobic sulfur sols to occur more rapidly and uniformly, with no remaining sol particles or aggregates. Moreover, graphene with increased conductivity could also facilitate the fabrication of higher sulfur content and loading cathodes with improved performance. Likewise, the current capacity of the sulfur cathodes at high rates is limited (74 mAh/g_{sulfur} at 2C), so increases in the conductivity of the carbon host could further improve this as well. One strategy to investigate would be the direct exfoliation of graphite, without the intermediate formation of graphene oxide. While most exfoliation strategies still introduce some degree of defects, including oxygen-containing defects, and the scalability of these methods requires improvement, the quality of the graphene prepared from these methods is typically more pristine, and may possess lower oxygen content.[328]

Investigation of Further Materials to Prevent Polysulfide Shuttling

The focus of Chapter 6 was the improved fabrication of rGO/S composites for sulfur cathodes. We did not focus in this work on the other main challenge facing sulfur cathodes – the dissolution of intermediate polysulfide species which can move out of the cathode and irreversibly deposit on the lithium anode, limiting the cycle life. We did demonstrate that without addressing polysulfide shuttling, the cycle life of the rGO/S cathodes is limited, and that by adding PEI into the sulfur cathode, which can bind to polysulfides via polar interactions and prevent them from leaving the cathode, the cycle life is significantly improved. However, polysulfide shuttling remains a significant challenge that has not been fully solved. Improved binders that can trap polysulfides in the sulfur cathode are needed. One relatively unexplored method of trapping polysulfides is via ionic interactions, which are typically much stronger than polar interactions or hydrogen bonding. The use of cationic polymeric binders in the sulfur cathode has been investigated,[329,330] but their limited commercial availability has prevented widespread study. Wang et al. demonstrated that cationic quaternary ammonium groups could be formed on PEI via a one-step reaction, and that these groups have polysulfide binding energies twice that of unmodified PEI.[331] Consequently, modification of binders with cationic groups is one promising direction to further address polysulfide shuttling.

7.2.2.3 Investigation of Full LiS Cell Performance

Most literature on lithium-sulfur batteries to date has focused on improving the performance of either the lithium anode or sulfur cathode alone. Indeed, in this thesis we focused separately on the lithium anode in Chapter 5 and sulfur cathode in Chapter 6. However, future work must also study the performance of full LiS cells. This is particularly critical when using a host material for lithium metal, as either this host or the sulfur cathode must be pre-lithiated before full cell assembly. Preliminary unpublished work in our group demonstrated that the rGO/S cathodes prepared in Chapter 6 can be lithiated to form Li_2S via reaction with n-butyllithium. However, further study is required in order to prepare full cells with either Li_2S cathodes or pre-lithiated host anodes.

7.2.2.4 Application of Doped LIG into Other Next-Generation Batteries

Finally, while we have focused in this thesis on the application of graphene-based electrodes into supercapacitors and lithium-sulfur batteries, this work has potential applications beyond these devices and chemistries. Notably, in our LIG work, we demonstrate a strategy to prepare high surface area,

heteroatom-doped LIG from sustainable precursors. LIG has particularly been studied as a conductive, porous scaffold for air cathodes. It has almost always been implemented with specific transition metal oxide catalysts for the ORR/OER reactions,[99–101] except for one study that demonstrated that LIG that had been oxidized via O_2 plasma is also a suitable catalyst for air cathodes.[98] Our salt-induced doping provides a potentially simpler and more widely tunable approach to introduce dopants into LIG, and demonstrated improved kinetics over LIG from pristine PFA in Chapter 5. Thus, the salt-induced templating and doping of LIG studied here may also be a key strategy for the development of electrodes for other next-generation batteries, such as metal-air batteries.

References

(1) IPCC. *Synthesis Report of the IPCC Sixth Assessment Report*; 2023.

(2) Environment and Climate Change Canada. *A Healthy Environment and a Healthy Economy: Canada's Strengthened Climate Plan to Create Jobs and Support People, Communities and the Planet*; 2020.

(3) Pope, M. A.; Aksay, I. A. Structural Design of Cathodes for Li-S Batteries. *Adv. Energy Mater.* **2015**, *5* (16), 1500124.

(4) Lin, Z.; Liang, C. Lithium-Sulfur Batteries: From Liquid to Solid Cells. *J. Mater. Chem. A* **2015**, *3* (3), 936–958.

(5) Choi, N. S.; Chen, Z.; Freunberger, S. A.; Ji, X.; Sun, Y. K.; Amine, K.; Yushin, G.; Nazar, L. F.; Cho, J.; Bruce, P. G. Challenges Facing Lithium Batteries and Electrical Double-Layer Capacitors. *Angew. Chemie - Int. Ed.* **2012**, *51* (40), 9994–10024.

(6) Cleaver, T.; Kovacik, P.; Marinescu, M.; Zhang, T.; Offer, G. Commercializing Lithium Sulfur Batteries: Are We Doing the Right Research? *J. Electrochem. Soc.* **2018**, *165* (1), A6029–A6033.

(7) Lin, D.; Liu, Y.; Cui, Y. Reviving the Lithium Metal Anode for High-Energy Batteries. *Nat. Nanotechnol.* **2017**, *12* (3), 194–206.

(8) Yu, M.; Li, R.; Wu, M.; Shi, G. Graphene Materials for Lithium–Sulfur Batteries. *Energy Storage Mater.* **2015**, *1*, 51–73.

(9) Borchardt, L.; Oschatz, M.; Kaskel, S. Carbon Materials for Lithium Sulfur Batteries—Ten Critical Questions. *Chem. – A Eur. J.* **2016**, *22* (22), 7324–7351.

(10) Liu, Z.; Bertolini, S.; Balbuena, P. B.; Mukherjee, P. P. Li_2S Film Formation on Lithium Anode Surface of Li − S Batteries. *ACS Appl. Mater. Interfaces* **2016**, *8*, 4700–4708.

(11) Zhang, L. L.; Zhao, X. S. Carbon-Based Materials as Supercapacitor Electrodes. *Chem. Soc. Rev.* **2009**, *38* (9), 2520.

(12) Raza, W.; Ali, F.; Raza, N.; Luo, Y.; Kim, K.-H.; Yang, J.; Kumar, S.; Mehmood, A.; Kwon, E. E. Recent Advancements in Supercapacitor Technology. *Nano Energy* **2018**, *52*, 441–473.

(13) Poonam; Sharma, K.; Arora, A.; Tripathi, S. K. Review of Supercapacitors: Materials and Devices. *J. Energy Storage* **2019**, *21*, 801–825.

(14) Novoselov, K. S.; Geim, A. K.; Morozov, S. V.; Jiang, D.; Zhang, Y.; Dubonos, S. V.; Grigorieva, I. V.; Firsov, A. A. Electric Field Effect in Atomically Thin Carbon Films. *Science.* **2004**, *306* (5696), 666–669.

(15) Novoselov, K. S.; Jiang, D.; Schedin, F.; Booth, T. J.; Khotkevich, V. V.; Morozov, S. V.; Geim, A. K. Two-Dimensional Atomic Crystals. *Proc. Natl. Acad. Sci.* **2005**, *102* (30), 10451–10453.

(16) Chabot, V.; Higgins, D.; Yu, A.; Xiao, X.; Chen, Z.; Zhang, J. A Review of Graphene and Graphene Oxide Sponge: Material Synthesis and Applications to Energy and the Environment. *Energy Environ. Sci.* **2014**, *7* (5), 1564.

(17) Yi, M.; Shen, Z. A Review on Mechanical Exfoliation for the Scalable Production of Graphene. *J. Mater. Chem. A* **2015**, *3* (22), 11700–11715.

(18) Zhang, Y.; Zhang, L.; Zhou, C. Review of Chemical Vapor Deposition of Graphene and Related Applications. *Acc. Chem. Res.* **2013**, *46* (10), 2329–2339.

(19) Marcano, D. C.; Kosynkin, D. V; Berlin, J. M.; Sinitskii, A.; Sun, Z.; Slesarev, A.; Alemany, L. B.; Lu, W.; Tour, J. M. Improved Synthesis of Graphene Oxide. *ACS Nano* **2010**, *4* (8), 4806–4814.

(20) Liu, Y.; Zhang, R.; Wang, J.; Wang, Y. Current and Future Lithium-Ion Battery Manufacturing. *iScience* **2021**, *24* (4), 102332.

(21) Liu, N.; Gao, Y. Recent Progress in Micro-Supercapacitors with In-Plane Interdigital Electrode Architecture. *Small* **2017**, *13* (45), 1701989.

(22) Chen, R.; Chen, Y.; Xu, L.; Cheng, Y.; Zhou, X.; Cai, Y.; Mai, L. 3D-Printed Interdigital Electrodes for Electrochemical Energy Storage Devices. *J. Mater. Res.* **2021**, *36* (22), 4489–4507.

(23) Hawes, G. F.; Rehman, S.; Rangom, Y.; Pope, M. A. Advanced Manufacturing Approaches for Electrochemical Energy Storage Devices. *Int. Mater. Rev.* **2022**, *68* (3), 323-364.

(24) Lin, J.; Peng, Z.; Liu, Y.; Ruiz-Zepeda, F.; Ye, R.; Samuel, E. L. G.; Yacaman, M. J.;

Yakobson, B. I.; Tour, J. M. Laser-Induced Porous Graphene Films from Commercial Polymers. *Nat. Commun.* **2014**, *5* (1), 5714.

(25) Wang, H.; Pilon, L. Accurate Simulations of Electric Double Layer Capacitance of Ultramicroelectrodes. *J. Phys. Chem. C* **2011**, *115* (33), 16711–16719.

(26) Booth, F. Dielectric Constant of Polar Liquids at High Field Strengths. *J. Chem. Phys.* **1955**, *23* (3), 453–457.

(27) Aguirre, J. C.; Ferreira, A.; Ding, H.; Jenekhe, S. A.; Kopidakis, N.; Asta, M.; Pilon, L.; Rubin, Y.; Tolbert, S. H.; Schwartz, B. J.; Dunn, B.; Ozolins, V. Panoramic View of Electrochemical Pseudocapacitor and Organic Solar Cell Research in Molecularly Engineered Energy Materials (MEEM). *J. Phys. Chem. C* **2014**, *118* (34), 19505–19523.

(28) Chen, R.; Yu, M.; Sahu, R. P.; Puri, I. K.; Zhitomirsky, I. The Development of Pseudocapacitor Electrodes and Devices with High Active Mass Loading. *Adv. Energy Mater.* **2020**, *10* (20), 1903848.

(29) Linden, D.; Reddy, T. B. *Handbook of Batteries*, 3rd ed.; McGraw-Hill: New York, 2002.

(30) Bard, A. J.; Faulkner, L. R. *Electrochemical Methods: Fundamentals and Applications*, 2nd ed.; John Wiley & Sons, Inc.: New York, 2001.

(31) Goodenough, J. B.; Park, K. S. The Li-Ion Rechargeable Battery: A Perspective. *J. Am. Chem. Soc.* **2013**, *135* (4), 1167–1176.

(32) Lain, M. J.; Brandon, J.; Kendrick, E. Design Strategies for High Power vs. High Energy Lithium Ion Cells. *Batteries* **2019**, *5* (4), 64.

(33) Mathis, T. S.; Kurra, N.; Wang, X.; Pinto, D.; Simon, P.; Gogotsi, Y. Energy Storage Data Reporting in Perspective—Guidelines for Interpreting the Performance of Electrochemical Energy Storage Systems. *Adv. Energy Mater.* **2019**, *9* (39), 1902007.

(34) Obreja, V. V. N. Supercapacitors Specialities - Materials Review. *AIP Conf. Proc.* **2014**, *1597* (February 2015), 98–120.

(35) Park, J.-K. J. K. Principles and Applications of Lithium Secondary Batteries. *Princ. Appl. Lithium Second. Batter.* **2012**, 380.

(36) Nishi, Y. The Development of Lithium Ion Secondary Batteries. *Chem. Rec.* **2001**, *1*, 406–

413.

(37) Mizushima, K.; Jones, P. C.; Wiseman, P. J.; Goodenough, J. B.; K. Mizushima, P.Jones, P. W. Li_xCoO_2 (0<x<1): A New Cathode Material for Batteries of High Energy Density. *Mater. Res. Bull.* **1980**, *15*, 783–789.

(38) Brodie, B. C. XIII. On the Atomic Weight of Graphite. *Philos. Trans. R. Soc. London* **1859**, *149* (149), 249–259.

(39) Staudenmaier, L. Verfahren Zur Darstellung Der Graphitsäure. *Berichte der Dtsch. Chem. Gesellschaft* **1898**, *31* (2), 1481–1487.

(40) Hummers, W. S.; Offeman, R. E. Preparation of Graphitic Oxide. *J. Am. Chem. Soc.* **1958**, *80* (6), 1339–1339.

(41) Dimiev, A. M.; Tour, J. M. Mechanism of Graphene Oxide Formation. *ACS Nano* **2014**, *8* (3), 3060–3068.

(42) Pei, S.; Cheng, H. M. The Reduction of Graphene Oxide. *Carbon* **2012**, *50* (9), 3210–3228.

(43) He, H.; Klinowski, J.; Forster, M.; Lerf, A. A New Structural Model for Graphite Oxide. *Chem. Phys. Lett.* **1998**, *287* (1–2), 53–56.

(44) Lerf, A.; He, H.; Forster, M.; Klinowski, J. Structure of Graphite Oxide Revisited. *J. Phys. Chem. B* **1998**, *102* (23), 4477–4482.

(45) Yu, W.; Sisi, L.; Haiyan, Y.; Jie, L. Progress in the Functional Modification of Graphene/Graphene Oxide: A Review. *RSC Adv.* **2020**, *10* (26), 15328–15345.

(46) Chung, C.; Kim, Y.; Shin, D.; Ryoo, S.; Hong, B. H.; Min, D. Biomedical Applications of Graphene and Graphene Oxide. *Acc. Chem. Res.* **2013**, *46* (10), 2211–2224.

(47) Moon, I. K.; Lee, J.; Ruoff, R. S.; Lee, H. Reduced Graphene Oxide by Chemical Graphitization. *Nat. Commun.* **2010**, *1* (1), 73.

(48) Pei, S.; Zhao, J.; Du, J.; Ren, W.; Cheng, H.-M. Direct Reduction of Graphene Oxide Films into Highly Conductive and Flexible Graphene Films by Hydrohalic Acids. *Carbon* **2010**, *48* (15), 4466–4474.

(49) Schniepp, H. C.; Li, J.-L.; McAllister, M. J.; Sai, H.; Herrera-Alonso, M.; Adamson, D. H.;

Prud'homme, R. K.; Car, R.; Saville, D. A.; Aksay, I. A. Functionalized Single Graphene Sheets Derived from Splitting Graphite Oxide. *J. Phys. Chem. B* **2006**, *110* (17), 8535–8539.

(50) Zhou, M.; Wang, Y.; Zhai, Y.; Zhai, J.; Ren, W.; Wang, F.; Dong, S. Controlled Synthesis of Large-Area and Patterned Electrochemically Reduced Graphene Oxide Films. *Chem. - A Eur. J.* **2009**, *15* (25), 6116–6120.

(51) Zhou, Y.; Bao, Q.; Tang, L. A. L.; Zhong, Y.; Loh, K. P. Hydrothermal Dehydration for the "Green" Reduction of Exfoliated Graphene Oxide to Graphene and Demonstration of Tunable Optical Limiting Properties. *Chem. Mater.* **2009**, *21* (13), 2950–2956.

(52) Williams, G.; Seger, B.; Kamat, P. V. TiO_2 -Graphene Nanocomposites. UV-Assisted Photocatalytic Reduction of Graphene Oxide. *ACS Nano* **2008**, *2* (7), 1487–1491.

(53) Zhu, Y.; Murali, S.; Stoller, M. D.; Velamakanni, A.; Piner, R. D.; Ruoff, R. S. Microwave Assisted Exfoliation and Reduction of Graphite Oxide for Ultracapacitors. *Carbon* **2010**, *48* (7), 2118–2122.

(54) Cote, L. J.; Cruz-Silva, R.; Huang, J. Flash Reduction and Patterning of Graphite Oxide and Its Polymer Composite. *J. Am. Chem. Soc.* **2009**, *131* (31), 11027–11032.

(55) Zhou, Y.; Bao, Q.; Varghese, B.; Ai Ling Tang, L.; Tan, C. K.; Sow, C. H.; Loh, K. P.; Tang, L. A. L.; Tan, C. K.; Sow, C. H.; Loh, K. P. Microstructuring of Graphene Oxide Nanosheets Using Direct Laser Writing. *Adv. Mater.* **2010**, *22* (1), 67–71.

(56) Sokolov, D. A.; Shepperd, K. R.; Orlando, T. M. Formation of Graphene Features from Direct Laser-Induced Reduction of Graphite Oxide. *J. Phys. Chem. Lett.* **2010**, *1* (18), 2633–2636.

(57) Zhang, Y.; Guo, L.; Wei, S.; He, Y.; Xia, H.; Chen, Q.; Sun, H.; Xiao, F. Direct Imprinting of Microcircuits on Graphene Oxides Film by Femtosecond Laser Reduction. *Nano Today* **2010**, *5*, 15–20.

(58) Xia, J.; Chen, F.; Li, J.; Tao, N. Measurement of the Quantum Capacitance of Graphene. *Nat. Nanotechnol.* **2009**, *4* (8), 505–509.

(59) El-Kady, M. F.; Shao, Y.; Kaner, R. B. Graphene for Batteries, Supercapacitors and Beyond. *Nat. Rev. Mater.* **2016**, *1* (7), 16033.

(60) Miller, J. R.; Outlaw, R. A.; Holloway, B. C. Graphene Double-Layer Capacitor with ac Line-

Filtering Performance. *Science.* **2010**, *329* (5999), 1637–1639.

(61) Yan, J.; Wei, T.; Shao, B.; Ma, F.; Fan, Z.; Zhang, M.; Zheng, C.; Shang, Y.; Qian, W.; Wei, F. Electrochemical Properties of Graphene Nanosheet/Carbon Black Composites as Electrodes for Supercapacitors. *Carbon* **2010**, *48* (6), 1731–1737.

(62) Pham, D. T.; Lee, T. H.; Luong, D. H.; Yao, F.; Ghosh, A.; Le, V. T.; Kim, T. H.; Li, B.; Chang, J.; Lee, Y. H. Carbon Nanotube-Bridged Graphene 3D Building Blocks for Ultrafast Compact Supercapacitors. *ACS Nano* **2015**, *9* (2), 2018–2027.

(63) She, Z.; Ghosh, D.; Pope, M. A. Decorating Graphene Oxide with Ionic Liquid Nanodroplets: An Approach Leading to Energy-Dense, High-Voltage Supercapacitors. *ACS Nano* **2017**, *11* (10), 10077–10087.

(64) Lashkari, S.; Ozhukil Valappil, M.; Pal, R.; Pope, M. A. Electrolyte-Mediated Assembly of Graphene-Based Supercapacitors Using Adsorbed Ionic Liquid/Non-Ionic Surfactant Complexes. *J. Mater. Chem. A* **2023**, *11* (21), 11222–11234.

(65) Liu, C.; Yu, Z.; Neff, D.; Zhamu, A.; Jang, B. Z. Graphene-Based Supercapacitor with an Ultrahigh Energy Density. *Nano Lett.* **2010**, *10* (12), 4863–4868.

(66) Luo, J.; Jang, H. D.; Huang, J. Effect of Sheet Morphology on the Scalability of Graphene-Based Ultracapacitors. *ACS Nano* **2013**, *7* (2), 1464–1471.

(67) Xu, Q.; Yang, G.; Fan, X.; Zheng, W. Improving the Quantum Capacitance of Graphene-Based Supercapacitors by the Doping and Co-Doping: First-Principles Calculations. *ACS Omega* **2019**, *4* (8), 13209–13217.

(68) Sruthi, T.; Kartick, T. Route to Achieving Enhanced Quantum Capacitance in Functionalized Graphene Based Supercapacitor Electrodes. *J. Phys. Condens. Matter* **2019**, *31* (47), 475502.

(69) Zhu, J.; Childress, A. S.; Karakaya, M.; Dandeliya, S.; Srivastava, A.; Lin, Y.; Rao, A. M.; Podila, R. Defect-Engineered Graphene for High-Energy- and High-Power-Density Supercapacitor Devices. *Adv. Mater.* **2016**, *28* (33), 7185–7192.

(70) Wang, G.; Shen, X.; Yao, J.; Park, J. Graphene Nanosheets for Enhanced Lithium Storage in Lithium Ion Batteries. *Carbon* **2009**, *47* (8), 2049–2053.

(71) Dahn, J. R.; Zheng, T.; Liu, Y.; Xue, J. S. Mechanisms for Lithium Insertion in Carbonaceous

Materials. *Science.* **1995**, *270* (5236), 590–593.

(72) Lee, G. W.; Ryu, J. H.; Han, W.; Ahn, K. H.; Oh, S. M. Effect of Slurry Preparation Process on Electrochemical Performances of $LiCoO_2$ Composite Electrode. *J. Power Sources* **2010**, *195* (18), 6049–6054.

(73) Liu, D.; Chen, L.-C.; Liu, T.-J.; Fan, T.; Tsou, E.-Y.; Tiu, C. An Effective Mixing for Lithium Ion Battery Slurries. *Adv. Chem. Eng. Sci.* **2014**, *04* (04), 515–528.

(74) Ahmed, S.; Nelson, P. A.; Gallagher, K. G.; Dees, D. W. Energy Impact of Cathode Drying and Solvent Recovery during Lithium-Ion Battery Manufacturing. *J. Power Sources* **2016**, *322*, 169–178.

(75) Park, J. H.; Park, J. K.; Lee, J. W. Stability of $LiNi_{0.6}Mn_{0.2}Co_{0.2}O_2$ as a Cathode Material for Lithium-Ion Batteries against Air and Moisture. *Bull. Korean Chem. Soc.* **2016**, *37* (3), 344–348.

(76) Meyer, C.; Weyhe, M.; Haselrieder, W.; Kwade, A. Heated Calendering of Cathodes for Lithium-Ion Batteries with Varied Carbon Black and Binder Contents. *Energy Technol.* **2020**, *8* (2), 1900175.

(77) Lee, D.; Ahn, S. Investigation of Laser Cutting Width of $LiCoO_2$ Coated Aluminum for Lithium-Ion Batteries. *Appl. Sci.* **2017**, *7* (9), 914.

(78) Eser, J. C.; Wirsching, T.; Weidler, P. G.; Altvater, A.; Börnhorst, T.; Kumberg, J.; Schöne, G.; Müller, M.; Scharfer, P.; Schabel, W. Moisture Adsorption Behavior in Anodes for Li-Ion Batteries. *Energy Technol.* **2020**, *8* (2), 1801162.

(79) Huttner, F.; Haselrieder, W.; Kwade, A. The Influence of Different Post-Drying Procedures on Remaining Water Content and Physical and Electrochemical Properties of Lithium-Ion Batteries. *Energy Technol.* **2020**, *8* (2), 1900245.

(80) Zwicker, M. F. R.; Moghadam, M.; Zhang, W.; Nielsen, C. V. Automotive Battery Pack Manufacturing – a Review of Battery to Tab Joining. *J. Adv. Join. Process.* **2020**, *1*, 100017.

(81) Liu, L.; Weng, Q.; Lu, X.; Sun, X.; Zhang, L.; Schmidt, O. G. Advances on Microsized On-Chip Lithium-Ion Batteries. *Small* **2017**, *13* (45), 1701847.

(82) Zhu, Z.; Kan, R.; Hu, S.; He, L.; Hong, X.; Tang, H.; Luo, W. Recent Advances in High-

Performance Microbatteries: Construction, Application, and Perspective. *Small* **2020**, *16* (39), 2003251.

(83) Scherer, G. W. Theory of Drying. *J. Am. Ceram. Soc.* **1990**, *73* (1), 3–14.

(84) Pang, Y.; Cao, Y.; Chu, Y.; Liu, M.; Snyder, K.; MacKenzie, D.; Cao, C. Additive Manufacturing of Batteries. *Adv. Funct. Mater.* **2020**, *30* (1), 1906244.

(85) Zhu, C.; Liu, T.; Qian, F.; Chen, W.; Chandrasekaran, S.; Yao, B.; Song, Y.; Duoss, E. B.; Kuntz, J. D.; Spadaccini, C. M.; Worsley, M. A.; Li, Y. 3D Printed Functional Nanomaterials for Electrochemical Energy Storage. *Nano Today* **2017**, *15*, 107–120.

(86) Wei, T.; Ahn, B. Y.; Grotto, J.; Lewis, J. A. 3D Printing of Customized Li-Ion Batteries with Thick Electrodes. *Adv. Mater.* **2018**, *30* (16), 1703027.

(87) El-Kady, M. F.; Strong, V.; Dubin, S.; Kaner, R. B. Laser Scribing of High-Performance and Flexible Graphene-Based Electrochemical Capacitors. *Science.* **2012**, *335* (6074), 1326–1330.

(88) Jiang, H.; Ye, X.; Zhu, Y.; Yue, Z.; Wang, L.; Xie, J.; Wan, Z.; Jia, C. Flexible Solid-State Supercapacitors with High Areal Performance Enabled by Chlorine-Doped Graphene Films with Commercial-Level Mass Loading. *ACS Sustain. Chem. Eng.* **2019**, *7* (23), 18844–18853.

(89) Wan, Z.; Streed, E. W.; Lobino, M.; Wang, S.; Sang, R. T.; Cole, I. S.; Thiel, D. V; Li, Q. Laser-Reduced Graphene: Synthesis, Properties, and Applications. *Adv. Mater. Technol.* **2018**, *3*, 1700315.

(90) Trusovas, R.; Račiukaitis, G.; Niaura, G.; Barkauskas, J.; Valušis, G.; Pauliukaite, R. Recent Advances in Laser Utilization in the Chemical Modification of Graphene Oxide and Its Applications. *Adv. Opt. Mater.* **2016**, *4* (1), 37–65.

(91) Wang, F.; Wang, K.; Zheng, B.; Dong, X.; Mei, X.; Lv, J.; Duan, W.; Wang, W. Laser-Induced Graphene: Preparation, Functionalization and Applications. *Mater. Technol.* **2018**, *33* (5), 340–356.

(92) Pope, M. A.; Aksay, I. A. Four-Fold Increase in the Intrinsic Capacitance of Graphene through Functionalization and Lattice Disorder. *J. Phys. Chem. C* **2015**, *119* (35), 20369–20378.

(93) Peng, Z.; Lin, J.; Ye, R.; Samuel, E. L. G.; Tour, J. M. Flexible and Stackable Laser-Induced Graphene Supercapacitors. *ACS Appl. Mater. Interfaces* **2015**, *7*, 3414–3419.

(94) Peng, Z.; Ye, R.; Mann, J. A.; Zakhidov, D.; Li, Y.; Smalley, P. R.; Lin, J.; Tour, J. M. Flexible Boron-Doped Laser-Induced Graphene Microsupercapacitors. *ACS Nano* **2015**, *9* (6), 5868–5875.

(95) Wang, F.; Mei, X.; Wang, K.; Dong, X.; Gao, M.; Zhai, Z.; Lv, J.; Zhu, C.; Duan, W.; Wang, W. Rapid and Low-Cost Laser Synthesis of Hierarchically Porous Graphene Materials as High-Performance Electrodes for Supercapacitors. *J. Mater. Sci.* **2019**, *54*, 5658–5670.

(96) Zhang, Z.; Song, M.; Hao, J.; Wu, K.; Li, C.; Hu, C. Visible Light Laser-Induced Graphene from Phenolic Resin: A New Approach for Directly Writing Graphene-Based Electrochemical Devices on Various Substrates. *Carbon* **2018**, *127*, 287–296.

(97) Cai, J.; Lv, C.; Watanabe, A. Cost-Effective Fabrication of High-Performance Flexible All-Solid-State Carbon Micro-Supercapacitors by Blue-Violet Laser Direct Writing and Further Surface Treatment. *J. Mater. Chem. A* **2016**, *4* (5), 1671–1679.

(98) Zhang, J.; Ren, M.; Wang, L.; Li, Y.; Yakobson, B. I.; Tour, J. M. Oxidized Laser-Induced Graphene for Efficient Oxygen Electrocatalysis. *Adv. Mater.* **2018**, *30* (21), 1707319.

(99) Ren, M.; Zhang, J.; Tour, J. M. Laser-Induced Graphene Synthesis of Co_3O_4 in Graphene for Oxygen Electrocatalysis and Metal-Air Batteries. *Carbon* **2018**, *139*, 880–887.

(100) Ren, M.; Zhang, J.; Tour, J. M. Laser-Induced Graphene Hybrid Catalysts for Rechargeable Zn-Air Batteries. *ACS Appl. Energy Mater.* **2019**, *2* (2), 1460–1468.

(101) Ren, M.; Zhang, J.; Fan, M.; Ajayan, P. M.; Tour, J. M. Li-Breathing Air Batteries Catalyzed by MnNiFe/Laser-Induced Graphene Catalysts. *Adv. Mater. Interfaces* **2019**, *6* (19), 1901035.

(102) Aslam, S.; Sagar, R. U. R.; Liu, Y.; Anwar, T.; Zhang, L.; Zhang, M.; Mahmood, N.; Qiu, Y. Graphene Decorated Polymeric Flexible Materials for Lightweight High Areal Energy Lithium-Ion Batteries. *Appl. Mater. Today* **2019**, *17*, 123–129.

(103) Shim, H. C.; Tran, C. Van; Hyun, S.; In, J. Bin. Three-Dimensional Laser-Induced Holey Graphene and Its Dry Release Transfer onto Cu Foil for High-Rate Energy Storage in Lithium-Ion Batteries. *Appl. Surf. Sci.* **2021**, *564* (March), 150416.

(104) Zhou, C.; Zhang, K.; Hong, M.; Yang, Y.; Hu, N.; Su, Y.; Zhang, L.; Zhang, Y. Laser-Induced MnO/Mn_3O_4/N-Doped-Graphene Hybrid as Binder-Free Anodes for Lithium Ion Batteries.

Chem. Eng. J. **2020**, *385*, 123720.

(105) Huang, Y.; Field, R.; Chen, Q.; Peng, Y.; Walczak, M. S.; Zhao, H.; Zhu, G.; Liu, Z.; Li, L. Laser Induced Molybdenum Sulphide Loading on Doped Graphene Cathode for Highly Stable Lithium Sulphur Battery. *Commun. Chem.* **2019**, *2* (1), 138.

(106) Zhou, C.; Li, M.; Hong, M.; Hu, N.; Yang, Z.; Zhang, L.; Zhang, Y. Laser-Induced Micro-Explosion to Construct Hierarchical Structure as Efficient Polysulfide Mediators for High-Performance Lithium-Sulfur Batteries. *Chem. Eng. J.* **2021**, *421* (P1), 129707.

(107) Ye, R.; Peng, Z.; Wang, T.; Xu, Y.; Zhang, J.; Li, Y.; Nilewski, L. G.; Lin, J.; Tour, J. M. In Situ Formation of Metal Oxide Nanocrystals Embedded in Laser-Induced Graphene. *ACS Nano* **2015**, *9* (9), 9244–9251.

(108) Dosi, M.; Lau, I.; Zhuang, Y.; Simakov, D. S. A.; Fowler, M. W.; Pope, M. A. Ultrasensitive Electrochemical Methane Sensors Based on Solid Polymer Electrolyte-Infused Laser-Induced Graphene. *ACS Appl. Mater. Interfaces* **2019**, *11*, 6166–6173.

(109) Tao, L.-Q.; Tian, H.; Liu, Y.; Ju, Z.-Y.; Pang, Y.; Chen, Y.-Q.; Wang, D.-Y.; Tian, X.-G.; Yan, J.-C.; Deng, N.-Q.; Yang, Y.; Ren, T.-L. An Intelligent Artificial Throat with Sound-Sensing Ability Based on Laser Induced Graphene. *Nat. Commun.* **2017**, *8* (1), 14579.

(110) Rahimi, R.; Ochoa, M.; Yu, W.; Ziaie, B. Highly Stretchable and Sensitive Unidirectional Strain Sensor via Laser Carbonization. *ACS Appl. Mater. Interfaces* **2015**, *7*, 4463–4470.

(111) Tan, K. W.; Jung, B.; Werner, J. G.; Rhoades, E. R.; Thompson, M. O.; Wiesner, U. Transient Laser Heating Induced Hierarchical Porous Structures from Block Copolymer – Directed Self-Assembly. *Science.* **2015**, *349* (6243), 54–58.

(112) Tittle, C. M.; Yilman, D.; Pope, M. A.; Backhouse, C. J. Robust Superhydrophobic Laser-Induced Graphene for Desalination Applications. *Adv. Mater. Technol.* **2018**, *3*, 1700207.

(113) Li, Y.; Luong, D. X.; Zhang, J.; Tarkunde, Y. R.; Kittrell, C.; Sargunaraj, F.; Ji, Y.; Arnusch, C. J.; Tour, J. M. Laser-Induced Graphene in Controlled Atmospheres: From Superhydrophilic to Superhydrophobic Surfaces. *Adv. Mater.* **2017**, *29* (27), 1700496.

(114) Kyerematen, N. A.; Brousse, T.; Pech, D. Microsupercapacitors as Miniaturized Energy-Storage Components for on-Chip Electronics. *Nat. Nanotechnol.* **2017**, *12* (1), 7–15.

(115) Ling, Y.; Zhuang, X.; Xu, Z.; Xie, Y.; Zhu, X.; Xu, Y.; Sun, B.; Lin, J.; Zhang, Y.; Yan, Z. Mechanically Assembled, Three-Dimensional Hierarchical Structures of Cellular Graphene with Programmed Geometries and Outstanding Electromechanical Properties. *ACS Nano* **2018**, *12*, 12456–12463.

(116) Kim, M.; Gu, M. G.; Jeong, H.; Song, E.; Jeon, J. W.; Huh, K.-M.; Kang, P.; Kim, S.-K.; Kim, B. G. Laser Scribing of Fluorinated Polyimide Films to Generate Microporous Structures for High-Performance Micro-Supercapacitor Electrodes. *ACS Appl. Energy Mater.* **2021**, *4* (1), 208–214.

(117) Chyan, Y.; Ye, R.; Li, Y.; Singh, S. P.; Arnusch, C. J.; Tour, J. M. Laser-Induced Graphene by Multiple Lasing: Toward Electronics on Cloth, Paper, and Food. *ACS Nano* **2018**, *12* (3), 2176–2183.

(118) Ye, R.; Chyan, Y.; Zhang, J.; Li, Y.; Han, X.; Kittrell, C.; Tour, J. M. Laser-Induced Graphene Formation on Wood. *Adv. Mater.* **2017**, *29*, 1702211.

(119) Zhu, C.; Zhao, D.; Wang, K.; Dong, X.; Duan, W.; Wang, F.; Gao, M.; Zhang, G. Direct Laser Writing of Graphene Films from a Polyether Ether Ketone Precursor. *J. Mater. Sci.* **2019**, *54* (5), 4192–4201.

(120) Jiao, L.; Chua, Z.; Moon, S.; Song, J.; Bi, G.; Zheng, H.; Lee, B.; Koo, J. Laser-Induced Graphene on Additive Manufacturing Parts. *Nanomaterials* **2019**, *9* (1), 90.

(121) Yu, W.; Peng, Y.; Cao, L.; Zhao, W.; Liu, X. Free-Standing Laser-Induced Graphene Films for High-Performance Electromagnetic Interference Shielding. *Carbon* **2021**, *183*, 600–611.

(122) Cao, L.; Zhu, S.; Pan, B.; Dai, X.; Zhao, W.; Liu, Y.; Xie, W.; Kuang, Y.; Liu, X. Stable and Durable Laser-Induced Graphene Patterns Embedded in Polymer Substrates. *Carbon* **2020**, *163*, 85–94.

(123) Le, T. D.; Park, S.; An, J.; Lee, P. S.; Kim, Y. J. Ultrafast Laser Pulses Enable One-Step Graphene Patterning on Woods and Leaves for Green Electronics. *Adv. Funct. Mater.* **2019**, *29* (33), 1902771.

(124) Han, X.; Ye, R.; Chyan, Y.; Wang, T.; Zhang, C.; Shi, L.; Zhang, T.; Zhao, Y.; Tour, J. M. Laser-Induced Graphene from Wood Impregnated with Metal Salts and Use in Electrocatalysis. *ACS Appl. Nano Mater.* **2018**, *1* (9), 5053–5061.

(125) Qu, W.; Zhao, Z.; Wang, J.; Dong, F.; Xu, H.; Sun, X.; Jin, H. Direct Laser Writing of Pure Lignin on Carbon Cloth for Highly Flexible Supercapacitors with Enhanced Areal Capacitance. *Sustain. Energy Fuels* **2021**, *5* (14), 3744–3754.

(126) Alhajji, E.; Zhang, F.; Alshareef, H. N. Status and Prospects of Laser-Induced Graphene for Battery Applications. *Energy Technol.* **2021**, *9* (10), 2100454.

(127) Dominko, R.; Vizintin, A.; Aquilanti, G.; Stievano, L.; Helen, M. J.; Munnangi, A. R.; Fichtner, M.; Arcon, I. Polysulfides Formation in Different Electrolytes from the Perspective of X-Ray Absorption Spectroscopy. *J. Electrochem. Soc.* **2018**, *165* (1), A5014–A5019.

(128) Ding, N.; Zhou, L.; Zhou, C.; Geng, D.; Yang, J.; Chien, S. W. Building Better Lithium-Sulfur Batteries: From $LiNO_3$ to Solid Oxide Catalyst. *Sci. Rep.* **2016**, No. 6, 33154.

(129) Xue, W.; Miao, L.; Qie, L.; Wang, C.; Li, S.; Wang, J.; Li, J. Gravimetric and Volumetric Energy Densities of Lithium-Sulfur Batteries. *Curr. Opin. Electrochem.* **2017**, *6* (1), 92–99.

(130) Vehicle Technologies Office. Electric Vehicle Battery Pack Costs in 2022 Are Nearly 90% Lower than in 2008, according to DOE Estimates https://www.energy.gov/eere/vehicles/articles/fotw-1272-january-9-2023-electric-vehicle-battery-pack-costs-2022-are-nearly (accessed Jun 28, 2023).

(131) Fotouhi, A.; Auger, D.; O'Neill, L.; Cleaver, T.; Walus, S. Lithium-Sulfur Battery Technology Readiness and Applications—A Review. *Energies* **2017**, *10* (12), 1937.

(132) Tikekar, M. D.; Choudhury, S.; Tu, Z.; Archer, L. A. Design Principles for Electrolytes and Interfaces for Stable Lithium-Metal Batteries. *Nat. Energy* **2016**, *1* (9), 16114.

(133) Chazalviel, J. N. Electrochemical Aspects of the Generation of Ramified Metallic Electrodeposits. *Phys. Rev. A* **1990**, *42* (12), 7355–7367.

(134) Cheng, X. B.; Zhang, R.; Zhao, C. Z.; Wei, F.; Zhang, J. G.; Zhang, Q. A Review of Solid Electrolyte Interphases on Lithium Metal Anode. *Adv. Sci.* **2016**, *3* (3), 1500213.

(135) Judez, X.; Zhang, H.; Li, C.; Eshetu, G. G.; González-Marcos, J. A.; Armand, M.; Rodriguez-Martinez, L. M. Review—Solid Electrolytes for Safe and High Energy Density Lithium-Sulfur Batteries: Promises and Challenges. *J. Electrochem. Soc.* **2018**, *165* (1), A6008–A6016.

(136) Monroe, C.; Newman, J. The Impact of Elastic Deformation on Deposition Kinetics at

Lithium/Polymer Interfaces. *J. Electrochem. Soc.* **2005**, *152* (2), A396.

(137) Li, N. W.; Yin, Y. X.; Yang, C. P.; Guo, Y. G. An Artificial Solid Electrolyte Interphase Layer for Stable Lithium Metal Anodes. *Adv. Mater.* **2016**, *28* (9), 1853–1858.

(138) Pang, Q.; Liang, X.; Shyamsunder, A.; Nazar, L. F. An In Vivo Formed Solid Electrolyte Surface Layer Enables Stable Plating of Li Metal. *Joule* **2017**, *1* (4), 871–886.

(139) Pang, Q.; Liang, X.; Kochetkov, I. R.; Hartmann, P.; Nazar, L. F. Stabilizing Lithium Plating by a Biphasic Surface Layer Formed In Situ. *Angew. Chemie - Int. Ed.* **2018**, *57* (31), 9795–9798.

(140) Choudhury, S.; Tu, Z.; Stalin, S.; Vu, D.; Fawole, K.; Gunceler, D.; Sundararaman, R.; Archer, L. A. Electroless Formation of Hybrid Lithium Anodes for Fast Interfacial Ion Transport. *Angew. Chemie - Int. Ed.* **2017**, *56* (42), 13070–13077.

(141) Ding, F.; Xu, W.; Graff, G. L.; Zhang, J. G.; Sushko, M. L.; Chen, X.; Shao, Y.; Engelhard, M. H.; Nie, Z.; Xiao, J.; Liu, X.; Sushko, P. V.; Liu, J.; Zhang, J. G. Dendrite-Free Lithium Deposition via Self-Healing Electrostatic Shield Mechanism. *J. Am. Chem. Soc.* **2013**, *135* (11), 4450–4456.

(142) Qian, J.; Henderson, W. A.; Xu, W.; Bhattacharya, P.; Engelhard, M.; Borodin, O.; Zhang, J. G. High Rate and Stable Cycling of Lithium Metal Anode. *Nat. Commun.* **2015**, *6* (1), 6362.

(143) Ma, G.; Wen, Z.; Wu, M.; Shen, C.; Wang, Q.; Jin, J.; Wu, X. A Lithium Anode Protection Guided Highly-Stable Lithium–Sulfur Battery. *Chem. Commun.* **2014**, *50* (91), 14209–14212.

(144) Lin, D.; Liu, Y.; Chen, W.; Zhou, G.; Liu, K.; Dunn, B.; Cui, Y. Conformal Lithium Fluoride Protection Layer on Three-Dimensional Lithium by Nonhazardous Gaseous Reagent Freon. *Nano Lett.* **2017**, *17* (6), 3731–3737.

(145) Jing, H.-K.; Kong, L.-L.; Liu, S.; Li, G.-R.; Gao, X.-P. Protected Lithium Anode with Porous Al_2O_3 Layer for Lithium–Sulfur Battery. *J. Mater. Chem. A* **2015**, *3* (23), 12213–12219.

(146) Li, Q.; Zeng, F. L.; Guan, Y. P.; Jin, Z. Q.; Huang, Y. Q.; Yao, M.; Wang, W. K.; Wang, A. B. Poly(Dimethylsiloxane) Modified Lithium Anode for Enhanced Performance of Lithium-Sulfur Batteries. *Energy Storage Mater.* **2018**, *13*, 151–159.

(147) Kang, I. S.; Lee, Y.-S.; Kim, D.-W. Improved Cycling Stability of Lithium Electrodes in

Rechargeable Lithium Batteries. *J. Electrochem. Soc.* **2013**, *161* (1), A53–A57.

(148) Chen, L.; Huang, Z.; Shahbazian-Yassar, R.; Libera, J. A.; Klavetter, K. C.; Zavadil, K. R.; Elam, J. W. Directly Formed Alucone on Lithium Metal for High-Performance Li Batteries and Li-S Batteries with High Sulfur Mass Loading. *ACS Appl. Mater. Interfaces* **2018**, *10* (8), 7043–7051.

(149) Liu, F.; Xiao, Q.; Wu, H. B.; Shen, L.; Xu, D.; Cai, M.; Lu, Y. Fabrication of Hybrid Silicate Coatings by a Simple Vapor Deposition Method for Lithium Metal Anodes. *Adv. Energy Mater.* **2018**, *8* (6), 1701744.

(150) Kozen, A. C.; Lin, C. F.; Zhao, O.; Lee, S. B.; Rubloff, G. W.; Noked, M. Stabilization of Lithium Metal Anodes by Hybrid Artificial Solid Electrolyte Interphase. *Chem. Mater.* **2017**, *29* (15), 6298–6307.

(151) Jiang, S.; Lu, Y.; Lu, Y.; Han, M.; Li, H.; Tao, Z.; Niu, Z.; Chen, J. Nafion/Titanium Dioxide-Coated Lithium Anode for Stable Lithium-Sulfur Batteries. *Chem. - An Asian J.* **2018**, *13* (10), 1379–1385.

(152) Zheng, G.; Lee, S. W.; Liang, Z.; Lee, H. W.; Yan, K.; Yao, H.; Wang, H.; Li, W.; Chu, S.; Cui, Y. Interconnected Hollow Carbon Nanospheres for Stable Lithium Metal Anodes. *Nat. Nanotechnol.* **2014**, *9* (8), 618–623.

(153) Yan, K.; Lee, H. W.; Gao, T.; Zheng, G.; Yao, H.; Wang, H.; Lu, Z.; Zhou, Y.; Liang, Z.; Liu, Z.; Chu, S.; Cui, Y. Ultrathin Two-Dimensional Atomic Crystals as Stable Interfacial Layer for Improvement of Lithium Metal Anode. *Nano Lett.* **2014**, *14* (10), 6016–6022.

(154) Huang, S.; Tang, L.; Najafabadi, H. S.; Chen, S.; Ren, Z. A Highly Flexible Semi-Tubular Carbon Film for Stable Lithium Metal Anodes in High-Performance Batteries. *Nano Energy* **2017**, *38* (June), 504–509.

(155) Zhao, Y.; Sun, Q.; Li, X.; Wang, C.; Sun, Y.; Adair, K. R.; Li, R.; Sun, X. Carbon Paper Interlayers: A Universal and Effective Approach for Highly Stable Li Metal Anodes. *Nano Energy* **2018**, *43* (2018), 368–375.

(156) Huang, C.; Xiao, J.; Shao, Y.; Zheng, J.; Bennett, W. D.; Lu, D.; Saraf, L. V.; Engelhard, M.; Ji, L.; Zhang, J.; Li, X.; Graff, G. L.; Liu, J. Manipulating Surface Reactions in Lithium-Sulphur Batteries Using Hybrid Anode Structures. *Nat. Commun.* **2014**, *5* (1), 3015.

(157) Li, Q.; Zhu, S.; Lu, Y. 3D Porous Cu Current Collector/Li-Metal Composite Anode for Stable Lithium-Metal Batteries. *Adv. Funct. Mater.* **2017**, *27* (18), 1606422.

(158) Lin, D.; Zhao, J.; Sun, J.; Yao, H.; Liu, Y.; Yan, K.; Cui, Y. Three-Dimensional Stable Lithium Metal Anode with Nanoscale Lithium Islands Embedded in Ionically Conductive Solid Matrix. *Proc. Natl. Acad. Sci.* **2017**, *114* (18), 4613–4618.

(159) Lin, D.; Liu, Y.; Liang, Z.; Lee, H. W.; Sun, J.; Wang, H.; Yan, K.; Xie, J.; Cui, Y. Layered Reduced Graphene Oxide with Nanoscale Interlayer Gaps as a Stable Host for Lithium Metal Anodes. *Nat. Nanotechnol.* **2016**, *11* (7), 626–632.

(160) Cheng, X. B.; Peng, H. J.; Huang, J. Q.; Zhang, R.; Zhao, C. Z.; Zhang, Q. Dual-Phase Lithium Metal Anode Containing a Polysulfide-Induced Solid Electrolyte Interphase and Nanostructured Graphene Framework for Lithium-Sulfur Batteries. *ACS Nano* **2015**, *9* (6), 6373–6382.

(161) Xie, J.; Wang, J.; Lee, H. R.; Yan, K.; Li, Y.; Shi, F.; Huang, W.; Pei, A.; Chen, G.; Subbaraman, R.; Christensen, J.; Cui, Y. Engineering Stable Interfaces for Three-Dimensional Lithium Metal Anodes. *Sci. Adv.* **2018**, *4* (7), 2–10.

(162) Jeong, J.; Chun, J.; Lim, W.-G.; Kim, W. B.; Jo, C.; Lee, J. Mesoporous Carbon Host Material for Stable Lithium Metal Anode. *Nanoscale* **2020**, *12* (22), 11818–11824.

(163) Gong, H.; Chen, Y.; Chen, S.; Xu, C.; Yang, Y.; Ye, Y.; Huang, Z.; Ning, R.; Cui, Y.; Bao, Z. Fast-Charging of Hybrid Lithium-Ion/Lithium-Metal Anodes by Nanostructured Hard Carbon Host. *ACS Energy Lett.* **2022**, *7* (12), 4417–4426.

(164) Kim, J.; Lee, J.; Yun, J.; Choi, S. H.; Han, S. A.; Moon, J.; Kim, J. H.; Lee, J.; Park, M. Functionality of Dual-Phase Lithium Storage in a Porous Carbon Host for Lithium-Metal Anode. *Adv. Funct. Mater.* **2020**, *30* (15), 1910538.

(165) Shi, P.; Li, T.; Zhang, R.; Shen, X.; Cheng, X.-B.; Xu, R.; Huang, J.-Q.; Chen, X.-R.; Liu, H.; Zhang, Q. Lithiophilic LiC_6 Layers on Carbon Hosts Enabling Stable Li Metal Anode in Working Batteries. *Adv. Mater.* **2019**, *31* (8), 1807131.

(166) Chen, C.; Guan, J.; Li, N. W.; Lu, Y.; Luan, D.; Zhang, C. H.; Cheng, G.; Yu, L.; Lou, X. W. Lotus-Root-Like Carbon Fibers Embedded with Ni–Co Nanoparticles for Dendrite-Free Lithium Metal Anodes. *Adv. Mater.* **2021**, *33* (24), 2100608.

(167) Liu, H.; Di, J.; Wang, P.; Gao, R.; Tian, H.; Ren, P.; Yuan, Q.; Huang, W.; Liu, R.; Liu, Q.; Feng, M. A Novel Design of 3D Carbon Host for Stable Lithium Metal Anode. *Carbon Energy* **2022**, *4* (4), 654–664.

(168) Yi, J.; Chen, J.; Yang, Z.; Dai, Y.; Li, W.; Cui, J.; Ciucci, F.; Lu, Z.; Yang, C. Facile Patterning of Laser-Induced Graphene with Tailored Li Nucleation Kinetics for Stable Lithium-Metal Batteries. *Adv. Energy Mater.* **2019**, *9* (38), 1901796.

(169) Chen, X.; Chen, X. R.; Hou, T. Z.; Li, B. Q.; Cheng, X. B.; Zhang, R.; Zhang, Q. Lithiophilicity Chemistry of Heteroatom-Doped Carbon to Guide Uniform Lithium Nucleation in Lithium Metal Anodes. *Sci. Adv.* **2019**, *5* (2), 1–9.

(170) Pei, A.; Zheng, G.; Shi, F.; Li, Y.; Cui, Y. Nanoscale Nucleation and Growth of Electrodeposited Lithium Metal. *Nano Lett.* **2017**, *17* (2), 1132–1139.

(171) Kelton, K. F.; Greer, A. L. Heterogeneous Nucleation. In *Pergamon Materials Series*; Elsevier, 2010; Vol. 15, pp 165–226.

(172) Ely, D. R.; García, R. E. Heterogeneous Nucleation and Growth of Lithium Electrodeposits on Negative Electrodes. *J. Electrochem. Soc.* **2013**, *160* (4), A662–A668.

(173) Yan, K.; Lu, Z.; Lee, H. W.; Xiong, F.; Hsu, P. C.; Li, Y.; Zhao, J.; Chu, S.; Cui, Y. Selective Deposition and Stable Encapsulation of Lithium through Heterogeneous Seeded Growth. *Nat. Energy* **2016**, *1* (3), 16010.

(174) Chen, Q.; Yang, Y.; Zheng, H.; Xie, Q.; Yan, X.; Ma, Y.; Wang, L.; Peng, D.-L. Electrochemically Induced Highly Ion Conductive Porous Scaffolds to Stabilize Lithium Deposition for Lithium Metal Anodes. *J. Mater. Chem. A* **2019**, *7* (19), 11683–11689.

(175) Zhang, Y.; Luo, W.; Wang, C.; Li, Y.; Chen, C.; Song, J.; Dai, J.; Hitz, E. M.; Xu, S.; Yang, C.; Wang, Y.; Hu, L. High-Capacity, Low-Tortuosity, and Channel-Guided Lithium Metal Anode. *Proc. Natl. Acad. Sci.* **2017**, *114* (14), 3584–3589.

(176) Fan, H.; Gao, C.; Dong, Q.; Hong, B.; Fang, Z.; Hu, M.; Lai, Y. Silver Sites Guide Spatially Homogeneous Plating of Lithium Metal in 3D Host. *J. Electroanal. Chem.* **2018**, *824*, 175–180.

(177) Zhang, H.; Liao, X.; Guan, Y.; Xiang, Y.; Li, M.; Zhang, W.; Zhu, X.; Ming, H.; Lu, L.; Qiu,

J.; Huang, Y.; Cao, G.; Yang, Y.; Mai, L.; Zhao, Y.; Zhang, H. Lithiophilic-Lithiophobic Gradient Interfacial Layer for a Highly Stable Lithium Metal Anode. *Nat. Commun.* **2018**, *9* (1), 3729.

(178) Nagy, K. S.; Kazemiabnavi, S.; Thornton, K.; Siegel, D. J. Thermodynamic Overpotentials and Nucleation Rates for Electrodeposition on Metal Anodes. *ACS Appl. Mater. Interfaces* **2019**, *11* (8), 7954–7964.

(179) Evers, S.; Nazar, L. F. New Approaches for High Energy Density Lithium-Sulfur Battery Cathodes. *Acc. Chem. Res.* **2013**, *46* (5), 1135–1143.

(180) Li, G. C.; Hu, J. J.; Li, G. R.; Ye, S. H.; Gao, X. P. Sulfur/Activated-Conductive Carbon Black Composites as Cathode Materials for Lithium/Sulfur Battery. *J. Power Sources* **2013**, *240*, 598–605.

(181) Makimura, Y.; Ohzuku, T. Lithium Insertion Material of $LiCo_{1/3}Ni_{1/3}Mn_{1/3}O_2$ for Advanced Lithium-Ion Batteries. *J. Power Sources* **2003**, *119–121*, 156–160.

(182) Zhang, Y.; Bakenov, Z.; Zhao, Y.; Konarov, A.; Doan, T. N. L.; Malik, M.; Paron, T.; Chen, P. One-Step Synthesis of Branched Sulfur/Polypyrrole Nanocomposite Cathode for Lithium Rechargeable Batteries. *J. Power Sources* **2012**, *208*, 1–8.

(183) Zhao, Q.; Hu, X.; Zhang, K.; Zhang, N.; Hu, Y.; Chen, J. Sulfur Nanodots Electrodeposited on Ni Foam as High-Performance Cathode for Li–S Batteries. *Nano Lett.* **2015**, *15* (1), 721–726.

(184) Zheng, J.; Tian, J.; Wu, D.; Gu, M.; Xu, W.; Wang, C.; Gao, F. Lewis Acid − Base Interactions between Polysulfides and Metal Organic Framework in Lithium Sulfur Batteries. *Nano Lett.* **2014**, *14*, 2345–2352.

(185) Ji, X.; Lee, K. T.; Nazar, L. F. A Highly Ordered Nanostructured Carbon–Sulphur Cathode for Lithium–Sulphur Batteries. *Nat. Mater.* **2009**, *8* (6), 500–506.

(186) Jin, K.; Zhou, X.; Zhang, L.; Xin, X.; Wang, G.; Liu, Z. Sulfur/Carbon Nanotube Composite Film as a Flexible Cathode for Lithium-Sulfur Batteries. *J. Phys. Chem. C* **2013**, *117* (41), 21112–21119.

(187) Liu, J.; Liu, B.; Wang, C.; Huang, Z.; Hu, L.; Ke, X.; Liu, L.; Shi, Z.; Guo, Z. Walnut Shell-Derived Activated Carbon: Synthesis and Its Application in the Sulfur Cathode for Lithium-

Sulfur Batteries. *J. Alloys Compd.* **2017**, *718*, 373–378.

(188) Rao, M.; Song, X.; Liao, H.; Cairns, E. J. Carbon Nanofiber – Sulfur Composite Cathode Materials with Different Binders for Secondary Li/S Cells. *Electrochim. Acta* **2012**, *65*, 228–233.

(189) Kim, K. R.; Yu, S.; Sung, Y. Enhancement of Cycle Performance of Li–S Batteries by Redistribution of Sulfur. *Chem. Commun.* **2016**, *52* (6), 1198–1201.

(190) Yu, X.; Pan, H.; Zhou, Y.; Northrup, P.; Xiao, J.; Bak, S.; Liu, M.; Nam, K.-W. W.; Qu, D.; Liu, J.; Wu, T.; Yang, X.-Q. Q. Direct Observation of the Redistribution of Sulfur and Polysufides in Li-S Batteries During the First Cycle by In Situ X-Ray Fluorescence Microscopy. *Adv. Energy Mater.* **2015**, *5* (16), 1500072.

(191) Li, G.; Wang, S.; Zhang, Y.; Li, M.; Chen, Z.; Lu, J. Revisiting the Role of Polysulfides in Lithium-Sulfur Batteries. *Adv. Mater.* **2018**, *30* (22), 1705590.

(192) Choi, Y. S.; Kim, S.; Choi, S. S.; Han, J. S.; Kim, J. D.; Jeon, S. E.; Jung, B. H. Effect of Cathode Component on the Energy Density of Lithium–Sulfur Battery. *Electrochim. Acta* **2004**, *50* (2–3), 833–835.

(193) Yao, X.; Huang, N.; Han, F.; Zhang, Q.; Wan, H.; Mwizerwa, J. P.; Wang, C.; Xu, X. High-Performance All-Solid-State Lithium-Sulfur Batteries Enabled by Amorphous Sulfur-Coated Reduced Graphene Oxide Cathodes. *Adv. Energy Mater.* **2017**, *7* (17), 1602923.

(194) Zhang, S. S. Liquid Electrolyte Lithium/Sulfur Battery: Fundamental Chemistry, Problems, and Solutions. *J. Power Sources* **2013**, *231*, 153–162.

(195) Elazari, R.; Salitra, G.; Talyosef, Y.; Grinblat, J.; Scordilis-Kelley, C.; Xiao, A.; Affinito, J.; Aurbach, D. Morphological and Structural Studies of Composite Sulfur Electrodes upon Cycling by HRTEM, AFM and Raman Spectroscopy. *J. Electrochem. Soc.* **2010**, *157* (10), A1131.

(196) Lei, D.; Shi, K.; Ye, H.; Wan, Z.; Wang, Y.; Shen, L.; Li, B.; Yang, Q.-H.; Kang, F.; He, Y.-B. Progress and Perspective of Solid-State Lithium-Sulfur Batteries. *Adv. Funct. Mater.* **2018**, *28* (38), 1707570.

(197) Fu, K. (Kelvin); Gong, Y.; Hitz, G. T.; McOwen, D. W.; Li, Y.; Xu, S.; Wen, Y.; Zhang, L.;

Wang, C.; Pastel, G.; Dai, J.; Liu, B.; Xie, H.; Yao, Y.; Wachsman, E. D.; Hu, L. Three-Dimensional Bilayer Garnet Solid Electrolyte Based High Energy Density Lithium Metal-Sulfur Batteries. *Energy Environ. Sci.* **2017**, *10* (7), 1568–1575.

(198) Nagao, M.; Hayashi, A.; Tatsumisago, M. Sulfur–Carbon Composite Electrode for All-Solid-State Li/S Battery with Li_2S–P_2S_5 Solid Electrolyte. *Electrochim. Acta* **2011**, *56* (17), 6055–6059.

(199) Pang, Q.; Liang, X.; Kwok, C. Y.; Kulisch, J.; Nazar, L. F. A Comprehensive Approach toward Stable Lithium–Sulfur Batteries with High Volumetric Energy Density. *Adv. Energy Mater.* **2017**, *7* (6), 1601630.

(200) Liang, X.; Hart, C.; Pang, Q.; Garsuch, A.; Weiss, T.; Nazar, L. F. A Highly Efficient Polysulfide Mediator for Lithium–Sulfur Batteries. *Nat. Commun.* **2015**, *6* (1), 5682.

(201) Wang, Z.; Zhang, S.; Zhang, L.; Lin, R.; Wu, X.; Fang, H.; Ren, Y. Hollow Spherical Carbonized Polypyrrole/Sulfur Composite Cathode Materials for Lithium/Sulfur Cells with Long Cycle Life. *J. Power Sources* **2014**, *248*, 337–342.

(202) Zhou, G.; Yin, L.-C.; Wang, D.-W.; Li, L.; Pei, S.; Gentle, I. R.; Li, F.; Cheng, H.-M. Fibrous Hybrid of Graphene and Sulfur Nanocrystals for High-Performance Lithium–Sulfur Batteries. *ACS Nano* **2013**, *7* (6), 5367–5375.

(203) Chong, W. G.; Xiao, Y.; Huang, J. Q.; Yao, S.; Cui, J.; Qin, L.; Gao, C.; Kim, J. K. Highly Conductive Porous Graphene/Sulfur Composite Ribbon Electrodes for Flexible Lithium-Sulfur Batteries. *Nanoscale* **2018**, *10* (45), 21132–21141.

(204) Evers, S.; Nazar, L. F. Graphene-Enveloped Sulfur in a One Pot Reaction: A Cathode with Good Coulombic Efficiency and High Practical Sulfur Content. *Chem. Commun.* **2012**, *48* (9), 1233–1235.

(205) Zu, C.; Manthiram, A. Hydroxylated Graphene-Sulfur Nanocomposites for High-Rate Lithium-Sulfur Batteries. *Adv. Energy Mater.* **2013**, *3* (8), 1008–1012.

(206) Pan, H.; Chen, J.; Cao, R.; Murugesan, V.; Rajput, N. N.; Han, K. S.; Persson, K.; Estevez, L.; Engelhard, M. H.; Zhang, J.-G. G.; Mueller, K. T.; Cui, Y.; Shao, Y.; Liu, J. Non-Encapsulation Approach for High-Performance Li–S Batteries through Controlled Nucleation and Growth. *Nat. Energy* **2017**, *2* (10), 813–820.

(207) Han, J.; Xi, B.; Feng, Z.; Ma, X.; Zhang, J.; Xiong, S.; Qian, Y. Sulfur–Hydrazine Hydrate-Based Chemical Synthesis of Sulfur@graphene Composite for Lithium–Sulfur Batteries. *Inorg. Chem. Front.* **2018**, *5* (4), 785–792.

(208) Chen, H.; Wang, C.; Dong, W.; Lu, W.; Du, Z.; Chen, L. Monodispersed Sulfur Nanoparticles for Lithium–Sulfur Batteries with Theoretical Performance. *Nano Lett.* **2015**, *15* (1), 798–802.

(209) Wang, C.; Chen, H.; Dong, W.; Ge, J.; Lu, W.; Wu, X.; Guo, L.; Chen, L. Sulfur–Amine Chemistry-Based Synthesis of Multi-Walled Carbon Nanotube–Sulfur Composites for High Performance Li–S Batteries. *Chem. Commun.* **2014**, *50* (10), 1202–1204.

(210) Steudel, R. Aqueous Sulfur Sols. In *Elemental Sulfur and Sulfur-Rich Compounds I. Topics in Current Chemistry*; Steudel, R., Ed.; Springer, Berlin, Heidelberg, 2003; pp 153–166.

(211) Steudel, R.; Göbel, T.; Holdt, G. The Molecular Composition of Hydrophilic Sulfur Sols Prepared by Acid Decomposition of Thiosulfate [1]. *Zeitschrift für Naturforsch. B* **1988**, *43* (2), 203–218.

(212) von Weimarn, P. P.; Malyschew, B. W. Etne Einfachste Methode Zur Darstellung Yon P, S, Se Und Te in Kolloldem Zustand. *Kolloid-Z* **1911**, *8*, 216.

(213) von Weimarn, P. P. *Kolloid- chem. Beihefte* **1926**, *22*, 38.

(214) Ghosh, D.; Gad, M.; Lau, I.; Pope, M. A. Trapping and Redistribution of Hydrophobic Sulfur Sols in Graphene-Polyethyleneimine Networks for Stable Li-S Cathodes. *Adv. Energy Mater.* **2018**, *8* (27), 1801979.

(215) Deng, N.; Kang, W.; Liu, Y.; Ju, J.; Wu, D.; Li, L.; Samman, B.; Cheng, B. A Review on Separators for Lithium-Sulfur Battery: Progress and Prospects. *J. Power Sources* **2016**, *331*, 132–155.

(216) Liang, X.; Liu, Y.; Wen, Z.; Huang, L.; Wang, X.; Zhang, H. A Nano-Structured and Highly Ordered Polypyrrole-Sulfur Cathode for Lithium-Sulfur Batteries. *J. Power Sources* **2011**, *196* (16), 6951–6955.

(217) Deng, Y.; Xu, H.; Bai, Z.; Huang, B.; Su, J.; Chen, G. Durable Polydopamine-Coated Porous Sulfur Core-Shell Cathode for High Performance Lithium-Sulfur Batteries. *J. Power Sources* **2015**, *300*, 386–394.

(218) Liu, J.; Nara, H.; Yokoshima, T.; Momma, T.; Osaka, T. Li_2S Cathode Modified with Polyvinylpyrrolidone and Mechanical Milling with Carbon. *J. Power Sources* **2015**, *273*, 1136–1141.

(219) Nishi, Y. The Dawn of Lithium-Ion Batteries. *Electrochem. Soc. Interface* **2016**, *25* (3), 71–74.

(220) Schueller, O. J. A.; Brittain, S. T.; Marzolin, C.; Whitesides, G. M. Fabrication and Characterization of Glassy Carbon MEMS. *Chem. Mater.* **1997**, *9* (6), 1399–1406.

(221) Joo, S. H.; Choi, S. J.; Oh, I.; Kwak, J.; Liu, Z.; Terasaki, O.; Ryoo, R. Ordered Nanoporous Arrays of Carbon Supporting High Dispersions of Platinum Nanoparticles. *Nature* **2001**, *412*, 169–172.

(222) Kelly, T. L.; Gao, T.; Sailor, M. J. Carbon and Carbon/Silicon Composites Templated in Rugate Filters for the Adsorption and Detection of Organic Vapors. *Adv. Mater.* **2011**, *23*, 1776–1781.

(223) He, L.; Li, D.; Zhang, G.; Webley, P. A.; Zhao, D.; Wang, H. Synthesis of Carbonaceous Poly(Furfuryl Alcohol) Membrane for Water Desalination. *Ind. Eng. Chem. Res.* **2010**, *49* (9), 4175–4180.

(224) Song, C.; Wang, T.; Jiang, H.; Wang, X.; Cao, Y.; Qiu, J. Gas Separation Performance of C/CMS Membranes Derived from Poly(Furfuryl Alcohol) (PFA) with Different Chemical Structure. *J. Memb. Sci.* **2010**, *361* (1–2), 22–27.

(225) Pranger, L.; Tannenbaum, R. Biobased Nanocomposites Prepared by In Situ Polymerization of Furfuryl Alcohol with Cellulose Whiskers or Montmorillonite Clay. *Macromolecules* **2008**, *41* (22), 8682–8687.

(226) Ling, H. Y.; Su, Z.; Chen, H.; Hencz, L.; Zhang, M.; Tang, Y.; Zhang, S. Biomass-Derived Poly(Furfuryl Alcohol)–Protected Aluminum Anode for Lithium-Ion Batteries. *Energy Technol.* **2019**, 1800995.

(227) Zhu, J.; Childress, A. S.; Karakaya, M.; Dandeliya, S.; Srivastava, A.; Lin, Y.; Rao, A. M.; Podila, R. Defect-Engineered Graphene for High-Energy- and High- Power-Density Supercapacitor Devices. *Adv. Mater.* **2016**, *28*, 7185–7192.

(228) Chen, J.; Han, Y.; Kong, X.; Deng, X.; Park, H. J.; Guo, Y.; Jin, S.; Qi, Z.; Lee, Z.; Qiao, Z.; Ruoff, R. S.; Ji, H. The Origin of Improved Electrical Double-Layer Capacitance by Inclusion of Topological Defects and Dopants in Graphene for Supercapacitors. *Angew. Chem. Int. Ed.* **2016**, *55*, 13822–13827.

(229) Irisarri, E.; Ponrouch, A.; Palacin, M. R. Hard Carbon Negative Electrode Materials for Sodium-Ion Batteries. *J. Electrochem. Soc.* **2015**, *162* (14), A2476–A2482.

(230) Yao, J.; Wang, H.; Liu, J.; Chan, K.-Y. Y.; Zhang, L.; Xu, N. Preparation of Colloidal Microporous Carbon Spheres from Furfuryl Alcohol. *Carbon* **2005**, *43* (8), 1709–1715.

(231) Ferrari, A. C.; Robertson, J. Interpretation of Raman Spectra of Disordered and Amorphous Carbon. *Phys. Rev. B* **2000**, *61* (20), 14095–14107.

(232) Szczurek, A.; Fierro, V.; Thébault, M.; Pizzi, A.; Celzard, A. Structure and Properties of Poly(Furfuryl Alcohol)-Tannin PolyHIPEs. *Eur. Polym. J.* **2016**, *78*, 195–212.

(233) Burket, C. L.; Rajagopalan, R.; Marencic, A. P.; Dronvajjala, K.; Foley, H. C. Genesis of Porosity in Polyfurfuryl Alcohol Derived Nanoporous Carbon. *Carbon* **2006**, *44*, 2957–2963.

(234) Bertarione, S.; Bonino, F.; Cesano, F.; Jain, S.; Zanetti, M.; Scarano, D.; Zecchina, A. Micro-FTIR and Micro-Raman Studies of a Carbon Film Prepared from Furfuryl Alcohol Polymerization. *J. Phys. Chem. B* **2009**, *113* (31), 10571–10574.

(235) Choura, M.; Belgacem, N. M.; Gandini, A. Acid-Catalyzed Polycondensation of Furfuryl Alcohol: Mechanisms of Chromophore Formation and Cross-Linking. *Macromolecules* **1996**, *29* (11), 3839–3850.

(236) Ferrari, A. C.; Meyer, J. C.; Scardaci, V.; Casiraghi, C.; Lazzeri, M.; Mauri, F.; Piscanec, S.; Jiang, D.; Novoselov, K. S.; Roth, S.; Geim, A. K. Raman Spectrum of Graphene and Graphene Layers. *Phys. Rev. Lett.* **2006**, *97*, 187401.

(237) Holmberg, P.; Fokine, M. Thermometric Study of CO_2-Laser Heated Optical Fibers in Excess of 1700°C Using Fiber Bragg Gratings. *J. Opt. Soc. Am. B* **2013**, *30* (7), 1835.

(238) Kandola, B. K.; Horrocks, A. R. Complex Char Formation in Flame-Retarded Fibre-Intumescent Combinations -- II. Thermal Analytical Studies. *Polym. Degrad. Stab.* **1996**, *54* (2-3), 289–303.

(239) Bao, C.; Guo, Y.; Yuan, B.; Hu, Y.; Song, L. Functionalized Graphene Oxide for Fire Safety Applications of Polymers: A Combination of Condensed Phase Flame Retardant Strategies. *J. Mater. Chem.* **2012**, *22* (43), 23057–23063.

(240) Wicklein, B.; Kocjan, A.; Salazar-Alvarez, G.; Carosio, F.; Camino, G.; Antonietti, M.; Bergström, L. Thermally Insulating and Fire-Retardant Lightweight Anisotropic Foams Based on Nanocellulose and Graphene Oxide. *Nat. Nanotechnol.* **2015**, *10* (3), 277–283.

(241) Lee, Y. R.; Kim, S. C.; Lee, H.; Jeong, H. M.; Raghu, A. V; Reddy, K. R.; Kim, B. K. Graphite Oxides as Effective Fire Retardants of Epoxy Resin. *Macromol. Res.* **2011**, *19* (1), 66–71.

(242) Higginbotham, A. L.; Lomeda, J. R.; Morgan, A. B.; Tour, J. M. Graphite Oxide Flame-Retardant Polymer Nanocomposites. *ACS Appl. Mater. Interfaces* **2009**, *1*, 2256–2261.

(243) Bae, J. J.; Yoon, J. H.; Jeong, S.; Moon, B. H.; Han, J. T.; Jeong, H. J.; Lee, G.; Hwang, H. R.; Lee, Y. H.; Jeong, S. Y.; Lim, S. C. Sensitive Photo-Thermal Response of Graphene Oxide for Mid-Infrared Detection. *Nanoscale* **2015**, *7*, 15695–15700.

(244) Bhattacharjya, D.; Kim, C.; Kim, J.; You, I.; In, J. Bin; Lee, S.-M. Fast and Controllable Reduction of Graphene Oxide by Low-Cost CO_2 Laser for Supercapacitor Application. *Appl. Surf. Sci.* **2018**, *462*, 353–361.

(245) Krishnan, D.; Kim, F.; Luo, J.; Cruz-Silva, R.; Cote, L. J.; Jang, H. D.; Huang, J. Energetic Graphene Oxide: Challenges and Opportunities. *Nano Today* **2012**, *7*, 137–152.

(246) Qiu, Y.; Guo, F.; Hurt, R.; Külaots, I. Explosive Thermal Reduction of Graphene Oxide-Based Materials: Mechanism and Safety Implications. *Carbon* **2014**, *72*, 215–223.

(247) Krishnan, D.; Raidongia, K.; Shao, J.; Huang, J. Graphene Oxide Assisted Hydrothermal Carbonization of Carbon Hydrates. *ACS Nano* **2014**, *8* (1), 449–457.

(248) Shtein, M.; Nadiv, R.; Buzaglo, M.; Kahil, K.; Regev, O. Thermally Conductive Graphene-Polymer Composites: Size, Percolation, and Synergy Effects. *Chem. Mater.* **2015**, *27* (6), 2100–2106.

(249) Li, A.; Zhang, C.; Zhang, Y.-F. Thermal Conductivity of Graphene-Polymer Composites: Mechanisms, Properties, and Applications. *Polymers* **2017**, *9*, 437.

(250) Slopiecka, K.; Bartocci, P.; Fantozzi, F. Thermogravimetric Analysis and Kinetic Study of Poplar Wood Pyrolysis. *Appl. Energy* **2012**, *97*, 491–497.

(251) Williams, P. T.; Besler, S. Pyrolysis - Thermogravimetric Analysis of Tyres and Tyre Components. *Fuel* **1995**, *74* (9), 1277–1283.

(252) Comesaña, R.; Gómez, M. A.; Álvarez, M. A.; Eguía, P. Thermal Lag Analysis on a Simulated TGA-DSC Device. *Thermochim. Acta* **2012**, *547*, 13–21.

(253) Gracia-Fernández, C.; Álvarez-García, B.; Gómez-Barreiro, S.; López-Beceiro, J.; Artiaga, R. Significant Hidden Temperature Gradients in Thermogravimetric Tests. *Polym. Test.* **2018**, *68*, 388–394.

(254) Beckert, M.; Menzel, M.; Tölle, F. J.; Bruchmann, B.; Mülhaupt, R. Nitrogenated Graphene and Carbon Nanomaterials by Carbonization of Polyfurfuryl Alcohol in the Presence of Urea and Dicyandiamide. *Green Chem.* **2015**, *17* (2), 1032–1037.

(255) Liu, X.; Kang, J.; Dai, Y.; Dong, C.; Guo, X.; Jia, X. Graphene-Like Nitrogen-Doped Carbon Nanosheet Prepared from Direct Calcination of Dopamine Confined by g-C_3N_4 for Oxygen Reduction. *Adv. Mater. Interfaces* **2018**, *5*, 1800303.

(256) Hu, C.; Zhou, Y.; Ma, R.; Liu, Q.; Wang, J. Reactive Template Synthesis of Nitrogen-Doped Graphene-like Carbon Nanosheets Derived from Hydroxypropyl Methylcellulose and Dicyandiamide as Efficient Oxygen Reduction Electrocatalysts. *J. Power Sources* **2017**, *345*, 120–130.

(257) Gu, D.; Zhou, Y.; Ma, R.; Wang, F.; Liu, Q.; Wang, J. Facile Synthesis of N-Doped Graphene-Like Carbon Nanoflakes as Efficient and Stable Electrocatalysts for the Oxygen Reduction Reaction. *Nano-Micro Lett.* **2018**, *10*, 29.

(258) Thekkekara, L. V; Chen, X.; Gu, M. Two-Photon-Induced Stretchable Graphene Supercapacitors. *Sci. Rep.* **2018**, *8*, 11722.

(259) Lamberti, A.; Clerici, F.; Fontana, M.; Scaltrito, L. A Highly Stretchable Supercapacitor Using Laser-Induced Graphene Electrodes onto Elastomeric Substrate. *Adv. Energy Mater.* **2016**, *6*, 1600050.

(260) Hawes, G. F.; Yilman, D.; Noremberg, B. S.; Pope, M. A. Supercapacitors Fabricated via

Laser-Induced Carbonization of Biomass-Derived Poly(Furfuryl Alcohol)/Graphene Oxide Composites. *ACS Appl. Nano Mater.* **2019**, *2* (10), 6312–6324.

(261) Mullins, M. J.; Liu, D.; Sue, H.-J. Mechanical Properties of Thermosets. In *Thermosets*; Elsevier, 2012; pp 28–61.

(262) Qu, C.; Hu, J.; Liu, X.; Li, Z.; Ding, Y. Morphology and Mechanical Properties of Polyimide Films: The Effects of UV Irradiation on Microscale Surface. *Materials* **2017**, *10* (11), 1329.

(263) Ma, C. -C M.; Goang, D. Y.; Han, J. L.; Hsieh, K. H. Interpenetrating Polymer Networks of Polyurethane and Furfuryl Alcohol, I. Morphology and mechanical properties. *Die Angew. Makromol. Chemie* **1994**, *214*, 39–56.

(264) Kherroub, D. E.; Belbachir, M.; Lamouri, S. Synthesis of Poly(Furfuryl Alcohol)/Montmorillonite Nanocomposites by Direct in-Situ Polymerization. *Bull. Mater. Sci.* **2015**, *38* (1), 57–63.

(265) Hayashi, J.; Kazehaya, A.; Muroyama, K.; Watkinson, A. P. Preparation of Activated Carbon from Lignin by Chemical Activation. *Carbon* **2000**, *38* (13), 1873–1878.

(266) Li, J.; Li, X.; Han, G.; Liu, C.; Wang, X. Salt-Template Hydrothermal Carbonization for Pd NP- Loaded Porous Carbonaceous Material. **2019**, *14* (2), 3630–3650.

(267) Shen, Y.; Linnow, K.; Steiger, M. Crystallization Behavior and Damage Potential of Na_2SO_4–NaCl Mixtures in Porous Building Materials. *Cryst. Growth Des.* **2020**, *20* (9), 5974–5985.

(268) Wei, Z. F.; Zhang, Y. H.; Zhao, L. J.; Liu, J. H.; Li, X. H. Observation of the First Hydration Layer of Isolated Cations and Anions through the FTIR-ATR Difference Spectra. *J. Phys. Chem. A* **2005**, *109* (7), 1337–1342.

(269) Rodriguez-Navarro, C.; Doehne, E.; Sebastian, E. How Does Sodium Sulfate Crystallize? Implications for the Decay and Testing of Building Materials. *Cem. Concr. Res.* **2000**, *30* (10), 1527–1534.

(270) Swanson, H. E.; McMurdie, H. F.; Morris, M. C.; Evans, E. H.; Paretzkin, B. *Standard X-Ray Diffraction Powder Patterns, National Bureau of Standards*; 1974.

(271) Wu, J. Bin; Lin, M. L.; Cong, X.; Liu, H. N.; Tan, P. H. Raman Spectroscopy of Graphene-Based Materials and Its Applications in Related Devices. *Chem. Soc. Rev.* **2018**, *47* (5), 1822–

1873.

(272) Karimi, G.; Lau, I.; Fowler, M.; Pope, M. Parametric Study of Laser-induced Graphene Conductive Traces and Their Application as Flexible Heaters. *Int. J. Energy Res.* **2021**, *45* (9), 13712–13725.

(273) Ming, J.; Wu, Y.; Liang, G.; Park, J.-B.; Zhao, F.; Sun, Y.-K. Sodium Salt Effect on Hydrothermal Carbonization of Biomass: A Catalyst for Carbon-Based Nanostructured Materials for Lithium-Ion Battery Applications. *Green Chem.* **2013**, *15* (10), 2722.

(274) Yoon, H.; Nah, J.; Kim, H.; Ko, S.; Sharifuzzaman, M.; Barman, S. C.; Xuan, X.; Kim, J.; Park, J. Y. A Chemically Modified Laser-Induced Porous Graphene Based Flexible and Ultrasensitive Electrochemical Biosensor for Sweat Glucose Detection. *Sensors Actuators B Chem.* **2020**, *311*, 127866.

(275) Zhang, X.; Schiros, T.; Nordlund, D.; Shin, Y. C.; Kong, J.; Dresselhaus, M.; Palacios, T. X-Ray Spectroscopic Investigation of Chlorinated Graphene: Surface Structure and Electronic Effects. *Adv. Funct. Mater.* **2015**, *25* (26), 4163–4169.

(276) Abdul Razzaq, A.; Yao, Y.; Shah, R.; Qi, P.; Miao, L.; Chen, M.; Zhao, X.; Peng, Y.; Deng, Z. High-Performance Lithium Sulfur Batteries Enabled by a Synergy between Sulfur and Carbon Nanotubes. *Energy Storage Mater.* **2019**, *16* (March 2018), 194–202.

(277) Bagri, A.; Mattevi, C.; Acik, M.; Chabal, Y. J.; Chhowalla, M.; Shenoy, V. B. Structural Evolution during the Reduction of Chemically Derived Graphene Oxide. *Nat. Chem.* **2010**, *2* (7), 581–587.

(278) Wahlqvist, M.; Shchukarev, A. XPS Spectra and Electronic Structure of Group IA Sulfates. *J. Electron Spectros. Relat. Phenomena* **2007**, *156–158*, 310–314.

(279) Yang, Z.; Dai, Y.; Wang, S.; Yu, J. In Situ Incorporation of a S, N Doped Carbon/Sulfur Composite for Lithium Sulfur Batteries. *RSC Adv.* **2015**, *5*, 78017–78025.

(280) Lin, Y. C.; Chen, Y. Y.; Yu, B. Y.; Lin, W. C.; Kuo, C. H.; Shyue, J. J. Sputter-Induced Chemical Transformation in Oxoanions by Combination of C_{60}^{+} and Ar^{+} Ion Beams Analyzed with X-Ray Photoelectron Spectrometry. *Analyst* **2009**, *134* (5), 945–951.

(281) Kakaei, K.; Hamidi, M.; Husseindoost, S. Chlorine-Doped Reduced Graphene Oxide

Nanosheets as an Efficient and Stable Electrode for Supercapacitor in Acidic Medium. *J. Colloid Interface Sci.* **2016**, *479*, 121–126.

(282) Arvas, M. B.; Gürsu, H.; Gencten, M.; Sahin, Y. Preparation of Different Heteroatom Doped Graphene Oxide Based Electrodes by Electrochemical Method and Their Supercapacitor Applications. *J. Energy Storage* **2021**, *35*, 102328.

(283) Chen, X.; Chen, X.; Xu, X.; Yang, Z.; Liu, Z.; Zhang, L.; Xu, X.; Chen, Y.; Huang, S. Sulfur-Doped Porous Reduced Graphene Oxide Hollow Nanosphere Frameworks as Metal-Free Electrocatalysts for Oxygen Reduction Reaction and as Supercapacitor Electrode Materials. *Nanoscale* **2014**, *6* (22), 13740–13747.

(284) McCrory, C. C. L.; Jung, S.; Ferrer, I. M.; Chatman, S. M.; Peters, J. C.; Jaramillo, T. F. Benchmarking Hydrogen Evolving Reaction and Oxygen Evolving Reaction Electrocatalysts for Solar Water Splitting Devices. *J. Am. Chem. Soc.* **2015**, *137* (13), 4347–4357.

(285) Ai, C.; Chernyshova, I. V.; Gawron, E. L.; Ponnurangam, S.; Birss, V. I. Electrochemistry of New Generation Conformal Polyaniline/Carbon Scaffolds with Monodispersed Nanopores and High Capacitance. *J. Mater. Chem. C* **2022**, *10* (6), 2271–2280.

(286) Valipour, A.; Hamnabard, N.; Meshkati, S. M. H.; Pakan, M.; Ahn, Y. Effectiveness of Phase- and Morphology-Controlled MnO_2 Nanomaterials Derived from Flower-like δ-MnO_2 as Alternative Cathode Catalyst in Microbial Fuel Cells. *Dalt. Trans.* **2019**, *48* (16), 5429–5443.

(287) Avval, T. G.; Cushman, C. V.; Bahr, S.; Dietrich, P.; Meyer, M.; Thißen, A.; Linford, M. R. Dimethyl Sulfoxide by Near-Ambient Pressure XPS. *Surf. Sci. Spectra* **2019**, *26* (1), 014020.

(288) Wood, K. N.; Noked, M.; Dasgupta, N. P. Lithium Metal Anodes: Toward an Improved Understanding of Coupled Morphological, Electrochemical, and Mechanical Behavior. *ACS Energy Lett.* **2017**, *2* (3), 664–672.

(289) Mohammadi, A.; Monconduit, L.; Stievano, L.; Younesi, R. Measuring the Nucleation Overpotential in Lithium Metal Batteries: Never Forget the Counter Electrode! *J. Electrochem. Soc.* **2022**, *169* (7), 070509.

(290) Shi, F.; Pei, A.; Vailionis, A.; Xie, J.; Liu, B.; Zhao, J.; Gong, Y.; Cui, Y. Strong Texturing of Lithium Metal in Batteries. *Proc. Natl. Acad. Sci.* **2017**, *114* (46), 12138–12143.

(291) Liu, H.; Cheng, X.-B.; Jin, Z.; Zhang, R.; Wang, G.; Chen, L.-Q.; Liu, Q.-B.; Huang, J.-Q.; Zhang, Q. Recent Advances in Understanding Dendrite Growth on Alkali Metal Anodes. *EnergyChem* **2019**, *1* (1), 100003.

(292) Zheng, J.; Kim, M. S.; Tu, Z.; Choudhury, S.; Tang, T.; Archer, L. A. Regulating Electrodeposition Morphology of Lithium: Towards Commercially Relevant Secondary Li Metal Batteries. *Chem. Soc. Rev.* **2020**, *49* (9), 2701–2750.

(293) Li, S.; Jiang, M.; Xie, Y.; Xu, H.; Jia, J.; Li, J. Developing High-Performance Lithium Metal Anode in Liquid Electrolytes: Challenges and Progress. *Adv. Mater.* **2018**, *30* (17), 1706375.

(294) Guan, X.; Wang, A.; Liu, S.; Li, G.; Liang, F.; Yang, Y.-W.; Liu, X.; Luo, J. Controlling Nucleation in Lithium Metal Anodes. *Small* **2018**, *14* (37), 1801423.

(295) Monroe, C.; Newman, J. The Effect of Interfacial Deformation on Electrodeposition Kinetics. *J. Electrochem. Soc.* **2004**, *151* (6), A880.

(296) Badeda, J.; Huck, M.; Sauer, D. U.; Kabzinski, J.; Wirth, J. Basics of Lead–Acid Battery Modelling and Simulation. In *Lead-Acid Batteries for Future Automobiles*; Elsevier, 2017; pp 463–507.

(297) Heinritz, A.; Binninger, T.; Patru, A.; Schmidt, T. J. Asymmetric Butler–Volmer Kinetics of the Electrochemical Ce(III)/Ce(IV) Redox Couple on Polycrystalline Au Electrodes in Sulfuric Acid and the Dissociation Field Effect. *ACS Catal.* **2021**, *11* (13), 8140–8154.

(298) Boyle, D. T.; Kong, X.; Pei, A.; Rudnicki, P. E.; Shi, F.; Huang, W.; Bao, Z.; Qin, J.; Cui, Y. Transient Voltammetry with Ultramicroelectrodes Reveals the Electron Transfer Kinetics of Lithium Metal Anodes. *ACS Energy Lett.* **2020**, *5* (3), 701–709.

(299) Buiel, E.; Dahn, J. R. Li-Insertion in Hard Carbon Anode Materials for Li-Ion Batteries. *Electrochim. Acta* **1999**, *45* (1), 121–130.

(300) Manthiram, A.; Fu, Y.; Chung, S.; Zu, C.; Su, Y. Rechargeable Lithium–Sulfur Batteries. *Chem. Rev.* **2014**, *114* (23), 11751–11787.

(301) Pang, Q.; Liang, X.; Kwok, C. Y.; Nazar, L. F. Advances in Lithium–Sulfur Batteries Based on Multifunctional Cathodes and Electrolytes. *Nat. Energy* **2016**, *1* (9), 16132.

(302) Hsieh, A. G.; Punckt, C.; Korkut, S.; Aksay, I. A. Adsorption of Sodium Dodecyl Sulfate on

Functionalized Graphene Measured by Conductometric Titration. *J. Phys. Chem. B* **2013**, *117* (26), 7950–7958.

(303) Voorhees, P. W. The Theory of Ostwald Ripening. *J. Stat. Phys.* **1985**, *38* (1–2), 231–252.

(304) Fan, X.; Zhang, Y.; Li, J.; Yang, K.; Liang, Z.; Chen, Y.; Zhao, C.; Zhang, Z.; Mai, K. A General Dissolution–Recrystallization Strategy to Achieve Sulfur-Encapsulated Carbon for an Advanced Lithium–Sulfur Battery. *J. Mater. Chem. A* **2018**, *6* (25), 11664–11669.

(305) Kaban, I.; Nowak, R.; Bruzda, G.; Xi, L.; Sobczak, N.; Eckert, J.; Giebeler, L. Wettability and Work of Adhesion of Liquid Sulfur on Carbon Materials for Electrical Energy Storage Applications. *Carbon* **2016**, *98*, 702–707.

(306) Fu, Y.; Manthiram, A. Orthorhombic Bipyramidal Sulfur Coated with Polypyrrole Nanolayers As a Cathode Material for Lithium–Sulfur Batteries. *J. Phys. Chem. C* **2012**, *116* (16), 8910–8915.

(307) Smeraldi, J.; Ganesh, R.; Safarik, J.; Rosso, D. Statistical Evaluation of Photon Count Rate Data for Nanoscale Particle Measurement in Wastewaters. *J. Environ. Monit.* **2012**, *14* (1), 79–84.

(308) Garcia, A. A.; Druschel, G. K. Elemental Sulfur Coarsening Kinetics. *Geochem. Trans.* **2014**, *15* (1), 11.

(309) Kuczyńska-Zemła, D.; Kwaśniak, P.; Sotniczuk, A.; Spychalski, M.; Wieciński, P.; Zdunek, J.; Ostrowski, R.; Garbacz, H. Microstructure and Mechanical Properties of Titanium Subjected to Direct Laser Interference Lithography. *Surf. Coatings Technol.* **2019**, *364*, 422–429.

(310) Eckert, B.; Steudel, R. Molecular Spectra of Sulfur Molecules and Solid Sulfur Allotropes. In *Elemental Sulfur und Sulfur-Rich Compounds II. Topics in Current Chemistry*; Steudel, R., Ed.; Springer, Berlin, Heidelberg, 2003; pp 31–98.

(311) McAllister, M. J.; Li, J.; Adamson, D. H.; Schniepp, H. C.; Abdala, A. A.; Liu, J.; Herrera-Alonso, M.; Milius, D. L.; Car, R.; Prud'homme, R. K.; Aksay, I. A. Single Sheet Functionalized Graphene by Oxidation and Thermal Expansion of Graphite. *Chem. Mater.* **2007**, *19* (18), 4396–4404.

(312) Kim, M. S.; Kim, M. S.; Do, V.; Lim, Y. R.; Nah, I. W.; Archer, L. A.; Cho, W. Il. Designing Solid-Electrolyte Interphases for Lithium Sulfur Electrodes Using Ionic Shields. *Nano Energy* **2017**, *41*, 573–582.

(313) He, J.; Manthiram, A. 3D CoSe@C Aerogel as a Host for Dendrite-Free Lithium-Metal Anode and Efficient Sulfur Cathode in Li–S Full Cells. *Adv. Energy Mater.* **2020**, *10* (41), 2002654.

(314) Li, H.; Chao, D.; Chen, B.; Chen, X.; Chuah, C.; Tang, Y.; Jiao, Y.; Jaroniec, M.; Qiao, S.-Z. Z. Revealing Principles for Design of Lean-Electrolyte Lithium Metal Anode via in Situ Spectroscopy. *J. Am. Chem. Soc.* **2020**, *142* (4), 2012–2022.

(315) Gao, Y.; Yan, Z.; Gray, J. L.; He, X.; Wang, D. D.; Chen, T.; Huang, Q.; Li, Y. C.; Wang, H.; Kim, S. H.; Mallouk, T. E.; Wang, D. D. Polymer–Inorganic Solid–Electrolyte Interphase for Stable Lithium Metal Batteries under Lean Electrolyte Conditions. *Nat. Mater.* **2019**, *18* (4), 384–389.

(316) Nanda, S.; Bhargav, A.; Manthiram, A. Anode-Free, Lean-Electrolyte Lithium-Sulfur Batteries Enabled by Tellurium-Stabilized Lithium Deposition. *Joule* **2020**, *4* (5), 1121–1135.

(317) Jiang, W.; Yin, L.; Chen, H.; Paschall, A. V.; Zhang, L.; Fu, W.; Zhang, W.; Todd, T.; Yu, K. S.; Zhou, S.; Zhen, Z.; Butler, M.; Yao, L.; Zhang, F.; Shen, Y.; Li, Z.; Yin, A.; Yin, H.; Wang, X.; et al. NaCl Nanoparticles as a Cancer Therapeutic. *Adv. Mater.* **2019**, *31* (46), 1904058.

(318) Kim, K. Y.; Choi, H.; Tran, C. Van; In, J. Bin. Simultaneous Densification and Nitrogen Doping of Laser-Induced Graphene by Duplicated Pyrolysis for Supercapacitor Applications. *J. Power Sources* **2019**, *441*, 227199.

(319) Li, L.; Zhang, J.; Peng, Z.; Li, Y.; Gao, C.; Ji, Y.; Ye, R.; Kim, N. D.; Zhong, Q.; Yang, Y.; Fei, H.; Ruan, G.; Tour, J. M. High-Performance Pseudocapacitive Microsupercapacitors from Laser-Induced Graphene. *Adv. Mater.* **2016**, *28*, 838–845.

(320) Peng, Z.; Jia, J.; Ding, H.; Yu, H.; Shen, Y.; Zhang, J.; Tao, W.; Zhang, C.; Wang, J.; Cheng, H. High-Energy All-in-One Micro-Supercapacitors Based on ZnO Mesoporous Nanosheet-Decorated Laser-Induced Porous Graphene Foams. *J. Mater. Res.* **2021**, *36* (9), 1927–1936.

(321) Zhang, C.; Peng, Z.; Huang, C.; Zhang, B.; Xing, C.; Chen, H.; Cheng, H.; Wang, J.; Tang, S. High-Energy All-in-One Stretchable Micro-Supercapacitor Arrays Based on 3D Laser-

Induced Graphene Foams Decorated with Mesoporous ZnP Nanosheets for Self-Powered Stretchable Systems. *Nano Energy* **2021**, *81*, 105609.

(322) Duy, L. X.; Peng, Z.; Li, Y.; Zhang, J.; Ji, Y.; Tour, J. M. Laser-Induced Graphene Fibers. *Carbon* **2018**, *126*, 472–479.

(323) Luong, D. X.; Subramanian, A. K.; Silva, G. A. L. L.; Yoon, J.; Cofer, S.; Yang, K.; Owuor, P. S.; Wang, T.; Wang, Z.; Lou, J.; Ajayan, P. M.; Tour, J. M. Laminated Object Manufacturing of 3D-Printed Laser-Induced Graphene Foams. *Adv. Mater.* **2018**, *30* (28), 1707416.

(324) Chu, T.; Park, S.; Fu, K. 3D Printing-Enabled Advanced Electrode Architecture Design. *Carbon Energy* **2021**, *3* (3), 424–439.

(325) Zhao, J.; Lu, H.; Zhang, Y.; Yu, S.; Malyi, O. I.; Zhao, X.; Wang, L.; Wang, H.; Peng, J.; Li, X.; Zhang, Y.; Chen, S.; Pan, H.; Xing, G.; Lu, C.; Tang, Y.; Chen, X. Direct Coherent Multi-Ink Printing of Fabric Supercapacitors. *Sci. Adv.* **2021**, *7* (3), 1–14.

(326) Tran, T. X.; Choi, H.; Che, C. H.; Sul, J. H.; Kim, I. G.; Lee, S. M.; Kim, J. H.; In, J. Bin. Laser-Induced Reduction of Graphene Oxide by Intensity-Modulated Line Beam for Supercapacitor Applications. *ACS Appl. Mater. Interfaces* **2018**, *10* (46), 39777–39784.

(327) Cai, J.; Lv, C.; Hu, C.; Luo, J.; Liu, S.; Song, J.; Shi, Y.; Chen, C.; Zhang, Z.; Ogawa, S.; Aoyagi, E.; Watanabe, A. Laser Direct Writing of Heteroatom-Doped Porous Carbon for High-Performance Micro-Supercapacitors. *Energy Storage Mater.* **2020**, *25*, 404–415.

(328) Parviz, D.; Irin, F.; Shah, S. A.; Das, S.; Sweeney, C. B.; Green, M. J. Challenges in Liquid-Phase Exfoliation, Processing, and Assembly of Pristine Graphene. *Adv. Mater.* **2016**, *28* (40), 8796–8818.

(329) Liao, J.; Ye, Z. Quaternary Ammonium Cationic Polymer as a Superior Bifunctional Binder for Lithium-Sulfur Batteries and Effects of Counter Anion. *Electrochim. Acta* **2018**, *259*, 626–636.

(330) Ling, M.; Yan, W.; Kawase, A.; Zhao, H.; Fu, Y.; Battaglia, V. S.; Liu, G. Electrostatic Polysulfides Confinement to Inhibit Redox Shuttle Process in the Lithium Sulfur Batteries. *ACS Appl. Mater. Interfaces* **2017**, *9* (37), 31741–31745.

(331) Wang, H.; Ling, M.; Bai, Y.; Chen, S.; Yuan, Y.; Liu, G.; Wu, C.; Wu, F. Cationic Polymer Binder Inhibit Shuttle Effects through Electrostatic Confinement in Lithium Sulfur Batteries. *J. Mater. Chem. A* **2018**, *6* (16), 6959–6966.

(332) Bird, R. B.; Stewart, W. E.; Lightfoot, E. N. *Transport Phenomena*, 2nd ed.; John Wiley & Sons, Inc., 2002.

(333) Laughton, M. A.; Say, M. G. *Electrical Engineer's Reference Book*, Fourteenth.; Butterworths: London, 2013.

(334) *"Physical Constants of Inorganic Compounds," in CRC Handbook of Chemistry and Physics*, 103rd Edit.; Rumble, J. R., Ed.; CRC Press/Taylor & Francis: Boca Raton, FL.

(335) Michael F. Ashby. Material Profiles. In *Materials and Design*; Elsevier, 2010; pp 194–249.

(336) *"Thermal Conductivity of Crystalline Dielectrics," in CRC Handbook of Chemistry and Physics*, 103rd Edit.; Rumble, J. R., Ed.; CRC Press/Taylor & Francis: Boca Raton, FL.

(337) Harald Mehling, L. F. C. *Heat and Cold Storage with PCM*; Mewes, D., Mayinger, F., Eds.; Springer, 2008.

(338) Pauselli, C.; Gola, G.; Ranalli, G.; Mancinelli, P.; Trippetta, F.; Ballirano, P.; Verdoya, M. Thermal Conductivity of Triassic Evaporites. *Geophys. J. Int.* **2021**, *227* (3), 1715–1729.

(339) Chase Jr., M. W. NIST-JANAF Thermochemical Tables, 4th Edition. *J. Phys. Chem. Ref. Data, Monogr. 9* **1998**, 1–1951.

(340) Alipoori, S.; Mazinani, S.; Aboutalebi, S. H.; Sharif, F. Review of PVA-Based Gel Polymer Electrolytes in Flexible Solid-State Supercapacitors: Opportunities and Challenges. *J. Energy Storage* **2020**, *27*, 101072.

(341) Ivanov, A. A. Electrical Conductivity of Aqueous Acids in Binary and Ternary Water-Electrolyte Systems. *Russ. J. Inorg. Chem.* **2008**, *53* (12), 1948–1963.

(342) Henrie, J.; Kellis, S.; Schultz, S. M.; Hawkins, A. Electronic Color Charts for Dielectric Films on Silicon. *Opt. Express* **2004**, *12* (7), 1464.

(343) Sasson, R.; Wright, R.; Arakawa, E. T. T.; Khare, B. N. N.; Sagan, C. Optical Properties of Solid and Liquid Sulfur at Visible and Infrared Wavelengths. *Icarus* **1985**, *64* (3), 368–374.

Appendix A:
Supplementary Information for Chapter 3

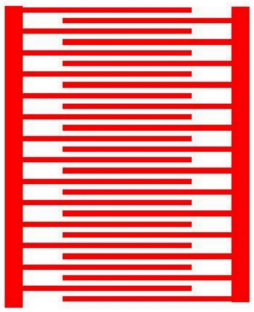

Figure A1: Illustration of microsupercapacitor electrode design. The full device is composed of 28 fingers, 14 on each electrode, with each finger being 1.5 cm in length and 350 μm in width with 450 μm of space between each other. The electrolyte is applied to a 1 cm wide region in the center, giving an active area of both electrodes of approximately 0.98 cm^2.

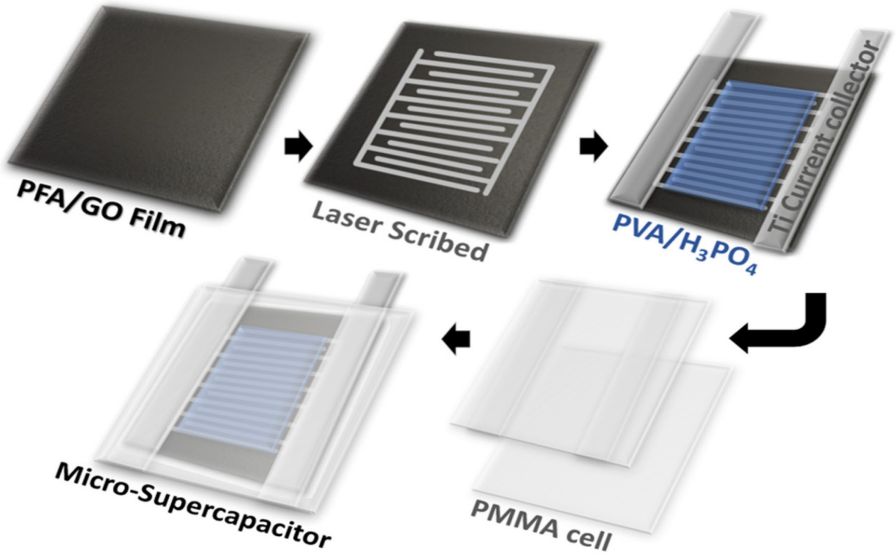

Figure A2: Scheme of microsupercapacitor fabrication and assembly procedure. PFA/GO composites are drop cast onto a PET substrate. Following drying/solidification of the polymer, the film is laser scribed to obtain the interdigitated electrode design. The gel-based PVA/H_3PO_4 electrolyte is then applied on the surface of the device, and a 24 hour rest period ensures wetting and penetration of the electrolyte into the pores of the material. The device is then assembled with titanium foil current collectors in a custom PMMA cell.

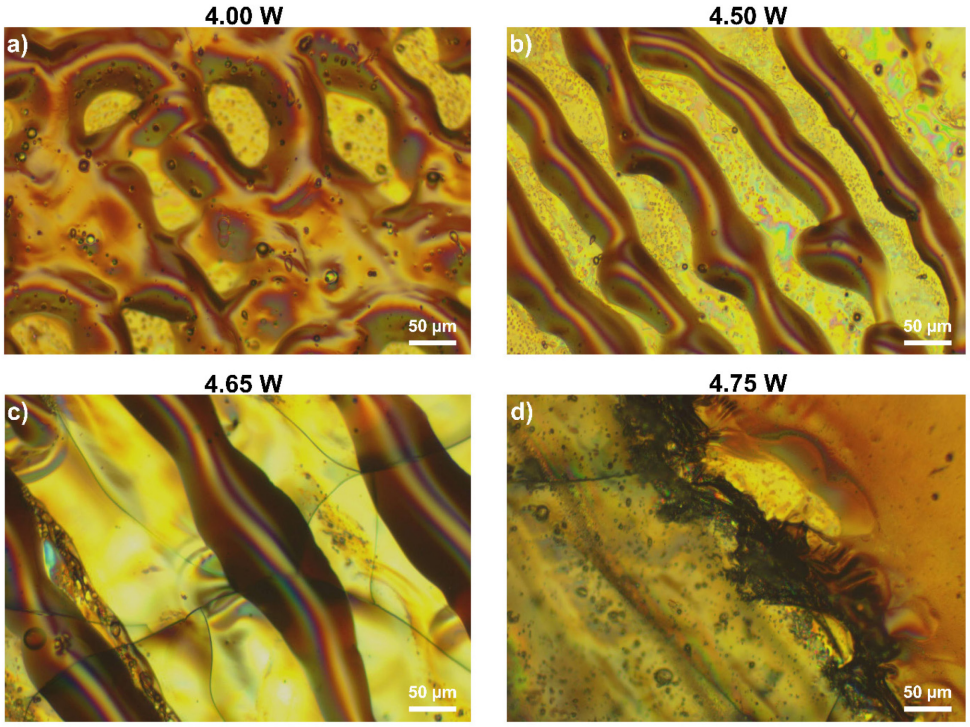

Figure A3: Optical microscopy images of the effect of laser power on PFA films spincoated on glass. All were scribed at 1 mm/s with a single laser pass. Yellow areas in a) and b) correspond to unconverted PFA, while brown areas correspond to the decomposition product. The yellow areas in c) correspond to bare glass substrate with PFA material ablated, along with cracks evident tin the substrate. The brown lines again correspond to decomposition product. In d), the black line marks the edge of the laser scribed material, with un-scribed PFA on the right side, and fully ablated PFA on the left.

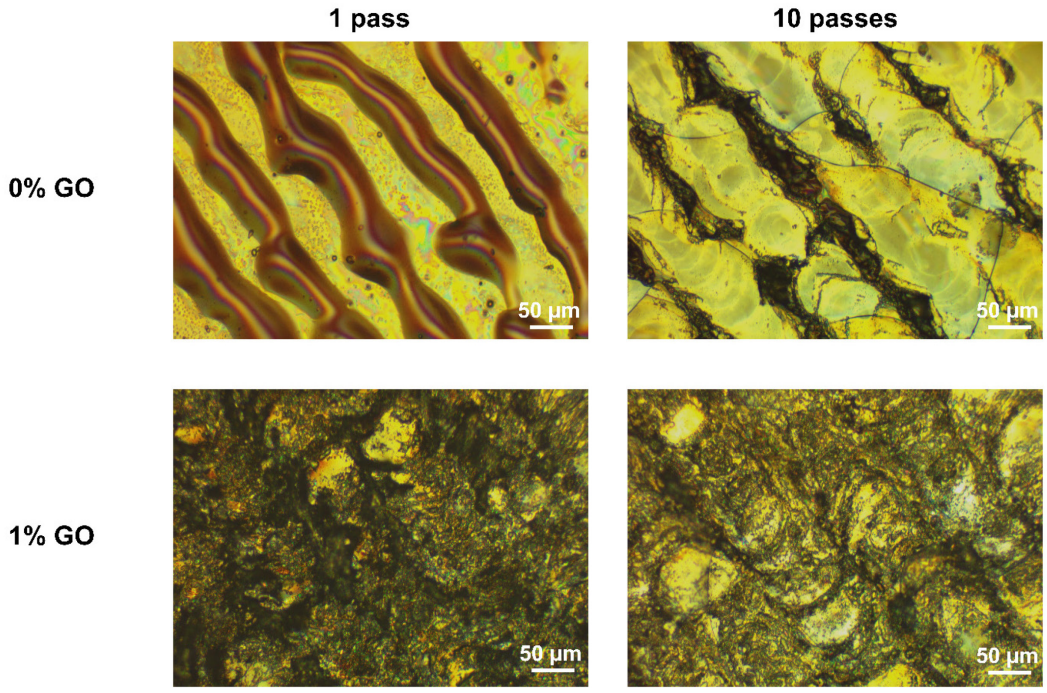

Figure A4: Optical microscopy images of the effect of multiple laser passes on PFA and PFA/1% GO films spincoated on glass. Laser scribing was performed at 4.5 W and 1 mm/s. Multiple laser passes of the PFA films with no GO result in disconnected black lines, with most material ablated, and no conductivity. The yellow areas for PFA/1 pass correspond to unconverted PFA, while the yellow areas for PFA/10 passes correspond to bare glass substrate where PFA has been ablated, as evidenced by the cracks in the glass substrate. Laser irradiation of films with 1% GO results in formation of a black, conductive product, for both 1 laser pass and 10 laser passes.

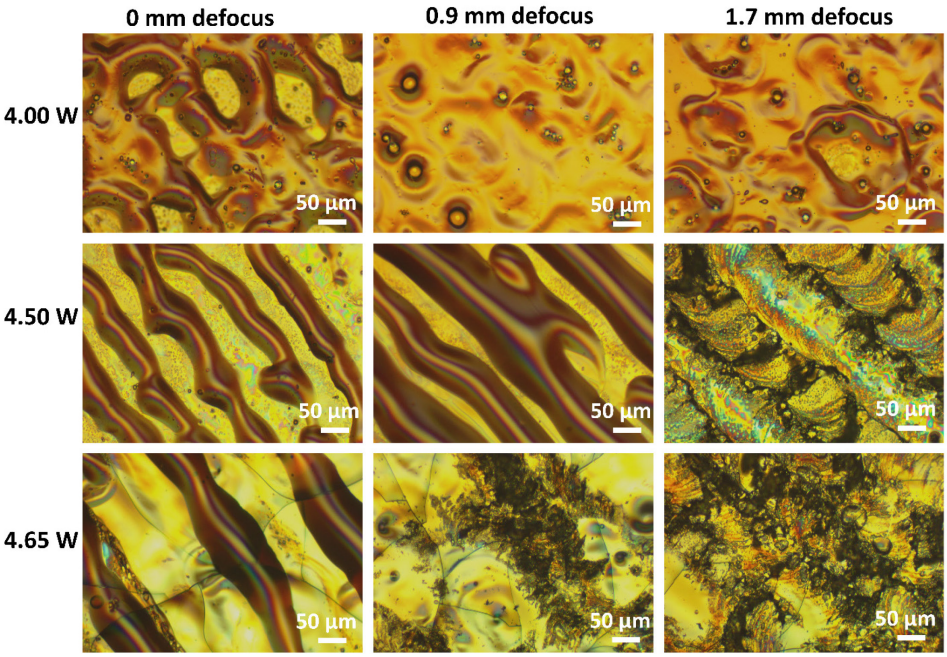

Figure A5: Optical microscopy images of the effect of laser defocusing on pure PFA films spin coated on glass. All films were scribed at 1 mm/s with a single laser pass. Brown areas in all films correspond to a decomposition product of PFA. Yellow areas at powers of 4.00 W and 4.50 W correspond to unconverted PFA, while yellow areas above 4.65 W correspond to bare glass substrate, where PFA has been ablated, as evidenced by the cracks in the glass substrate. Increasing the defocusing and the laser power enables a defocus of 1.7 mm and a laser power of 4.65 W to result in a black film. However, the film possesses poor conductivity, with most material ablated.

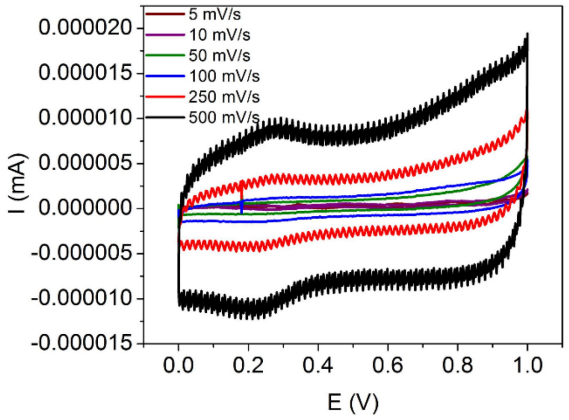

Figure A6: Cyclic voltammetry of supercapacitors prepared from PFA films laser scribed at 4.5 W, 10 mm/s, and a defocus of 1.7 mm with varying scan rates. The maximum currents achieved are in the nA range at 500 mV/s, and are too low and noisy to accurately calculate a specific capacitance. These electrochemical results indicate that there are no laser settings that enable the carbonization of PFA into a conductive material suitable for application as an electrode material for supercapacitors.

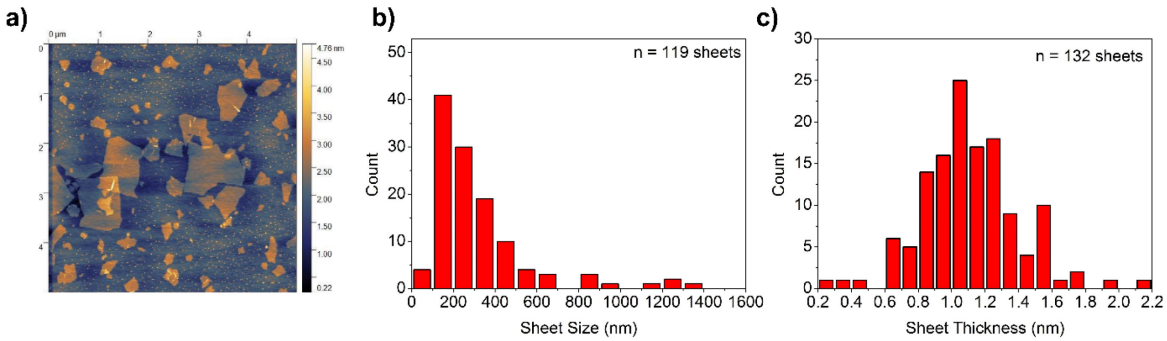

Figure A7: Atomic force microscopy (AFM) characterization of spincoated GO on mica substrate. a) AFM image of spincoated GO. b) Distribution of measured lateral GO sheet sizes. c) Distribution of measured GO sheet thicknesses. The GO sheets have an average thickness of 1.1 nm ± 0.3 nm, indicating that they have been exfoliated into monolayers in solution, and possess lateral flake sizes ranging from sub-100 nm to 1.4 micron.

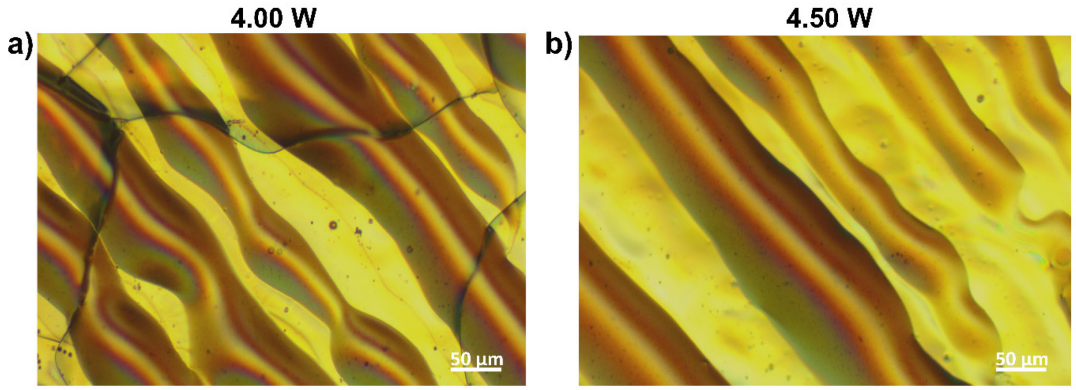

Figure A8: Optical microscopy images of the effect of laser power on PFA/0.1% GO films spincoated on glass. All were scribed at 1 mm/s with a single laser pass. At powers above 4.5 W, the film is ablated. The brown lines correspond to an insulating PFA decomposition product, while the yellow areas correspond to either unconverted or ablated PFA.

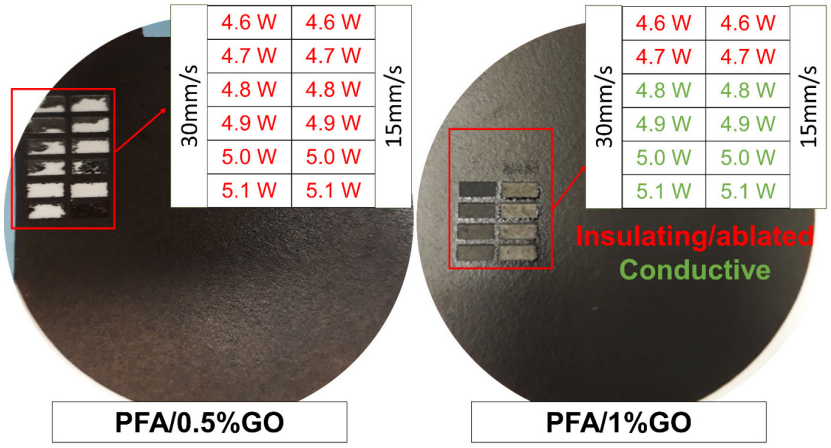

Figure A9: PFA/0.5% GO, and PFA/1% GO drop cast on cellulose substrates, and the effect of laser irradiation at powers ranging from 4.6 W to 5.1 W at different speeds of 30 mm/s and 15 mm/s. In the case of PFA/0.5% GO, the film is either degraded to form an insulating product at low powers, or fully ablated at higher powers. Under no laser conditions is a conductive film formed on the PFA/0.5% GO sample. At 1 wt.% GO, a conductive black product is formed upon laser irradiation, without ablation of the film for powers ranging from 4.8 W to 5.1 W for both speeds of 15 mm/s and 30 mm/s.

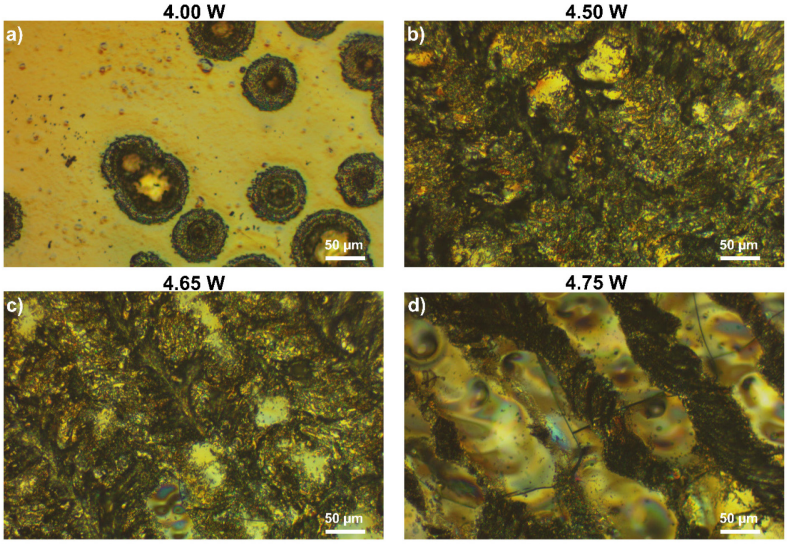

Figure A10: Optical microscopy images of the effect of laser power on PFA/1% GO films spincoated on glass. All were scribed at 1 mm/s with a single laser pass. As seen in b) and c), laser irradiation results in the formation of black, conductive material at 4.50 W and 4.65 W. As seen in d), black material is still present for increased powers such as 4.75 W, but most material appears ablated. At lower powers, such as 4.00 W in a), black circles are present in optical microscope images of the films, but are disconnected and do not result in a conductive network. At even lower powers, there is no observable change in the morphology or colour of the films, indicating that the laser power is too low to induce any carbonization or degradation of the PFA/GO composite. In a), the yellow areas correspond to unconverted PFA, while in d), the yellow areas correspond to bare glass substrate where PFA has been ablated, as evidenced by the cracks in the substrate.

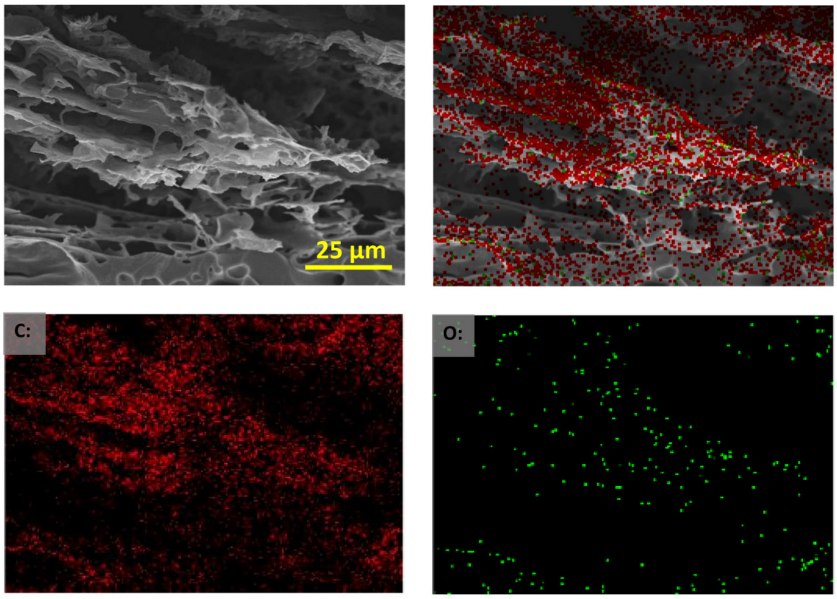

Figure A11: EDS mapping of cryogenically-fractured cross-section of laser-scribed PFA/1% GO. SEM images indicate that the material has a fibrous morphology. EDS mapping indicates that both carbon and oxygen are present in the material, and that it consists of 96.8 at.% carbon and 3.2 at.% oxygen, confirming the conversion of the polymer into a carbonized structure.

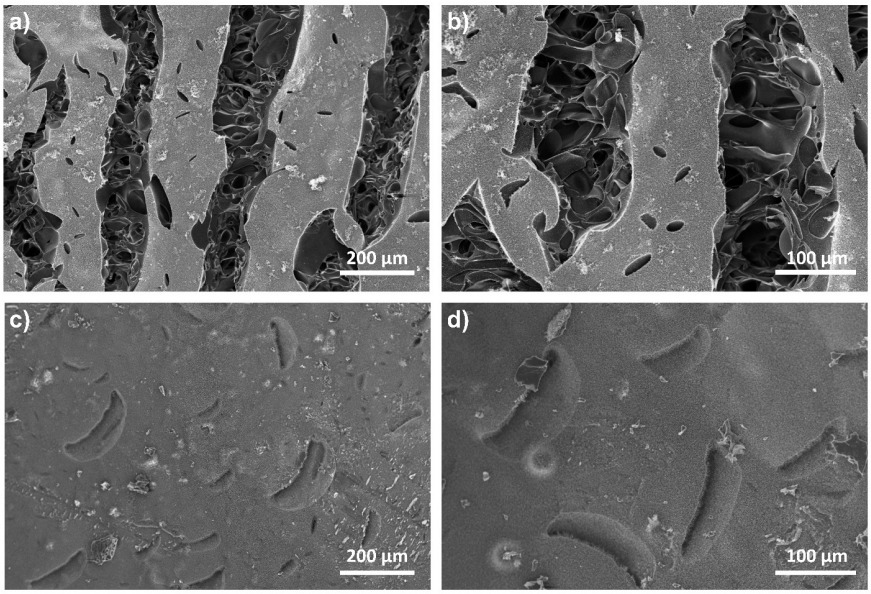

Figure A12: SEM images of chars formed from burning samples of PFA a), b) with no GO, and c), d) with 1% GO.

TGA Analysis of Thermal Conductivity of PFA Composites with and without GO:

In order to investigate any thermal effects of GO on PFA, TGA was performed on PFA/0% GO and PFA/1% GO powders at varying heating rates. Shifts in the profile of the TGA curve are expected at different heating rates, with curves shifting to higher temperatures at higher heating rates.[250,251] This effect results partly from the kinetics of the decomposition, and partly from thermal lag, which is attributed to heat transfer limitations.[250,251] The magnitude of thermal lag has been related to the thermal diffusivity of the measured material, which is, in turn, directly related to the thermal conductivity of the material.[252,253] Thus, it is expected that smaller shifts in the TGA curves should be observed for materials with higher thermal diffusivity, and larger changes should be observed for materials with lower thermal diffusivity. The TGA curves for PFA/0% GO and PFA/1% GO at scan rates of 5 °C/min, 10 °C/min, and 20 °C/min are shown in Fig. A11 a) and c) below. There is a significant difference in the TGA profile and carbon yield of samples with and without GO. Samples with GO have a distinct plateau from approximately 200 °C to 300 °C which is absent in the samples without GO at all scan rates. This plateau is the most distinct difference in the TGA profiles, indicating increased thermal stability of the PFA/1% GO composite in this temperature range, and resulting in an increased carbon yield.

The derivative TGA curves for PFA with 0% GO and 1% GO are presented in Fig. A11 b) and d). In both cases, two major peaks are present, with maxima in the ranges of 130 – 170 °C and 350 – 420 °C. In the case of 1% GO, only these two peaks are present, while the 0% PFA sample possesses multiple broad shoulders. We have extracted key thermal parameters from this analysis and tabulated them in Table A1.

To assess differences in thermal diffusivity, shifts in the T_{max} value with scan rate should be analyzed. However, in both the 0% and 1% GO cases, there is some shift in the shape of the ~400 °C degradation peak, leading to erroneous shifts in the T_{max} value. As such, we instead compared the shift of the ~150 °C degradation peak, which retained a constant shape and relative intensity for all samples. The T_{max} values for this peak, labelled $T_{max,\ 150°C}$, are listed in Table A1. The percentage change of the T_{max} values compared to the value at 5 °C/min are also tabulated, and the values are similar for samples with and without GO, indicating that there is not a significant difference in the thermal diffusivity, and, assuming a similar heat capacity and density of the two materials, that there is no significant difference in the thermal conductivity of the two samples in this temperature range. However, it should be noted that the

derivative curves for samples with GO retain a more consistent peak shape, while samples without GO display significant differences in the heights and shapes of peaks in the 250 – 500 °C range.

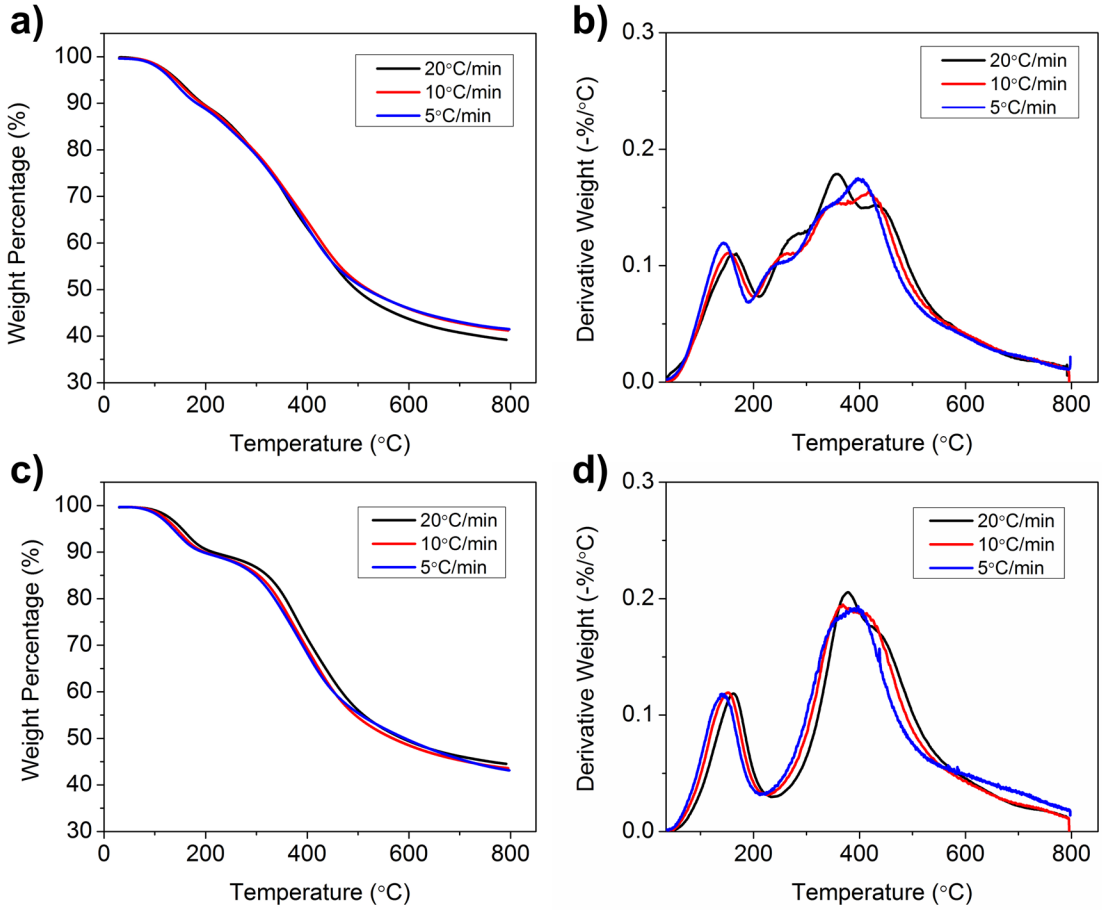

Figure A13: a) TGA and b) derivative weight curve for PFA/0% GO. c) TGA and d) derivative weight curve for PFA/1% GO.

Table A1: Summary of thermal parameters extracted from TGA of PFA/0% GO and PFA/1% GO at varying heating rates.

	Scan rate (°C/min)	$T_{max,\ 150°C}$ (°C)	Percentage Change from 5 °C/min (%)	Char Residue/ Carbon Yield (%)
0% GO	20	167.5	16.9	39.3
	10	152.0	6.1	41.2
	5	143.3	0.0	41.5
1% GO	20	162.2	15.4	44.7
	10	152.5	8.5	43.6
	5	140.5	0.0	43.1

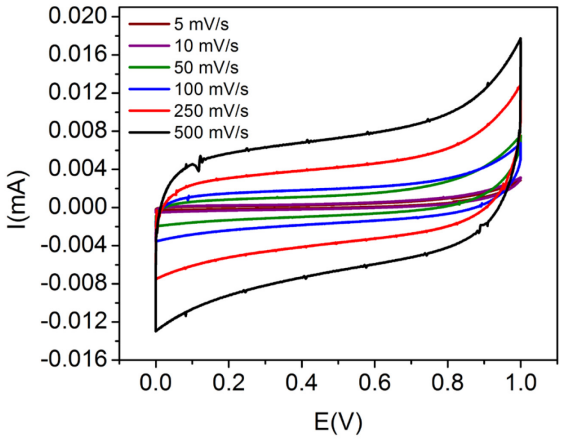

Figure A14: Cyclic voltammetry of laser-scribed PFA/1% GO supercapacitors at varying scan rates. The devices display the pseudo-rectangular shape expected. Despite the high conductivity of the laser-scribed PFA/1% GO, supercapacitors prepared from this material exhibit a specific capacitance of only 34 μF/cm² at 5 mV/s.

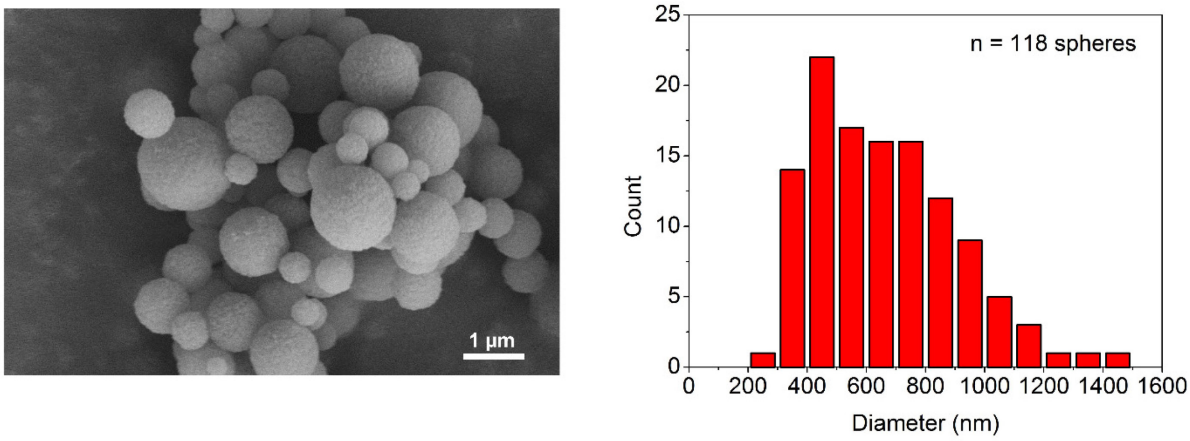

Figure A15: Characterization of PFA microspheres prepared from the emulsion polymerization of PFA. The histogram shows the diameter of the microspheres as measured via SEM. The microspheres range in size from approximately 280 nm to 1.5 μm and possess an average diameter of 670 nm.

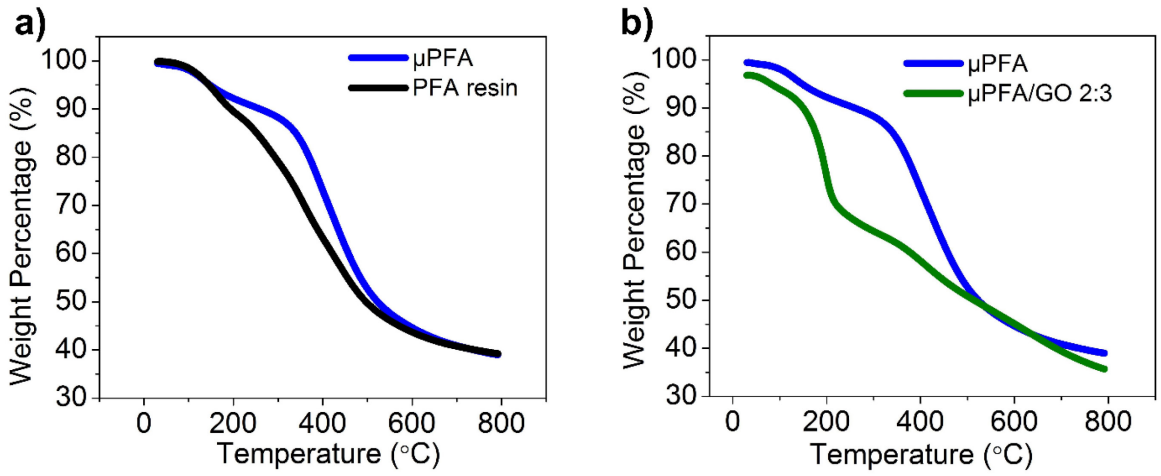

Figure A16: Thermogravimetric analysis (TGA) of PFA microspheres and PFA/GO composites. a) TGA curves of PFA resin and PFA microspheres. b) TGA curves of PFA microspheres and µPFA/GO 2:3 composite. The carbon yields of the µPFA, PFA resin, and µPFA/GO 2:3 are 39.2%, 39.3%, and 36.9% respectively. TGA was performed at 20 °C/min under nitrogen environment, to best approximate the rapid heating of the laser scribing process.

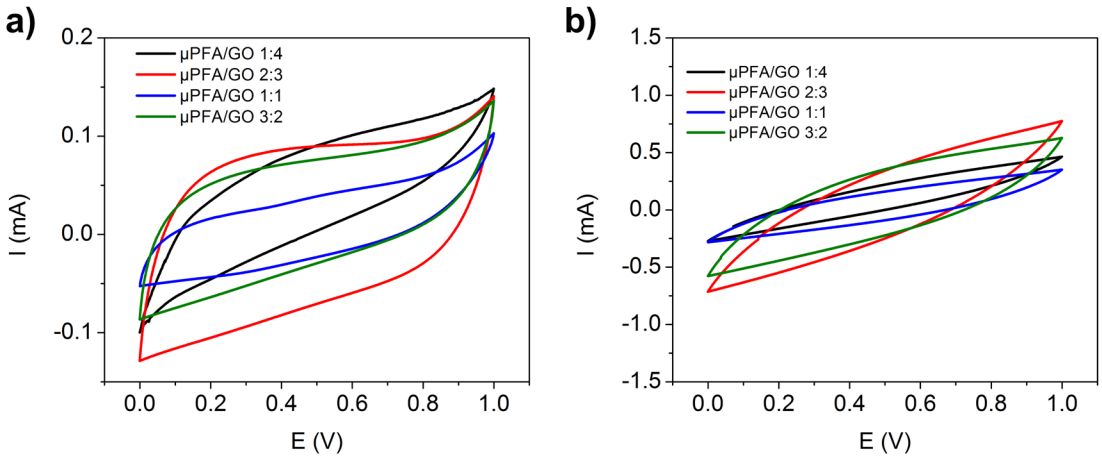

Figure A17: Electrochemical performance of µPFA/GO composites of varying µPFA/GO ratios, drop cast onto PET substrates at lower loadings of ~1.15 mg/cm^2. a) Cyclic voltammetry at 5 mV/s. b) Cyclic voltammetry at 100 mV/s. At all scan rates tested, the µPFA/GO 2:3 ratio had the highest specific capacitance and was therefore selected for further characterization and optimization.

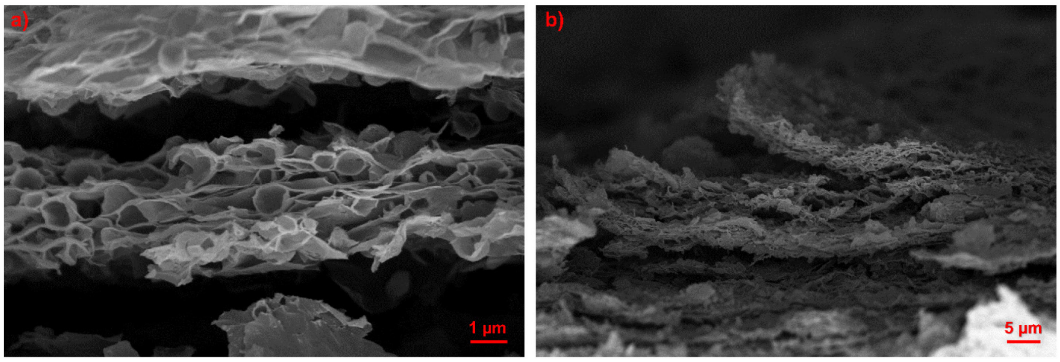

Figure A18: Cross-sectional SEM images of laser-scribed µPFA/GO 2:3. a) Cross-sectional SEM images of laser-scribed µPFA/GO 2:3 showing hollow or broken carbonized PFA microspheres. b) Lower magnification cross-sectional SEM images of laser-scribed µPFA/GO 2:3 indicates larger separated flakes of material likely due to rapid gas evolution during photothermal heating.

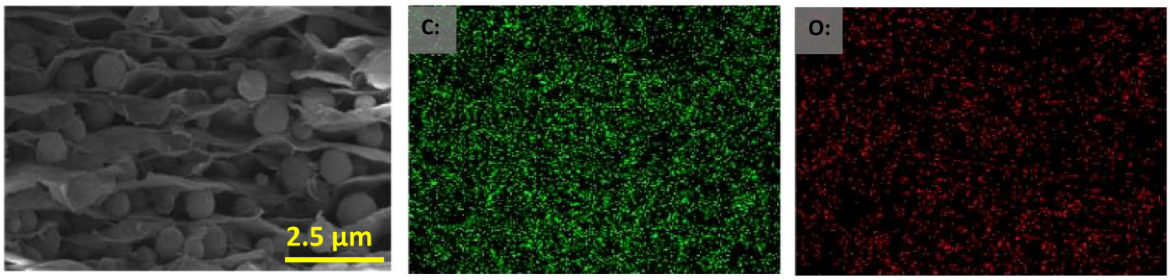

Figure A19: EDS mapping of cross-section of µPFA/GO 2:3 prior to laser scribing. The SEM image shows the structure of the composite, with layers of GO sheets and PFA microspheres well dispersed with each other. EDS mapping indicates that the composite consists of 18.7 at.% oxygen and 81.3 at.% carbon, with both randomly distributed over the whole composite.

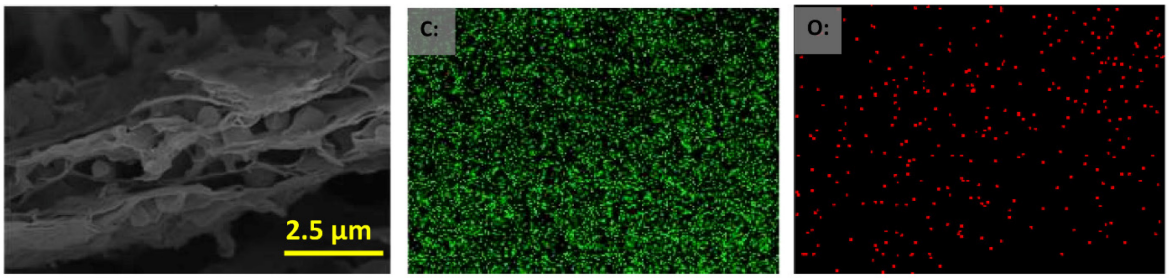

Figure A20: EDS mapping of cross-section of laser-scribed µPFA/GO 2:3. The SEM image shows the structure of the laser-scribed composite, with layers of rGO sheets and carbonized PFA microspheres still present. EDS mapping indicates that the composite consists of 0.9 at.% oxygen and 99.1 at.% carbon following laser irradiation. Both the carbon and oxygen contents are randomly distributed across the whole composite. Thus, both the GO sheets and PFA microspheres are carbonized upon laser-irradiation.

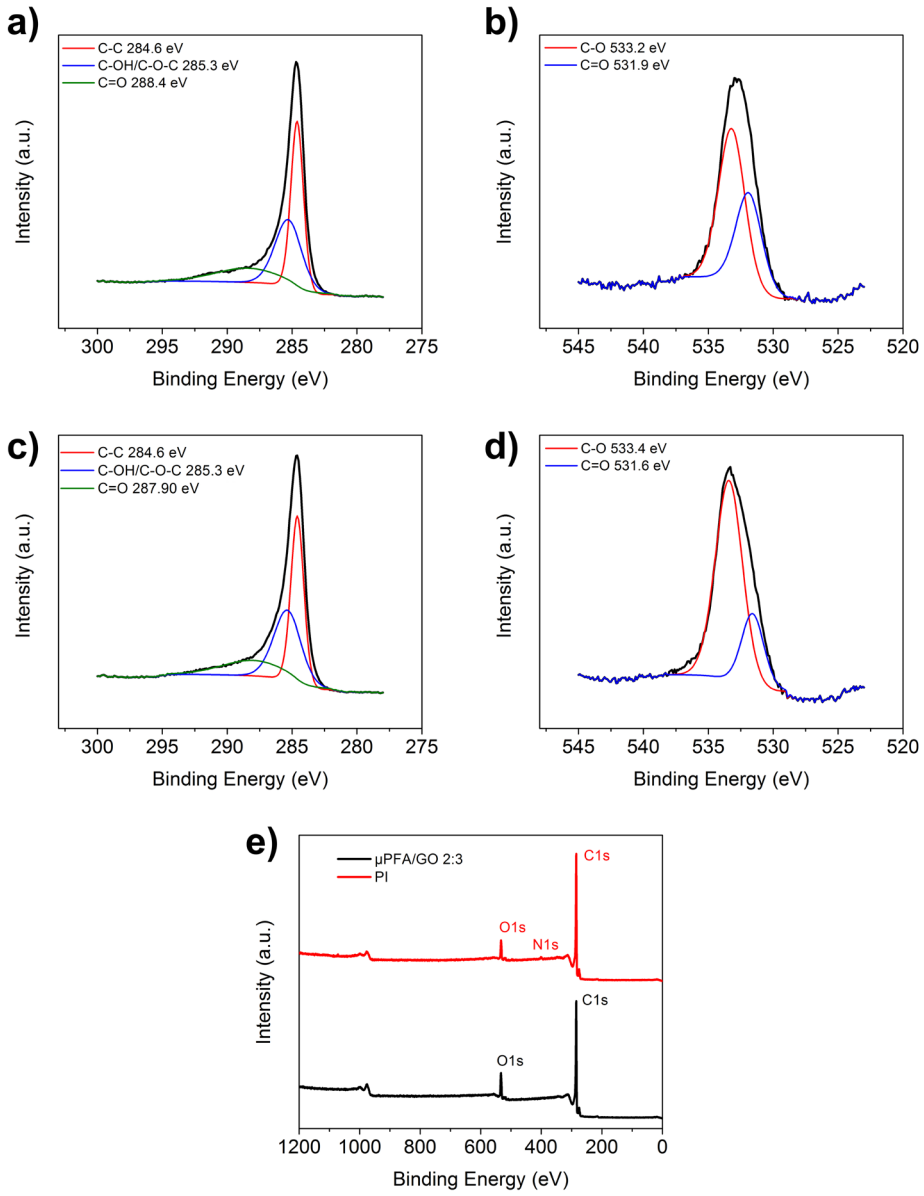

Figure A21: X-ray photoelectron spectroscopy of laser-scribed PI and µPFA/GO 2:3. a) High resolution C1s XPS spectrum for LIG from PI. b) High resolution O1s XPS spectrum for LIG from PI. c) High resolution C1s XPS spectrum for LIG from µPFA/GO 2:3. d) High resolution O1s XPS spectrum for LIG from µPFA/GO 2:3. e) XPS survey spectra of LIG from PI and LIG from µPFA/GO 2:3. From the survey spectrum, the C/O ratio of LIG from PI is 16.9, while the C/O ratio of LIG from µPFA/GO 2:3 is 11.2. The high resolution C 1s spectra for both LIG from PI and from µPFA/GO 2:3 are very similar, with a strong C-C peak at 284.6 eV, and weaker C=O and C-OH/C-O-C peaks. There are differences in the O 1s spectra for the two materials. Both possess C-O and C=O peaks, but the ratio of the two is different, with a stronger C-O peak and weaker C=O peak for the µPFA/GO 2:3 material. This corresponds well with the chemical structure of the polymers, where PFA has fewer carbonyl groups than PI.

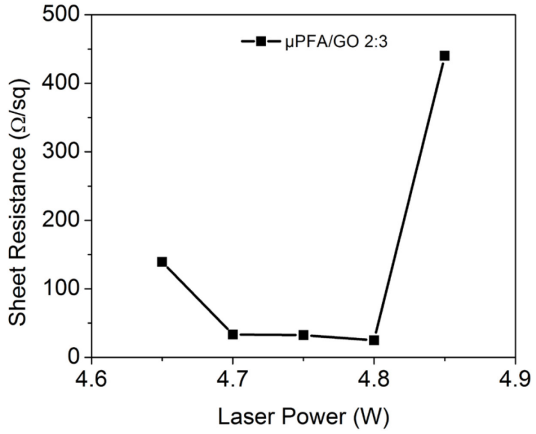

Figure A22: Sheet resistance of laser-scribed μPFA/GO 2:3 with laser power. The μPFA/GO 2:3 material carbonizes at lower laser powers than PFA/1% GO (4.65 to 4.85 W compared to 4.8 to 5.1 W). The sheet resistances (25 – 440 Ω/sq) are in the same range as LIG from PFA/1% GO and from PI. Taking into account the thinner LIG layer of this material (20 μm ± 10 μm), this results in a conductivity of 20 S/cm ± 15 S/cm.

Raman Characterization of Varying Ratios of μPFA/GO:

It is challenging to experimentally assess the structure of the carbonized PFA within the composite, as it is not easily isolated from the surrounding rGO. One of the only possible experimental methods to assess the differences in these two carbon materials is Raman spectroscopy. Still, the Raman spectra of the μPFA/GO 2:3 material appear similar to a pure rGO spectrum. In order to elucidate any differences between this material and rGO, we have performed extensive Raman spectroscopy analysis of LIG prepared from different ratios of μPFA and GO. We firstly prepared carbonized μPFA through pyrolysis at 700 °C, and prepared LIG from pure GO films. We then prepared films with varying ratios of μPFA and GO (3:2, 1:1, and 2:3), laser scribed all films with the same conditions, and measured Raman spectra on different samples and different areas of the LIG formed. An example of each spectrum is presented in a), though it should be noted that there are significant variations among spectra depending on the area of the sample measured, and thus each spectrum represented is only a single example. The variations in the Raman spectra for each sample are expected and have been previously reported for LIG from PI,[24] as, due to the Gaussian-like distribution of heat from the laser, the LIG material formed at the center of a scribed line will be different than the material at the edge. The results of the analysis of varying μPFA and GO ratios are shown in b)-f). Various parameters were assessed, including the I_D/I_G ratio, I_G/I_{2D} ratio, and the FWHM of the D, G, and 2D peaks. In order to assess if

changes in these parameters stemmed from a physical mixture of glassy carbon (carbonized μPFA) and rGO, representative full spectra from LIG from GO and thermally carbonized μPFA were added in a linear combination matching the various PFA/GO ratios. The theoretically calculated linear combination spectra were then fit and each parameter was then extracted. For further theoretical comparison, the weighted average of each individual parameter (not full spectrum) was also calculated, i.e.:

$$I_D/I_G \; value \; for \; PFA/GO \; 3{:}2 \; = (0.6 \times I_D/I_G \; value \; for \; PFA) \; + (0.4 \times I_D/I_G \; value \; for \; GO)$$

Each of the calculated theoretical values were compared to experimental values obtained from three to eight spectra from each sample type. Deviations from the theoretical values indicate that the LIG material is different than a purely physical mixture of glassy carbon and graphene.

In terms of the I_D/I_G ratio, the calculated theoretical values are higher than the experimental values, especially for the 1:1 and 2:3 ratios, for which the theoretical values are outside of the standard deviation of the samples. This indicates that there are fewer defects in the carbon material formed than predicted by a physical mixture of glassy carbon and graphene. The results for the I_G/I_{2D} ratio further support the formation of a different material, with significantly lower I_G/I_{2D} ratios than theoretical obtained for all μPFA/GO ratios. Similarly to the I_D/I_G ratios, while the I_G/I_{2D} ratios decrease with increasing GO content, the values for all ratios are similar to that of pure rGO. The decreased I_G/I_{2D} ratios indicate the formation of a few-layer graphene structure. Notably, the 2:3 ratio, which was the optimal ratio utilized in our manuscript, possesses a lower average I_D/I_G ratio and I_G/I_{2D} ratio than LIG prepared from pure GO.

We also examined the effect of the ratio of μPFA/GO on the FWHM of each peak. While the effects are more subtle than the I_D/I_G and I_G/I_{2D} ratios, there are still observable differences. The FWHM of all three peaks is highest for the thermally carbonized PFA, most notably for the D and 2D peaks, for which its FHWM is more than twice that of rGO. Again, for all peaks, there are some PFA/GO ratios that result in lower FWHMs than those predicted theoretically. Interestingly, there is not a clear trend in the FWHM of each peak with increasing GO content, but this could be partially attributed to the large standard deviation in each of these parameters.

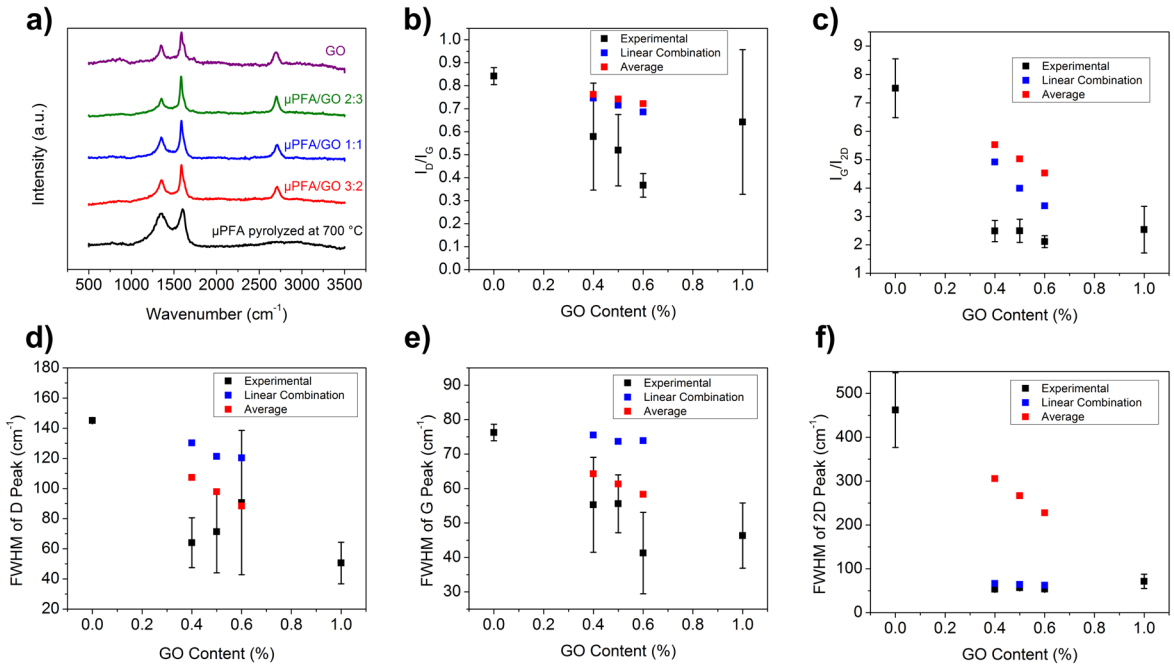

Figure A23: Raman spectroscopy analysis of LIG prepared from mixtures of μPFA and GO in varying ratios. a) Examples of spectra for LIG prepared from varying ratios of μPFA and GO, as well as for pure μPFA pyrolyzed at 700 °C and LIG from pure GO. b) I_D/I_G ratio, c) I_G/I_{2D} ratio, d) FWHM of D peak, e) FWHM of G peak, and f) FWHM of 2D peak for experimental spectra, and theoretical values from linear combinations of the spectra as well as weighted averages.

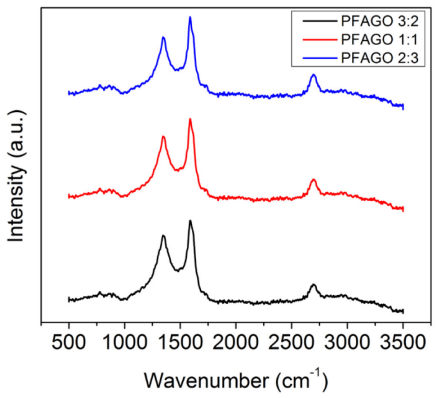

Figure A24: Theoretical Raman spectra prepared via linear combinations of pyrolyzed μPFA and LIG from GO.

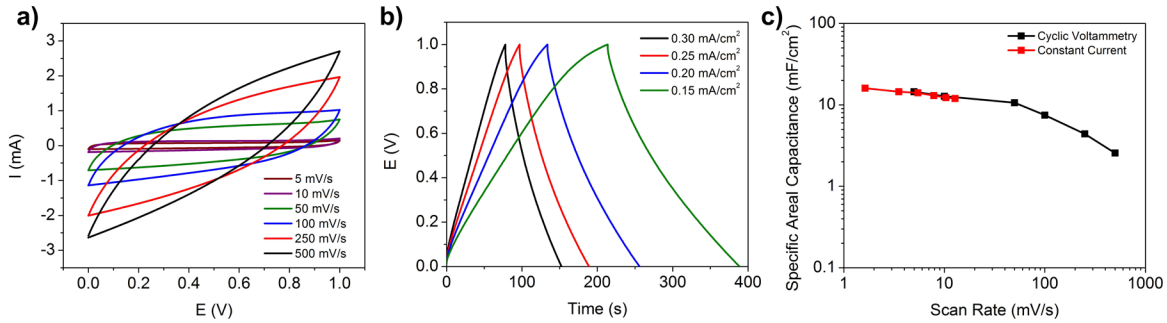

Figure A25: Electrochemical performance of µPFA/GO 2:3 after 11 days. a) Cyclic voltammetry of the µPFA/GO 2:3 supercapacitor at varying scan rates. b) Galvanostatic charging and discharging of the µPFA/GO 2:3 supercapacitor at varying current densities. c) Specific areal capacitances of the µPFA/GO 2:3 supercapacitor from both cyclic voltammetry and galvanostatic charging and discharging with varying scan rates. The capacitance increases to 14.5 mF/cm^2 at 5 mV/s. The increased capacitance is suspected to arise from increased electrolyte wetting over time.

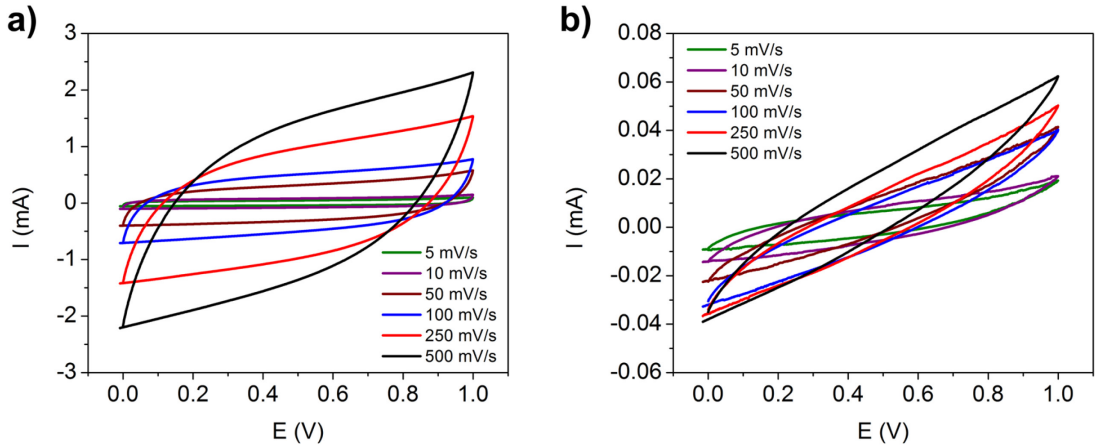

Figure A26: Electrochemical performance of PI-based and GO-based LIG supercapacitors. GO-based devices were prepared by drop casting a GO dispersion onto PET substrates, while commercial PI films were utilized. Both were scribed under various laser conditions, and the parameters resulting in the lowest sheet resistance were used to prepare devices. a) Cyclic voltammetry of PI LIG supercapacitor at varying scan rates. The device achieves a specific capacitance of 9.2 mF/cm^2 at 5 mV/s. b) Cyclic voltammetry of GO LIG supercapacitor at varying scan rates. The device achieves a specific capacitance of 0.97 mF/cm^2 at 5 mV/s.

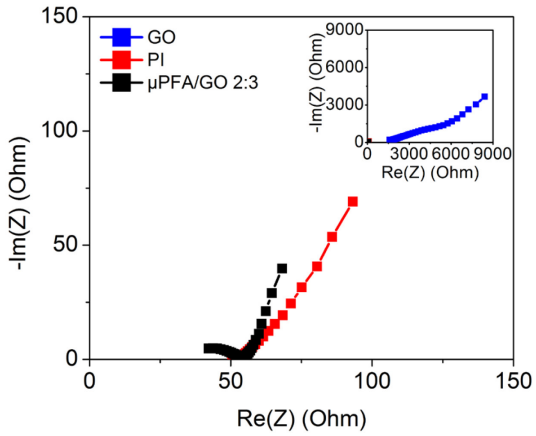

Figure A27: Electrochemical Impedance Spectroscopy (EIS): Nyquist plot of LIG supercapacitors prepared from µPFA/GO 2:3, PI, and GO. Curves for the µPFA/GO and PI-based devices are similar; however the slope of the µPFA/GO material in the low-frequency regime is higher than that of the PI-based device, indicating the stronger capacitive behaviour of the µPFA/GO-based device. It should be noted that the relatively high ESR in these devices is likely due to the interdigitated electrode design, which possesses longer pathways for both electronic and ionic transport. A full discussion of the sources of resistance in these interdigitated devices can be found in Appendix B.

Appendix B:
Supplementary Information for Chapter 4

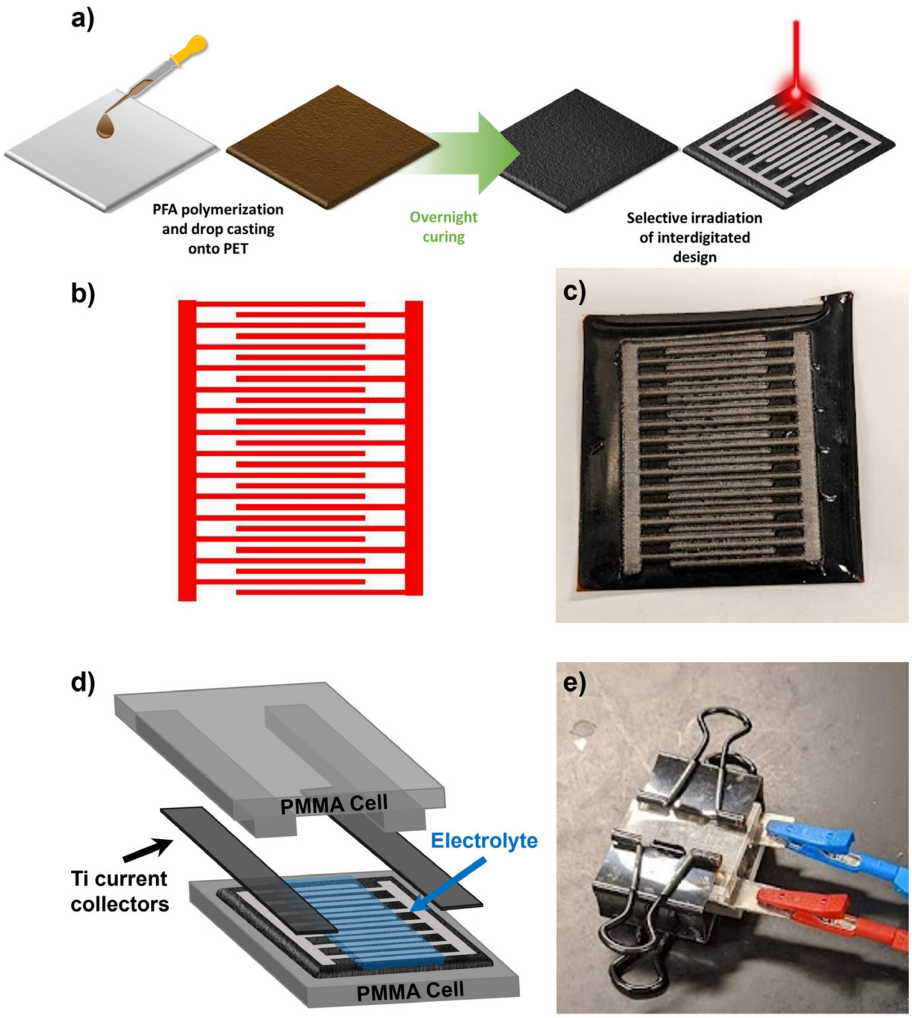

Figure B1: a) Scheme of fabrication of PFA-based LIG supercapacitor. b) Electrode design used to laser scribe PFA-based supercapacitors. c) Photo of laser-scribed PFA film, prior to coating with electrolyte. d) Schematic of supercapacitor testing cell. e) Photo of supercapacitor testing cell.

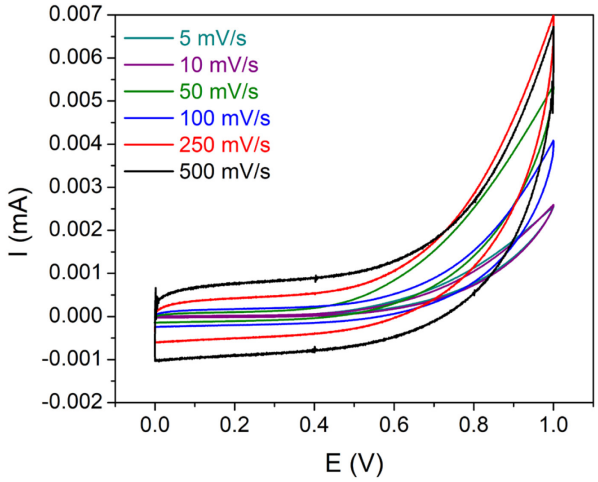

Figure B2: Cyclic voltammetry (CV) curves demonstrating electrochemical performance of supercapacitor prepared from LIG from PFA/no salt. The CV curves indicate that irreversible faradaic reactions occur with LIG-based electrodes formed from pristine PFA at around ~1 V, which may be a result of residual, uncarbonized polymer and functional groups with poor electrochemical stability.

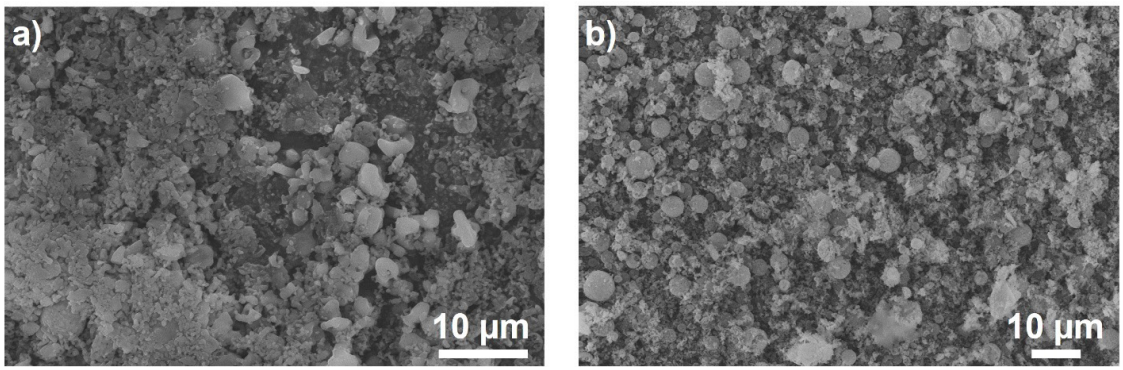

Figure B3: a) and b) SEM images of spray-dried Na_2SO_4 particles, demonstrating the variation in the different particle sizes and shapes recovered after spray-drying.

Mechanical Properties of PFA and PFA/Salt Films:

Following salt addition, we investigated the mechanical properties of the films. As PFA is a thermosetting resin, this depends strongly on the curing time and temperature. We cured films overnight at 80 °C in order to ensure complete polymerization and cross-linking was obtained. Moreover, in order to ensure that we could form the thickest layer of LIG possible without ablating the PFA films, we cast 400-600 µm thick films. These relatively thick films are not highly flexible. However, as seen in **Figure B4**, thinner fully cured PFA films are highly flexible and can be bent around a 1.5 cm cylinder without cracking. Introduction of salt microparticles into the PFA makes the film more brittle, and at high salt loadings the high viscosity of the mixture makes it challenging to cast thin films, but ~350 µm thick films of PFA/25% Na_2SO_4 are still flexible and can be bent around a 2.8 cm diameter cylinder without cracking.

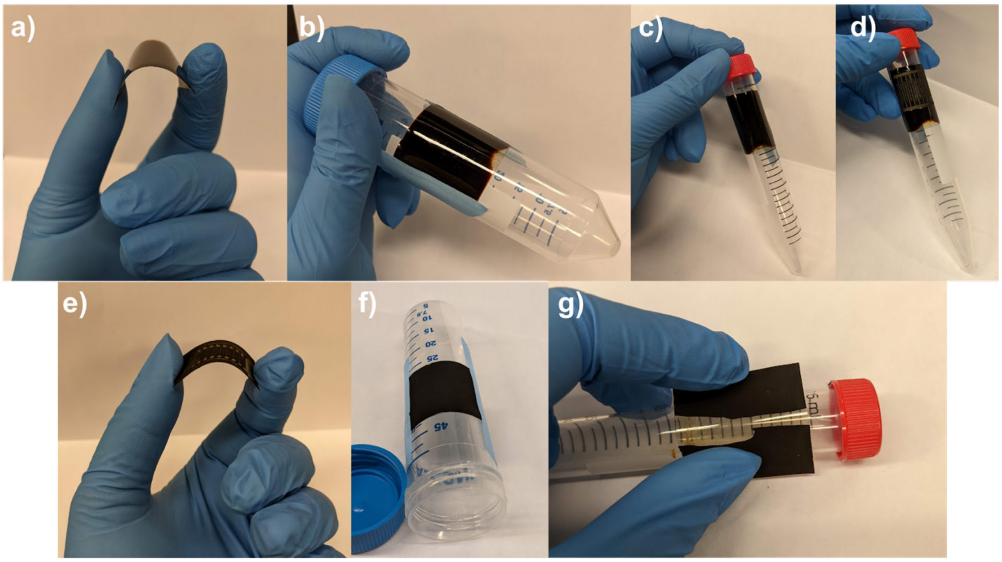

Figure B4: Flexibility of PFA and PFA/salt films. a) – d) Flexibility of ~160 µm thick PFA film without salt. a) Film bent by hand, b) film bent around 2.8 cm diameter cylinder, c) film bent around 1.5 cm diameter cylinder, and d) film bent around 1.5 cm diameter cylinder with LIG electrode pattern scribed on surface. No crack formation was observed. e) – g) Flexibility of ~350 µm thick PFA/25% Na_2SO_4 film. e) Film scribed with LIG electrode pattern and bent by hand, f) film bent around 2.8 cm diameter cylinder without any crack formation, g) film bent around 1.5 cm diameter cylinder causes film to crack.

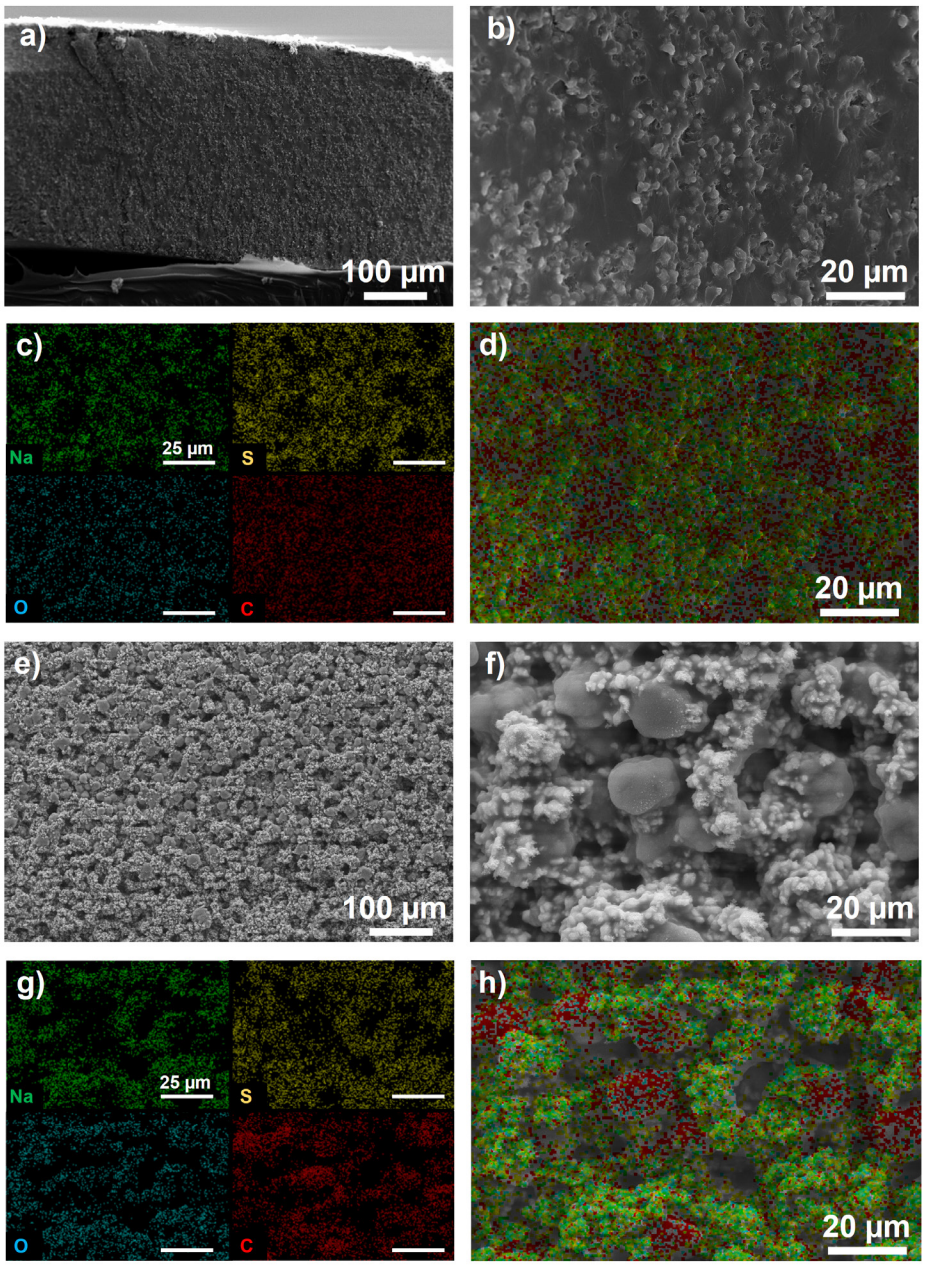

Figure B5: SEM images and EDS mapping of PFA/25% Na_2SO_4 composite. a,b) SEM images of freeze-fractured cross-sections of PFA/25% Na_2SO_4 composite. c) EDS mapping of Na, S, O, and C of b), and d) SEM image in b) with EDS mapping overlay to demonstrate the distribution of the different elements. e, f) Top-down SEM images of PFA/25% Na_2SO_4 composite surface. g) EDS mapping of Na, S, O and C of f), and h) SEM image in f) with EDS mapping overlay to demonstrate the distribution of the different elements.

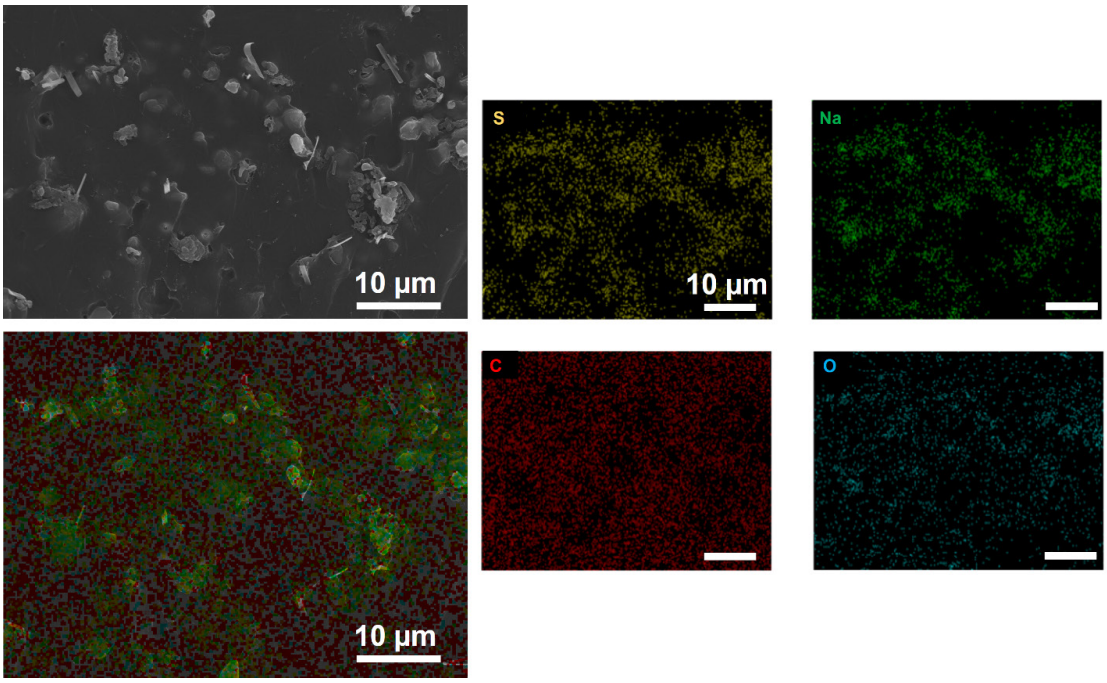

Figure B6: EDS mapping of PFA/10% Na_2SO_4 cross-section.

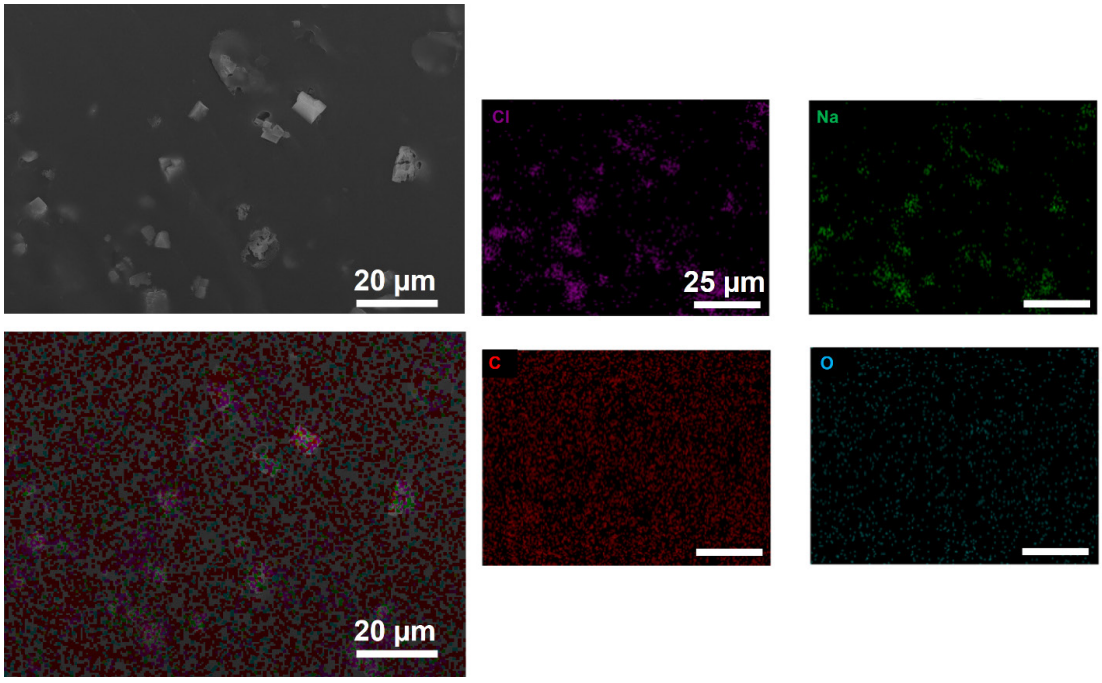

Figure B7: EDS mapping of PFA/10% NaCl cross-section.

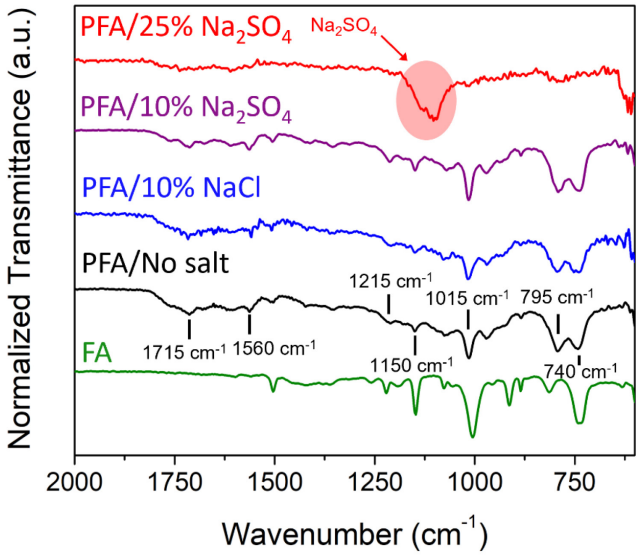

Figure B8: Expanded and labelled fingerprint region of FTIR of FA and PFA composites with and without salt. PFA without salt, with 10% NaCl and with 10% Na_2SO_4 all possess peaks at 1150 cm^{-1}-1215 cm^{-1}, and 1015 cm^{-1} from the asymmetric and symmetric stretching of =C-O-C groups belonging to 2-substituted furan rings, ~1560 cm^{-1} from the stretching mode of conjugated C=C bonds or ring vibrations, 795 cm^{-1} from 2,5-disubstituted furan rings, and 740 cm^{-1} from monosubstituted furan heterocycles.[232–235]

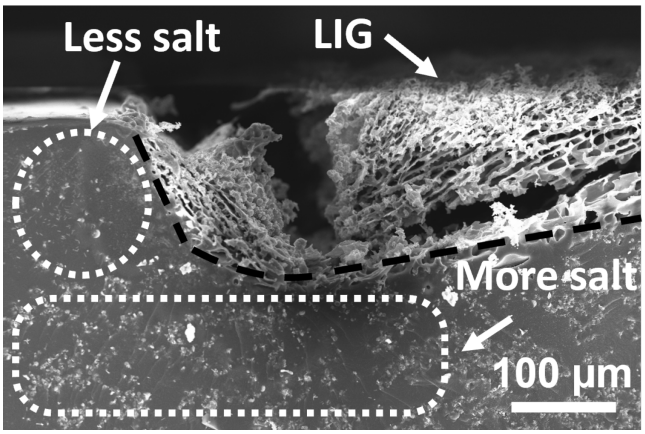

Figure B9: SEM image of cross-section of LIG from PFA/10% Na_2SO_4, demonstrating that more salt particles are present deeper in the film, indicating some settling of particles during curing. Note that the disconnection of the LIG from the PFA substrate is likely due to the fracturing of the cross-section in liquid nitrogen.

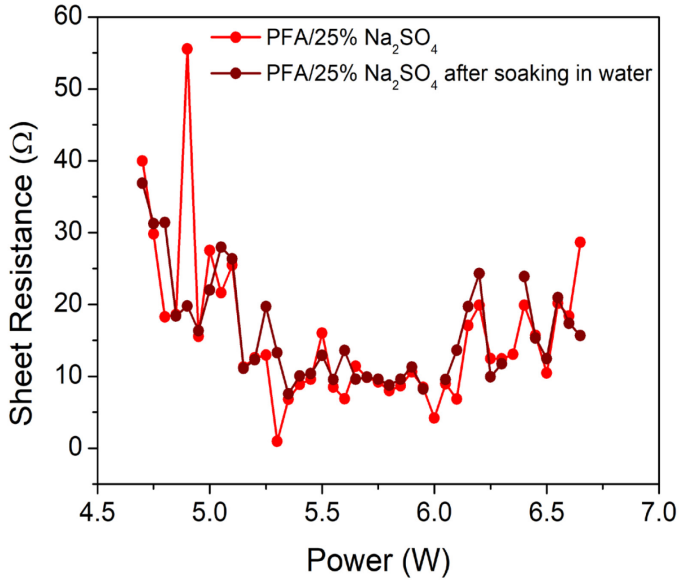

Figure B10: Sheet resistance of LIG from PFA/25% Na_2SO_4 before and after soaking sample in water overnight to dissolve salt coating the LIG surface.

Table B1: XRD Peak Assignment for Spray-dried NaCl

2θ (°)	**Peak Assignment**
27.6	(111)
31.8	(200)
45.7	(220)
56.8	(222)
66.5	(400)
75.4	(420)
84.2	(422)

Table B2: XRD Peak Assignment for Spray-dried Na_2SO_4

2θ (°)	**Peak Assignment**
19.0	(111) Phase V
28.0	(131) Phase V
29.0	(040) Phase V
32.1	(311) Phase V
33.8	(022) Phase V
38.6	(222) Phase V
48.8	(351) Phase V
54.6	(062) Phase V
22.6	(111) Phase III
23.6	(120) Phase III
25.5	(200) Phase III
31.8	(211) Phase III
34.0	(031) Phase III
37.8	(022) Phase III
46.2	(222) Phase III
48.3	(240) Phase III
52.5	(331) Phase III
58.1	(033) Phase III
59.0	(242) Phase III
64.0	(431) Phase III

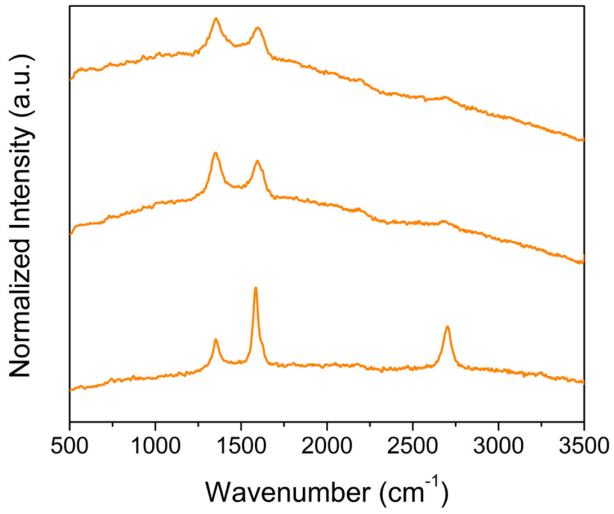

Figure B11: Raman spectra of different areas of LIG from PFA/no salt irradiated at 5.85 W.

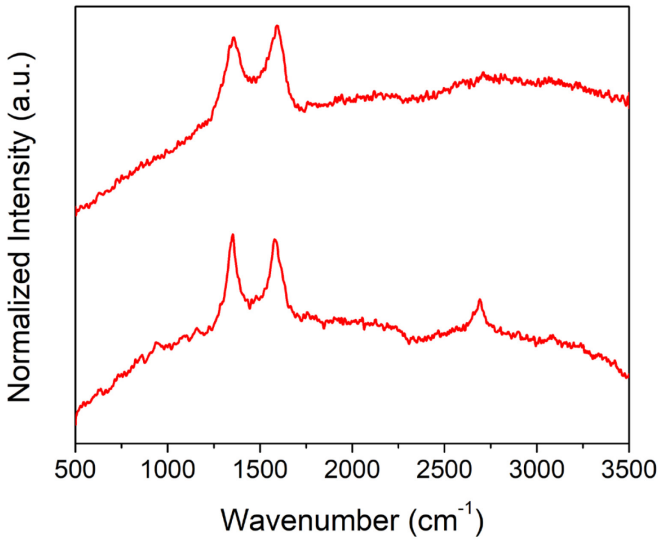

Figure B12: Raman spectra of different areas of LIG from PFA/25% Na_2SO_4 irradiated at 6.65 W.

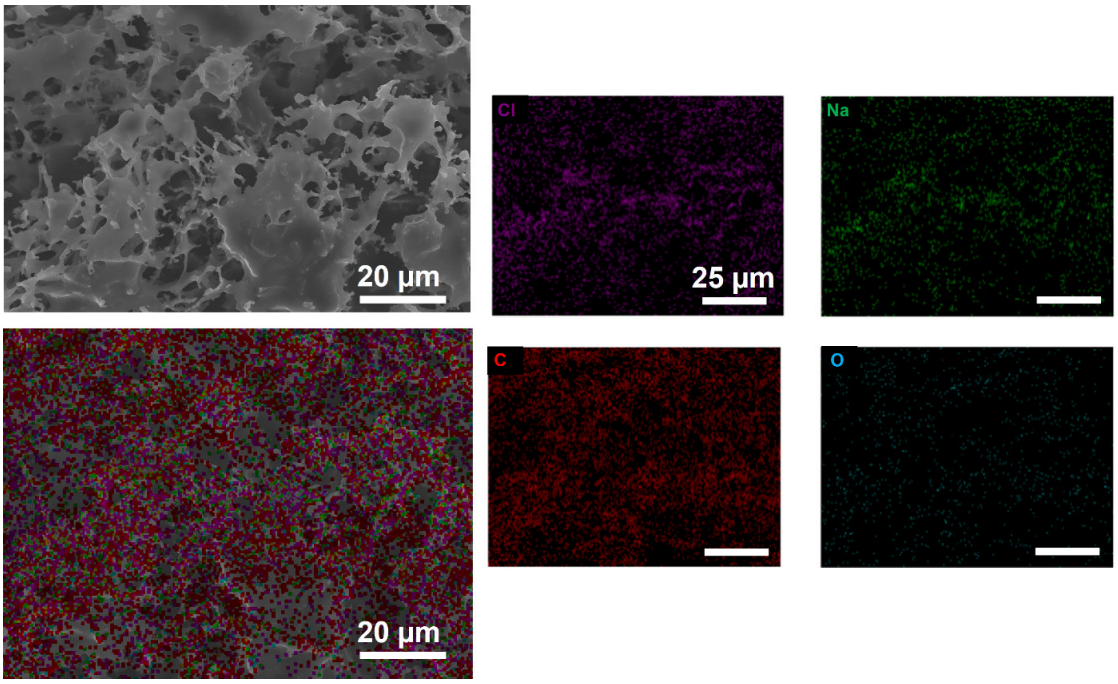

Figure B13: EDS mapping of LIG from PFA/10% NaCl, top down.

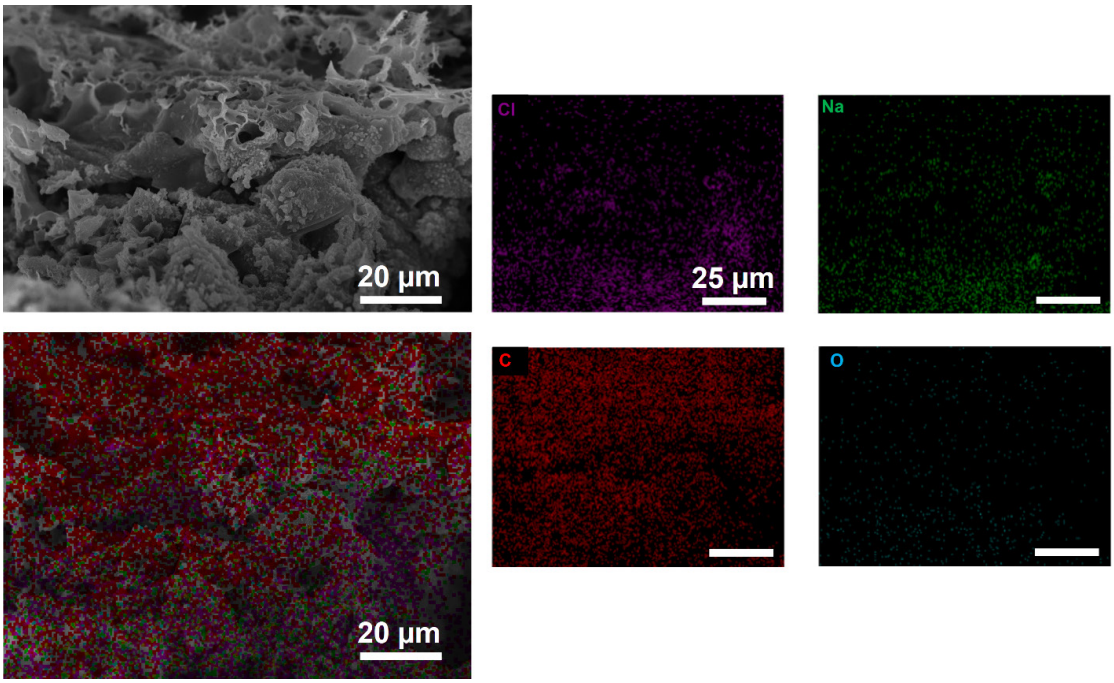

Figure B14: EDS mapping of LIG from PFA/10% NaCl, cross-section.

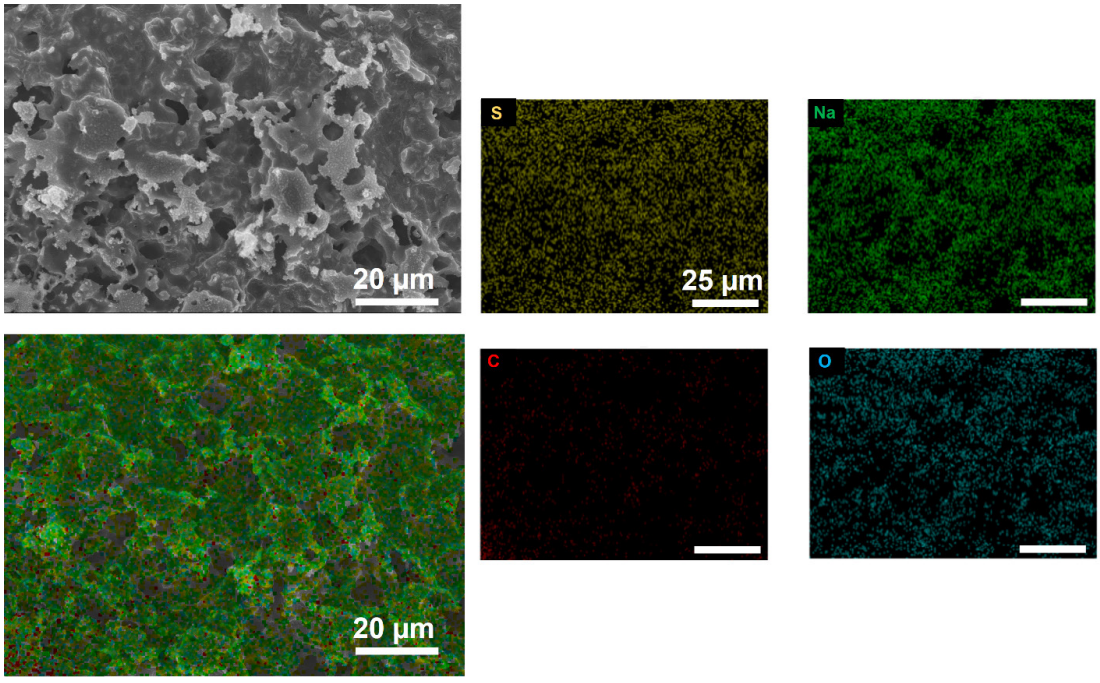

Figure B15: EDS mapping of LIG from PFA/25% Na_2SO_4, top down.

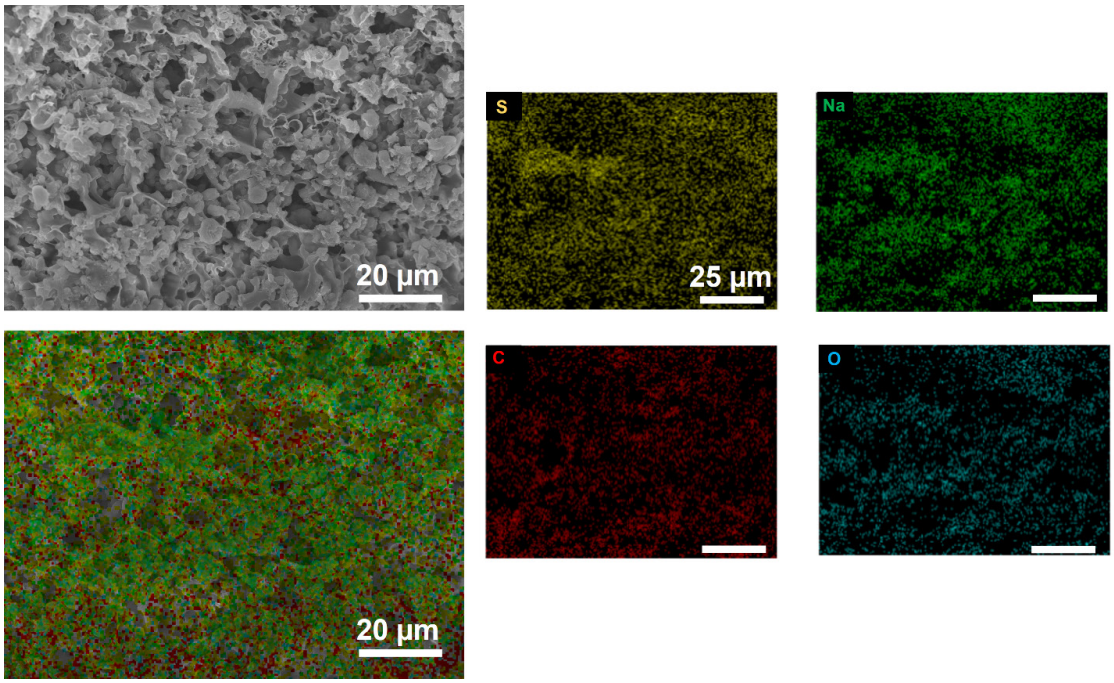

Figure B16: EDS mapping of LIG from PFA/25% Na_2SO_4, cross-section.

Thermal Modeling Details:

A complete description of thermal diffusion through the PFA/salt composite is extremely complicated. However, in order to estimate the thermal penetration depth and the resulting carbonization zone during the laser irradiation, the composite can be regarded as a homogeneous material with an effective thermal conductivity and the thermal diffusion is interpreted as a quantity averaged over a volume that is large with respect to the scale of the heterogeneity but small with respect to the overall dimensions of the heat conduction system. For unconsolidated inclusion of particles (salts) in a continuous solid phase (PFA resin), effective thermal conductivity and diffusivity of the PFA/salt composites are estimated as a function of salt loading using thermo-physical properties of the individual constituents of the composite.[332] Assuming a constant heat flux, the relative thermal penetration depth, δ_T, as the laser beam scans the composite can be estimated by[332]

$$\delta_T = \sqrt{\alpha t} \tag{B.1}$$

where α is the effective thermal diffusivity of the composite and t is the exposure time of the composite to the laser beam which is equal to

$$t = \frac{d}{U} \tag{B.2}$$

Here d and U are the laser beam diameter and scanning speed, respectively. The laser beam diameter is assumed to be 100 μm, and scanning speeds of 5 mm/s to 40 mm/s were considered for the calculation.

The effective thermal conductivity and diffusivity of the PFA-salt composites are estimated through the following correlations:

$$\frac{k_{\text{eff}}}{k_0} = \frac{(1-\varphi)+\beta\varphi(k_1/k_0)}{(1-\varphi)+\beta\varphi} \tag{B.3}$$

in which

$$\beta = \frac{1}{3}\sum_{i=1}^{3}\left[1+\left(\frac{k_1}{k_0}-1\right)g_i\right]^{-1} \tag{B.4}$$

where k_1 and k_0 are thermal conductivities of salt and PFA resin, respectively, k_{eff} is the effective thermal conductivity of the PFA/salt composite, and φ is the volume fraction of the salt in the composite. The g_i are shape factors for the salt in the PFA resin which for the unconsolidated solid particles are as follows: $g_1 = g_2 = \frac{1}{8}$ and $g_3 = \frac{3}{4}$.

The density and specific heat of the PFA/salt composites are calculated through mixing rule as follows:

$$\rho_{\text{eff}} = \rho_1\varphi + (1-\varphi)\rho_0 \tag{B.5}$$

$$c_{\text{eff}} = c_1\varphi + (1-\varphi)c_0 \tag{B.6}$$

where subscripts 1 and 2 represent salt and PFA resin, respectively. The effective thermal diffusivity of the PFA/salt composite is

$$\alpha = \frac{k_{\text{eff}}}{\rho_{\text{eff}}c_{\text{eff}}} \tag{B.7}$$

The LIG process is highly dynamic, meaning that the thermal and optical properties of the material rapidly evolve as soon as carbonization begins, and the thermal properties of several of our materials are not widely reported, and as such, this model serves as only a rough estimate of the thermal properties of the composites before carbonization begins.

Table B3: Assumptions Used for Modeling of Thermal Properties of PFA/Salt Composites

Parameter	**Value**
Film thickness, L	350 μm
Laser beam diameter, D	100 μm
Minimum laser rastering velocity, U_1	5 mm/s
Maximum laser rastering velocity, U_2	40 mm/s
Density of PFA, ρ_{PFA} (kg/m^3)	1300 [333]
Density of NaCl, ρ_{NaCl} (kg/m^3)	2170 [334]
Density of Na_2SO_4, ρ_{Na2SO4} (kg/m^3)	2700 [334]
Thermal conductivity of PFA, k_{PFA} (W/m·K)	0.15 [333,335]
Thermal conductivity of NaCl, k_{NaCl} (W/m·K)	6.5 [336]
Thermal conductivity of Na_2SO_4, k_{Na2SO4} (W/m·K)	0.6 ($Na_2SO_4 \cdot 10H_2O$),[337] 1.6 ($CaSO_4 \cdot 4H_2O$)[338]
Heat capacity of PFA, $C_{P,PFA}$ (J/kg·K)	1500 [335]
Heat capacity of NaCl, $C_{P,NaCl}$ (J/kg·K)	864 [339]
Heat capacity of Na_2SO_4, $C_{P,Na2SO4}$ (J/kg·K)	899 [339]

Notes on Modeling Parameters:

The thermal modeling serves as a rough, qualitative estimate of the effects of introducing salt particles into the PFA on the composite thermal properties. While accurate thermal data is available for some materials, such as NaCl, many of the other parameters are estimates. The density, thermal conductivity, and heat capacity of PFA have not been reported to the best of our knowledge, and as such, we used model values from Bakelite, a phenol-formaldehyde resin with similar properties. Similarly, only some thermal values are available for Na_2SO_4. The density and heat capacity of anhydrous Na_2SO_4 (an average of phase III and phase V) have been reported and used here. However, the thermal conductivity has not been reported for anhydrous Na_2SO_4 to the best of our knowledge. As this is a key parameter in the model, we have included different estimates and plotted the variation. The thermal conductivity of $Na_2SO_4 \cdot 10H_2O$ is 0.6 W/m·K. We expect that the decahydrate form of Na_2SO_4 will have different thermal properties than the anhydrous form. Many inorganic minerals possess thermal conductivities >1 W/m·K[338] (including NaCl at 6.5 W/m·K) – as such we also ran a model using an estimated thermal conductivity of 1.6 W/m·K based on gypsum ($CaSO_4 \cdot 4H_2O$), which, while still a hydrate, is a less hydrated sulfate salt.

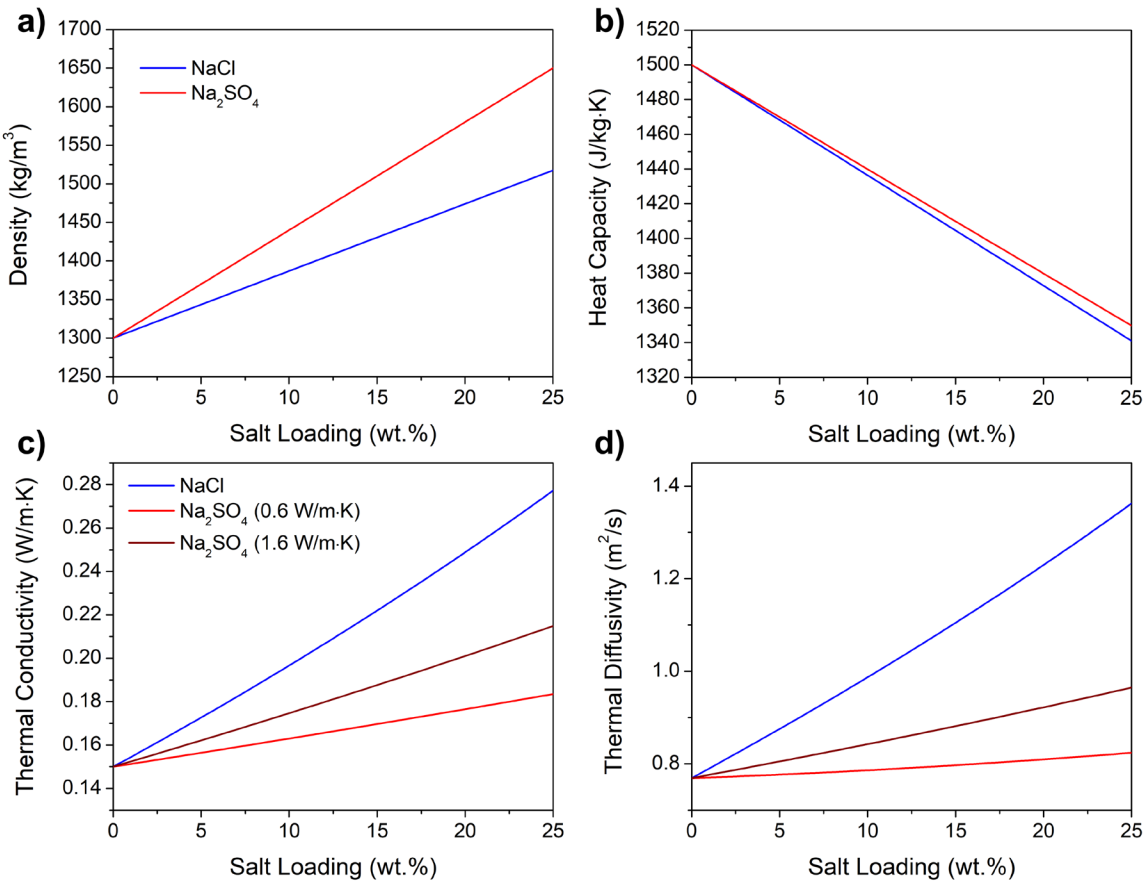

Figure B17: Modeling of a) density, b) heat capacity, c) thermal conductivity, and d) thermal diffusivity of PFA/salt composites with salt loading for NaCl and Na_2SO_4. Note that two different thermal conductivities were used for pure Na_2SO_4 (0.6 W/m·K and 1.6 W/m·K) as discussed with Table B3.

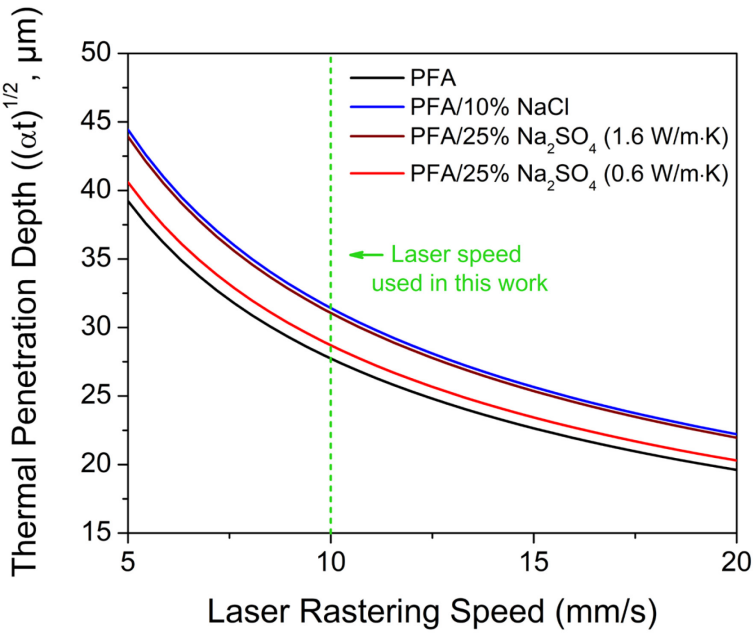

Figure B18: Modeling of estimated heat penetration depth $(\alpha t)^{1/2}$ for PFA/salt composites with laser rastering speed, for 10% NaCl and 25% Na_2SO_4. The experimental laser speed used in this work, 10 mm/s, is marked with a dotted line. Note that two different thermal conductivities were used for pure Na_2SO_4 (0.6 W/m·K and 1.6 W/m·K) as discussed with Table B3. We observe that at laser speeds of 10 mm/s, for PFA/no salt the estimated penetration depth is approximately 28 μm. The addition of 10% NaCl or 25% Na_2SO_4 into the PFA increases the penetration depth to ~32 μm and ~29-31 μm, respectively. Experimentally, the LIG thickness is greater than the estimated heat penetration depth, which we expect is a result of other mechanisms including the expansion of the LIG as gases escape during rapid carbonization, and due to potential differences in the IR absorptivity or transmissivity of the composites with the addition of salt particles, which we did not consider in this model.

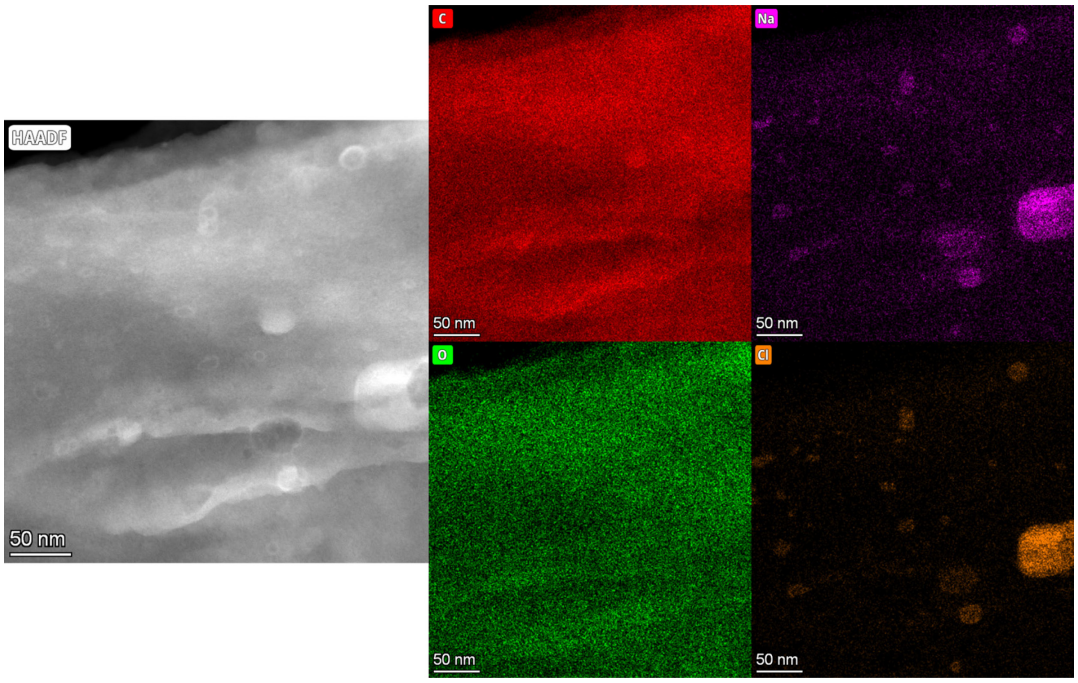

Figure B19: TEM EDS mapping of LIG from PFA/10% NaCl at higher magnification.

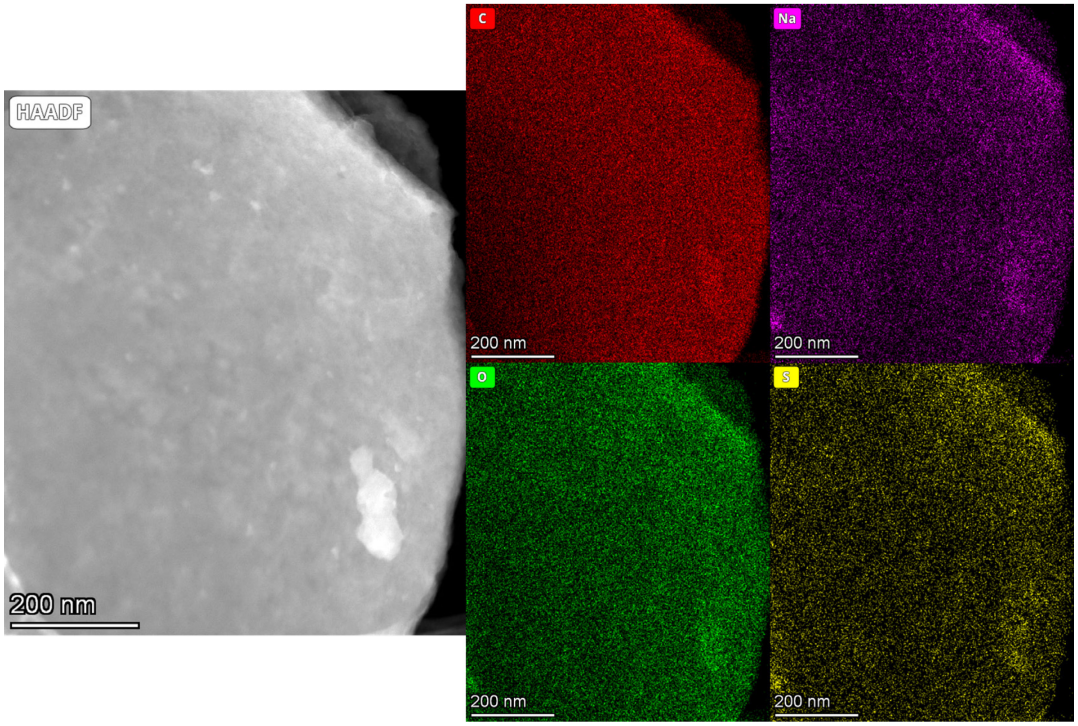

Figure B20: TEM EDS mapping of LIG from PFA/25% Na_2SO_4 at higher magnification.

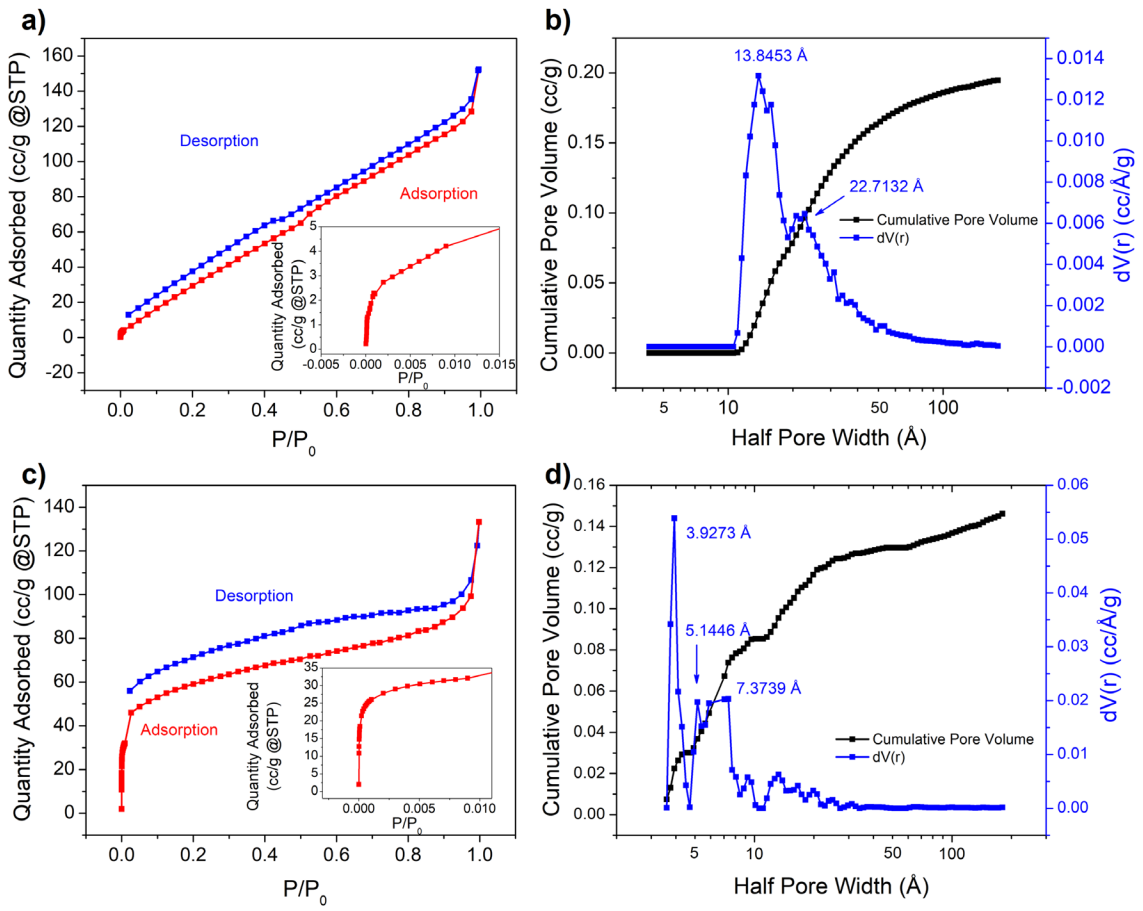

Figure B21: a,c) Full nitrogen adsorption and desorption isotherms and b,d) DFT pore size distributions for a,b) LIG from PFA/10% NaCl and c,d) PFA/25% Na_2SO_4. Both samples are both microporous and mesoporous.

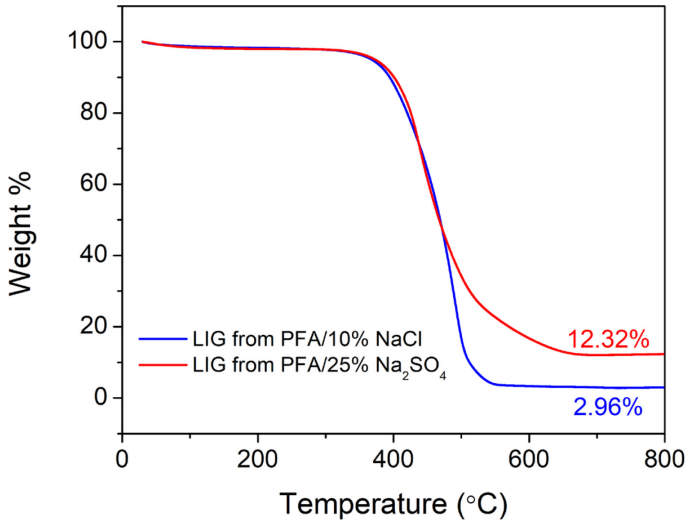

Figure B22: TGA analysis of LIG from PFA/10% NaCl and PFA/15% Na_2SO_4 after soaking in water to remove residual salt and after performing BET analysis. TGA was performed at 5 °C/min under air, to burn away all carbon and determine the amount of remaining salt in the samples.

Table B4: XPS Fitting Parameters for LIG from PFA/no salt

Peak	Deconvoluted Peaks	Position (eV)	FWHM	% Area
C1s	C-C	284.4	0.94	34.5
	C-O	285.1	1.75	44.0
	C=O	286.2	3.27	21.5
O1s	C-O	533.9	1.52	38.6
	C=O	532.5	1.96	61.4

Table B5: XPS Fitting Parameters for LIG from PFA/10% NaCl

Peak	Deconvoluted Peaks	Position (eV)	FWHM	% Area
C1s	C-C	284.8	1.13	7.7
	C-O	285.6	1.88	42.5
	C=O/C-Cl	286.8	2.90	46.7
	-COO	289.5	1.89	3.1
O1s	C-O	533.9	2.93	87.5
	C=O	532.3	1.90	12.5
Cl2p	$Cl^- 2p_{3/2}$	199.1	1.35	32.4
	$Cl^- 2p_{1/2}$	200.7	1.35	16.2
	C-Cl $2p_{3/2}$	200.6	1.90	34.2
	C-Cl $2p_{1/2}$	202.2	1.90	17.1

Table B6: XPS Fitting Parameters for LIG from PFA/25% Na_2SO_4

Peak	Deconvoluted Peaks	Position (eV)	FWHM	% Area
C1s	C-C	284.6	1.03	7.8
	C-O/C-S	285.5	1.46	31.5
	C=O	286.2	2.90	44.0
	-COO	289.6	1.83	16.7
O1s	C-O	533.9	1.05	2.5
	C=O	532.5	1.75	67.8
	SO_4^{2-}	531.6	1.48	29.8
S2p	SO_4^{2-} $2p_{3/2}$	169.1	1.83	50.5
	SO_4^{2-} $2p_{1/2}$	170.2	1.83	25.3
	C-S $2p_{3/2}$	163.5	2.89	13.9
	C-S $2p_{1/2}$	164.7	2.89	6.9
	$Na_2(SO_3)_2$	166.9	0.86	3.5

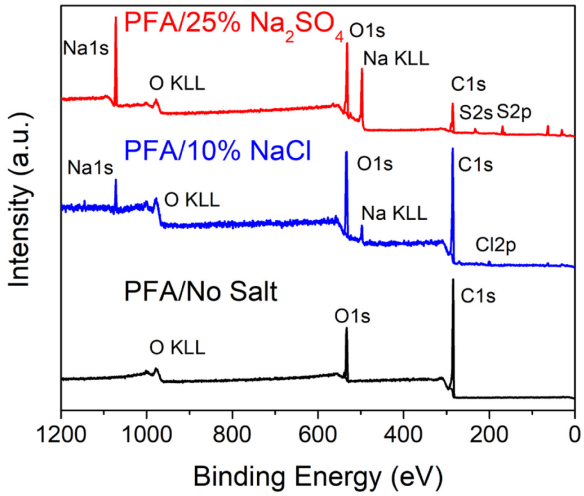

Figure B23: XPS survey spectra of LIG from PFA/no salt, PFA/10% NaCl, and PFA/25% Na_2SO_4.

Table B7: Average Areal Capacitance of LIG Devices from PFA with Varying Salt Loadings at 5 mV/s

Salt Loading	Areal Capacitance (mF/cm^2)
No Salt	0.008
5% NaCl	6.5
10% NaCl	5.7
5% Na_2SO_4	0.99
10% Na_2SO_4	1.7
15% Na_2SO_4	8.4
20% Na_2SO_4	25.6
25% Na_2SO_4	19.7
30% Na_2SO_4	15.2

Effect of Salt Particle Size and Dissolved Salt on Capacitance

In order to determine if the capacitance boost occurs as a result of the dispersed salt particles or from dissolved salt in the system, the performance of PFA/10% Na_2SO_4 devices prepared as discussed with spray-dried salt particles was compared to the performance of devices which were prepared by first stirring the FA, EtOH, and spray-dried Na_2SO_4 after tip sonication for 24 hours in order to dissolve any salt, and then centrifuged to remove all solid salt particles. The polymerization was then carried out via addition of the oxalic acid catalyst after centrifugation. The centrifuged samples exhibited extremely low areal capacitances of 0.8 µF/cm^2 at 5 mV/s and 0.5 µF/cm^2 at 100 mV/s, even lower than PFA/no salt films, indicating that if any Na_2SO_4 dissolves throughout the polymerization, it does not result in a boost in the final device capacitance. The performance of PFA/10% Na_2SO_4 devices prepared with 2 µm spray-dried Na_2SO_4 particles was also compared to devices prepared with non-spray-dried salt particles, with an average particle size of 373 µm, to determine the effect of the size of the salt particles on the capacitance. PFA/10% Na_2SO_4 samples with non-spray-dried particles also exhibit a much lower capacitance than with spray-dried particles, achieving 0.21 mF/cm^2 at 5 mV/s and 0.08 mF/cm^2 at 100 mV/s, compared to an average of 1.7 mF/cm^2 at 5 mV/s and 0.62 mF/cm^2 at 100 mV/s for spray-dried particles. Notably, similar results are achieved for centrifuged samples and non-spray-dried samples with NaCl. These results indicate that only small, well-dispersed solid salt particles can enable a significant boost in capacitance.

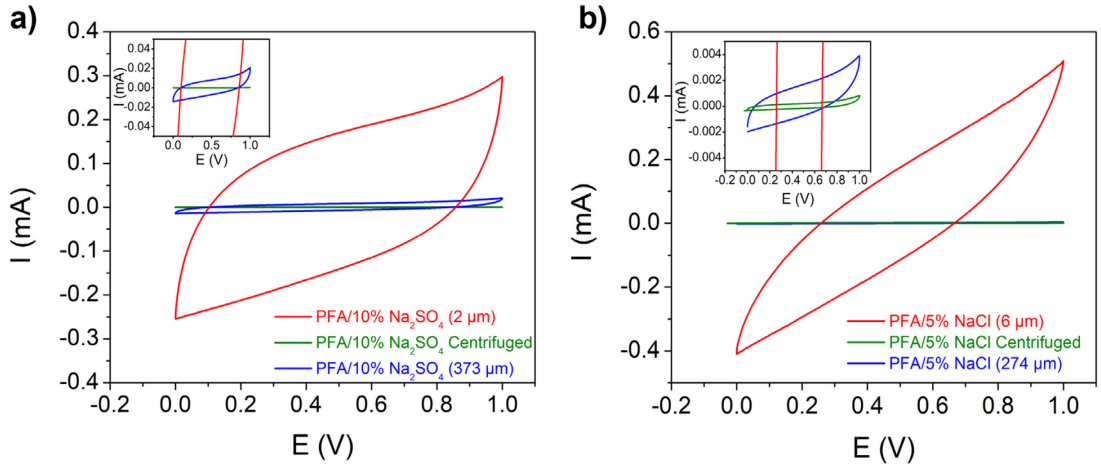

Figure B24: CV curves at 100 mV/s of LIG supercapacitors from a) PFA/10% Na_2SO_4 (spray-dried, 2 µm particles), PFA/10% Na_2SO_4 Centrifuged, and PFA/10% Na_2SO_4 (non-spray-dried, 373 µm particles) and b) PFA/5% NaCl (spray dried, 6 µm particles), 5% NaCl Centrifuged, and 5% NaCl (not spray dried, 274 µm particles).

Table B8: Average Areal Capacitance of PFA/25% Na_2SO_4 LIG Devices with Scan Rate

Scan Rate (mV/s)	Average Areal Capacitance (mF/cm^2)
5	19.7 ± 3.0
10	14.7 ± 2.0
50	10.9 ± 3.7
100	7.6 ± 2.1
250	5.9 ± 2.8
500	4.3 ± 2.3

Sources of Cell Resistance:

There is a slight tilt to the CV curves from PFA/salt devices, which stems from several sources of resistance in our devices. Unlike a typical sandwich configuration supercapacitor, the interdigitated electrode design possesses longer pathways for both electronic transport (resistance along each 1.5 cm long finger is ~360 Ω based on sheet resistance) and ionic conduction (~450 μm between each finger, compared to ~25 μm thick separators in conventional cells). We note that while the resistance along a single finger is ~360 Ω, because 14 fingers are in parallel on each electrode, the total resistance is only ~26 Ω. Because there are two electrodes effectively in series in the full device, the total resistance from the LIG should be ~51 Ω. However, our experimental ESR is only ~26 Ω, which is likely due to the scribed fingers being slightly wider than 350 μm and the fact that the bus bars overlap significantly with the fingers, shortening the overall length of each finger substantially. We observe an IR drop of ~55-60 mV in GCD cycling at 2 mA/cm^2 (1 mA), which would give a similar but slightly higher device resistance of ~55-60 Ω, which may be due to variation as the device cycles. Furthermore, all testing is done with a PVA gel-based electrolyte, which has achieved ionic conductivities of 0.002 – 12 mS/cm in literature,[340] while typical aqueous electrolytes such as 1 M H_2SO_4 possesses conductivities >100 mS/cm.[341] However, gel-based electrolytes are the most common choice for LIG-based devices with novel architectures to prevent electrolyte leakage. This interdigitated electrode design demonstrates the capabilities of the LIG approach to prepare next generation device architectures, but further optimization is required to achieve cell resistances comparable to liquid electrolyte sandwich configurations.

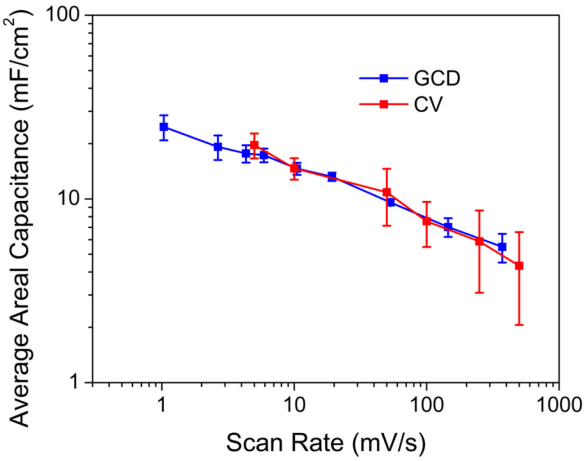

Figure B25: Average areal capacitance for LIG supercapacitors from PFA/25% Na_2SO_4 with scan rate from both CV and GCD data.

Table B9: Average Areal Capacitance of PFA/25% Na_2SO_4 LIG Devices with Current Density

Current Density (mA/cm^2)	Average Areal Capacitance (mF/cm^2)
0.05	24.7 ± 3.8
0.1	19.2 ± 2.9
0.2	17.3 ± 1.5
0.3	14.6 ± 1.1
0.5	13.2 ± 0.7
1	9.6 ± 0.3
2	7.0 ± 0.8
4	5.5 ± 1.0

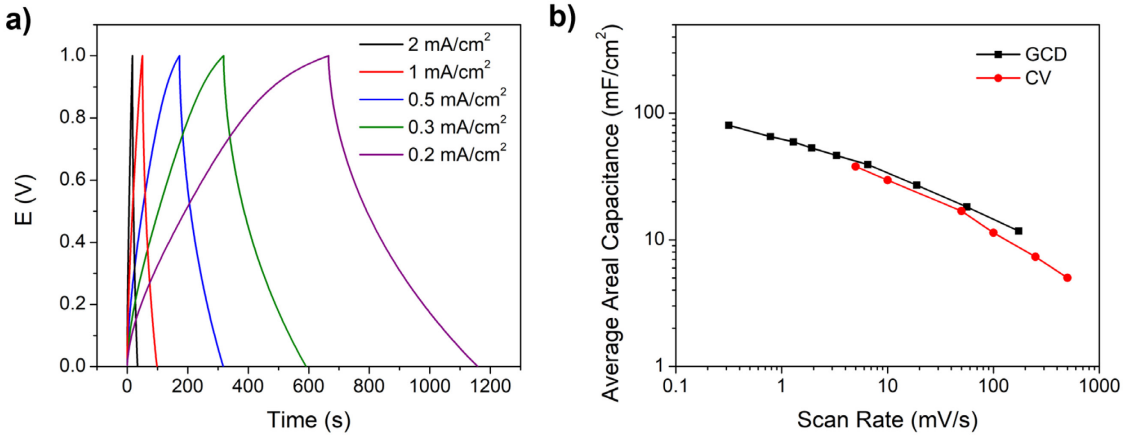

Figure B26: a) GCD curves for high-performing PFA/20% Na_2SO_4 device. b) Average areal capacitance for two high-performing PFA/20% Na_2SO_4 devices with scan rate from both CV and GCD data.

Table B10: Average Areal Capacitance of PFA/20% Na_2SO_4 LIG Devices with Current Density

Current Density (mA/cm^2)	Average Areal Capacitance (mF/cm^2)
0.05	80.4
0.1	65.2
0.2	53.2
0.3	46.3
0.5	39.3
1	27.0
2	18.2
4	11.8

Effect of Residual Salt in LIG on Supercapacitor Performance:

We further investigated the effect of the residual surface-coating salt in the LIG on the capacitance of the LIG-based supercapacitors by soaking devices in water overnight to dissolve out the salt, and then testing their performance, as seen in **Figure B27**. We observed a slight boost in performance after salt dissolution, to 27.6 mF/cm^2 at 5 mV/s. We also tested the effect of salt dissolution on a second electrode design, where the electrode fingers are spaced further apart (~750 µm), leading to higher expected cell resistances. In this case, we observe a slight decrease in capacitance at low scan rates, but a much more dramatic increase at high scan rates (0.35 mF/cm^2 to 3.0 mF/cm^2 at 500 mV/s), indicating that salt dissolution could be a strategy to further improve device performance to some degree.

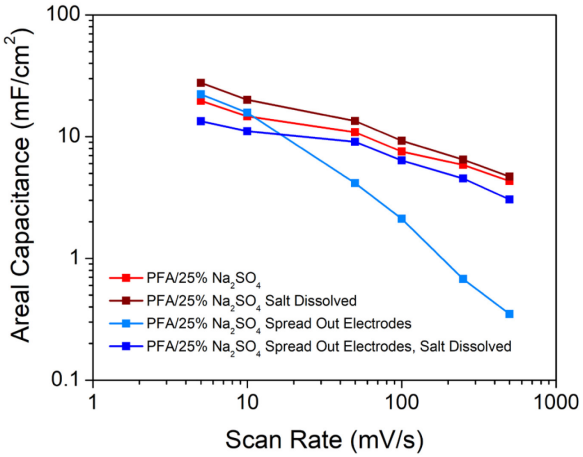

Figure B27: Effect of surface-coating salt on PFA/salt supercapacitors. For "Salt Dissolved" devices, samples were soaked in DI water overnight to dissolve out residual salt in the LIG, and then tested as supercapacitors. Device performance increases slightly for PFA/25% Na_2SO_4 devices soaked in water overnight. For devices prepared with a spread out electrode design, devices were prepared with 18 fingers total, each measuring 350 µm thick, with ~750 µm space between the fingers. For devices with spread out electrode design, a slight decrease in performance is seen with salt dissolution at low scan rates, but a significant increase in capacitance is achieved at high scan rates.

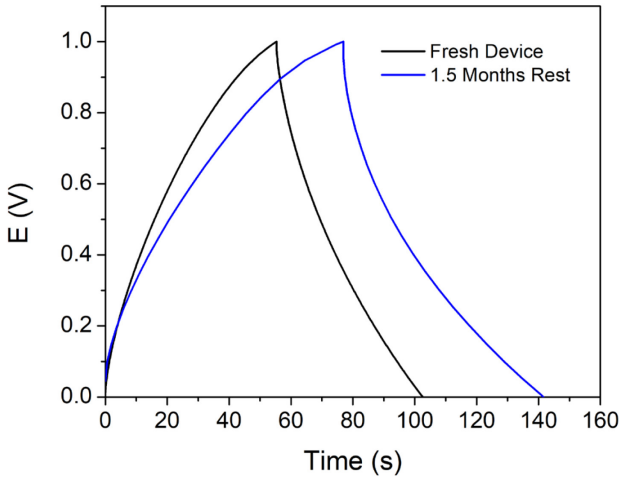

Figure B28: Variation in capacitance for PFA/25% Na_2SO_4 devices with time resting (not cycling). GCD curves at 0.5 mA/cm^2 demonstrate an increase in capacitance observed after samples were rested for 1.5 months.

Appendix C:
Supplementary Information for Chapter 5

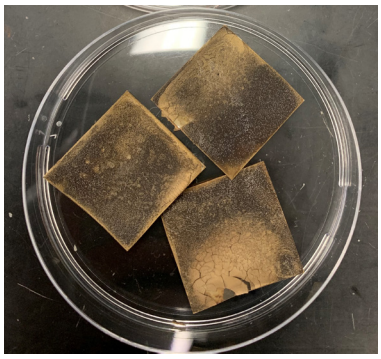

Figure C1: PFA/10% $Li_2B_4O_7$ films, exhibiting heterogeneous composition and cracking.

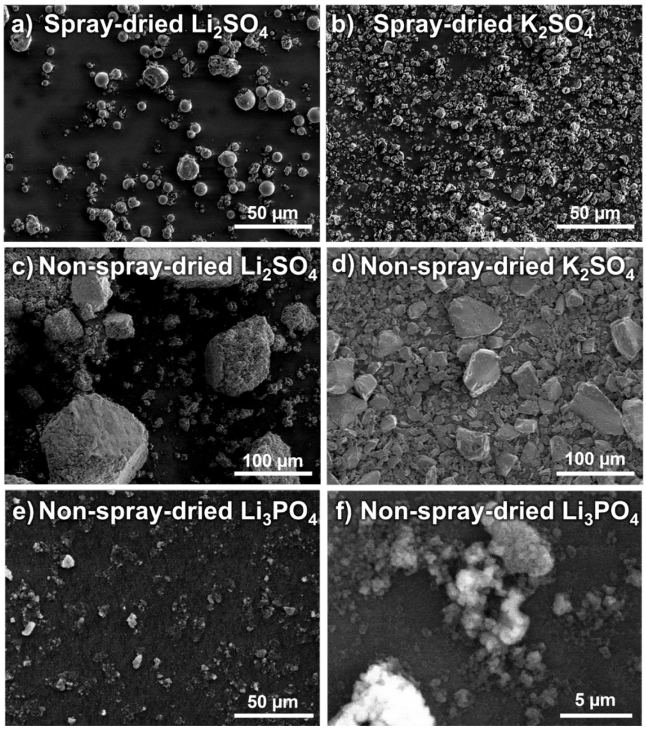

Figure C2: SEM images of spray-dried salt particles. a) Spray-dried Li_2SO_4, b) spray-dried K_2SO_4, c) non-spray-dried Li_2SO_4, d) non-spray-dried K_2SO_4, e) spin-coated Li_3PO_4 and f) higher magnification image of spin-coated Li_3PO_4. Li_3PO_4 was not spray dried due to limited water solubility, but to attempt to estimate the particle size, the commercial powder was dispersed in ethanol at 5 wt.% and spin coated on silicon. However, significant particle aggregation prevented quantitative particle size analysis.

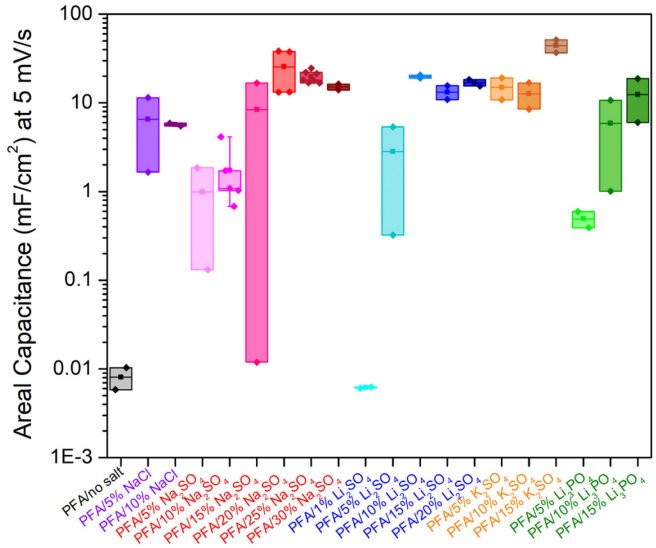

Figure C3: Areal capacitance of LIG supercapacitors from various salt loadings at 5 mV/s, plotted on a logarithmic axis.

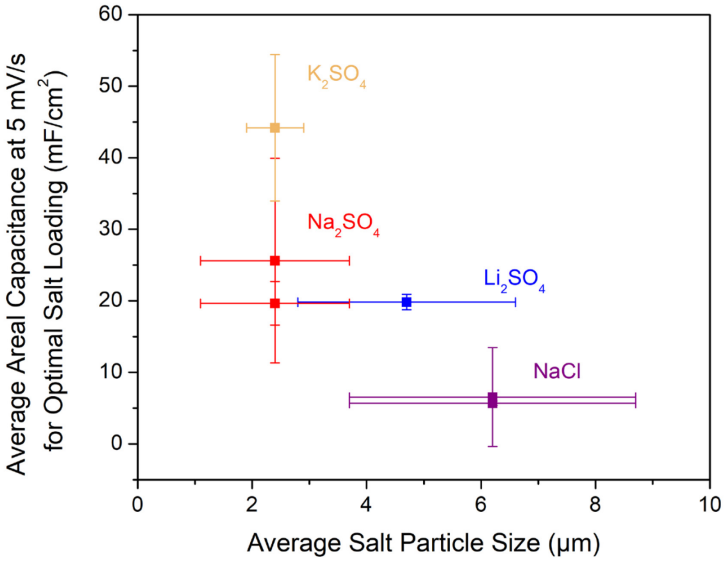

Figure C4: Average areal capacitance at 5 mV/s for optimal salt loading with salt particle size. The optimal salt loadings, resulting in the highest average capacitance, are 15% K_2SO_4, 10% Li_2SO_4, 20-25% Na_2SO_4, and 5-10% NaCl. Two different loadings are included for Na_2SO_4 and NaCl, as the maximum areal capacitance resulted in higher standard deviation between samples (5% NaCl, 20% Na_2SO_4), while the second highest areal capacitance exhibited much lower variation between samples.

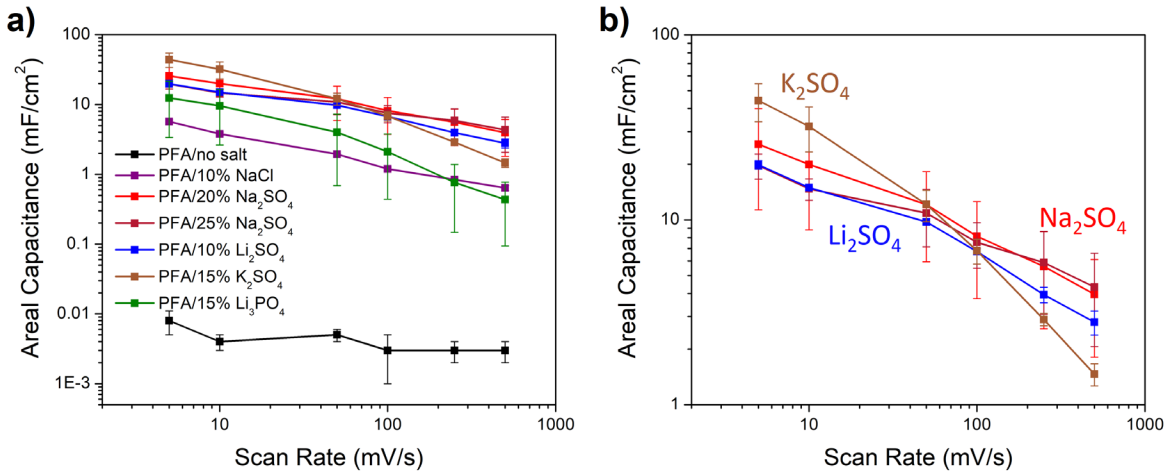

Figure C5: a) Areal capacitance of LIG from PFA with various salts, at optimal loading, with scan rate. b) Areal capacitance of LIG from PFA with sulfate salts, at optimal loading, with scan rate. Both 20% and 25% Na_2SO_4 are included as 20% Na_2SO_4 has a higher average capacitance, but also more sample variability.

Table C1: XPS Fitting Parameters for LIG from PFA/5% Li_2SO_4

Peak	Deconvoluted Peaks	Position (eV)	FWHM	% Area
C1s	C-C	284.34	1.38	42.67
	C-O/C-S	285.65	1.67	44.91
	C=O	287.18	1.98	10.77
	COO	289.66	3.00	1.65
O1s	C=O/C-SO_2-C	531.64	2.13	34.05
	C-O	533.62	2.05	65.95
S2p	C-S $2p_{3/2}$	163.42	1.28	26.14
	C-S $2p_{1/2}$	164.58	1.28	13.36
	C-SO-C $2p_{3/2}$	165.11	1.81	22.72
	C-SO-C $2p_{1/2}$	166.27	1.81	11.61
	C-SO_2-C $2p_{3/2}$	167.99	2.00	10.33
	C-SO_2-C $2p_{1/2}$	169.15	2.00	5.28
	SO_4^{2-} $2p_{3/2}$	169.60	2.00	6.99
	SO_4^{2-} $2p_{1/2}$	170.76	2.00	3.57

Table C2: XPS Fitting Parameters for LIG from PFA/10% Li_2SO_4

Peak	Deconvoluted Peaks	Position (eV)	FWHM	% Area
C1s	C-C	284.38	1.56	51.19
	C-O/C-S	285.65	1.77	35.74
	C=O	287.12	2.43	10.68
	COO	289.70	3.00	2.39
O1s	C=O/C-SO_2-C	531.71	2.28	51.94
	C-O	533.63	1.81	48.06
S2p	C-S $2p_{3/2}$	163.41	1.28	27.32
	C-S $2p_{1/2}$	164.57	1.28	13.96
	C-SO-C $2p_{3/2}$	164.95	2.00	14.80
	C-SO-C $2p_{1/2}$	166.11	2.00	7.56
	C-SO_2-C $2p_{3/2}$	168.08	1.45	15.75
	C-SO_2-C $2p_{1/2}$	169.24	1.45	8.05
	SO_4^{2-} $2p_{3/2}$	169.60	2.00	8.31
	SO_4^{2-} $2p_{1/2}$	170.76	2.00	4.25

Table C3: XPS Fitting Parameters for LIG from PFA/15% Li_2SO_4

Peak	Deconvoluted Peaks	Position (eV)	FWHM	% Area
C1s	C-C	284.39	1.46	42.45
	C-O/C-S	285.65	1.84	31.70
	C=O	287.16	2.59	18.82
	COO	289.70	3.00	7.03
O1s	C=O/C-SO_2-C	531.88	2.20	65.74
	C-O	533.67	2.03	34.26
S2p	C-S $2p_{3/2}$	163.47	1.26	15.69
	C-S $2p_{1/2}$	164.63	1.26	8.02
	C-SO-C $2p_{3/2}$	164.99	2.00	13.76
	C-SO-C $2p_{1/2}$	166.15	2.00	7.03
	C-SO_2-C $2p_{3/2}$	167.85	1.56	17.27
	C-SO_2-C $2p_{1/2}$	169.01	1.56	8.83
	SO_4^{2-} $2p_{3/2}$	169.60	2.00	19.46
	SO_4^{2-} $2p_{1/2}$	170.76	2.00	9.94

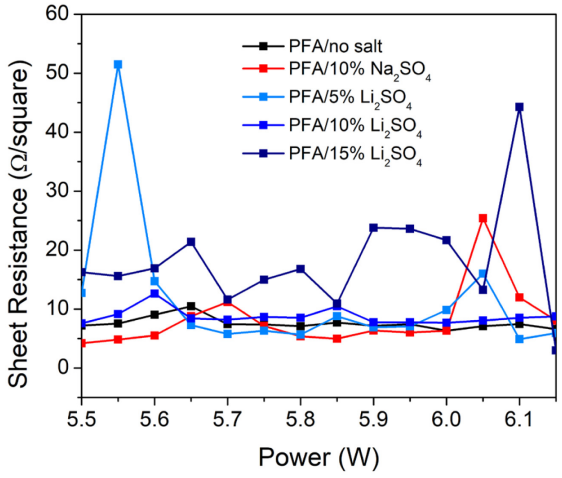

Figure C6: Sheet resistance of LIG from PFA/no salt, PFA/10%Na_2SO_4, PFA/5% Li_2SO_4, PFA/10% Li_2SO_4, and PFA/15% Li_2SO_4 with laser power, before salt dissolution.

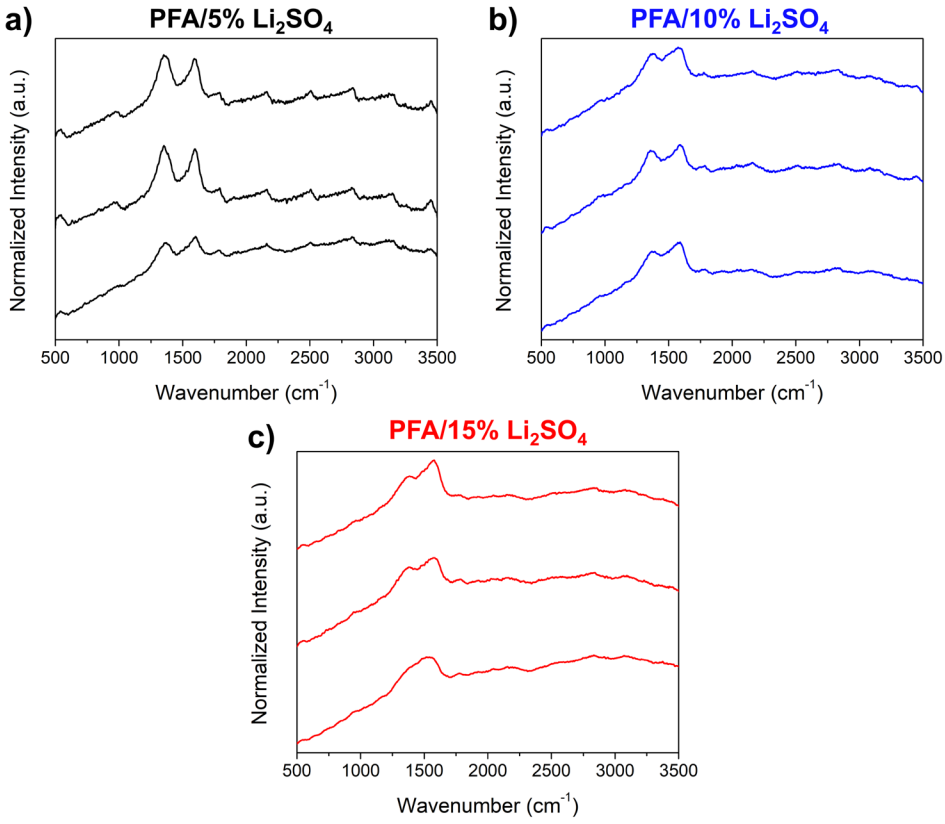

Figure C7: Raman spectra of LIG from PFA/5% Li_2SO_4, PFA/10% Li_2SO_4, and PFA/15% Li_2SO_4 at 5.85 W, before salt dissolution.

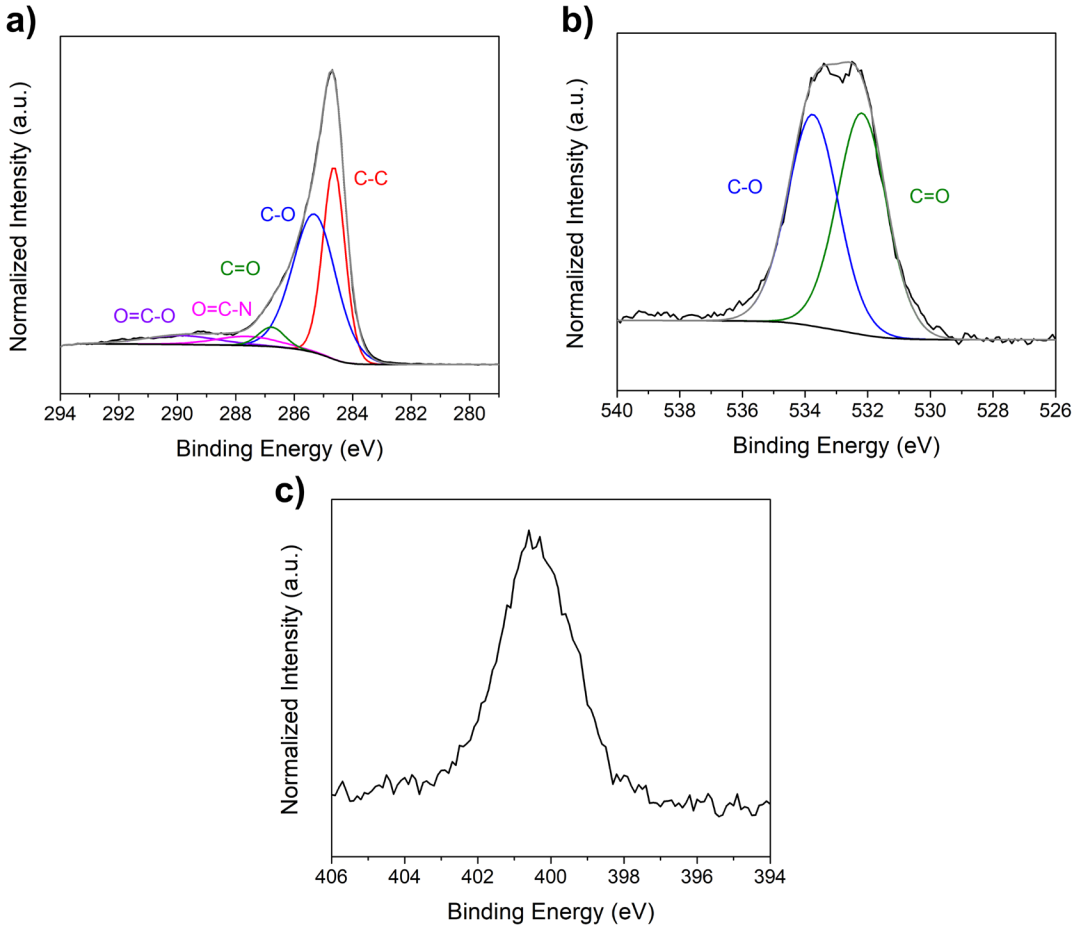

Figure C8: XPS of LIG from PI. a) C1s spectrum, b) O1s spectrum, and c) N1s spectrum. The N1s spectrum was not deconvoluted due to the significant overlap of several functional groups in the same binding energy range.

Table C4: XPS Fitting Parameters for LIG from PI

Peak	Deconvoluted Peaks	Position (eV)	FWHM	% Area
C1s	C-C	284.6	0.89	35.4
	C-O	285.3	1.74	50.0
	C=O	286.8	1.05	4.2
	O=C-N	287.6	2.59	4.9
	O=C-O	289.9	3.00	5.5
O1s	C-O	533.8	1.90	49.3
	C=O	532.2	1.87	50.7

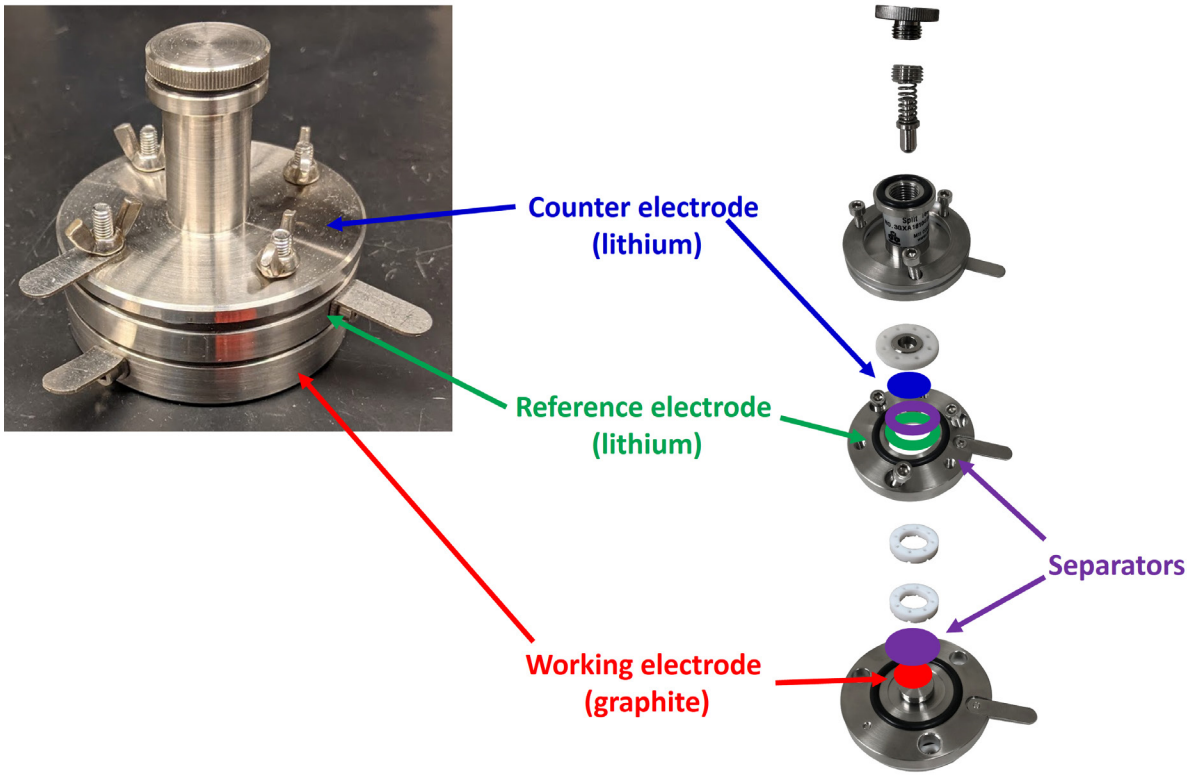

Figure C9: Three-electrode split test cell setup.

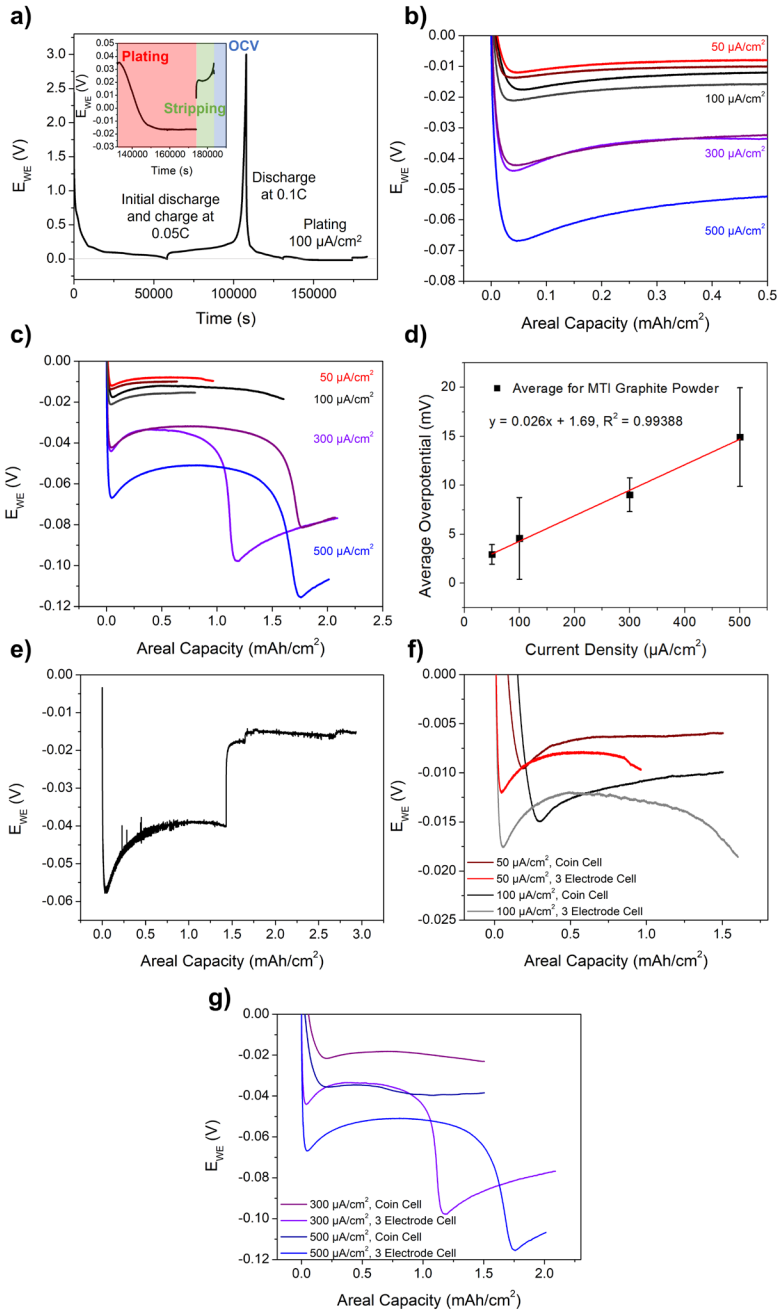

Figure C10: Three-electrode lithium nucleation on graphite. a) Pre-lithiation process before plating. b) Voltage profiles for lithium nucleation on graphite at different current densities up to 0.5 mAh/cm^2. c) Full voltage profiles for lithium nucleation and plating at different current densities, showing second dip in voltage profile at high current densities, indicating shorting of reference and counter electrodes in 3 electrode set up. d) Linear fit of average overpotentials for lithium nucleation with current density. e) Example of noisy plating curves observed with 3 electrode setup, likely due to poor reference electrode contact. Comparison of voltage profiles for lithium nucleation on graphite for coin cell and 3 electrode setups at f) 50 and 100 µA/cm^2 and g) 300 and 500 µA/cm^2.

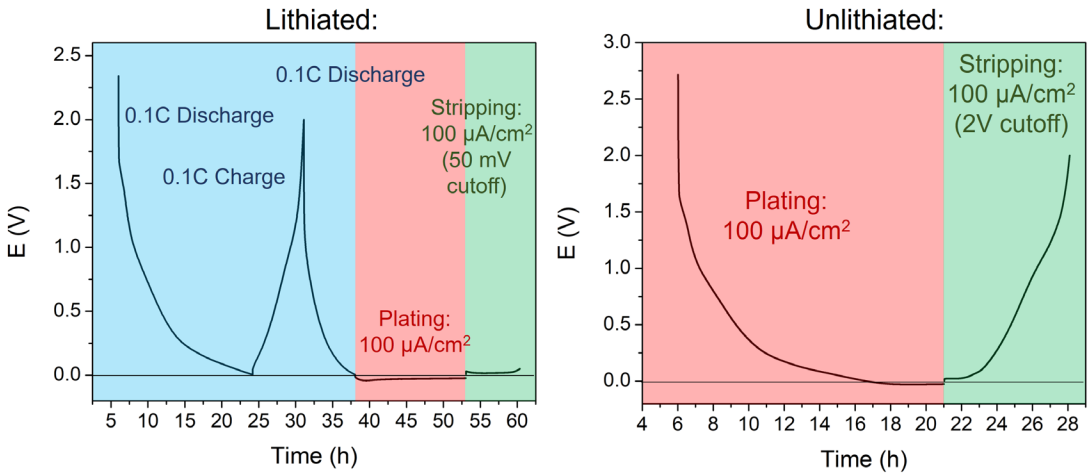

Figure C11: Testing methods for lithiated and unlithiated cells.

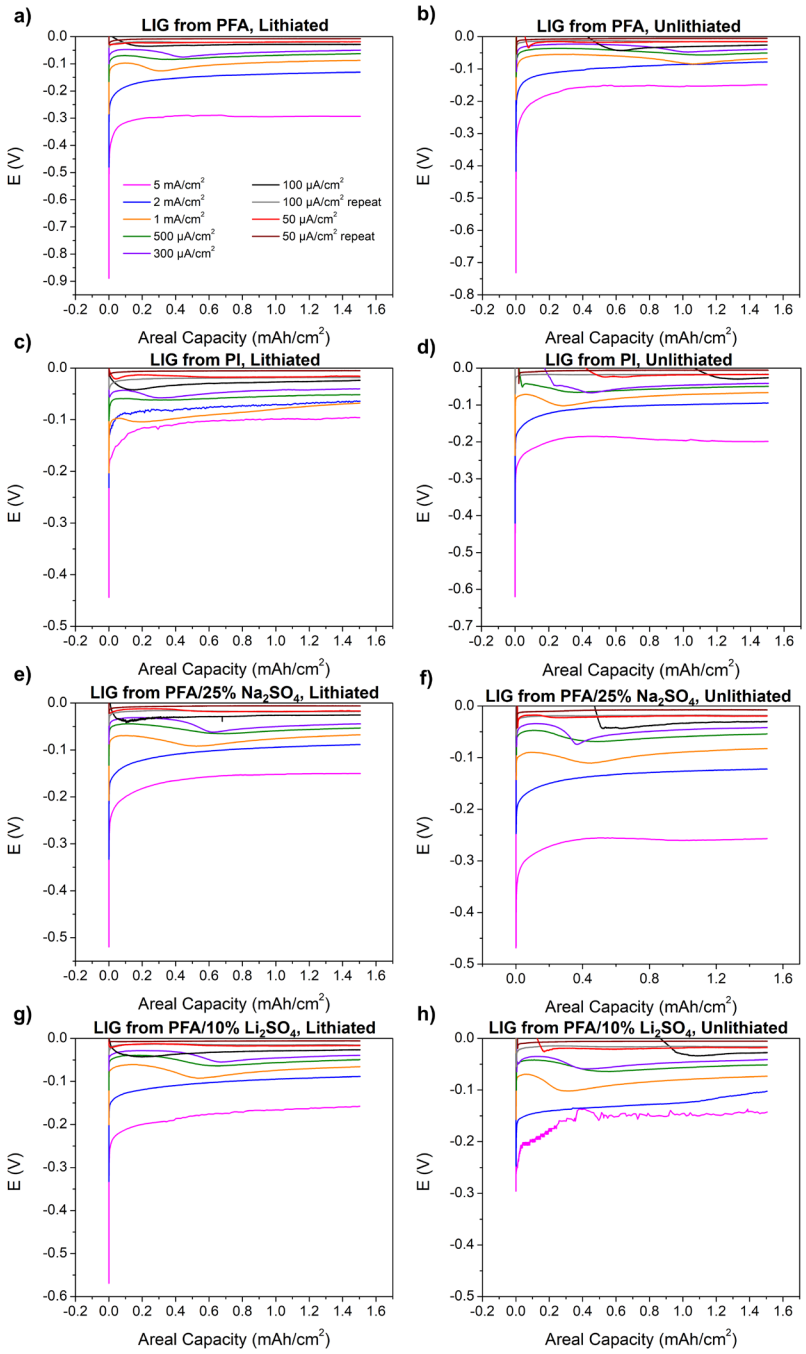

Figure C12: Voltage profiles for lithium plating on a) lithiated LIG from PFA, b) unlithiated LIG from PFA, c) lithiated LIG from PI, d) unlithiated LIG from PI, e) lithiated LIG from PFA/25% Na_2SO_4, f) unlithiated LIG from PFA/25% Na_2SO_4, g) lithiated LIG from PFA/10% Li_2SO_4, and h) unlithiated LIG from PFA/10% Li_2SO_4.

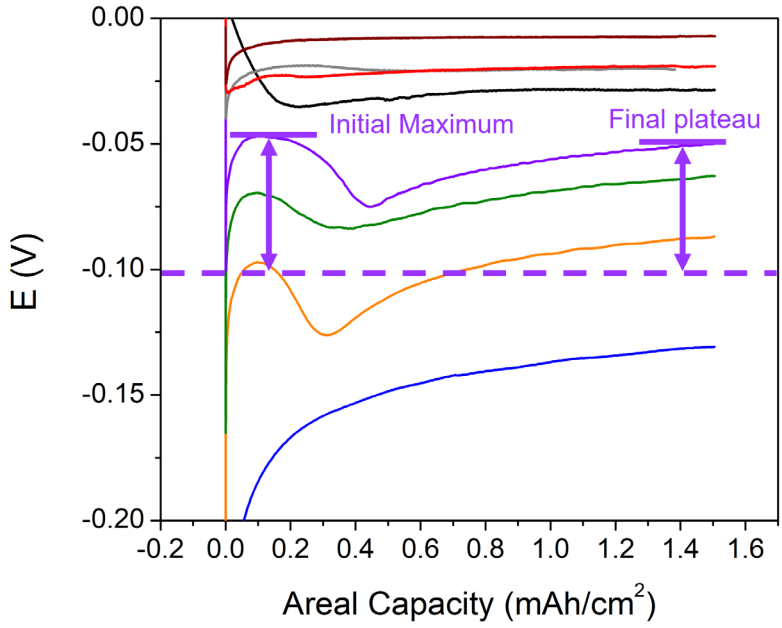

Figure C13: Example of calculating overpotential from initial maximum and final plateau for plating curves with second dip.

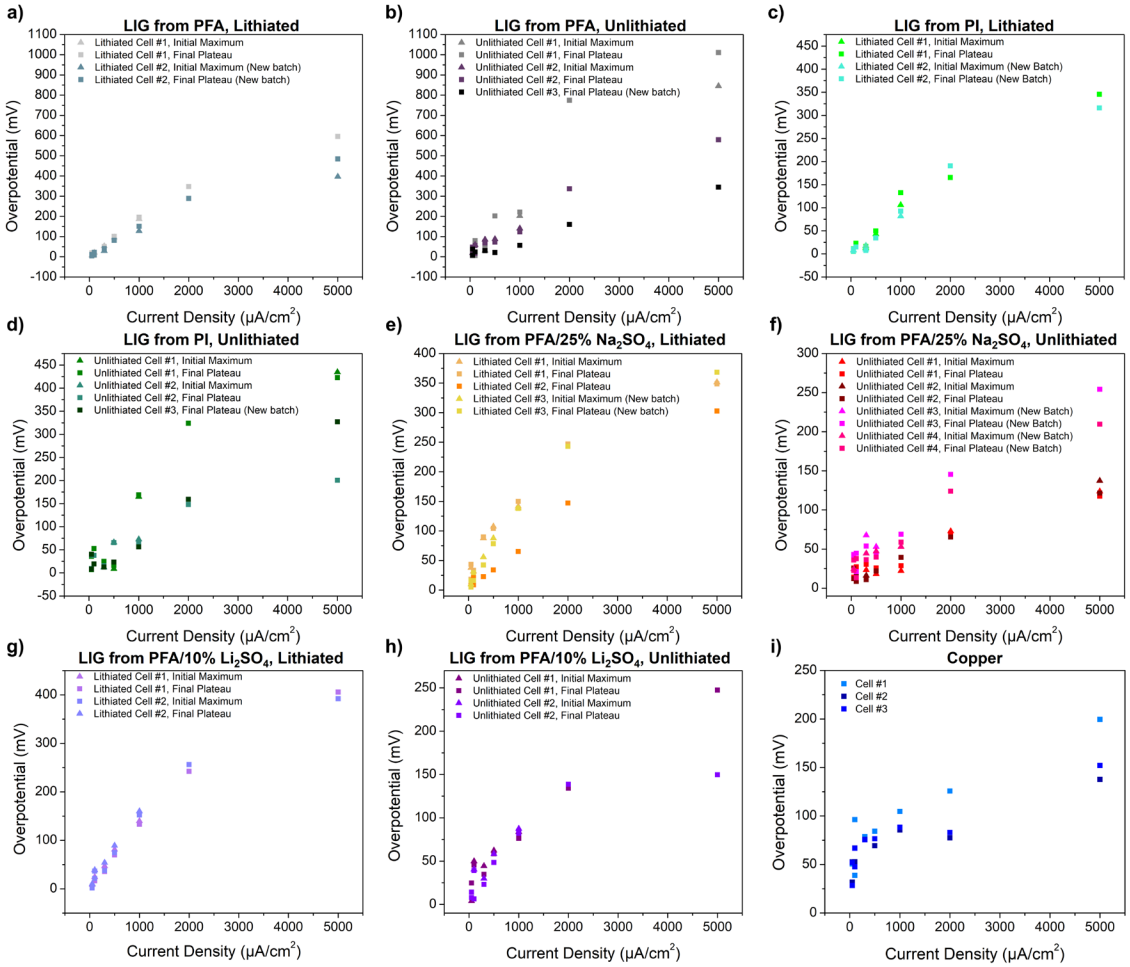

Figure C14: Summary of overpotentials calculated with current density for a) lithiated LIG from PFA, b) unlithiated LIG from PFA, c) lithiated LIG from PI, d) unlithiated LIG from PI, e) lithiated LIG from PFA/25% Na_2SO_4, f) unlithiated LIG from PFA/25% Na_2SO_4, g) lithiated LIG from PFA/10% Li_2SO_4, h) unlithiated LIG from PFA/10% Li_2SO_4, and i) copper.

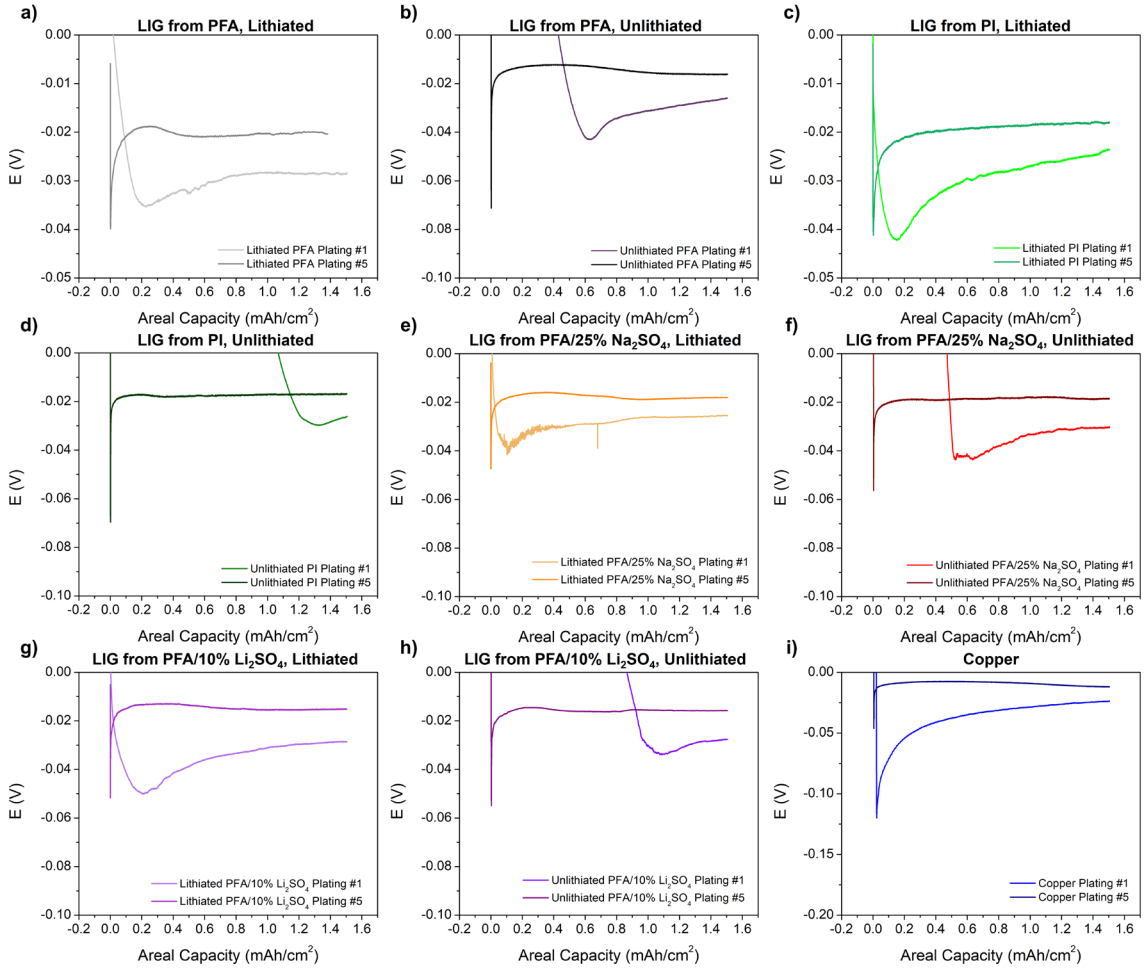

Figure C15: Variation in 100 μA/cm^2 voltage profile for 1st plating and 5th plating.

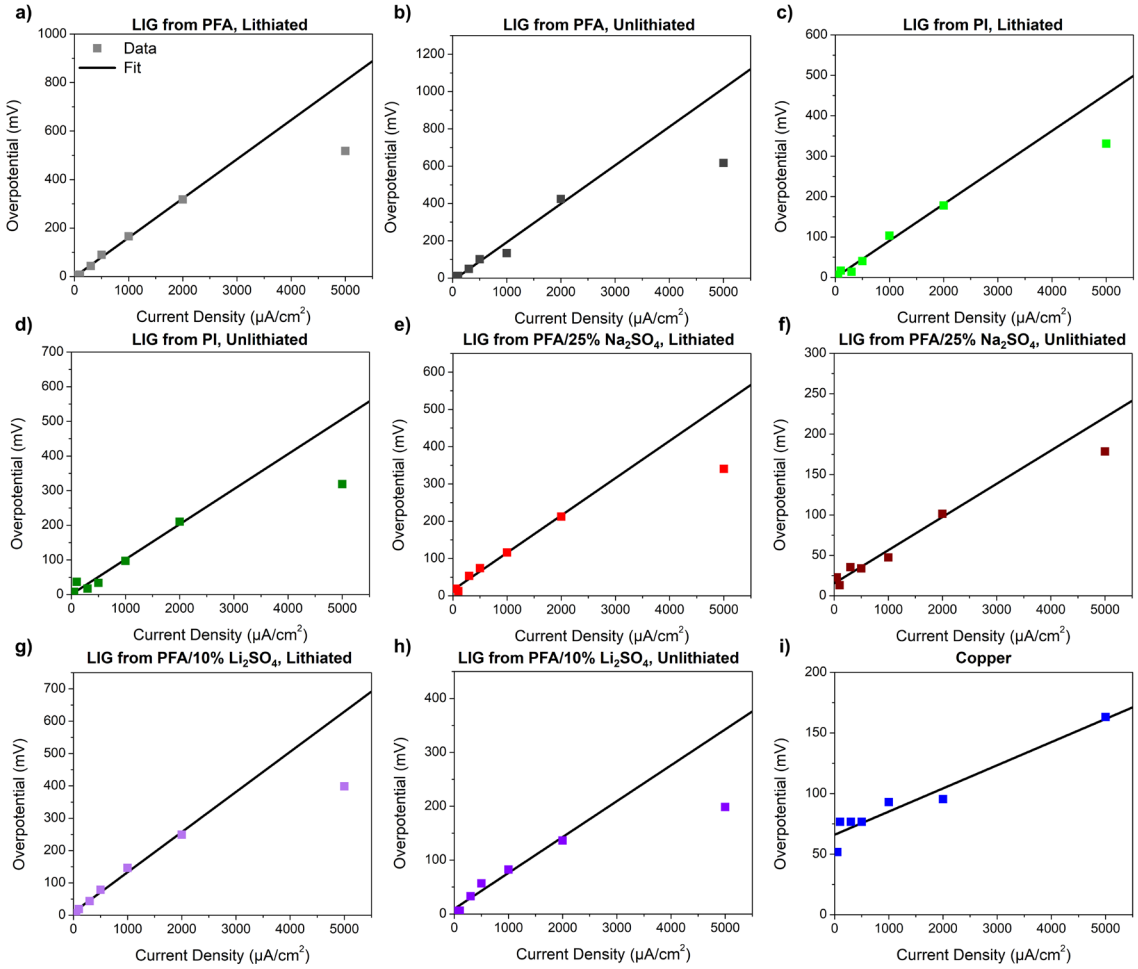

Figure C16: Linear fit to current density-overpotential data, using low overpotential assumption of Butler-Volmer equation.

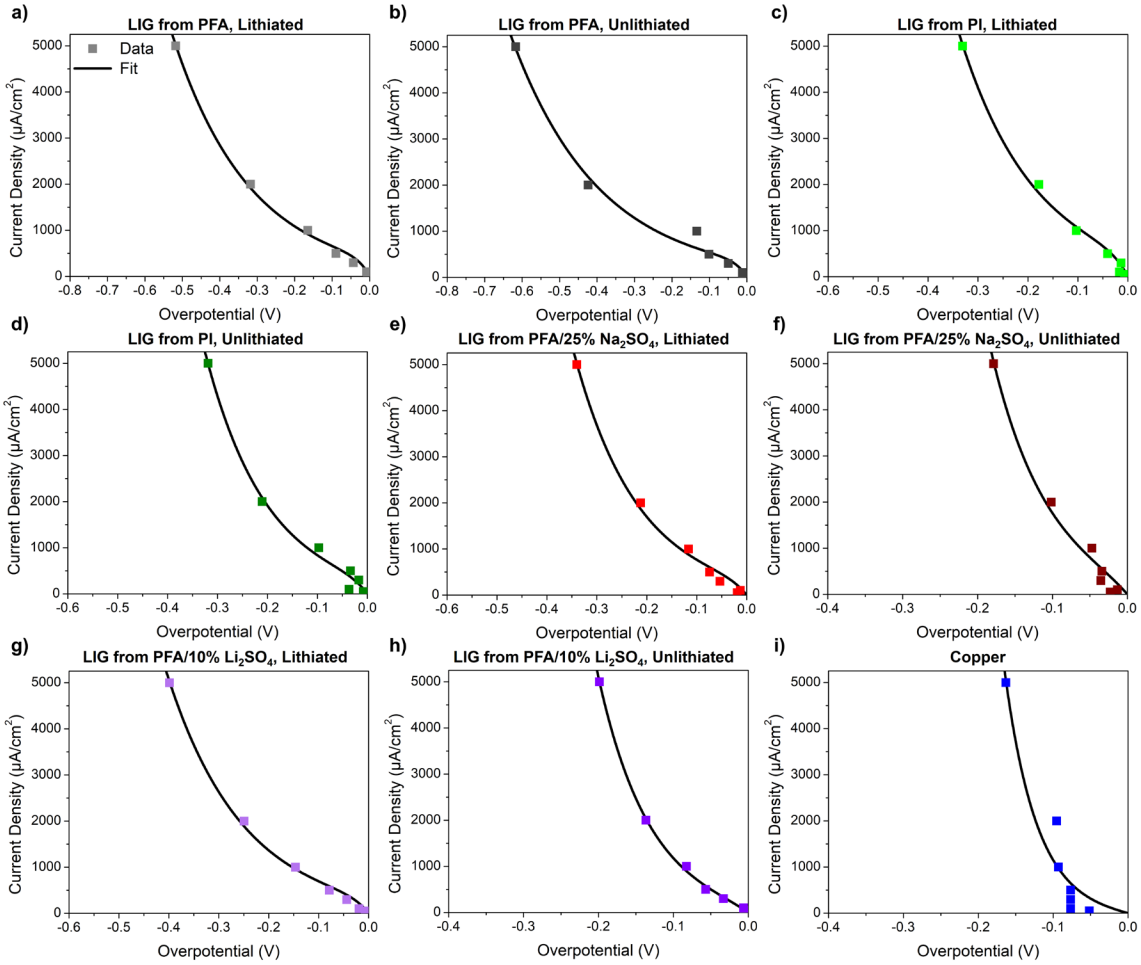

Figure C17: Fit of overpotential-current density data to full Butler-Volmer equation without mass transfer effects.

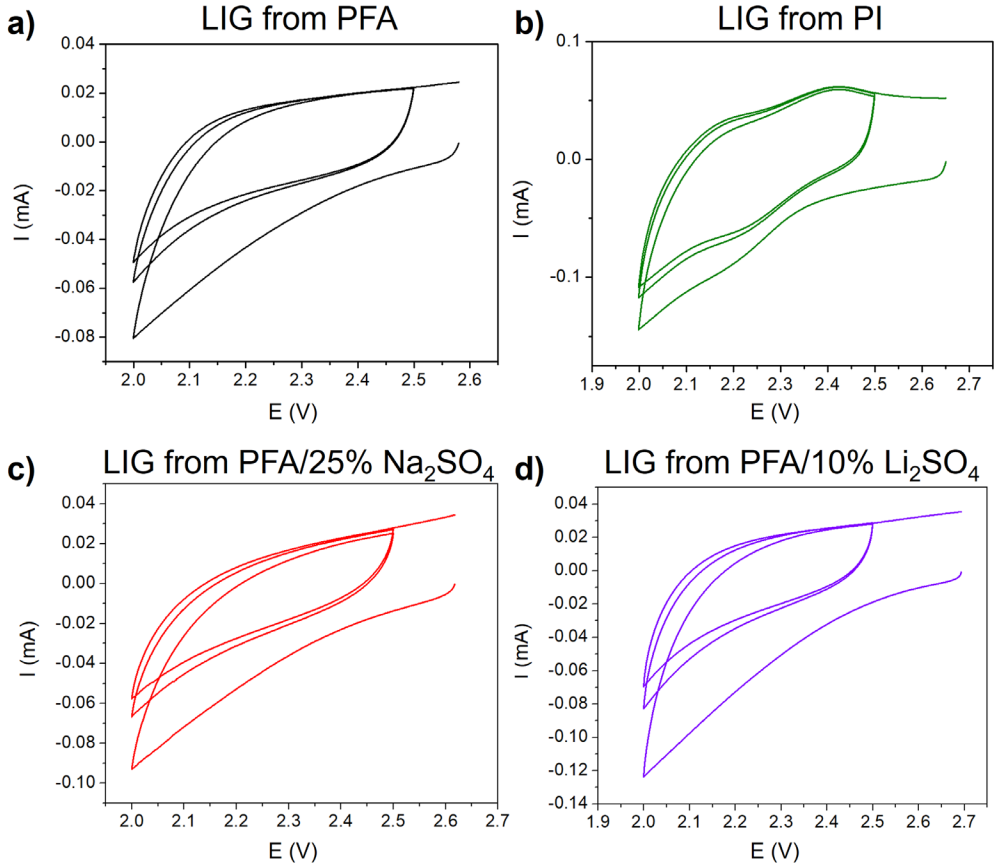

Figure C18: CV curves for different LIG materials, used to determine the ECSA.

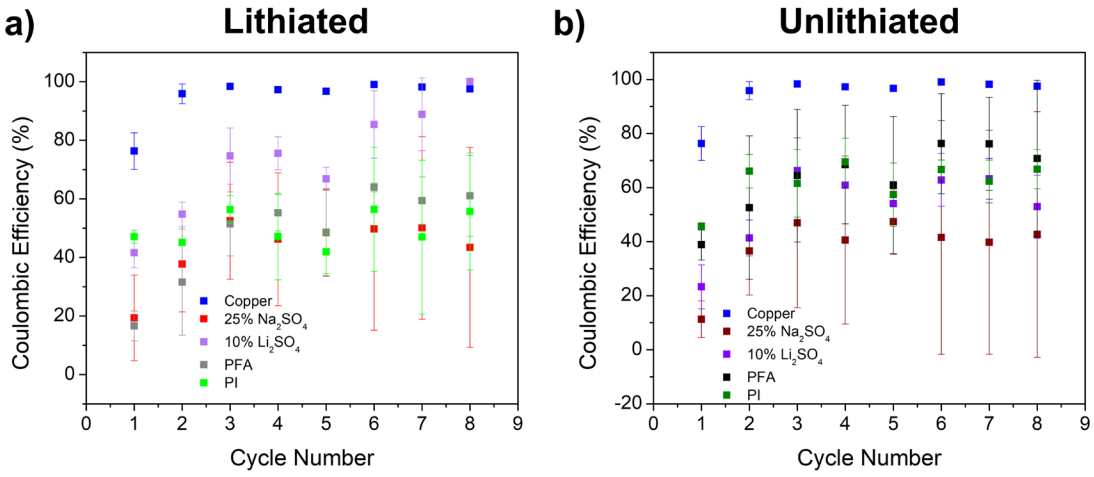

Figure C19: Average coulombic efficiency for a) lithiated and b) unlithiated samples in plating study. Plating at each cycle was performed at different current densities, but stripping was performed at 100 μA/cm^2.

Appendix D:
Supplementary Information for Chapter 6

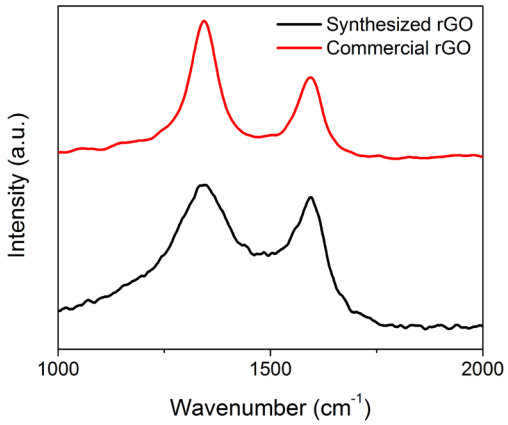

Figure D1: Raman spectra of synthesized rGO from high temperature reduction of GO (black) and commercial rGO (red). The G peak at ~1580 cm^{-1} stems from the graphitic sp^2 structure, while the D peak at ~1350 cm^{-1} is associated with defects and disorder in the material. The I_D/I_G ratio of the commercial rGO is higher than synthesized rGO at 1.54 ± 0.14 vs 0.75 ± 0.05, indicating that the structure is more disordered. The I_D/I_G ratio of rGO prepared from thermal reduction of GO follows a nonmonotonic relationship with temperature, and is known to remain fairly constant at reduction temperatures below 1100 °C and drop significantly at higher reduction temperatures as functional groups and defects are removed with annealing.[92]

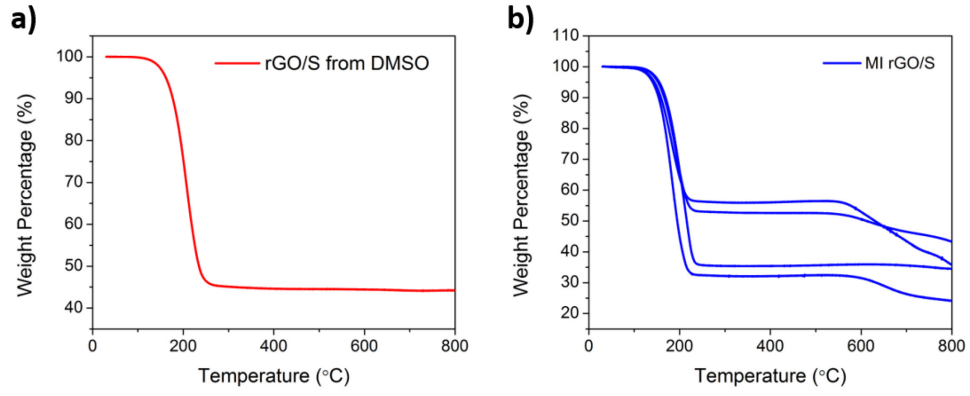

Figure D2: a) TGA of rGO/S active material prepared from 4 mM SDS and DMSO. Active material consists of 45% rGO and 55% sulfur. TGA analysis indicates that 55.5% sulfur is present in the sample. b) TGA of rGO/S active material prepared from melt imbibition of 45% rGO and 55% sulfur. 4 repeats of the same sample indicate that the sample is highly inhomogeneous, with an average sulfur concentration of 55.8%.

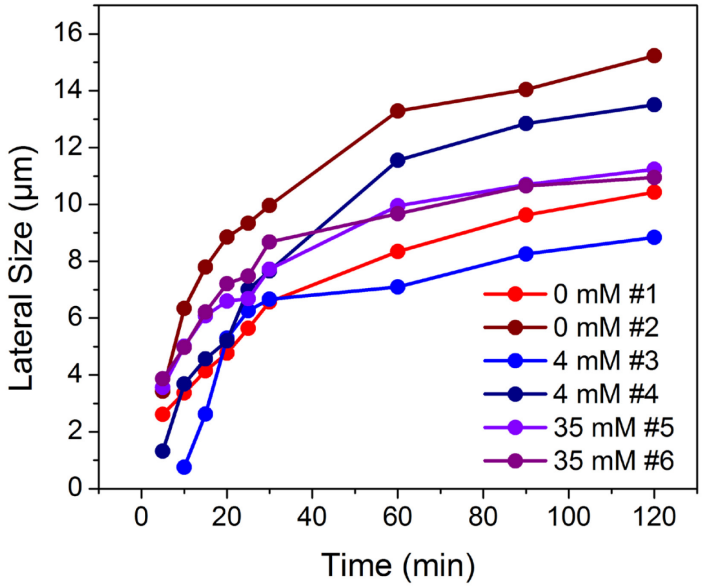

Figure D3: Lateral crystal size over time for crystals seen in Figure 6.2, grown on HOPG substrate using 0.2 M sulfur dissolved in DMSO, a 1:10 ratio of DMSO/water, and SDS concentrations of 0 mM, 4 mM, and 35 mM. The numbers correspond to the number of each crystal as labelled in Figure 6.2 in Chapter 6.

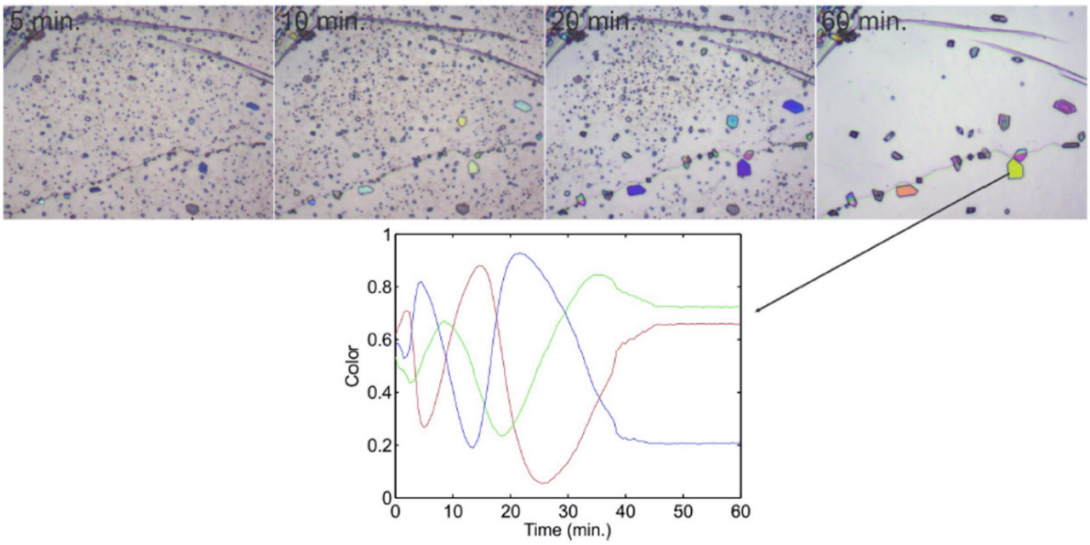

Figure D4: OM images of sulfur crystal growth from hydrophobic sulfur sol from 1:20 THF to water, 35 mM SDS in water and saturated sulfur in THF, where the color of one crystal is tracked over time in RGB, demonstrating the oscillations in color over time as the crystal grows in thickness. After ~2 min, the RGB values are approximately: 71% (R), 46% (G), 54% (B), which is a pink color. Using a standard color chart for thin film color with thickness for oxide,[342] and converting the scale using the average index of refraction of sulfur (n = 1.99),[343] it can be determined that the crystal is ~200 nm thick after 2 min of growth. After 60 min of growth, the crystal is a yellow-green color, and it can be determined that the crystal is ~400 nm thick.

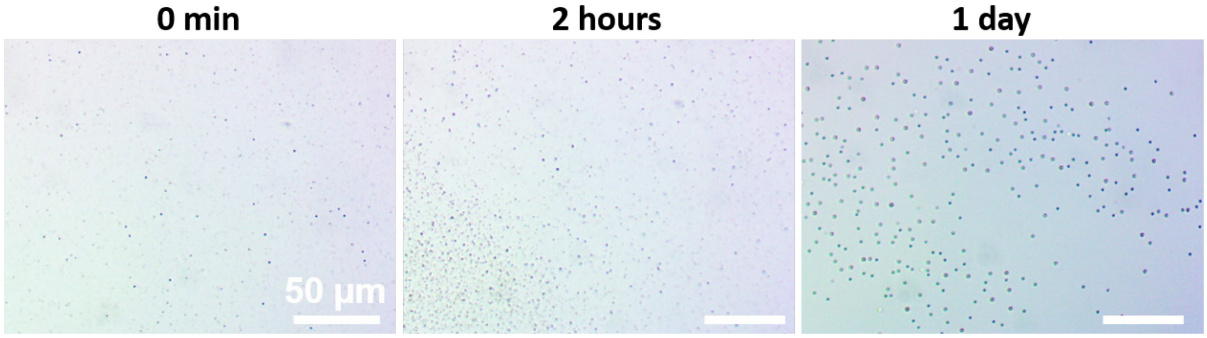

Figure D5: Control sample where sulfur sol prepared from 0.2 M sulfur, 35 mM SDS in water and ratio of 1:10 DMSO/water was drop cast onto glass substrate. Unlike on HOPG, no crystal growth is observed, even after 1 day.

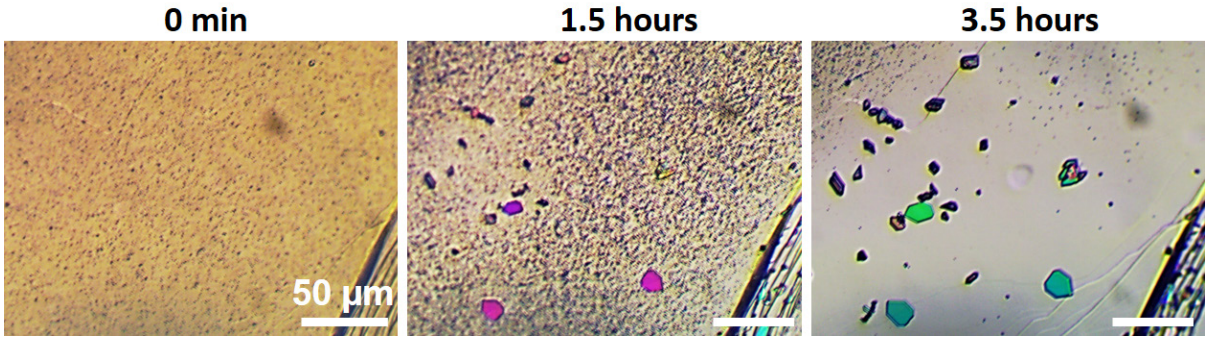

Figure D6: OM images of sulfur crystal growth from hydrophobic sulfur sol from 1:10 DMSO to water, 35 mM SDS in water and 11.8 mg/mL (0.37 M) sulfur in DMSO.

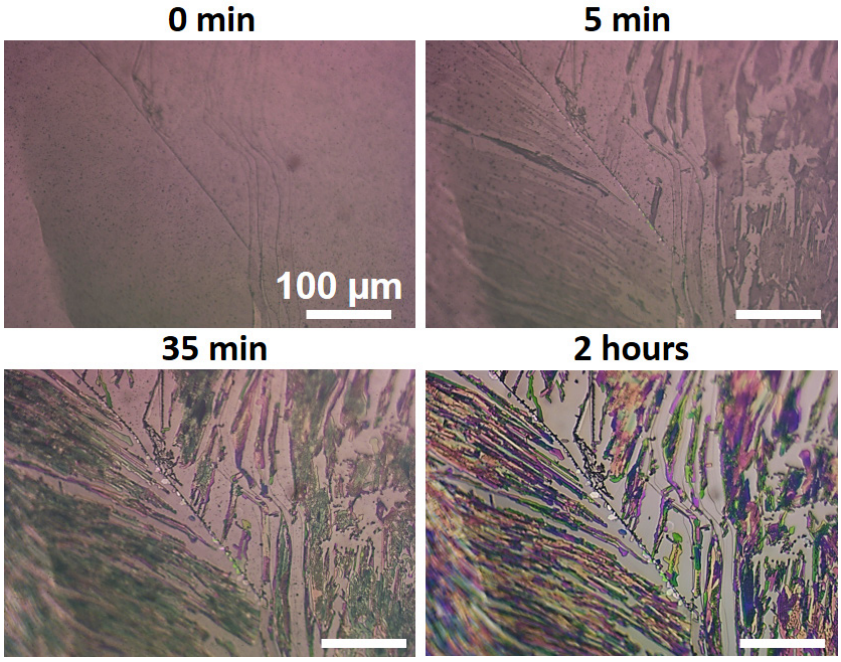

Figure D7: OM images of sulfur crystal growth from hydrophobic sulfur sol from 1:10 THF to water, 35 mM SDS in water and 11.8 mg/mL (0.37 M) sulfur in THF.

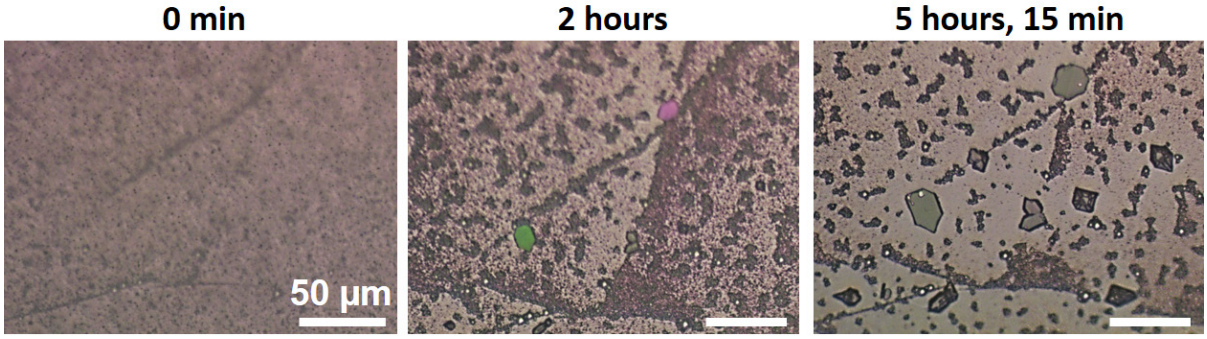

Figure D8: OM images of sulfur crystal growth from hydrophobic sulfur sol from 1:10 DMSO to water, 35 mM SDS in water and 40 mg/mL (1.25 M) sulfur in DMSO.

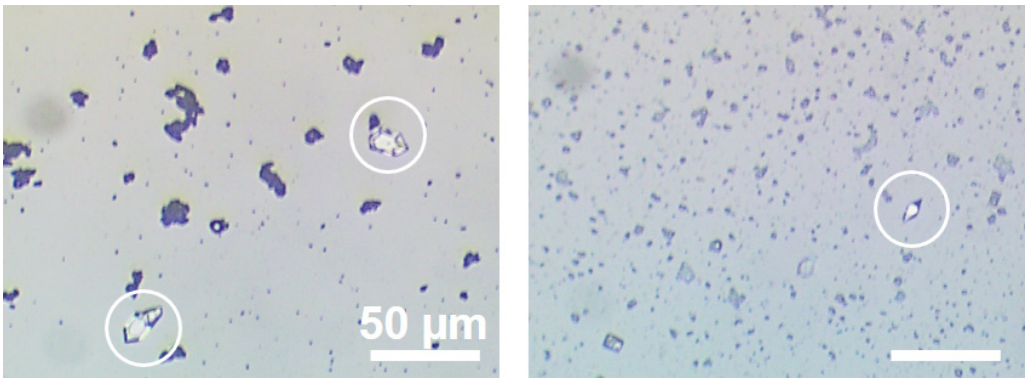

Figure D9: OM images of sulfur crystals from hydrophobic sulfur sol from 1:10 DMSO to water, 35 mM SDS in water and 40 mg/mL (1.25 M) sulfur in DMSO on glass (control) after 5 hours. Bipyramidal crystals are circled.

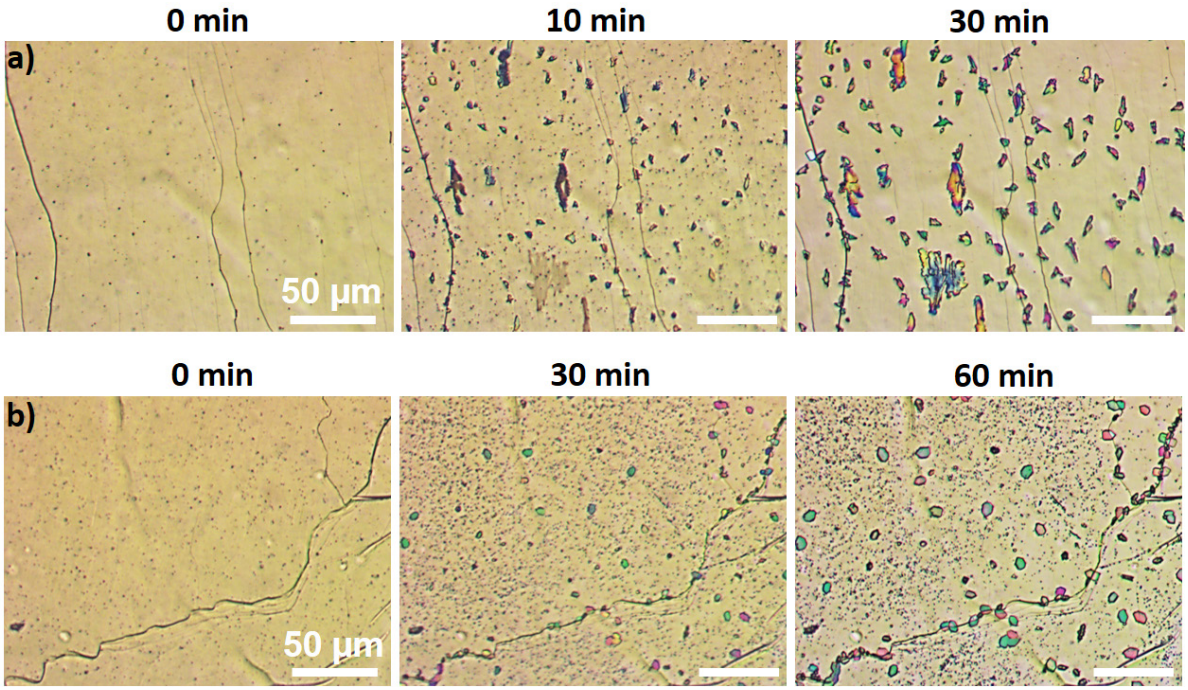

Figure D10: Optical microscopy of sulfur sol growth on HOPG from 1:10 DMSO/water, 0.2 M sulfur, using 35 mM a) Triton X-100 and b) CTAB.

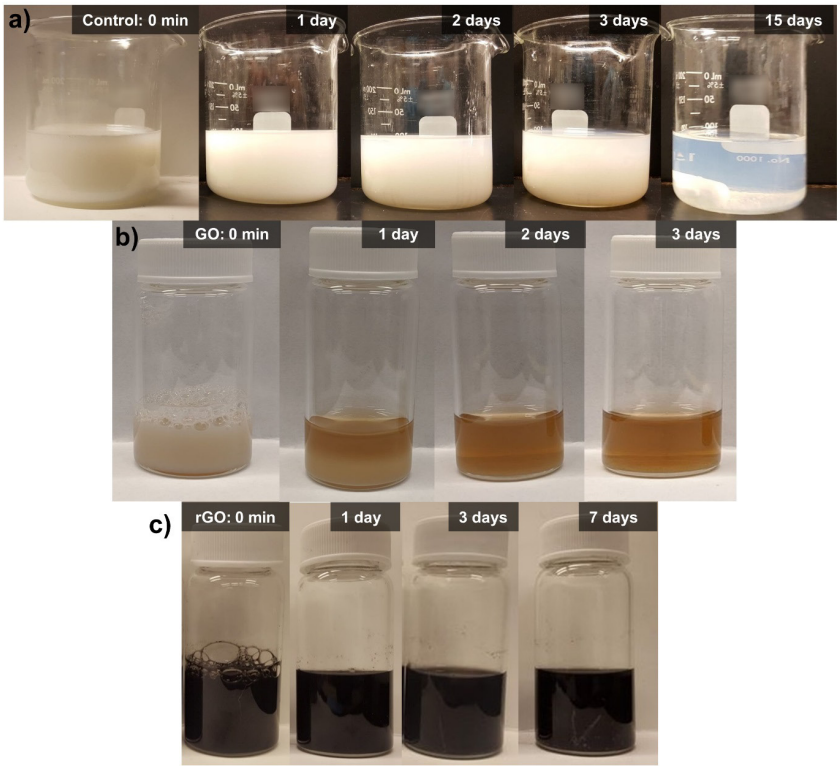

Figure D11: Photos of bulk samples over time to observe settling of sol prepared from 35 mM SDS and a 1:10 ratio of DMSO/water for a) control with no carbon material, b) GO, and c) rGO. In the control case, the cloudy sol is still present after 3 days, although some homogeneously nucleated crystals are observed at the bottom of the beaker in the OM images. The sol is observed to mostly clear 15 days after formation. In the case of GO, the sol clears within 2-3 days, and homogeneously nucleated crystals are observed at the bottom of the vial as seen in the OM images. The GO remains dispersed. In the case of the rGO, the settling of homogenously nucleated crystals is not observed. The clearing of the sol in the solution is not visible due to the opaque nature of the rGO dispersion, which remains intact after one week.

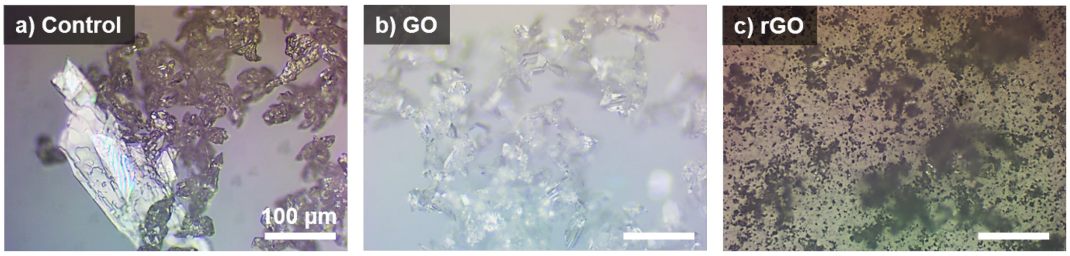

Figure D12: Optical microscopy of settled material three days after the formation of hydrophobic sulfur sol using 35 mM SDS, 0.2 M sulfur, and a 1:10 ratio of THF/water for a) control sample with no carbon material, b) GO, and c) rGO. The ratio of carbon nanomaterial to sulfur was 45% to 55% to mimic a conventional sulfur cathode.

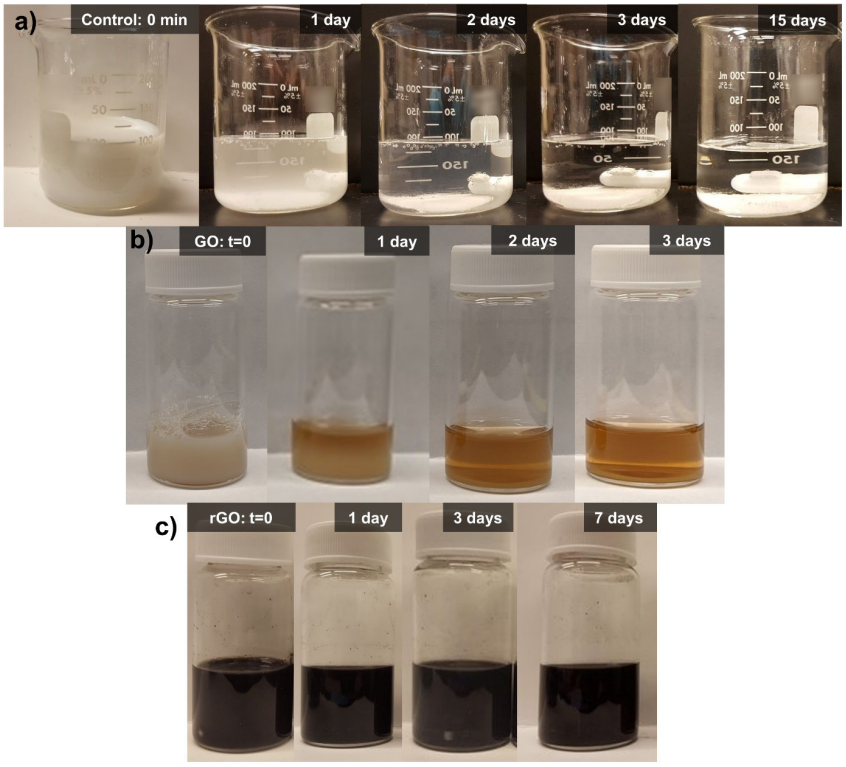

Figure D13: Photos of bulk samples over time to observe settling of sol prepared from 35 mM SDS and a 1:10 ratio of THF/water for a) control with no carbon material, b) GO, and c) rGO. In the control case, the sol clears fully within 3 days, resulting in purely homogenously nucleated sulfur crystals collected at the bottom of the beaker. In the case of GO, the sol also clears within 2-3 days, and homogeneously nucleated crystals are observed at the bottom of the vial as seen in the OM images. The GO remains dispersed. In the case of the rGO, the settling of homogenously nucleated crystals is not observed. The clearing of the sol in the solution is not visible due to the opaque nature of the rGO dispersion, which remains intact after one week.

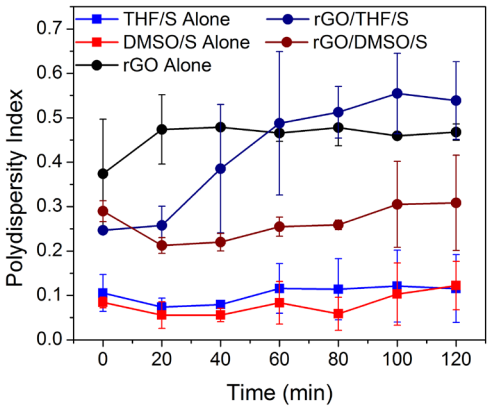

Figure D14: Average polydispersity index (PDI) of different sulfur sol samples over time during DLS measurements. All samples possess PDI values below 0.7, indicating that they are suitable for DLS analysis.

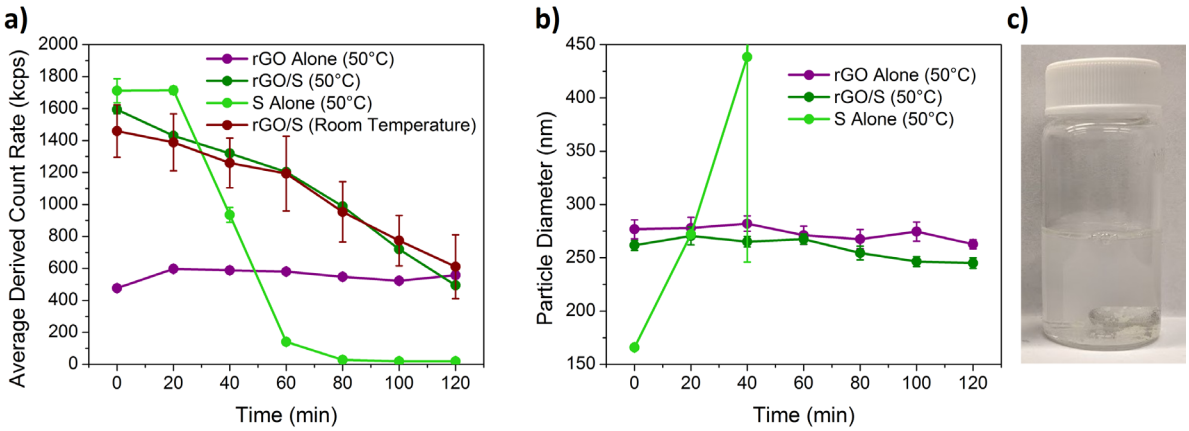

Figure D15: DLS study at increased temperature of 50 °C. a) Average derived count rate of rGO alone, and DMSO-based rGO/S and S alone at 50 °C, compared to DMSO-based rGO/S at room temperature. The 50 °C sample demonstrates similar behaviour to the room temperature sample, with a slightly more rapid decrease in count rate, but within the error bars of the room temperature measurement. The sulfur sol alone at 50 °C precipitates quickly out of solution, leading to the drop in count rate. b) Average hydrodynamic diameter of rGO alone, rGO/S, and S alone at 50 °C. rGO/S and rGO alone maintain similar sizes across the 2 hours, while the sulfur sol particles grow rapidly in size, followed by precipitation in the solution after approximately 1 hour. c) Photo of the vial containing the sulfur sol sample after the 2 hour experiment, with solid sulfur crystals settled at the bottom of the vial.

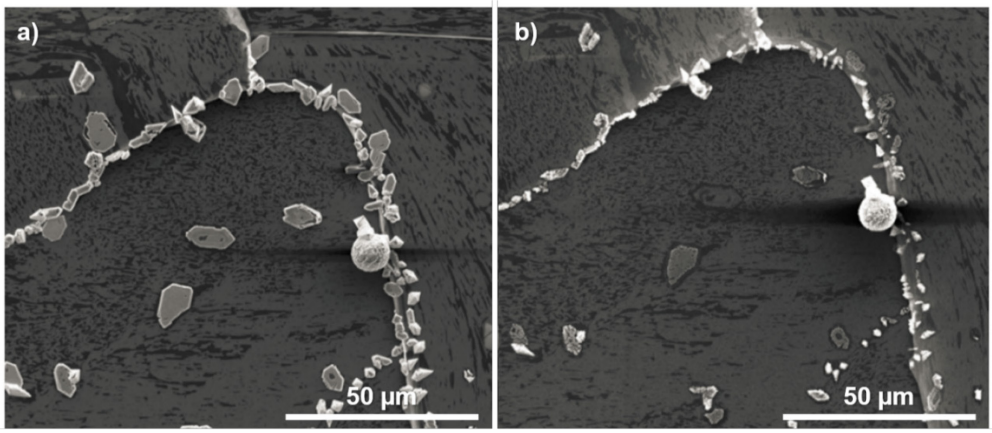

Figure D16: Rapid sublimation of sulfur under high vacuum conditions imaged in an environmental SEM immediately after switching from 1 torr water to 10^{-5} torr. The time interval between the two pictures is approximately 3 minutes.

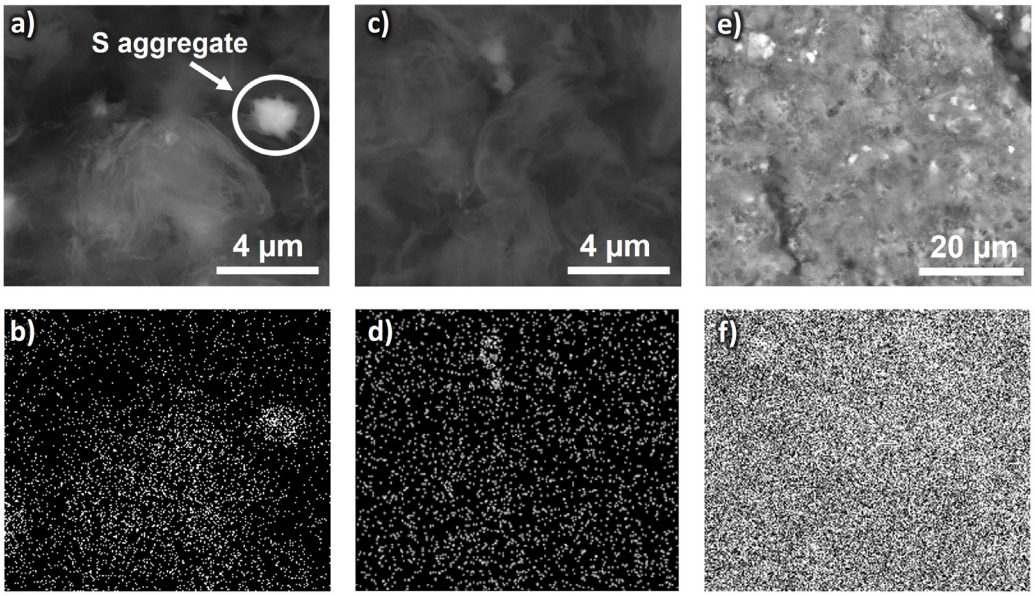

Figure D17: BSE SEM images and EDS maps of rGO/S composite from DMSO-based sol. a) SEM image of morphology of rGO/S composite prepared from DMSO-based sol with a sulfur aggregate and b) corresponding S EDS map. c) SEM image of rGO/S in area with no sulfur aggregates and d) corresponding S EDS map. e) Lower magnification SEM image of the rGO/S composite and f) corresponding S EDS map.

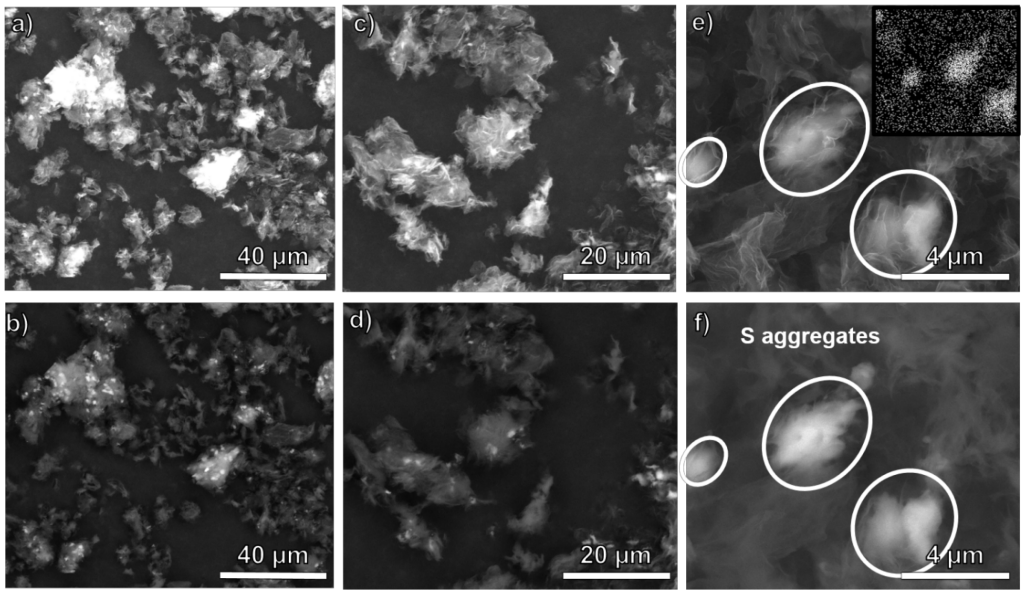

Figure D18: Further SEM images of DMSO-based rGO/S active material composite. a), c), e) SEM images of rGO/S composite using secondary electron detector. b), d), f) Corresponding SEM images using backscattered electron detector. In e), subset is an EDS map of sulfur distribution.

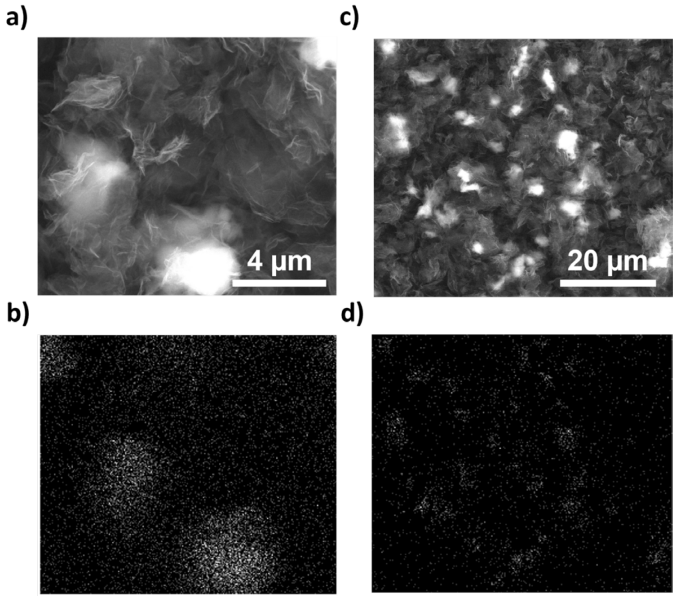

Figure D19: SEM imaging and EDS mapping of sulfur in rGO/THF/S composites. a) SEM image of morphology of rGO/S composite prepared from THF-based sol and b) corresponding S EDS map. c) Lower magnification SEM image of the rGO/S composite and d) corresponding S EDS map.

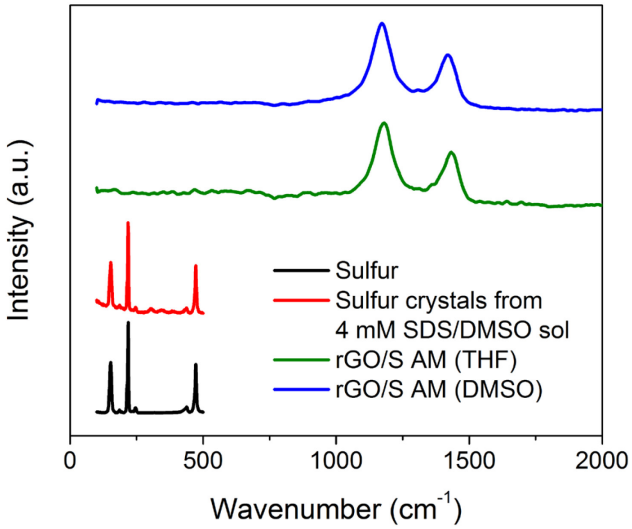

Figure D20: Raman analysis of rGO/S active material prepared from 4 mM SDS and a ratio of 45% rGO and 55% sulfur. No characteristic peaks for sulfur are observed in multiple scans of different areas of the active material powder prepared from sols using THF and DMSO as the organic solvent.

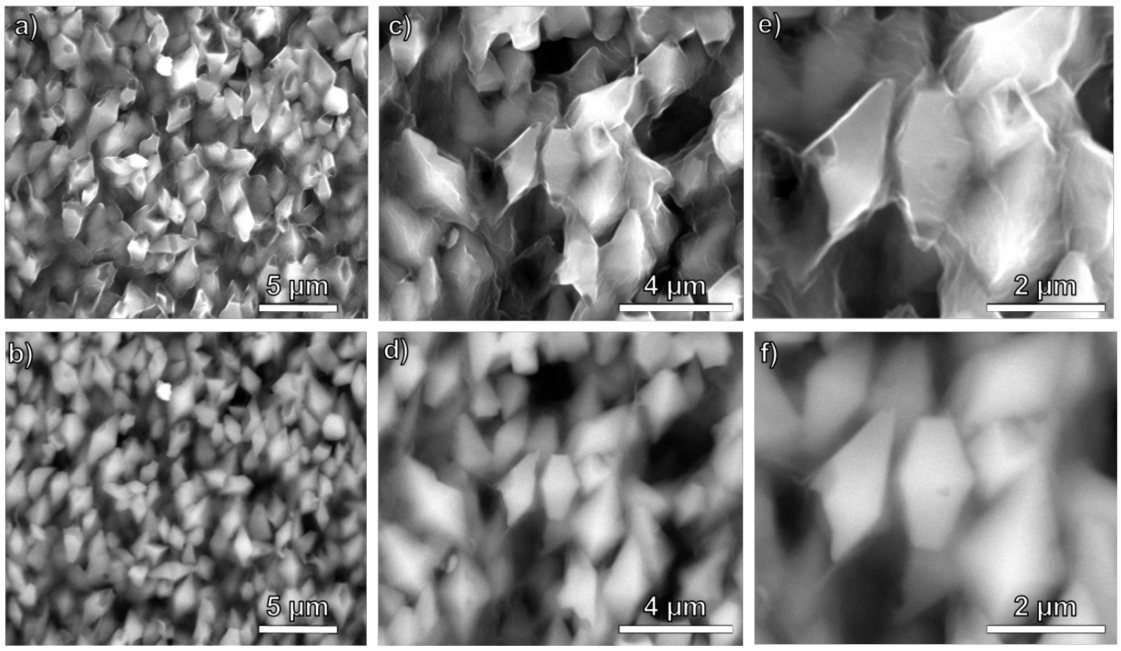

Figure D21: SEM images of GO/S composite. a), c), and e) Secondary electron images of GO/S composite, and b), d), and f) corresponding backscattered electron images.

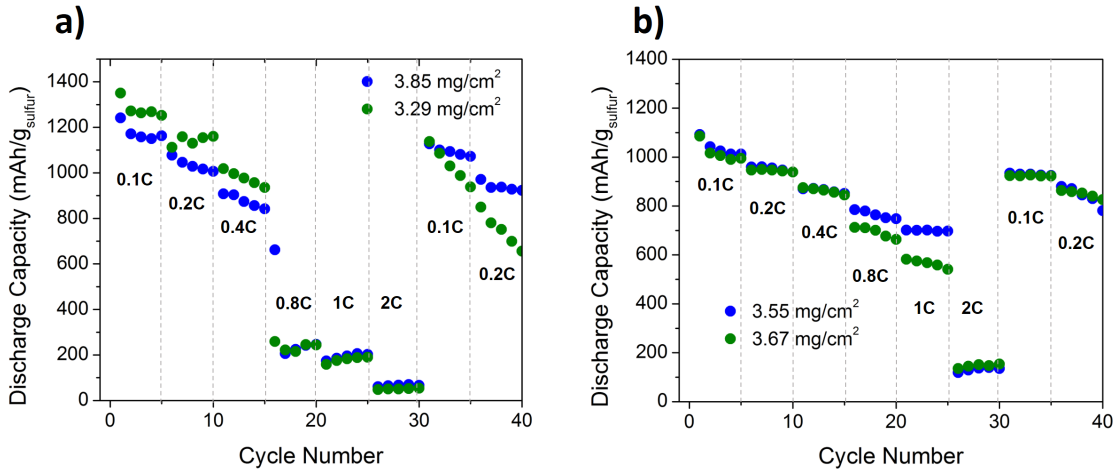

Figure D22: Electrochemical performance of rGO/THF/S cells. a) Discharge capacity for cells with 45% rGO, 55% sulfur, and with no added binder or conductive additives. b) Discharge capacity for cells with 10% binder and 20% carbon black.

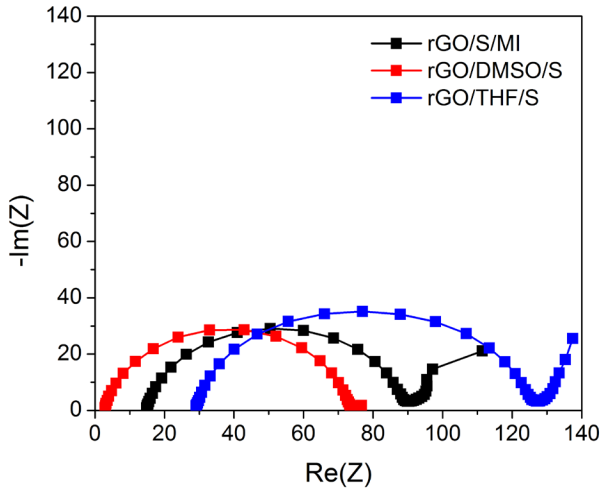

Figure D23: EIS of rGO/S cathodes prepared from DMSO- and THF-based sols and melt imbibition. EIS spectra vary across multiple cells, with THF-based samples demonstrating significant variability. The average charge transfer resistances determined from EIS from multiple cells for the three sample types are 68.5 Ω ± 6.2 Ω for DMSO samples, 90.8 Ω ± 25.6 Ω for THF samples, and 70.0 Ω ± 7.7 Ω for melt imbibed samples.

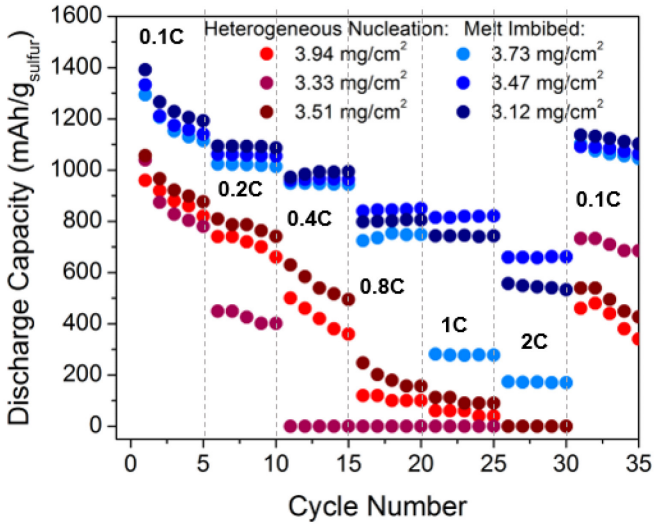

Figure D24: Electrochemical performance of Ketjen black cathodes prepared from 45% rGO, 55% sulfur and no added binder or conductive additive. Red circles are samples prepared from heterogeneous nucleation from hydrophobic sulfur sol (4 mM SDS in water, 0.2 M sulfur in DMSO, 1:10 ratio of DMSO/water) and blue circles are samples prepared from melt imbibition.

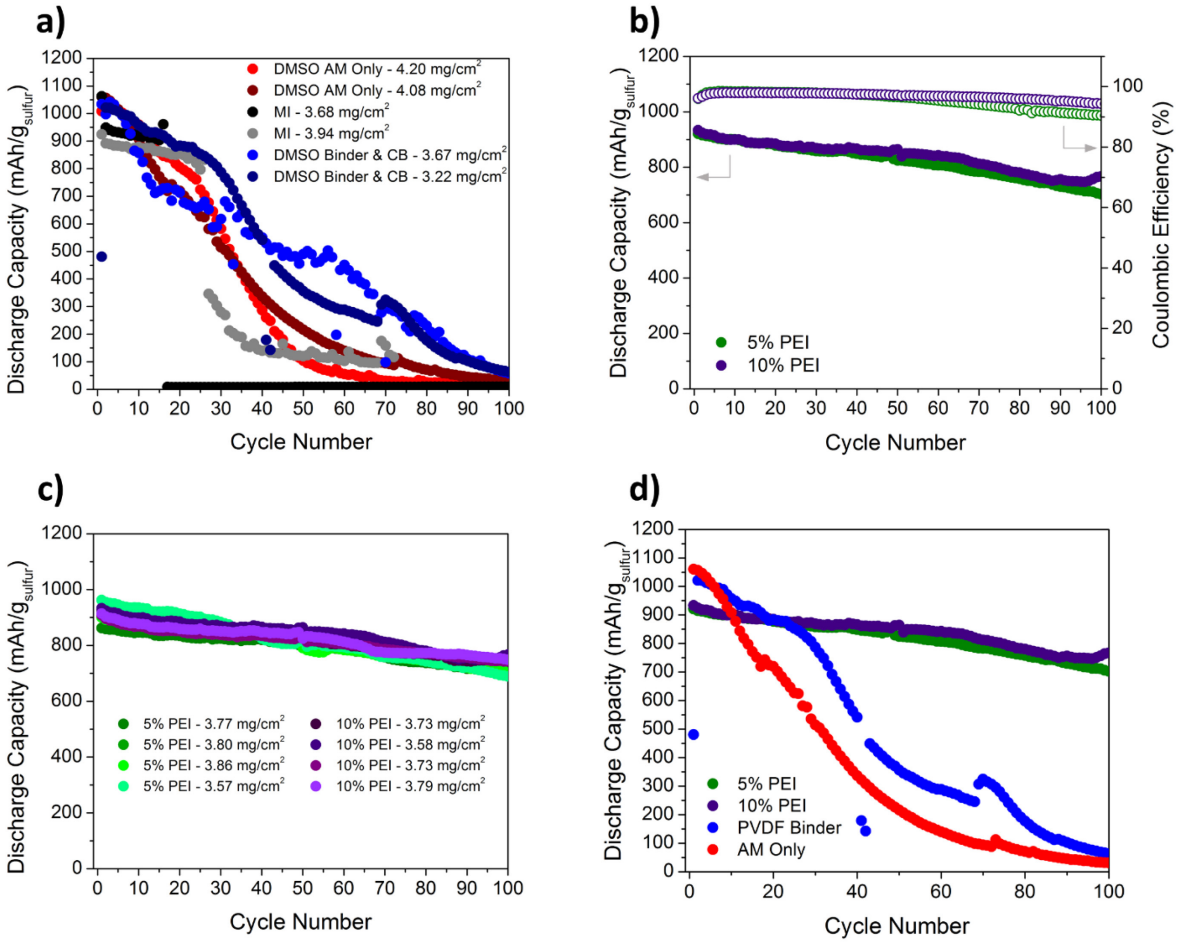

Figure D25: Cycle life of rGO/S cells at 0.5C. a) Cycle life of rGO/DMSO/S cells, including both AM only cells and cells with binder and CB, and cycle life of rGO/S/MI cells for comparison. All cells exhibit rapid capacity fading due to unaddressed polysulfide shuttling and lithium anode degradation. b) Cycle life of rGO/DMSO/S cells with 5% and 10% PEI, demonstrating remarkably improved capacity retention. c) Cycle life of 4 cells each of rGO/DMSO/S cells with 5% and 10% PEI, demonstrating the repeatability of their stable cycling performance. d) Comparison of cycle life of rGO/DMSO/S cathodes with and without PEI, demonstrating that further optimization of these cathodes is expected to result in cathodes with high initial capacities and stable long term cycling.

Calculation of Energy Density:

The practical full cell energy density (E) of the cells was calculated as follows:

$$E = F \cdot Q_C \cdot U \tag{D.1}$$

where Q_C is the cathode discharge capacity, U is the cell voltage, and F is a correction factor to account for inactive components in the cell. F can be calculated by considering inactive cell components (f_∞, mg/mg S) that scale with the sulfur loading (t), and components that do not scale with the sulfur loading (f_0, in mg/cm^2):

$$F = \frac{t}{f_\infty t + f_0} \tag{D.2}$$

The f_∞ parameter takes into account inactive components such as the amount of electrolyte, binder, conductive additive, and minimum mass of lithium required on the anode side for a specific loading of sulfur. The f_0 parameter takes into account the mass of fixed inactive cell components such as the current collectors and separator. The parameters and the assumptions made can be seen in Tables D1-D2. We performed the energy density calculation three different ways to demonstrate the effect of different assumptions on the calculated value. In the first calculation, we assume a 5% stoichiometric excess of lithium paired with the sulfur cathode. This represents an absolute maximum energy density achievable for our sulfur cathodes with a perfect lithium anode. In this case, lithium is a component of f_∞. While in a theoretical cell, a stoichiometric amount of lithium would be paired with the sulfur, in practice significant excess (>100-200%) is required due to SEI formation and growth during cycling. Additionally, thin films of lithium metal would require a current collector to support them. As such, in the second calculation, we instead assume a more practical and conservative system with a lithium anode with significant stoichiometric excess, at a constant thickness. This enables lithium to act as both the active material and replace the need for an added current collector. We assume a form that is commercially available – 125 μm thick foils from FMC Corp. As such, the lithium metal is a component of f_0 and not f_∞. In the third calculation, we again assume the use of 125 μm thick lithium foil, and also consider the effect of excess electrolyte used in practice to compensate for the unoptimized lithium anode and SEI formation.

The power density (P) for all of the cells was also calculated as follows:

$$P = E/t_d \tag{D.3}$$

where t_d is the discharge time.

For all energy density calculations:

Table D1: Assumptions made in energy density analysis for density of materials

Density of carbon	2.2	g/cm^3
Density of sulfur	1.96	g/cm^3
Density of electrolyte	0.965	g/cm^3
Density of lithium metal	0.534	g/cm^3
Density of binder	1.78	g/cm^3
Density of membrane material	0.91	g/cm^3 (polypropylene)

Table D2: Assumptions made in energy density analysis for void space

Cathode porosity	35	% of total cathode volume
Membrane porosity	55	% of total membrane volume

Energy density calculation #1: 5% stoichiometric excess of lithium:

Table D3: Assumptions made in energy density analysis for thicknesses

Current collector	16	µm thick Al
Membrane	25	µm

Table D4: Calculation of mass density of cell components that do not scale with active material loading (f_0)

f_0	Current collector	4.32	mg/cm^2 (theoretical)
	Membrane	1.03	mg/cm^2 (measured in lab)
	Electrolyte in membrane	1.33	mg/cm^2
	Total f(0)	6.68	mg/cm^2

Table D5: Calculation of mass density of cell components that scale with active material loading (f_∞) for AM Only cells (i.e. no binder or carbon black)

f_∞	Electrolyte	0.46	mg/mg S
	Binder	0	mg/mg S
	Carbon	0.82	mg/mg S
	Lithium	1.05	mg/mg S
	Sulfur	1	mg/mg S
	Total f(∞)	3.33	mg total/mg S

Table D6: Calculation of mass density of cell components that scale with active material loading (f_∞) for cells with PVDF binder and carbon black

f_∞	Electrolyte	0.66	mg/mg S
	Binder	0.26	mg/mg S
	Carbon	1.34	mg/mg S
	Lithium	1.05	mg/mg S
	Sulfur	1	mg/mg S
	Total f(∞)	4.30	mg total/mg S

Table D7: Calculated practical energy densities for rGO/DMSO/S cells with no added binder or CB (45% rGO, 55% sulfur) at various C rates

Cell 1: 3.90 mg/cm^2			Cell 2: 3.90 mg/cm^2			Cell 3: 3.59 mg/cm^2		
C Rate	Capacity (mAh/g)	Energy Density (Wh/kg)	C Rate	Capacity (mAh/g)	Energy Density (Wh/kg)	C Rate	Capacity (mAh/g)	Energy Density (Wh/kg)
0.1C	1241.59	529.61	0.1C	1141.00	486.70	0.1C	1304.18	540.44
0.2C	1110.48	474.29	0.2C	967.83	412.84	0.2C	1140.60	472.66
0.4C	1020.87	436.77	0.4C	924.52	394.36	0.4C	1080.88	447.91
0.8C	718.47	313.77	0.8C	775.03	330.60	0.8C	972.01	402.79
1C	508.66	231.44	1C	662.63	282.65	1C	667.48	276.60

Table D8: Calculated practical energy densities for rGO/DMSO/S cells with binder and CB (Active material: 45% rGO, 55% sulfur, ratio of active material/PVDF/CB = 70:10:20) at various C rates

Cell 1: 3.70 mg/cm^2			Cell 2: 3.67 mg/cm^2		
C Rate	Capacity (mAh/g)	Energy Density (Wh/kg)	C Rate	Capacity (mAh/g)	Energy Density (Wh/kg)
0.1C	1219.85	429.19	0.1C	1300.29	456.39
0.2C	1062.86	373.96	0.2C	1160.82	407.44
0.4C	974.42	342.84	0.4C	1108.68	389.14
0.8C	891.67	313.73	0.8C	1054.47	370.11
1C	814.13	286.44	1C	969.72	340.37

Energy density calculation #2: 125 µm thick lithium foil:

Table D9: Assumptions made in energy density analysis for thicknesses

Current collector	16	µm thick Al
Lithium metal	125	µm thick
Membrane	25	µm

Table D10: Calculation of mass density of cell components that do not scale with active material loading (f_0)

f_0	Current collector	4.32	mg/cm^2 (theoretical)
	Membrane	1.03	mg/cm^2 (measured in lab)
	Electrolyte in membrane	1.33	mg/cm^2
	Anode	6.68	mg/cm^2 (assumes 125 μm Li foil)
	Total f(0)	13.36	mg/cm^2

Table D11: Calculation of mass density of cell components that scale with active material loading (f_∞) for AM Only cells (i.e. no binder or carbon black)

f_∞	Electrolyte	0.46	mg/mg S
	Binder	0	mg/mg S
	Carbon	0.82	mg/mg S
	Sulfur	1	mg/mg S
	Total f(∞)	2.28	mg total/mg S

Table D12: Calculation of mass density of cell components that scale with active material loading (f_∞) for cells with PVDF binder and carbon black

f_∞	Electrolyte	0.66	mg/mg S
	Binder	0.26	mg/mg S
	Carbon	1.34	mg/mg S
	Sulfur	1	mg/mg S
	Total f(∞)	3.25	mg total/mg S

Table D13: Calculated practical energy densities for rGO/DMSO/S cells with no added binder or CB (45% rGO, 55% sulfur) at various C rates

Cell 1: 3.90 mg/cm^2			Cell 2: 3.90 mg/cm^2			Cell 3: 3.59 mg/cm^2		
C Rate	Capacity (mAh/g)	Energy Density (Wh/kg)	C Rate	Capacity (mAh/g)	Energy Density (Wh/kg)	C Rate	Capacity (mAh/g)	Energy Density (Wh/kg)
0.1C	1241.59	468.06	0.1C	1141.00	430.14	0.1C	1304.18	467.40
0.2C	1110.48	418.63	0.2C	967.83	364.86	0.2C	1140.60	408.78
0.4C	1020.87	384.85	0.4C	924.52	348.53	0.4C	1080.88	387.38
0.8C	718.47	270.85	0.8C	775.03	292.17	0.8C	972.01	348.36
1C	508.66	191.76	1C	662.63	249.80	1C	667.48	239.22

Table D14: Calculated practical energy densities for rGO/DMSO/S cells with binder and CB (Active material: 45% rGO, 55% sulfur, ratio of active material/PVDF/CB = 70:10:20) at various C rates

Cell 1: 3.70 mg/cm^2			Cell 2: 3.67 mg/cm^2		
C Rate	Capacity (mAh/g)	Energy Density (Wh/kg)	C Rate	Capacity (mAh/g)	Energy Density (Wh/kg)
0.1C	1219.85	381.97	0.1C	1300.29	405.42
0.2C	1062.86	332.82	0.2C	1160.82	361.93
0.4C	974.42	305.12	0.4C	1108.68	345.68
0.8C	891.67	279.21	0.8C	1054.47	328.77
1C	814.13	254.93	1C	969.72	302.35

Energy density calculation #3: 125 µm thick lithium foil and excess electrolyte:

The previously calculated energy densities reflect the energy density of our sulfur cathodes when paired with an optimized lithium anode, and do not consider the mass of excess electrolyte added into the cell, beyond what fills the porosity of the cathode and membrane. In practice, excess electrolyte must be added to the cell to wet all cell components effectively, and due to the use of an unoptimized lithium anode, which consumes electrolyte during SEI formation, breakage, and growth during cycling. While the optimization of the lithium anode is not the focus of this work, we have also calculated the energy density of these cells, taking into account the effect of excess electrolyte (90 µL total per cell). We still consider the use of excess lithium, using a commercially available 125 micron thick foil. Since a constant volume of electrolyte was used in all cells regardless of sulfur loading, and as excess electrolyte is predominantly added to wet all components and for anode performance, the excess electrolyte is included in the f_0 term here. f_∞ is assumed to be same as above for the two different types of cells (with and without binder).

Table D15: Example calculation of mass density of cell components that do not scale with active material loading (f_0) when considering excess electrolyte

f_0	Current collector	4.32	mg/cm^2 (theoretical)
	Membrane	1.03	mg/cm^2 (measured in lab)
	Electrolyte in membrane	1.33	mg/cm^2
	Excess electrolyte	25.71	mg/cm^2
	Anode	6.68	mg/cm^2 (assumes 125 µm Li foil)
	Total f(0)	39.08	mg/cm^2

Table D16: Example calculation of excess electrolyte for 3.90 mg/cm^2 AM only cell, based on 90 μL electrolyte volume

Total electrolyte	0.09	mL
Total electrolyte mass	86.85	mg
Electrolyte in f_∞ (scaling with sulfur loading)	1.79	mg/cm^2
Cathode area	1.27	cm^2
Electrolyte in cathode	2.26	mg
Membrane area	2.85	cm^2
Electrolyte in membrane	3.80	mg
Excess electrolyte	80.78	mg
Coin cell area	3.14	cm^2
Excess electrolyte per coin cell area	25.71	mg/cm^2

Table D17: Values of f_0 calculated with excess electrolyte for cells with AM only (no binder or CB)

f_0	Cell loading (mg/cm^2)	3.90	Excess electrolyte (mg/cm^2)	25.71	Total f_0 (mg/cm^2)	39.08
		3.90		25.71		39.08
		3.59		25.77		39.13

Table D18: Values of f_0 calculated with excess electrolyte for cells with binder and CB

f_0	Cell loading (mg/cm^2)	3.67	Excess electrolyte (mg/cm^2)	25.46	Total f_0 (mg/cm^2)	38.83
		3.70		25.45		38.82

Table D19: Calculated practical energy densities for rGO/DMSO/S cells with no added binder or CB (45% rGO, 55% sulfur) at various C rates when considering excess electrolyte

Cell 1: 3.90 mg/cm^2			Cell 2: 3.90 mg/cm^2			Cell 3: 3.59 mg/cm^2		
C Rate	Capacity (mAh/g)	Energy Density (Wh/kg)	C Rate	Capacity (mAh/g)	Energy Density (Wh/kg)	C Rate	Capacity (mAh/g)	Energy Density (Wh/kg)
0.1C	1241.59	217.09	0.1C	1141.00	199.50	0.1C	1304.18	212.78
0.2C	1110.48	194.41	0.2C	967.83	169.22	0.2C	1140.60	186.09
0.4C	1020.87	179.03	0.4C	924.52	161.65	0.4C	1080.88	176.35
0.8C	718.47	128.61	0.8C	775.03	135.51	0.8C	972.01	158.59
1C	508.66	94.87	1C	662.63	115.86	1C	667.48	108.90

Table D20: Calculated practical energy densities for rGO/DMSO/S cells with binder and CB (Active material: 45% rGO, 55% sulfur, ratio of active material/PVDF/CB = 70:10:20) at various C rates when considering excess electrolyte

Cell 1: 3.70 mg/cm^2			Cell 2: 3.67 mg/cm^2		
C Rate	Capacity (mAh/g)	Energy Density (Wh/kg)	C Rate	Capacity (mAh/g)	Energy Density (Wh/kg)
0.1C	1219.85	190.80	0.1C	1300.29	202.09
0.2C	1062.86	166.24	0.2C	1160.82	180.41
0.4C	974.42	152.41	0.4C	1108.68	172.31
0.8C	891.67	139.47	0.8C	1054.47	163.88
1C	814.13	127.34	1C	969.72	150.71

Summary of energy densities using different methods:

Table D21: Calculated practical energy densities for rGO/DMSO/S cells with no added binder or CB (45% rGO, 55% sulfur) at various C rates for three different calculation methods

C Rate	Cell 1: 3.90 mg/cm^2			Cell 2: 3.90 mg/cm^2			Cell 3: 3.59 mg/cm^2		
	Energy Density (Wh/kg) (Method 1 – 5% excess Li)	Energy Density (Wh/kg) (Method 2 – 125 µm thick Li)	Energy Density (Wh/kg) (Method 3 - 125 µm thick Li & excess electrolyte)	Energy Density (Wh/kg) (Method 1 – 5% excess Li)	Energy Density (Wh/kg) (Method 2 – 125 µm thick Li)	Energy Density (Wh/kg) (Method 3 - 125 µm thick Li & excess electrolyte)	Energy Density (Wh/kg) (Method 1 – 5% excess Li)	Energy Density (Wh/kg) (Method 2 – 125 µm thick Li)	Energy Density (Wh/kg) (Method 3 - 125 µm thick Li & excess electrolyte)
0.1C	529.61	468.06	217.09	486.70	430.14	199.50	540.44	467.40	212.78
0.2C	474.29	418.63	194.41	412.84	364.86	169.22	472.66	408.78	186.09
0.4C	436.77	384.85	179.03	394.36	348.53	161.65	447.91	387.38	176.35
0.8C	313.77	270.85	128.61	330.60	292.17	135.51	402.79	348.36	158.59
1C	231.44	191.76	94.87	282.65	249.80	115.86	276.60	239.22	108.90

Table D22: Calculated practical energy densities for rGO/DMSO/S cells with binder and CB (Active material: 45% rGO, 55% sulfur, ratio of active material/PVDF/CB = 70:10:20) at various C rates for three different calculation methods

C Rate	Cell 1: 3.70 mg/cm^2			Cell 2: 3.67 mg/cm^2		
	Energy Density (Wh/kg) (Method 1 – 5% excess Li)	Energy Density (Wh/kg) (Method 2 – 125 µm thick Li)	Energy Density (Wh/kg) (Method 3 - 125 µm thick Li & excess electrolyte)	Energy Density (Wh/kg) (Method 1 – 5% excess Li)	Energy Density (Wh/kg) (Method 2 – 125 µm thick Li)	Energy Density (Wh/kg) (Method 3 - 125 µm thick Li & excess electrolyte)
0.1C	429.19	381.97	190.80	456.39	405.42	202.09
0.2C	373.96	332.82	166.24	407.44	361.93	180.41
0.4C	342.84	305.12	152.41	389.14	345.68	172.31
0.8C	313.73	279.21	139.47	370.11	328.77	163.88
1C	286.44	254.93	127.34	340.37	302.35	150.71